Chris Mi, M. Abul Masrur and David Wenzhong Gao

Hybrid Electric Vehicles

Principles and Applications with Practical Perspectives

WILEY

HYBRID ELECTRIC VEHICLES

HYBRID ELECTRIC VEHICLES

PRINCIPLES AND APPLICATIONS WITH PRACTICAL PERSPECTIVES

Chris Mi
University of Michigan–Dearborn, USA

M. Abul Masrur
University of Detroit Mercy, USA

David Wenzhong Gao
University of Denver, USA

WILEY
A John Wiley & Sons, Ltd., Publication

This edition first published 2011

Registered office
John Wiley & Sons Ltd, The Atrium, Southern Gate, Chichester, West Sussex, PO19 8SQ, United Kingdom

Library of Congress Cataloguing-in-Publication Data

Mi, Chris.
Hybrid Electric Vehicles: Principles and Applications with Practical Perspectives / Chris Mi, M. Abul Masrur, David Wenzhong Gao.
p. cm.
Includes bibliographical references and index.
ISBN 978-0-470-74773-5 (cloth)
1. Hybrid electric vehicles. I. Masrur, Abul. II. Gao, David. III. Title.
TL221.15.M545 2011
629.22′93–dc22

2011002521

A catalogue record for this book is available from the British Library.

Print ISBN: 978-0-470-74773-5
ePDF ISBN: 978-1-119-99890-7
oBook ISBN: 978-1-119-99891-4
ePub ISBN: 978-1-119-97011-8
Mobi ISBN: 978-1-119-97012-5

Typeset in 10/12pt Times Roman by Laserwords Private Limited, Chennai, India

Contents

About the Authors

Chris Mi is Associate Professor of Electrical and Computer Engineering and Director of DTE Power Electronics Laboratory at the University of Michigan – Dearborn, Dearborn, MI, USA. Dr Mi is a leading expert in electric and hybrid vehicles, and has presented tutorials and seminars on the subject for the Society of Automotive Engineers (SAE), the IEEE, National Society of Professional Engineers, and major automotive manufacturers and suppliers, including GM, Ford, Chrysler, and Delphi. He has also presented tutorials in China, Korea, Italy, Singapore, and Mexico. He has published more than 100 articles and delivered more than 50 invited talks and keynote speeches, as well as serving as a panelist.

Dr. Mi is the recipient of the 2009 Distinguished Research Award of the University of Michigan–Dearborn, the 2007 SAE Environmental Excellence in Transportation (also known as E2T) Award for "Innovative Education and Training Program in Electric, Hybrid and Fuel Cell Vehicles," the 2005 Distinguished Teaching Award of the University of Michigan–Dearborn, the IEEE Region 4 Outstanding Engineer Award, and the IEEE Southeastern Michigan Section Outstanding Professional Award. He is also the recipient of the National Innovation Award (1992) and the Government Special Allowance Award (1994) from the China Central Government. In December 2007, Dr. Mi became a member of the Eta Kappa Nu, the Electrical and Computer Engineering Honor Society, for being "a leader in education and an example of good moral character."

Dr. Mi holds BS and MS degrees from Northwestern Polytechnical University, Xi'an, China, and a PhD from the University of Toronto, Canada. He was the Chief Technical Officer of 1Power Solutions from 2008 to 2010 and worked with General Electric Company from 2000 to 2001. From 1988 to 1994, he was a member of the faculty of Northwestern Polytechnical University, and from 1994 to 1996 he was an Associate Professor and Associate Chair in the Department of Automatic Control Systems, Xi'an Petroleum University, China.

Dr. Mi is the Associate Editor of *IEEE Transactions on Vehicular Technology*, Associate Editor of *IEEE Transactions on Power Electronics – Letters*, associate editor of the *Journal of Circuits, Systems, and Computers* (2007–2009); editorial board member of *International Journal of Electric and Hybrid Vehicles*; editorial board member of *IET Transactions on Electrical Systems in Transportation*; a Guest Editor of *IEEE Transactions on Vehicular Technology, Special Issue on Vehicle Power and Propulsion* (2009–2010), and Guest Editor of *International Journal of Power Electronics, Special Issue on Vehicular Power Electronics and Motor Drives* (2009–2010). He served as the Vice Chair

(2006, 2007) and Chair (2008) of the IEEE Southeastern Michigan Section. He was the General Chair of the Fifth IEEE International Vehicle Power and Propulsion Conference held in Dearborn, MI, September 7–11, 2009. He has also served on the review panel for the National Science Foundation, the US Department of Energy (2006–2010), and the Natural Science and Engineering Research Council of Canada (2010).

Dr. Mi is one of the two Topic Coordinators for the 2011 IEEE International Future Energy Challenge Competition.

M. Abul Masrur received his PhD in electrical engineering from the Texas A & M University, College Station, TX, USA, in 1984. Dr. Masrur is an Adjunct Professor at the University of Detroit Mercy, where he has been teaching courses on Advanced Electric and Hybrid Vehicles, Vehicular Power Systems, Electric Drives and Power Electronics. He was with the Scientific Research Labs., Ford Motor Co., between 1984 and 2001 and was involved in research and development related to electric drives and power electronics, advanced automotive power system architectures, electric active suspension systems for automobiles, electric power assist steering, and standalone UPS protection design, among other things.

Since April 2001, Dr. Masrur has been with the US Army RDECOM-TARDEC (R&D) where he has been involved in vehicular electric power system architecture concept design and development, electric power management, and artificial intelligence-based fault diagnostics in electric drives. He has written over 70 publications, many of which are in public domain international journals and conference proceedings. He also owns eight US patents, two of which are also patented in Europe and one in Japan. He received the Best Automotive Electronics Paper Award from the IEEE Vehicular Technology Society in 1998 for his papers proposing novel vehicular power system architectures in *IEEE Transactions on Vehicular Technology*, and in 2006 was a joint recipient of the SAE Environmental Excellence in Transportation Award – Education, Training, & Public Awareness (or E2T) for a tutorial course he had been jointly presenting on hybrid vehicles.

Dr. Masrur is a Senior Member of the IEEE and from 1999–2007 he served as an Associate Editor (Vehicular Electronics Section) of *IEEE Transactions on Vehicular Technology*. He also served as Chair of the Motor-Subcommittee of the IEEE Power & Energy Society – Electric Machinery Committee for two years ending in December 2010.

David Wenzhong Gao is an Associate Professor of Electrical and Computer Engineering and Director of Renewable Energy and Power Electronics Laboratory at the University of Denver, Denver, CO, USA. Dr. Gao has conducted extensive research in the areas of hybrid electric vehicles, renewable energy, electric power systems, and smart grids, and has published more than 100 papers in international journals and conference proceedings. He presented a tutorial course "Modeling and Simulation Tools for Vehicle Power System" at the US Army Vetronics Institute in Warren, MI, in 2006. In September 2007, he was elected as a member of Sigma Xi. He is a member of Eta Kappa Nu, the Electrical and Computer Engineering Honor Society, and served as a HKN Faculty Advisor. Since June 2003, he has been a Senior Member of the IEEE. He received the Best Paper Award in the Complex Systems Track at the 2002 Hawaii International Conference on System Sciences (HICSS) in January 2002.

Dr. Gao holds a BS degree from Northwestern Polytechnical University, Xi'an, China, an MS degree from Northeastern University, Shenyang, China, and a PhD from Georgia Institute of Technology, Atlanta, USA.

Dr. Gao is the Editor of *IEEE Transactions on Sustainable Energy* and has been an active reviewer for leading journals such as *IEEE Transactions on Vehicular Technology*, *IEEE Transactions on Power Electronics*, *IEEE Transactions on Smart Grid*, *IEEE Transactions on Energy Conversion*, *IEEE Transactions on Sustainable Energy*, *IET Renewable Power Generation*, *IEEE Transactions on Power Delivery*, *IEEE Transactions on Power Systems*, as well as for conferences such as IEEE Vehicular Power and Propulsion Conference (VPPC) and IEEE Power and Energy Society General Meeting. He was a Technical Co-chair on the Organizing Committee of the IEEE Vehicular Power and Propulsion Conference, held in Dearborn, MI, USA, September 7–11, 2009. He has also served on the grant review panel for the US National Science Foundation, the US Department of Energy, and the Natural Sciences and Engineering Research Council of Canada.

Preface

It is well recognized today that hybrid electric vehicle (HEV) and electric vehicle (EV) technologies are vital to the overall automotive industry and also to the user, in terms of both better fuel economy and a better effect on the environment. Over the past decade, these technologies have taken a significant leap forward. As they have developed, the literature in the public domain has also grown accordingly, in the form of publications in conference proceedings and journals, and also in the form of textbooks and reference books. Why then was the effort made to write this book? The question is legitimate. The authors observed that existing textbooks have topics like drive cycle, fuel economy, and drive technology as their main focus. In addition, the authors felt that the main focus of such textbooks was on regular passenger automobiles. It is against this backdrop that the authors felt a wider look at the technology was necessary. By this, it is meant that HEV technology is one which is applicable not just to regular automobiles, but also to other vehicles such as locomotives, off-road vehicles (construction and mining vehicles), ships, and even to some extent to aircraft. The authors believe that the information probably exists, but not specifically in textbook form where the overall viewpoint is included. In fact, HEV technology is not new – a slightly different variant of it was present many years ago in diesel–electric locomotives. However, the availability of high-power electronics and the development of better materials for motor technology have made it possible to give a real boost to HEV technology during the past decade or so, making it viable for wider applications.

A textbook, unlike a journal paper, has to be reasonably self-contained. Hence the authors decided to review the basics, including power electronics, electric motors, and storage elements like batteries, capacitors, flywheels, and so on. All these are the main constituent elements of HEV technology. Also included is a discussion on the system-level architecture of the vehicles, modeling and simulation methods, transmission and coupling. Drive cycles and their meaning, and optimization of the vehicular power usage strategy (and power management), have also been included. The issue of dividing power between multiple sources lies within the domain of power management. Power management is an extremely important matter in any power system where more than one source of power is used. These sources may be similar or diverse in nature: that is, they could be electrical, mechanical, chemical, and so on; and even if they all could be similar, they might potentially have different characteristics. Optimization involves a decision on resource allocation in such situations. Some of these optimization methods actually exist in and are used by the utility industry, but have lately attracted significant interest in vehicular applications. To make the book relatively complete and more holistic in nature,

the topics of applications to off-road vehicles, locomotive, ships, and aircraft have been included as well. In the recent past, the interface between a vehicle and the utility grid for plug-in capabilities has become important, hence the inclusion of topics on plug-in hybrid and vehicle-to-grid or vehicle-to-vehicle power transfer. Also presented is a discussion on diagnostics and prognostics, the reliability of the HEV from a system-level perspective, electromechanical vibration and noise vibration harshness (NVH), electromagnetic compatibility and electromagnetic interference (EMC/EMI), and overall life cycle issues. These topics are almost non-existent in the textbooks on HEVs known to the authors. In fact some of the topics have not been discussed much in the research literature either, but are all very important issues. The success of a technology is ultimately manifested in the form of user acceptance and is intimately connected with the mass manufacture of the product. It is not sufficient for a technology to be good; unless a technology, particularly the ones meant for ordinary consumers, can be mass produced in a relatively inexpensive manner, it may not have much of an impact on society. This is very much valid for HEVs as well. The book therefore concludes with a chapter on commercialization issues in HEVs.

The authors have significant industrial experience in many of the technical areas covered in the book, as reflected in the material and presentation. They have also been involved in teaching both academic and industrial professional courses in the area of HEV and EV systems and components. The book evolved to some extent from the notes used in these courses. However, significant amounts of extra material have been added, which is not covered in those courses.

It is expected that the book will fill some of the gaps in the existing literature and in the areas of HEV and EV technologies for both regular and off-road vehicles. It will also help the reader to get a better system-level perspective of these.

There are 15 chapters, the writing of which was shared among the three authors. Chris Mi is the main author of Chapter 1, Chapter 4, Chapter 5, Chapter 9, and Chapter 10. M. Abul Masrur is the main author of Chapter 2, Chapter 6, Chapter 7, Chapter 8, Chapter 14, and Chapter 15. David Wenzhong Gao is the main author of Chapter 3, Chapter 11, Chapter 12, and Chapter 13.

Since this is the first edition of the book, the authors very much welcome any input and comments from readers, and will ensure that any corrections or amendments as needed are incorporated into future editions.

The authors are grateful to all those who helped to complete the book. In particular, a large portion of the material presented is the result of many years of work by the authors as well as other members of their research groups at the University of Michigan–Dearborn, Tennessee Technological University, and University of Denver. Thanks are due to the many dedicated staff and graduate students who made enormous contributions and provided supporting material to this book.

The authors also owe debts of gratitude to their families, who gave tremendous support and made sacrifices during the process of writing this book.

Sincere acknowledgment is made to various sources that granted permission to use certain materials or pictures in this book. Acknowledgments are included where those materials appear. The authors used their best efforts to get approval to use those materials which are in the public domain and on open Internet web sites. Sometimes the original sources of the materials (in some web sites in particular) no longer exist or could not be

traced. In these cases the authors have noted where they found the materials and expressed their acknowledgment. If any of these sources were missed, the authors apologize for that oversight, and will rectify this in future editions of the book if brought to the attention of the publisher. The names of any product or supplier referred to in this book are provided for information only and are not in any way to be construed as an endorsement (or lack thereof) of such product or supplier by the publisher or the authors.

Finally, the authors are extremely grateful to John Wiley & Sons, Ltd and its editorial staff for giving them the opportunity to publish this book and helping in all possible ways. Finally, the authors acknowledge with great appreciation the efforts of the late Ms. Nicky Skinner of John Wiley & Sons, who initiated this book project on behalf of the publisher, but passed away in an untimely way very recently, and so did not see her efforts come to successful fruition.

1

Introduction

Modern society relies heavily on fossil fuel-based transportation for economic and social development – freely moving goods and people. There are about 800 million cars in the world and about 250 million motor vehicles on the road in the United States according to the US Department of Transportation's estimate [1]. In 2009, China overtook the United States to become the world's largest auto maker and auto market, with output and sales respectively hitting 13.79 and 13.64 million units in that year [2]. With further urbanization, industrialization, and globalization, the trend of rapid increase in the number of personal automobiles worldwide is inevitable. The issues related to this trend become evident because transportation relies heavily on oil. Not only are the oil resources on Earth limited, but also the emissions from burning oil products have led to climate change, poor urban air quality, and political conflict. Thus, global energy system and environmental problems have emerged, which can be attributed to a large extent on personal transportation.

Personal transportation offers people the freedom to go wherever and whenever they want. However, this freedom of choice creates a conflict, leading to growing concerns about the environment and concerns about the sustainability of human use of natural resources.

First, the world faces a serious challenge in energy demand and supply. The world consumes approximately 85 million barrels of oil every day but there are only 1300 billion barrels of proven reserves of oil. At the current rate of consumption, the world will run out of oil in 42 years [3]. New discoveries of oil reserves are at a slower pace than the increase in demand. Among the oil consumed, 60% is used for transportation [4]. The United States consumes approximately 25% of the world's total oil [5]. Reducing oil consumption in the personal transportation sector is essential to achieve energy and environmental sustainability.

Second, the world faces a great challenge from global climate change. The emissions from burning fossil fuels increase the carbon dioxide (CO_2) concentration (also referred to as greenhouse gas or GHG emissions) in the Earth's atmosphere. The increase in CO_2 concentration leads to excessive heat being captured on the Earth's surface, which leads to a global temperature increase and extreme weather conditions in many parts of the world. The long-term consequences of global warming can lead to rising sea levels and instability of ecosystems.

Hybrid Electric Vehicles: Principles and Applications with Practical Perspectives, First Edition.
Chris Mi, M. Abul Masrur and David Wenzhong Gao.

Gasoline and diesel fuel-powered vehicles are among the major contributors to CO_2 emissions. In addition, there are other emissions from conventional fossil fuel-powered vehicles, including carbon monoxide (CO) and nitrogen oxides (NO and NO_2, or NO_x) from burning gasoline; hydrocarbons or volatile organic compounds (VOCs) from evaporated, unburned fuel; and sulfur oxide and particulate matter (soot) from burning diesel fuel. These emissions cause air pollution and ultimately affect human and animal health.

Third, society needs sustainability but the current model is far from it. Cutting fossil fuel usage and reducing carbon emissions are part of the collective effort to retain human uses of natural resources within sustainable limits. Therefore, future personal transportation should provide enhanced freedom, sustainable mobility, and sustainable economic growth and prosperity for society. In order to achieve these, vehicles driven by electricity from clean, secure, and smart energy are essential.

Electrically-driven vehicles have many advantages and challenges. Electricity is more efficient than the combustion process in a car. Well-to-wheel studies show that, even if the electricity is generated from petroleum, the equivalent miles that can be driven by 1 gallon (3.8 l) of gasoline is 108 miles (173 km) in an electric car, compared to 33 miles (53 km) in an internal combustion engine (ICE) car [6–8]. In a simpler comparison, it costs 2 cents per mile to use electricity (at US $0.12 per kWh) but 10 cents per mile to use gasoline (at $3.30 per gallon) for a compact car.

Electricity can be generated through renewable sources, such as hydroelectric, wind, solar, and biomass. On the other hand, the current electricity grid has extra capacity available at night when usage of electricity is off-peak. It is ideal to charge electric vehicles (EVs) at night when the grid has extra energy capacity available.

High cost, limited driving range, and long charging time are the main challenges for battery-powered EVs. Hybrid electric vehicles (HEVs), which use both an ICE and an electric motor to drive the vehicle, overcome the cost and range issues of a pure EV without the need to plug in to charge. The fuel consumption of HEVs can be significantly reduced compared to conventional gasoline engine-powered vehicles. However, the vehicle still operates on gasoline/diesel fuel.

Plug-in hybrid electric vehicles (PHEVs) are equipped with a larger battery pack and a larger-sized motor compared to HEVs. PHEVs can be charged from the grid and driven a limited distance (20–40 miles) using electricity, referred to as charge-depletion (CD) mode operation. Once the battery energy has been depleted, PHEVs operate similar to a regular HEV, referred to as charge-sustain (CS) mode operation, or extended range operation. Since most of the personal vehicles are for commuting and 75% of them are driven only 40 miles or less daily [9], a significant amount of fossil fuel can be displaced by deploying PHEVs capable of a range of 40 miles of purely electricity-based propulsion. In extended range operation, a PHEV works similar to a HEV by using the onboard electric motor and battery to optimize the engine and vehicle system operation to achieve higher fuel efficiency. Thanks to the larger battery power and energy capacity, the PHEV can recover more kinetic energy during braking, thereby further increasing fuel efficiency.

1.1 Sustainable Transportation

The current model of the personal transportation system is not sustainable in the long run because the Earth has limited reserves of fossil fuel, which provide 97% of all transportation energy needs at the present time [10]. To understand how sustainable transportation can be achieved, let us look at the ways energy can be derived and the ways vehicles are powered.

The energy available to us can be divided into three categories: renewable energy, fossil fuel-based non-renewable energy, and nuclear energy. Renewable energy includes hydropower, solar, wind, ocean, geothermal, biomass, and so on. Non-renewable energy includes coal, oil, and natural gas. Nuclear energy, though abundant, is not renewable since there are limited resources of uranium and other radioactive elements on Earth. In addition, there is concern on nuclear safety (such as the recent accident in Japan due to earthquake and tsunami) and nuclear waste processing in the long term. Biomass energy is renewable because it can be derived from wood, crops, cellulose, garbage, and landfill. Electricity and hydrogen are secondary forms of energy. They can be generated by using a variety of sources of original energy, including renewable and non-renewable energy. Gasoline, diesel, and syngas are energy carriers derived from fossil fuel.

Figure 1.1 shows the different types of sources of energy, energy carriers, and vehicles. Conventional gasoline/diesel-powered vehicles rely on liquid fuel which can only be derived from fossil fuel. HEVs, though more efficient and consuming less fuel than conventional vehicles, still rely on fossil fuel as the primary energy. Therefore, both conventional cars and HEVs are not sustainable. EVs and fuel cell vehicles rely on electricity and hydrogen, respectively. Both electricity and hydrogen can be generated from renewable energy sources, therefore they are sustainable as long as only renewable energy sources are used for the purpose. PHEVs, though not totally sustainable, offer the advantages of both conventional vehicles and EVs at the same time. PHEVs can

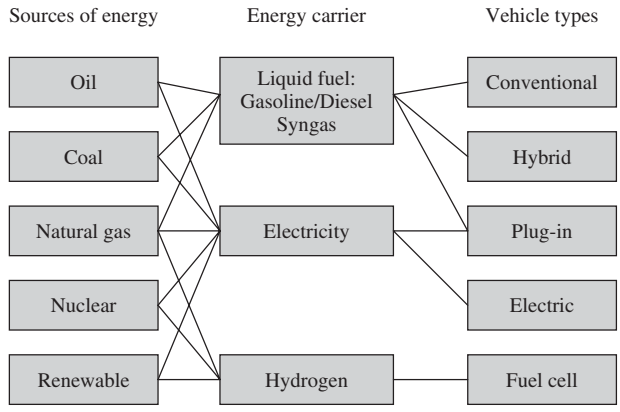

Figure 1.1 A sustainable transportation model (hc, hydrocarbon; co, carbon monoxide; nox, nitrogen oxides; pm, particulate matter)

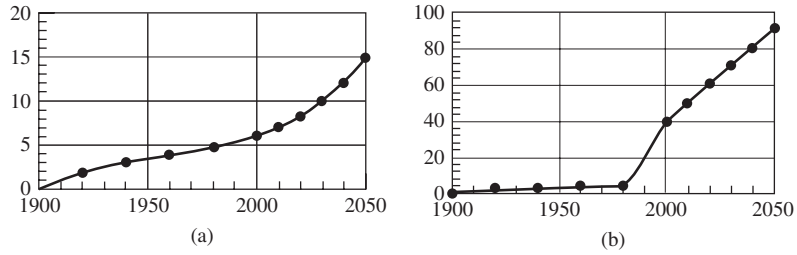

Figure 1.2 Trends of world population and vehicles sold per year. (a) World population, in billion barrels. (b) Passenger cars sold per year, in millions

displace fossil fuel usage by using grid electricity. They are not the ultimate solution for sustainability but they build a pathway to future sustainability.

1.1.1 Population, Energy, and Transportation

The world's population is growing at a rapid pace, as shown in Figure 1.2 [11]. At the same time, personal vehicle sales are also growing at a rapid pace, as shown in Figure 1.2 (www.dot.gov, also http://en.wikipedia.org/wiki/Passenger_vehicles_in_the_United_States). There is a clear correlation between population growth and the number of vehicles sold every year.

Fuel economy, as used in the United States, evaluates how many miles can be driven with 1 gallon of gas, or miles per gallon (MPG). Fuel consumption, as used in most countries in the world, evaluates the gasoline (or diesel) consumption in liters for every 100 km the car is driven (l per 100 km). The US Corporate Average Fuel Economy Standard, known as the CAFÉ standard, sets the fuel economy for passenger cars at 27.5 MPG from 1989 to 2008 [12]. With an average 27.5 MPG fuel economy, an average 15 000 miles driven per year, and 250 million cars on the road, the United States would consume 136 billion gallons of gasoline per year. This is equivalent to 7 billion barrels of oil, or 0.5% of all the proven oil reserves on Earth.

China surpassed the United States in 2009 to become the second largest vehicle market in the world, with more than 13 million motor vehicles sold in 2009. Growth has been in double digits for five consecutive years. In 2009, overall vehicle sales dropped 20% worldwide due to the global financial crisis, but China's car market still grew by more than 6%, along with its sustained economic growth of close to 10%. China used to be self-sufficient in oil supplies, but is now estimated to import 40% of its oil consumption (http://data.chinaoilweb.com/crudeoil-import-data/index.html).

In addition to industrialized countries such as Japan and Germany which have high demand for oil imports, developing countries such as India and Brazil have also seen tremendous growth in car sales in the past five years. These countries face the same challenges in oil demand and environmental aspects. Figure 1.3 shows crude oil consumption and demand per day by country [13].

Figure 1.4 shows the history and projections of oil demand and production (http://www.eia.doe.gov/steo/contents.html). Many analysts believe in the theory of peak oil at the present time, which predicts that oil production is at its peak in history, and

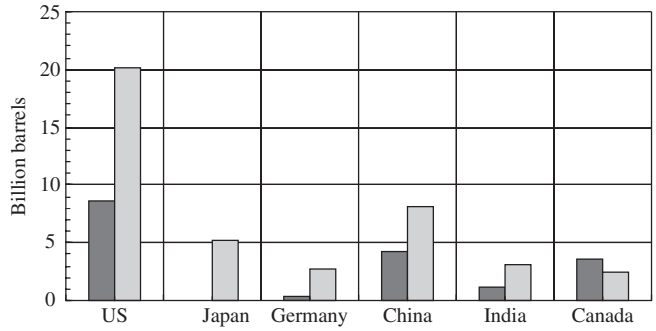

Figure 1.3 Average crude oil consumption per day by country in 2008, in million barrels. The left column for each country is the production and the right column is the consumption [13]

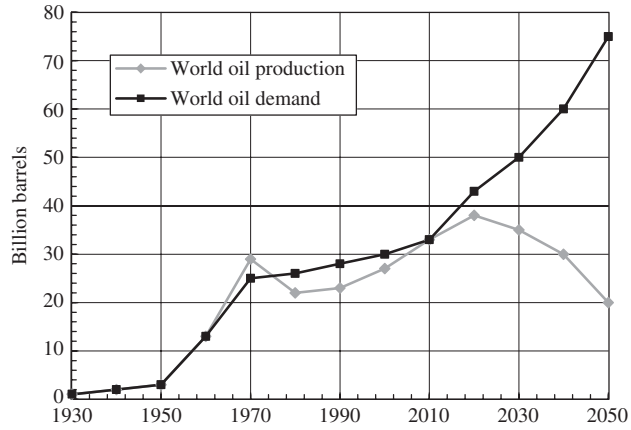

Figure 1.4 World oil demand and depletion history and projections

will soon be below oil demand. The gap generated by demand and production will cause another and probably eventual energy crisis without careful planning beforehand.

1.1.2 Environment

Carbon emissions from burning fossil fuel are the primary source of GHG emissions that lead to global environment and climate change. Figure 1.5 shows the fossil carbon emissions from 1900 to the present time [14]. The most dramatic increase of GHG emissions has happened in the last 100 years. Associated with the increase of GHG emissions is the global temperature increase. Figure 1.6 shows the global mean land–ocean temperature change from 1880 to the present, using the period of 1951–1980 temperature as the basis for comparison (http://data.giss.nasa.gov/gistemp/graphs/).

As an example of how car emissions contribute to GHG emissions, Figure 1.7 shows the emissions of a typical passenger car during a cold start. Modern cars are equipped with

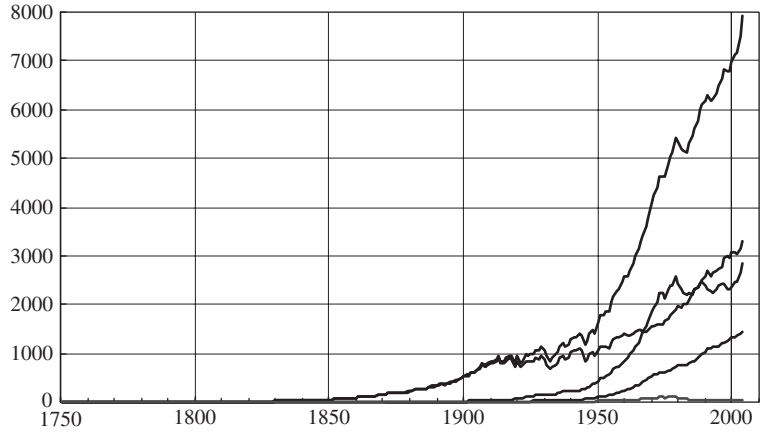

Figure 1.5 Global fossil carbon emissions from 1800 to 2004 [14]. On the right tip points, from top to bottom: total CO_2; oil; coal; cement production; and other. (Courtesy Oak Ridge National Laboratory.)

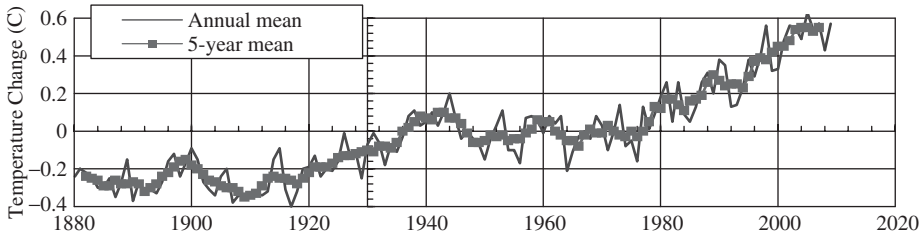

Figure 1.6 Global annual mean surface air temperature change. Data from http://data.giss.nasa.gov/gistemp/graphs/. (Courtesy NASA.)

catalytic converters to reduce emissions from the car tailpipes/exhausts. But the catalytic converter needs to heat up to approximately 350 °C in order to function efficiently. It has been estimated that 70–80% of the total emissions occur during the first two minutes after a cold start during a standard driving cycle.

1.1.3 Economic Growth

Economic growth relies heavily on energy supply. For example, from 1999 to 2009, China's economy attained an average growth rate of more than 10%. In the same period, energy demand increased by more than 15% per year. In the early 1990s, China's oil production was sufficient to support its own economy, but by the year 2009, China imported a large portion of its oil consumption, estimated at 40% (http://data.chinaoilweb.com/crude-oil-import-data/index.html).

Figure 1.8 shows the energy consumption per capita, in kilograms of oil equivalent [13]. It is evident that developing countries are still well below the level of the developed countries. To reach sustainability, the global economy must embark on a new model.

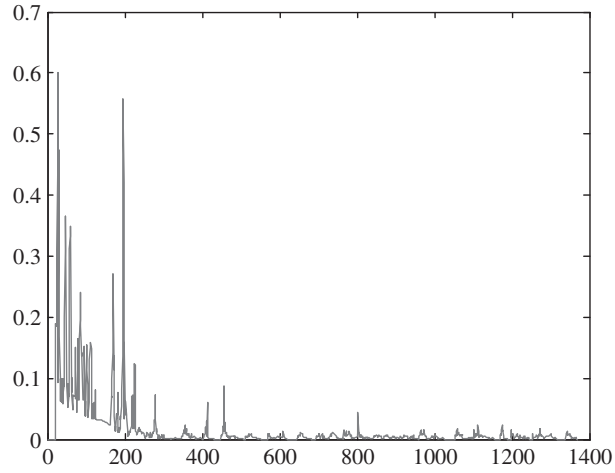

Figure 1.7 Typical emissions of a passenger car during cold starting (Shown in figure is the total emissions in grams, which contains hc – hydrocarbon; co – carbon monoxide; nox – nitrogen oxide; pm – particular matter)

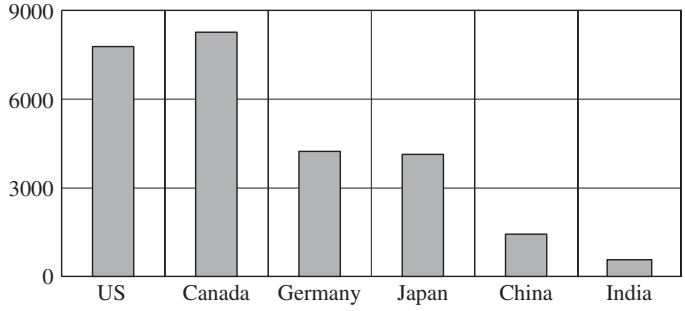

Figure 1.8 Energy consumption per capital in 2006 in kilograms of oil equivalent

1.1.4 New Fuel Economy Requirement

In 2009, the US government announced its new CAFÉ standard, requiring that all car manufacturers achieve an average fuel economy of 35 MPG by 2020. This is equivalent to 6.7 l/100 km. The new requirement is a major increase in fuel economy in the United States in 20 years, and represents approximately a 40% increase from the current standard as shown in Figure 1.9. This new legislation is a major step forward to effectively reduce energy consumption and GHG emissions. To achieve this goal, a mixed portfolio is necessary for all car manufacturers.

First, auto makers must shift from large cars and pickup trucks to smaller vehicles to balance the portfolio. Second, auto makers must continue to develop technology that supports fuel efficiency improvements in conventional gasoline engines. Lastly and most importantly, auto makers have to increase HEV and PHEV production.

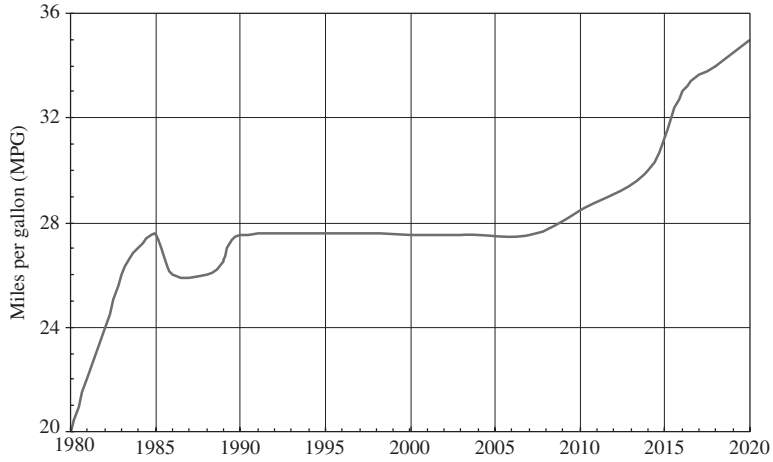

Figure 1.9 Fuel economy evolution in the United States (CAFÉ requirements)

1.2 A Brief History of HEVs

EVs were invented in 1834, that is, about 60 years earlier than gasoline-powered cars, which were invented in 1895. By 1900, there were 4200 automobiles sold in the United States, of which 40% were electric cars (http://sites.google.com/site/petroleumhistoryresources/Home/cantankerous-combustion).

Dr Ferdinand Porsche in Germany built probably the world's first HEV in 1898, using an ICE to spin a generator that provided power to electric motors located in the wheel hubs (http://en.wikipedia.org/wiki/Ferdinand_Porsche). Another hybrid vehicle, made by the Krieger Company in 1903, used a gasoline engine to supplement the power of the electric motor which used electricity from a battery pack (http://www.hybridcars.com/history/history-of-hybrid-vehicles.html). Both hybrids are similar to the modern series HEV.

Also in the 1900s, a Belgian car maker, Pieper, introduced a 3.5 hp "Voiturette" in which the small gasoline engine was mated to an electric motor under the seat (http://en.wikipedia.org/wiki/Voiturette). When the car was cruising, its electric motor was used as a generator to charge the batteries. When the car was climbing a grade, the electric motor, mounted coaxially with the gas engine, helped the engine to drive the vehicle. In 1905, a US engineer, H. Piper, filed a patent for a petrol–electric hybrid vehicle. His idea was to use an electric motor to assist an ICE, enabling the vehicle to achieve 25 mph. Both hybrid designs are similar to the modern parallel HEV.

In the United States, there were a number of electric car companies in the 1920s, with two of them dominating the EV markets – Baker of Cleveland and Woods of Chicago. Both car companies offered hybrid electric cars. However, the hybrid cars were more expensive than gasoline cars, and sold poorly.

HEVs, together with EVs, faded away by 1930 and the electric car companies all failed. There were many reasons leading to the disappearance of the EV and HEV. When compared to gasoline-powered cars, EVs and HEVs:

- were more expensive than gasoline cars due to the large battery packs used;
- were less powerful than gasoline cars due to the limited power from the onboard battery;
- had limited range between each charge;
- and needed many hours to recharge the onboard battery.

In addition, urban and rural areas lacked accessibility to electricity for charging electric and hybrid cars.

The major progress in gasoline-powered cars also hastened the disappearance of the EV and HEV. The invention of starters made the starting of gasoline engines easier, and assembly line production of gasoline-powered vehicles, such as the Model-T by Henry Ford, made these vehicles a lot more affordable than electric and hybrid vehicles.

It was not until the Arab oil embargo in 1973 that the soaring price of gasoline sparked new interest in EVs. The US Congress introduced the Electric and Hybrid Vehicle Research, Development, and Demonstration Act in 1976 recommending the use of EVs as a mean of reducing oil dependency and air pollution. In 1990, the California Air Resource Board (CARB), in consideration of the smog affecting Southern California, passed the zero emission vehicle (ZEV) mandate, which required 2% of vehicles sold in California to have no emissions by 1998 and 10% by 2003. California car sales have approximately a 10% share of the total car sales in the United States. Major car manufacturers were afraid that they might lose the California car market without a ZEV. Hence, every major auto maker developed EVs and HEVs. Fuel cell vehicles were also developed in this period. Many EVs were made, such as GM's EV1, Ford's Ranger pickup EV (Figure 1.10), Honda's EV Plus, Nissan's Altra EV, and Toyota's RAV4 EV.

In 1993, the US Department of Energy set up the Partnership for Next Generation Vehicle (PNGV) program to stimulate the development of EVs and HEVs. The partnership was a cooperative research program between the US government and major auto corporations, aimed at enhancing vehicle efficiency dramatically. Under this program, the three US car companies demonstrated the feasibility of a variety of new automotive technologies, including a HEV that can achieve 70 MPG. This program was cancelled in 2001 and was transitioned to the Freedom CAR (Cooperative Automotive Research),

Figure 1.10 Ford Electric Ranger

which is responsible for the current HEV, PHEV, and battery research programs under the US Department of Energy.

Unfortunately, the EV program faded away by 2000, with thousands of EV programs terminated by the auto companies. This is due partially to the fact that consumer acceptance was not overwhelming, and partially to the fact that the CARB relaxed its ZEV mandate.

The world's automotive history turned to a new page in 1997 when the first modern hybrid electric car, the Toyota Prius, was sold in Japan. This car, along with Honda's Insight and Civic HEVs, has been available in the United States since 2000. These early HEVs marked a radical change in the types of cars offered to the public: vehicles that take advantage of the benefits of both battery EVs and conventional gasoline-powered vehicles. At the time of writing, there are more than 40 models of HEVs available in the marketplace from more than 10 major car companies.

1.3 Why EVs Emerged and Failed in the 1990s, and What We Can Learn from It

During the 1990s, California had a tremendous smog and pollution problem that needed to be addressed. The CARB passed a ZEV mandate that required car manufacturers to sell ZEVs if they wanted to sell cars in California. This led to the development of electric cars by all major car manufacturers. Within a few years, there were more than 10 production EVs available to consumers, such as the GM EV1, the Toyota RAV4, the Ford Ranger, and so on.

Unfortunately, the EV market collapsed in the late 1990s. What caused the EV industry to fail? The reasons were mixed, depending on how one looks at it, but the following were the main contributors to the collapse of EVs in the 1990s:

- **Limitations of EVs:** These concerned the limited range (most EVs provided 60–100 miles, compared to 300 or more miles from gasoline-powered vehicles); long charging time (eight or more hours); high cost (40% more expensive than gasoline cars); and limited cargo space in many of the EVs available.
- **Cheap gasoline:** The operating cost (fuel cost) of cars is insignificant in comparison to the investment that an EV owner makes in buying an EV.
- **Consumers:** Consumers believed that large sports utility vehicles (SUVs) and pickup trucks were safer to drive and convenient for many other functions, such as towing. Therefore, consumers preferred large SUVs instead of smaller efficient vehicles (partly due to the low gasoline prices).
- **Car companies:** Automobile manufacturers spent billions of dollars in research, development, and deployment of EVs, but the market did not respond very well. They were losing money in selling EVs at that time. Maintenance and servicing of EVs were additional burdens on the car dealerships. Liability was a major concern, though there was no evidence that EVs were less safe than gasoline vehicles.
- **Gas companies:** EVs were seen as a threat to gas companies and the oil industry. Lobbying by the car and gasoline companies of the federal government and the California government to drop the mandate was one of the key factors leading to the disappearance of EVs in the 1990s.

- **Government:** The CARB switched at the last minute from a mandate for EVs to hydrogen vehicles.
- **Battery technology:** Lead acid batteries were used in most EVs in the 1990s. The batteries were large and heavy, and needed a long time to charge.
- **Infrastructure:** There was limited infrastructure for recharging batteries.

As we strive for a way toward sustainable transportation, lessons from history will help us prevent the same mistakes happening again. In the current context of HEV and PHEV development, we must overcome many barriers in order to succeed:

- **Key technology:** That is, batteries, power electronics, and electric motors. In particular, without significant breakthroughs in batteries and with gasoline prices continuing at low levels, there will be significant obstacles for large-scale deployment of EVs and PHEVs.
- **Cost:** HEVs and PHEVs cost significantly more than their gasoline counterparts. Efforts need to be made to cut component and system cost. When savings in fuel can quickly recover the investment in the HEV, consumers will switch to HEVs and PHEVs rapidly.
- **Infrastructure:** This needs to be ready for the large deployment of PHEVs, including electricity generation for increased demand by PHEVs and increased renewable energy generation, and for rapid and convenient charging of grid PHEVs.
- **Policy:** Government policy has a significant impact on the deployment of many new technologies. Favorable policies include taxation, standards, consumer incentives, investment in research, development, and manufacture of advanced technology products will all have a positive impact on the deployment of HEV and PHEV.
- **Approach:** An integrated approach that combine high-efficiency engines, vehicle safety, and smarter roadways will ultimately help form a sustainable future for personal transportation.

1.4 Architectures of HEVs

A HEV is a combination of a conventional ICE-powered vehicle and an EV. It uses both an ICE and an electric motor/generator for propulsion. The two power devices, the ICE and the electric motor, can be connected in series or in parallel from a power flow point of view. When the ICE and motor are connected in series, the HEV is a series hybrid in which only the electric motor is providing mechanical power to the wheels. When the ICE and the electric motor are connected in parallel, the HEV is a parallel hybrid in which both the electric motor and the ICE can deliver mechanical power to the wheels.

In a HEV, liquid fuel is still the source of energy. The ICE is the main power converter that provides all the energy for the vehicle. The electric motor increases system efficiency and reduces fuel consumption by recovering kinetic energy during regenerative braking, and optimizes the operation of the ICE during normal driving by adjusting the engine torque and speed. The ICE provides the vehicle with an extended driving range therefore overcoming the disadvantages of a pure EV.

In a PHEV, in addition to the liquid fuel available on the vehicle, there is also electricity stored in the battery, which can be recharged from the electric grid. Therefore, fuel usage can be further reduced.

In a series HEV or PHEV, the ICE drives a generator (referred to as the I/G set). The ICE converts energy in the liquid fuel to mechanical energy and the generator converts the mechanical energy of the engine output to electricity. An electric motor will propel the vehicle using electricity generated by the I/G set. This electric motor is also used to capture the kinetic energy during braking. There will be a battery between the generator and the electric motor to buffer the electric energy between the I/G set and the motor.

In a parallel HEV or PHEV, both the ICE and the electric motor are coupled to the final drive shaft through a mechanical coupling mechanism, such as a clutch, gears, belts, or pulleys. This parallel configuration allows both the ICE and the electric motor to drive the vehicle either in combined mode, or separately. The electric moor is also used for regenerative braking and for capturing the excess energy from the ICE during coasting.

HEVs and PHEVs can also have either the series–parallel configuration or a more complex configuration which usually contains more than one electric motor. These configurations can generally further improve the performance and fuel economy of the vehicle with added component cost.

1.4.1 Series HEVs

Figure 1.11 shows the configuration of a series HEV. In this HEV, the ICE is the main energy converter that converts the original energy in gasoline to mechanical power. The mechanical output of the ICE is then converted to electricity using a generator. The electric motor moves the final drive using electricity generated by the generator or electricity stored in the battery. The electric motor can receive electricity directly from the engine, or from the battery, or both. Since the engine is decoupled from the wheels, the engine speed can be controlled independently of vehicle speed. This not only simplifies the control of the engine, but, most importantly, can allow operation of the engine at its optimum speed to achieve the best fuel economy. It also provides flexibility in locating the engine on the vehicle. There is no need for the traditional mechanical transmission in a series HEV. Based on the vehicle operating conditions, the propulsion components on a series HEV can operate with different combinations:

- **Battery alone:** When the battery has sufficient energy, and the vehicle power demand is low, the I/G set is turned off, and the vehicle is powered by the battery only.

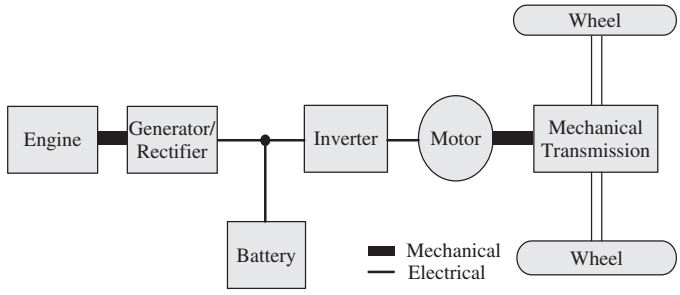

Figure 1.11 The architecture of a series HEV

- **Combined power:** At high power demands, the I/G set is turned on and the battery also supplies power to the electric motor.
- **Engine alone:** During highway cruising and at moderately high power demands, the I/G set is turned on. The battery is neither charged nor discharged. This is mostly due to the fact that the battery's state of charge (SOC) is already at a high level but the power demand of the vehicle prevents the engine from turning, or it may not be efficient to turn the engine off.
- **Power split:** When the I/G is turned on, the vehicle power demand is below the I/G optimum power, and the battery SOC is low, then a portion of the I/G power is used to charge the battery.
- **Stationary charging:** The battery is charged from the I/G power without the vehicle being driven.
- **Regenerative braking:** The electric motor is operated as a generator to convert the vehicle's kinetic energy into electric energy and charge the battery.

A series HEV can be configured in the same way that conventional vehicles are configured, that is, the electric motor in place of the engine as shown in Figure 1.11. Other choices are also available, such as wheel hub motors. In this case, as shown in Figure 1.12, there are four electric motors, each one installed inside each wheel. Due to the elimination of transmission and final drive, the efficiency of the vehicle system can be significantly increased. The vehicle will also have all-wheel drive (AWD) capability. However, controlling the four electric motors independently is a challenge.

1.4.2 Parallel HEVs

Figure 1.13 shows the configuration of a parallel hybrid. In this configuration, the ICE and the electric motor can both deliver power in parallel to the wheels. The ICE and the electric motor are coupled to the final drive through a mechanism such as a clutch, belts, pulleys, and gears. Both the ICE and the motor can deliver power to the final drive, either in combined mode, or each separately. The electric motor can be used as a generator to

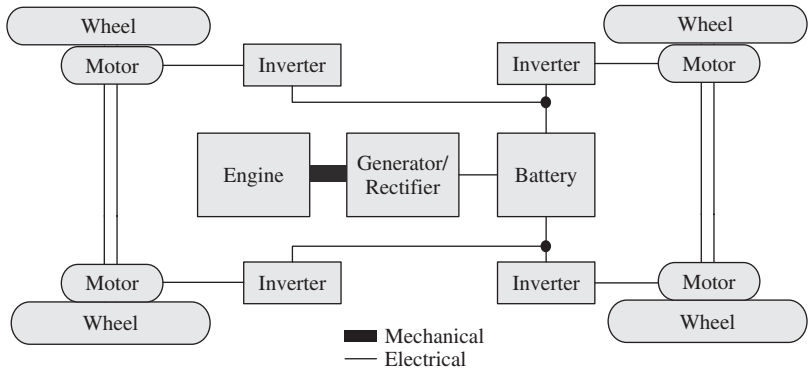

Figure 1.12 Hub motor configuration of a series HEV

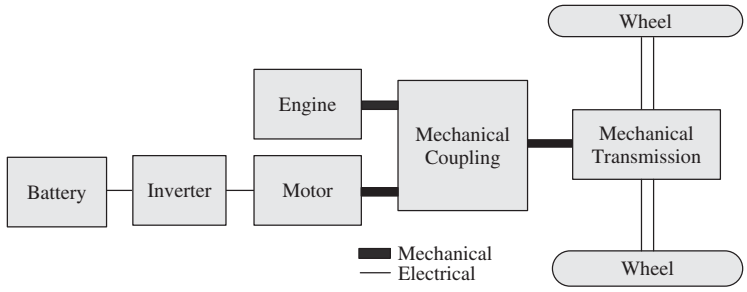

Figure 1.13 The architecture of a parallel HEV

recover the kinetic energy during braking or absorbing a portion of power from the ICE. The parallel hybrid needs only two propulsion devices, the ICE and the electric motor, which can be used in the following mode:

- **Motor-alone mode:** When the battery has sufficient energy, and the vehicle power demand is low, then the engine is turned off, and the vehicle is powered by the motor and battery only.
- **Combined power mode:** At high power demand, the engine is turned on and the motor also supplies power to the wheels.
- **Engine-alone mode:** During highway cruising and at moderately high power demands, the engine provides all the power needed to drive the vehicle. The motor remains idle. This is mostly due to the fact that the battery SOC is already at a high level but the power demand of the vehicle prevents the engine from turning off, or it may not be efficient to turn the engine off.
- **Power split mode:** When the engine is on, but the vehicle power demand is low and the battery SOC is also low, then a portion of the engine power is converted to electricity by the motor to charge the battery.
- **Stationary charging mode:** The battery is charged by running the motor as a generator and driven by the engine, without the vehicle being driven.
- **Regenerative braking mode:** The electric motor is operated as a generator to convert the vehicle's kinetic energy into electric energy and store it in the battery. Note that, in regenerative mode, it is in principle possible to run the engine as well, and provide additional current to charge the battery more quickly (while the propulsion motor is in generator mode) and command its torque accordingly, that is, to match the total battery power input. In this case, the engine and motor controllers have to be properly coordinated.

1.4.3 Series–Parallel HEVs

The series–parallel HEV shown in Figure 1.14 incorporates the features of both series and parallel HEVs. Therefore, it can be operated as a series or parallel HEV. In comparison to a series HEV, the series–parallel HEV adds a mechanical link between the engine and the final drive, so the engine can drive the wheels directly. When compared to a parallel HEV, the series–parallel HEV adds a second electric motor that serves primarily as a generator.

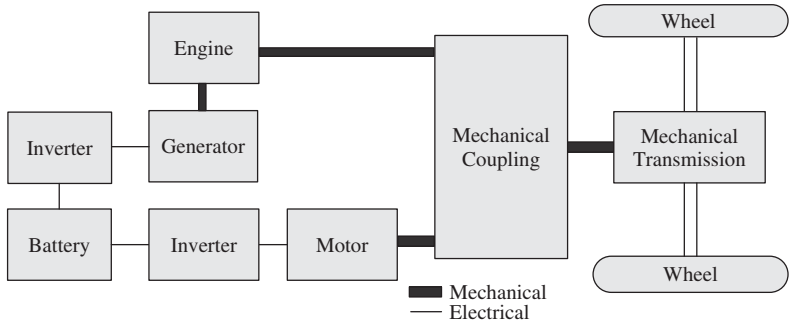

Figure 1.14 The architectures of a series–parallel HEV

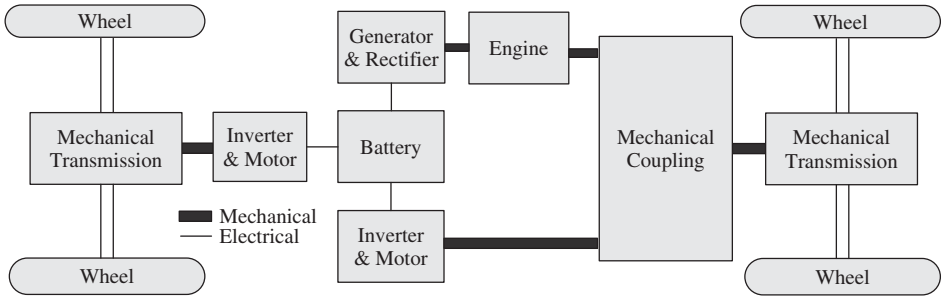

Figure 1.15 The electrical four-wheel drive system using a complex architecture

Because a series–parallel HEV can operate in both parallel and series modes, the fuel efficiency and drivability can be optimized based on the vehicle's operating condition. The increased degree of freedom in control makes the series–parallel HEV a popular choice. However, due to increased components and complexity, it is generally more expensive than series or parallel HEVs.

1.4.4 Complex HEVs

Complex HEVs usually involve the use of planetary gear systems and multiple electric motors (in the case of four/all-wheel drive). One typical example is a four-wheel drive (4WD) system that is realized through the use of separate drive axles, as shown in Figure 1.15. The generator in this system is used to realize series operation as well as to control the engine operating condition for maximum efficiency. The two electric motors are used to realize all-wheel drive, and to realize better performance in regenerative braking. They may also enhance vehicle stability control and antilock braking control by their use.

1.4.5 Diesel Hybrids

HEVs can also be built around diesel vehicles. All topologies explained earlier, such as series, parallel, series–parallel, and complex HEVs, are applicable to diesel hybrids.

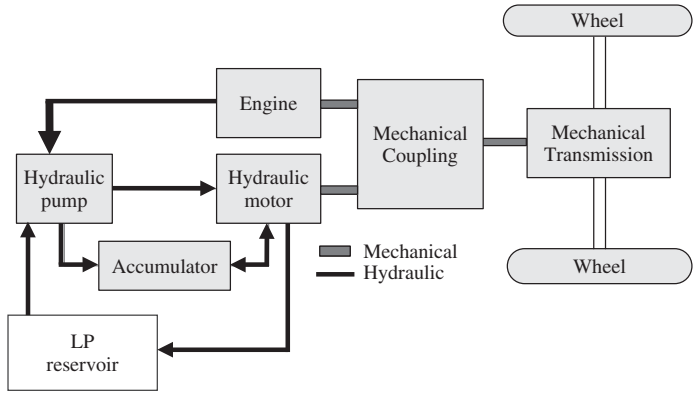

Figure 1.16 A parallel hydraulic hybrid vehicle (LP, Low Pressure)

Due to the fact that diesel vehicles can generally achieve higher fuel economy, the fuel efficiency of hybridized diesel vehicles can be even better when compared to their gasoline counterparts.

Vehicles such as delivery trucks and buses have unique driving patterns and relatively low fuel economy. When hybridized, these vehicles can provide significant fuel savings. Hybrid trucks and buses can be series, parallel, series–parallel, or complex structured and may run on gasoline or diesel.

Diesel locomotives are a special type of hybrid. A diesel locomotive uses a diesel engine and generator set to generate electricity. It uses electric motors to drive the train. Even though a diesel locomotive can be referred to as a series hybrid, in some architectures there is no battery for the main drive system to buffer energy between the I/G set and the electric motor. This special configuration is sometimes referred to as simple hybrid. In other architectures, batteries are used and can help reduce the size of the generator, and can also be used for regenerative energy capture. The batteries, in this case, can also be utilized for short-term high current due to torque needs, without resorting to a larger generator.

1.4.6 Other Approaches to Vehicle Hybridization

The main focus of this book is on HEVs, that is, electric–gasoline or electric–diesel hybrids. However, there exist other types of hybridization methods that involve other types of energy storage and propulsion, such as compressed air, flywheels, and hydraulic systems. A typical hydraulic hybrid is shown in Figure 1.16. Hydraulic systems can provide a large amount of torque, but due to the complexity of the hydraulic system, a hydraulic hybrid is considered only for large trucks and utility vehicles where frequent and extended period of stops of the engine are necessary.

1.4.7 Hybridization Ratio

Some new concepts have also emerged in the past few years, including full hybrid, mild hybrid, and micro hybrid. These concepts are usually related to the power rating

of the main electric motor in a HEV. For example, if the HEV contains a fairly large electric motor and associated batteries, it can be considered as a full hybrid. On the other hand, if the size of the electric motor is relatively small, then it may be considered as a micro hybrid.

Typically, a full hybrid should be able to operate the vehicle using the electric motor and battery up to a certain speed limit and drive the vehicle for a certain amount of time. The speed threshold is typically the speed limit in a residential area. The typical power rating of an electric motor in a full hybrid passenger car is approximately 50–75 kW.

The micro hybrid, on the other hand, does not offer the capability to drive the vehicle with the electric motor only. The electric motor is merely for starting and stopping the engine. The typical rating of electric motors used in micro hybrids is less than 10 kW. A mild hybrid is in between a full hybrid and a micro hybrid.

An effective approach for evaluating HEVs is to use a hybridization ratio to reflect the degree of hybridization of a HEV. In a parallel hybrid, the hybridization ratio is defined as the ratio of electric power to the total powertrain power. For example, a HEV with a motor rated at 50 kW and an engine rated at 75 kW will have a hybridization ratio of $50/(50+75)\,\text{kW} = 40\%$. A conventional gasoline-powered vehicle will have a 0% hybridization ratio and a battery EV will have a hybridization ratio of 100%. A series HEV will also have a hybridization ratio of 100% due to the fact that the vehicle is capable of being driven in EV mode.

1.5 Interdisciplinary Nature of HEVs

HEVs involve the use of electric machines, power electronics converters, and batteries, in addition to conventional ICEs and mechanical and hydraulic systems. The interdisciplinary nature of HEV systems can be summarized as in Figures 1.17. The HEV field involves engineering subjects beyond traditional automotive engineering, which was mechanical engineering oriented. Power electronics, electric machines, energy storage systems, and control systems are now integral parts of the engineering of HEVs and PHEVs.

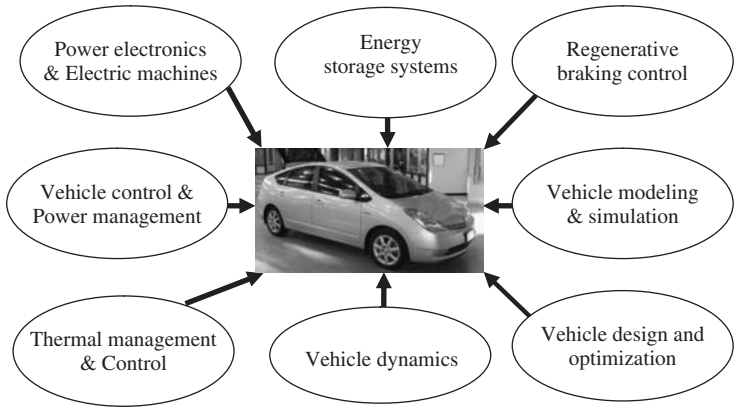

Figure 1.17 The general nature and required engineering field by HEVs

In addition, thermal management is also important in HEVs and PHEVs, where the power electronics, electric machines, and batteries all require a much lower temperature to operate properly, compared to a non-hybrid vehicle's powertrain components. Modeling and simulation, vehicle dynamics, and vehicle design and optimization also pose challenges to the traditional automotive engineering field due to the increased difficulties in packaging the components and associated thermal management systems, as well as the changes in vehicle weight, shape, and weight distribution.

1.6 State of the Art of HEVs

In the past 10 years, many HEVs have been deployed by the major automotive manufacturers. Figure 1.18 shows HEV sales in the United States from 2000 to 2009, and predictions (http://electricdrive.org/index.php?ht=d/Articles/cat_id/5514/pid/2549). Figure 1.19 shows the US HEV sales breakdown by manufacturer. It is clear that HEV sales have grown significantly over the last 10 years. In 2008, these sales had a downturn which is consistent with conventional car sales that dropped more than 20% in 2008 from the previous year. Another observation is that most HEV sales belong to Toyota, which manufactured the earliest modern HEV, the Prius, and also makes most of the models available (including the Lexus).

Table 1.1 shows the current HEVs available in the United States, along with a comparison to the base model of gasoline-powered cars (www.toyota.com, www.ford.com, www.gm.com, http://www.nissanusa.com/, www.honda.com, www.chrysler.com). In the case of the Toyota Prius, the comparison is made to the Toyota Corolla. It can be seen that the price of HEVs is generally 40% more than that of their base models. The increase in fuel economy in HEVs is also significant, in particular for city driving.

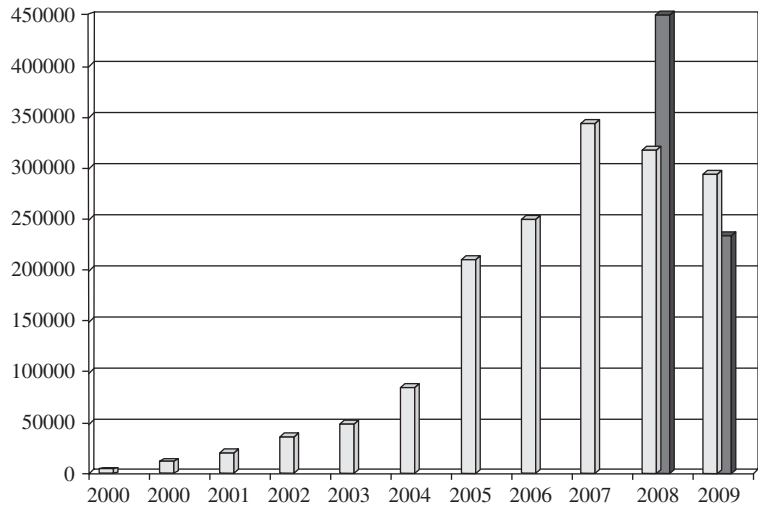

Figure 1.18 Total HEVs sold in the United States from 2000 to 2009 (in thousands): left bar, actual sales number; right bar, predicted**

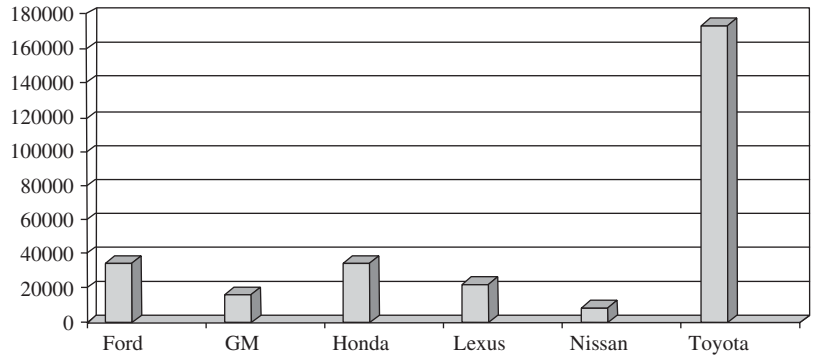

Figure 1.19 Breakdown of HEV sales by model** in the United States in 2009 (in thousands)

Figure 1.20 The Toyota Prius (2010 model)

1.6.1 The Toyota Prius

Toyota produced the world's first mass-marketed modern HEV in 1997, the Prius, as shown in Figure 1.20. The worldwide sales of the Prius exceeded 1 million units in 2009. It uses a planetary gear set to realize continuous variable transmission (CVT). Therefore, conventional transmission is not needed in this system. As shown in Figure 1.21, the engine is connected to the carrier of the planetary gear while the generator is connected to the sun gear. The ring gear is coupled to the final drive, as is the electric motor. The planetary gear set also acts as a power/torque split device. During normal operations, the ring gear speed is determined by the vehicle speed, while the generator speed can be controlled such that the engine speed is in its optimum efficiency range.

Table 1.1 Partial list of HEVs available in the United States

Manufacturer	Model	HEV price (US $)	Base model price (US $)	Price increase (%)	HEV MPG City	HEV MPG Hwy	Base MPG City	Base MPG Hwy	Increase in MPG (%) City	Increase in MPG (%) Hwy
Toyota	Prius[a]	22 800	15 450	47.6	51	48	26	35	96	37
	Camry	26 400	19 595	34.7	33	34	22	33	50	3
	Highlander	34 900	25 855	35.0	27	25	20	27	35	12
Ford/Mercury	Fusion	27 950	19 695	41.9	41	36	22	34	86	6
	Escape	29 860	21 020	42.1	34	31	22	28	55	11
	Mariner	30 105	23 560	27.8	34	31	21	28	62	11
	Milan	31 915	21 860	46.0	41	26	23	34	78	−24
Honda	Insight[b]	19 800	15 655	26.5	40	43	26	34	54	26
	Civic	23 800	15 655	52.0	40	45	26	34	54	32
Nissan	Altima	26 780	19 900	34.6	35	33	23	32	52	3
Lexus	RX 450h	42 685	37 625	13.4	32	28	18	25	78	12
	GS 450h	57 450	54 070	6.3	22	25	17	24	29	4
	LS 600h	108 800	74 450	46.1	20	22	16	23	25	−4
GM GMC, Chevrolet, and Cadillac Saturn[c]	Tahoe	50 720	37 280	36.1	21	22	15	21	40	5
	Yukon	51 185	38 020	34.6	21	22	15	21	40	5
	Sierra	38 710	20 850	85.7	21	22	15	22	40	0
	Malibu	22 800	21 825	4.5	26	34	22	33	18	3
	Escalade	73 425	62 495	17.5	21	22	13	20	62	10
	Silverado	38 340	29 400	30.4	22	21	13	17	69	24
Chrysler Dodge	Aspen[d]	44 700	40 000	11.8	18	19	15	20	38	6
	Durango[d]	45 900	40 365	13.7	18	19	15	20	38	6

[a] Comparison to Corolla.
[b] Comparison to Civic.
[c] Saturn Brand vehicle including Vue and Saturn Aura are not offered.
[d] Chrysler Aspen uses similar platform as Durango but is no longer offered.

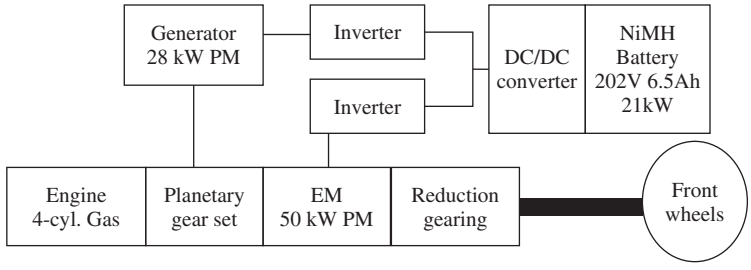

Figure 1.21 The powertrain layout of the Toyota Prius (EM, Electric Machine; PM, Permanent Magnet)

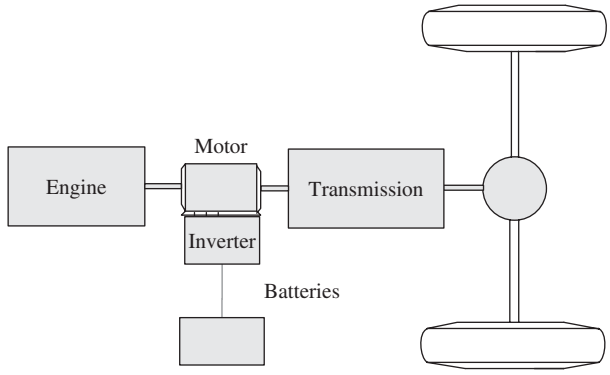

Figure 1.22 The powertrain layout of the Honda Civic hybrid

The 6.5 Ah, 21 kW nickel metal hydride battery pack is charged by the generator during coasting and by the propulsion motor (in generation mode) during regenerative braking. The engine is shut off during low-speed driving.

The same technology has been used in the Camry hybrid, the Highlander hybrid, and the Lexus brand hybrids. However, the Highlander and the Lexus brand hybrids add a third motor at the rear wheel. The drive performance, such as for acceleration and braking, can thus be further improved.

1.6.2 The Honda Civic

The Honda Civic hybrid has an electric motor mounted between the ICE and the CVT, as shown in Figure 1.22. The electric motor either provides assistance to the engine during high power demand, or splits the engine power during low power demand.

1.6.3 The Ford Escape

The Escape hybrid from the Ford Motor Company (Figure 1.23) is the first hybrid in the SUV category. The Escape hybrid adopted the same planetary gear concept as the Toyota system.

1.6.4 The Two-Mode Hybrid

The GM two-mode hybrid transmission was initially developed by GM (Alison) in 1996, and later advanced by GM, Chrysler, BMW, and Mercedes-Benz with a joint venture named Global Hybrid Cooperation in 2005. The GM two-mode hybrids (Figure 1.24) use two planetary gear sets and two electric machines to realize two different operating modes, namely, high-speed mode and low-speed mode. Detailed operation of the two-mode hybrid will be discussed in Chapter 4.

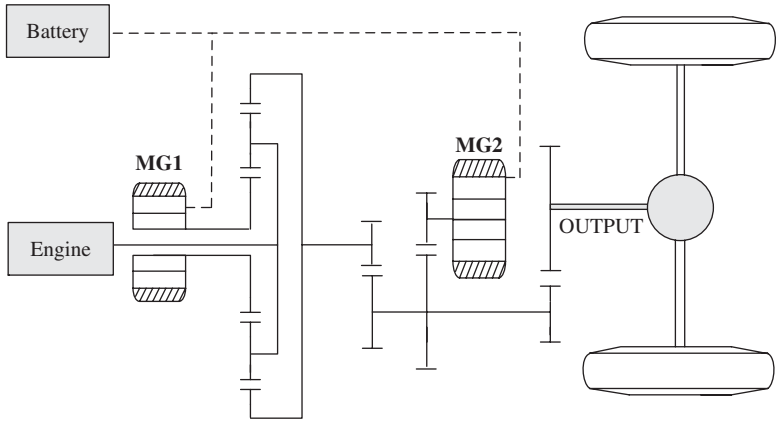

Figure 1.23 The Ford Escape hybrid SUV

Figure 1.24 The Chrysler Aspen two-mode hybrid

1.7 Challenges and Key Technology of HEVs

HEVs can overcome some of the disadvantages of battery-powered pure EVs and gasoline-powered conventional vehicles. These advantages include optimized fuel economy and reduced emissions when compared to conventional vehicles, and increased range, reduced charging time, and reduced battery size (hence reduced cost) when compared to pure EVs.

However, HEVs and PHEVs still face many challenges, including higher cost when compared to conventional vehicles; electromagnetic interference caused by high-power components; and safety and reliability concerns due to increased components and complexity, packaging of the system, vehicle control, and power management:

- **Power electronics and electric machines:** The subject of power electronics and electric motors is not new. However, the use of power electronics in a vehicle environment

poses significant challenges. Environmental conditions, such as extreme high and low temperatures, vibration, shock, and transient behavior are very different from what electric motors and power electronic converters have been used to. Challenges in power electronics in a HEV include packaging, size, cost, and thermal management.

- **Electromagnetic interference:** High-frequency switching and high-power operation of power electronics and electric motors will generate abundant electromagnetic noise that will interfere with the rest of the vehicle system if not dealt with properly.
- **Energy storage systems:** Such systems are a major challenge for HEVs and PHEVs. The pulsed power behavior and energy content required for the best performance are typically difficult for conventional batteries to satisfy. Life cycle and abuse tolerance are also critical for vehicle applications. At the present time, nickel metal hydride batteries are used by most HEVs and lithium-ion batteries are targeted by PHEVs. Ultracapacitors have also been considered in some special applications where power demand is a major concern. Flywheels have also been investigated. The limitations of the current energy storage systems are unsatisfactory power density and energy density, limited life cycle, high cost, and potential safety issues.
- **Regenerative braking control:** Recovering the kinetic energy during braking is a key feature of HEVs and PHEVs. However, coordinating regenerative braking with the hydraulic/frictional braking system presents a major challenge as far as safety and braking performance are concerned.
- **Power management and vehicle control:** HEVs involve the use of multiple propulsion components that require harmonious coordination. Hence, power management is a critical aspect of vehicle control functions in a HEV. A optimized vehicle controller can help achieve better fuel efficiency in a HEV.
- **Thermal management:** Power electronics, electric machines, and batteries all require a much lower operating temperature than a gasoline engine. A separate cooling loop is necessary in a HEV.
- **Modeling and simulation, vehicle dynamics, vehicle design, and optimization:** Due to the increased number of components in a HEV, packaging of the components in the same space is a challenge. Associated vehicle dynamics, vehicle design, and modeling and simulation all involve major challenges.

1.8 The Invisible Hand–Government Support

Without government support, the HEV and PHEV may take longer to succeed in the marketplace due to their high cost and other limitations. As far as consumers are concerned, there are two kinds of buyers of HEVs. One kind expects to save money over time by saving fuel consumption; the other buys the hybrid because of environmental concerns. The payback period, or the time it takes for the owner to recover the investment in a HEV due to fuel savings, depends greatly on the price of gasoline.

Take the Toyota Prius as an example. This HEV is priced at $22 800 while the conventional similar model, the Corolla, is only $15 450. The fuel savings are 96% in city driving and 37% in highway driving. Assume an owner drives an average 10 000 miles in the city and 5000 miles on the highway annually. Then the annual fuel consumption for the base model and for the hybrid will be as follows:

Conventional:	10 000 miles/26 MPG + 5000/35 MPG = 527 gallons
HEV:	10 000 miles/51 MPG + 5000/48 MPG = 300 gallons

At $2.50 per gallon, the fuel savings are $568 per year. In other words, it would take 13 years to make up the cost difference between the two vehicles. However, if gasoline were to cost $6.5 per gallon, it would only take five years to recover the cost differences.

Consider the Ford Escape SUV as another example. This HEV is priced at $29 860 while the conventional model is priced at $21 020. Assume an owner drives an average 10 000 miles in the city and 5000 miles on the highway annually. Then the annual fuel consumption for the base model and for the hybrid will be as follows:

Conventional:	10 000 miles/22 MPG + 5000/28 MPG = 633 gallons
HEV:	10 000 miles/34 MPG + 5000/31 MPG = 455 gallons

The total fuel saved is 178 gallons. At $2.50 per gal, the fuel savings are $455 per year, so it would take 19 years to make up the difference. However, if gasoline were to cost $6.5 per gallon, it would take 7.5 years to recover the cost difference.

Government incentives can make a difference in this scenario. Table 1.2 lists the tax credits available on certain HEVs by the US federal government (http://www.irs.gov/businesses/article/0,,id=223736,00.html). If we take the Ford Escape HEV as an example, when the tax credit is considered the recovery time of investment would be 5 and 13 years, respectively, for gasoline prices of $6.5 and $2.5 per gallon.

A few states and metropolitan cities in the United States, such as California and Washington DC, allow access of HEVs to the high-occupancy-vehicle (HOV) lane. Due to the fact that a significant amount of time can be saved by driving in the HOV lane, some consumers are motivated to buy a HEV or PHEV for their daily commuting to save time.

Some other states, such as Colorado and California, have separate incentives in addition to those from the federal government. A number of private companies such as Google, Bank of America, STMicroelectronics, and Hyperion reward their employees for buying or leasing a HEV. It is interesting to note that the motivation of the companies toward such investment by their employees may be to allow them to spend time in the office rather than in traffic.

In 2009, the US president announced funding to the amount of $2.4 billion for PHEV development that supported 48 projects being undertaken by major car manufacturers and automotive suppliers. The projects support the development of batteries and electric drive components as well as the deployment of electric drive vehicles. The president of the United States set the goal of reaching 1 million plug-in hybrids by 2015. Additional incentives are in place for PHEV developers and consumers.

At the time of writing, China, Japan, the European Union, and many other countries around the world have initiated support for the development, demonstration, and deployment of EVs, PHEVs, and associated battery and electric drive components.

Table 1.2 Available tax credits for HEVs sold in the United States (http://www.irs.gov/businesses/article/0,,id=223736,00.html)

Model year	Make	Model	Credit amount ($)
2011	BMW	Active Hybrid 750i	900
		Active Hybrid Li	900
		Active Hybrid X6	1550
2011	Cadillac	Escalade Hybrid (2WD and 4WD)	2200
2011	Chevrolet	Tahoe Hybrid C1500 2WD	2200
		Tahoe Hybrid K1500 4WD	2200
		Silverado Hybrid C15 2WD	2200
		Silverado Hybrid K15 4WD	2200
2011	GMC	Sierra Hybrid C15 2WD	2200
		Sierra Hybrid K15 4WD	2200
		Yukon Hybrid C1500 2WD	2200
		Yukon Hybrid K1500 4WD	2200
		Yukon Denali Hybrid K1500 4WD	2200
2011	Mercedes-Benz	ML450 Hybrid	2200
2011	Nissan	Altima Hybrid	2350
2011	Porsche	Cayenne S Hybrid	1800

However, hybridization of vehicles is not the ultimate solution for sustainability, though it builds the pathway to a sustainable future. The technology developed along this pathway will allow the necessary transition from fossil fuel-based transportation to ultimate electrification of the transportation sector.

Electrification alone will not suffice sustainability. There will be a need for a coordinated effort along this critical path, including smarter urban planning, public transient systems, high-speed rail networks, and smarter and safer vehicles and roads. There will also be a need for a collective effort by multiple stakeholders. The power industry must increase its renewable energy and cleaner energy generation. Governments will need to develop fast rail transportation systems in and among dense metropolitan areas.

References

1. Table 1060. State Motor Vehicle Registrations: 1990 to 2007, http://www.census.gov/compendia/statab/2010/tables/10s1060.pdf (accessed September 12, 2010).
2. China's Auto Sales Rebound in August after July's Monthly Decline, http://news.xinhuanet.com/english2010/business/2010-09/09/c_13487102.htm (accessed September 12, 2010). Also, http://www.bloomberg.com/apps/news?pid=newsarchive&sid=aqqmjRJpc4Uk (accessed September 12, 2010).
3. Owen, N.A., Inderwildi, O.R., and King, D.A. (2010) The status of conventional world oil reserves – hype or cause for concern? *Energy Policy*, **38**, 4743 http://dx.doi.org/10.1016%2Fj.enpol.2010.02.026 (accessed September 12, 2010).
4. US Oil Demand by End-Use Sector (1950–2004), http://www.eia.doe.gov/pub/oil_gas/petroleum/analysis_publications/oil_market_basics/dem_image_us_cons_sector.htm (accessed September 12, 2010).
5. International Energy Outlook. United States Energy Information Administration (2007) Petroleum and Other Liquid Fuels, May, http://www.eia.doe.gov/oiaf/archive/ieo07/pdf/oil.pdf (accessed September 12, 2010).

6. Williamson, S.S. and Emadi, A. (2005) Comparative assessment of hybrid electric and fuel cell vehicles based on comprehensive well-to-wheels efficiency analysis. *IEEE Transactions on Vehicular Technology*, **54** (3), 856–862.
7. Imai, S., Takeda, N., and Horii, Y. (1997) Total efficiency of a hybrid electric vehicle. Proceedings of the Power Conversion Conference, Nagaoka.
8. Rousseau, A. and Sharer, P. (2004) Comparing Apples to Apples: Well-to-wheel Analysis of Current ICE and Fuel Cell Vehicle Technologies. Argonne National Laboratory, http://www.transportation.anl.gov/pdfs/HV/300.pdf (accessed January 27, 2011).
9. Sanna, L. (2005) Driving the Solution – the Plug-in hybrid Vehicle, http://mydocs.epri.com/docs/CorporateDocuments/EPRI_Journal/2005-Fall/1012885_PHEV.pdf (accessed January 27, 2011).
10. The Energy Report, http://www.window.state.tx.us/specialrpt/energy/exec/fuel.html (accessed January 27, 2011).
11. World Population, http://www.google.com/publicdata?ds=wb-wdi&met=sp_pop_totl&tdim=true&dl=en&hl=en&q=world+population (accessed January 27, 2011).
12. Annual Update on the Automotive Fuel Economy Program, http://icsw.nhtsa.gov/cars/rules/CAFE/overview.htm (accessed January 27, 2011).
13. The World Factbook, Oil Consumption by Country, https://www.cia.gov/library/publications/the-world-factbook/rankorder/2174rank.html (accessed January 27, 2011).
14. Global, Regional, and National Fossil Fuel CO_2 Emissions, http://web.archive.org/web/20080508060713/http://cdiac.esd.ornl.gov/trends/emis/tre_glob.htm (accessed January 27, 2011).

2

Concept of Hybridization of the Automobile

2.1 Vehicle Basics

2.1.1 Constituents of a Conventional Vehicle

Present-day engine-propelled automobiles have evolved over many years. Today's automobiles initially started with steam propulsion and later transitioned into ones based on the internal combustion engine (ICE). The focus of this section will be on ICE vehicles. So, the vehicles we use nowadays have diesel or gasoline (or petrol, as it is called in countries outside North America) engines. The engine provides the power to drive the vehicle. An illustration of an ICE is shown in Figure 2.1.

The engine has a chamber where gasoline or diesel is ignited, which creates a very high pressure to drive the pistons. A piston is connected through a reciprocating arm to a crankshaft, as shown in Figure 2.1. The crankshaft is connected to a flywheel which is then connected to a transmission system. The purpose of the transmission system is to match the torque speed profile of the engine to the torque speed profile of the load. Figure 2.2 shows a simplified diagram of a transmission system connected to an engine and a few intermediate devices.

The shaft from the transmission system is ultimately connected to the wheels through some additional mechanical interfaces such as differential gears. The overall vehicular system is shown in Figure 2.3 with the basic system-level constituent elements in a present-day vehicle.

Figure 2.3a, b shows the cutaway views of a hybrid and a regular vehicle which indicate the complexity and tight packaging of numerous components within the confines of a small space in present-day automobiles.

2.1.2 Vehicle and Propulsion Load

The power generated from the engine is ultimately used to drive a load. In an automobile this load includes the road resistance due to friction, uphill or downhill drive related

Hybrid Electric Vehicles: Principles and Applications with Practical Perspectives, First Edition.
Chris Mi, M. Abul Masrur and David Wenzhong Gao.

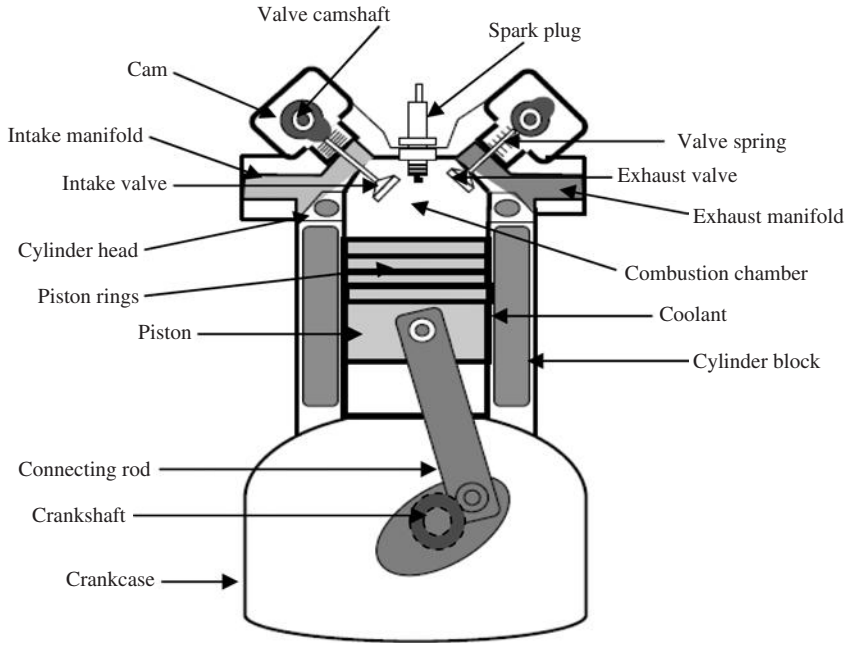

Figure 2.1 Cutaway view of an ICE

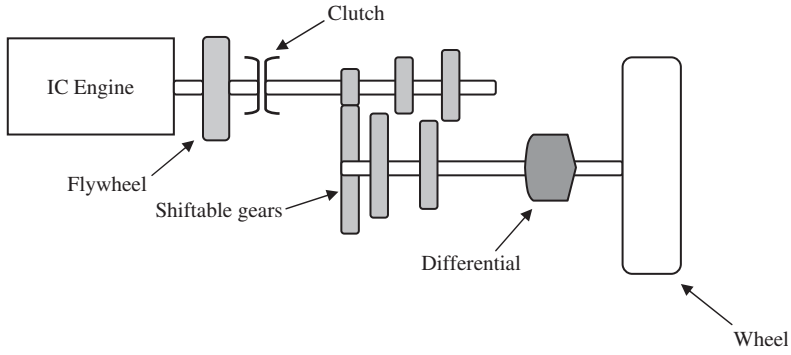

Figure 2.2 Transmission system and engine connected together

to the road profile, and the environmental effect of, for example, the wind, rain, snow, and so on. In addition, some of the energy developed in the vehicle is wasted in overcoming the internal resistance within the vehicle's components and subsystems, none of which are 100% efficient. Examples of such subsystems or components include the radiator fan, various pumps, whether electrical or mechanical, motors for the wipers, window lift, and so on. These items are just a few examples from a whole list of vehicular loads. The energy lost in these devices is released eventually as heat and expelled into the atmosphere.

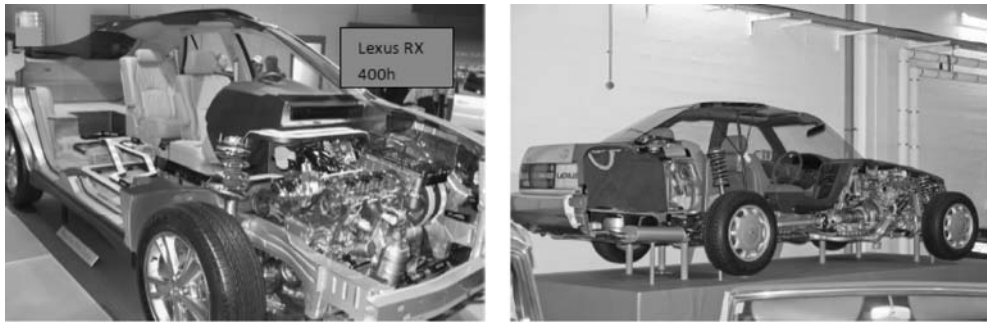

(a) (b)

Figure 2.3 (a) Cutaway view of a Lexus RX 400h. (b) Cutaway view of a Lexus LS 400. (Courtesy Wikimedia, http://en.wikipedia.org/wiki/File:Lexus_RX_400h_cutaway_model.jpg; http://commons.wikimedia.org/wiki/File:Lexus_Cutaway_LS_400.jpg.)

Normally "load" can be related to the amount of opposing force or torque. But a more scientific definition of load comes from the fact that it is not defined by a single number or numerical value. Load is a collection of a set of numbers defined by the speed–torque or speed–force characteristics in the form of a table or graph, that is, through a mathematical equation relating speed and torque. Similarly the engine is also defined by speed–torque characteristics in the form of a table or graph, that is, through a mathematical equation. The operating point of the combination of the engine and the load system together will then be at the intersection of these characteristics. This situation is shown in Figure 2.4.

A complete vehicle or automotive system has various loads. Some of these are electrical devices, and others are mechanical devices. The electrical loads are normally run at a low voltage (nominally 12 V). The reason for this, i.e. running the non-propulsion loads at

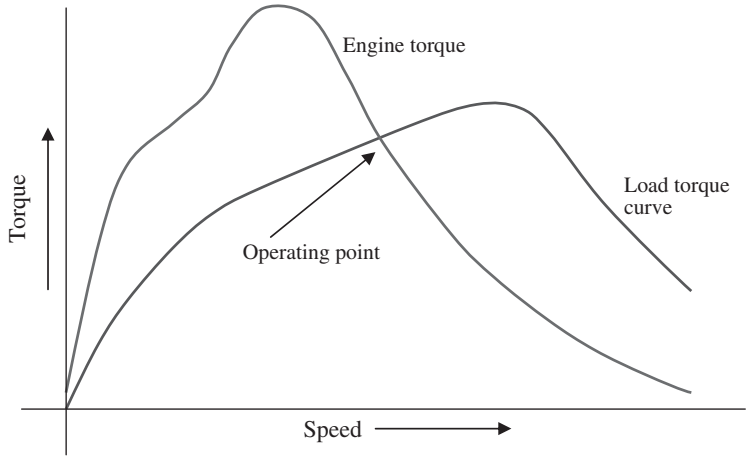

Figure 2.4 Load and engine characteristics of a vehicle

low voltage, is primarily related to safety issues. There is an existing manufacturing base for many of these non-propulsion loads (as indicated below), where it is easier to take advantage of the situation and use the existing low-voltage components, rather than transform the voltage system. Examples of these loads are:

- brakes – mechanical (hydraulic or low-voltage electrically assisted);
- air-conditioner – generally mechanical;
- radiator fan – can be belt driven mechanically (or low-voltage electrical);
- various pumps – can be mechanical (or low-voltage electrical);
- window lift – electrical;
- door locks – electrical;
- wipers – electrical;
- various lights – non-motor load, low-voltage electrical;
- radio, TV, GPS – non-motor, low-voltage electrical;
- various controllers – for example, engine controller, transmission controller, vehicle body controller;
- and various computational microprocessors – non-motor, low-voltage electrical.

2.1.3 Drive Cycles and Drive Terrain

Since a vehicle will be driven through all kinds of road profiles and environmental conditions, to exactly know beforehand about which loads the vehicle will encounter under all circumstances is difficult. It is of course possible for one to perform experiments and place sensors etc. to monitor the speed and torque of a vehicle, but to do so under all circumstances for all vehicle platforms is simply impossible. Hence, for the sake of engineering studies, a few limited situations have been developed which more or less cover typical road profiles and the terrains one can expect to encounter. Using a few of these profiles, one can create or synthesize various arbitrary road profiles. Such profiles can involve things like driving within a city, on a highway, across some special uphill or downhill terrain, to name but a few. Drive cycles only provide time, and corresponding speed fluctuations, and labels attached to these tell us what kind of drive cycle it is, for example, city, highway, and so on. Drive cycle data by itself does not reveal the terrain; it is the label attached to the data which tells what the drive cycle has undergone. One possible drive cycle is shown in Figure 2.5 (www.epa.gov/oms/standards/light-duty/udds.htm).

So, if a vehicle goes through different driving situations, partly city, partly highway, and so on, then one can obtain speed vs. time data by synthesizing multiple typical drive cycles.

The question then arises about the ways to utilize the drive cycle information. Assume that we want to know about the fuel economy of a particular vehicle X. It is not sufficient to say that vehicle X does 25 MPG. We also need to say under what conditions this was obtained. That is, whether it was under a city drive cycle, or highway drive cycle, and so on. Then one can compare another vehicle Y against X, under similar drive cycle conditions, and make a fair comparison.

As there are different kinds of drive cycles, that of a passenger car cannot be compared against the drive cycle of a refuse truck or a postal mail vehicle, since they have very

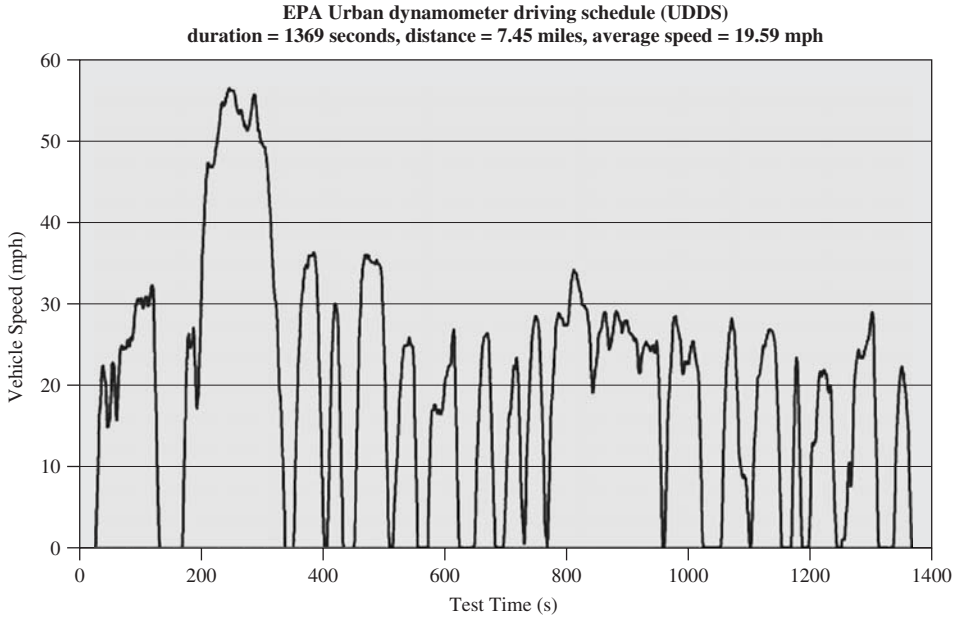

Figure 2.5 A typical automotive drive cycle. (Courtesy US EPA, www.epa.gov/oms/standards/light-duty/udds.htm.)

different kinds of stop and go driving. Similarly the drive cycle of a heavy mining vehicle cannot be compared with the above either. We will say more about this in a later chapter on off-road vehicles. The bottom line is that drive cycles allow us to make a fair comparison between vehicles, in terms of fuel economy in particular, and also in terms of performance.

Finally, it should be noted that a drive cycle concerns the road profile through which a vehicle goes and hence is a situation external to the vehicle. However, the response of a vehicle to a given drive cycle, in terms of fuel economy, will be different depending on whether the vehicle is a regular ICE vehicle, fully electric vehicle (EV), hybrid electric vehicle (HEV), and so on. Hence the discussion on drive cycles above applies to the other types of vehicles as well, as discussed below.

2.2 Basics of the EV

2.2.1 Why EV?

Although these days people talk more about HEVs which have become very popular, their underlying system is complex because it has two propulsion sources. A pure EV is relatively simpler since it has only one source of energy, that is, a battery or perhaps a fuel cell. Similarly its propulsion is performed by an electric motor and the need for an ICE is not there. If the ICE is gone, the vehicle will not need any fuel injectors, various complicated engine controllers, and all the other peripherals associated with the engine and transmission. With a reduced parts count and a simpler system, it will be more reliable as well.

In addition, an EV is "virtually" a zero-emission vehicle (since nothing has technically zero emissions in a true global sense). Of course, if one considers the ultimate source of energy, by tracing the path backward from the battery to the utility industry, it will be found that the location of pollution has been essentially shifted from the vehicle to elsewhere. Furthermore, an EV is virtually quiet. In fact it can be so quiet that people have even talked about introducing artificial noise in the vehicle so that they can hear it, which is something important to know from a safety point of view. It should also be recognized that if the battery or the fuel cell technology, the single weak link in terms of technological maturity, were fully mature, that is, able to provide the necessary power and energy within a compact size and weight, the HEV would probably not be necessary. Obviously, the EV is on everyone's wish list and can be considered to be the real culminating point of automotive technology.

From a technical viewpoint, the EV has another benefit. In the ICE, which is a reciprocating engine, the torque produced is pulsating in nature. The flywheel helps smooth the torque which would otherwise cause vibration. In the EV the motor can create a very smooth torque and, in fact, it is possible to do away with the flywheel, thus saving material and manufacturing cost, in addition to reducing weight. And finally, the efficiency of an ICE (gasoline to shaft torque) is very low. The engine itself has about 30–37% efficiency for a gasoline and about 40% for a diesel engine, but by the time the power arrives at the wheel, the efficiency is just 5–10%. On the other hand, the efficiency of the electric motor is very high, on the order of 90%. The battery and power electronics to drive the motor also have high efficiency. If each of these components has an efficiency on the order of 90%, by the time the battery energy leaves the motor shaft, the overall efficiency will be something like 70%. This is still substantially higher than that in the ICE.

2.2.2 *Constituents of an EV*

As noted earlier, an EV is simpler than a HEV. Its basic system-level constituents are shown in Figure 2.6.

The complete EV consists of not only the electric drive and power electronics for propulsion, but also other subsystems to make the whole system work. In Figure 2.6, one needs a battery (or a fuel cell) to provide the electrical energy. This is shown by the block on the left which provides power to drive the electric motor. The motor is part of the EV powertrain, labeled as EVPT on the right. For each of these items, battery or EVPT, there is a controller. The battery controller can control the charging or discharging, and similarly the EVPT controller will control the speed or torque of the motor by controlling the power electronics. It should be realized that even though the blocks in the diagram are shown to be at quite different positions, in reality they could be physically very close. The reason is due to packaging and also, by positioning them nearby, it is possible to reduce the high-current and high-voltage cable lengths. Similarly, although the controllers named the FC controller (for Fuel Cell controller or battery controller) and the EVPT controller are shown separately to indicate separate functionality, in reality they could be part of the same physical box and could even share the same microprocessors to achieve their functions. These aspects are subtle design issues involving cost and packaging. In addition, there is a box shown as the "Interface." This is the controller box that receives signals and also power, both high voltage for propulsion and low voltage for certain specific devices

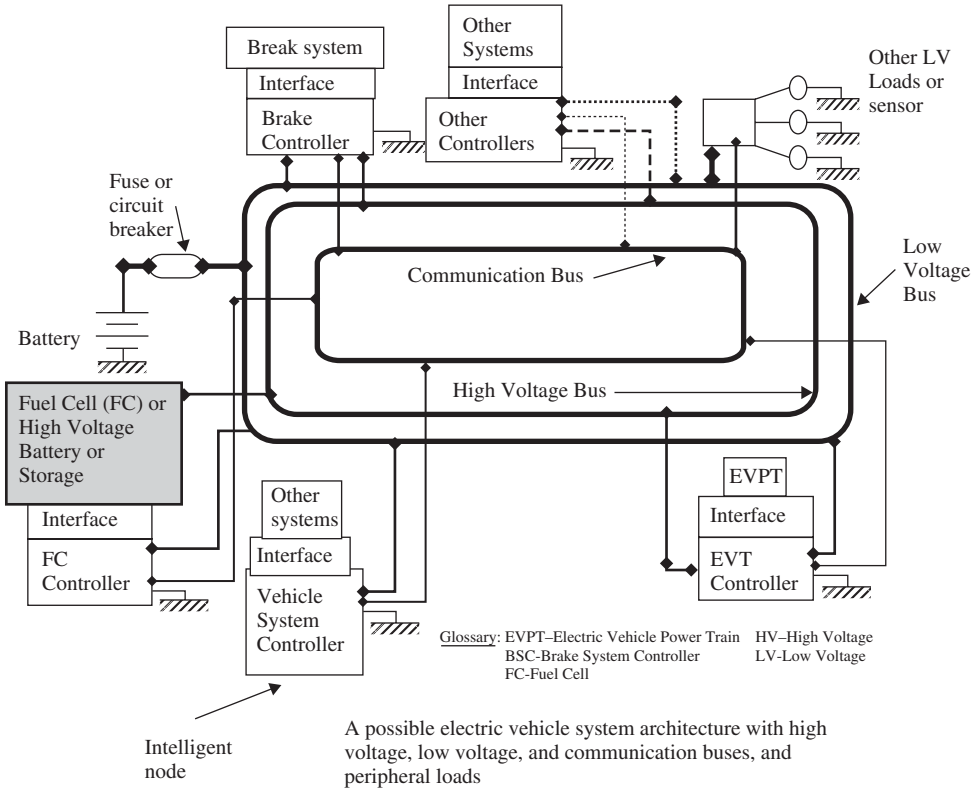

Figure 2.6 System-level diagram of an EV. (From [1], © [2008] IEEE.)

which operate at low voltage, and then through the "interface" function channelizes them to the EVPT motor or the high-voltage battery. Again, these function separation blocks may be merged when physically integrating the system.

In addition to the above blocks, there are various other blocks, for example, the vehicle controller, which can receive signals on the velocity of the vehicle, driver pedal position, and so on, and make a decision whether additional torque is needed from the motor or not. Based on that information it can send the signal to the EVPT controller with the appropriate torque request. Similarly the brake controller can receive signals corresponding to brake pedal position, vehicle velocity, and so on, and decide how much brake force is needed. It can also receive signals like the battery's state of charge and can figure out whether the opportunity of regenerative braking is present. If it is possible, it can then send signals to the EVPT controller to carry this out. All this illustrates the importance of continuous flow of information and signals between various control blocks and corresponding decision making in each subsystem.

Information transmission between various blocks is normally done through a controller area network (CAN) bus. This is basically a type of computer network where a single wire can contain multiple information or communication signals multiplexed together. Some sort of protocol has to be used when multiple signals are to be shared. In other words,

there is some sort of priority-based signal flow when trying to share the same physical medium. For relatively slow signals, for example, to turn the door lock switch, one can afford to wait, whereas for very important functions like braking and steering, which are safety functions, the signals need to be transmitted immediately. There are some newer protocols which can allow such activities. In addition, for safety-critical functions, it may be necessary to have additional hardware-based backup communication mechanisms, so as to avoid failures.

2.2.3 *Vehicle and Propulsion Loads*

There is a significant amount of commonality between the loads in an EV and a regular automobile. Hence, just like a regular vehicle, some of these loads are electrical devices and others are mechanical devices. As noted earlier, those loads which are electrical normally run at a low voltage (nominally 12 V), with the exception of the propulsion load, that is, the propulsion motor, which runs at a high voltage (several hundred volts). The reason for this has to do with safety primarily. And, of course, the existing manufacturing base for many of these non-propulsion loads can be used to advantage by using the existing low-voltage components, rather than transforming the voltage system. Examples of these loads are same as those noted in Section 2.1.2:

- propulsion or traction motor – high-voltage electrical load;
- brake motor (if a fully or partially electrical brake system is used) – low voltage;
- air-conditioner motor (if electrical) – low voltage;
- radiator fan (if electrical) – low voltage;
- various pumps (if electrical) – low voltage;
- window lift – low voltage;
- door locks – electrical;
- wipers – electrical;
- various lights – non-motor load, low-voltage electrical;
- radio, TV, GPS – non-motor, low-voltage electrical;
- various controllers, for example, engine controller, transmission controller, vehicle body controller; and
- various computational microprocessors, digital signal processors (DSPs) – non-motor, low-voltage electrical.

The above list more or less covers the various loads in the vehicle, including propulsion loads. The propulsion load can be several kilowatts for a mild hybrid vehicle regenerative braking system, up to say 50 kW or a few hundred kilowatts for propulsion in a hybrid vehicle. The various pumps and fans can be only a few hundred or less watts, whereas some small motors like door lock motors could be just a few tens of watts. Similarly the lights can range from a few tens to about a hundred watts.

The above loads are fed by the battery, the generator, or a combination of the two. We can also see from Figure 2.6 that the non-propulsion loads are fed by the low-voltage battery. This low voltage can be derived either by a part of the main high-voltage battery system, or through the transformation of the high-voltage system by a DC–DC

downconverter; it could even be a totally separate low-voltage battery with its own generator system to charge it. In other words, more than one architecture is possible for the low-voltage system.

2.3 Basics of the HEV

2.3.1 Why HEV?

In the previous section we discussed the architecture of a purely EV. As we saw, the EV propulsion uses an electric motor for propulsion. The energy comes from the battery (or perhaps a fuel cell). The battery bank in a pure EV can be quite large if the vehicle is to go a few hundred miles on one full charge to begin with. The reason for this is that battery technology, as it stands today, does not have a very high energy density for a given weight and size, compared to a liquid fuel like gasoline. Although new batteries like lithium-ion batteries have a much higher energy density than the existing lead acid or nickel metal hydride batteries, it is still much lower compared to liquid fuel.

As noted earlier, the HEV is a complex system since it has two propulsion sources. Comparatively a pure EV is simpler since it has only one source of energy, namely, a battery or perhaps a fuel cell. In the EV the propulsion is produced by only the electric motor and there is no ICE. This removes the need for fuel injectors, complicated engine controllers, and all other peripherals. Hence, with a reduced parts count, the system is simpler and more reliable.

Of course, there is an efficiency improvement in the HEV compared to the ICE, but it will still be lower than in the EV. The overall efficiency will depend on the relative size of the ICE and the electric propulsion motor power.

A variant of the HEV is found in locomotives and in very high powered off-road vehicles. In a number of variants of such systems there is no battery. The ICE is used to drive a generator which creates AC power. This power is translated to DC and then to another AC power required to drive an electric motor. The problem with this system is that the engine has to be run continuously to produce the electricity. The advantage is that it does not need a battery. Furthermore, the ICE can be run at an optimal speed to achieve the best possible efficiency. One problem with this system is that it does not lend itself to regenerative energy recovery during braking. The battery helps regenerative energy recovery by allowing storage and it can also be coordinated more optimally in terms of when the ICE or the electric motor should be run. More on this will be presented in a later chapter.

2.3.2 Constituents of a HEV

As noted earlier, an EV is simpler than a HEV. The basic system-level constituents for a HEV are shown in Figure 2.7 [1].

As we can see, the only difference between this diagram and the one for the EV is that this one has an additional subsystem called IC engine, along with the necessary interface and the controller. Otherwise the two diagrams are identical.

All the other items and the discussion are the same as for the EV.

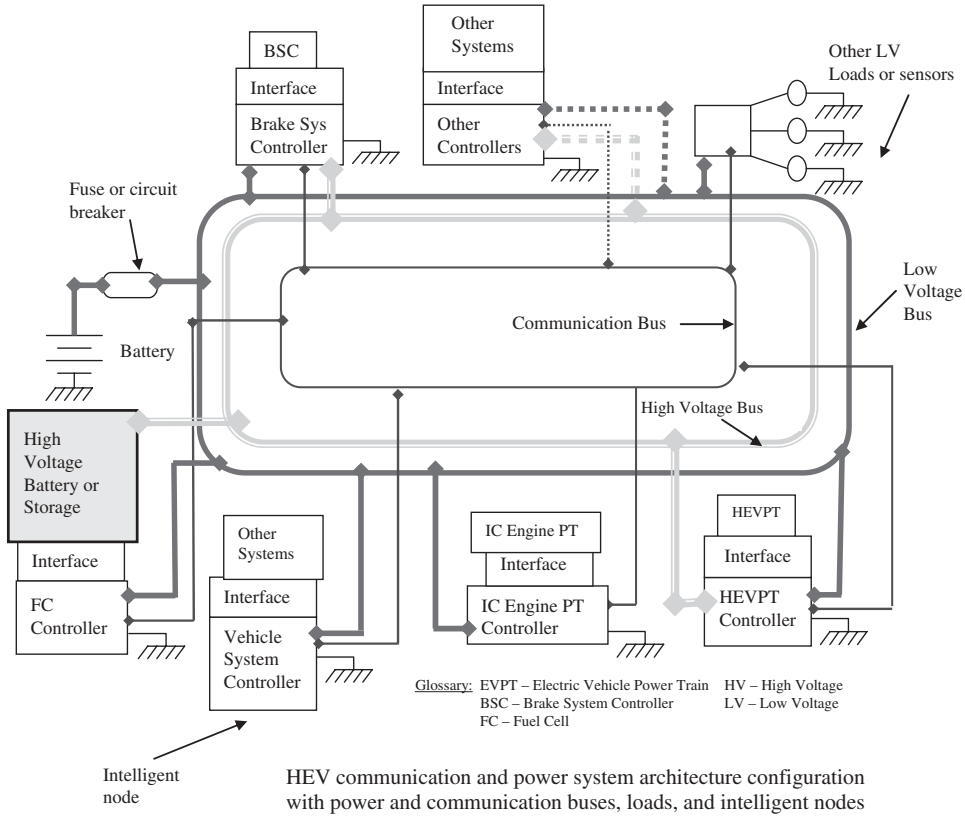

Figure 2.7 System-level diagram of a HEV. (From [1], © [2008] IEEE.)

2.4 Basics of Plug-In Hybrid Electric Vehicle (PHEV)

2.4.1 Why PHEV?

The PHEV, as the name suggests, differs from a HEV only by the fact that it allows one to plug in a cable running from the vehicle to a household utility wall socket at home or elsewhere to charge the vehicle's battery. To extend the flexibility of the system, it is also possible in principle to use the engine and/or the battery system in the vehicle to generate AC power and feed it back to the utility grid. Since plug-in allows a fair amount of external utility system energy to drive the vehicle, it is helpful to use a larger battery than in a regular HEV. A larger battery is not a required part of the PHEV, but having one definitely benefits fuel economy and also increases the range of the vehicle when fully charged. In a HEV, using a much larger battery may not necessarily be the optimal choice in terms of design, since the ICE is always capable of kicking in, when the battery needs to be charged. People sometimes think that a large battery is mandatory for a PHEV, which may not be the case. How large the battery can be depends on the

packaging space available in the vehicle. If the battery size is small, then the benefits from the PHEV will be merely incremental, whereas if it is too big then it can be very expensive and will take longer to recharge from the utility system. Note also that the household utility system may have some limitations on how much current it can sustain in charging a battery system, hence some safeguards are necessary for the plug-in. Since the cost of utility energy at present is much lower than the price of gasoline, it makes sense to use the PHEV, where possible.

2.4.2 *Constituents of a PHEV*

The same diagram as before, that is, Figure 2.5, applies to a PHEV. The only difference is that it now has an extra connecting socket in the vehicle, from where a lead can be pulled out and plugged into the wall utility outlet. Obviously, when the vehicle is connected to a utility outlet, its propulsion motor is not needed and neither is the ICE, as far as turning the wheels is concerned. However, the vehicle may still need to use auxiliary loads (normally low-voltage loads at 12 V), the air-conditioner (can be low voltage as well), or the heater and some lights. Hence it is appropriate to deliver those loads at low voltage. If fast charging of the battery is necessary, it will also be appropriate to run the ICE and use the propulsion motor as a generator, or have a separate generator for this purpose. Depending on the scheme used, changes in the gear train system are called for. Even though the whole process of interconnection between the utility and the PHEV system is simple in principle, there are quite a few considerations to be taken into account, as will be obvious from the possible architecture for such a vehicle shown in Figure 2.8.

From Figure 2.8 it is apparent that in order to charge the battery, one path goes directly from the wall outlet to the battery, through a transformer isolation and a rectifier or DC–DC converter combination. This situation is directly involved with the plug-in part of the system. The bottom part of the figure shows that the charging process is done

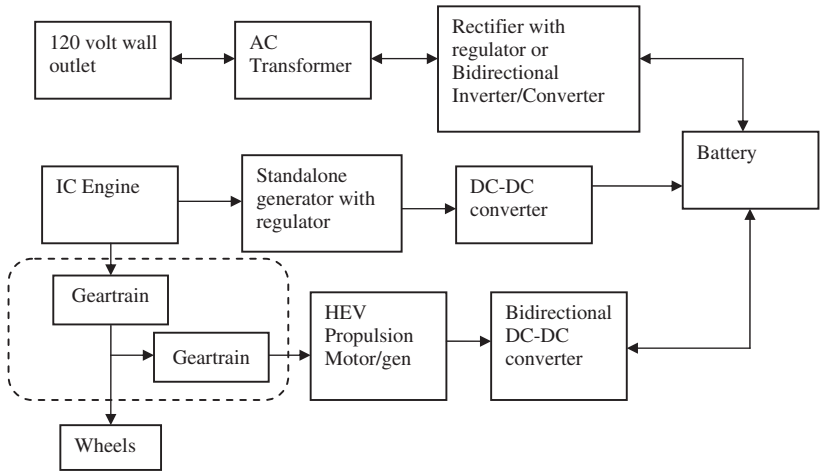

Figure 2.8 A possible architecture for the plug-in hybrid vehicle and home outlet interface

by either driving a standalone alternator, or using the propulsion motor itself run as a generator, ultimately charging the battery. Of course, it is understood that, when plugged in, the vehicle is stationary and the wheels are not moving. Even though the process indicated in the bottom part of Figure 2.8 is not involved with directly with the plug-in, an overall power management process has to coordinate both the plug-in and the ICE, since there may be a situation when fast charging becomes necessary, and both the plug-in and the ICE (in generation mode) need to run concurrently. Finally, note the inclusion of a bidirectional converter in the plug-in part of the figure. This covers the possibility that in future the utility regulations may allow power to be fed back into the utility grid from the vehicle, assuming it has enough power to do so. This issue is not an immediate consideration within the automotive industry at present. However, the possibility may in fact help use the vehicle as an emergency generator to light a home in case there is a utility power failure.

2.4.3 Comparison between the HEV and PHEV

Fundamentally the only difference between the HEV and PHEV is related to the upper part of Figure 2.8, where the wall outlet is used to charge the battery. The size of the battery may be substantially different. In addition, as indicated above, the plug-in system has to be properly coordinated with the rest of the charging process and the overall power management in the vehicular system.

2.5 Basics of Fuel Cell Vehicles (FCVs)

2.5.1 Why FCV?

The FCV architecture is most closely related to the pure EV. If the power source in the EV is replaced by a fuel cell system, then potentially it could replace the battery in the EV. Even in a HEV with an ICE, if the electrical energy source for propulsion were replaced by a fuel cell, it could still be classified as a FCV, though in reality it would be a HEV. Of course, as discussed in other parts of this book on the fuel cell, it needs chemical energy in the form of either hydrogen gas which can be directly used as fuel, or natural gas with appropriate reformers. It is also possible to have certain other kinds of liquid fuels along with reformers so that the fuel can be transformed to hydrogen. In such cases it is possible do the hydrogen reformation and creation, and hydrogen consumption, by the fuel cell simultaneously, so that no additional storage for the hydrogen is necessary. Without reformers and conversion and use as it is produced, the hydrogen has to be stored in a tank. As long as sufficient fuel is present, the cell will run. Note that the fuel cell does not run on its own initially, and some warm-up is necessary. For that purpose a relatively small battery can be used, but as soon as the fuel cell is started, it will be self-sustaining and the initial energy drawn from the battery to warm up the fuel cell can soon be replenished. Advantages of the fuel cell are that it is virtually pollution free and quiet. But at present the technology has still to mature before it can replace the existing ICE-based hybrid vehicles.

2.5.2 Constituents of a FCV

The same figure which was used for the EV applies here. It can be seen from Figure 2.6 that the high-voltage source is already labeled as either a battery or fuel cell. The constituent elements are, therefore, identical to the EV.

2.5.3 Some Issues Related to Fuel Cells

One of the problems with the fuel cell is that it is a unidirectional device, that is, it can deliver power output, but, unlike a battery or ultracapacitor, it cannot receive any power back. Obviously then, the fuel cell has to be ruled out for any regenerative efforts in a vehicle. This implies that a battery or an ultracapacitor has to be introduced in order to gain a regenerative capability. It is not just for regenerative braking that a storage battery or an ultracapacitor is necessary; such storage elements also serve as mechanism by which the fuel cell can be started. This is important for both series and parallel hybrid vehicles. The battery or ultracapacitor has to be designed to meet such a starting current capability for at least half a minute, if not for longer. In addition, based on the typical drive cycle of the vehicle, an assessment has to be made about the regenerative needs of the vehicle during braking and the size of the battery or ultracapacitor should be large enough for the worst case scenario.

The second problem with the fuel cell is its sensitivity in terms of individual cell voltage. This gives an indication of the health of the fuel cell condition. If the cell voltages show a difference, that can indicate a problem. Fuel cells generally cannot handle large transients, hence a battery often helps reduce the size of fuel cell needed and protects it during large transients in the dynamic process.

The fuel cell, not the cell per se but rather the whole module, along with all the peripheral devices like a compressor, water disposal mechanism, and warming system, together lead to a relatively low overall system efficiency.

Reference

1. Masrur, M.A. (2008) Penalty for fuel economy – system level perspectives on the reliability of hybrid electric vehicles during normal and graceful degradation operation. *IEEE Systems Journal*, **2** (4), 476–483.

3

HEV Fundamentals

3.1 Introduction

Hybrid electric vehicles (HEVs) are vehicles that combine an internal combustion engine (ICE) with an electrical traction system. It usually consists of either two or more sources of energy storage devices or two or more power sources onboard the vehicle. HEVs are synonymous with vehicles that offer high fuel economy and lower emissions when compared to conventional gasoline vehicles. Hybrid vehicles combine the ICE and electrical traction machine in an efficient way so as to utilize the most desirable characteristics of both. In HEVs, the ICE is mainly used for steady state operation while the electric machine powertrain is mainly used for dynamic operation. Some of the advantages offered by HEVs are as follows:

- Efficiency-improving technology such as regenerative braking which is not available in conventional vehicles.
- Less engine idling and efficient engine operation leading to better fuel economy.
- Better drivability since electric motor characteristics better match the road load.
- Potential to reduce the emission of greenhouse gases.
- Reduced fossil fuel consumption.

HEVs can be classified based on the configuration of the drivetrain as series hybrid, parallel hybrid, series–parallel hybrid, complex hybrid, and plug-in hybrid. In this chapter, the fundamentals involving series and parallel hybrids will be the focus since advanced hybrids are covered in other chapters.

In general, when we design a HEV, we need to select the ratings for the propulsion engine, traction electric motor, generator, and energy storage based on the desired vehicle performance. After the initial design, we need to verify if the vehicle performance specifications are met. The design usually requires a modeling and simulation program and may take several iterations before final design. Thus in this chapter, we will mainly discuss vehicle road load modeling, how to specify vehicle performance and fuel economy, and two design examples for series hybrid and parallel hybrid vehicles.

Hybrid Electric Vehicles: Principles and Applications with Practical Perspectives, First Edition.
Chris Mi, M. Abul Masrur and David Wenzhong Gao.

3.2 Vehicle Model

In this section, the vehicle is modeled as a road load. The vehicle and the associated forces are illustrated in Figure 3.1 [1].

Consider a vehicle of mass M_v, moving at a velocity v, up a slope of angle α (in degrees). The propulsion force for the vehicle to move forward is termed the tractive force or driving force F_{te}. This force has to overcome rolling resistance F_{rr}, aerodynamic drag F_{ad}, the climbing resistance force F_{rg} (the component of the vehicle's weight acting down the slope), and the force to accelerate the vehicle (the acceleration force), if the velocity is not constant. The first three terms are summed together and labeled the road load force F_{RL}. The base road load force or simply road load is as follows:

$$F_{RL} = F_{rr} + F_{ad} + F_{rg} \tag{3.1}$$

The rolling resistance is produced by the hysteresis of the tire at the surface with the roadway. Under most circumstances, rolling resistance depends on the coefficient of rolling friction between the tire and the road C_f, the normal force F_N due to the vehicle's weight $M_v g$, and the gravitational acceleration g. However, if the vehicle is at rest and the force applied to the road is not great enough to overcome the rolling resistance, then the rolling resistance must exactly cancel out the applied tractive force to keep the vehicle from moving. Thus, the equation for rolling resistance is

$$\begin{aligned} F_{rr} &= -F_{te} && \text{if } v = 0 \text{ and } F_{te} < C_f M_v g \cos\left(\frac{\alpha\pi}{180^\circ}\right) \\ F_{rr} &= -C_f M_v g \cos\left(\frac{\alpha\pi}{180^\circ}\right) && \text{otherwise} \end{aligned} \tag{3.2}$$

The aerodynamic drag depends on the air density ρ (kg/m^3), coefficient of drag C_d, frontal area of the vehicle A, and the vehicle speed v. The equation for the aerodynamic drag is as follows:

$$F_{ad} = 0.5\rho C_d A v^2 \operatorname{sgn}(v) \tag{3.3}$$

where

$$\begin{aligned} \operatorname{sgn}(v) &= +1 \text{ if } v > 0 \\ &= -1 \text{ if } v < 0 \end{aligned}$$

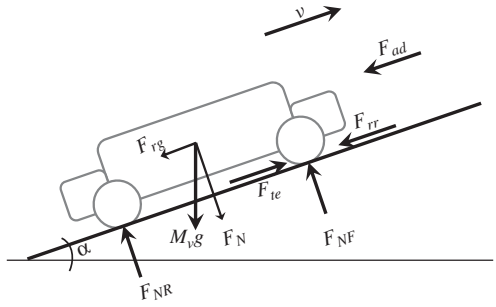

Figure 3.1 Vehicle model

The force due to the road grade depends on the mass of the vehicle M_v, road angle in degrees α, and gravitational acceleration g. The equation for this force is

$$F_{rg} = -M_v g \sin\left(\frac{\alpha\pi}{180^\circ}\right) \tag{3.4}$$

The road load curves of a vehicle for varying road angles are shown in Figure 3.2. The vehicle parameters are listed in Table 3.1. It can be observed that the road load increases with the velocity and with road angle.

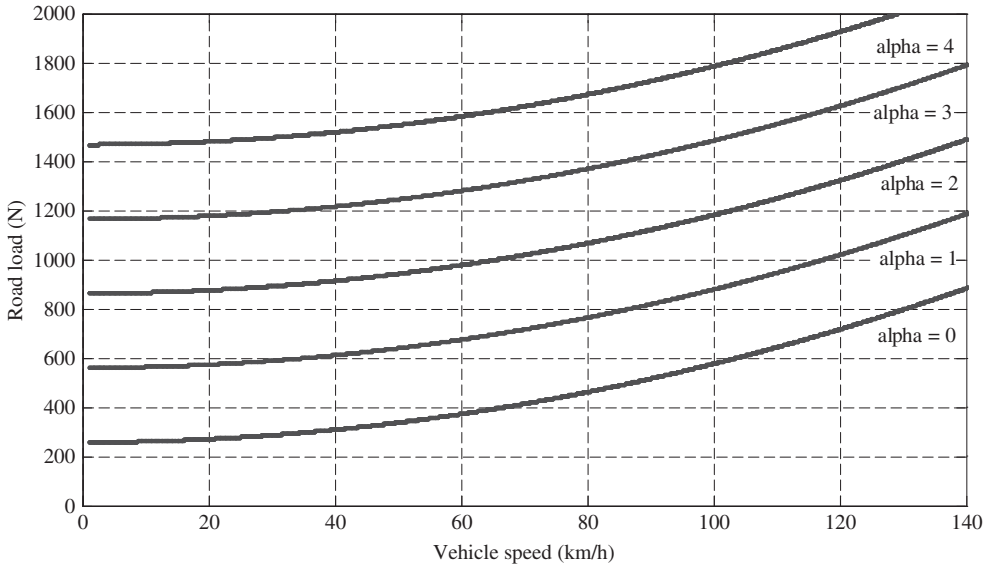

Figure 3.2 Road load characteristics for road angle $\alpha = 0^\circ$–4°

Table 3.1 Parameters for simulated vehicle

Parameters	Value	Unit
Vehicle mass	1767	kg
Gravity	9.81	m/s^2
Rolling friction	0.015	–
Air density	1.225	kg/m^3
Aerodynamic drag coefficient	0.35	–
Frontal area	1.93	m^2
Wheel inertia	3.2639	kg/m^2
Wheel radius	0.2794	m
Headwind speed	0	m/s

The acceleration force is the force needed to accelerate the vehicle, governed by Newton's second law. This force will provide the linear acceleration of the vehicle,

$$F_{acc} = M_v a = M_v \frac{dv}{dt} \tag{3.5}$$

Thus, the total tractive effort is the sum of all the above forces:

$$F_{te} = F_{rr} + F_{ad} + F_{rg} + F_{acc} \tag{3.6}$$

The vehicle's velocity is calculated by integrating the vehicle's acceleration with the starting value set to 0 km/h at $t = 0$ seconds. It is equal to

$$V = \frac{1}{M_v} \int_{t=0}^{t} \left(F_{te} - F_{rr} - F_{ad} - F_{rg}\right) dt \tag{3.7}$$

In the case of an ICE-driven vehicle, the vehicle tractive force comes from the engine shaft torque. So, the axle torque and engine torque are related by the following:

$$T_{axle} = (T_{ICE})\,(GR_{trans})\left(GR_{diff}\right)(\eta_{trans})\left(\eta_{diff}\right) \tag{3.8}$$

where T denotes torque, GR denotes gear ratio, η denotes efficiency, subscript "*trans*" denotes transmission, and subscript "*diff*" denotes differential. Thus, the tractive force is

$$F_{te} = \frac{T_{axle}}{\text{tire radius}} \tag{3.9}$$

In the case of series hybrid vehicles, the tractive force comes from traction motor shaft torque; in the case of parallel hybrid vehicles, the tractive force comes from the summation of torque produced by the ICE and electric traction motor.

3.3 Vehicle Performance

For any vehicle design, the performance constraints to be met must be defined first. These constraints are different depending on the vehicle type and size. From the powertrain point of view, typical performance specifications include initial acceleration, cruise speed, maximum speed, gradability, drive range, and so on. Acceleration rate is the minimum time required to accelerate the vehicle from 0 to a specified speed such as 40, 60, or 80 mph. Sometimes acceleration rate from a lower speed to a higher speed is specified; for example, from 40 to 60 mph. Maximum acceleration is limited by maximum tractive power and roadway condition. The gradability is the maximum grade that a vehicle can move along at a certain speed with the maximum tractive force available from the powertrain. Drive range refers to the distance, in miles or kilometers, that a vehicle can travel with a full tank of fuel and/or fully charged batteries before refueling or recharging. Satisfactory drive range of an electric vehicle (EV) or HEV is crucial for market acceptance.

The US PNGV's (Partnership for a New Generation of Vehicle's) performance goal for mid-size vehicles is as follows:

- 0–60 mph: $\leq$12 seconds
- 40–60 mph: $\leq$5.3 seconds

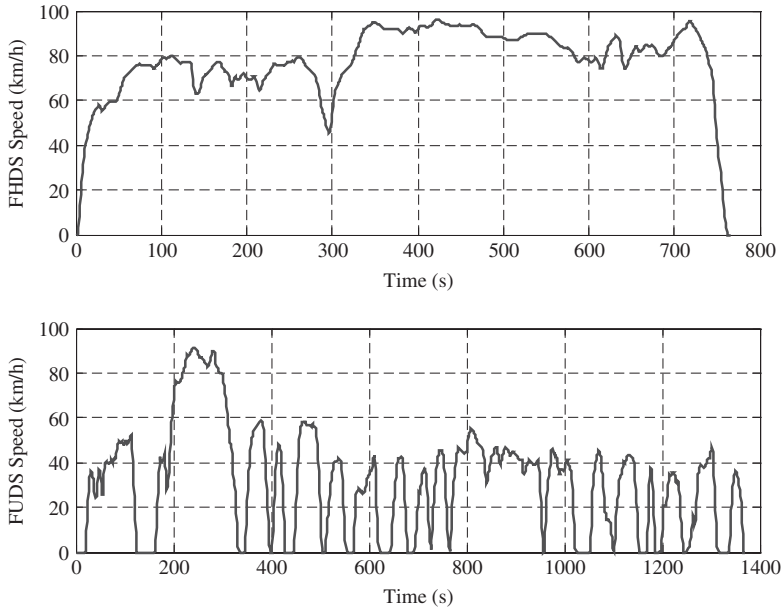

Figure 3.3 The FHDS and FUDS drive cycles

- 0–85 mph: $\leq$23.4 seconds
- Maximum speed: 85 mph
- Maximum grade at 55 mph: 6.5%.

Drive cycles are standard vehicle speed versus time profile for testing vehicle performance, fuel economy, and emissions. For example, the Federal Highway Driving Schedule (FHDS) and Federal Urban Driving Schedule (FUDS) are plotted in Figure 3.3.

The required power for operating a vehicle can be calculated from the driving cycles, depending on the mass of the vehicle. For example, the required power for driving a vehicle with a total weight of 1380 kg under US06 driving cycle is shown in Figure 3.4. US06, the aggressive driving cycle, was proposed by the US Environmental Protection Agency (EPA) to measure fuel economy and emissions. The positive power is due to acceleration while the negative power is due to deceleration. Part of the negative power corresponding to braking can be recovered through regeneration in the HEV.

Different drive cycles in different areas all over the world are used to test dynamic performance and fuel economy of different types of vehicles. At present, the drive cycles mostly come from Europe, North America, and Japan. China is also developing its own drive cycles based on Chinese road systems.

Listed in Table 3.2 are eight example drive cycles [2]: CYC_HWFET, CYC_HWFET_MTN, CYC_NYCTRUCK, CYC_NYGCT, CYC_NEWYORKBUS, CYC_UDDS_HDV, CYC_BEIJINGBUS, and CYC_CONSTANT.

From the data shown in Table 3.2, each drive cycle has different characteristics. But in general, the idle time percentage, number of stops, and time percentage in a particular speed zone affect fuel economy the most. For example, in the UDDS_HDV drive cycle,

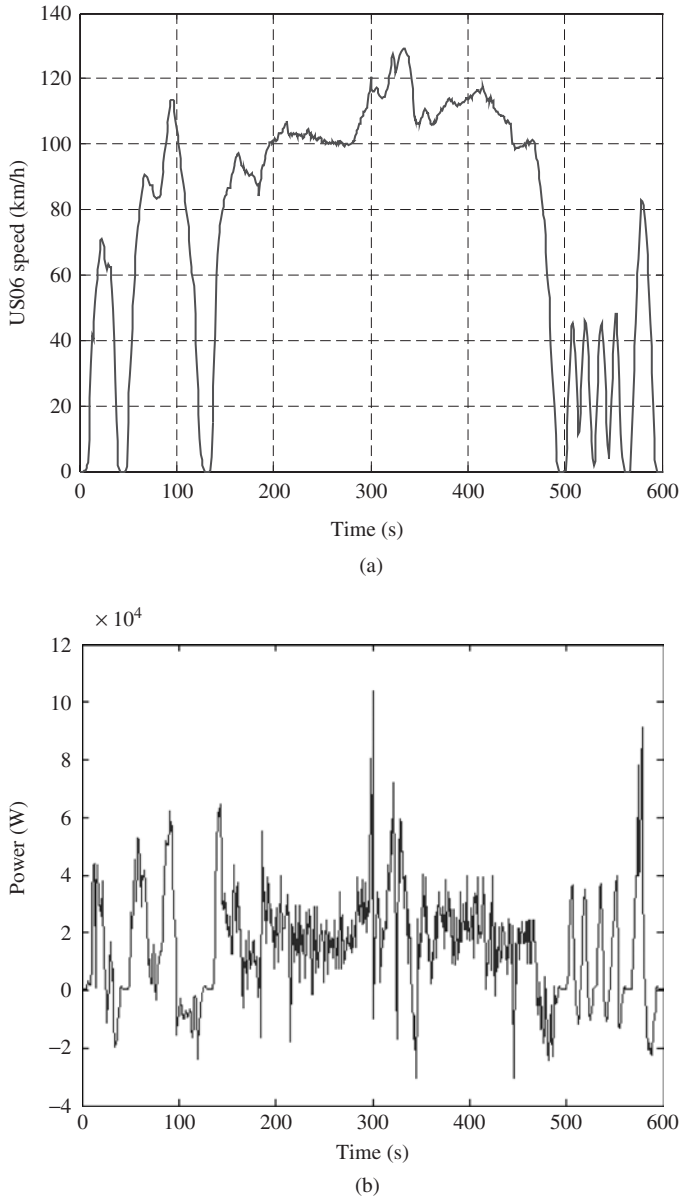

Figure 3.4 (a) The US06 drive cycle and (b) vehicle required electric power under US06 driving cycle

Table 3.2 The characteristics of example driving cycles

Drive cycle	Idle time (percentage of total time)	Stops	Time percentage in specific speed zone
CONSTANT	4	0	≤16 km/h 100%
NYGCT	68.3	5	≤5 km/h 82%
NEWYORKBUS	67.3	11	≤6 km/h 75%
NYCTRUCK	52.1	20	≤12 km/h 70%
HWFET_HTN	0.7	1	≥70 km/h 85%
HWFET	0.7	1	≥70 km/h 85%
UDDS_HDV	33	14	≤20 km/h 80%
BEIJINGBUS	59.1	23	≤20 km/h 85%

a vehicle has 14 stops and starts, 33% idle time, and runs at a lower speed of 20 km/h or less during 80% of the driving time period.

The fuel economy refers to how many miles a vehicle can travel with the consumption of per unit of fuel. One common unit is miles per gallon or MPG. For EVs or HEVs, miles per gallon gasoline equivalent (MPGGE) is used to measure how many miles a vehicle can travel with the consumption of energy equivalent to the amount released from combustion of 1 gallon of gasoline. Fuel economy of HEVs also depends on the drive cycles. Thus, sometimes, composite fuel economy or combined fuel economy is used. For example, composite fuel economy can be computed as the weighted average of the state of charge (SOC) balanced fuel economy values during the city drive cycle and highway drive cycle, as given below [3]:

$$\text{Composite fuel economy} = \frac{1}{\frac{0.55}{\text{City\_FE}} + \frac{0.45}{\text{Hwy\_FE}}} \tag{3.10}$$

where City_FE and Hwy_FE denote the city and highway fuel economy values, respectively.

Based on the vehicle road load modeling in the previous section, we can perform a parametric design study for vehicle design. For example, we can see how vehicle performance is affected by changing the values for C_f, A, C_d, and M_v.

3.4 EV Powertrain Component Sizing

In this section, several examples are given to illustrate fundamental concepts and methods for EV component sizing.

As discussed earlier, when we size the powertrain of an EV, we must ensure sufficient tractive force for the vehicle to:

- accelerate from zero speed to a certain speed within a required time limit;
- overcome wind resistance force if headwind speed is non-zero;
- overcome aerodynamic force;
- overcome rolling resistance;
- climb a certain slope (grade).

Example 3.1: As an example, let us find the approximate rating of an EV powertrain with a vehicle weight of 1364 kg. First, let us determine the forces needed to accelerate at 4.47 m/s^2, assuming that aerodynamic, rolling, and hill-climbing force counts for an extra 10% of the needed acceleration force.

$$\begin{aligned} F_{te} &= 1.1 \times \text{mass} \times \text{acceleration} \\ &= 1.1 \times 1364 \times 4.47 \text{ m/s}^2 \\ &= 6704 \text{ N} \end{aligned}$$

Then, let us determine the average power needed to accelerate the vehicle from 0 to 96.5 km/h (60 mph):

$$\begin{aligned} \text{Energy required} &= \text{mass} \times V^2/2 \\ &= 1364 \times (26.8 \text{ m/s})^2/2 \\ &= 489839 \text{ J} \end{aligned}$$

Time required for the vehicle to accelerate from 0 to 96.5 km/h is

$$\begin{aligned} \text{Time} &= (26.8 \text{ m/s}^2)/(4.47 \text{ m/s}^2) \\ &= 6 \text{ s} \\ \text{Average power} &= \text{force} \times \text{distance/seconds} = \text{energy/time} \\ &\approx 81.7 \text{ kW (peak power } P_{\max} = F_{te} \times V \approx 180 \text{ kW)} \end{aligned}$$

Example 3.2: Let us determine the tractive force needed for a 1364 kg vehicle to accelerate to 96.5 km/h in 10 seconds, assuming a constant acceleration. The total power required for acceleration is

$$\begin{aligned} \text{Acceleration } a &= V/t = 26.8/10 = 2.68 \text{ m/s}^2 \\ \text{Force } F_{te} &= \text{mass} \times \text{acceleration} = 1364 \times 2.68 \text{ m/s}^2 = 3657 \text{ N} \\ \text{Final power} &= F_{te} \times V = 3657 \times 26.8 = 98 \text{ kW (at a speed of 60 mph)} \end{aligned}$$

In this example, a constant acceleration is assumed. In real life, the acceleration near 60 mph will be greatly reduced. Therefore, the actual power needed to accelerate the vehicle is much less than 98 kW:

$$\text{Average power} = \text{final power}/2 = 49 \text{ kW}$$

Example 3.3: Assume that the vehicle accelerates according to a sine wave (Figure 3.5, top plot) to a final speed of 60 mph and ignore all other resistances. Let us find the tractive force needed for the 3000 lb vehicle to accelerate.

$$V = \int a dt = \int a_m \sin \omega t dt = -(a_m/\omega)\cos \omega t|_0^t = a_m(1 - \cos \omega t)/\omega$$

$$V_{final} = 60 \text{ mph} = 60 \times 1608/3600 = 26.8 \text{ m/s}$$

$$a_m(1 - \cos \pi)/\omega = 26.8 \qquad (\omega t = \pi \text{ at } 10 \text{ s}, \omega = 0.314)$$

$$\therefore a_m = 0.314 \times 26.8/2 = 4.2 \text{ m/s}^2$$

$$a = 4.2 \sin 0.314t$$

$$F = \text{mass} \times a = 3000/2.2 \times 4.2 \sin 0.314t = 5727 \sin 0.314t$$

$$P = FV = 5727 \sin 0.314t \times 4.2(1 - \cos 0.314t)/0.314$$

$$= 76 \sin 0.314t - 38 \sin 0.628t$$

$$P_{\max} \approx 90 \text{ kW}$$

P is also illustrated in Figure 3.5, bottom plot, where the two terms in P are plotted separately.

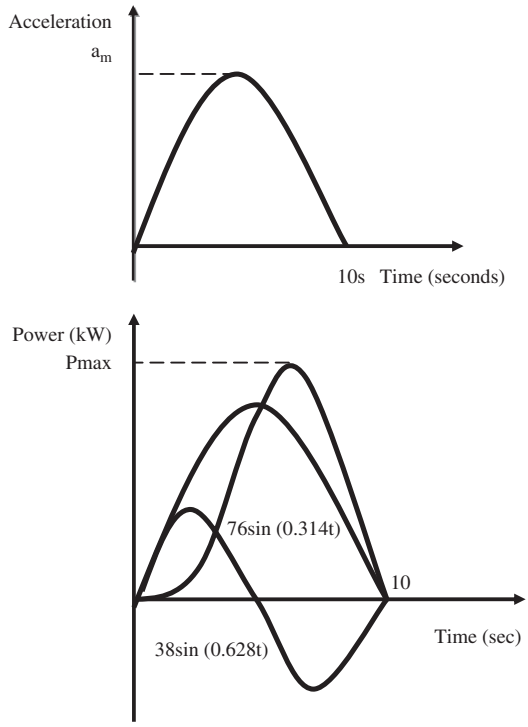

Figure 3.5 Vehicle acceleration and power

Example 3.4: In this example, we will compare the resistive and the acceleration forces of a vehicle. The acceleration force was computed in Example 3.2 where the acceleration force is 3657 N (accelerate to 60 mph in 10 seconds). The vehicle mass is 1364 kg.

1. Aerodynamic force: Consider the vehicle with the following:
   (a) Aerodynamic drag coefficient 0.109
   (b) Air density 1.16 kg/m^3
   (c) Frontal area 1.543 m^2 (or 16.6 ft^2)
   Then the aerodynamic force at 60 mph (96 km/h) is

$$F_{ad} = 0.5 \times 1.16 \times 0.109 \times 1.543 \times 26.82 = 70 \text{ N}$$

2. Rolling resistance: Consider the vehicle with a rolling coefficient of 0.02. Thus the rolling resistance force is

$$F_{rr} = 0.02 \times 1364 \times 9.8 = 270 \text{ N}$$

3. Hill-climbing resistance: Consider the vehicle with a grade of 0.5°. Thus the hill-climbing force is

$$F_{rg} = mg \times \sin\alpha = 1364 \times 9.8 \times \sin 0.5^\circ = 117 \text{ N}$$

The total resistance force on the highway is (except for acceleration)

$$F_{RL} = F_{ad} + F_{rr} + F_{rg} = 70 + 270 + 117 = 457 \text{ N}$$

$$P_r = F_{RL}V = 457 \times 26.8 \text{ m/s} = 12.3 \text{ kW(at top speed)}$$

Note that the dragging force accounts only $P_r/P_{\max} = 12.3\,\text{kW}/98\,\text{kW} = 12.5\%$ of the total tractive force.

Further, note that the power required for a vehicle to cruise on a highway at 60 mph is only about 6% of the power needed to accelerate the vehicle from 0 to 60 mph in 10 seconds. Since most electric motors can be designed to overload for a short time, a motor can be designed at much lower ratings.

Note also that an electric motor can have an efficiency (including controller) of over 90%, while an engine only has an efficiency less than 30%. Furthermore, an ICE does not have the transient overload capability as does a motor. This is why the rated power of ICE is usually much higher than required for highway cruising.

Now let us briefly look at the braking in an EV. Energy is wasted during braking in conventional vehicles, but the braking energy can be partially recovered in EVs and HEVs. Consequently, the performance of the antilock brake system (ABS) can be improved in HEVs/EVs and traction control is easier to achieve in HEVs/EVs.

Let us compute the energy expected when bringing a 1364 kg vehicle to a halt from a speed of 60 mph in 10 seconds:

$$\text{Energy} = \tfrac{1}{2} \times \text{mass} \times V^2 = \tfrac{1}{2} \times 1364 \times (26.8 \text{ m/s})^2$$
$$= 489709 \text{ J} = 0.136 \text{ kWh}$$

Using an average speed of 30 mph, the vehicle will travel 44 ft/s or 440 ft in 10 seconds. Assuming an average drag force of 100 lbf, the drag loss is

$$100 \times 4.455 \times 440/3.28 = 59762 \text{ J} = 0.0166 \text{ kWh}$$

The energy that can potentially be recovered is $0.136 - 0.0166 = 0.1194$ kWh.

The design of the complete propulsion system is a complex issue involving numerous variables, constraints, considerations, and judgment, which is beyond the scope of this book. The power and energy requirement from the powertrain is determined from a given set of vehicle cruising and acceleration specifications. EV/HEV design is an iterative process and requires many engineers from multiple disciplines to collaborate to meet design goals. Thus:

- Electrical and mechanical engineers design the electric motor for the EV or the combination of electric motor and ICE for HEVs.
- Power electronics engineers design the power conversion circuit which links the energy source with the electric motor.
- Control engineers working in conjunction with the power electronics engineers develop the propulsion control system.
- Electrochemists and chemical engineers design the energy source based on the energy requirement and guidelines of the vehicle manufacturer.

3.5 Series Hybrid Vehicle*

In the series hybrid powertrain, as illustrated in Figure 3.6, the mechanical output from the ICE is converted into electrical energy using a generator and the electrical energy is either used to charge the battery or is bypassed from the battery to the electric traction motor which propels the wheels. With respect to power electronics components, an AC–DC converter for charging the batteries and a DC–AC inverter for traction motor propulsion are required. In a series configuration, the engine is decoupled from the road load so the engine will not undergo abrupt changes in operating conditions and will have little idling time, thus emissions are reduced and this is better for the environment. Some other advantages of series hybrids are flexibility in the location of the engine–generator set and simplicity in design. However, three propulsion components are needed: the ICE, generator, and motor. This results in a longer chain of energy transmission and so the

* © [2005] IEEE. Reprinted, with permission.

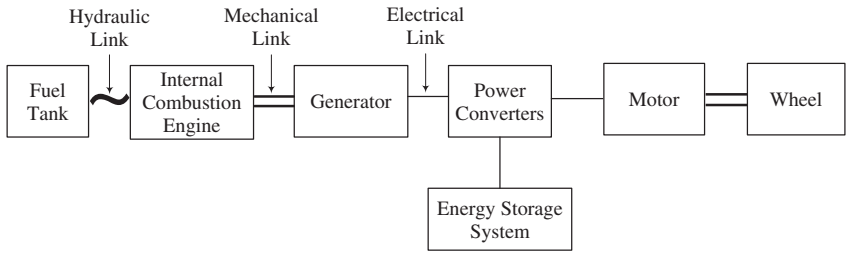

Figure 3.6 Series HEV powertrain

efficiency of series hybrids is generally lower than parallel hybrids. The motor must be designed for the maximum sustained power that the vehicle may require, such as when climbing a high grade. Nevertheless, the vehicle operates below the maximum power most of the time. All three drivetrain components need to be sized for maximum power for long-distance, sustained, and high-speed driving, otherwise the batteries will discharge fairly quickly, leaving the ICE to supply all the power through the generator. An example application for a series hybrid is in locomotive drives.

The fuel cell EV is one type of series hybrid and will be used as a design example for it [4]. In the fuel cell EV, the energy storage devices can be batteries or ultracapacitors or both. The fuel cell system supplies the base power while the battery/ultracapacitor supplies peak power for fast acceleration and captures the braking energy for regeneration. The hybridization degree is defined as

$$HD = \frac{P_{ESS}}{P_{ESS} + P_{fc}} \tag{3.11}$$

where P_{ESS} is the power of the energy storage device and P_{fc} is the fuel cell power. An HD of 0 corresponds to a pure fuel cell vehicle, and an HD of 1 corresponds to a pure EV such as a battery electric vehicle (BEV). In a hybrid fuel cell powertrain, a good control strategy is necessary to manage the power flow considering the largely different characteristics of each component. The two types of hybrid fuel cell powertrains to be studied are illustrated in Figure 3.7(a) and (b). The operating modes of this series hybrid include: (i) battery or ultracapacitor-alone mode in which the fuel cell is turned off; (ii) fuel cell-alone mode; (iii) combined mode in which both the fuel cell and energy storage provide power to the road load; (iv) fuel cell power split mode in which the fuel cell provides power for the vehicle road load and charging the battery or ultracapacitor; and (v) regenerative braking mode in which energy storage recuperates part of the braking energy.

To compare the fuel economy and performance of the two types of fuel cell hybrid powertrains, four fuel cell hybrid vehicles are designed in ADVISOR. The first design case in ADVISOR is the default fuel cell vehicle with a battery and is used as a baseline vehicle (input file name: FUEL_CELL_defaults_in). The hypothetical small car is roughly based on a 1994 Saturn SL1 vehicle with the main data listed in Table 3.3. The fuel cell is the type of ambient pressure hydrogen fuel cell system. A one-speed gearbox is used for the transmission. The powertrain controller uses the hybrid with a thermostat control strategy as defined in ADVISOR [3, 5]. In brief, the fuel cell is controlled to be off when the energy storage SOC achieves a predetermined upper limit and is controlled to be on

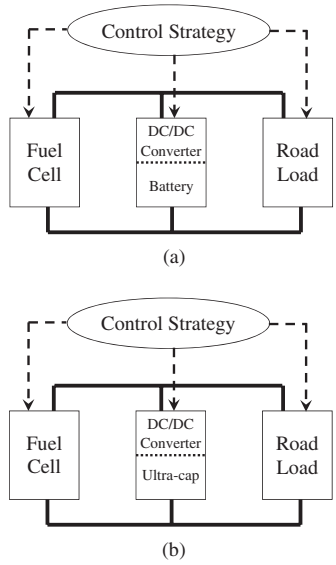

Figure 3.7 Configurations of fuel cell hybrid powertrains

Table 3.3 Assumed parameters for the vehicle

Parameters	Value	Unit
Vehicle glider mass, m	592	kg
Gravity, g	9.81	m/s^2
Rolling resistance coefficient, f_r	0.009	–
Transmission efficiency, η_t	0.92	–
Air density, ρ_a	1.2	kg/m^3
Aerodynamic drag coefficient, C_d	0.335	–
Frontal area, A_f	2.0	m^2
Wheel radius	0.282	m
Average electrical accessory load	700	W
Vehicle cargo mass	136	kg
Electric motor mass	91	kg
Fuel cell system mass	223	kg

when the SOC drops below a predetermined lower limit. The designs of the fuel cell and energy storage are described in more detail below.

In the hybrid powertrain, the fuel cell supplies the base power, P_e, to meet the vehicle power requirement for cruising and/or driving on a road with a grade [6, 7]:

$$P_e = \frac{(mgf_r + \frac{1}{2}\rho_a C_d A_f V^2 + mgi)V}{1000\eta_t \eta_{em}} \tag{3.12}$$

where m is the vehicle total mass (assumed to be 1380 kg), i is the road grade, and η_{em} is the motor average efficiency (assumed to be 0.90). Then, by calculation, P_e is 13.1 kW at

a cruising speed of 60 mph (96 km/h) on a flat road; P_e is 42.1 kW at a maximum speed of 95 mph (152 km/h) on a flat road; and P_e is 50.0 kW if the maximum grade at 55 mph is 10%. This determines the size of the fuel cell for steady driving.

The maximum total electric power required for vehicle acceleration from 0 to 60 mph in 11 seconds is [8]

$$P_{tot} = \frac{\left(mgf_r + \frac{1}{2}\rho_a C_d A_f V^2 + m\delta\frac{dv}{dt}\right)V}{1000\eta_t\eta_{em}}, \tag{3.13}$$

where δ is the mass factor (assumed to be 1.035). The maximum P_{tot} is computed to be 124.8 kW.

Based on the above calculation, the net peak power of the fuel cell system is designed to be 50 kW and the battery size at least 75 kW (including electrical accessory load). A Westinghouse 75 kW (continuous) AC induction motor/inverter with a peak efficiency of 0.92 is used in the powertrain.

In summary, the four design cases are:

- **Case 1 (baseline):** 25 modules of lead acid (Hawker Genesis 12 V, 26 Ah 10EP VRLA) batteries are used; battery peak power is 86.35 kW; total vehicle mass is 1380 kg.
- **Case 2:** 85 cells of Maxwell ultracapacitors are used; ultracapacitor peak power is 86.0 kW; total vehicle mass is 1140 kg (the same hybridization degree as Case 1).
- **Case 3:** 170 cells of ultracapacitors are used (twice those in Case 2); ultracapacitor peak power is 172.0 kW; total vehicle mass is 1174 kg.
- **Case 4:** 50 modules of lead acid battery are used (twice those in Case 1); battery peak power is 172.8 kW; total vehicle mass is 1655 kg.

As a double check, the total required electric power under the US06 driving cycle for Case 1 is given in Figure 3.4(b). Note that the maximum total power required is about 105 kW at a time instant near 300 seconds. This is close to (but smaller than) the above maximum P_{tot} of 124.4 kW. So our design does satisfy the vehicle road load power requirement.

The assumptions for the battery and ultracapacitor are given in Table 3.4 [3, 9]. The peak power, energy storage capacity, weight, and cost of the two types of fuel cell hybrid powertrains are compared in Table 3.5.

Note that the designed fuel cell vehicles have large power rating energy storage devices because the fuel cell vehicle is a series hybrid [10]. Thus, the fuel cell system can be considered as an auxiliary power unit, which is controlled to run at its optimum efficiency region.

Table 3.4 Energy storage system assumptions

	Weight per cell (kg)	Specific power (W/kg)	Specific energy (Wh/kg)	Cost ($/kW)
Battery	11	314.6	28.4	10
Ultracapacitor	0.408	2500	6	15

Table 3.5 Energy storage system comparison

	Peak power (kW)	HD	Energy storage capacity (kWh)	Weight (kg)	Cost ($)
Case 1 (battery)	86.4	0.63	7.81	275	864
Case 2 (ultracapacitor)	86.4	0.63	0.21	35	1296
Case 3 (ultracapacitor)	172	0.78	0.42	71	2580
Case 4	172.8	0.78	15.62	550	1728

In the simulation studies, energy management strategies (series thermostat control strategy [11]) remain the same in all cases. The highest desired SOC is 0.8; the lowest desired SOC is 0.4. The initial SOC for the battery and ultracapacitor is set to the same value (0.7) for all cases. The simulations are run under three different driving schedules: UDDS (Urban Dynamometer Driving Schedule), HWFET (Highway Fuel Economy Test), and US06 (aggressive driving cycle). The fuel economy in terms of MPGGE for the four cases is compared in Table 3.6. The MPGGE is calculated based on the lower heating value of gasoline (42.6 kJ/g), density of gasoline (749 g/l), and total energy consumption from the energy storage system. The detailed definition of MPGGE is given in [3].

From the numbers in the table, Case 2 with an ultracapacitor has a higher fuel economy than Case 1. Increasing the modules of the ultracapacitor from Case 2 to Case 3 does not increase fuel economy (the difference is small). Increasing the modules of batteries from Case 1 to Case 4 decreases fuel economy.

The simulated vehicle performance is listed in Table 3.7. Specifically, the performance indices include the times for the vehicle to accelerate from 0 to 60 mph, from 40 to 60 mph, and from 0 to 85 mph; the maximum achievable speed; and the maximum sustainable grade at 55 mph. The last row also lists the PNGV performance constraints for a mid-size car [9]. From the numbers given, Case 1 has a better performance than Case 2. Increasing the modules of the ultracapacitor from Case 2 to Case 3 greatly improves the vehicle performance. As a result, the fuel cell–ultracapacitor hybrid (Case 3) has a much better performance than the baseline fuel cell–battery hybrid (Case 1). Increasing the modules of batteries from Case 1 to Case 4 also improves the vehicle performance.

From the simulation results in Tables 3.6 and 3.7, with the same hybridization degree (0.63), the fuel cell–ultracapacitor hybrid vehicle's fuel economy is higher by about 30% than its battery counterpart, but the performance is worse. If more ultracapacitors are used with a hybridization degree of 0.78, the vehicle performance can be improved tremendously, while the fuel economy is maintained roughly at the same high level.

Overall, the fuel cell–ultracapacitor hybrid is better since ultracapacitors can more effectively assist the fuel cell to meet transient power demand. If more ultracapacitors

Table 3.6 Fuel economy (MPGGE)

	Case 1	Case 2	Case 3	Case 4
UDDS (four cycles, 29.8 miles (47.7 km))	58.5	75.8	73.3	50.9
HWFET (four cycles, 41 miles (66 km))	78.7	84.4	83.2	74.7
US06 (four cycles, 32 miles (51 km))	58.7	64.1	63.1	56.8

Table 3.7 Simulated vehicle performance

	0–60 mph (s)	40–60 mph (s)	0–85 mph (s)	Maximum speed (mph)	Maximum grade at 55 mph (%)
Case 1	11.1	5.8	22	97.6	9.8
Case 2	19.2	13.6	44.5	95.0	12.0
Case 3	6.9	3.2	36	95.1	11.7
Case 4	8.2	4.0	16	97.2	8.0
PNGV constraints	≤12	≤5.3	≤23.4	85	6.5

are added, the performance is improved, while the fuel economy remains high. Although battery modules can also be increased for a fuel cell–battery hybrid, only the performance can be improved, while the fuel economy will be decreased as shown by Case 4. The battery has a higher specific energy than an ultracapacitor. But in a charge-sustaining hybrid powertrain, this is not necessarily an advantage since the range is determined by the fuel tank volume. As demonstrated in this chapter, higher specific power characteristics of ultracapacitors are a big advantage for hybrid fuel cell powertrains, which can enhance both the fuel economy and vehicle acceleration performance. In addition, the characteristics of allowing a wide variation of SOC also enable the ultracapacitor to more effectively assist the fuel cell to meet the vehicle power demand and to help achieve a better performance and higher fuel economy.

3.6 Parallel Hybrid Vehicle

In a parallel hybrid powertrain, more than one energy source can provide propulsion power. In this hybrid system, the ICE and the motor are coupled in many possible ways. The propulsion force may be supplied by the ICE alone, by the electric motor alone, or both. The electric motor can operate as an electric generator to charge the battery during regenerative braking or when the ICE output power is greater than the required power at the wheels. A smaller ICE and a smaller motor can be selected to obtain a similar performance in the non-hybrid counterpart. Parallel hybrids can offer lower cost as compared to series hybrids. However, one disadvantage is that the former need a complex control system. In a parallel hybrid vehicle, the ICE and the electric motor can separately provide the propulsion force. Figure 3.8 shows a block diagram for one possible parallel hybrid vehicle, which is a "through the road" four-wheel-drive hybrid.

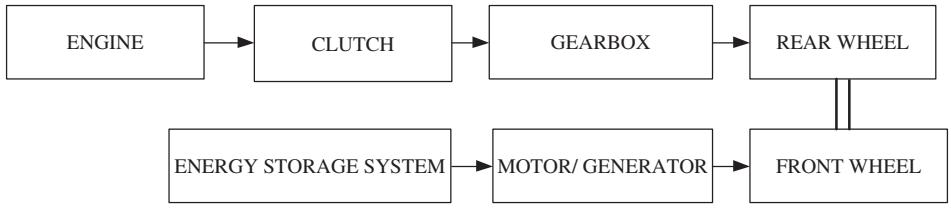

Figure 3.8 "Through the road" parallel hybrid powertrain

Based on the location of the gearbox or transmission, the parallel hybrid can be further classified as follows:

1. **Pre-transmission parallel hybrid:** This is also known as the engine–transmission–motor system. In this system, the gearbox is located on the main drive shaft after the torque coupler; as a result, the gear speed ratios apply on both the engine and the electric motor. Power flow is summed at the gearbox. Also the torque from the motor is added to the torque of the engine at the gearbox input shaft.
2. **Post-transmission parallel hybrid:** This is also known as the engine–motor–transmission system. In this system, the gearbox is located before the torque coupler as a result, gearbox speed ratios apply only on the engine. In this system, the torque from the motor is added to the torque of the engine at the gearbox output shaft.
3. **"Through the road" parallel hybrid:** This belongs to the class of parallel hybrids. The ICE-based powertrain propels one axle and the electric traction motor propels another axle. The design of the hybrid powertrain is simplified since the above two powertrains are decoupled.

3.6.1 Electrically Peaking Hybrid Concept

The electrically peaking hybrid (ELPH) concept was proposed by the HEV Research Group from Texas A&M University, and is a parallel control strategy. The electric traction motor is controlled to accommodate the acceleration and deceleration power while the ICE is controlled to provide the average power of the vehicle load. The main goal of this control strategy is to operate the ICE in the high-efficiency torque–speed region and thus increase ICE fuel economy while reducing harmful emissions. Also, the battery SOC is maintained within a predetermined range by this control strategy during the vehicle driving period [12].

In this section, the design of a parallel hybrid vehicle is given as an example. The design is done in a hierarchical manner starting at the system level and ending at the component level. The system design starts by defining the performance constraints to be met, such as the initial acceleration, cruise velocity, maximum velocity, gradability, and so on. The system is designed so as to meet the above criteria with minimum power. The performance specification for the present vehicle is given below:

- **Acceleration:** from 0 to 100 km/h in 16 seconds.
- **Gradability:** 5° at 100 km/h and maximum 25° at 60 km/h.
- **Speed:** 160 km/h (ICE only), 140 km/h (electric motor only).

The parameters and constants used in the calculations are given in Table 3.1. In this design, a single gear ratio and ideal loss-free gears are chosen for simplicity. The primary energy source in the parallel hybrid is decided based on the energy management strategy used. In this design example, the ELPH control strategy is implemented. Component sizing is selected in such a way that the battery SOC can be controlled within a predetermined range.

In the first step of this design, the power ratings of the ICE and the electric motor are estimated based on vehicle performance requirements or specifications. First, an electric

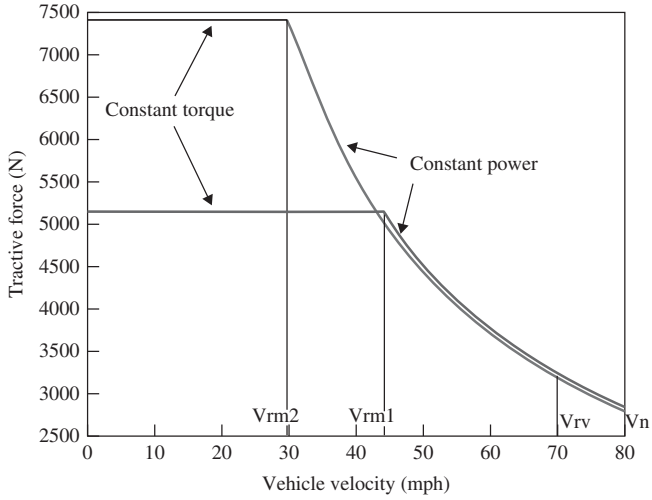

Figure 3.9 Example tractive force and vehicle velocity curve corresponding to electric traction motor

motor is designed based on ELPH strategy, which meets both the acceleration and the road load requirements. The motor operates in three regions as shown in Figure 3.9 according to the different vehicle speed range. The motor is a variable frequency induction-type motor [13]. The first region, called the constant torque/force region, extends from 0 to the rated motor speed (v_{rm}), corresponding to the motor rated power. From the base speed up to the maximum speed (v_n), the motor runs in the constant power region. The motor runs in the natural mode if it is operated beyond v_n. The torque decreases roughly according to the inverse of speed squared in this high-speed region. Note that the natural mode is not shown in the figure and v_{rv} represents the vehicle's rated speed. Generally, the motor is operated in the constant torque region for rapid acceleration. The corresponding motor efficiency plot is shown in Figure 3.10. The following motor loss constants are assumed in plotting the motor efficiency: copper losses $k_c = 1.5$, iron losses $k_i = 0.1$, windage losses $k_w = 0.0001$, and motor constant losses = 20 [13].

The differential equation describing the performance of the hybrid vehicle is given by

$$a = \frac{dv}{dt} = \frac{F_{te} - F_{RL}}{K_m m} \tag{3.14}$$

where F and F_{RL} are the motive and road load forces, respectively. Assuming the road load to be 0 for simplicity and $K_m = 1$, then the above equation becomes

$$a = \frac{dv}{dt} = \frac{F}{m} \tag{3.15}$$

A vehicle with a mass of 1767 kg moving with an acceleration of 1.7361 m/s^2 requires an average force of 3067.7 N at the tire/road interface, approximately 857 N m at the wheels. Note that this is the torque required to accelerate the vehicle, not to overcome the base load. It can be seen from Figure 3.11 that the vehicle meets the acceleration performance of 0–100 km/h in 16 seconds.

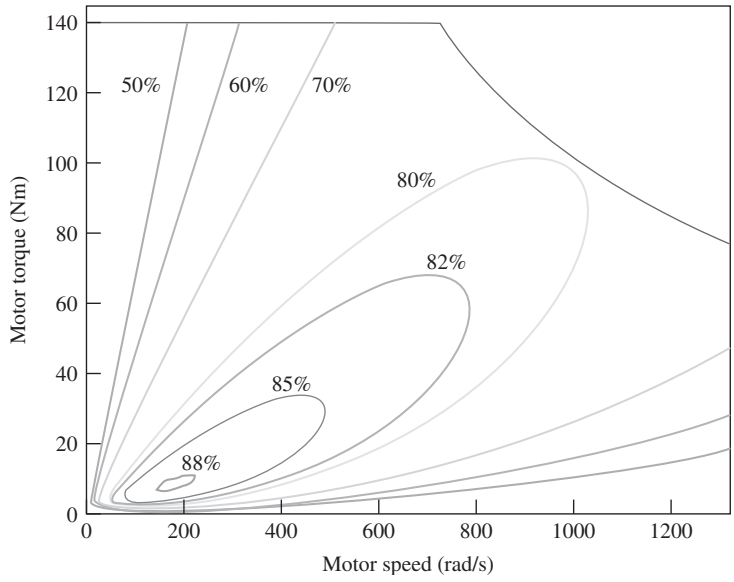

Figure 3.10 Motor efficiency plot

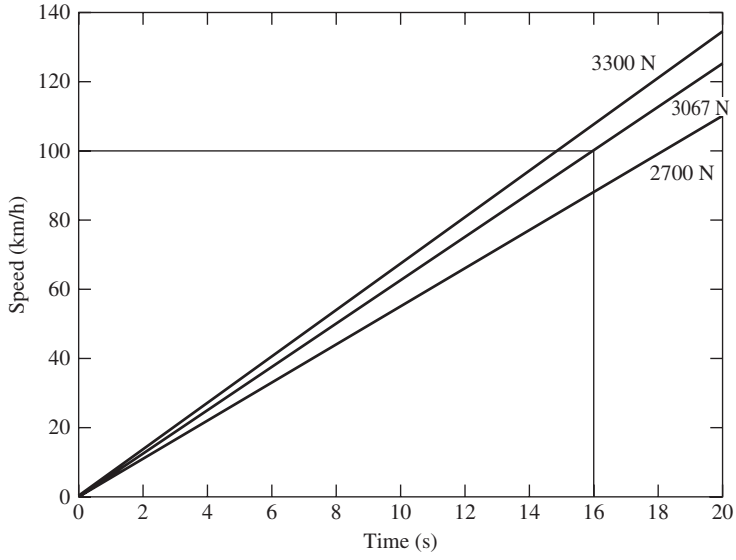

Figure 3.11 Acceleration performance with zero road load

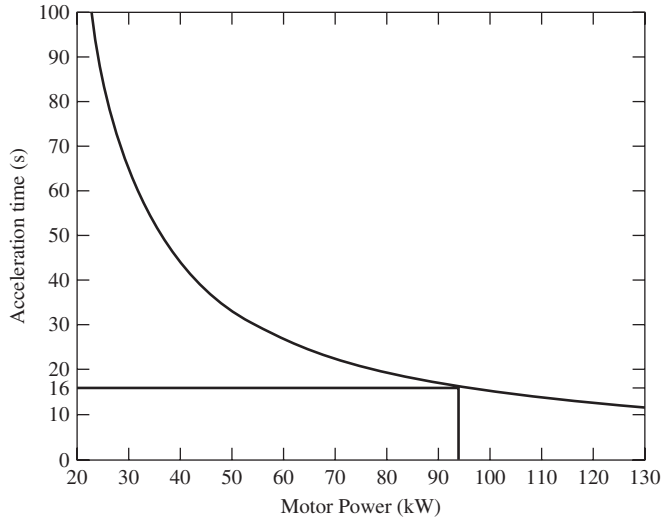

Figure 3.12 Motor power requirement to meet 0–100 km/h in 16 seconds

The power requirement to meet the acceleration performance is given in Figure 3.12, at approximately 95 kW.

Integrating the above acceleration equation for a time period of t_f and for a final velocity of v_{rv}, we get

$$m \int_0^{V_{rv}} \frac{dv}{F} = \int_0^{t_f} dt \tag{3.16}$$

The left integral can be separated into two integrals, one for a constant torque region and one for a constant power region,

$$m \int_0^{V_{rm}} \frac{dv}{Pm/v_{rm}} + m \int_{V_{rm}}^{V_{rv}} \frac{dv}{Pm/v} = t_f \tag{3.17}$$

Solving for Pm gives

$$Pm = \frac{m}{2t_f}\left(v_{rm}^2 + v_{rv}^2\right) \tag{3.18}$$

The fact that the power requirement will be minimum if the motor is operated in the constant power region can be obtained from this equation. To find the minimum power, we take the derivative of Pm with respect to v_{rm} and set the derivative to 0. This will yield the solution

$$v_{rm} = 0 \tag{3.19}$$

Therefore, if the motor is accelerating from 0 to v_{rv} in t_f seconds in the constant power region alone, the power requirement is minimum; in fact, this power is half of the required

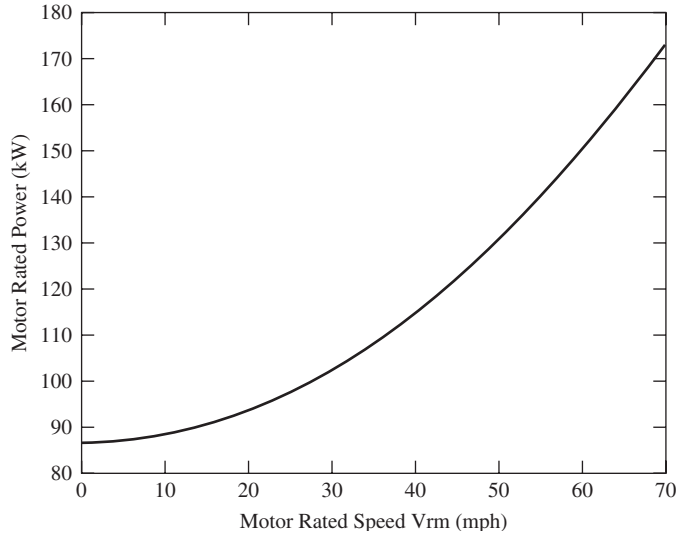

Figure 3.13 Motor rated power as a function of motor rated speed during acceleration

power when the motor is operated entirely in the constant torque region. The motor power dependence on the motor rated speed is shown in Figure 3.13. It can be seen that the power required decreases as the constant power region increases and it is minimum when the motor is completely operated in the constant power region. The effect of extending the constant power range is shown in Figure 3.14. Defining the constant power range ratio as v_{rm}/v_{rv}, it can be seen from Figure 3.14 that, with a ratio of about 1:4, the

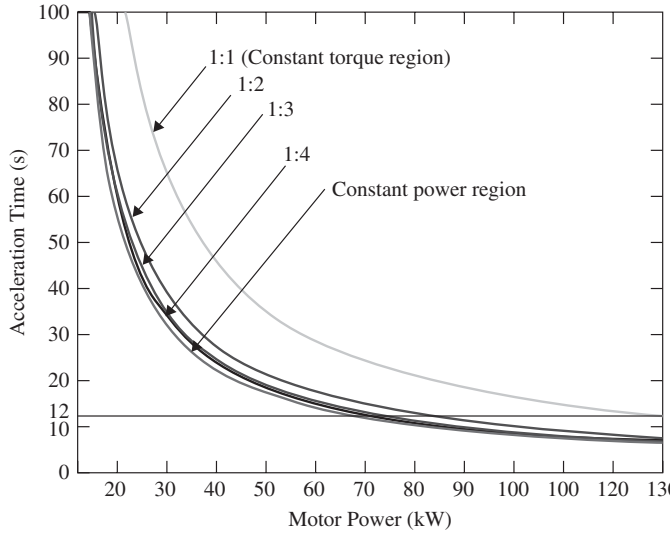

Figure 3.14 Motor power as a function of constant power range

decrease in the required Pm for a certain t_f becomes less significant. Here, a ratio of 1:1 corresponds to the purely constant torque region. Note here that as the constant power range is increased, the torque required increases as shown in Figure 3.9. So, a trade-off has to be made between motor power and motor torque depending upon the requirements. Note also that the previous discussion for the required motor power is obtained based on neglecting the road load force. When this road load force is included, we have the following equation:

$$m\int_{0}^{V_{rm}} \frac{dv}{(Pm/v_{rm}) - F_{RL}} + m\int_{V_{rm}}^{V_{rv}} \frac{dv}{(Pm/v) - F_{RL}} = t_f \tag{3.20}$$

It can be seen from Figure 3.12 that a 95 kW motor is needed to meet the acceleration performance. But the power requirement should also meet the maximum vehicle velocity requirement. The motor power demand with vehicle speed for different grade angles is shown in Figure 3.15. The following equation is used in plotting Figure 3.15 with $\eta_t = 0.92$:

$$P_e = \frac{v}{1000\eta_t}\left(C_f mg + 0.5\rho C_d A_f v^2 + mg\sin\frac{\alpha\pi}{180^\circ}\right) \tag{3.21}$$

where η_t is the transmission efficiency.

The power demand required depends on the maximum vehicle speed and the maximum road angle to be climbed. In our case, the requirement is 140 km/h (ICE alone) and 160 km/h (electric motor alone); then from Figure 3.15 the power requirement of the motor is about 38 kW. Note here that the power required to meet the maximum speed of the vehicle is less than the power required to meet the acceleration performance. In order to meet both requirements, a motor power of 95 kW is chosen.

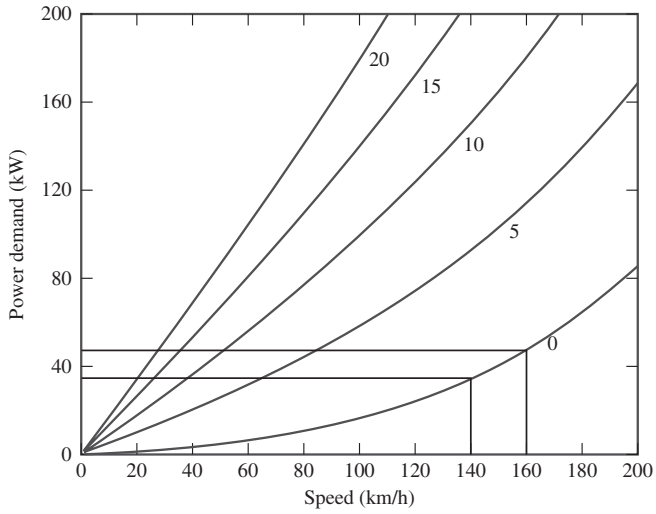

Figure 3.15 Vehicle power demand at zero acceleration with vehicle speed at different road grades

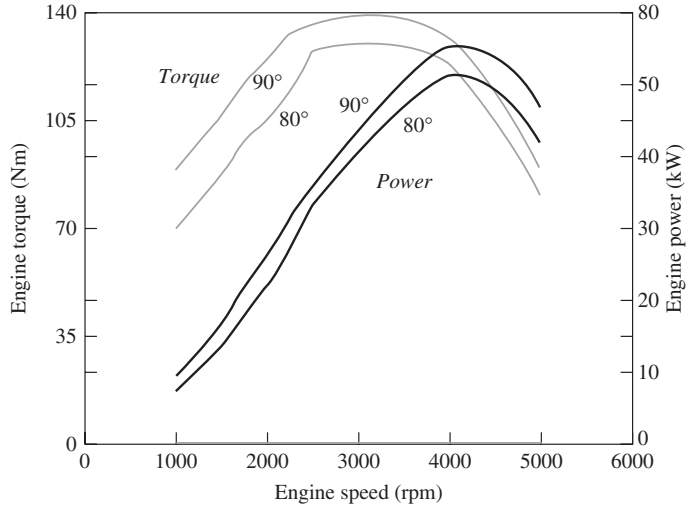

Figure 3.16 ICE torque–speed characteristics

3.6.2 ICE Characteristics

A 55 kW ICE's torque–speed and power–speed characteristics with different throttle angles of 80° and 90° are shown in Figure 3.16. This plot is obtained by using a two-dimensional lookup table [14].

Figure 3.16 clearly indicates that, for high-torque outputs, the ICE must be operated at moderate speeds. Also, the efficiency of the ICE (not shown in the figure) is high at moderate speeds. In the ELPH control strategy, the ICE needs to be sized so as to provide the road load power and to recharge the batteries. From Figure 3.15, to achieve 160 km/h on ICE alone the power needed is 45 kW. If we assume an extra power demand of 10 kW for hotel loads such as air-conditioner, lighting, and other auxiliary loads, then the size of the ICE needs to be at least 55 kW.

3.6.3 Gradability Requirement

So far, two vehicle components, the motor and ICE, are designed to meet the acceleration and maximum speed requirements. Now, let us double check gradability requirements. Figure 3.17 shows the required vehicle power at grade angles of 0°, 5°, 10°, 15°, 20°, and 25°.

It can be seen from Figure 3.17 that approximately 60 kW and 140 kW are required to meet the gradability requirements of 100 km/h at 5° grade and 60 km/h at 25° grade, respectively. The available power from the vehicle is the sum of available powers from both the traction motor and ICE. The available power of the vehicle is 150 kW (95 kW from the motor and 55 kW from the ICE). Thus, the available power is greater than the two gradability power requirements. Hence, these requirements are met by our design.

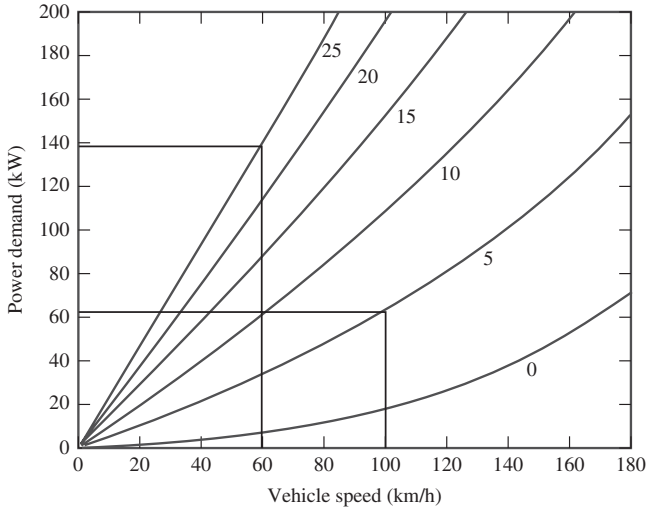

Figure 3.17 Vehicle power demand curves with respect to vehicle velocity and grade angle

3.6.4 Selection of Gear Ratio from ICE to Wheel

In this design, a single gear ratio was assumed for simplicity. Here, we relax the single ratio specification and find out the required gear ratio from engine to drive wheel. Gears are mechanical devices used to gain a mechanical advantage through an increase in torque or reduction in speed. Gear ratio is the ratio of the ICE speed (rad/s) multiplied by the tire radius (m) with respect to the vehicle speed (m/s). In Figure 3.18, the vehicle power

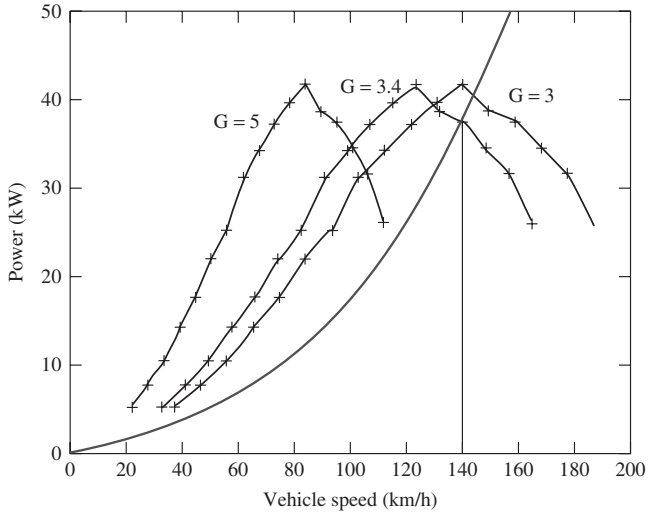

Figure 3.18 Gear ratio from ICE to drive wheel (the curve with '+' marks represents ICE power and the curve without '+' marks represents vehicle power)

demand curve (Figure 3.15) at zero road grade is plotted on the same graph as the engine power curves (Figure 3.16) at 90° throttle angle under different gear ratios [8]. The ratio curve on which these two curves touch each other, satisfying the maximum speed constraint and the available ICE power, corresponds to the minimum gear ratio required to meet the performance constraints. It can be seen from Figure 3.18 that a gear ratio of 3.4 is required to sustain a speed of 140 km/h in ICE-only operating mode.

In a similar fashion, the gear ratio of the electric motor to drive wheel can be determined.

3.7 Wheel Slip Dynamics

In this section, vehicle wheel slip dynamics is briefly discussed. As the power delivered to the wheels increases, vehicle acceleration eventually becomes limited by traction power. In power-limited acceleration, the vehicle reaches its maximum acceleration because the engine cannot deliver any more traction power. In acceleration with limited traction, the engine can and does deliver more power, but the traction force from the tires to the road surface cannot be further increased, resulting in limited acceleration. This is due to the nonlinear characteristics of the coefficient of friction between the tire and road surface. A schematic of a single-wheel braking model and the corresponding free body diagram is shown in Figure 3.19 [15].

In this figure, the normal force z balances the vehicle weight F_z. F_x is the tire reaction force, which is produced by the friction between the tire and road surface. This tire reaction force will cause a torque that drives the wheel forward with an angular velocity ω. On the contrary, the braking torque T_b counteracts F_x and slows down the wheel's forward rotational motion. The dynamic motion equations can be written following Newton's laws:

$$m\frac{dv}{dt} = -F_x \tag{3.22}$$

$$J\frac{d\omega}{dt} = rF_x - T_b\,\mathrm{sgn}(\omega) \tag{3.23}$$

$$0 = Z - F_z \tag{3.24}$$

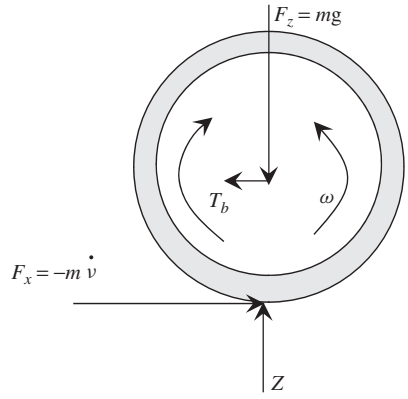

Figure 3.19 Model of quarter car forces and torques

where

v = longitudinal speed at which the wheel moves along the vehicle
ω = angular velocity of the wheel
F_z = vehicle weight force
Z = normal force due to road reaction force
F_x = tire reaction force due to friction
r = wheel radius
J = wheel inertia
T_b = braking torque.

The tire friction force is given by

$$F_x = F_z \mu\,(\lambda, \mu_H, \alpha) \tag{3.25}$$

where the friction coefficient μ is a nonlinear function of λ, μ_H, and α; λ is longitudinal tire slip; μ_H is the friction coefficient between the tire and road; and α is the slip angle of the wheel.

If the tire friction force exceeds the force given by the above equation, the tire slips excessively and enters dynamic friction, where the coefficient of friction decreases dramatically, that is, it brakes traction.

The longitudinal slip is defined by

$$\lambda = \frac{v - \omega r}{v} \tag{3.26}$$

which quantifies the normalized difference between the vehicle speed v and the linear speed at the radius of the wheel corresponding to the wheel rotational speed ω. If $\lambda = 0$, the wheel is in free motion with no friction force between the tire and road surface. If $\lambda = 1$, the wheel is in a locked condition without any rotational motion ($\omega = 0$) and thus only sliding friction is present.

The longitudinal tire friction force is usually obtained by curve-fitting road test data. The so-called *magic formula* of Pacejka gives a good representation of the longitudinal friction characteristic [16, 17], as expressed by the following equation:

$$y(x) = D \sin(C \arctan(Bx - E(Bx - \arctan(Bx)))) \tag{3.27}$$

The function parameters B, C, D, and E are determined based on curve-fitting. A more simple dependence of the friction coefficient as a function of slip can be given by unimodal friction characteristics [18]

$$\mu(\lambda) = 1.18(1 - e^{-10\lambda}) - \lambda/2 \tag{3.28}$$

An example friction coefficient as a function of slip is shown in Figure 3.20. In the figure, the curve of the friction coefficient (μ) can be divided into two regions: to the left of 0.3, where the friction coefficient increases as slip value increases; and to the right of 0.3, where the friction coefficient decreases until the wheel locking condition ($\lambda = 1$) as slip value increases. Note that the curve in Figure 3.20 is different for different road

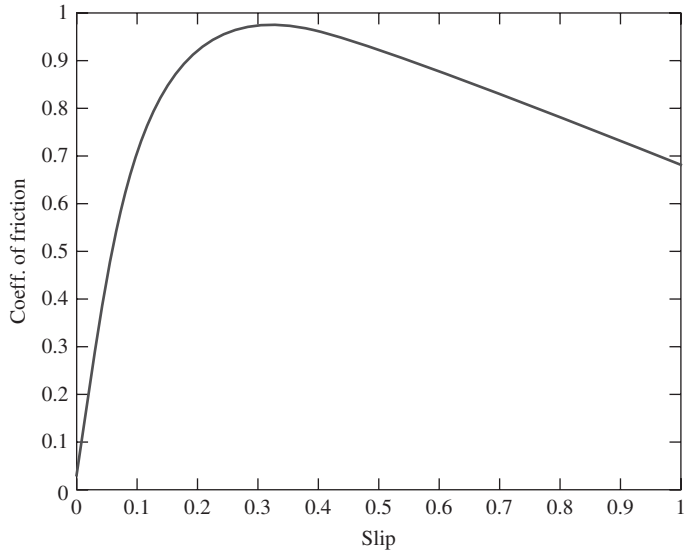

Figure 3.20 Friction coefficient (μ) and dependence on slip (λ)

conditions such as dry asphalt, wet asphalt, gravel, and packed snow [18]. Understandably, the friction coefficient is much higher for dry asphalt than for snow.

References

1. Gillespie, T.D. (1992) *Fundamentals of Vehicle Dynamics*, SAE, Warrendale, PA.
2. Fu, Jianfu and Gao, Wenzhong (2009) Principal component analysis based on drive cycles for hybrid electric vehicle. 5th IEEE Vehicular Power and Propulsion Conference, September 7–11, Dearborn, MI.
3. Brooker, A., Haraldsson, K., Hendricks, T. *et al*. (2002) ADVISOR Documentation, Version 2002, National Renewable Energy Laboratory.
4. Gao, W. (2005) Performance comparison of a hybrid fuel cell – battery powertrain and a hybrid fuel cell – ultracapacitor powertrain. *IEEE Transactions on Vehicular Technology*, **54** (3), 846–855.
5. ADVISOR 2004 Documentation, http://www.avl.com.
6. Gao, Y. and Ehsani, M. (2001) Systematic design of fuel-cell powered hybrid vehicle drive train. Future Transportation Technology Conference, August 20–22, Costa Mesa, CA, paper 2001-01-2532.
7. Ehsani, M., Gao, Y., and Butler, K.L. (1999) Application of electrically peaking hybrid propulsion system to a full-size passenger car simulation design verification. *IEEE Transactions on Vehicular Technology*, **48** (6), 1779–1787.
8. Rahman, Z., Butler, K.L., and Ehsani, M. (1999) Designing parallel hybrid electric vehicles using V-ELPH 2.01. Proceedings of the American Control Conference, June 2–4, San Diego, CA.
9. Markel, T., Zolot, M., Wipke, K.B., and Pesaran, A.A. (2003) Energy storage requirements for hybrid fuel cell vehicles. Advanced Automotive Battery Conference, June 10–13, Nice, France.
10. Wipke, K.B., Markel, T., and Nelson, D. (2001) Optimizing energy management strategy and degree of hybridization for a hydrogen fuel cell SUV. 18th Electric Vehicle Symposium, EVS 18, Berlin, Germany.
11. Rahman, Z., Butler, K.L., and Ehsani, M. (1999) Design studies of a series hybrid heavy-duty transit bus using V-ELPH 2.01. Proceedings of the 49th IEEE Vehicular Technology Conference, May, Houston, TX, Vol. 3, pp. 2268–2272.
12. Butler, K.L., Ehsani, M., and Kamath, P. (1999) A MATLAB-based modeling and simulation package for electric and hybrid electric vehicle design. *IEEE Transactions on Vehicular Technology*, **48** (6), 1770–1778.

13. Jefferson, C.M. and Barnard, R.H. (2002) *Hybrid Vehicle Propulsion*, WIT Press, Southampton.
14. Larminie, J. and Lowry, J. (2003) *Electric Vehicle Technology Explained*, John Wiley & Sons, Ltd, Chichester.
15. Johansen, T.A., Petersen, I., Kalkkuhl, J., and Ludemann, J. (2003) Gain-scheduled wheel slip control in automotive brake systems. *IEEE Transactions on Control Systems Technology*, **11** (6), 799–811.
16. Bakker, E., Pacejka, H., and Lidner, L. (1989) A New Tire Model with an Application in Vehicle Dynamics Studies. SAE Paper No. 890087, pp. 101–113.
17. Bakker, E., Nyborg, L., and Pacejka, H. (1987) Tyre Modeling for Use in Vehicle Dynamics Studies. SAE Paper No. 870421, pp. 190–204.
18. Olson, B.J., Shaw, S.W., and Stépán, G.S. (2003) Nonlinear dynamics of vehicle traction. *Vehicle System Dynamics*, **40** (6), 377–399.

4

Advanced HEV Architectures and Dynamics of HEV Powertrain

There are various hybrid powertrain architectures which are in use. The general goals of a hybrid transmission design are to realize the different operating modes of a hybrid vehicle system, such as the capability to run motor-alone mode, engine-alone mode, combined mode, power split mode, regenerative braking mode, and stationary charging operations. In addition, it is important to be able to control engine power and speed during hybrid operations so that better fuel economy and lower emissions can be achieved for all ranges of vehicle speeds and power demands. Lastly, the system design should be easy to implement and control, and bear low overall cost. This chapter discusses the principles of a few advanced hybrid electric powertrain architectures. These architectures include the popular GM two-mode hybrid and its variations, dual-clutch-based hybrid, Tsai's hybrid, Zhang's hybrid, Renault hybrid, and Timken hybrid.

The steady state operating modes and torque/speed relationships are presented first. Then, the HEV powertrain dynamics will be briefly discussed for the Toyota hybrid transmission.

4.1 Principle of Planetary Gears

Many hybrids in the marketplace today use a planetary gear train to replace the traditional automatic transmission such as continuous variable transmission (CVT). The engine, motor, and generator together form a type of transmission that can provide electric continuous variable transmission, known as e-CVT.

A planetary gear train has one or more planetary gears orbiting around a sun gear or central axis of the train. Therefore, there is a moving axis in planetary gear trains (carrier). A pictorial representation of a planetary train is shown in Figure 4.1. As can be seen, there are three axes in total: the sun axis, planet carrier axis, and ring axis. The possible relative motions among these axes make planetary gear trains very interesting.

Among the three shafts of a planetary gear train, any shaft can be treated as the input shaft or output shaft. Hence, a combination will be either two input shafts and one output

Hybrid Electric Vehicles: Principles and Applications with Practical Perspectives, First Edition.
Chris Mi, M. Abul Masrur and David Wenzhong Gao.

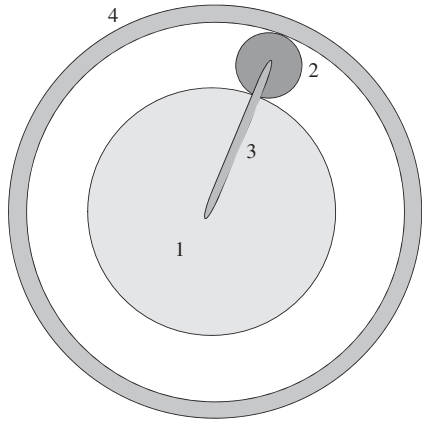

Figure 4.1 A planetary gear train: 1, the sun gear; 2, the planetary gear; 3, the arm or planet carrier; and 4, the ring gear

shaft, or one input shaft and two output shafts. In some applications, one of the gear sets is grounded so that only one input and one output is available.

To understand the speed/torque relationships inside a planetary gear train, we can first look at the relationship between a simple set of gears. The linear velocity of the edge of a wheel relative to its center is defined as follows:

$$V = \omega r \tag{4.1}$$

In simple gears, two wheels are put in contact with each other. The two wheels will travel at the same linear speeds. Hence, the speed relationship of the two wheels is

$$\frac{\omega_1}{\omega_2} = \frac{r_2}{r_1} \tag{4.2}$$

The relationship between a gear's radius and a gear's tooth number can be written as $2\pi r_i = pN_i$, where N is the tooth number and p is the pitch (arc distance between two adjunct teeth). If gear i and gear j are in contact, then they must have the same circular pitch p in order to transfer the movement.

Therefore, we have

$$\frac{r_i}{r_j} = \frac{N_i}{N_j} \tag{4.3}$$

This expression is valid for any gear with an angular movement with respect to one point. For the planetary gear train shown in Figure 4.2, there are two contact points: point A between the sun gear and the planet gear; and point B between the planet gear and the ring gear. The linear velocities of the contact points can be obtained using two different paths for each point:

For point A:

$$v_a = \omega_s r_s \tag{4.4}$$

$$v_a = \omega_p r_p - \omega_c r_a \tag{4.5}$$

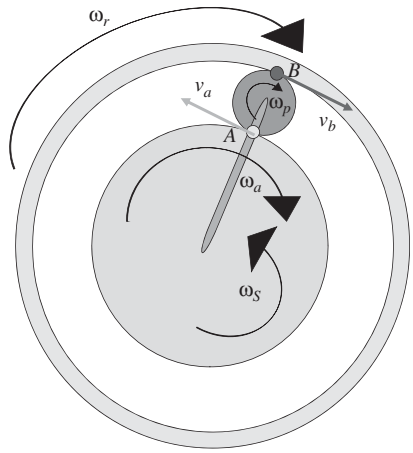

Figure 4.2 The operation of a planetary gear train

For point B:

$$v_b = \omega_r r_r \tag{4.6}$$

$$v_b = \omega_p r_p + \omega_c r_a \tag{4.7}$$

The directions of the various components' rotation have been chosen so that the movement of the planetary train is feasible. Thus, we have the following two equations:

$$\omega_s r_s = \omega_p r_p - \omega_c r_a \tag{4.8}$$

$$\omega_r r_r = \omega_p r_p + \omega_c r_a \tag{4.9}$$

After manipulation, we get

$$\omega_r r_r = \omega_s r_s + 2\omega_c r_a$$

But $r_a = r_r - r_p$ and $2r_p + r_s = r_r$, so $r_a = (r_r + r_s)/2$. Therefore, we get

$$\omega_r r_r = \omega_s r_s + \omega_c (r_s + r_r) \tag{4.10}$$

In order to make use of the expression easier, the clockwise direction will be considered positive and the anticlockwise direction negative. As can be seen in the above figure, not all the angular velocities have the same direction. So, we can rewrite the above equation by including the correct reference direction:

$$\omega_r r_r = -\omega_s r_s + \omega_c (r_s + r_r) \tag{4.11}$$

Since

$$2\pi r_i = pN_i \tag{4.12}$$

we have

$$\omega_r N_r + \omega_s N_s = \omega_c (N_s + N_r) \tag{4.13}$$

or

$$\frac{N_r}{N_s + N_r}\omega_r + \frac{N_s}{N_s + N_r}\omega_s = \omega_c \tag{4.14}$$

As mentioned earlier, two inputs are required before a planetary gear set can be uniquely analyzed. If a gear is grounded, its velocity is zero; nevertheless this zero velocity constitutes one of the input values.

4.2 Toyota Prius and Ford Escape Hybrid Powertrain

The Toyota Prius and the Ford Escape use similar powertrain transmissions as shown in Figure 4.3 as well as in Figure 1.23. There are an engine, two electric machines, and a planetary gear train in the transmission. The engine is connected to the carrier, electric motor MG1 is connected to the ring gear as well as the final drive, and the generator MG2 is connected to the sun gear. Hence, the speed and torque relationships are

$$\omega_e = \frac{N_r}{N_r + N_s}\omega_m + \frac{N_s}{N_r + N_s}\omega_g \tag{4.15}$$

where $\omega_e, \omega_m,$ and ω_g are the speed of the engine, the motor, and the generator, respectively.

Since there is no clutch, the planetary gear is always running whenever the vehicle is moving. It can be seen from the above equation and the diagram of the powertrain that the speed of the motor is directly proportional to the linear speed of the vehicle through the radius of the front tires and the final drive ratio. The ring gear speed and the motor speed are identical.

There are four different operating modes:

- **Mode 0:** Launch and backup – the motor is powered from the battery; the vehicle is driven by the motor only:

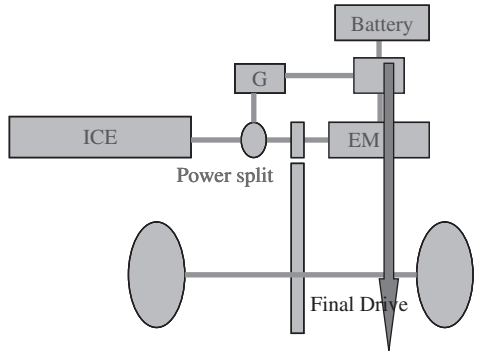

$$T_{out} = \frac{N_2}{N_1}\omega_m \tag{4.16}$$

- **Mode 1:** Cruising, or e-CVT mode 1:

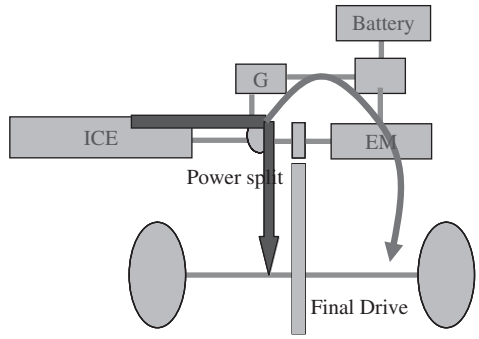

$$T_r = \frac{N_r}{N_r + N_s} T_e \tag{4.17}$$

$$T_g = \frac{N_s}{N_r + N_s} T_e \tag{4.18}$$

$$T_{out} = \frac{N_2}{N_1} T_r \tag{4.19}$$

$$T_m = 0 \tag{4.20}$$

- **Mode 2:** Sudden acceleration, e-CVT mode 2:

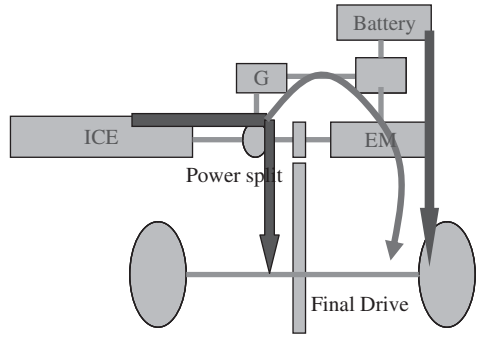

$$T_r = \frac{N_r}{N_r + N_s} T_e \tag{4.21}$$

$$T_g = \frac{N_s}{N_r + N_s} T_e \tag{4.22}$$

$$T_{out} = \frac{N_2}{N_1} (T_r + T_m) \tag{4.23}$$

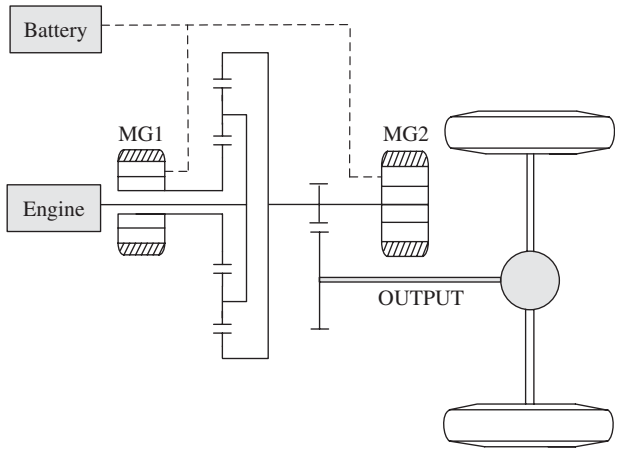

Figure 4.3 The Toyota Prius transmission

- **Mode 3:** Regenerative braking – the motor MG1 is operating as a generator to produce electricity to charge the battery and at the same time provide braking torque to the final drive. This operation is the reverse of launch and backup operation.

During normal operation (e-CVT or acceleration mode), the speed of the engine is controlled by the torque on the generator. Basically, the generator power is adjusted so that the engine turns at the desired speed. Hence, by adjusting the generator speed, the engine can operate at a relatively constant speed while the vehicle is driven at different speeds.

In the Prius, the engine is limited from 0 to 4000 rpm. The motor is limited by a small negative revolution per minute for reverse and up to 6000 rpm (~103 mph or 165 km/h). The generator is limited to ±5500 rpm. The ring gear and sun gear each have 78 and 30 teeth respectively. The four planetary gears each have 23 teeth. The final drive ratio is 3.93 and the wheel radius is 0.287 m. Hence, $\omega_e = 0.7222\omega_m + 0.2778\omega_g$.

The control strategy is as follows. For a given vehicle speed, and a desired output power determined by the drive cycle, or driver inputs, the desired operating point of the engine can be determined based on the maximum efficiency curve of the engine. From the vehicle speed and engine speed, the desired generator speed can then be calculated. The generator speed is regulated through the inverter by controlling the output power of the generator (either as generator or motor). Motor torque is determined by looking at the difference between the total vehicle torque demand and the engine torque that is delivered to the ring gear. The battery provides power to the motors along with the electricity generated by the engine.

Example 4.1: Consider a planetary gear train-based transmission with an engine (carrier) providing 100 kW at 2000 rpm optimum operating point. The ring gear has 72 teeth and the sun gear has 30 teeth. The final drive ratio is 3.7865, and the

wheel radius 0.283 m. (i) For a vehicle speed of 45 mph or 20.6 m/s, the power demand under heavy acceleration at this speed is 120 kW. Find the speed and power for each component, assuming no losses. (ii) For a vehicle speed of 70 mph, or 32.7 m/s, when cruising the power demand is 70 kW. Calculate the speed and power of each component.

Solution:

$$\omega_e = \frac{N_r}{N_r + N_s}\omega_r + \frac{N_s}{N_r + N_s}\omega_s = 0.706\omega_r + 0.294\omega_s$$

1. At 45 mph, the ring gear (same as motor speed) is calculated from the above to be 2632 rpm. Therefore, the sun gear (generator) speed needs to be 482 rpm in order to operate the engine at 2000 rpm:

$$T_c(\text{engine}) = P_{engine}/\omega_{engine(carrier)} = 477\,\text{Nm}$$

$$T_r(\text{Ring\_gear}) = \frac{N_r}{N_r + N_s}T_c = 0.706 \times 477 = 337\,\text{Nm}$$

$$T_s(\text{generator}) = \frac{N_s}{N_r + N_s}T_c = 0.294 \times 477 = 140\,\text{Nm}$$

$$P_c(\text{engine}) = 100\,\text{kW}$$

$$P_r(\text{Ring\_gear}) = T_r\omega_r = 337 \times 2 \times \pi \times 2632/60 = 92.9\,\text{kW}$$

$$P_s(\text{generator}) = T_s\omega_s = 140 \times 2 \times \pi \times 482/60 = 7.1\,\text{kW}$$

$$P_c(\text{engine}) = P_r + P_s$$

$$P_{vehicle} = 120\,\text{kW}$$

$$P_m(\text{motor}) = P_{vehicle} - P_r = 27.1\,\text{kW}$$

$$P_{bat} = P_m - P_s = 20\,\text{kW}$$

2. At 70 mph, the ring gear (same as motor speed) is calculated from the above to be 4080 rpm. Therefore, the sun gear (generator) speed needs to be −2995 rpm in order to operate the engine at 2000 rpm:

$$T_c(\text{engine}) = P_{engine}/\omega_{engine(carrier)} = 477\,\text{Nm}$$

$$T_r(\text{Ring\_gear}) = \frac{N_r}{N_r + N_s} T_c = 0.706 \times 477 = 337\,\text{Nm}$$

$$T_s(\text{generator}) = \frac{N_s}{N_r + N_s} T_c = 0.294 \times 477 = 140\,\text{Nm}$$

$$P_c(\text{engine}) = 100\,\text{kW}$$

$$P_r(\text{Ring\_gear}) = T_r \omega_r = 337 \times 2 \times \pi \times 4080/60 = 144\,\text{kW}$$

$$P_s(\text{generator}) = T_s \omega_s = 140 \times 2 \times \pi \times (-2995)/60 = -44\,\text{kW}$$

$$P_{vehicle} = 70\,\text{kW}$$

$$P_m(\text{motor}) = P_{vehicle} - P_r = -74\,\text{kW}$$

$$P_{bat} = P_m - P_s = -30\,\text{kW}$$

4.3 GM Two-Mode Hybrid Transmission

The GM two-mode hybrid electric powertrain (or transmission) is shown in Figure 4.4 [1, 2]. This powertrain consists of two planetary gear sets P1 and P2; two electric machines MG1 and MG2; and three clutches C1, C2, and C3. The powertrain is capable of providing e-CVT for both high-speed and low-speed operations, hence two-mode. The two-mode concept can be referred and compared to the Toyota and Ford hybrid electric vehicle powertrain whose operation is limited to only one mode. In principle, two-mode operation can provide more flexibility for transmission control, increase drivability, improve vehicle performance, and improve fuel economy.

The GM two-mode hybrid transmission was initially developed by GM (Alison) in 1996, and later advanced by GM, Chrysler, BMW, and Mercedes-Benz in a joint venture named Global Hybrid Cooperation in 2005.

4.3.1 Operating Principle of the Two-Mode Powertrain

In the GM two-mode hybrid transmission, the engine is connected to the ring gear of planetary gear P1 through clutch C1. Electric machine MG1 is connected to the sun gear of P1. The carrier of P1 is connected to the final drive through the output shaft. MG2 is connected to the sun gear of planetary P2. The carrier of P2 is also connected to the output shaft. There is a dual-position clutch that connects either the ring gear of P2 to ground, or the ring gear of P2 to the shaft of MG1. Through control of C2 and C3, different operating

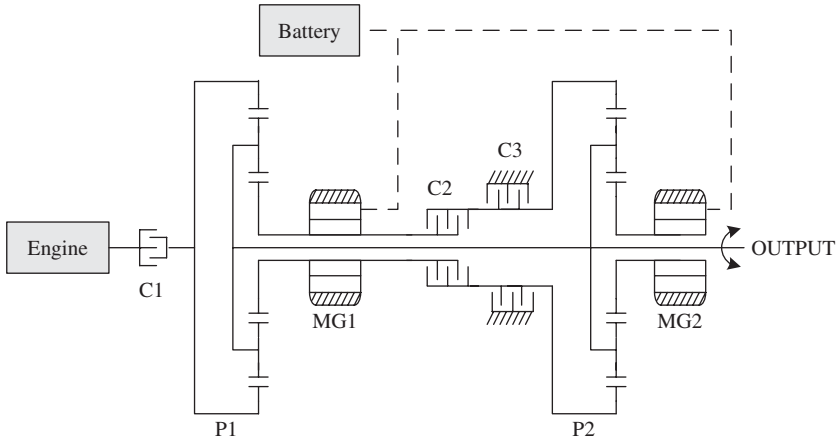

Figure 4.4 GM two-mode hybrid transmission

modes can be realized. The engine in this system can be kept at the best speed and torque combinations to achieve the best fuel economy by controlling the input/output of the two electric machines. The engine may be stopped or idle during vehicle launch and backup, as well as at low power demand. At cruising conditions, the engine efficiency is further enhanced by cylinder deactivation, also known as Active Fuel Management (GM) or the Multi-Displacement System (Chrysler). Note that this discussion is generic and may not be the same as those implemented in a real vehicle by the automobile manufacturers.

In the following derivations, ω is the angular velocity, T is torque, N is the number of teeth of a gear, and P is power. Subscript s stands for sun gear, r for ring gear, c for planetary carrier, 1 for planetary gear set 1, 2 for planetary gear set 2, g for motor/generator 1, or MG1, m for motor/generator 2, or MG2, and *out* is for output or final drive.

4.3.2 Mode 0: Vehicle Launch and Backup

During vehicle launch and backup, the system is operating in motor-alone mode (Mode 0). C2 is open and C3 is engaged to ground the ring gear of P2. In this mode, there are two possibilities for engine operation, either off or idle at cranking speed (approximately 800 rpm) by adjusting MG1 speed. MG1 torque is not transmitted to the final drive. MG2 provides the needed torque to launch the vehicle forward or backward. Figure 4.5 shows the power flow during launch and backup. The speed/torque relationships are

$$\omega_{out} = \frac{N_{s2}}{N_{s2} + N_{r2}} \omega_m \tag{4.24}$$

$$T_{out} = \frac{N_{s2} + N_{r2}}{N_{s2}} T_m \tag{4.25}$$

In the final implementation, C1 was eliminated. Therefore, the engine is always connected to the ring gear of P1. Since the carrier of P1 is always connected to the

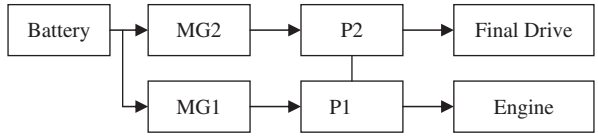

Figure 4.5 Power flow during launch and backup

final drive, MG1 needs to be controlled so that the engine is either at zero or at a certain speed:

$$\omega_g = \frac{N_{s1} + N_{r1}}{N_{s1}}\omega_{c1} - \frac{N_{r1}}{N_{s1}}\omega_e \tag{4.26}$$

If the engine is maintained at 800 rpm without fuel injection, there are still friction losses but the engine can be ignited at any time without delay. If the engine is controlled to be at zero speed, then MG1 will need to be controlled so that the ring gear of P1 reaches 800 rpm before the engine can be started. In this case, the engine is controlled by cylinder deactivation.

4.3.3 Mode 1: Low Range

Mode 1 is also called the low-range or low-speed mode. In this mode, C1 is engaged, C2 is open, and C3 is engaged. The second planetary gear works as a speed reduction gear for MG2. Figure 4.6 illustrates the mechanical connections of the transmission. The engine may be controlled by partial cylinder deactivation to further save fuel and reduce emissions based on vehicle power demand. The torque and speed relationships during steady state operations can be expressed as

$$T_g = \frac{N_{s1}}{N_{r1}}T_e \tag{4.27}$$

$$\omega_{c1} = \frac{N_{r1}}{N_{s1} + N_{r1}}\omega_e + \frac{N_{s1}}{N_{s1} + N_{r1}}\omega_g \tag{4.28}$$

$$\omega_{out} = \omega_{c2} = \omega_{c1} = \frac{N_{s2}}{N_{s2} + N_{r2}}\omega_m \tag{4.29}$$

$$T_{out} = \frac{N_{r1} + N_{s1}}{N_{r1}}T_e + \frac{N_{s2} + N_{r2}}{N_{s2}}T_m \tag{4.30}$$

The different operations in Mode 1 can be described as follows:

1. **Engine alone (CVT 1):** MG2 is off (freewheel) and MG1 can be either in motoring mode or in generating mode. When MG1 is in motoring mode, P1 acts as a speed coupling mechanism to couple the speed of the engine and MG1. When MG1 is in generating mode, engine power is split between the final drive and MG1 with power generated by MG1 charging the battery. Since the battery can quickly be charged fully, this mode is generally brief.

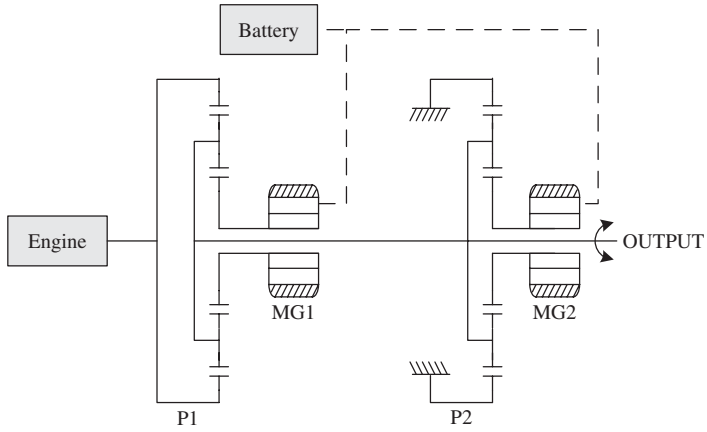

Figure 4.6 Low range

2. **Combined mode (CVT 2):** MG2 is turned on to assist the driving. P2 acts as a torque coupling mechanism to add the torque of the engine (P1 carrier portion) and MG2. If needed, both MG1 and MG2 can work in motoring mode to maximize the driving torque.
3. **Power split mode (CVT 3):** MG2 is in generating mode to charge the battery. MG1 can be either motoring or generating.

4.3.4 Mode 2: High Range

Mode 2 is also called the high-range or high-speed mode. C1 is engaged, C2 is engaged, but C3 is open. In this mode, the sun gear of P1 is connected to the ring gear of P2 through MG1, that is, MG1, S1, and R2 will have the same speed. Figure 4.7 shows the mechanical

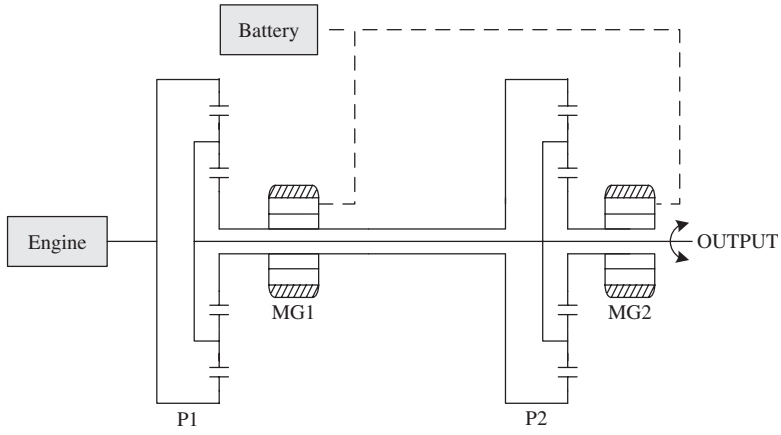

Figure 4.7 High range

connections of the transmission in Mode 2. In this operating mode, the engine is generally kept at a constant speed to achieve the best fuel economy. MG1 and MG2 are controlled in either motoring or generating mode depending on the vehicle speed and power demand. The torque and speed relationships during steady state operation are as follows:

$$T_g = \frac{N_{s1}}{N_{r1}} T_e + \frac{N_{r2}}{N_{s2}} T_m \tag{4.31}$$

$$\omega_{c1} = \frac{N_{r1}}{N_{s1} + N_{r1}} \omega_e + \frac{N_{s1}}{N_{s1} + N_{r1}} \omega_g \tag{4.32}$$

$$\omega_{c2} = \frac{N_{r2}}{N_{s2} + N_{r2}} \omega_g + \frac{N_{s2}}{N_{s2} + N_{r2}} \omega_m \tag{4.33}$$

$$\omega_{c2} = \omega_{c1} \tag{4.34}$$

$$\omega_{r2} = \omega_{s1} = \omega_g \tag{4.35}$$

$$T_{fd} = \frac{N_{r1} + N_{s1}}{N_{r1}} T_e + \frac{N_{s2} + N_{r2}}{N_{s2}} T_m \tag{4.36}$$

Similar to Mode 1, the engine may be controlled by partial cylinder deactivation to further save fuel and reduce emission based on vehicle power demand.

4.3.5 Mode 3: Regenerative Braking

During regenerative braking, C1 is open, C2 is open, and C3 is engaged to ground the ring gear of P2 (Mode 3). The engine and MG1 are off or freewheel. MG2 provides the needed braking torque for the vehicle and, at the same time, stores regenerative braking energy in the onboard battery. Figure 4.8 shows the power flow during regenerative braking. The speed/torque relationship is

$$\omega_m = \frac{N_{s2} + N_{r2}}{N_{s2}} \omega_{out} \tag{4.37}$$

$$T_m = \frac{N_{s2}}{N_{s2} + N_{r2}} T_{out} \tag{4.38}$$

Hydraulic/frictional braking may be controlled in coordination with regenerative braking to maximize the braking torque and/or maintain vehicle stability and prevent wheel locking. In this case, MG2 only provides a portion of the braking torque.

4.3.6 Transition from Mode 0 to Mode 3

In general, transition is performed at a condition that can minimize mechanical disturbance to the overall vehicle system. The vehicle is generally launched by MG2 with the engine

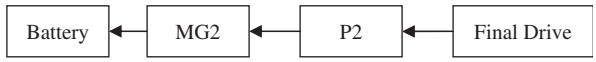

Figure 4.8 Power flow in regenerative braking

off (Mode 0). MG1 is turned on before transitioning to Mode 1 such that the engine speed reaches approximately 800 rpm. Transition from Mode 0 to Mode 1 is characterized by the engine turning on. This typically happens when the power demand reaches a certain limit such that MG2 is no longer capable of providing the needed torque. The power demand is a combination of vehicle speed, acceleration demand, vehicle load, and road conditions.

Transition from Mode 1 to Mode 2 happens when the sun gear of P1 and the ring gear of P2 reach the same speed. In other words, since the ring gear of P1 is grounded (zero speed), transition from Mode 1 to Mode 2 will happen when the sun gear of P1 or MG1 reaches zero speed. Similarly, transition from Mode 2 to Mode 1 also happens when the speed of MG1 reaches zero.

Transition from Mode 1 to Mode 3, or Mode 2 to Mode 3, is triggered by a braking request from the driver (brake pedal is pressed).

Example 4.2: Both planetary gear sets have 30 teeth for the sun gear and 70 teeth for the ring gear. The engine is kept at 800 rpm in Mode 0, ramped up from 800 to 2000 rpm in Mode 1, and kept at 2000 rpm in Mode 2. The wheel radius is 0.28 m. Vehicle speed V is in kilometers per hour and ranges from −40 to 160 km/h. The final drive gear ratio (including axle) is 3.3.

Solution: The final drive speed is a function of vehicle speed V:

$$\omega_{out} = (V \times 1000/3600/0.28) \times 3.3 \times 60/2\pi = 31.2\,\mathrm{V(rpm)}$$

In Mode 0, the engine is kept at 800 rpm and the speed of the ring gear of P2 is zero. Therefore,

$$\omega_m = \frac{N_{s2} + N_{r2}}{N_{s2}}\omega_{c2} = 3.33\omega_{out}$$

$$\omega_e = 800\,\mathrm{rpm}$$

$$\omega_g = \frac{N_{s1} + N_{r1}}{N_{s1}}\omega_{c1} - \frac{N_{r1}}{N_{s1}}\omega_e = 3.33\omega_{out} - 2.33\omega_e$$

In Mode 1, the engine speed will ramp up from 800 to 2000 rpm. Note that the engine can be turned on or kept idling. Engine on/off is determined by vehicle power demand. The speed relationships are the same as in Mode 0.

When the speed of the sun gear of P1 reaches zero, the vehicle will shift from Mode 1 to Mode 2. In Mode 2, the engine speed is kept at 2000 rpm. The speed relationships are

$$\omega_e = 2000\,\mathrm{rpm}$$

$$\omega_g = \frac{N_{s1} + N_{r1}}{N_{s1}}\omega_{c1} - \frac{N_{r1}}{N_{s1}}\omega_e = 3.33\omega_{out} - 2.33\omega_e$$

$$\omega_m = \frac{N_{s2} + N_{r2}}{N_{s2}}\omega_{c2} - \frac{N_{r2}}{N_{s2}}\omega_{r2} = 3.33\omega_{out} - 2.33\omega_g$$

Figure 4.9 shows the speeds of the system: engine, MG1, MG2, and final drive.

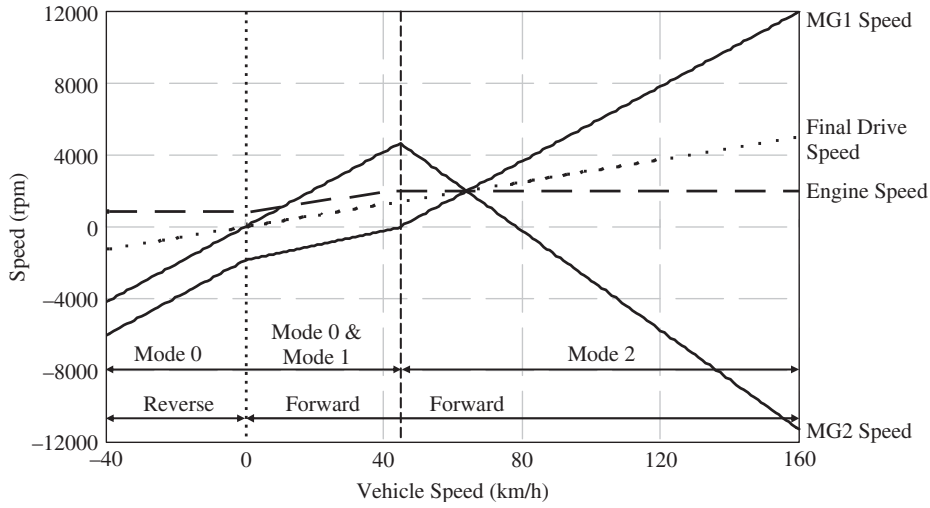

Figure 4.9 Speed relationships of the two-mode transmission in Example 4.2

Example 4.3: Planetary gear set 1 has 35 teeth for the sun gear and 65 teeth for the ring gear. Planetary gear set 2 has 30 teeth for the sun gear and 70 teeth for the ring gear. The engine is kept at 0 rpm in Mode 0, ramped up from 0 to 3000 rpm in Mode 1, and kept at 3000 rpm in Mode 2. The wheel radius is 0.28 m. Vehicle speed V is in kilometers per hour and ranges from −40 to 160 km/h. The final drive gear ratio (including axle) is 3.

Solution: The final drive speed is a function of vehicle speed V:

$$\omega_{out} = (V \times 1000/3600/0.28) \times 3.3 \times 60/2\pi = 31.2\,\mathrm{V(rpm)}$$

In Mode 0, the engine is kept at 0 rpm and the speed of the ring gear of P2 is zero. Therefore,

$$\omega_m = \frac{N_{s2} + N_{r2}}{N_{s2}}\omega_{c2} = 3.33\omega_{out}$$

$$\omega_g = \frac{N_{s1} + N_{r1}}{N_{s1}}\omega_{c1} = 2.86\omega_{out}$$

In Mode 1, the engine speed will ramp up from 0 to 3000 rpm. Note that the engine can be turned on or kept idling. Engine on/off is determined by vehicle

power demand. The speed relationships are

$$\omega_m = \frac{N_{s2} + N_{r2}}{N_{s2}}\omega_{c2} = 3.33\omega_{out}$$
$$\omega_g = \frac{N_{s1} + N_{r1}}{N_{s1}}\omega_{c1} - \frac{N_{r1}}{N_{s1}}\omega_e = 2.86\omega_{out} - 1.86\omega_e$$

When the speed of the sun gear of P1 reaches zero, the vehicle will shift from Mode 1 to Mode 2. In Mode 2, the engine speed is kept at 3000 rpm. The speed relationships are

$$\omega_e = 3000\,\text{rpm}$$
$$\omega_m = \frac{N_{s2} + N_{r2}}{N_{s2}}\omega_{c2} - \frac{N_{r2}}{N_{s2}}\omega_{r2} = 3.33\omega_{out} - 2.33\omega_g$$
$$\omega_g = \frac{N_{s1} + N_{r1}}{N_{s1}}\omega_{c1} - \frac{N_{r1}}{N_{s1}}\omega_e = 2.86\omega_{out} - 1.86\omega_e$$

Figure 4.10 shows the speeds of the system: engine, MG1, MG2, and final drive.

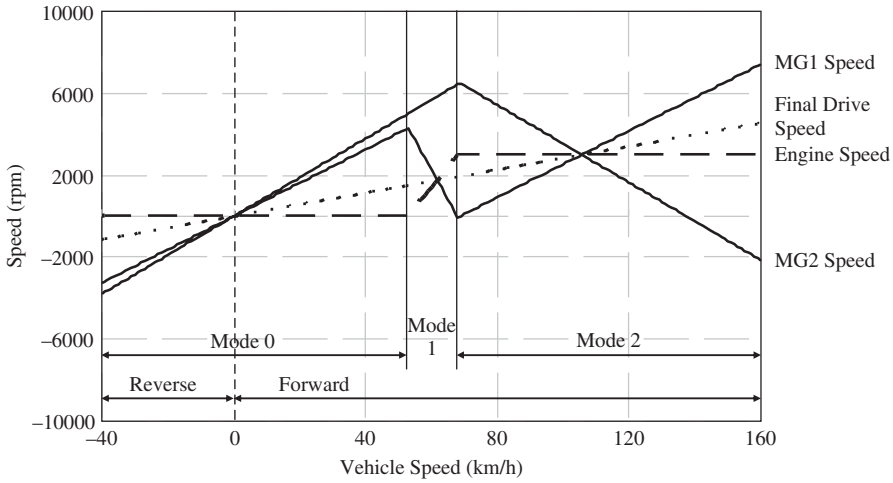

Figure 4.10 Speed relationships of the two-mode transmission in Example 4.3

4.4 Dual-Clutch Hybrid Transmissions*

There are a few variants of automatic transmissions such as automated manual transmission (AMT), CVT, and dual-clutch transmission (DCT). Each of these technologies has

* © [2009] IEEE. Reprinted, with permission, from 2009 IEEE VPPC Conference

Table 4.1 Qualitative comparison of automatic and manual transmissions

Aspects	Automatic transmission	Manual transmission	Desired transmission
Cost	Expensive	Lower	Low
Efficiency	Moderate	High	High
Ease of use	Easy	Hard	Easy
Comfort	Good	Poor	Good

its own penetration levels in different regions of the world (North America, Europe, or Japan). The advantages of DCT include high efficiency, low cost, and driving comfort. Conservative estimates peg DCT technology to be around 10% of the global market by 2015. Table 4.1 compares the advantages and disadvantages of CVT, AMT, and DCT.

DCT technology is well suited for high-torque diesel engines and high-revving gas engines alike. Some of the major drivers for DCT include:

- flexible and software tunability;
- gear ratio flexibility the same as that of manual lay shaft transmissions allowing greater compatibility with any engine characteristic.

4.4.1 Conventional DCT Technology

A typical DCT architecture has a lay shaft with synchronizers used for maximum efficiency. It also has launch clutches (either wet or dry) used with electronics, along with mechanical or hydraulic actuation systems to achieve the automatic shifting. Lay shaft transmissions yield an efficiency of 96% or better as compared to 85–87% efficiency of automatic transmissions [3, 4].

Figure 4.11 shows the diagram of a DCT-based transmission. It is a typical setup often found in all of the latest vehicle models with a DCT. It consists of two coaxial shafts each having the odd and even gears. It is tantamount to having two transmissions, hence the name.

In a DCT system, the two clutches are connected to two separate sets of gears. The odd gear set is connected to one of the clutches and the even gear set to the other clutch. It is necessary to preselect the gears to realize the benefits of the DCT system. Accordingly, the off-going clutch is released simultaneously as the on-coming clutch is engaged. This gives an uninterrupted torque supply to the driveline during the shifting process. This preselection of gears can be implemented using either complicated controllers such as fuzzy logic or simple ones such as selections based on the next anticipated vehicle speed.

4.4.2 Gear Shift Schedule

Initially, when the vehicle starts, gear N1i is synchronized. Therefore, engine torque is transmitted to the final drive through gears N1i and N1m. Vehicle speed increases as the odd clutch engages. When vehicle speed reaches a certain threshold, gear N2i is

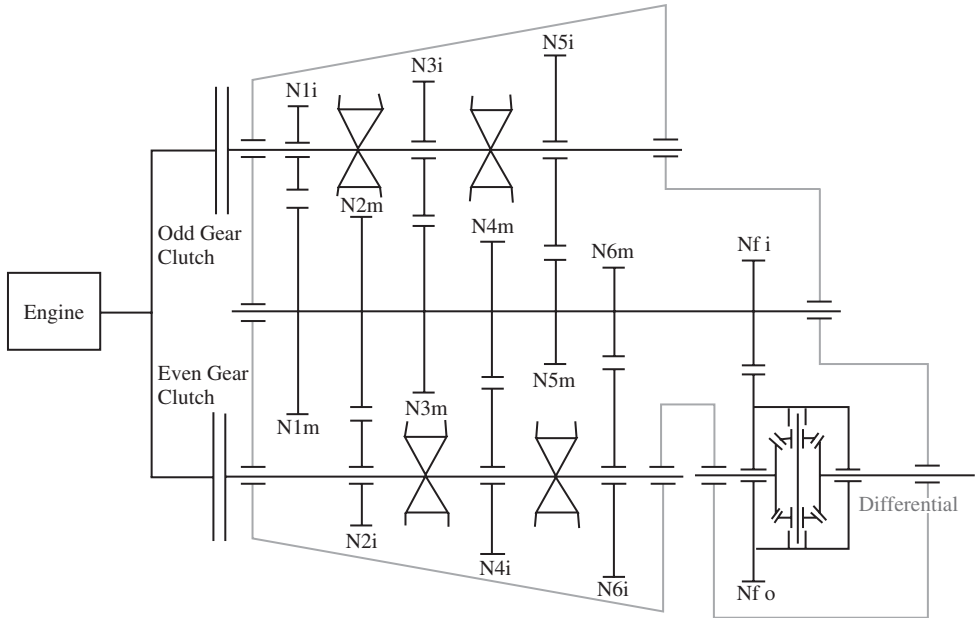

Figure 4.11 Dual-clutch transmission. Note that the reverse gear is omitted in the diagram

synchronized. As the even clutch engages (the odd clutch disengages), engine torque is shifted from gear N1i to N2i. Hence engine torque is transmitted through gear N2i and N2m. As vehicle speed increases, N3i is synchronized. Then the odd clutch would engage and the even clutch would disengage. This process will continue until the vehicle speed becomes stable (from N3i to N4i, from N4i to N5i, and from N5i to N6i).

During downshift, the process is reversed. For example, assume initially that N4i is synchronized and the even clutch is engaged. During downshift, N3i is synchronized before the even clutch opens. When the even clutch disengages and the odd clutch engages, engine torque is transferred from N4i to N3i. Similarly, N2i would be synchronized before the even clutch engages.

Since all transitions in a DCT are managed by gear synchronizers and two clutches, there is no need for a torque converter in DCT. The transitions (gear shifting and torque shifting) are very smooth. Control of the synchronizers and clutches, or shift controller, is computerized in the vehicle. The shift controller decides the upshifts or the downshifts of the transmission as per the gear shift schedule as shown from left to right in Figure 4.12. This controller intelligently preselects the higher or the lower gear depending on the current and desired vehicle velocity.

4.4.3 DCT-Based Hybrid Powertrain

The diagram for a DCT-based hybrid powertrain is shown in Figure 4.13 [5]. The transmission is a six-speed AMT. The hybrid powertrain consists of two motors with each coupled mechanically onto the two shafts using a standard gear reduction. Due to the

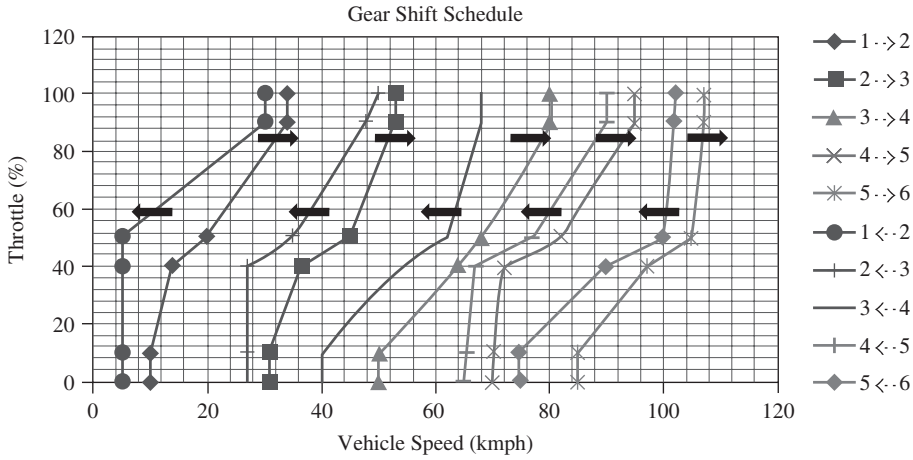

Figure 4.12 Gear shift schedule

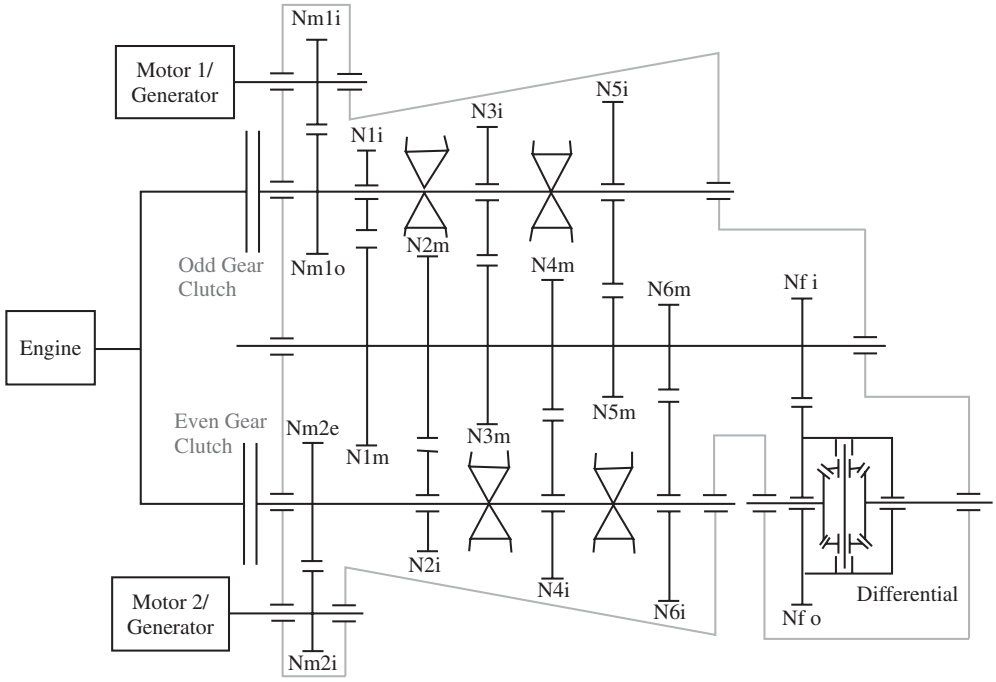

Figure 4.13 Hybrid powertrain based on dual-clutch transmissions. Reverse gear is not needed due to the fact that the motors can be used to back up the vehicle

presence of the motor/generator, the vehicle can be reversed without the reverse gear. The odd shaft houses gears 1, 3, and 5, and the even shaft houses gears 2, 4, and 6. The two motors can also be operated as generators as needed by the hybrid control strategy.

4.4.4 Operation of DCT-Based Hybrid Powertrain

The DCT-based hybrid powertrain shown in Figure 4.13 has seven operating modes when the vehicle is in motion and one additional operating mode for standstill charging.

4.4.4.1 Motor-Alone Mode

The vehicle is always launched in the motor-only mode unless the battery's state of charge (SOC) is below the minimum level. In this mode the gears are selected according to the shift logic controller. The vehicle operates in this mode up to a maximum speed defined by the controller, provided the SOC is greater than the minimum SOC for the battery as per the system design. Since the engine does not operate in this mode, the dual clutches are disengaged to prevent any backlash to the engine. Either motor can be used for the launch and backup of the vehicle. The equations for this mode are

$$\omega_o = \frac{\omega_m}{i_g i_a i_m} \tag{4.39}$$

$$T_o = i_a i_g i_m \times T_m \tag{4.40}$$

4.4.4.2 Combined Mode

This mode is selected when a high torque is required for situations such as sudden acceleration or climbing a grade. This mode is also selected if the vehicle speed becomes more than the maximum speed defined by the controller in the motor-alone mode. Both the engine and the motor provide the propulsion power to the drive shaft. Depending on the vehicle speed, the transmission shift controller selects the proper dual clutch and the gears. The power flow is shown in Figure 4.14. The equations for this mode are

$$\omega_o = \frac{\omega_m}{i_g i_a i_m} = \frac{\omega_e}{i_g i_a} \tag{4.41}$$

$$T_o = i_g i_a i_m T_m + i_g i_a T_e \tag{4.42}$$

4.4.4.3 Engine-Alone Mode

This mode involves the engine as the only source of propulsion. The engine controller ensures that the engine transmits power to the lowest possible gear ratio such that the engine remains in the best efficiency window. The equations for this mode are

$$\omega_o = \frac{\omega_e}{i_g i_a} \tag{4.43}$$

$$T_o = i_a i_g \times T_e \tag{4.44}$$

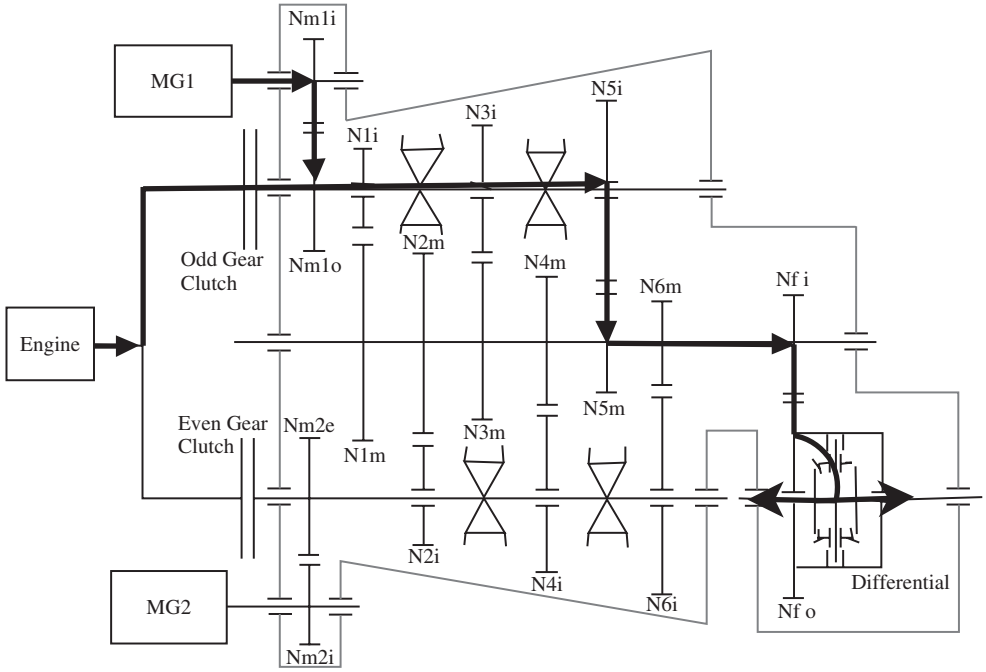

Figure 4.14 Power flow in the combined mode

4.4.4.4 Regenerative Braking Mode

The motor is coupled to the output shaft through gears and it can function as a generator as well. It is used to recover the energy during braking to charge the battery. Depending on the current clutch that is used, the controller decides which motor is to be operated in this mode. In case the motor torque is not sufficient to brake the vehicle, a conventional braking system is used to supplement the braking demand.

The equations for this mode are

$$\omega_{in} = \frac{\omega_m}{i_m i_g i_a} \tag{4.45}$$

$$T_{in} = -i_m i_a i_g \times T_m \tag{4.46}$$

4.4.4.5 Power Split Mode

This mode is used to charge the battery when the vehicle is in motion. The controller decides on this mode if the engine supplies more power than that required to drive the vehicle. The excess power is then used to charge the battery. The motor on the same lay shaft that drives the output shaft is selected to act as the generator to charge the battery.

The motor controller selects the correct motor depending on the shaft that is transmitting the power to the final drive. The equations for this mode are

$$\omega_o = \frac{\omega_m}{i_a i_m i_g} = \frac{\omega_e}{i_a i_g} \tag{4.47}$$

$$T_o = i_a i_g T_e - T_m \tag{4.48}$$

4.4.4.6 Standstill Charge Mode

This mode can be used to crank-start the engine or charge the battery when the vehicle is in standstill position. The controller opts for this mode when the battery SOC is lower than the minimum SOC level permitted by the design. This is the only operating mode when the engine is cranked and the vehicle is in standstill position. Since the vehicle is not moving and no power is transmitted to the drive train, all the gears are disengaged for safety. The kinematic equations for this mode are

$$\omega_o = 0 \tag{4.49}$$

$$T_e = T_m i_m \tag{4.50}$$

$$\omega_e = \frac{\omega}{i_m} \tag{4.51}$$

4.4.4.7 Series Hybrid Mode

This mode offers a very interesting option for the DCT-based hybrid powertrain. The engine is operated in a region near its sweet spot (by adaptively changing the gear ratios) so that the torque generated from the engine is used by one of the motors to generate electricity. This electricity is then used by another motor on the other shaft to drive the vehicle. This therefore gives an option of having the DCT-based hybrid powertrain operating as a series hybrid. The kinematic equations for this mode are

$$\omega_o = \frac{\omega_m}{i_a i_m i_g} \tag{4.52}$$

$$T_o = T_m i_m i_g i_a \tag{4.53}$$

4.5 Hybrid Transmission Proposed by Zhang *et al*.*

An alternate hybrid transmission was proposed to use one electric motor, a planetary gear set, and four fixed gears to realize automated transmission and CVT for a parallel hybrid, as shown in Figure 4.15 [6]. The design is based on the concept of AMTs. It uses a combination of lay shaft gearing and planetary gearing for power transmission. The lay shaft gears on the input shaft and the motor shaft freewheel unless engaged by the shifter–synchronizer assemblies. The carrier of the planetary gear train is connected with the input shaft that picks up the engine torque. The sun is connected with the motor shaft

* © [2006] ASME. Reprinted, with permission, from IASME Journal of Mechanical Design

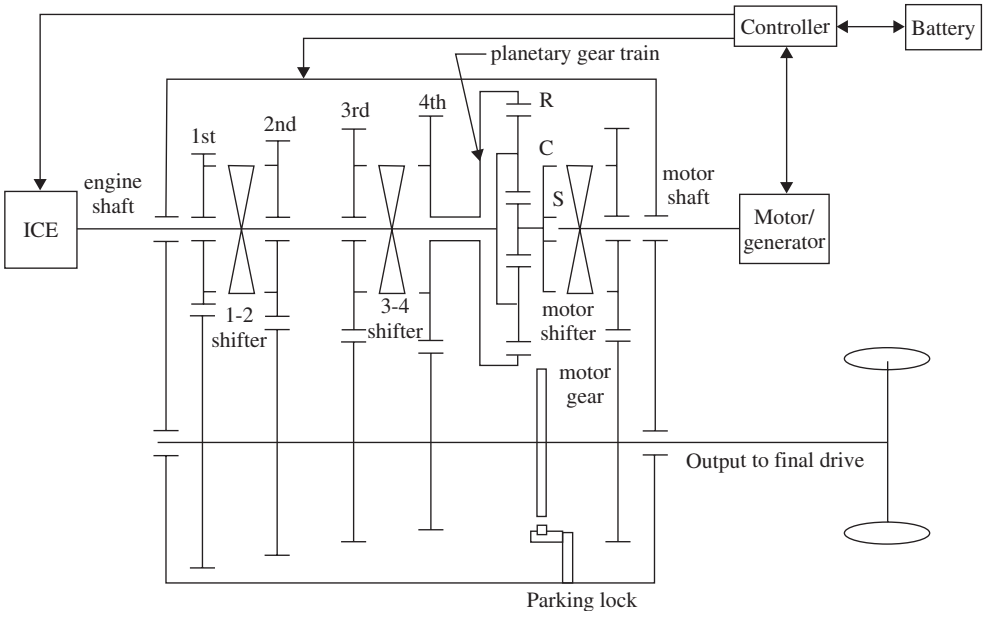

Figure 4.15 Hybrid transmission proposed by Zhang *et al.*

if so engaged. One motor is used either as the driving assisting unit or as the generator in charging and regenerative braking operations. Mode switching and gear shifting are realized by shifters actuated by computer and controlled step motors as in an AMT. The hybrid system has five operating modes for vehicle driving and one standstill mode for emergency or convenience operations. The six operating modes and the related kinematics are described in the following.

4.5.1 Motor-Alone Mode

The vehicle is always launched in the motor-alone mode. In this mode, the motor shaft is engaged by the shifter and power is transmitted to the final drive by the motor gears. Vehicle backup is realized by reversing the motor rotation. All other gears freewheel in this mode. The operating parameters for the engine and the motor in this mode are related by the following equations:

$$\omega_o = \frac{\omega_m}{i_m} \tag{4.54}$$

$$T_o = i_m T_m \tag{4.55}$$

where ω_o and ω_m are the angular velocities of the output shaft and the motor respectively, T_o and T_m are the output torque and the motor torque respectively, and i_m is the motor gear ratio.

4.5.2 Combined Power Mode

The combined mode is used when high power is required in situations such as accelerating and hill climbing. In this mode the motor shaft and one of the lay shaft pairs are engaged. One of the four available gears as shown in Figure 4.15 can be selected according to the vehicle operating condition. The motor and the engine operate at speeds that are mechanically linked by the gear ratios to drive the vehicle jointly, with the operating parameters related as follows:

$$\omega_o = \frac{\omega_e}{i_k} = \frac{\omega_m}{i_m} \tag{4.56}$$

$$T_o = i_k T_e + i_m T_m \tag{4.57}$$

where ω_e and T_e are the angular velocity and the torque of the engine respectively, and i_k (with $k = 1–4$) is the gear ratio of the lay shaft gear pairs.

4.5.3 Engine-Alone Mode

The engine-alone mode is the most efficient mode for highway cruising. In this mode, a lay shaft gear pair with low gear ratio is engaged to transmit the engine torque to the output shaft with the motor shaft in neutral. The vehicle runs like a conventional vehicle in this mode. The operating parameters are linked by the lay shaft gear ratio:

$$\omega_o = \frac{\omega_e}{i_k} \tag{4.58}$$

$$T_o = i_k T_e \tag{4.59}$$

4.5.4 Electric CVT Mode

The electric CVT mode provides two degrees of freedom for vehicle operation control that allows optimization of engine operation for best fuel economy. In this mode, the engine drives the vehicle and powers the generator for battery charging at the same time. The sun gear of the planetary gear train is coupled to the motor shaft by the shifter and the fourth lay shaft gear is coupled to the ring gear. The operating parameters of the system are governed by the characteristics of the planetary gear train as follows:

$$\omega_m = \frac{N_s + N_r}{N_s}\omega_e - \frac{N_r}{N_s} i_4 \omega_o \tag{4.60}$$

$$T_m = T_s = \frac{N_s}{N_s + N_r} T \tag{4.61}$$

$$T_o = T_r i_4 = \frac{N_r}{N_s + N_r} i_4 T_e \tag{4.62}$$

where N_r and N_s are the number of teeth of the ring gear and sun gear, respectively; T_r and T_s are the ring gear torque and sun gear torque which are distributed from the engine torque at a constant proportion. The output torque T_o and the angular velocity ω_o are determined by the vehicle driving condition. The engine torque and the torque provided to the generator are determined by optimizing the engine efficiency. In the

electric CVT mode, the engine speed ω_e is optimized at the point for the highest efficiency corresponding to the required torque. The generator speed ω_m is controlled such that the engine speed and torque are optimized.

4.5.5 *Energy Recovery Mode*

In the energy recovery mode, the motor is coupled to the output shaft through the motor gear pair by the shifter and functions as a generator. The relations for the operating parameters are the same as that in the motor-alone mode, with the power flow reversed.

4.5.6 *Standstill Mode*

In this mode, the motor is engaged by the shifter to the sun gear and the parking locker is applied to lock the output shaft (ring gear). The lay shaft gears freewheel. This mode can be used to crank-start the engine or use the engine to charge a low battery at standstill. It can also be used as a generator for household electricity or other conveniences if a bidirectional power converter is provided. The parameters are

$$\omega_e = \frac{N_s}{N_r + N_s}\omega_m \tag{4.63}$$

$$T_m = \frac{N_s}{N_r + N_s}T_e \tag{4.64}$$

4.6 Renault IVT Hybrid Transmission

In the Renault infinite variable transmission (IVT) as shown in Figure 4.16, there are two electric motors MG1 and MG2, two planetary gears sets P1 and P2, but no clutches [7]. MG1 is connected to the sun gear of P1; MG2 is connected to the sun gear of P2; the engine is connected to the carrier of P2 as well as the ring gear of P1; the carrier of P1 and the ring gear of P2 are coupled together and connected to the final drive. The system is capable of providing infinite variable transmission by controlling the two electric motors to match the vehicle speed while optimizing operation of the engine.

Since there are no clutches, there is only one operating mode. The steady state torque–speed relationships are as follows:

$$\omega_e = \omega_{c2} = \frac{N_{r2}}{N_{s2} + N_{r2}}\omega_o + \frac{N_{s2}}{N_{s2} + N_{r2}}\omega_{mg2} \tag{4.65}$$

$$\omega_o = \omega_{c1} = \frac{N_{r1}}{N_{s1} + N_{r1}}\omega_e + \frac{N_{s1}}{N_{s1} + N_{r1}}\omega_{mg1} \tag{4.66}$$

$$T_o = T_{r2} + T_{c1} = \frac{N_{r2}}{N_{s2} + N_{r2}}T_e + \frac{N_{r1} + N_{s1}}{N_{s1}}T_{mg1} \tag{4.67}$$

$$T_{mg2} = \frac{N_{s2}}{N_{s2} + N_{r2}}T_e \tag{4.68}$$

$$T_{mg1} = \frac{N_{r2}}{N_{r2}}T_e \tag{4.69}$$

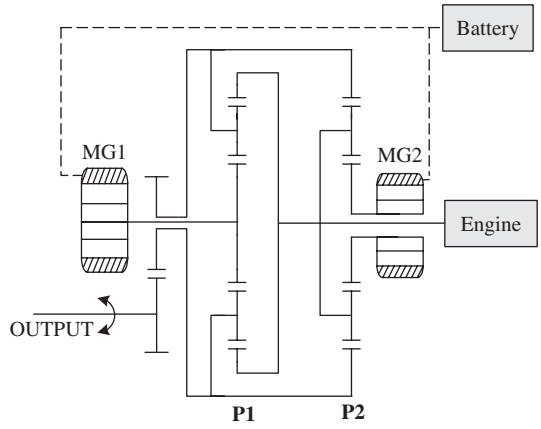

Figure 4.16 Renault two-mode transmission

4.7 Timken Two-Mode Hybrid Transmission

The Timken hybrid powertrain shown in Figure 4.17 is also a two-mode hybrid system [8]. The transmission contains two electric motors, MG1and MG2; two planetary gears, P1 and P2; two clutches, C1 and C2; and two locks, B1 and B2.

The engine is connected to the ring gear of P1; MG1 is connected to the sun gear of P1 and via a clutch (C2) to the ring gear of P2; MG2 is connected to the sun gear of P2; the carrier of P2 is connected to the output shaft; the carrier of P1 is connected through C1 to the output shaft, or can locked by B1. By controlling the two clutches and two locks, the system can operate in high range or low range based on vehicle operating conditions.

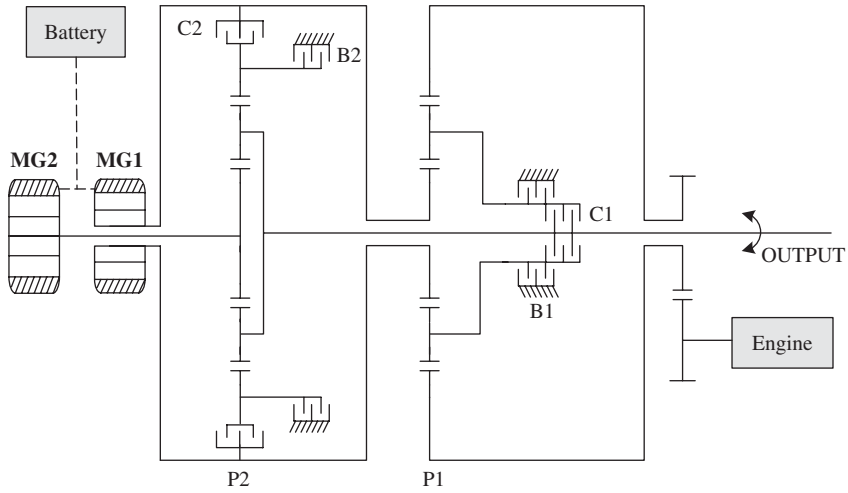

Figure 4.17 Timken two-mode transmission

4.7.1 Mode 0: Launch and Reverse

The vehicle can be launched by MG2. In this mode, B2 locks the ring gear of P2. MG2 torque is transferred through the sun gear of P2 to the carrier of P2. Since the sun gear of P1 is coupled to the ring gear of P2, the sun gear of P1 is also locked. In this case, the carrier of P1 needs to be locked by B1 so that the engine is stalled as well. The equations are

$$\omega_{mg2} = \omega_{s2} = \frac{N_{s2}}{N_{s2} + N_{r2}}\omega_o \tag{4.70}$$

$$T_o = \frac{N_{s2} + N_{r2}}{N_{s2}} T_{mg2} \tag{4.71}$$

4.7.2 Mode 1: Low-Speed Operation

In this mode, B2 locks the ring gear of P2; C1 engages the engine, as shown in Figure 4.18. The operation of this mode is exactly the same as the GM two-mode hybrid.

4.7.3 Mode 2: High-Speed Operation

In high-speed operation, C1 engages the carrier of P1; C2 engages MG1 (Figure 4.19). The sun gear of P1, the ring gear of R2, and MG1 will have the same speed. This mode is also the same as the GM two-mode hybrid powertrain.

4.7.4 Mode 4: Series Operating Mode

The powertrain can also operate in series mode by locking the carrier of P1 and ring gear of P2. In this mode (Figure 4.20), engine power is delivered to MG1 through the sun

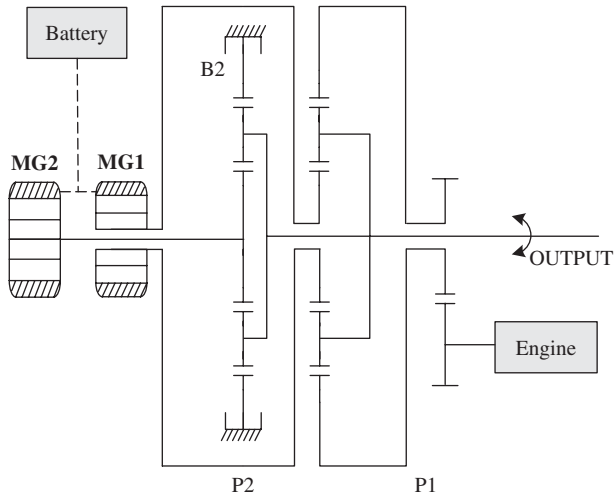

Figure 4.18 Low-speed mode of the Timken two-mode transmission

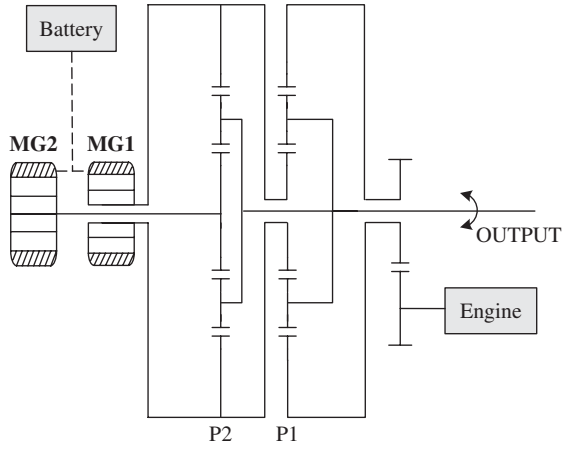

Figure 4.19 High-speed mode of the Timken two-mode transmission

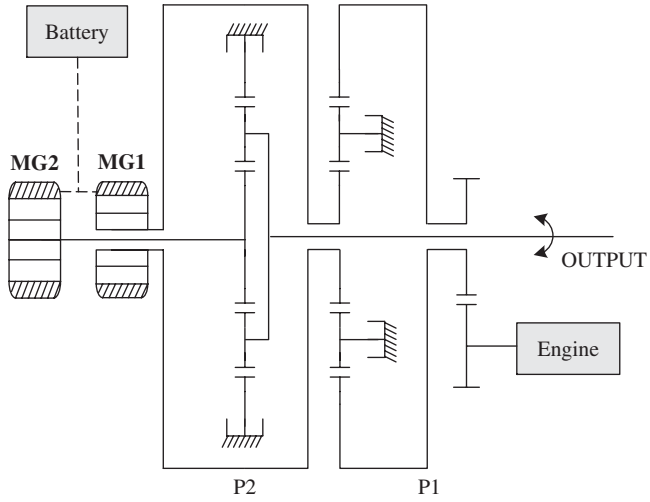

Figure 4.20 Series operating mode of the Timken two-mode transmission

gear of P1 (with the carrier locked). The electricity generated by MG1 will be delivered to MG2 which drives the sun gear of P2 which in turn drives the carrier of P2 with the ring gear locked. The torque-speed equations are

$$\omega_o = \omega_{c2} = \frac{N_{s2}}{N_{s2} + N_{r2}} \omega_{mg2} \tag{4.72}$$

$$\omega_{mg1} = -\frac{N_{r1}}{N_{s1}} \omega_e \tag{4.73}$$

$$T_o = \frac{N_{r2} + N_{s2}}{N_{s2}} T_{mg2} \tag{4.74}$$

$$T_{mg1} = \frac{N_{s1}}{N_{r1}} T_e \tag{4.75}$$

4.7.5 Mode Transition

Similar to any other hybrid powertrain, the transition between different modes needs to happen at the moment when mechanical disturbance to the system can be minimized. For example, with the carrier of P1 locked to B1, the engine can be started by MG1. In order to engage the carrier of P1 with the final drive shaft, first B1 needs to be released; then the speed of MG1 will be controlled such that C1 will accelerate to the same speed as the final drive shaft; and then C1 will engage the carrier of P1 to the final drive shaft. Similarly, in order to engage the ring gear of P2 to the sun gear of P1 (and MG1), the sun gear speed of P1 and MG1 is first brought down to zero and then C2 is engaged.

4.8 Tsai's Hybrid Transmission

In the hybrid system proposed by Tsai as shown in Figure 4.21, the transmission includes one electric motor, two clutches, two planetary gear sets, and two locks [9, 10].

There are 14 different combinations of operating modes based on the different configurations of the clutches and locks, but there are only seven valid modes:

C1	C2	B1	B2	State	Additional modes
0	0	0	0	None	—
0	0	0	1	None	—
0	0	1	0	Motor alone	Engine idle, generator/regen.
0	0	1	1	None	—
0	1	0	0	Engine + motor	Motor, generator/regen.
0	1	0	1	Engine alone	Motor stationary
0	1	1	0	None	—
0	1	1	1	None	—
1	0	0	0	Engine alone/CVT	Generator/charging
1	0	0	1	Engine + motor	Motor stationary
1	0	1	0	Engine + motor	Motor, generator/regen.
1	0	1	1	None	—
1	1	0	0	Engine + motor	Motor, generator/regen.
1	1	0	1	None	—
1	1	1	0	None	—
1	1	1	1	None	—

From [9]. © [2001] ASME. Reprinted, with permission, from *ASME Journal of Mechanical Design*.

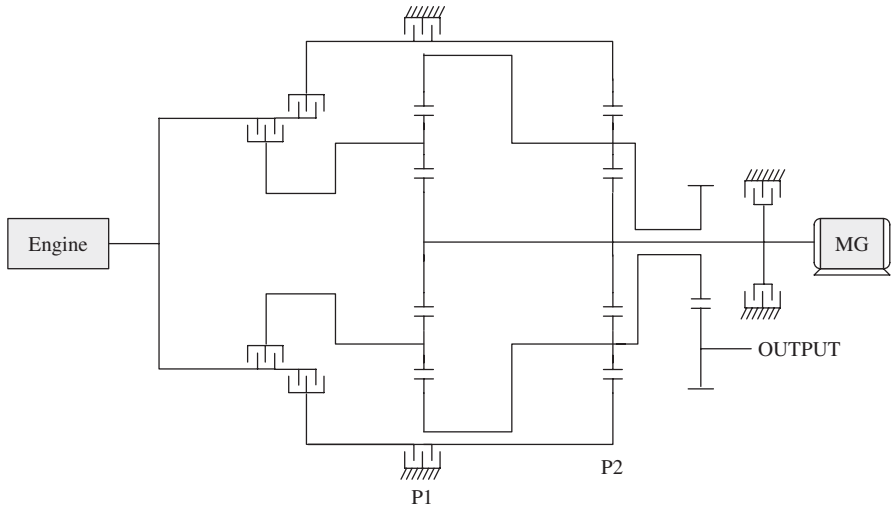

Figure 4.21 A multimode hybrid transmission proposed by Tsai *et al.** [9] (© [2001] ASME. Reprinted, with permission, from *ASME Journal of Mechanical Design*.)

The speed/torque relationships can be written in two conditions, that is, C1 engage or C2 engage.

When C1 engages (B1 freewheel)

$$\omega_e = \frac{N_{s1}}{N_{s1}+N_{r1}}\omega_m + \frac{N_{r1}}{N_{s1}+N_{r1}}\omega_o \tag{4.76}$$

$$T_o = \frac{N_{r1}}{N_{s1}+N_{r1}}T \tag{4.77}$$

$$T_m = \frac{N_{s1}}{N_{s1}+N_{r1}}T_e \tag{4.78}$$

When C1 engages (B1 lock)

$$\omega_e = \frac{N_{s1}}{N_{s1}+N_{r1}}\omega_m + \frac{N_{r1}}{N_{s1}+N_{r1}}\omega_o \tag{4.79}$$

$$\omega_o = \frac{N_{s2}}{N_{s2}+N_{r2}}\omega_m \tag{4.80}$$

$$T_o = \frac{N_{r1}}{N_{s1}+N_{r1}}T_e + \frac{N_{s2}+N_{r2}}{N_{s2}}T_m \tag{4.81}$$

When C2 engages

$$\omega_o = \frac{N_{s2}}{N_{s2}+N_{r2}}\omega_m + \frac{N_{r2}}{N_{s2}+N_{r2}}\omega_e \tag{4.82}$$

$$\frac{N_{s2}+N_{r2}}{N_{r2}}T_e = \frac{N_{s2}+N_{r2}}{N_{s2}}T_m \tag{4.83}$$

* The permission is from Figure 4.21, and the table before Figure 4.21

When C1 and C2 engage

$$\omega_o = \omega_m = \omega_e \tag{4.84}$$

$$T_o = T_m = T \tag{4.85}$$

4.9 Hybrid Transmission with Both Speed and Torque Coupling Mechanism

The hybrid configuration proposed by Ehsani *et al*. in [11] uses one electric motor, three clutches, and two locks to achieve both speed coupling and torque coupling functions (Figure 4.22) [11]:

- **Mode 0:** Vehicle launch and backup (motor-alone mode), and regenerative braking. C1 open, C2 closed, C3 open, L1 closed, and L2 open. Only the motor torque is transmitted to the final drive. The sun gear of the planetary gear is locked. The torque/speed relationships are

$$\omega_{out} = \frac{N_r}{N_s + N_r}\omega_m \tag{4.86}$$

$$T_{out} = \frac{N_s + N_r}{N_r}T_m \tag{4.87}$$

- **Mode 1:** Engine-alone mode. C1 closed, C2 open, C3 open, L1 open, L2 closed. In this mode, the motor is off – only the engine is transferring torque to the final drive. The ring gear is locked. The torque/speed relationships are

$$\omega_{out} = \frac{N_s}{N_s + N_r}\omega_e \tag{4.88}$$

$$T_{out} = \frac{N_s + N_r}{N_s}T_e \tag{4.89}$$

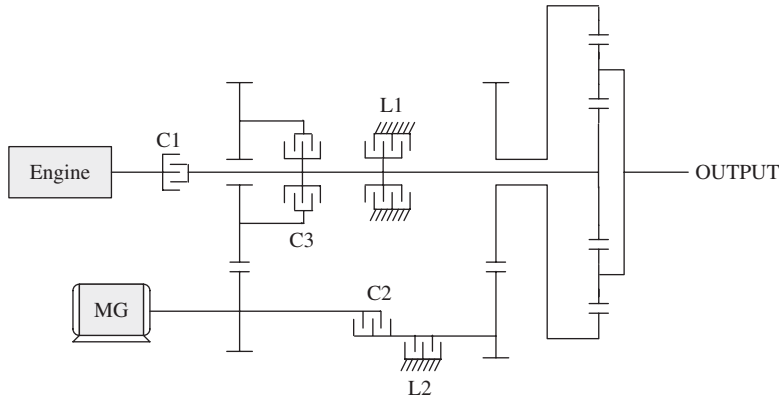

Figure 4.22 A hybrid transmission proposed in [11]

- **Mode 2:** Low-speed mode. C1 closed, C2 open, C3 closed, L1 open, L2 closed. In this mode, the engine torque and the motor torque are added to provide the maximum drivetrain torque for acceleration needs. The ring gear is locked and the motor torque is added to the engine shaft. The torque/speed relationships are

$$\omega_{out} = \frac{N_s}{N_s + N_r}\omega_e \tag{4.90}$$

$$\omega_m = \frac{N_1}{N_2}\omega_e \tag{4.91}$$

$$T_{out} = \frac{N_s + N_r}{N_s}\left(T_e + \frac{N_1}{N_2}T_m\right) \tag{4.92}$$

- **Mode 3:** Combined and power split mode (CVT). C1 closed, C2 closed, C3 open, L1 open, L2 open. In this mode, the motor and the engine output are coupled to the planetary gear on the sun gear and ring gear, respectively. The output and input relationships are

$$\omega_{out} = \frac{N_s}{N_s + N_r}\omega_e + \frac{N_r}{N_s + N_r}\omega_m \tag{4.93}$$

$$T_{out} = \frac{N_s + N_r}{N_s}T_e = \frac{N_s + N_r}{N_r}T_m \tag{4.94}$$

The vehicle could be running between Mode 2 and Mode 3 during highway cruising.

Mode transition in this transmission is complicated. In order to reduce mechanical disturbance, the locks have to be engaged at zero speed and the clutches have to be engaged when the two sides of the gears have similar speeds.

4.10 Toyota Highlander and Lexus Hybrid, E-Four-Wheel Drive

The Toyota Highlander and Lexus hybrid vehicles feature an electric four-wheel drive, or e-four, with the front wheels driven by a planetary gear-based hybrid powertrain, and the rear wheels driven by an electric motor. The generalized schematics are shown in Figure 4.23.

In the above scheme, the engine is connected to the carrier of the planetary gear set, the generator is connected to the sun gear, and the ring gear is connected to the final drive of the front axle. The total powertrain torque available during any driving condition is

$$T_{out} = \frac{N_r}{N_s + N_r}T_e + \frac{N_1}{N_2}T_{m1} + \frac{N_3}{N_4}T_{m2} \tag{4.95}$$

The generator torque is

$$T_g = \frac{N_s}{N_s + N_r}T_e \tag{4.96}$$

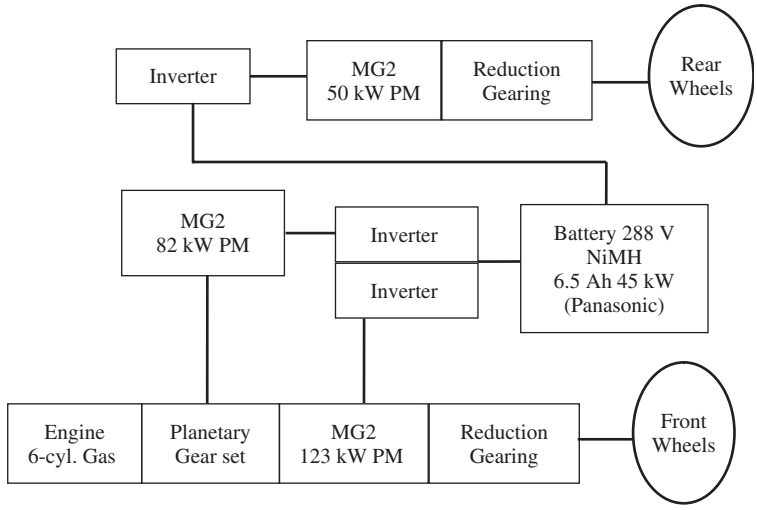

Figure 4.23 Schematics of electric four-wheel-drive hybrid system

The power relationship, when neglecting losses, is

$$P_{out} = P_{m1} + P_{m2} + P_r \tag{4.97}$$

$$P_e = P_r + P_g \tag{4.98}$$

$$P_{m1} + P_{m2} = P_g + P_B \tag{4.99}$$

A simplified version of the e-four is shown in Figure 4.24 with the goal of reducing the overall system cost (http://reviews.cnet.com/suv/2006-toyota-highlander-hybrid/1707-10868_7-31352761.html). In comparison to the above configurations, this configuration has significant cost advantage and is simple to fabricate and manufacture, because it does not involve any modification to the front axle design. However, this design does not allow flexibility of engine speed control. Besides, the system is not very efficient during power

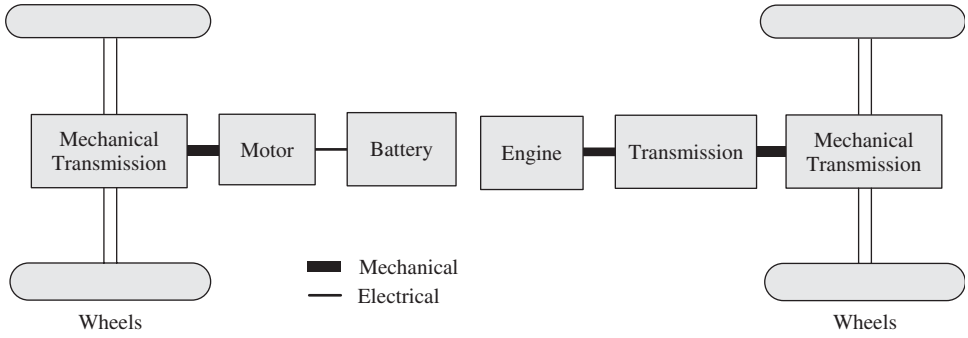

Figure 4.24 Hybrid powertrain with separate driving axles

split mode operation, because engine power needs to be transferred through the vehicle body to the rear axle and then to the electric motor. The total torque of the powertrain is

$$T_{out} = k_e T_e + k_m T_m \tag{4.100}$$

where k_e and k_m are the gear ratios of the engine transmission and motor transmission, respectively.

4.11 CAMRY Hybrid

In the Camry hybrid (Figure 4.25), there are two planetary gear sets. The engine, generator, and planetary gear set 1 are configured the same way as in the Prius, that is, the engine is coupled to the carrier, and the generator is coupled to the sun gear. However, the ring gear is connected to a counter gear which is also connected to the ring gear of the motor speed reduction planetary gear. The motor is connected to the sun gear of planetary gear set 2, and the carrier of planetary gear set 2 is grounded. The multifunction gear connects the counter gear and the final drive.

The ring gear speed can be calculated from the vehicle speed:

$$\omega_r = \frac{N_2}{N_1}\frac{N_4}{N_3} i_{fd} V \tag{4.101}$$

The engine and generator satisfy

$$\omega_e = \frac{N_{r1}}{N_{r1} + N_{s1}}\omega_r + \frac{N_{s1}}{N_{r1} + N_{s1}}\omega_g \tag{4.102}$$

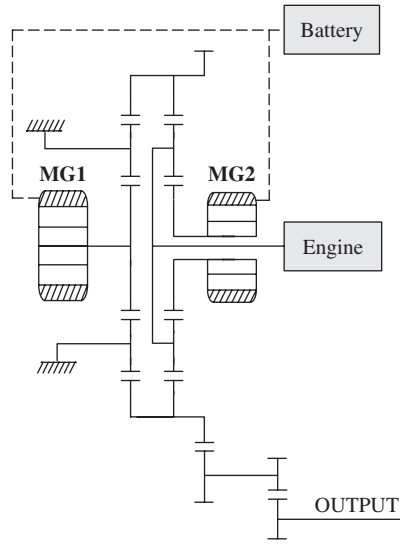

Figure 4.25 Toyota Camry hybrid transmission

The motor and the ring gear satisfy

$$\omega_r = -\frac{N_{s2}}{N_{r2}}\omega_m \tag{4.103}$$

The torque at the final drive is

$$T_{out} = \left(\frac{N_{r2}}{N_{s2}}T_m + \frac{N_{r1}}{N_{r1}+N_{s1}}T_e\right)\frac{N_2}{N_1}\frac{N_4}{N_3}i_{fd} \tag{4.104}$$

4.12 Chevy Volt Powertrain

The Chevy Volt from GM (Figure 4.26) has been described as an extended range electric vehicle, or EREV. The exact powertrain configuration is not yet public. However, a number of sources have suggested that the Volt employs two electric motors and a planetary gear set, along with the engine and three clutches [12, 13]. The Volt is equipped with a 16 kWh lithium-ion battery pack, a 125 kW induction motor, and a 1.41 four-cylinder engine. The initial driving range of 25–50 miles (40–80 km) can be achieved by using energy from the onboard battery, and additional driving range can be achieved by using gasoline.

In the Volt's transmission, MG1 is the main drive motor which is connected to the sun gear of the planetary system. The ring gear can be grounded through clutch C3, or connected to MG1 by engaging clutch C2. The carrier is connected to the final drive. The engine can be connected to MG1 through clutch C1. MG1 can be either connected to the engine to become a generator through C1, or connected to the ring gear to become a motor through C2.

The operation of the system can be described as follows:

- **Mode 1:** Single-motor driving mode. In this mode, MG1 drives the sun gear with the ring gear locked by C3. The torque of the motor is transmitted through the carrier to the final drive. The engine and MG2 are idle. All driving power is provided by the

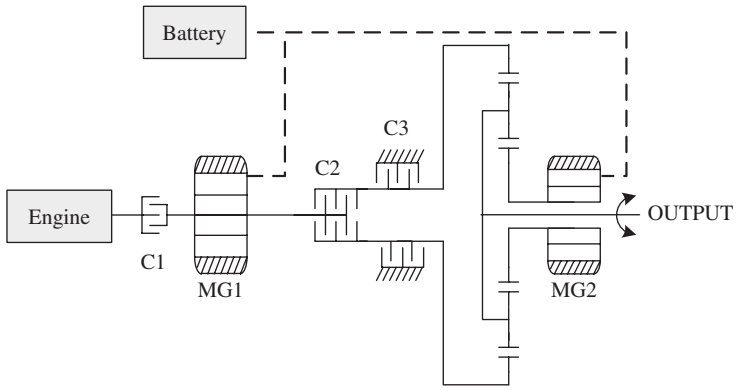

Figure 4.26 The Chevy Volt transmission

battery. This mode is suitable for launch, backup, low-speed driving, and cruising. The equation is

$$T_{out} = \frac{N_s}{N_s + N_r} T_{MG1} \tag{4.105}$$

- **Mode 2:** Dual-motor driving mode. In this mode, MG2 is connected to the ring gear through C2, with C3 disengaged. The engine is idle with C1 open. Both motors receive power from the battery to drive the carrier which delivers torque to the final drive. The equations are

$$\omega_{out} = \frac{N_s}{N_s + N_r} \omega_{MG1} + \frac{N_r}{N_s + N_r} \omega_{MG2} \tag{4.106}$$

$$T_{out} = \frac{N_s}{N_s + N_r} T_{MG1} = \frac{N_r}{N_s + N_r} T_{MG2} \tag{4.107}$$

  Since the speed of the two motors is added, this can achieve a high cruising speed for the vehicle. Hence, the authors believe this mode is used for highway cruising with the battery only.
- **Mode 3:** Extended driving range. In this mode, C1 is engaged so the engine drives MG2 which is now a generator. C2 is open and C3 is engaged to lock the ring gear. Electricity generated by MG2 is delivered to MG1 through power inverters. Only MG1 is driving the final drive. Hence, the output torque expression is the same as in Mode 1:

$$T_{out} = \frac{N_s}{N_s + N_r} T_{MG1} \quad \text{and} \quad T_{MG2} = kT_e \tag{4.108}$$

  where k is the gear ratio between the engine and MG2.
- **Mode 4:** With the engine turned on and C1 engaged, C3 is engaged as well (but C2 is open). Now, a portion of the engine torque can be transmitted to the ring gear to drive the carrier, which delivers the combined engine and MG1 torque to the final drive. Another portion of the engine torque is still used to drive MG2 to generate electricity. This mode is suitable for high-speed and heavy accelerations. Thus,

$$kT_e = T_{MG2} + T_r \tag{4.109}$$

$$\omega_{out} = \frac{N_s}{N_s + N_r} \omega_{MG1} + \frac{N_r}{N_s + N_r} \omega_{MG2} \tag{4.110}$$

- **Regenerative braking mode:** The engagement of the clutches is the same as in Mode 1. The only difference is that the wheels are now driving MG1 to generate electricity and at the same time generating the required braking torque to slow down the vehicle.

4.13 Dynamics of Planetary-Based Transmissions

4.13.1 Non-ideal Gears in the Planetary System

In the previous sections, the torque/speed relations were given under the assumption that the losses of transmission/gears are neglected, and the kinetic motion is also neglected.

When gear losses are considered, the torque equations of a planetary gear set in steady state can be expressed as

$$T_r + \xi_r \omega_r = \frac{N_r}{N_r + N_s}(T_c - \xi_c \omega_c) \tag{4.111}$$

$$T_s + \xi_s \omega_s = \frac{N_s}{N_r + N_s}(T_c - \xi_c \omega_c) \tag{4.112}$$

where ξ_c, ξ_r, and ξ_s stand for the frictional loss of the carrier, ring gear, and sun gear, respectively.

When the dynamics of the transmission is considered, there will also be transients in the transmission. For any given rotational system, the rotational dynamics can be written as

$$T_{in} = T_{out} + J\frac{d\omega}{dt} \tag{4.113}$$

In the following, the dynamics of the Toyota Prius planetary gear-based hybrid transmission is further analyzed. The analysis of other systems should be very similar.

When gear losses are considered, the torque relationships of the Prius transmission are

$$T_r + \xi_r \omega_r = \frac{N_r}{N_r + N_s}(T_e - \xi_c \omega_c) \tag{4.114}$$

$$T_g + \xi_s \omega_s = \frac{N_s}{N_r + N_s}(T_e - \xi_c \omega_c) \tag{4.115}$$

$$T_o = T_r + \frac{N_{m1}}{N_{m2}}(T_m - \xi_m \omega_m) \tag{4.116}$$

where ξ is the friction coefficient of each gear, and subscript m represents motor; r, ring gear; s, sun gear; c, carrier; g, generator; e, engine. ξ_m is the motor output gear.

4.13.2 Dynamics of the Transmission

The inertias of the final drive shaft and axle are transferred to the output shaft of the transmission [2]

$$J_{fd} = \frac{1}{G_a^2} J_a + J_{fd\_sh} \tag{4.117}$$

where the subscripts are: a, axle; and sh, final drive shaft. G_a is the final drive gear ratio. The final drive and the ring gear are coupled directly to the motor shaft. Therefore, on the motor shaft, the total inertia is

$$J_{ma} = J_m + J_r + J_{fd} \tag{4.118}$$

The sun gear is coupled to the generator. Therefore, the total generator shaft inertia is

$$J_{gq} = (J_s + J_g) \tag{4.119}$$

The engine shaft inertia is the total of the engine crankshaft and the carrier

$$J_e = J_{crank} + J_c \tag{4.120}$$

where J_{crank} is the crankshaft inertia. From generator to carrier,

$$J_{gc} = \frac{(N_r + N_s)N_r}{N_s^2}(J_g + J_s) \tag{4.121}$$

The generator shaft inertia can be transferred to the motor shaft and engine shaft. The equivalent inertias of the engine shaft and the motor shaft are

$$J_{eq} = J_e + \frac{(N_r + N_s)^2}{N_s^2} J_{gq} \tag{4.122}$$

$$J_{mq} = J_{ma} + \frac{N_r^2}{N_s^2} J_{gq} \tag{4.123}$$

On the generator shaft,

$$T_g = \frac{N_s}{N_s + N_r}\left(T_e - \xi_c\omega_c - J_{eq}\dot{\omega}_e - J_{gc}\dot{\omega}_m\right) - \xi_s\omega_s \tag{4.124}$$

On the output shaft,

$$\begin{aligned} T_o = {} & T_m - \xi_m\omega_m + \frac{N_r}{N_r + N_s}(T_e - \xi_c\omega_c) \\ & - \left(\frac{N_r}{N_r + N_s} J_{eq} + J_{gc}\right)\dot{\omega}_e - \left(\frac{N_r}{N_r + N_s} J_{gc} + J_{mq}\right)\dot{\omega}_m \end{aligned} \tag{4.125}$$

This torque will drive the final drive shaft at a certain speed. Due to slip of the wheels, $\lambda = (\omega r - V)/V$, there exists a traction force $F_{fd} = mg\mu(\lambda)$, where $\mu(\lambda)$ is the traction coefficient. This traction force is to overcome the resistive force of the vehicle during driving:

$$F_{fd} = mg\mu(\lambda) = mg\sin\alpha + \frac{1}{2}C_D A_F \rho V^2 + mg(C_0 + C_1 V^2) + m\frac{dV}{dt} \tag{4.126}$$

4.14 Conclusions

It should be noted that most planetary gear-based HEVs, including the Toyota, Ford, and GM two-mode hybrids, do not include a separate dedicated starter for the engine. The engine is started by one of the motors/generators at an appropriate condition. Due to the fact that the engine usually starts at the time when the drive needs more power, such as on acceleration, there is usually a "jerk" or "hiccup" because a portion of the motor torque is diverted to start the engine. The battery has limited power capability.

Another issue that many drivers have experienced is the weakness of the 14 V battery used to supply power to the vehicle's auxiliary power, such as for wipers, headlights, entertainment systems, power steering, hydraulic compressor, and so on.

The authors feel that, if a starter–alternator is added, the "jerk" during acceleration can be eliminated because the engine may be started by the 14 V onboard battery. Besides, this starter can also be used to charge the 14 V battery when the engine is on which may also ease the burden on the 14V battery.

In the case of the Toyota and Ford hybrid systems, an additional clutch between the engine and the planetary gear system could smooth acceleration.

Control of these powertrains is complicated. Often an advanced control algorithm is needed to manage the system. Fuzzy logic, dynamic programming, and wavelet transforms are popular in the power management of complex hybrid vehicles.

References

1. Holmes, A.G. and Schmidt, M.R. (2002) Hybrid electric powertrain including a two-mode electrically variable transmission. US Patent US6478705 B1, November 12, 2002.
2. Miller, J.M. (2006) Hybrid electric vehicle propulsion system architectures of the e-CVT type. *IEEE Transactions on Power Electronics*, **21** (3), 756–767.
3. Kulkarni, M., Shim, T., and Zhang, Y. (2007) Shift dynamics and control of dual-clutch transmissions. *Mechanism and Machine Theory*, **42** (2), 168–182.
4. Liu, Y., Qin, D., Jiang, H., and Zhang, Y. (2009) A systematic model for dynamics and control of dual clutch transmissions. *Journal of Mechanical Design*, **131**, 061012.
5. Joshi, A., Shah, N.P., and Mi, C. (2009) Modeling and simulation of a dual clutch hybrid vehicle powertrain. 5th IEEE Vehicle Power and Propulsion Conference, September 7–11, Dearborn, MI.
6. Zhang, Y., Lin, H., Zhang, B., and Mi, C. (2006) Performance modeling of a multimode parallel hybrid powertrain. *Journal of Mechanical Design, Transactions of the ASME*, **128** (1), 79–80.
7. Villeneuve, A. (2004) Dual mode electric infinitely variable transmission. Proceedings of the SAE TOPTECH Meeting on Continuously Variable Transmission, March 8–11, Detroit, MI , pp. 1–11.
8. Ai, X., Mohr, T., and Anderson, S. (2004) An electro-mechanical infinitely variable speed transmission. Proceedings of the SAE Congress Expo, March 8–11, Detroit, MI.
9. Tsai, L.W., Schultz, G.A., and Higuchi, N. (2001) A novel parallel hybrid transmission. *Journal of Mechanical Design, Transactions of the ASME*, **123**, 161–168.
10. Schultz, G.A., Tsai, L.W., Higuchi, N., and Tong, I.C. (2001) Development of a novel parallel hybrid transmission. SAE 2001 World Congress, March, Detroit, MI.
11. Ehsani, M., Gao, Y., and Emadi, A. (2009) *Modern Electric, Hybrid Electric, and Fuel Cell Vehicles: Fundamentals, Theory, and Design*, 2nd edn, Power Electronics and Applications Series, CRC Press, Boca Raton, FL.
12. Conlon, B.M., Savagian, P.J., Holmes, A.G., and Harpster, M.O. Jr. (2007) Output split electrically-variable transmission with electric propulsion using one or two motors. US Patent US2009/0082171 A1, filed September 10, 2007, and published March 26, 2009.
13. Amend, J.M. (2010) Charge up, Chevy Volt rises above sound, fury of introduction. *Ward's AutoWorld*, November.

5

Plug-in Hybrid Electric Vehicles

5.1 Introduction to PHEVs

Plug-in hybrid electric vehicles (PHEVs) have the potential to displace transportation fuel consumption by using grid electricity to drive the car. PHEVs can be driven initially using electric energy stored in the onboard battery, and an onboard gasoline engine can extend the driving range. In the 1990s and early 2000s, pure electric cars were not successful, one of the major reasons being the limited driving range of the battery-powered cars available at that time. For example, the GM electric vehicle (EV) had a range of about 100 miles (160 km) and the Ford Ranger electric truck had a range of approximately 60 miles (96 km).

5.1.1 PHEVs and EREVs

PHEVs are sometimes called range-extended electric vehicles (ReEVs) or extended range electric vehicles (EREVs), in the sense that these vehicles always have onboard gasoline or diesel that can be used to drive the vehicle for an extended distance when the onboard battery energy is depleted. Furthermore, these vehicles can provide high fuel economy during the extended driving range due to the large battery pack that can accept more regenerative braking energy and provide more flexibility for engine optimization during the extended driving range.

However, EREVs, such as the GM Chevy Volt, must be equipped with a full-sized electric motor so that pure electric driving can be realized for all kinds of driving conditions. It is shown that, for some driving conditions, all-electric drive sometimes does not provide the most benefits, given the limited battery energy available.

For example, the powertrain motor of a PHEV is rated at 125 kW, and the battery pack has a capacity of 16 kWh. This means that at full powertrain power, the battery needs to supply a power eight times its nominal capacity, or 8 C. This high power requirement not only is difficult to achieve, but also results in inevitable heavy losses inside the battery pack, which makes the drive system very inefficient.

Hybrid Electric Vehicles: Principles and Applications with Practical Perspectives, First Edition.
Chris Mi, M. Abul Masrur and David Wenzhong Gao.

Example 5.1: A 400 V, 16 kWh lithium-ion battery pack has an internal impedance of approximately 0.5 Ω. The motor and inverter have a combined efficiency of 90% and rated output of 125 kW. The rated current is 347 A on the DC side of the inverter. At this current, the battery will drop 174 V internally. In other words, the battery terminal voltage will be only 226 V at 347 A. This will result in a battery output power of 78 kW instead of 125 kW, and a loss inside the battery to an amount of 60.8 kW.

5.1.2 Blended PHEVs

Blended PHEVs have become more popular because of the reduced system cost (smaller electric motor, smaller battery pack, and lower battery power ratings), as well as the flexibility of optimizing fuel economy for different driving conditions. Compared to an EREV, a blended PHEV usually uses a parallel or complex configuration in which the engine and the motor can both drive the wheels directly. Since the engine is available for propulsion at high power demand, the size of the electric motor and the power requirement for the battery pack can be much smaller than the one in an EREV. Therefore, the cost of the vehicle is reduced.

Planetary gear-based hybrid vehicles, such as the Toyota Prius, and the GM two-mode hybrid, can be considered as parallel configurations since the electric motor (referred to as MG2 in Chapter 4) is in parallel with the engine output, while the generator (referred to as MG1 in Chapter 4) is used to realize the continuously variable transmission (CVT) and to optimize engine operation.

5.1.3 Why PHEV?

A survey [1, 2] showed that 78% of the US population drives an average of 40 miles (64 km) or less in their daily commuting. Figure 5.1 shows the distribution of daily miles driven versus percentage of population. Based on this survey, a PHEV with an electric range of 40 miles (or PHEV40) will satisfy the daily driving needs of 78% of the US population while driving on electricity in their daily commuting. Furthermore, people owning a 40 mile electric range PHEV but driving less than 40 miles daily will not need to refuel gasoline if they charge their car at night on a daily basis.

PHEVs can produce significant environmental and economic benefits for society. The advantages of PHEVs can be evaluated by how much fuel is displaced, as well as by how much pollution, including greenhouse gas (GHG) emissions, can be reduced. The main purpose for developing PHEVs can be summarized as follows:

1. **Displacement of fossil fuel consumption in the transportation sector:** Since PHEV owners will not need to refuel gasoline or need less gasoline, a significant amount of fossil fuel can be saved. This will have a long-term impact on the economy, environment, and political arena.
2. **Reduction of emissions:** Due to the reduced use of gasoline, a significant amount of emissions can be reduced due to the large deployment of PHEVs. Centralized generation of electricity is much more efficient and has much less emissions than

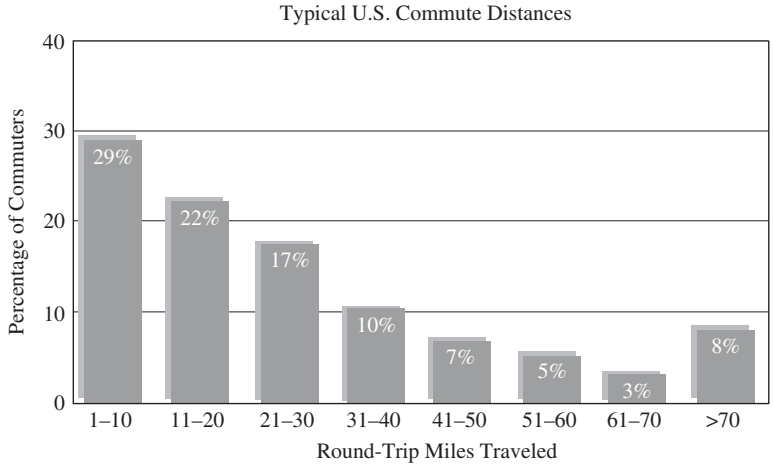

Data from the U.S. Bureau of Transportation show that 78% of commuters travel 40 miles or less each day-the expected battery-only range of PHEVs with routine overnight charging. For longer distances, the vehicles could run indefinitely in hybrid (gasoline/electric) mode.

Figure 5.1 Daily commuting distance versus population [1]. (Courtesy EPRI.)

gasoline-powered cars. Mitigation of emissions from urban (by cars) to remote areas (in power plants) where electricity is generated can also mitigate the heavy pollution in population-dense metropolitan areas. As more and more electricity in the future will come from renewable energy sources (which will be used by PHEVs), the emissions can be further reduced.

3. **Energy cost savings:** PHEVs use electricity for the initial driving range. Since electricity is cheaper than gasoline on an equivalent energy content basis, the cost per mile driven on electricity is cheaper than on gasoline. At the present time, gasoline costs about $3 per gallon in the United States, while electricity costs $0.12 per kWh. For a medium-size car, a gallon of gasoline can drive the car for about 30 miles, while a kilowatt hour of electricity can drive it 5 miles. This means that it will cost approximately $0.72 (or 6 kWh of electricity) to drive 30 miles while it costs $3 of gasoline to drive 30 miles. In other words, a driver can save $2.28 for 30 miles driven. However, PHEVs are generally more expensive than conventional cars due to an increased number of components, such as batteries and motors. The initial cost of the PHEV will take the owner some time to recover from fuel savings. At current fuel prices, it will take a number of years for the owner to recover the initial investment. As petroleum prices increase in the long run, the cost savings could be more advantageous. Also, as the production of PHEVs ramps up, their cost is expected to drop. Government incentives (tax rebates etc.) also help subsidize the initial cost of PHEVs. A differentiated electricity pricing structure could potentially help PHEVs. This potential structure will charge the consumer a lower rate if the PHEV is charged during off-peak times. Of course, the consumer still has the option to charge at any time.
4. **Maintenance cost savings:** PHEVs can generally save maintenance costs. Due to the extensive use of regenerative braking, braking system maintenance and repair is less

frequent, such as brake pad replacement, brake fluid change, and so on. Since the engine is not operating, or operating for much less time, there will be longer intervals for oil changes and other engine maintenance services.

5. **Backup power:** A PHEV can be used as a backup power source when a bidirectional charger is provided. A typical PHEV battery pack can provide a home or office with 3–10 kW of power for a few hours, and the onboard engine generator/motor can further extend the backup duration by using gasoline to generate electricity.
6. **End-of-life use of the battery:** Batteries that can no longer provide the desired performance in a PHEV can potentially be used for grid energy storage, which provides voltage regulation, system stability, and frequency regulation for a power grid. In particular, frequency regulation and stability become more and more important as more and more renewable energy generation is put on the power grid. These "retired" batteries, which may still have 30–50% of their original energy capacity, can provide this type of service.

5.1.4 Electricity for PHEV Use

Since PHEVs need to be charged from the power grid, the utility industry must be ready for the large deployment of PHEVs. Fortunately, the deployment of PHEVs will take place over a period of time, which will give the utility industry sufficient time to get ready.

PHEVs will be mostly charged at night. The electric power grid has capacity available at late evenings and nights when most of the PHEVs are charged. An Electric Power Research Institute (EPRI) study showed that with 1 million PHEVs plugged into the US grid, there is no need to build a single power plant in the United States [1]. With 10 million PHEVs on the road, the United States will only have to build three additional power plants (http://www.ornl.gov/info/ornlreview/v40_2_07/2007_plug-in_paper.pdf) [1–4].

On the other hand, electricity can be generated from a variety of sources, including nuclear and renewables such as hydroelectric, wind, photovoltaic, and ocean waves. Even coal-fired power plants will have advantages because there are more coal reserves than petroleum. By using renewable energy for PHEVs, it will significantly reduce the consumption of petroleum-based fossil fuel. Finally, centralized generation will reduce the total emissions and move the source of emissions to urban areas.

Figure 5.2 shows the current electricity generation portfolio in the United States [5]. Coal-fired power plants constitute the primary electricity generation in the world. However, it was estimated that the world has coal reserves for about 400 years at the current rate of consumption while petroleum will last only 40 years. It can also be seen that there is potential for renewable energy to grow.

5.2 PHEV Architectures

Figure 5.3 shows the architecture of a series PHEV. In the series configuration, the gasoline engine output is connected to a generator. The electricity generated by the generator can be used to charge the battery or supply power to the powertrain motor. The electric

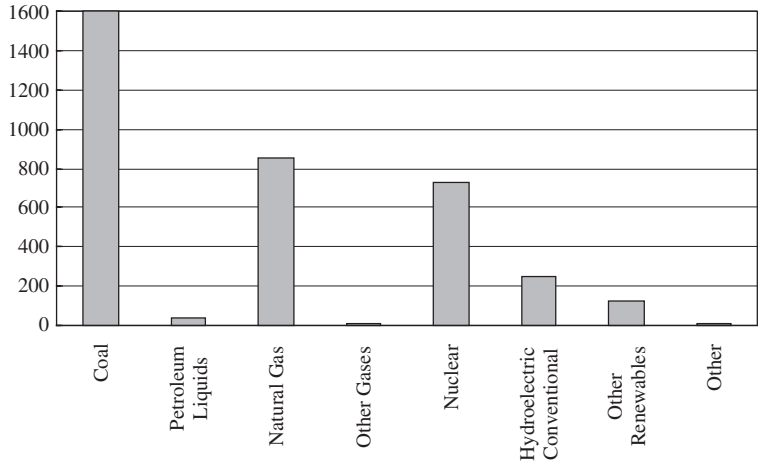

Figure 5.2 The US electricity generation portfolio [5]

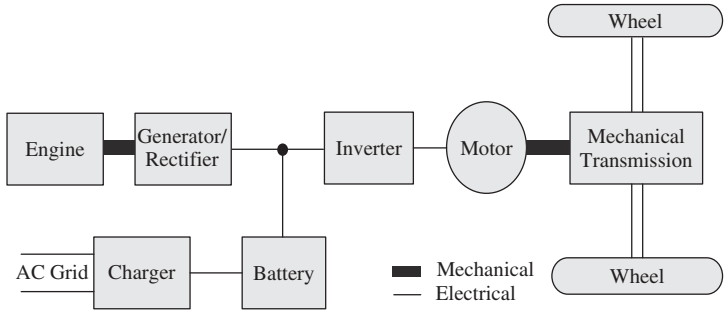

Figure 5.3 Series architecture of a PHEV

motor is the only component driving the wheels. The motor can be an induction motor, a switched reluctance motor, or a permanent magnet motor. The motor can be mounted on the vehicle in the same way as in a conventional vehicle, without the need for transmission. In-wheel hub motors can also be chosen. In the series configuration, the motor is designed to provide the torque needed for the vehicle to drive in all conditions. The engine/generator can be designed to provide the average power demand.

Parallel and complex hybrids can be designed as PHEVs as well. In parallel and complex configurations, the engine and the motor can both drive the wheels. Therefore, the motor size can be smaller than those in series configurations. In comparison to regular hybrid electric vehicles (HEVs), a parallel or complex PHEV will have a larger-sized battery pack that provides longer duration for extended electric drive. The engine is turned on whenever the vehicle's power demand is high.

5.3 Equivalent Electric Range of Blended PHEVs

For an EREV, the electric range can be easily calculated. For a blended PHEV, there may be no pure electric driving range available for some driving cycles. To find the equivalent electric range, it is useful to compare the fuel economy of a blended mode PHEV during charge-depletion (CD) mode to that of a comparable HEV.

Example 5.2: Assume there are two vehicles, one regular HEV and one PHEV, both using the same powertrain architecture and components. However, the PHEV has a larger battery pack of 11 kWh while the HEV has a 2 kWh battery pack. Neglect the weight difference of the two vehicles. The HEV has a fuel economy of 40 MPG. The PHEV has a fuel economy of 60 MPG during CD mode driving. The total CD mode range is 60 miles for the PHEV. It achieves 40 MPG during charge-sustaining (CS) mode driving.

This means that for 1 gallon of gasoline, the difference in distance between the two vehicles is 20 miles. Therefore, the equivalent electric range of this PHEV is 20 miles. However, it must be pointed out that the 20 mile electric range is realized within a total 60 miles, not the first 20 miles, like the EREV.

Example 5.3 (Similar to Example 5.2): The HEV has a fuel economy of 40 MPG and the PHEV has a fuel economy of 120 MPG during CD mode driving and 40 MPG during CS mode driving. The total CD mode range of the PHEV is 45 miles.

For the first 45 miles, at 120 MPG, the PHEV consumes 0.375 gallons of gasoline. For this amount of gasoline, the HEV will run 15 miles. The difference between the two vehicles is 30 miles, which can be considered as the equivalent electric range of the PHEV.

5.4 Fuel Economy of PHEVs

The fuel economy of conventional vehicles is evaluated by fuel consumption (liters) per 100 km, or miles per gallon. In the United States, the Environmental Protection Agency sets the methods for fuel economy certification. There are usually two numbers, one for city driving and one for highway driving. There is an additional fuel economy number that evaluates the combined fuel economy by combining the 55% city and 45% highway MPG numbers [6–8]:

$$FE_{MPG\_Combined} = \frac{1}{\frac{0.55}{FE_{city}} + \frac{0.45}{FE_{highway}}} \tag{5.1}$$

For pure EVs, the fuel economy is best described by electricity consumption for a certain range, for example, watt hour/mile or kWh/100 km. For example, a typical passenger car consumes 120–250 Wh/mile. In order to compare the fuel efficiency

of EVs with conventional gasoline or diesel vehicles, the energy content of gasoline is used to convert the numbers. Since 1 gallon of gasoline contains 33.7 kWh energy (http://www.eere.doe.gov), the equivalent fuel economy of an EV can be expressed as

$$FE_{gas\_equivalent} = \frac{1}{\text{Wh/mile}} \times 33\,700 \tag{5.2}$$

Therefore, a passenger car that consumes 240 Wh/mile will have an equivalent gasoline mileage of 140 MPG from the energy point of view.

5.4.1 Well-to-Wheel Efficiency

The above fuel efficiencies are also called tank-to-wheel efficiencies. This does not reflect the losses during the refining and distribution. It is sometimes easier to compare the overall fuel efficiencies of conventional vehicles and EVs. For gasoline, this efficiency is 83%, which reflects a lumped efficiency from the refining and distribution of gasoline. For electricity generation, this efficiency is 30.3%, which reflects a lumped efficiency that includes electricity generation of 32.8% (assume electricity is generated from gasoline) and distribution of electricity at 92.4%. Charge efficiency of the battery also needs to be reflected [9]. Thus,

$$FE_{EV\_well\_wheel} = \frac{1}{\text{Wh/mile}} \times 33\,700 \times \eta_{electricity} \tag{5.3}$$

$$FE_{ICEV\_well\_wheel} = FE_{mpg} \times \eta_{gasoline} \tag{5.4}$$

where $\eta_{electricity} = 30.3$ and $\eta_{gasoline} = 83\%$, and subscript *ICEV* stands for Internal Combustion engine Vehicle.

Example 5.4: A car of 30 MPG will have a well-to-wheel fuel efficiency of 24 MPG, and an EV that consumes 240 Wh/mile will have a well-to-wheel efficiency of 42.5 MPG.

5.4.2 PHEV Fuel Economy

For PHEVs, it is usually confusing as to which number should be used. Here, we discuss two different scenarios: all-electric capable PHEVs and blended PHEVs.

For all-electric capable PHEVs, it is useful to indicate the electric range, in miles or kilometers, and associated energy consumption during that range, in kilowatt hours/mile, and potentially gas equivalent MPG. Another set of numbers is needed to show the MPG during CS mode driving. A suggested label is shown in Figure 5.4.

For blended PHEVs, since there is no pure electric driving range, it is useful to label the fuel economy in CD and CS mode separately as shown in Figure 5.5. It may be preferred to include the electric energy consumption during CD mode as well.

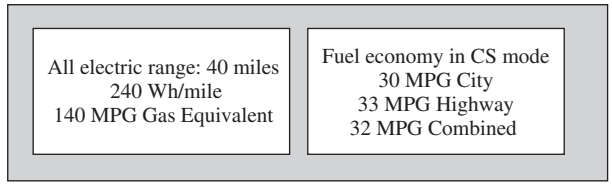

Figure 5.4 Fuel economy labeling for all-electric-capable PHEV

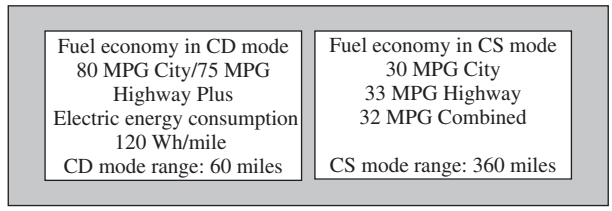

Figure 5.5 Fuel economy labeling for blended PHEV

5.4.3 Utility Factor

Another approach for fuel economy clarification is to use a utility factor. A utility factor is defined as the ratio of CD range of a PHEV to the total distances driven in daily commuting by all the US population. For example, a CD range of 20 miles will result in a utility factor of 40% (Figure 5.6). Using the utility factor, the combined fuel economy can be expressed as [6]

$$FE_{Gas\_equivalent} = \frac{1}{\frac{UF}{FE_{CD}} + \frac{1 - UF}{FE_{CS}}} \tag{5.5}$$

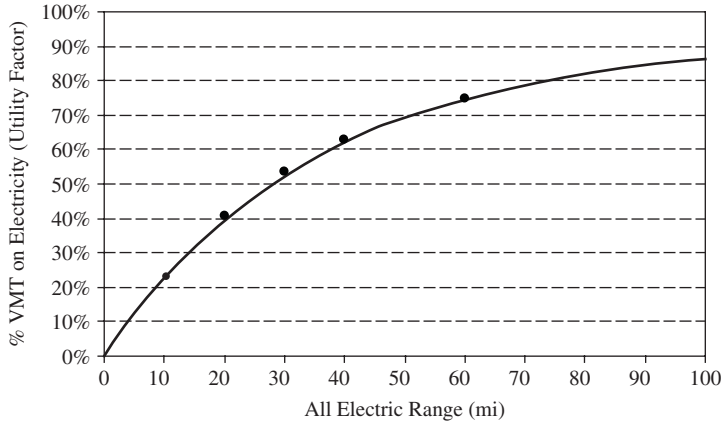

Figure 5.6 Definition of utility factor of PHEV (VMT, Vehicle Miles Traveled.)

where UF is the utility factor, and FE_{CD} and FE_{CS} are the fuel economy during CD and CS operation of a PHEV, respectively.

Example 5.5: In CD mode, a blended PHEV consumes 10 kWh of electric energy from the onboard battery and 1.5 l of gasoline in its first 64 km. Beyond 64 km, the car enters CS mode, which consumes 6.25 l of gasoline per 100 km. The car has a total range of 724 km. Calculate the fuel economy of the car.

- **Scenario 1:** In CD mode, since the car consumes 1.5 l of gasoline in its first 64 km, its fuel consumption is

$$FC_{CD,Gas} = 1.5/64 \times 100$$
$$= 2.34\,\text{l}/100\,\text{km or } 100\,\text{MPG, plus } 156\,\text{Wh/km electricity}$$

- **Scenario 2:** If the total energy consumption (gasoline and electricity) during CD mode is converted to gasoline equivalent, then the total energy consumption is

$$FC_{CD,Total} = \frac{2.34\,\text{l}}{100\,\text{km}} + \frac{15\,600\,\text{Wh}}{100\,\text{km}} \cdot \frac{1}{33\,700 \times 1.609} = 2.63\,\text{l}/100\,\text{km or } 89\,\text{MPG}$$

- **Scenario 3:** Beyond 64 km, its fuel consumption is

$$FC_{CS} = 6.25\,\text{l}/100\,\text{km or } 37.7\,\text{MPG}$$

- **Scenario 4:** The UF of this car is 0.62. The combined fuel economy by using the UF will be

$$FE_{Gas\_equivalent} = \frac{1}{\frac{UF}{FE_{CD}} + \frac{1-UF}{FE_{CS}}} = \frac{1}{\frac{0.62}{100} + \frac{1-0.62}{37.7}} = 61\,\text{MPG}$$

- **Scenario 5:** In this case, it is assumed that the car has a full tank of gasoline and a fully charged battery. It is then driven the full range of 724 km. If we consider the UF as the ratio of CD range versus total range, then the UF of this car is 64 km/724 km = 0.088. The overall fuel economy for the total range can be expressed as follows:

$$FE_{overall} = \frac{452\,\text{miles}}{\frac{40\,\text{miles}}{FE_{CD}} + \frac{412\,\text{miles}}{FE_{CS}}} = 40\,\text{MPG, plus } 10\,\text{kWh electricity}$$

5.5 Power Management of PHEVs

A PHEV involves the operating conditions of both CD mode and CS mode. Typically, when the battery is fully charged, the vehicle is operated in CD mode, and when the

battery state of charge (SOC) reaches a low threshold, it switches to CS mode. In CD mode, the vehicle will maximize the use of battery energy. In CS mode the vehicle will use gasoline to power the vehicle while maintaining the battery SOC at the same level.

During CD mode operation, the goal of vehicle power management is to minimize the total energy consumption by distributing power between the battery and the gasoline engine/generator for a given driving scenario. In other words, the goal of power management in a PHEV is to minimize the fuel consumption for a given drive scenario.

For a series PHEV (or EREV), if the drive distance is less than the nominal electric drive range, then it is possible to operate the vehicle in all-electric mode, hence no fuel is consumed. If the drive distance is longer than the electric range, then there are three possible approaches for operating the vehicle:

1. Operate the vehicle in electric mode until the battery is depleted to a preset threshold, then run in CS mode.
2. Operate the vehicle in a blended mode with the engine turning on at high power demands, and deplete the battery to the preset threshold at the end of the total driving cycle.
3. Operate the vehicle in a blended mode with the engine turning on at high power demands but with an optimal battery discharge policy, so the battery will be depleted to the preset threshold before the end of the total driving cycle.

In these approaches, since the total drive distance is the same, the one that consumes the least fuel will be the best choice. The fact that the battery will exhibit a large power loss at high power output in comparison to its output power, it may be advantageous to operate the vehicle in blended mode. The optimization problem can be expressed as

$$\min \{\text{fuel consumption}\}$$

Subject to a given distance and drive cycle

For a blended PHEV, since there is no pure electric range available, the goal of the power management is to minimize fuel consumption for a given drive cycle and given total battery energy available. This is strongly related to the characteristics of the power sources (battery and engine).

Figure 5.7 shows an idealized blended PHEV model for studying power management. In this model, the mechanical coupling and transmission losses are considered as part of the calculated vehicle power. The total vehicle power requested is satisfied by adding engine output and motor output

$$P_o = P_m + P_{eng} \tag{5.6}$$

and

$$P_b = P_m + p_b + p_m \tag{5.7}$$

where lower case p represents losses and upper case P represents total power or output power.

The vehicle power demand can be calculated using the driving cycle profile. Figure 5.8 shows the distribution of vehicle power demand. Figure 5.9 is the normalized power demand of the vehicle, where $f(P_o)$ represents the total time that the vehicle spends at a certain power demand P_o.

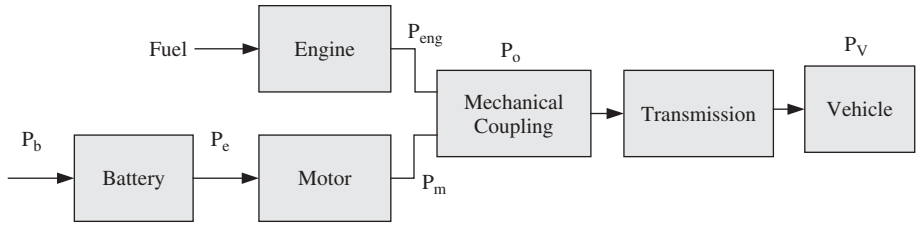

Figure 5.7 Idealized blended PHEV model for power management study

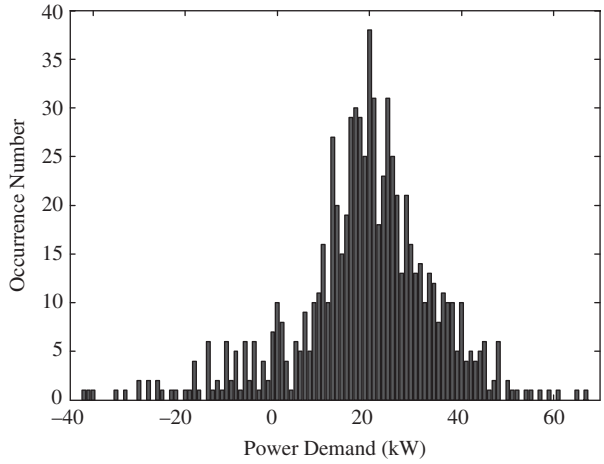

Figure 5.8 Power demand distribution in a passenger car under the US EPA's UDDS urban driving cycle. The horizontal axis is the power demand of the powertrain and the vertical axis is the occurrence of the power demand. The power demand is counted every second

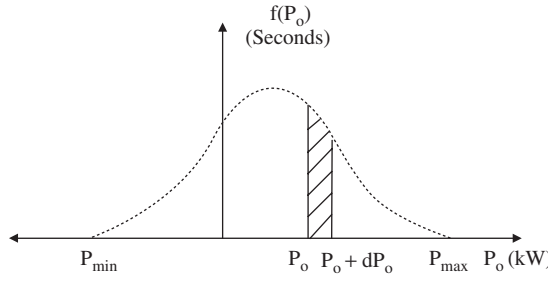

Figure 5.9 Normalized power demand distribution

The total battery energy consumed during the drive cycle is

$$E_b = \int_{P_{\min}}^{P_{\max}} P_b f\,(P_o)\,dP_o \tag{5.8}$$

The total fuel consumed is

$$F_e = \int_{P_{\min}}^{P_{\max}} f(P_{eng}) f\,(P_o)\,dP_o \tag{5.9}$$

where $f(P_{eng})$ is the fuel consumption of the engine for a given power output of P_{eng}.

The optimization problem is to minimize the total fuel consumption F_e for a given battery energy E_b = constant.

5.6 PHEV Design and Component Sizing

The main components of a PHEV are the powertrain motor and the battery pack. Using the vehicle resistive force and acceleration requirement, the driving motor can be sized. The total vehicle force is

$$F_{TR} = mg\sin\alpha + mgC_0 + mgC_1V^2 + \frac{1}{2}\rho C_D A_F V^2 + m\frac{dV}{dt} \tag{5.10}$$

where m is the vehicle mass, α is the road slope in radians, g is Earth's gravity, which is 9.8 m/s^2, C_0 and C_1 are rolling coefficients, ρ is air density, C_D is the aerodynamic coefficient, A_F is frontal area in meters squared, and V is vehicle speed. The total vehicle resistance is plotted in Figure 5.10.

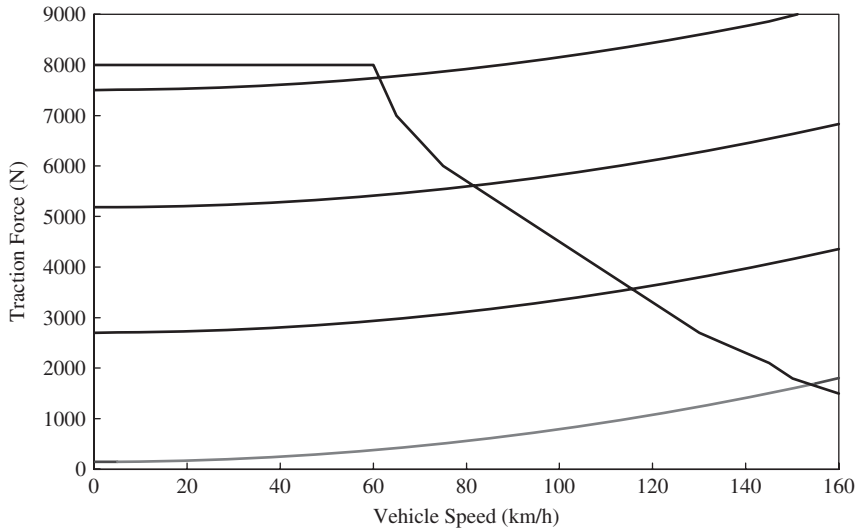

Figure 5.10 Traction force of a medium-sized passenger car

At any given vehicle speed, the power at the wheels is

$$P = F_{TR}V = \left(mg\sin\alpha + mgC_0 + mgC_1V^2 + \frac{1}{2}\rho C_D A_F V^2 + m\frac{dV}{dt}\right)V \tag{5.11}$$

5.7 Component Sizing of EREVs

Assume the driveline efficiency is η_d. For a PHEV to be capable of electric driving, the powertrain motor needs to be sized such that the motor can provide sufficient torque for all driving conditions, that is,

$$P_m = P/\eta_d \tag{5.12}$$

The total acceleration time and gradability of the vehicle are other design criteria for traction motor sizing. In general, the traction motor of an EREV is very similar to the design of a series HEV. For example, the typical power rating of a passenger car is about 125 kW, and the typical traction motor for a middle-sized sports utility vehicle (SUV) is about 150 kW.

The engine/generator set of an EREV is designed to provide average power during the extended driving range. In addition to the driveline need, auxiliary power needs should also be considered.

For the traction battery, there are two very important parameters: energy capacity and power capacity. Since the EREV is designed to operate under all kinds of conditions without turning on the engine during CD mode, the battery power rating needs to match the traction motor rating. For example, if the traction motor is rated at 125 kW output with a system efficiency of 95% (inverter + motor), then the battery needs to have a power capacity of 131.6 kW.

Another parameter of the battery pack is the energy capacity. This can be calculated based on the total electric range to be designed. For example, if a vehicle is designed to have an electric range of 64 km, and the vehicle consumes an average of 150 W per km in city driving, then the battery needs to be able to provide 9.6 kWh usable energy. If we allow the battery SOC only to go down to 30%, and consider the average efficiency of the battery to be 96%, then the nominal energy capacity of the battery will be 14.3 kWh.

Further, if we choose a battery pack that is composed of individual battery cells of 3.2 V, 40 Ah, then we will need 112 cells. Connecting all the cells in series will result in a nominal voltage of 358.4 V.

5.8 Component Sizing of Blended PHEVs

The design of the powertrain motor and engine of a blended PHEV is similar to the design of a parallel HEV. The only requirement is that the traction motor should be sized such that the vehicle can be driven in electric mode for the majority of city driving. For highway driving, the engine will provide power for the driving. In Figure 5.8, a motor rated at 50 kW will cover 95% of the city driving power demand.

The battery sizing is similar to the battery sizing of an ERVE, that is, the equivalent electric distance required for the PHEV. Since the focus is on city driving, the battery is sized to satisfy city driving cycles.

For example, if a blended PHEV is equipped with a powertrain motor of 50 kW with an efficiency of 95%, then the battery needs to be capable of providing 52.6 kW of power. If the desired city driving distance in electric mode is 40 km, and the power consumption is 160 W per km, then the battery needs to have a usable capacity of 6.4 kWh. Again, if we assume that battery SOC can only go down to 30%, and has an average efficiency of 95%, then the battery nominal capacity will be 9.6 kWh. If we choose battery cells rated at 3.75 V, 32 Ah each, then the total battery cells needed is 80. Connecting all cells in series will result in a nominal voltage of 300 V.

5.9 HEV to PHEV Conversions

At the time of writing, automotive companies are still in the process of developing PHEVs. Since there has been no mass-produced PHEV available for the past few years, regular HEVs have been converted to PHEVs by interested parties. Many independent conversions have been performed by various groups (such as Cal-Cars) and companies (such as A123 Hymotion, EEtrex, etc.) (http://www.eaa-phev.org/).

There are two potential ways to perform the conversion. One way is to replace the original battery pack (usually a nickel metal hydride (NiMH) battery) with a larger battery (usually lithium-ion batteries). Another way is to add an extra battery pack to the vehicle system.

Typical HEVs today are equipped with a NiMH battery pack ranging from 1.2 to 2.2 kWh. A converted PHEV will usually have a battery pack in the range of 7–16 kWh. This new or extra battery capacity will either make it possible to drive the vehicle in all-electric mode or significantly increase the fuel consumption of the car in the initial drive range.

5.9.1 Replacing the Existing Battery Pack

In this approach, the original battery pack is removed and a new battery pack is installed. In customized conversions of HEVs to PHEVs, the vehicle control is usually kept intact. In order to utilize the battery energy, usually the battery information is manipulated, or spoofed. One way of doing this is to replace the original battery ECU (Electronic Control Unit) with a new battery ECU that duplicates all the battery information. However, the real battery information is spoofed to a value such that the vehicle controller thinks there is sufficient energy and power from the battery so that it uses more battery energy to drive the car.

Another approach for spoofing the battery data is to use a gateway, as shown in Figure 5.11. The real battery information is sent to a gateway, which then sends manipulated battery data to the vehicle controller. The gateway can be part of the new battery ECU, or a standalone ECU.

Most HEVs use high-voltage (HV) NiMH batteries (HV battery). The power and energy available from the battery are typically determined by the battery SOC and battery temperature. The battery ECU constantly monitors the HV battery conditions, including temperature, voltage, and amperage, and calculates the SOC. When the vehicle is in motion, the HV battery goes through repetitive charge and discharge cycles (discharged during acceleration and charged during regenerative braking). The battery could also be

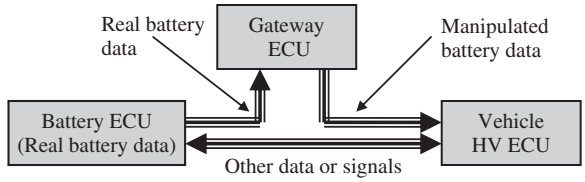

Figure 5.11 Gateway approach in the conversion of HEV to PHEV

charged by the motor/generator using engine power as necessary. The ECU calculates the SOC and sends charge/discharge requests to the vehicle ECU to maintain the SOC at a median level. In the Prius, for example, the target SOC is 60% within a ±20% band. When the SOC drops below the controlled region (40%), the battery ECU sends a request to the vehicle ECU, which then sends a request to the engine ECU to increase engine power to charge the battery. If the SOC increases to above the controlled region (80%), then the battery ECU sends a request to the vehicle ECU, which then sends a request to the motor so that the battery power is discharged by using the motor to drive the vehicle (either alone, or in combination with the engine).

Figure 5.12 shows a typical plot of battery power vs. the SOC of a HEV. The power available from the battery is closely related to the battery SOC. Only when the SOC is in a narrow range (55–80%) does the vehicle allow higher power from the battery. This approach is designed for battery life.

When a new and larger battery pack is added, the main goal is to use the battery energy as much as possible. The typical range is for the SOC to drop from 100% (fully charged) to 30% for a lithium-ion battery pack. Operating the battery below 30% will have a negative impact on battery health and life.

With no modification of the vehicle ECU, the SOC of the battery pack must be manipulated such that the vehicle will use more power from the battery. The mapping of the battery SCO for the limits shown in Figure 5.13 is as the follows. When the real battery SOC is above 30%, the real SOC is mapped to a range (60–75%) where the vehicle ECU will maximize the use of battery energy. When the real SOC drops below 30%, the calculation of the SOC is based on the original battery capacity:

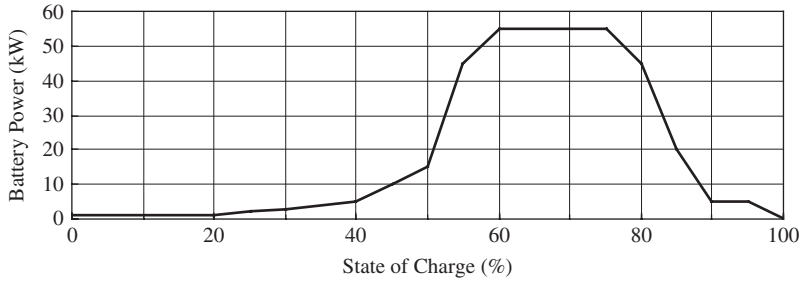

Figure 5.12 Typical battery power vs. SOC allowed by a HEV

Real battery SOC: [30%, 100%] ↔ Manipulated SOC: [60% . 75%]
Real battery SOC < 30% ↔ Manipulated SOC: Δ SOC + 60%

Figure 5.13 Actual and manipulated battery SOC information for powertrain control purposes in a converted PHEV

If $SOC_{real} > 0.3$, then

$$SOC_{real} = \frac{(Ah)_{new} - \int idt}{(Ah)_{new}} \tag{5.13}$$

$$SOC_{manipulated} = 60\% + 0.21(SOC_{real} - 0.3) \tag{5.14}$$

If $SOC_{real} < 0.3$, then

$$SOC_{manipulated} = \Delta SOC + 0.6 = \frac{\int idt}{(Ah)_{old}} + 0.6 \tag{5.15}$$

where $(Ah)_{old}$ is the capacity of the original pack, and $(Ah)_{new}$ is the capacity of the new pack.

5.9.2 *Adding an Extra Battery Pack*

A123 Systems' Hymotion approach (http://www.a123systems.com/hymotion/) is to add an extra battery back to the vehicle as shown in Figure 5.14. The energy of the extra battery pack is slowly released to the original battery pack to be used by the vehicle. Other than controlling the new battery pack, there is no change to the original electrical and control systems.

There may be a need for a DC–DC converter between the new lithium-ion battery pack (Li) and the original NiMH battery pack. The DC–DC converter will take energy from the lithium-ion battery and charge the NMH battery. In this way, the NiMH battery voltage is kept high. Since the battery ECU will reset the SOC of the NiMH battery pack based on the battery voltage, the energy that is charged to the NiMH battery is being used due to the detected high SOC.

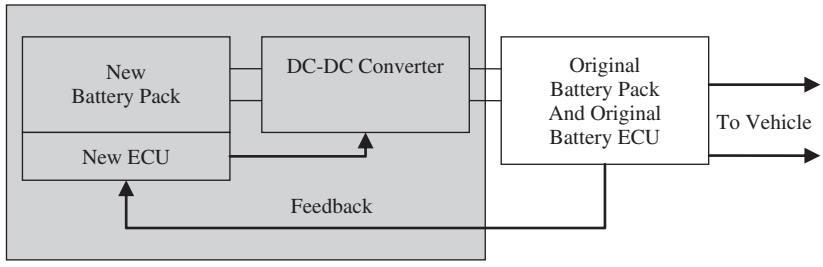

Figure 5.14 Adding an extra battery pack to the HEV

5.9.3 Converting Conventional Vehicles to PHEVs

Some vehicles, such as pickup trucks, have abundant space available. Hybrid Electric Vehicles Technology Inc. and Raser Inc. have each converted a conventional gasoline-powered pickup truck to a PHEV (http://hevt.com/flyers/HEVT%20Ford%20F150%20Pickup%20Truck%20Plug-in%20Hybrid%20Electric%20Conversion.pdf, http://www.rasertech.com/). In the former approach, the company kept the existing front axle as gasoline engine driven, but modified the rear axle by adding an induction motor and an extra battery pack. The vehicle controller needs to be modified to take advantage of the battery energy.

5.10 Other Topics on PHEVs

5.10.1 End-of-Life Battery for Electric Power Grid Support

In general, battery energy capacity tends to fade over time and over discharge cycles. Typical battery energy capacity as a function of time is shown in Figure 5.15.

With 70% SOC depletion, a lithium-ion battery can typically last 3000–4000 charge cycles. This is approximately 10 years for a PHEV. At that time, the battery capacity may be only 50% of its initial capacity. While this is not satisfactory for the car owner due to the reduced electric driving range, the battery itself may be used for other purposes, such as for electric grid support. Since there is less space/weight constraints for power grid applications, these batteries can be used for grid energy storage for peak shaving, frequency regulation, and stability control. When more and more renewable energy is connected to the electric power grid, stability of the grid becomes extremely important due to the intermittent nature of renewable energy generation.

5.10.2 Cold Start Emissions Reduction in PHEVs

Emissions during cold weather start of a vehicle have long been an issue. It has been shown (http://cfpub.epa.gov/ncer_abstracts/index.cfm/fuseaction/display.abstractDetail/abstract/1450/report/0) that the emissions from a vehicle during a cold weather start are significantly more than those during normal weather starting. In particular, the emissions during the first two minutes can be as much as 80% of the total emissions during a standard driving cycle (1400 seconds). This is due to the fact that vehicle emissions

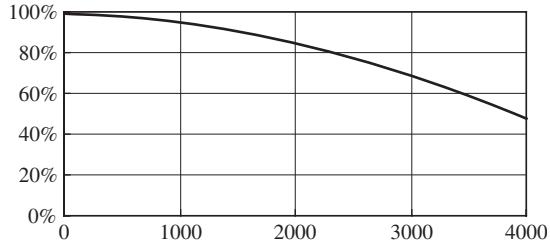

Figure 5.15 Typical battery capacity versus cycle life

are usually treated by a catalytic converter. A typical converter needs to heat up to function properly.

For conventional vehicles, a number of methods have been proposed to mitigate cold weather start emissions, such as catalytic heaters, novel materials, and so on.

It is possible to reduce cold start emissions in PHEVs by using the large onboard battery pack. The idea is to operate the vehicle in electric-only mode in the first few minutes and, at the same time, use electricity from the battery to warm up the catalytic converter to a certain temperature. Once the converter is normal and functional, the engine may be started as needed. However, almost all batteries do not work well under extremely cold weather conditions. Not only do the useful energy decrease and the internal impedance increase (efficiency drop), but also there is a negative impact on battery life if the discharge power is large. A reasonable compromise needs to be made in this regard.

5.10.3 Cold Weather/Hot Weather Performance Enhancement in PHEVs

The typical operating temperature range of a lithium-ion battery is from 0 to 50 °C. In extreme cold or hot weather conditions, the battery will exhibit large internal impedance and reduced power levels. In order to extend the driving distance and the battery life of a PHEV during cold weather conditions, additional measures may be necessary.

One method is to thermally insulate the battery pack so that no or very little heat exchange takes place between the battery cells and the ambient air, except at the cooling outlet. This thermal insulation will allow the battery to hold a steady temperature for an extended period of time during extreme cold or hot weather conditions. Another approach is to heat up the battery during cold weather by using an internal heater that consumes battery energy to warm up the battery pack. An additional method includes keeping the battery in trickle charge mode when plugged in to the power grid.

5.10.4 PHEV Maintenance

One issue of PHEVs is that if the driver always drives less than the electric range and is always charging the battery, the engine may never start. This could cause the fuel to go stale and some mechanical parts including ones in the engine to seize. Therefore, vehicles such as the Chevrolet Volt have been designed with an additional mode, namely, the maintenance mode [10]. This mode is activated either by the driver or automatically to operate the engine and the generator routinely to maintain the health of those components.

5.10.5 Safety of PHEVs

HEVs and PHEVs deal with high voltages and a large amount of energy in the battery pack. A PHEV is safe under normal drive conditions but safety can be an issue during charging (rain or wet plug), repair and service of the vehicle, as well as in a accident. Just like any HV system, the electrical system in a HEV or PHEV can be unsafe when mishandled. HV systems may cause electrical hazards if not handled properly, including electric shock, arcing, and blast [11].

The car's HV system is isolated from the ground and also isolated from the vehicle chassis. Therefore, electrical hazards can only arise when a person holds both the positive and the negative terminals of the HV system while repairing or servicing the car.

However, PHEVs must be plugged into an electrical outlet to charge the onboard battery. Advanced charging techniques, such as inductive and wireless charging, could potentially reduce the risk of electric shock during charging of the vehicle but will also reduce charge efficiency and increase system cost.

Charging the vehicle during rainy days with a contact charger can potentially cause leakage of current to the person handling the plug. Old and worn plugs and cables can cause current leakage. Therefore, extra caution needs to be taken when charging the vehicle. The leakage current can cause electric shocks, leading to muscle contraction, fibrillation, and tissue damage. A 10 mA current is enough to cause muscles to contract. A person may not be able to release the grip of his or her hand if it is exposed to sufficient electric current. If sufficient current goes through the chest, the person's chest muscle may paralyze and halt breathing.

More severe damage, such as fibrillation, can happen if the body's normal heartbeat is disrupted. The HV system, in particular the charger voltage from the electrical outlet, is enough to interrupt the brain current and cause the heart to stop beating. However, the current must follow a path through the body (hand to ground, hand to hand) in order for fibrillation to occur. Tissues can be damaged from prolonged exposure to electric shock due to heat concentration in the tissues.

The high-power, high-voltage connectors may become short-circuited during an accident and cause sparks or overheat, which could lead to a fire or explosion. After-market PHEVs typically have the battery installed at the back of the vehicle. This may be an issue during a rear collision. The added battery pack also shifts the weight center of the vehicle, which may cause stability problems during braking. Mass-produced PHEVs will have been designed taking battery weight into consideration, and the batteries are likely not to be installed in the crash zone. Safety disconnection devices such as a service plug and fast fuse will provide additional safety measures.

Extra care should be taken when working on a PHEV during maintenance and repair. For example, insulation gloves are necessary in order to avoid electric shock when handling the HV system. Terminals of cables need to be insulated if they are disconnected from their original place. Tools and instruments should have insulated handles when dealing with the battery and other HV components in the PHEV. In fact, the handling and safety measures in the EV, HEV, and PHEV are the same as those used in home electrical repairs.

5.11 Vehicle-to-Grid Technology

Vehicle-to-grid, or V2G, is a concept referring to the capability of bidirectional power and energy exchange between the power grid and the vehicle battery (http://www.ornl.gov/info/ornlreview/v40_2_07/2007_plug-in_paper.pdf) [3, 4]. With the bidirectional charger, the vehicle can be used a power backup for the home or office. It is also possible to use the PHEV battery to control the stability and regulate the frequency and voltage of the power grid, such as in a distributed power grid and with renewable energy generation.

PHEVs need to be charged from the electric power grid. During charging, the charger will generate inrush current, harmonics, and could cause the grid to malfunction if not coordinated properly.

In a broad sense, and in the foreseeable future, hundreds of thousands of PHEVs will be connected to the power grid as electric drive transportation prevails as our ultimate solution to becoming independent of fossil fuels. It is imperative to study the grid-to-vehicle (G2V) impact on power system operation and to consider various factors such as battery size, charging, PHEV distribution, and efficiency [12].

In order to optimize G2V it is important to educate consumers in the context of a "smart grid." They should be made aware of the fact that battery charging at night would improve utility generation efficiency, because at night-time the electricity is supplied by the base load generation units. Studies show that even with 50% penetration of PHEVs into the power system, no additional generating capacity or no new power plants are required [12]. Although there are concerns with PHEVs straining the grid, PHEVs, if properly managed, actually could help prevent brownouts, reduce the cost of electricity, and accommodate the integration of more renewable energy resources.

5.11.1 PHEV Battery Charging

There are three levels of charging for the PHEV depending on the voltage: single-phase AC 120 V, single-phase AC 240 V, and three-phase AC 480 V. The different voltage levels will affect the charging time, ranging from hours to tens of minutes. In general, there are four types of charging algorithms for PHEV: constant voltage, constant current, constant voltage and constant current, and pulse charging. These different charging algorithms require corresponding controller designs for power electronics circuits. In this section, the pulse charging technique is studied in detail through simulation. Here PHEVs are connected to an example distribution system. The case of 10 PHEVs has been considered for simulations in which the PHEVs are connected to an IEEE 13-bus distribution system. Figure 5.16 shows this distribution system together with PHEVs. The system is relatively small and highly loaded. For this study, the PHEVs are connected between nodes 692 and 675 of the distribution system.

The PHEVs connected to the distribution system via a single-phase transformer are charged by the pulse charging technique. Initially the battery is assumed to have a 90% SOC. The battery is charged by the DC–DC converter with pulse current until it reaches a 95% SOC.

The AC–DC converter connected to the distribution system draws unity power factor, which shows that the PHEV is utility friendly. Figure 5.17 shows the unity power factor for input current and voltage at the secondary side of the single-phase transformer. The input voltage has a 240 V rms value. The reference current is generated by a phase-locked loop (PLL) block. The secondary side voltage of the transformer is the input to the PLL. This in turn generates a sine wave to form the reference input current for the unity power factor controller.

5.11.2 Impact of G2V

The IEEE 13-bus distribution system [13, 14] with 10 PHEVs has been simulated to study the impact of connecting many PHEVs to the power system/grid. The case to be discussed

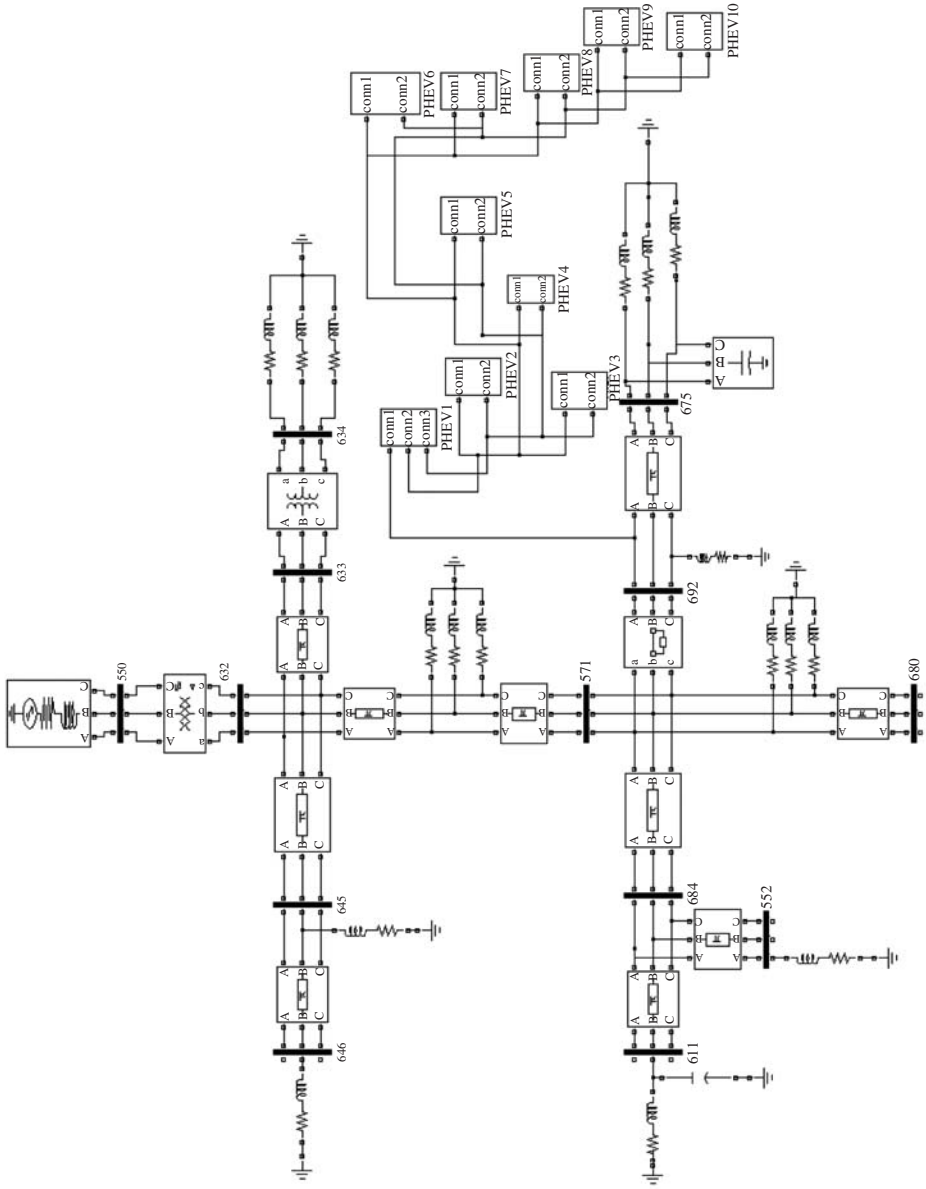

Figure 5.16 IEEE 13-bus distribution system with 10 PHEVs connected to phase A at node 692

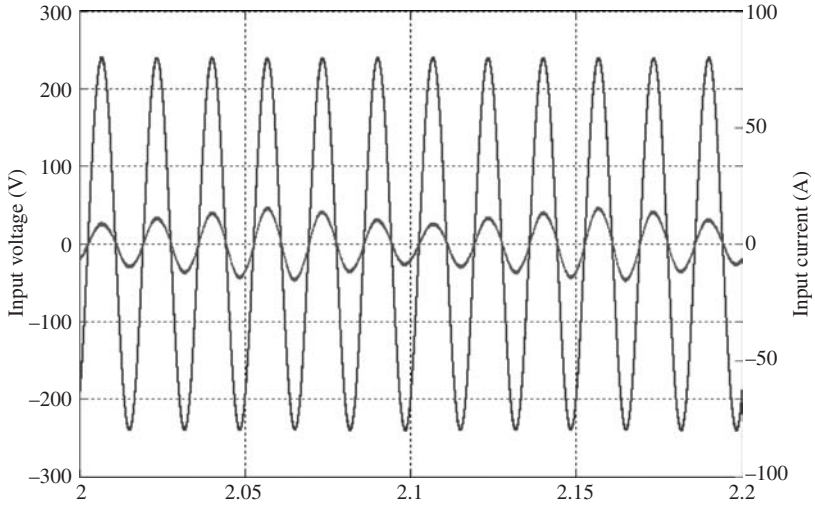

Figure 5.17 Unity power factor for input current and voltage during charging

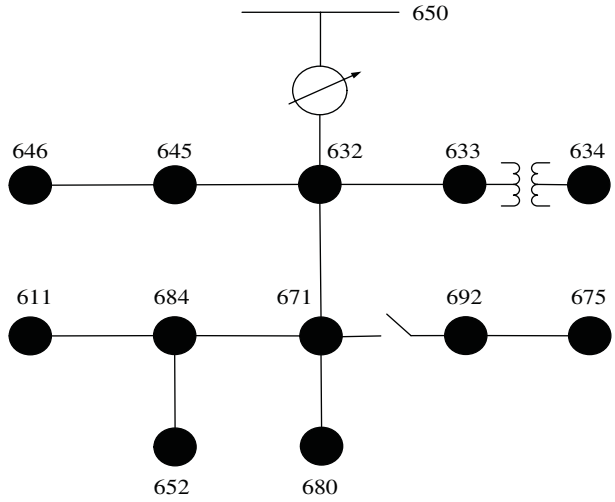

Figure 5.18 One-line diagram of IEEE 13-bus distribution system

here is that of connecting 10 PHEVs to the grid at node 692 of the distribution system via a step-down transformer rated at 4.16 kV/240 V. The substation transformer rating is 5000 kVA with a primary side rated voltage at 115 kV and secondary side rated voltage at 4.16 kV. The types of loads connected to the distribution system are unbalanced spot load and distributed load. Figure 5.18 shows a one-line diagram of the distribution system.

The distribution system has initially no PHEVs connected to it. After 0.3 seconds, 10 PHEVs are connected for charging the onboard batteries. The study is carried out with

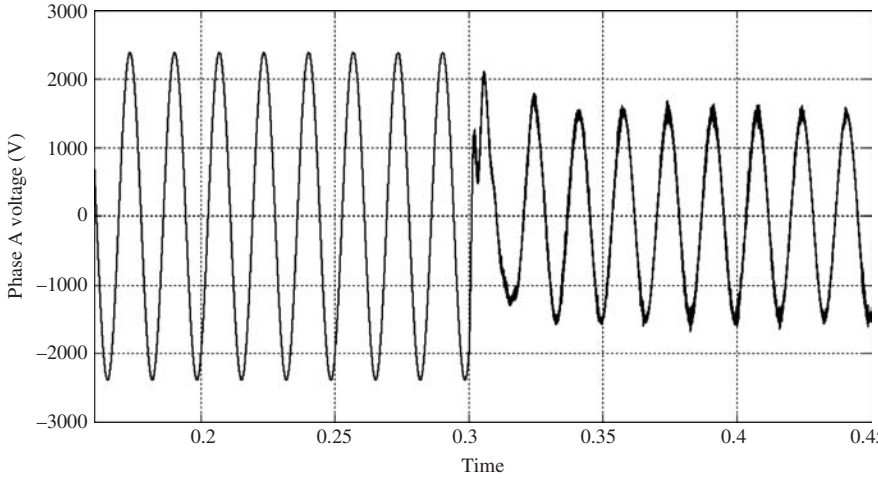

Figure 5.19 Phase A voltage with PHEV connected at $t = 0.3$ seconds

the simulation results to see the impact of PHEV charging on the grid voltage, current, and active power. Figure 5.19 shows the voltage of phase A at node 692. From the figure it can be clearly seen that phase A is heavily loaded when all the PHEVs are connected for charging; as a result the voltage in the line is reduced. The voltage drop is found to be 39%, which is not within permissible limits. When the voltage drops below a permissible value it has to be restored back to its original value. A capacitor bank can be used in cases where the voltage drop is below 20%. However, in this case the voltage drop is 39%, which is a very high value; local area generation will need to restore the voltage. At the generating end, automatic generation control (AGC) with a power system stabilizer (PSS) is usually used for maintaining voltage stability. Figure 5.20 shows the voltage waveform for sequential charging of PHEVs, where each PHEV is connected after 0.1 seconds. The voltage profile is greatly improved with the sequential charging method. In Figure 5.21 it can clearly be seen that after 0.3 seconds the value of the voltage is restored. Also, the total harmonic distortion (THD) of the grid side voltage was calculated after connecting the PHEVs. It was found to be 1.7%, which is well below the permissible value. Figure 5.22 shows a graph of the THD. Figure 5.23 shows the current of phase A at node 692. From the figure it can clearly be seen that the current increases after connecting a large number of PHEVs at $t = 0.3$ seconds. Figure 5.24 shows the current waveform for the sequential charging of PHEVs. The current waveform of phase A shown in Figure 5.25 clearly depicts that the current is also restored because of the PSS. Figure 5.26 shows the average real power of phase A at node 692 with and without the PHEVs. It can be seen from the figure that the active power consumption increases when a large number of PHEVs are connected for charging at the same time.

5.11.3 The Concept of V2G

The concept of V2G is that the energy stored within PHEV batteries can be utilized to send power back to the grid. The V2G technology supposes that if battery vehicles (BVs)

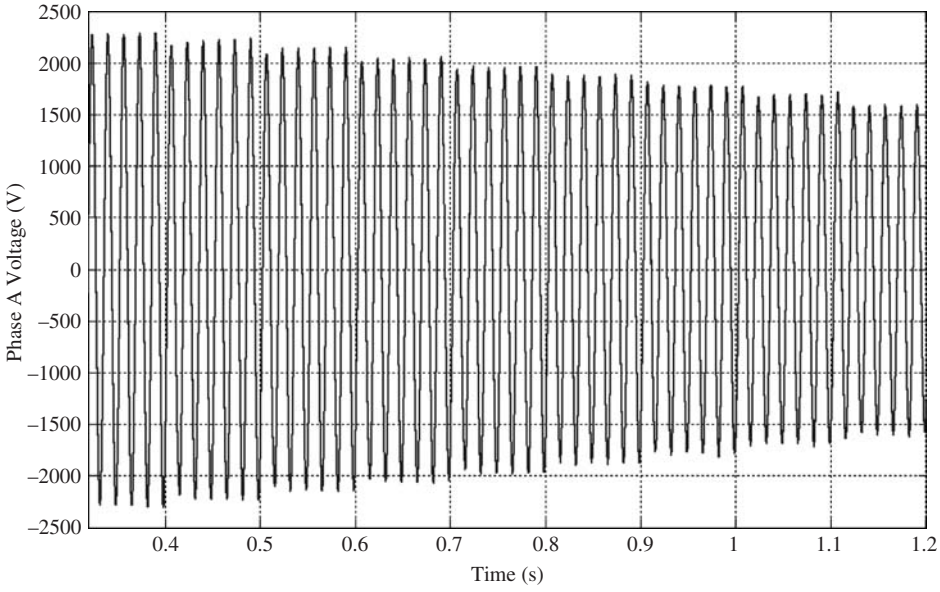

Figure 5.20 Phase A voltage for sequential charging of PHEVs

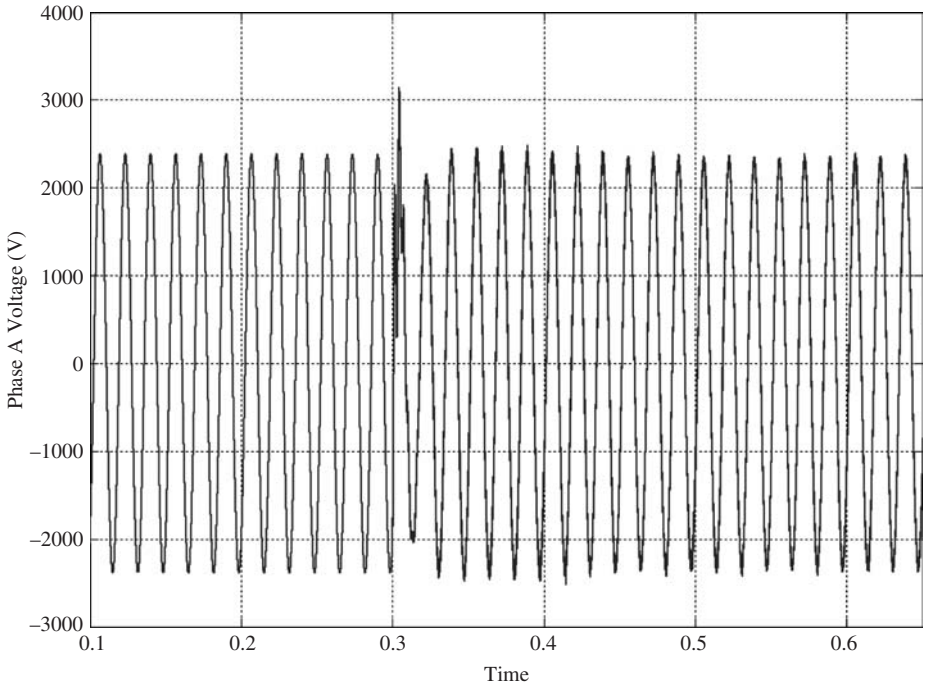

Figure 5.21 Phase A voltage restored at $t = 0.3$ seconds

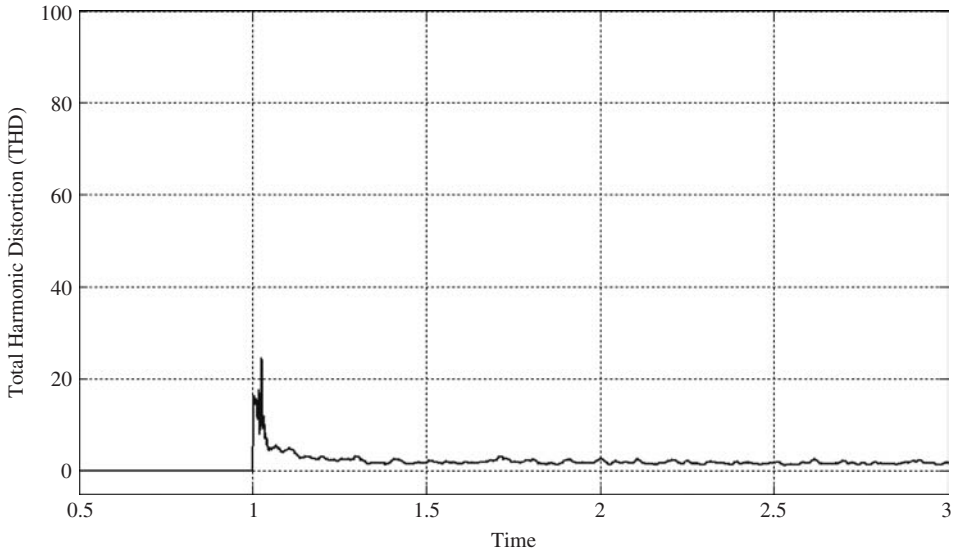

Figure 5.22 Total harmonic distortion (THD) of waveform input voltage

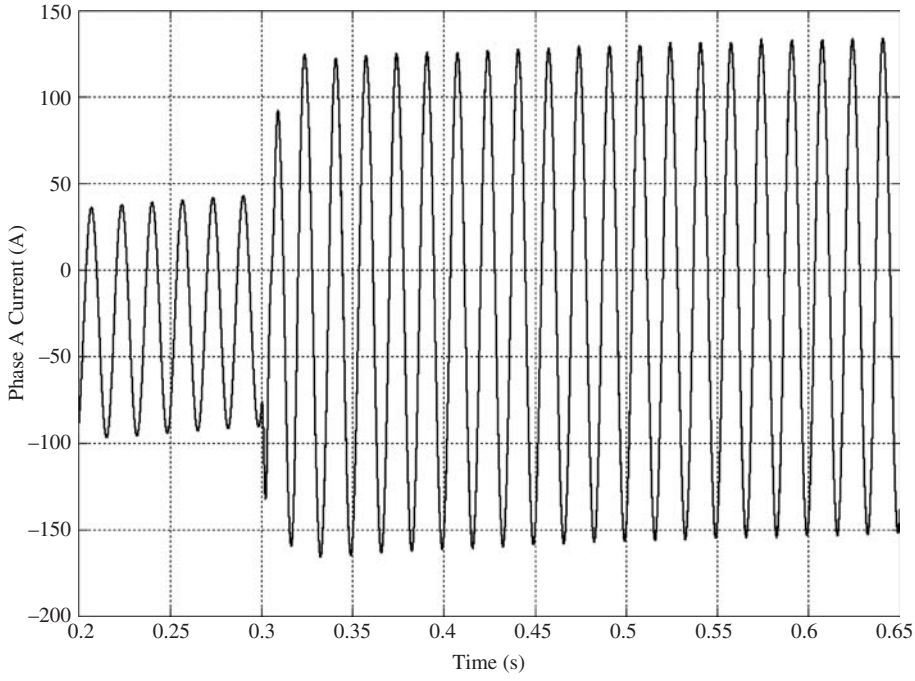

Figure 5.23 Phase A current and PHEVs connected at $t = 0.3$ seconds

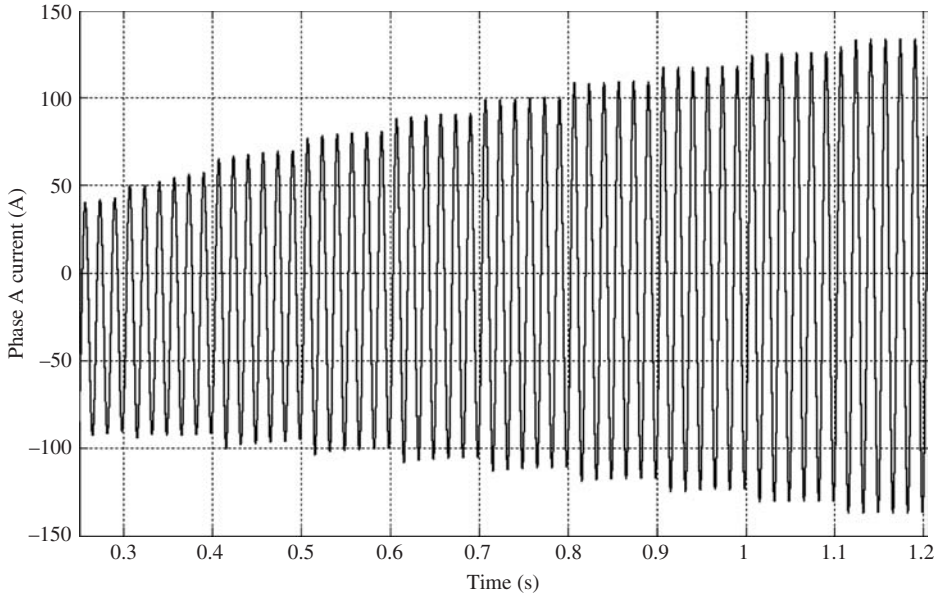

Figure 5.24 Phase A current for sequential charging of PHEVs

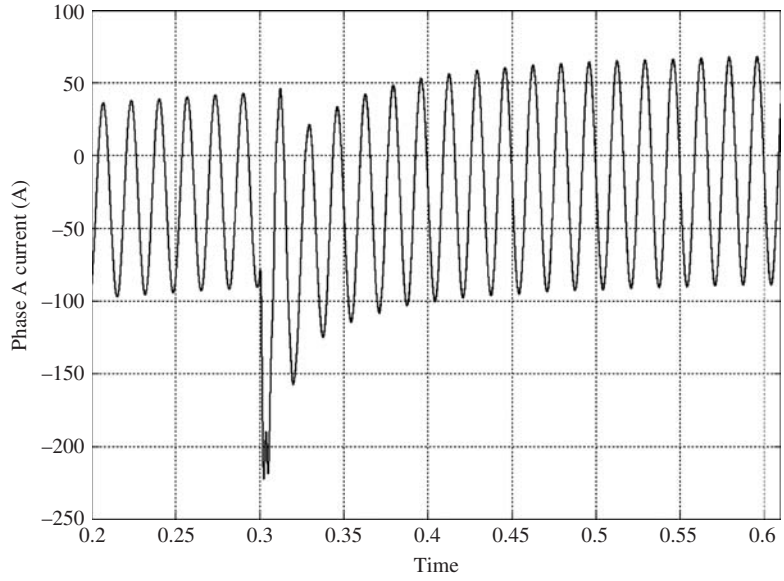

Figure 5.25 Phase A current restored at $t = 0.3$ seconds

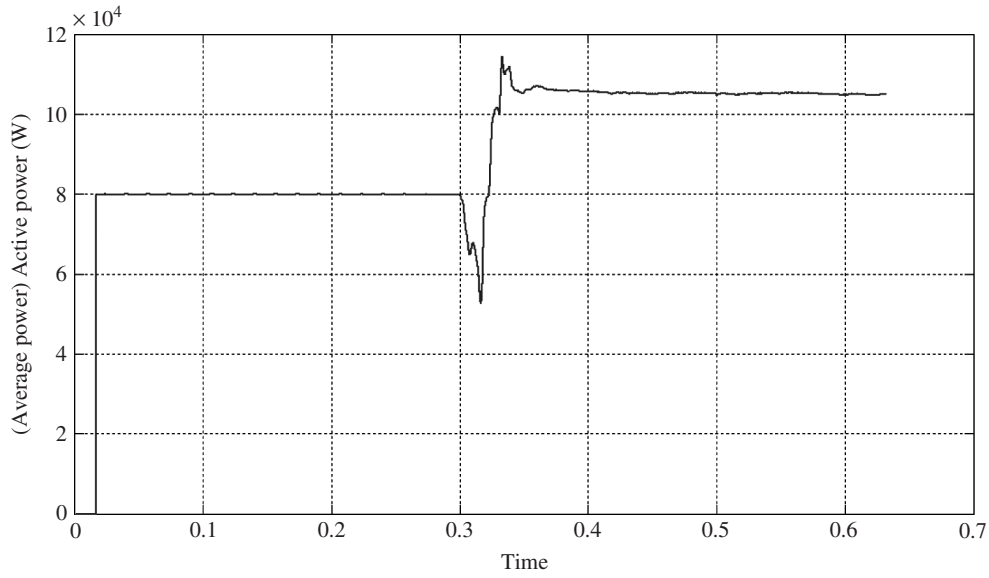

Figure 5.26 Phase A real power and PHEVs connected at $t = 0.3$ seconds

or PHEVs become widespread then they could supply peak load power with fast response when the vehicles are parked and are connected to charging stations [15, 16]. On average a car is driven for an hour per day and for rest of the day it is parked. Practically speaking, the amount of power drawn from the car can be around 10–20 kW. The V2G connection can provide a fast interface between the power system and the battery storage system of the PHEV. The system can produce both active and reactive power for the distribution system through proper control of the power electronics circuits, even though the batteries only store active power.

For EVs and PHEVs, the energy that can be used for V2G is limited by the onboard battery size. The unique aspect of power flow in PHEVs is that it is bidirectional, meaning that the vehicle can take power from the grid (during charging) and provide power (during discharge) to the grid. Apart from the concept of V2G, there is the concept of vehicle-to-home. The advantage of V2G is that it is parallel, which means within a grid any car can be used to power any home by feeding its power back to the grid. On the other hand, vehicle-to-home is limited in the sense that a single vehicle can supply only a single home.

PHEVs can be treated as distributed energy resources via V2G and can provide voltage and frequency regulation, spinning reserves, and electrical demand side management [12, 16]. The V2G functions can be classified into two categories: local services and broad area services. Local services include supplying backup power for local houses or businesses, peak shaving, and voltage stabilization or power quality improvement. Broad area services include ancillary services for the grid. Ancillary services are power services by which the grid operators maintain reliable operation of the grid.

5.11.4 Advantages of V2G

There are a number of advantages of introducing V2G into the power system. Some of the advantages are stated below (available at: http://www.udel.edu/V2G/docs/V2G-PUF-LetendKemp2002.pdf):

- **Improving security:** V2G inverters can respond quickly to control the effects of any disturbance as compared to the turbo-generator governor. This will help the power system to be more robust and reduce the vulnerability.
- **Improving reliability:** The advantage of locating the V2G system anywhere in the distribution system makes the backup supply available at a close distance even though it may not be installed at the consumer's location. This will have a major impact on consumer reliability as most interruptions are due to disturbances in the distribution networks.
- **Impact on generation:** By connecting a large number of PHEVs or V2G systems during daytime the peak power can be curtailed during the daily peak load period. Also, during the light-load period PHEVs can be connected to charge the battery system, thus allowing the base load generators to operate efficiently without the need to carry large amounts of spinning reserve.
- **Environmental advantage:** Using PHEVs can reduce environmental pollution. They can promote the reduction of greenhouse gas emissions by indirectly using clean electricity as transportation fuel.

5.11.5 Case Studies of V2G

The distribution system [14], as discussed previously, has been considered for carrying out V2G simulations. The aim here is to study power system behavior due to V2G technology. Two scenarios, namely, PHEV for peak shaving and PHEV for reactive power compensation, are discussed and simulated by using the IEEE distribution model system. The PHEV is connected to phase A of the line between nodes 692 and 675 of the distribution system via a step-down transformer rated at 4.16 kV/240 V:

- **Case 1: V2G for peak shaving:** If the battery has enough charge, for example, with a 95% SOC and if the PHEV is not in use, depending on the grid load condition the PHEV can send some power back to the grid. In this section the simulation results for V2G connection are presented. The control strategy for sending the power back to the grid is shown in Figure 5.27. From the figure it can be seen that the reference power is divided by the battery voltage, which forms the reference current for the battery. This in turn is compared to the actual battery discharging current and an error signal is generated. The error is then processed through a PI (Proportional Integrator) controller that forms the duty cycle, which is then compared to the carrier wave for generating the pulses for switching the IGBT (Insulated Gate Bipolar Transistor) of the converter. Figure 5.28 shows the active power being sent back to the grid. When the car is plugged in to the wall outlet, with the help of metering and the communication system the grid operator and consumer could interact and supply the available power to the grid. Such a case is depicted here where initially the power being supplied by the PHEV is 10 kW;

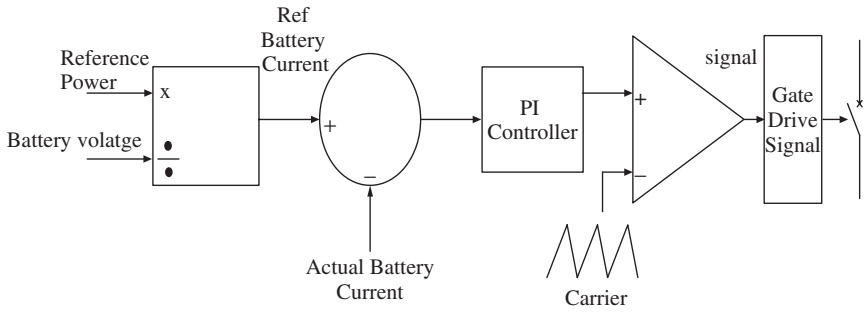

Figure 5.27 Control strategy for the battery system while sending the power back to the grid

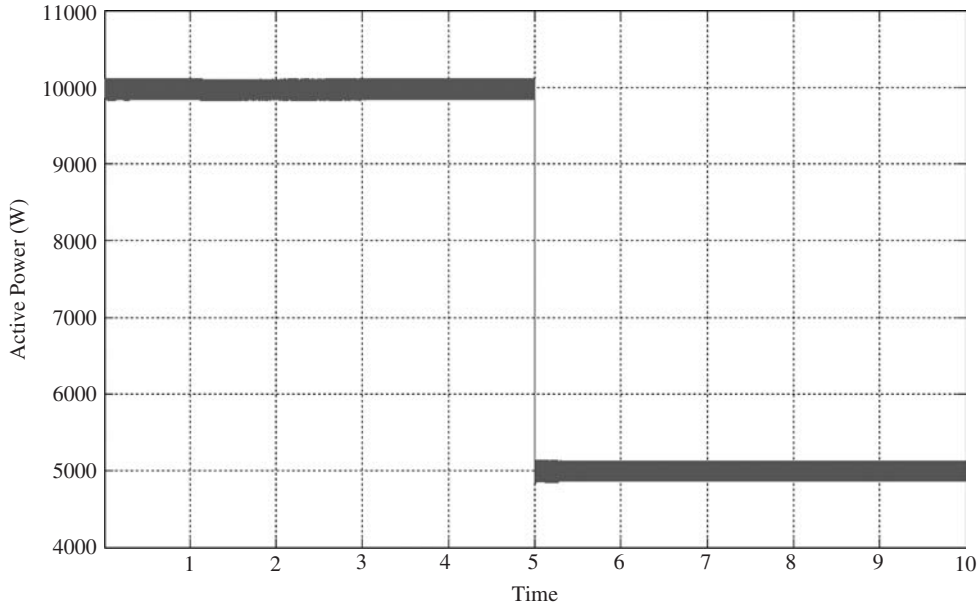

Figure 5.28 Real (active) power supplied by the battery

after time $t = 5$ seconds the power supplied is reduced to 5 kW. Figure 5.29 shows the input current and voltage are out of phase, meaning unity power factor when the power is delivered to the grid by the battery. This shows the utility-friendly nature of the charger. Also from the figure it can be seen that at time $t = 5$ seconds, when the power reduces from 10 to 5 kW the current at the grid side reduces correspondingly.

- **Case 2: Reactive power compensation:** A PHEV has the potential to act as a reactive power compensator for the power system. Capacitors are generally used for reactive power compensation in distribution networks. In Figures 5.30 and 5.31 the PHEV is shown as a reactive power compensator. Initially the PHEV is disconnected, and an inductive load is connected to the grid. From Figure 5.30 it can be seen that at the

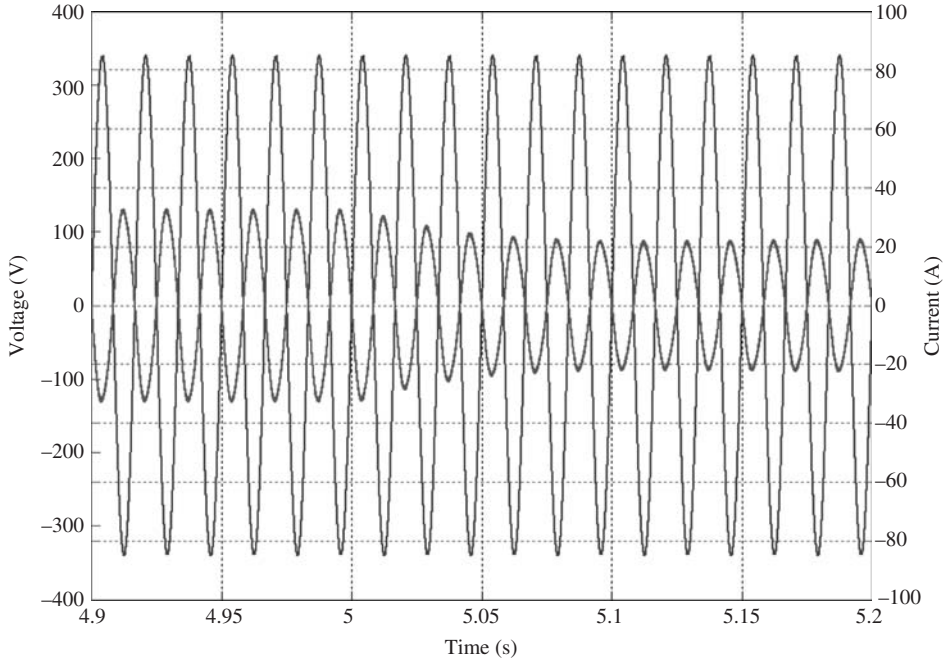

Figure 5.29 Input voltage and input current 180° out of phase during discharging

secondary side of the single-phase transformer at node 692, the current is lagging the voltage. After 0.5 seconds the PHEV charger is connected to the grid, and it can be seen in Figure 5.31 that the lagging current becomes in phase with the voltage. This demonstrates the reactive power compensation capability of the PHEV charger.

In this section, we briefly discussed the concept of G2V and V2G. Simulations were carried as an example to study the impact of connecting the PHEVs to the grid. From the results it can be seen that system voltage and current are greatly affected, hence local area generation with a PSS can be used to bring the system back to the normal state. V2G can partly spare the utility company from investing in creating spare capacity to meet electricity demand during peak hours. Some simulations are presented for cases where the PHEV is used for peak shaving and reactive power compensation. The bidirectional nature of the PHEV charger can prove to be beneficial during peak hours/periods. Also, the concept of reactive power compensation illustrates the fact that the PHEV can be used as an alternative to capacitors in distribution networks. On the other hand, a plug-in vehicle can also be designed to provide power for standby applications, through its V2G capability.

5.12 Conclusion

A PHEV equipped with a 10 kWh battery pack will require 8–10 hours of charging time at a regular 110 V/15 A outlet. Fast charging is only possible when higher power outlets

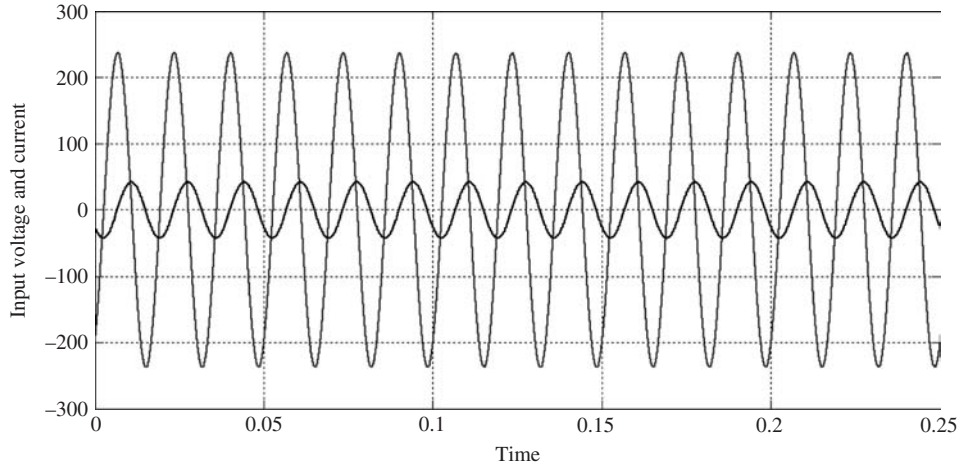

Figure 5.30 Current lagging voltage

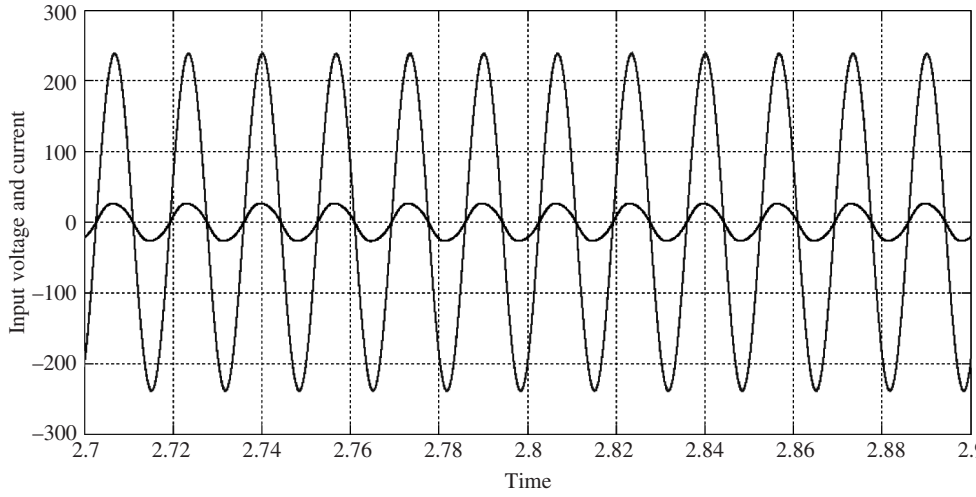

Figure 5.31 Reactive power compensation

are available, such as 110 V/50 A or 220 V/30 A, from which a 10 kWh battery back can be charged in less than two hours.

Finally, recycling of PHEV batteries has to be planned during the PHEV development phase, and be ready at the time of PHEV deployment. Continued or inappropriate use of batteries beyond their designed lifespan can lead to the release of toxic gasses, injury, or fire. Inappropriate disposal of batteries can contribute to the contamination of soil, water, and air. The lithium and other metals in lithium-ion batteries can be extracted for other uses when the lithium ion batteries are recycled.

References

1. Sanna, L. (2005) Driving the Solution – the Plug-in Hybrid Vehicle. http://mydocs.epri.com/docs/CorporateDocuments/EPRI_Journal/2005-Fall/1012885_PHEV.pdf (accessed February 2, 2011).
2. Douglas, J. (2008) Plug-in hybrids on the horizon – building a business case. *Journal of Electric Power Research Institute (EPRI)*, Spring.
3. Kempton, W. and Tomic, J. (2005) Vehicle-to-grid power implementation: from stabilizing the grid to supporting large-scale renewable energy. *Journal of Power Sources*, **144**, 28 0–294.
4. Gage, T.B. (2003) *Development and Evaluation of a Plug-in HEV with Vehicle-to-Grid Power Flow*, AC Propulsion, Inc., San Dimas, CA, CARB Grant Number ICAT 01-2, December 17.
5. Electric Power Annual, http://www.eia.doe.gov/cneaf/electricity/epa/figes1.html (accessed February 2, 2011).
6. SAE International (2009) Surface Vehicle Information Report SAE J2841 – Utility Factor Definitions for Plug-in Hybrid Electric Vehicles Using 2001 U.S. DOT National Household Travel Survey Data, March.
7. SAE International (1999) Surface Vehicle Recommended Practice SAE J1711 – Recommended Practice for Measuring the Exhaust Emissions and Fuel Economy of Hybrid-electric Vehicles, March.
8. United States Environmental Protection Agency (2006) Fuel Economy Labeling of Motor Vehicles: Revisions to Improve Calculation of Fuel Economy Estimates, Final Rule, 40 CFR Parts 86 and 600, December 27, 2006, http://www.epa.gov/fedrgstr/EPA-AIR/2006/December/Day-27/a9749.pdf.
9. Williamson, S.S. and Emadi, A. (2005) Comparative assessment of hybrid electric and fuel cell vehicles based on comprehensive well-to-wheels efficiency analysis. *IEEE Transactions on Vehicular Technology*, **54** (3), 856–862.
10. Maintenance Mode of the Chevrolet Volt, http://gm-volt.com/2010/08/17/chevrolet-volt-maintenance-mode/ (accessed February 2, 2011).
11. Ford Ranger EV User's Manual, http://www.eserviceinfo.com/download.php?fileid=18730 (accessed February 2, 2011).
12. Kramer, B., Chakraborty, S., and Kroposki, B. (2008) A review of plug-in vehicles and vehicle-to-grid capability. IEEE Industrial Electronics Conference IECON'08, November, Orlando, FL, pp. 2278–2283.
13. Kersting, W.H. (1991) Radial distribution test feeders. *IEEE Transactions on Power Systems*, **6** (3), 975–985.
14. Ma, W. and Jing, L. (1997) Distribution modeling and simulation based on MATLAB. 17th Conference of the Electric Power Supply Industry (CEPSi 2008), October, Macau SAR.
15. Haines, G., McGordon, A., and Jennings, P. (2009) The simulation of vehicle-to-home systems – using electric vehicle battery storage to smooth domestic electricity demand. Ecological Vehicles Renewable Energies, EVER'09, March, Monaco.
16. Kempton, W. and Tomić, J. (2005) Vehicle-to-grid power fundamentals: calculating capacity and net revenue. *Journal of Power Sources*, **144**, 268–279.

6

Special Hybrid Vehicles

6.1 Hydraulic Hybrid Vehicles

Although this book is primarily dedicated to issues related to hybrid electric vehicles, it should be appreciated that non-electric hybrid vehicles also are viable and can sometimes be more beneficial than an electric hybrid vehicle. Basically there are a few reasons for going hybrid in the first place, as follows:

- A normal internal combustion (IC) engine vehicle uses the engine over a wide speed range and hence the efficiency over this range is not the highest achievable efficiency in a particular engine.
- The maximum efficiency of IC engine propulsion is very low, on the order of 30%.
- The electric energy storage system, for example, battery and electric propulsion motor, both have high efficiency on the order of 80–90%.

Had it not been for the large size and cost, attributed to low energy storage per unit weight or volume capability of the battery, the pure electric vehicle probably would have replaced current vehicular technology. The next option, therefore, is the hybrid electric vehicle, where the IC engine can be used to optimally charge the battery and propulsion can be shared with the electrical method.

So, naturally, the question arises: is there anything else, other than IC engine propulsion, available? The answer is that the hydraulic system is one such option. In a hydraulic system the energy is stored in the form of a compressed fluid in a cylinder or by similar means. To pressurize the fluid, one needs power and energy, which come from the IC engine to activate a hydraulic pump. While extracting the energy one can use a hydraulic motor. In other words, the hydraulic pump is analogous to an electric generator, the hydraulic motor to an electric motor, the pressurized fluid in the cylinder to a battery. Thus we see that the hydraulic system has a one-to-one equivalence to an electrical system. Although typically people assume the theoretical efficiency of the hydraulic pump, motor, and storage to be very high, around 90%, in reality they will be nearer to 70%, which is

Hybrid Electric Vehicles: Principles and Applications with Practical Perspectives, First Edition.
Chris Mi, M. Abul Masrur and David Wenzhong Gao.

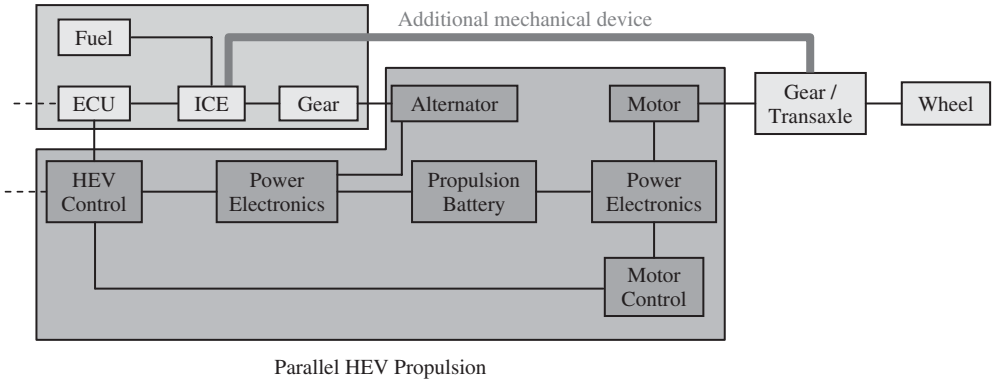

Figure 6.1 System-level diagram of HEV (ECU, Engine Control Unit; ICE, Internal Combustion Engine). (From [1], © [2008] IEEE.)

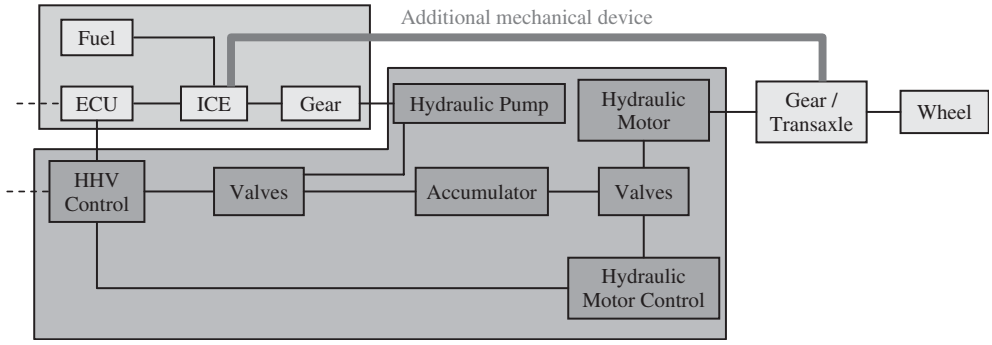

Figure 6.2 System-level diagram of HHV. (From [1], © [2008] IEEE.)

still much higher than an IC engine. Hence all the items noted above to justify the use of a hydraulic system in a hybrid vehicle hold true.

To illustrate the hydraulic hybrid system, consider the diagrams in Figures 6.1 and 6.2 [1] where a comparison of electric hybrid and hydraulic hybrid systems can be seen side by side through direct analogy. In these figures the shaded areas show the subsystems specific to the regular IC engine and the electric propulsion (Figure 6.1) and those specific to the hydraulic propulsion (Figure 6.2).

In the hydraulic hybrid vehicle (HHV) architecture shown in Figure 6.2, the alternator has been replaced by a hydraulic pump, the electric motor has been replaced by a hydraulic motor, the battery has been replaced by a hydraulic accumulator, the HEV controller has been replaced by a HHV controller, and the power electronics system has been replaced by the hydraulic valve system.

Figure 6.3 shows a full series hydraulic hybrid truck configuration [2]. The figure is consistent with the system-level diagram shown above. The accumulator includes a high-pressure (HP) accumulator containing some benign gas like nitrogen. The pressure in this

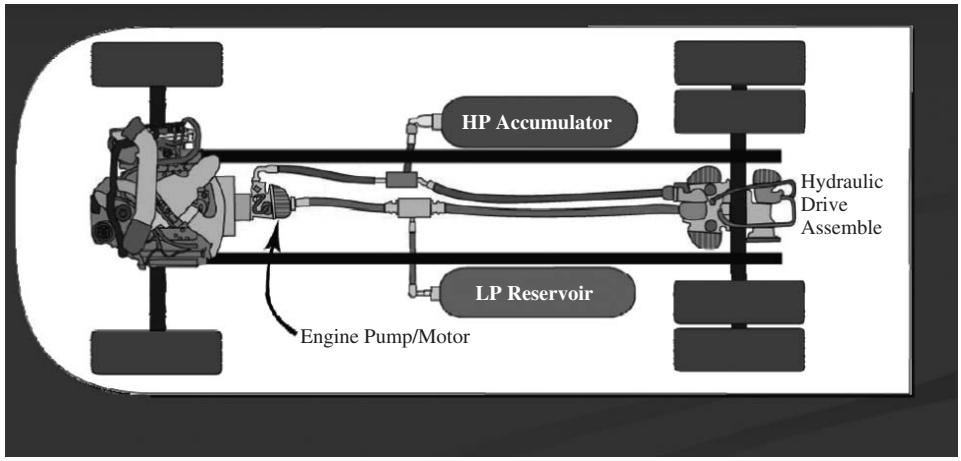

Figure 6.3 Physical architecture of HHV. (From [3]. Courtesy US EPA.)

cylinder can be as high as 3000–5000 psi (21–35 MPa), whereas the low-pressure (LP) cylinder pressure can be very low, on the order of a few hundred psi. The IC engine drives a pump, which takes the fluid from the LP cylinder side, pumps it to a very high pressure, and then delivers it to the HP cylinder side and the mechanical energy can be ultimately stored in the form of HP gas. To drive the vehicle's wheels, the HP fluid from the HP cylinder side passes through a hydraulic motor drive assembly. The hydraulic motor takes in the HP fluid, converts it to mechanical power at the wheels, and when the fluid has passed through the hydraulic motor, its pressure drops and it is transferred to the LP cylinder.

Thus, the hydraulic circuit is completed. Note that the amount of energy storage in the hydraulic accumulator system is rather low in terms of kilowatt hours per kilogram. For example, the energy storage density in a hydraulic accumulator can be about 1.9 Wh/kg [2], whereas a battery can have an energy density of 30–120 Wh/kg. However, the power density of a hydraulic system can be 2500 W/kg, whereas the electrical system power density can be about 650 W/kg. It is therefore apparent that the hydraulic hybrid system is very suitable for a high-power and relatively low-energy system, particularly where short bursts of high-power acceleration and deceleration are involved.

As we see from the previous discussion, in a hybrid hydraulic system, one can run the IC engine in the optimum efficiency zone of its operating curve and deliver the energy through the hydraulic system to the wheels. A few scenarios can take place here. If the energy needed by the vehicle propulsion matches the energy from the IC engine, the power generated will be used effectively in propulsion. Any excess energy will have to go to the accumulator for storage. The energy which is stored in the accumulator is rather low, hence this option cannot continue for long. If the HP accumulator cannot store any additional energy, then it will be necessary to change the engine operating point so as to match the propulsion need. However, even under this latter condition, it may be possible to stop the engine for a short while and use the energy from the hydraulic accumulator to propel the vehicle. The engine can be started again when the energy in the accumulator runs low. Thus it can be a type of stop and go situation.

One great benefit of having a hydraulic system for propulsion is due to the fact that it can eliminate the need for a massive conventional transmission system. Also, hydraulic fluid can be more easily moved from one point to another without the need for an elaborate transmission gearbox, other mechanical linkages, and so on. This concept can be used in a regular non-hybrid vehicle as well, where the conventional transmission system is replaced by the hydraulic system. But to be able to drive an IC engine at its most optimum point does need some sort of energy storage, which, in the case of a hydraulic hybrid, is an accumulator containing some gas. Without energy storage, it is not possible to realize the optimum operating point of the engine, simply because the average propulsion need in that case has to match the average power produced by the engine.

6.1.1 *Regenerative Braking in HHVs*

HHVs offer the benefit of regeneration when a vehicle is slowing down, and the ability to use the captured energy to accelerate again thereafter. As noted earlier, the specific energy of the hydraulic system or watt hours per kilogram is relatively low compared to a battery. However, it can still be good enough for braking applications, since, during braking, in general the power is high but the energy involved is typically low. Hence hydraulic storage can be quite adequate for the purpose. The regeneration process is shown in Figure 6.4 [3].

In this diagram it can be seen that the efficiencies of the hydraulic pump and motor are both a little over 90%. The efficiency of the accumulator (HP and LP together) is about 98%. Hence the efficiency of the whole regeneration process is about 82%. In another situation for a hybrid truck, the regenerative efficiency was shown to be 61%, which is still quite good.

One advantage of the hybrid hydraulic system is that the technology is very mature and has been around for many years. Components used in a hydraulic system, like the ones indicated in Figure 6.4, have a very high efficiency. Figures 6.5 and 6.6 show some of the typical hydraulic components used in a HHV [4].

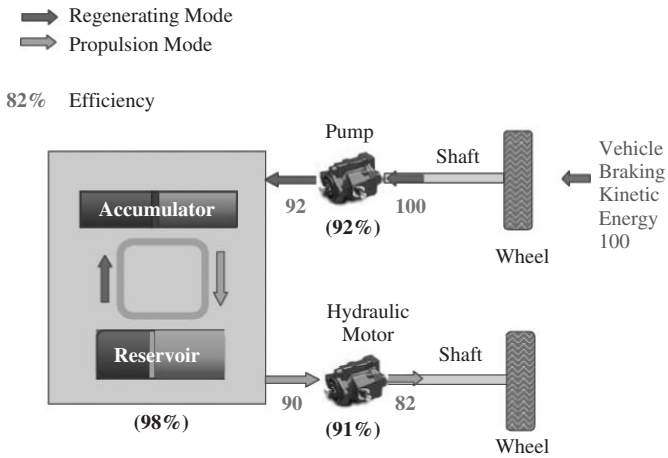

Figure 6.4 Regenerative braking efficiency distribution in HHV (From [3]. Courtesy US EPA.)

Figure 6.5 Bent-axis hydraulic motor. (From [4]. Courtesy Bosch-Rexroth.)

Figure 6.5 is a bent-axis hydraulic motor from Bosch-Rexroth. The nominal gas pressure at the entrance can be over 5000 psi, the maximum speed can be 4500 rpm, and the torque at 5100 psi can be 371 lb-ft (503 N m). This information is for a particular motor. The length of the unit excluding the geared shaft is about 5.15 in (13.1 cm). Hydraulic pumps also have similar appearance and characteristics.

Some accumulators are merely a cylinder with some valves to let the gas in or out with appropriate safety mechanisms. Other kinds of accumulators can be like the bladder type, in which a flexible bladder is submerged in a fluid or gas, and is pressurized to expand. It is the expansion of the bladder that pressurizes the gas in the accumulator. There are several working mechanisms for accumulators. In the hydro-pneumatic scheme a liquid pushes a piston, which then pushes a gas stored in the cylinder and compresses it, whereby energy is stored. The piston separates the liquid from the gas. Another type of accumulator is the diaphragm type.

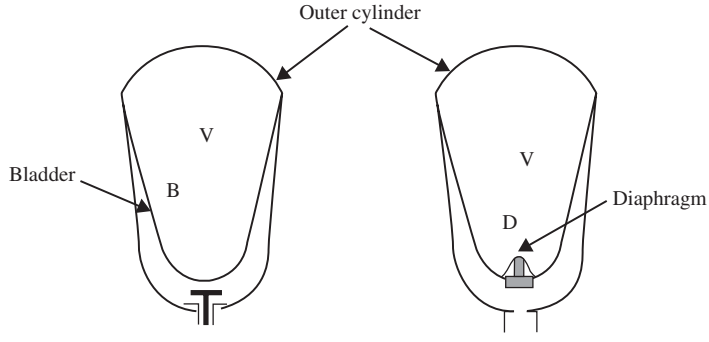

Figure 6.6 Bladder and diaphragm accumulators

Diagrams of some accumulators are shown in Figure 6.6, namely, diaphragm and bladder accumulators. The diagram on the right in Figure 6.6 shows a diaphragm accumulator. Here a diaphragm D is pushed by some fluid from the bottom, which then changes the volume V of the gas in the upper part of D, that is, between the diaphragm and the cylinder itself. The diagram on the left shows a bladder accumulator where the bladder B contains the gas (with volume V) which can be compressed. When the fluid enters the cylinder from the bottom, the bladder can expand or contract, thus energy can be stored in the gas when compressed and taken out from the gas when expanded. The energy is transferred through the fluid itself.

6.2 Off-road HEVs

Before discussing off-road HEVs, it is necessary to say a little about off-road vehicles in general. An off-road vehicle is any ground vehicle which does not, in general, use normal roads for its operation. Examples of such vehicles include predominantly construction vehicles and equipment, mining vehicles, agricultural vehicles like tractors, and so on. Some military vehicles also fall into this category. Off-road vehicles to be discussed in this section have quite different drive cycles and speed–torque demands, compared to a regular automobile.

Construction and mining vehicles, in particular, operate either under stationary conditions or at relatively low speeds. Very often they also operate over rough terrain. Thus an extremely rugged system is needed for a successful vehicle. The issue of emissions is not a matter of primary concern, due to the very nature of these vehicles. The prime requirement of these vehicles is very high power and torque. But in recent times, both fuel economy and pollution control have been focused to lead to a greener environment and, of course, economic operation. Hence the possibilities of using hybrid technology are being considered.

A qualitative discussion on the torque–speed requirement for the above vehicles and how to achieve it can be made at this point. Getting very high torque from a regular IC engine can lead to a very large transmission system or gearbox, and so on. To alleviate such difficulties, in the past hydraulic systems have been used. Hydraulic systems operate by continuously running an IC engine, which is a relatively low-torque, high-speed system. This IC engine is used to drive a hydraulic pump which can drive a hydraulic motor. Through the use of an incompressible fluid one can achieve very HP which can be transmitted to the drive end. However, it has been found that the hydraulic system, even though its technology is very mature, can cause certain problems. Examples of such problems are a complex plumbing system with pipes which, under rough terrain conditions, can cause fluid to leak. This can lead to degraded performance and eventually failure will take place. One disadvantage of hydraulic systems is that certain parasitic losses are unavoidable. Also, the IC engine does not operate at its optimum efficiency point all the time due to the nature of the torque–speed demand of the load.

Hence, lately various heavy off-road vehicle manufacturers, like those in the mining and construction equipment industries, have been concentrating on transforming their system to an electric hybrid type of propulsion. The word “hybrid” here may have a slightly different connotation than the regular HEV as in the automotive sector.

In very heavy vehicular applications like mining and construction, we noted earlier that a pure IC engine vehicle can lead to a very large transmission system capable of

providing the torque and power demands. This situation can be mitigated by using the IC engine to drive a generator or alternator, which in general will generate a variable speed (hence variable frequency) and variable (amplitude) voltage system. This variable frequency, variable amplitude voltage is then converted to a DC voltage of variable and ultimately constant value using a rectifier/regulator. The constant DC voltage is then translated into a three-phase AC system whose amplitude, frequency, and phase can be controlled electronically through the use of an appropriate power electronics converter. To be more precise, instantaneous variable voltage as a function of time can be generated by using power electronics. This three-phase voltage can then drive an electric motor to handle the vehicular load. Note that in the above system just described, one can avoid the use of a battery. Although the battery is a vital storage element in a regular HEV, in very large off-road vehicles the battery can require a very large and expensive system and hence it may be preferable to do without it. In other words, the system above is very similar or identical to a diesel–electric locomotive system.

Various architectures of off-road vehicles are possible, two of which are shown in Figures 6.7 and 6.8. The previous paragraph described the architecture of the system in Figure 6.7.

Note that the propulsion motor in this application can be any motor, but for very heavy mining applications, induction motors are found to be more robust and suitable in the rough environment, rather than a permanent magnet motor. The motor is then used to drive the wheels of the vehicle. Generally, off-road vehicles greater than 150 t in weight have two axles and two motors are used to drive these.

Although in the above architecture there is no battery, in principle a battery could be used for energy storage, but its size will be very large for such applications. In some

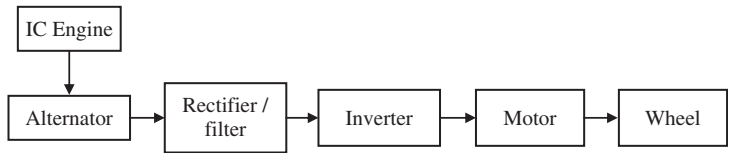

Figure 6.7 System-level architecture of a battery-less hybrid off-road vehicular system

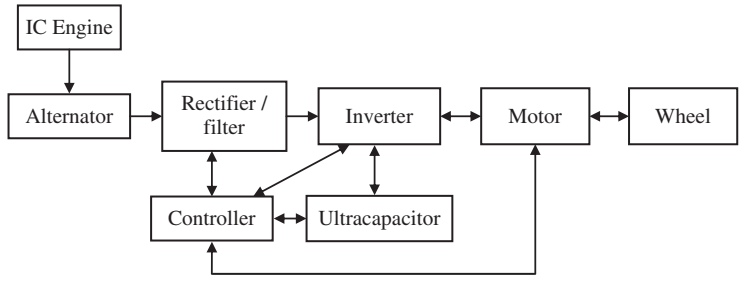

Figure 6.8 System-level architecture of a hybrid off-road vehicular system with ultracapacitor for storage

applications an ultracapacitor bank can also be used. The ultracapacitor normally has a high specific power, that is, it can provide very high bursts of power input to a device, but the duration will be very short and hence the energy involved will be small. During the slowing down of a vehicle or some of its movable parts, the mechanical energy can be transformed into electrical energy and stored in the ultracapacitor. The stored energy can be used to accelerate the vehicle if so needed at a later time. In this way regeneration can be utilized to save energy, thus leading to better system efficiency and fuel economy. An architecture for such a system with an ultracapacitor is shown Figure 6.8.

In the above architecture, if we want to drive the vehicle's wheels, the energy can come from the ultracapacitor or from the IC engine, which drives the alternator and then the rectifier creates direct current. The DC voltage from either the rectifier or the ultracapacitor can be translated to a proper AC voltage to drive the electric motor. The system will have the necessary switches, which can choose between the ultracapacitor and the alternator/rectifier. When the vehicle slows down, the controller commands the ultracapacitor, inverter, and alternator/rectifier to coordinate properly, so that energy flows from the motor side (with the motor operating as a generator) into the ultracapacitor, through the inverter.

It is interesting to look at some typical sizes involved in the off-road vehicles indicated above. For example:

- A Caterpillar Engine Model Cat 3524B EUI has gross power 2648 kW (3550 hp) and gross machine operating weight 623 690 kg (1 375 000 lb) (http://catsays.blogspot.com/2005/01/caterpillar-797b-mining-truck.html).
- A particular Komatsu model has gross horsepower 2611 kW (3500 hp) and weighs 505 755 kg (1 115 000 lb).
- A particular Liebherr model has gross horsepower 2722 kW (3650 hp) at 1800 rpm and weighs 592 tonnes (652.5 t).

The vehicles indicated above are huge in size, as is obvious from the specifications above and the pictures shown in Figure 6.9.

In the vehicles shown in Figure 6.9, Caterpillar uses a conventional powertrain, whereas Komatsu and Liebherr use hybrid (HEV) powertrains. Caterpillar is also now moving toward a HEV platform.

From the Komatsu information sheet, the system has the following specifications:

Alternating current	
Alternator	GTA-39
Dual impeller in-line blower	453 m^3/min (16 000 cfm)
Control	AC torque control system
Motorized wheels*	GDY106 AC induction traction motors
Ratio*	32.62 : 1
Speed (maximum)	64.5 km/h (40 mph)

*The authors most sincerely thank the Komatsu technical team who provided additional information on these items.

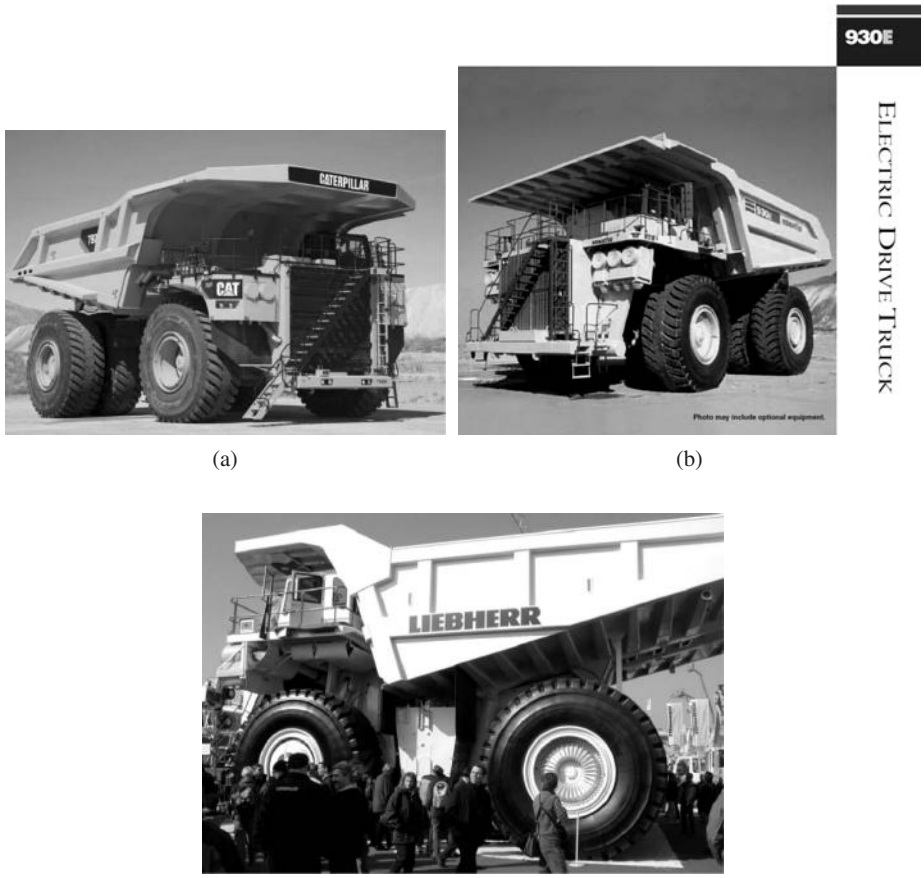

(a) (b)

(c)

Figure 6.9 Typical mining vehicles: (a) Caterpillar; (b) Komatsu; and (c) Liebherr. (Courtesy: (a) Caterpillar; (b) Komatsu; (c) Wikimedia.)

Although exact details of the systems are normally proprietary information, some commonality can be noticed between them and a reasonable idea about the sizes of the components can be obtained, based on the above information. For example, the traction motors in both the Komatsu and Liebherr models are induction motors. The alternators in the Komatsu vehicle (made by GE) have brushes, although brushless generators are also viable. The gear ratio reduction from motor to wheel is on the order of 28–42. The gross engine horsepower of the vehicles is about 2.6–2.7 MW. The inverter used to drive the motor generally uses an insulated bipolar gate transistor (IGBT) for switches. Assuming alternator and inverter efficiencies on the order of 0.95 each, the motor power input is about $2.6 \times 0.95 \times 0.95 = 2.35$ MW. For the Komatsu 930E-4SE, the retarding power is 4 MW short term and 3 MW continuous. So it is reasonable to assume that an induction motor on the order of half of that can be used, assuming two motors for the system, with one at each axle. Hence each of these induction motors can be considered to be

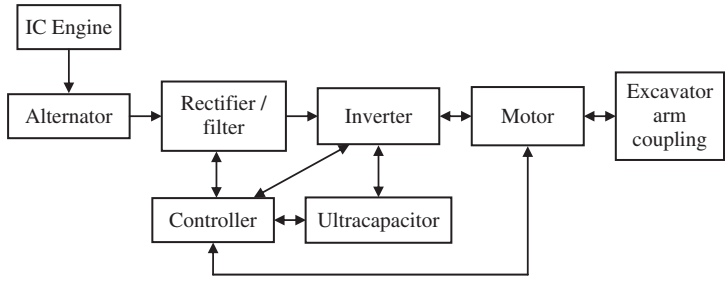

Figure 6.10 System-level architecture of hybrid excavator construction equipment with ultracapacitor for storage

about 1.5 MW. The vehicle at maximum speed amounts to a wheel revolution of about 84 rpm (assuming a tire diameter of about 4 m). With a gear ratio of about 32.62, the motor speed should be about 2700 rpm. Nominally, this leads to about 3000 rpm, which, at 50 Hz, leads to a four-pole induction motor. Such a motor is normally a common standard for such applications.

Another application of HEV in off-road vehicles involves a construction excavator. Here the use of the HEV concept is not in the vehicle propulsion, rather in the excavator arm movement. The excavator arms need very brief bursts of high power followed by low-power return and then slowdown of its speed to stop the arm. Such an application is very well catered for by using an IC engine driving a generator to produce electricity to drive the excavator arm motor, which is an electric drive. A possible architecture is shown in Figure 6.10.

This architecture is basically the same as the HEV architecture shown previously for the hauler propulsion. The only difference in this case is that the size is much smaller. It has been claimed that the Komatsu hybrid excavator leads to a fuel economy of around 25% and that some specific users have achieved fuel economies as high as 41%. A picture of the Komatsu PC 200-8 hybrid excavator is shown in Figure 6.11. These pictures are from the Komatsu web site (www.komatsu.com/CompanyInfo/press/2008051315113604588.html).

Some manufacturers prefer to use a battery instead of an ultracapacitor for the purpose of storage. An example is the New Holland excavator which uses a 36 hp diesel engine, 20 kW generator, and 288 V lithium battery. The choice of storage is highly dependent on exact usage and the duty cycle. If the vehicle is just a high-power excavator, then an ultracapacitor seems to be a suitable candidate. However, if in addition to the excavator application, there is any other auxiliary equipment needing energy which may not be immediately available from an ultracapacitor, a battery may be used. The duty cycle in terms of torque need, duration of the torque, auxiliary equipment used, cost, size, and similar factors all lead to the decision process in terms of what will be best: ultracapacitor or battery? Hence on this matter there is no unique answer.

Regarding the rating of the motor for the mining truck, the nominal DC link voltage rating of these motors can be around 2600 V, leading to about 1600 V line-to-line rms input to the three-phase motor. For a 1.2 MW motor this corresponds to about 541 A

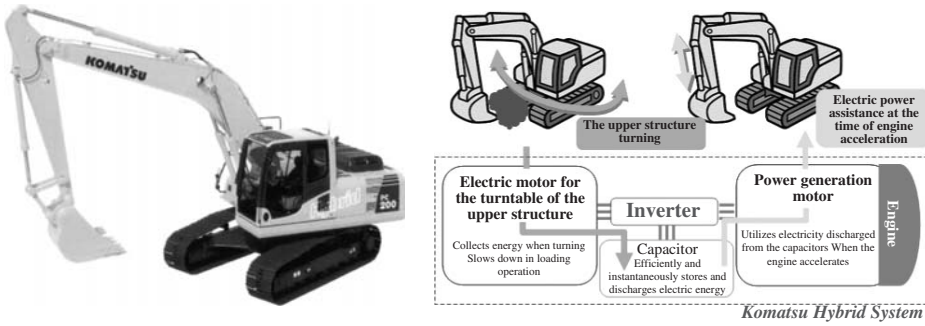

Figure 6.11 Komatsu hybrid excavator system. (Courtesy: Komatsu.)

AC rms, assuming a power factor of about 0.8. In this case the DC link current will be 1.2 MW/2600 = 461 A DC per motor. All these assume no additional loss in the system; the numbers merely give an idea of the voltage and current values. Some systems use 3.3 kV IGBT technology [5] to drive these motors, which is consistent with the above ratings indicated for the motor. For the excavator example above, the numbers are much lower. As in the paragraph immediately above, at 288 V DC, the DC link current will be about 70 A, the three-phase line-to-line rms for the motor will be about $0.612 \times 288 = 176$ V, and the motor current will be about 82 A for the excavator.

6.3 Diesel HEVs

Fundamentally the diesel HEV is nothing but a regular HEV, except that the IC engine is a diesel engine instead of a gasoline engine. It is well known that a diesel engine is more efficient than a gasoline engine, hence by combining a diesel engine with an electric drive, one can basically claim the best of both worlds. So, the question might arise: why should one not use a diesel hybrid and what are the motivations by not doing so? The following discussion will help throw some light on this issue.

The compression ratio of a diesel engine can be much higher than that of a gasoline engine, for example, it can be around 15–20 compared to 9–12 for the gasoline engine. The higher compression ratio means the engine has to be heavier in construction to sustain the pressure. At low speeds diesel engines are better in terms of fuel economy due to the absence of throttle vales, thus avoiding parasitic losses. Other benefits of diesel engines include lower greenhouse gas emissions like CO_2. Low-speed characteristics of diesel engines are better compared to gasoline engine, in terms of starting torque generation. The absence of an ignition system, and hence fewer components, leads to higher overall system reliability.

A diesel engine, being more efficient than its gasoline counterpart, obviously leads to smaller-sized engines, particularly at lower speeds. Hence for the same performance, and particularly during acceleration, it is more beneficial to use a diesel hybrid, within the same packaging size. This is especially beneficial in a parallel hybrid configuration, where both the diesel and electric propulsion will come into play to achieve performance

in terms of power and acceleration. This performance issue is of no consequence in a series hybrid, since propulsion is done only by the electric motor.

In transit buses, diesel hybrid technology leads to better benefits, due to the nature of the stop and go drive cycle and the need for acceleration at low speeds, which are very specifically offered by diesel hybrids. Hence they are ideal candidates for applications in buses and delivery trucks to name but a few. They are also suitable for very heavy-duty vehicles like mining vehicles, locomotives, and so on, in a series hybrid configuration which can help eliminate the need for a very heavy transmission (gearbox etc.) system. In these applications (mining, locomotives) the engine is used to run a generator, which can be run at an optimal speed. The electricity can then be coupled to a motor through some power electronics-based inverter.

If a comparison of diesel versus gasoline hybrid electrics is done on an equal basis, they can be briefly summarized as follows:

- A diesel engine operates more efficiently overall than a gasoline engine for a given size.
- A diesel engine has fewer components, hence can be considered to need less maintenance, compared to a gasoline engine.
- The higher the power need, the more important the size and cost become, therefore the diesel will have a better edge compared to the gasoline engine.

It therefore appears that there is a breakeven point in power requirement, above which diesels will prove more economical, in terms of both cost and fuel economy and overall life cycle maintenance, compared to their gaosline counterparts.

From this short overview of diesel engines, it can be concluded that the merits of diesel engines and electric propulsion, taken together, can lead to the best of both worlds, and to the most fuel-efficient vehicles, subject to the specific application needs noted above.

6.4 Electric or Hybrid Ships, Aircraft, Locomotives

The success of HEVs in automotive applications has led certain other vehicular areas to consider the technology as well. These include ships and aircraft, which are non-ground vehicles. Diesel–electric locomotives have already been using the technology in a slightly different form and we will discuss these as well.

6.4.1 Ships

Obviously, the need in a ship involves very large sizes of everything. It can be basically considered as an industrial power system, with both utility types of systems and a propulsion system. The overall power need in a ship could be anywhere from 1 MW to very close to 100 MW. The focus of this book, however, will be on propulsion and not on the overall electric power system in a ship.

Historically ships evolved in various stages, from steam- or diesel-based propulsion, to diesel–electric propulsion. Initially, the motors used in ship propulsion were DC motors. With the advent of power electronics, DC motors can be replaced with robust induction motors with very good control based on power electronics. The motors could also be

field-excited synchronous motors. The benefits of using these motors are in terms of both reliability and efficiency. In addition, recently the technology of pod propulsion has become popular [6]. In this scheme, the propulsion motor is located separately in a pod, which is physically secured at a distance from the main body of the ship. The power electronics system is located within the main body of the ship and electrical wiring is run to the pod, which houses the motor. The size of the pod can be very large, something like 10 or 12 ft (3.1 or 3.7 m) in diameter. The propulsion motor shaft is connected to the propellers. Also, the pod is capable of being turned through a full 360° if needed. This eliminates the need to have a rudder in the ship. Let us now look at the architecture of the ship propulsion system [7] shown in Figure 6.12.

This figure (Figure 6.12) more or less gives a complete overview of the possibilities in terms of generation, distribution, and propulsion in a ship. The choice of the particular architecture is dependent on the size and can affect the cost significantly. All the components mentioned above may not be suitable under all circumstances. If the ship generation system uses a diesel or gas turbine, then the overall ship system could be considered to be a hybrid system, whereas, if there is no mechanical power system, for example, if a fuel cell is the only source of power, then the ship will be a completely electric ship. Even if the power is generated by nuclear energy, ultimately, to get electricity, it will need some kind of electric generator, which in turn will need to be turned by non-electrical means, and in this case the ship may be considered in the hybrid vehicle category. Whether it

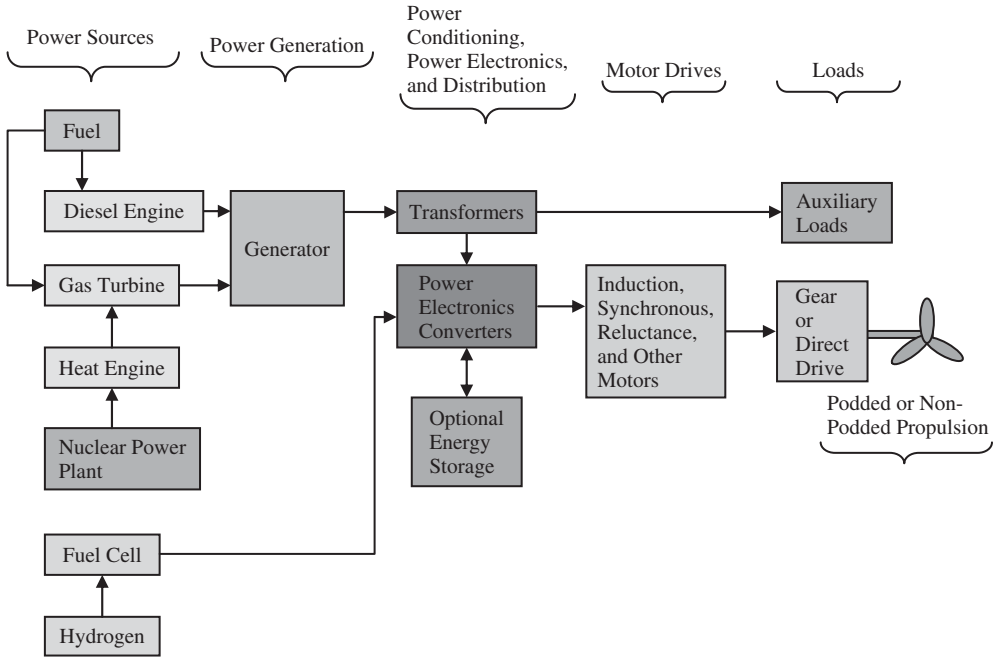

Figure 6.12 A generic electrical system architecture of a ship's electrical system. Paths shown by arrowhead lines entering a particular block merely imply multiple possibilities and do not necessarily indicate concurrent paths

will be hybrid in the sense of "propulsion" will depend on the exact propulsion means used, and what kind of devices are directly contributing toward propulsion.

So, a simpler subset of the above system can consist of a gas turbine as the prime mover, which drives a field-excited synchronous generator (or it could be a permanent magnet-based generator too). The advantage of a field-excited generator is the ability to control the voltage by controlling the magnetic field, and this can be done using semiconductors of relatively lower current rating. If a permanent magnet generator is used, the voltage control has to be at full power level at the stator terminal with much higher-rated semiconductors. The advantages of permanent magnet generators are of course higher efficiency and simplicity, with no need to use slip rings for the field. On the propulsion side, one can use synchronous or induction motors. Synchronous motors have to be doubly fed, whereas induction motors are just fed at the stators. The architecture of a possible system is shown in Figure 6.13.

The propulsion motor voltage can be rated at several hundred to several thousand volts, depending on the size and needs.

With the above architecture in mind, it will now be instructive to look at the pod propulsion we referred to previously. As its name suggests, pod propulsion is merely involved with the physical location of the propulsion motor. In other words, it is the items on the right of Figure 6.13, that is, the propulsion motor and the propeller, which belong to the pod directly. These two items are housed inside the pod. The pod itself is outside the ship's main body structure (below the stern), but of course secured to it through mechanical structures. The electric wiring runs from the main ship to the pod. So, the items shown inside the dot–dashed lines in Figure 6.13 are in the pod. Figure 6.14 shows what the pod looks like.

The figure is reasonably self-explanatory and describes the various components. The slip ring unit, obviously, has to be connected to the power system, which is located inside the main body of the ship. The picture of the man gives an idea of the size of the pod and its components.

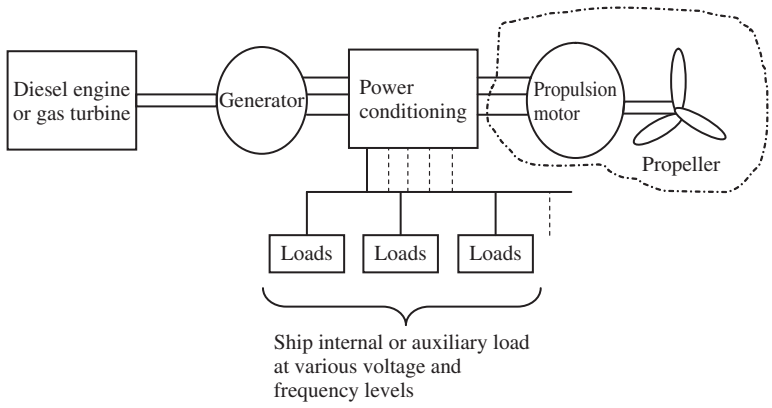

Figure 6.13 System architecture of a hybrid electric ship

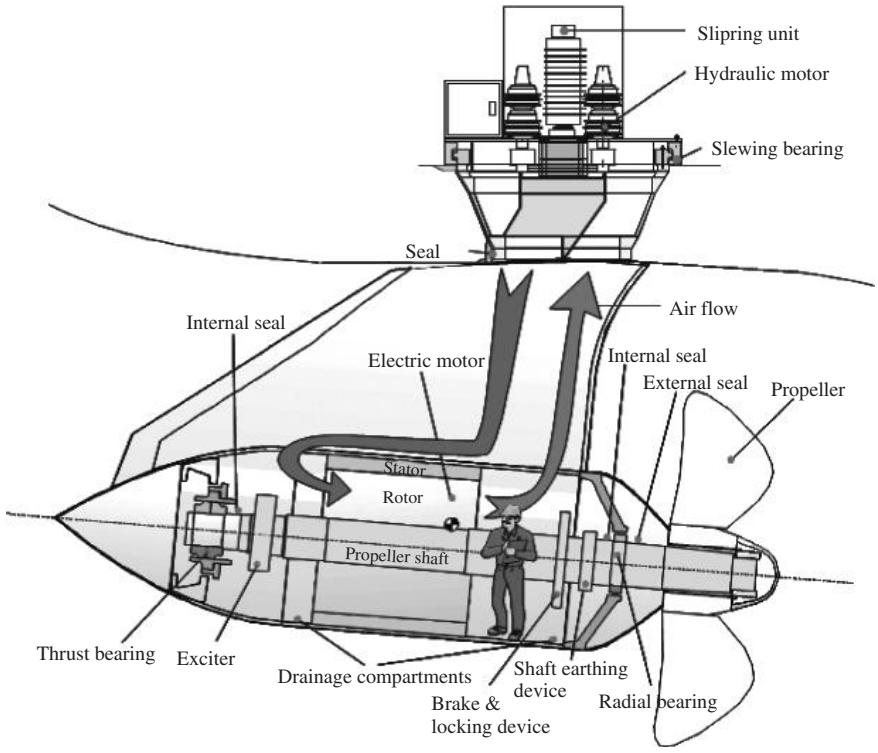

Figure 6.14 A pod propulsion system used in ships. (Courtesy Rolls-Royce plc.)

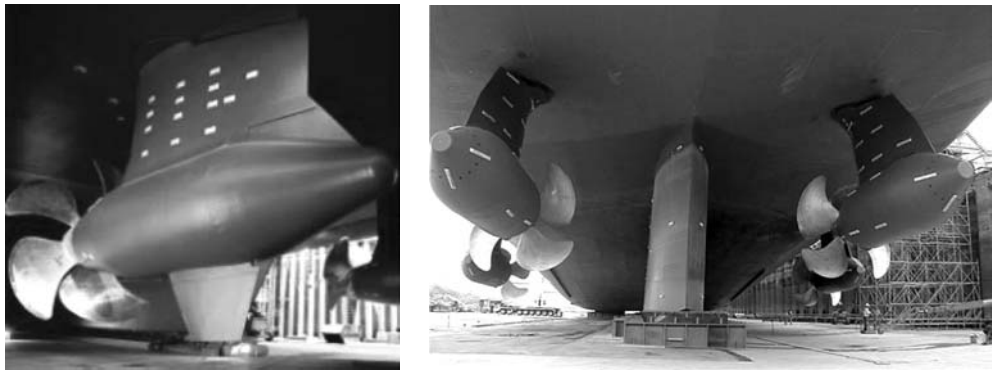

(a) (b)

Figure 6.15 External view of actual pod propulsion systems in a ship: left, Azipod® by ABB Oy (courtesy ABB); right, Mermaid pod by Rolls-Royce (Courtesy Rolls-Royce plc)

There are only a handful of pod manufacturers in the world. The main ones are ABB, Rolls-Royce, and Schottel. ABB makes the Azipod [8] and Rolls-Royce makes the Mermaid pod. Schottel has a low-power pod known as SEP or Schottel Electric Propulsion and there is a high-power version called Siemens Schottel Propulsion (SSP) in a joint venture with Siemens. The Azipod and the Mermaid are shown in Figure 6.15 to give an idea of their appearance.

6.4.2 *Aircraft*

Since this book is about electric and hybrid vehicles from a propulsion point of view, it might be instructive to consider an aircraft propulsion system and whether hybrid propulsion can be considered for the purpose or not. Let us begin by saying very briefly that at this point, with the energy technology available to us, electric and hybrid propulsion systems cannot be considered feasible. That said, we can continue with some explanation.

There are several fundamental issues which are different for aircraft compared to land or water-borne vehicles. First, why do we consider hybrid or electric technology? From our previous discussions in this book, the predominant considerations here are: (i) fuel economy, (ii) environmental friendliness, (iii) size, (iv) cost, (v) reliability, (vi) weight of mechanical transmission system in certain off-road applications, including locomotives, and finally (vii) the drive cycle of the vehicle. The choice of hybrid or electric vehicle is dependent on the trade-off between items (i) to (vii). The drive cycle of a ground vehicle can fluctuate according to city or highway driving. Water vehicles, particularly ocean-going ships (not excluding some smaller watersport and similar vehicles), and aircraft do not have a fluctuating drive cycle. Hence many of the considerations which are important in ground vehicles do not apply to these. Another consideration is available space. Ships have a lot of space available, whereas aircraft do not. Hence it is possible to place a high-power motor in a ship for propulsion, along with a big-sized battery, which may be unrealistic in an aircraft.

Consider a Boeing 747 type of commercial aircraft, which can need around some 90 MW of power during takeoff and about half of that during cruising, depending on the speed. Regardless of the technology used, accommodating a motor with that kind of power or having a means (battery or energy source) to drive it is unrealistic – at least with the current technology of motors and energy sources. Indeed, if the technology existed, we would have quieter aircraft, and they would, most likely in general, be safer as well in the event of crashes, in the absence of any combustible fuel and fire. Just to give an idea of specific energy and power, it may be instructive to refer to Table 6.1, from the "Battery University" web site, with some modifications.

An interesting thing to notice is that the power/passenger is lowest for a bike and highest in a 747 jumbo jet. However, the energy/passenger per kilometer is somewhat different – it is lowest in a bike, but highest in a ship. Interestingly, an SUV needs more energy/person/kilometer compared to the jet. The fourth row is the power at cruising, leading to the sixth row upon dividing by the number of passengers (i.e., the fifth row). This shows that power/passenger is very high in a jet and a ship. The number of passengers indicated above for the 747 and *Queen Mary 2* are slightly approximate, hence the sixth row is slightly different for those columns compared to those derived from fourth and fifth rows. But a ship has lot more space available, hence an electric ship is a viable

Table 6.1 Comparison of energy and power demands in different systems

Specifications/ power and energy demand	Boeing 747 (jumbo jet)	*Queen Mary* 2 or large ocean-going liner	Sports utility vehicle	Bicycle	Person on foot
Weight	369 t (fully loaded)	81 000 t	2.5 t	100 kg with person	80 kg (176 lb)
Cruising speed	900 km/h (560 mph)	52 km/h (32 mph)	100 km/h (62 mph)	20 km/h (12.5 mph)	5 km/h (3.1 mph)
Maximum power	77 000 kW (100 000 hp)	120 000 kW (160 000 hp)	200 kW (275 hp)	2000 W (professional)	2000 W
Power at cruising	65 000 kW (87 000 hp)	90 000 kW (120 000 hp)	130 kW (174 hp)	80 W (0.1 hp)	280 W (0.38 hp)
Number of passengers	450	3000	4	1	1
Power/passenger	140 kW	40 kW	50 kW	80 W	280 W
Energy/passenger per kilometer	580 kJ	2800 kJ	1800 kJ	14.4 kJ	200 kJ

Courtesy Battery University web site: http://batteryuniversity.com/parttwo-53.htm.

possibility, whereas a jet equivalent is not a viable option with the present technology. Thus, the only electric aircraft that we see today are some unmanned drones or very tiny propeller-driven planes.

With the above in mind, we can, however, discuss the work done on electric aircraft and where things stand at this time. As mentioned above, the equivalent of a jet engine using electrical means is not possible with currently available technology. To alleviate the problem of energy requirement, small solar aircraft have been designed using solar panels. Some of these will now be discussed.

A very recent example of a solar panel-based aircraft is shown in Figure 6.16. This aircraft, called "Helios Prototype," has been developed by NASA in the United States. It weighs 1600 lb (725 kg), has a wingspan of 247 ft (75.3 m), and a wing area of 1976 sq ft (184 m^2). The upper side of the wing contains the solar panels which are very thin, like a sheet of paper. The solar power is fed into backup lithium–sulfur batteries, so that the aircraft can fly in the absence of daylight.

Another aircraft is a hybrid, made by Falx Air Vehicles, from the UK (Figure 6.17). It has a tilt rotor, uses a 100 hp combustion engine, a solar array, and an electric motor rated at 240 hp peak power. The fuel consumption is claimed to be 10 l/h of flight. This is substantially lower than a regular helicopter, which consumers about 17 times more fuel.

It is obvious from the above that electric or hybrid aircraft are limited in size. The issue is in essence due to limitations of the energy storage mechanism and the extremely high power needed during takeoff by large commercial aircraft.

Figure 6.16 NASA's Helios Prototype solar aircraft. (Courtesy Wikimedia – original photo is from NASA.)

Figure 6.17 A hybrid electric solar aircraft by Falx Air. (Courtesy NewsUSA.com – copyright-free content.)

6.4.3 Locomotives

Locomotives evolved over more than 200 years, the steam locomotive being around in the early 1800s. The power demand in these vehicles could be anywhere from 3000 to 6000 hp on average, depending on the application. There are some exceptions where size could be even bigger. Diesel locomotives began replacing steam-based ones starting about a decade before the mid-twentieth century. They are easier to maintain than steam locomotives and are more efficient (www.railway-technical.com/st-vs-de.shtml). Purely electric locomotives were introduced in 1894 (www.itdh.com/resource.aspx?ResourceID=GREAT21) by Kálmán Kandó using a three-phase induction motor. This needed electrification of

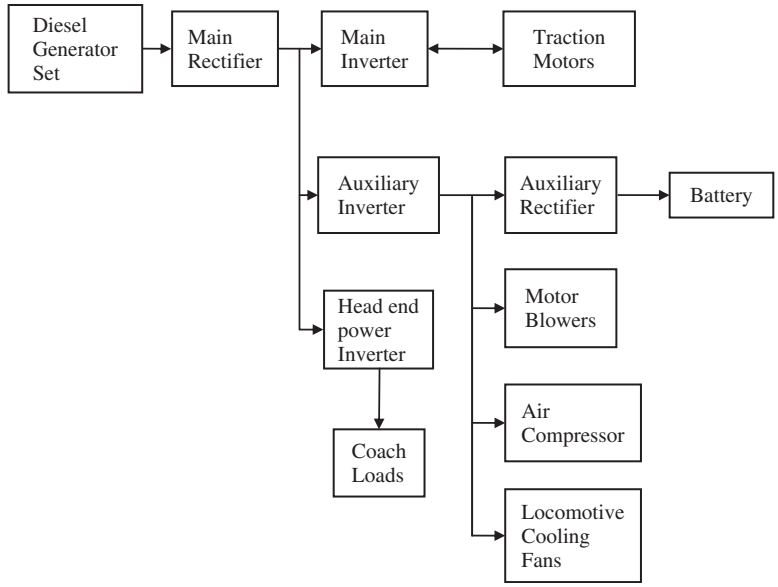

Figure 6.18 Electrical and propulsion system architecture for a diesel–electric locomotive

the railway track, however, to be successful in the long run. Then there was the gas turbine-based locomotive, where the gas turbine engine was used to run an electric generator, and the electricity was used to drive a propulsion motor. A gas turbine provides the benefit of high specific power density. But gas turbines suffer from a problem in that their efficiency drops after a certain engine speed, hence they become uneconomic in terms of fuel consumption. This is unlike a diesel engine, whose efficiency becomes flatter at a higher speed.

In view of the above, diesel engine-based locomotives are mostly used nowadays. The propulsion system is, however, implemented through an electric motor. There are a couple of main advantages why a diesel–electric system is used. First, if the propulsion were purely mechanical, then a rather large transmission system with gearbox etc. would be needed to create the needed torque in the wheels. Second, and particularly in short-haul trains where speed fluctuations will be encountered, a diesel engine with a finite (and a large) number of gears would need to be operated at different speeds other than the most optimum speed at which the efficiency is highest. By using a diesel–electric system, we can remove both of these issues. In this system, the diesel engine can be run at the most optimal speed, and a generator is run to produce electricity, which can be used to run a traction motor to drive the wheels. With the advent of power electronics, this system is rather easy to realize, using reliable and efficient traction motors, which can be an induction motor or a synchronous motor – either permanent magnet or field excited. With this background then, let us look at the basic architecture of the diesel–electric system (Figure 6.18).

In general, the traction motors are placed on each axle of the locomotive to drive the wheel pairs. A couple of diesel–electric locomotives [9] are shown in Figure 6.19.

Figure 6.19 Pictures of two diesel–electric locomotives by Siemens. (Courtesy Siemens AG.)

Figure 6.20 Picture of a large diesel–electric locomotive by Siemens. (Courtesy Siemens AG.)

One particular locomotive example is indicated in Figure 6.20 [10], with some technical specifications. Its diesel engine is rated at 4000 hp; the power at the wheels is 3350 hp. Six motors are used, one per axle. From the picture it is clearly seen that there are three axles in the front and three in the back. The motors are four-pole, squirrel cage, three-phase induction motors, maximum voltage 2030 V, with a 433 kW continuous power rating. So, the total motor power is 2598 kW, or about 3500 hp. The maximum speed of the motor is 3220 rpm, and there is a gear ratio of 85:16 between the motor and the wheel. Note that the squirrel cage induction motor is a very reliable device for such applications. Although specific power density can be somewhat smaller than in a permanent magnet motor, in a locomotive application where space may not be a premium, say in a small passenger car, this may be the ideal choice. In addition, induction motors are very resilient to temperature conditions, unlike permanent magnet motors.

It should be mentioned that in many applications there is no traction system battery in the locomotive (of course, to start the diesel engine it is necessary to have some starting mechanism, which can be electric, hydraulic, or pneumatic; if it is electric, a small starter battery will be needed). However, for capturing regenerative energy, it is necessary to have some storage battery, ultracapacitor, or a combination of the two, or even a flywheel

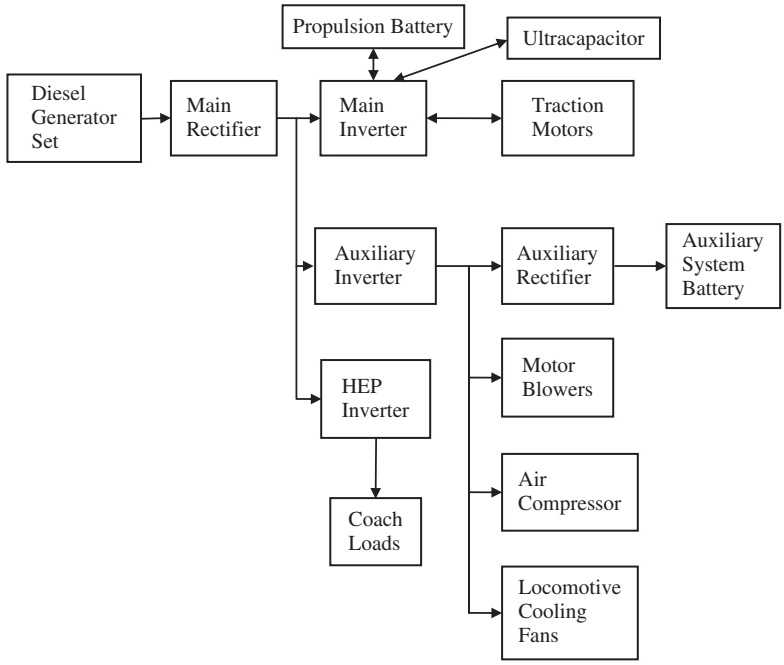

Figure 6.21 Electrical and propulsion system architecture for a diesel–electric locomotive including regenerative braking capability

storage unit, which can be used during regeneration. The regeneration can help improve fuel economy and is of more importance for short-haul trains and not so important for a long-haul train. The architecture of a locomotive system capable of regeneration is shown in Figure 6.21.

The system shown in this figure is essentially the same as the one before, except that it now has a propulsion battery and/or ultracapacitor, which can, if necessary, feed the propulsion motor. All the other principles mentioned above remain.

6.5 Other Industrial Utility Application Vehicles

Industrial utility vehicles normally include industrial fork lifts, airport tugs, golf carts, vehicles used in airports for internal transportation, to name but a few. Some of them indeed qualify as off-road vehicles as well. But we will specifically reserve the name off-road vehicles to describe relatively heavy-duty vehicles like mining vehicles, refuse trucks, excavators, and the like. In a more specific way, in many instances the industrial utility vehicles are used within relatively confined spaces compared to off-road vehicles. Hence industrial utility vehicle propulsion systems are sometimes seen using propane or other gas (including liquefied gas) fuel-based IC engines. The intent is to avoid exhaust-type pollution within a confined or closed space without adequate ventilation. However, to prevent noise pollution, in many cases the propulsion is purely electrical.

So, the question arises: where do these vehicles appear within the scope of HEVs? Before going into the issue in more detail, let us note that the main motivation behind HEVs is fuel economy and overall size reduction of transmission gearboxes, if possible. The first one, that is, fuel economy, is more important in the case of passenger vehicles, whereas the issue of transmission size reduction plays an important role in off-road vehicles, locomotives, and so on. It is in general true that if the size of the gearbox etc. can be reduced, a concomitant fuel economy will also take place. This is besides the fact that in locomotives, for example, one will also get fuel economy by running the IC engine at its most efficient point.

In an industrial utility vehicle, fuel economy is an issue, but noise reduction, pollution control, and reliability are more important. To that end, purely electric propulsion seems more attractive, which basically leads to a plug-in electric vehicle. This is generally suitable for indoor applications because, almost always, electricity will be available for charging the batteries of the vehicle for such applications. Therefore, multi-propulsion HEVs are not really very attractive for industrial utility vehicles which are operated within confined spaces and short drive cycles.

References

1. Masrur, M.A. (2008) Penalty for fuel economy – system level perspectives on the reliability of hybrid electric vehicles during normal and graceful degradation operation. *IEEE Systems Journal*, **2** (4), 476–483.
2. Kargul, J.J. (2007) Hydraulic hybrids – demonstration for port yard hostlers. EPA Presentation, July 11, 2007, http://www.epa.gov/otaq/presentations/diesel/hydraulic-hybrid-hostler.pdf (accessed February 2, 2011).
3. US EPA (2004) Clean automotive technology – innovation that works. World's First Full Hydraulic Hybrid SUV, Presented at 2004 SAE World Congress, http://www.epa.gov/oms/technology/420f04019.pdf (accessed February 2, 2011).
4. Rexroth-Bosch Group, Axial Piston Fixed Displacement Motor AA2FM (A2FM), Bosch product brochure.
5. Hierholzer, M., Bayerer, R., Porst, A., and Brunner, H. Improved Characteristics of 3.3kV IGBT Modules, http://www.scut-co.com/maindoc/techtrade/pdevice/eupec/documents/techsupport/ed_pcim_97.pdf (accessed February 2, 2011)
6. SINM (Studio di Ingegneria Navale e Meccanica) (2004) Focus on Propulsion Pods. Report 060/2004.
7. Hebner, R.E. (2005) Electric ship power system –research at the University of Texas at Austin. IEEE Electric Ship Technology Symposium, July.
8. ABB, The World's First Azimuthing Electric Propulsion Drive, http://www04.abb.com/global/seitp/seitp202.nsf/0/589ea2a5cd61753ec12570c002ab1d1 /$file/AzipodNew.pdf (accessed February 10, 2011).
9. Siemens Product Information, Diesel-Electric Locomotives.
10. Siemens Technical Information, Diesel-Electric Locomotive SD70MAC.

Further Reading

Caterpillar, http://catsays.blogspot.com/2005/01/caterpillar-797b-mining-truck.html (accessed February 2, 2011).

Comparing Battery Power, www.batteryuniversity.com/parttwo-53.htm (accessed February 2, 2011).

Hungarians in the History of Transport, www.itdh.com/resource.aspx?ResourceID=GREAT21 (accessed February 2, 2011).

Komatsu, http://www.komatsuamerica.com/default.aspx?p=equipment&f1=view&prdt_id=947 (accessed February 2, 2011).

Komatsu. http://www.komatsu.com/CompanyInfo/press http://www.epa.gov/oms/standards/light-duty/udds.htm (accessed February 2, 2011).
Wikimedia, http://commons.wikimedia.org/wiki/File:Liebherr_T282.jpg (accessed February 2, 2011).
http://sections.asme.org/Fairfield/FEBRUARY%2023,%202005%20FAIRFIELD,%20DOLAN%20SCHOOL%20OF%20BUSINESS.htm
http://www.copyrightfreecontent.com/auto/prius-of-the-skies/ (accessed February 2, 2011).
http://commons.wikimedia.org/wiki/File:Helios_Prototype_on_Lakebed_-_GPN-2000-000198.jpg (accessed February 2, 2011).

7

HEV Applications for Military Vehicles

7.1 Why HEVs Can Be Beneficial to Military Applications

There are several motivations, both direct and indirect, for HEVs for military applications. Military applications can include both direct vehicular applications, which are related to vehicular propulsion, and indirect applications in the sense of using electrically operated arms, or interfacing with the vehicular electrical system to create a microgrid to supply power to a military base etc.

One of the most important reasons for considering HEVs for military applications is the cost of fuel. Transporting fuel to the field through risky routes and over long distances can raise the cost of fuel significantly. The cost can rise from $1 in a regular civilian situation to $400 per gallon to carry fuel to the battlefield (http://www.defensesystems.com/Articles/2010/03/11/Defense-IT-3-Greens.aspx), and if an airlift is needed, the cost can rise to even $1000 per gallon. In general, the cost to carry fuel to the field is about $100 per gallon (http://www.environmentalleader.com/2010/05/28/us-commanders-want-deployable-renewable-energy-generation). The bottom line is that we can assume that the cost of fuel will be several hundred dollars per gallon in military situations. So, even a small percentage saving in fuel can imply huge cost savings to the tune of billions of dollars per year.

Other issues in military applications involve noise, both acoustic noise and heat signatures in the form of infrared radiation, which can be detected elsewhere. A quiet HEV can help significantly toward achieving goals of noise elimination.

Some indirect benefits of HEVs are as follows. When the military move to a combat zone, there may be bases and other infrastructures which need stationary applications of electricity at utility-level voltages. With multiple HEVs, when properly connected and interfaced, it becomes possible to create utility-level voltages to run various stationary equipment. This can be achieved by running the HEV battery (and, if necessary, the IC engines in the HEV). Several HEVs can, in fact, form a microgrid with a reasonably robust source of utility power. Of course, when interfacing several HEVs to generate electricity,

Hybrid Electric Vehicles: Principles and Applications with Practical Perspectives, First Edition.
Chris Mi, M. Abul Masrur and David Wenzhong Gao.

it will be necessary to do so properly through appropriate control electronics. This kind of utilization of vehicles for power generation can help significantly, in the sense that it can reduce the need for auxiliary power units, thus saving the cost and weight of acquiring them and transporting them to the field.

Depending on the architecture used in the HEV, for example, if it has hub motors in each of the wheels, or even one motor per axle for propulsion, and uses a series HEV (SHEV) architecture, it will have the advantage of redundancy in case one of the motors fails. Then the vehicle can run in a gracefully degradable mode, with a somewhat reduced performance, and moved to a safe zone as needed.

So, it can be seen that there are quite a few advantages in introducing HEVs for military applications.

7.2 Ground Vehicle Applications

7.2.1 Architecture – Series, Parallel, Complex

As in the regular commercial HEV architectures discussed in other chapters of this book, military vehicles can have similar architectures as well. A very informative research paper by Ucarol *et al*. [1] has made a comparison between an IC engine, SHEVs, and parallel HEVs. There, based on simulated studies, from the point of view of weight, the IC engine vehicle is lightest and the parallel HEV is slightly heavier. However, the series hybrid vehicle was found to be quite a bit heavier. This analysis, although done for a commercial vehicle, is equally applicable to military vehicles.

If an IC engine vehicle is considered as the baseline, then one can compare other architectures as follows. To match the performance of the baseline vehicle, obviously it is necessary to make the electric motor in a SHEV the same size as the IC engine in the baseline vehicle. The authors of this book believe that it is really not necessary to do this, but rather that the motor should be sized so that over a given drive cycle the average energy going out of the generator would be equal to the average energy consumed by the propulsion motor. The peak power can always be handled by the battery, which should be charged within its bounds. A similar thought process also applies to the decision making while selecting the size of the generator. The decision should be based on studies of different drive cycles and then presenting the worst case scenario. The key to this decision making lies in the battery or other storage and whether they can provide the maximum power needed or not. Only if the battery is kept in a completely floating condition all the time, and the power from the IC engine and generator is fed to the motor in parallel with the battery, will the generator be required to be equal in size to the maximum power demand. But the intent of the battery or any peak power source is in fact to address this eventuality of sudden peaks or higher demands, and hence IC engine size in SHEVs and the generator size could definitely be reduced.

In a parallel HEV, the size of the electric motor could even be less than half the size of that in a SHEV. Ucarol *et al*. [1] assign the balance of power, that is, any deficit between the load demand and the electric propulsion power, to the IC engine in the parallel HEV. This mechanism to split the power assignment between the motor and the IC engine in the parallel HEV assumes that the original IC engine in the baseline vehicle was chosen based on the maximum power needed under the worst possible drive cycle scenario.

There is also no generator in the PHEV in the study cited above. However, in some other architectures, like the Toyota Prius and GM two-mode hybrid, there is a generator that is separate from the main propulsion motor (which can be used as a generator as well). The reason for having this generator is very dependent on the strategy for control. Under certain conditions of the battery's state of charge (SOC) and power demand for propulsion, it may be necessary to provide additional charging to the battery, which is where this generator comes into play.

A very important part of the SHEV or parallel HEV is the battery or any other storage device like the ultracapacitor. Ucarol *et al*. [1] use the battery capacity, that is, ampere-hours, as the metric for the battery. But in fact the ampere-hour itself is not sufficient for specifying a battery. In addition, it is necessary to know the ampere or power rating of the battery so that during maximum power demand by the propulsion motor, the battery, in conjunction with the generator, is able to provide it. These are vital decision-making processes in creating the design specifications for a HEV.

The discussion above applies to both gasoline and diesel-based vehicles. Military vehicles are mostly diesel engine based. Improvements in diesel engine technology will always help these vehicles. But hybridization will always be usable to achieve even better fuel economy and other benefits regardless of the diesel engine technology.

The next question to be addressed is the choice of architecture in military vehicles for the purpose of hybridization, that is, whether it should be series, parallel, or complex. The question can be best answered depending on what the priority is – is it fuel economy, size or weight, or reliability? If fuel economy is of utmost priority, then the choice should be a parallel HEV. If size and light weight are of concern due to the requirement to carry the vehicle within an aircraft, and so on, then a parallel HEV will be better than a SHEV. In general, the SHEV will be to some extent heavier than the PHEV, hence this fact also might affect fuel economy slightly. On the other hand, if performance of the vehicle is of utmost concern, that is, power output, it may be beneficial to use the SHEV architecture, which might help remove heavier transmissions and provide high power on demand very quickly due to the ability to control the motor much faster than an IC engine. Reliability considerations might be better addressed in general by using a parallel HEV, because of the redundancy in propulsion by IC engine and the motor. Reliability is not to be underestimated in a military vehicle. However, the parallel HEV is more complex in terms of control, and introduces complexity in its mechanical coupling. A thorough study of failure modes of these devices is needed before a decision can be conclusively made on this matter of reliability.

Another issue accompanying reliability in military vehicular systems is maintenance. It appears that maintenance of a SHEV is somewhat simpler for several reasons. Its control is simpler. Its mechanical linkage, unlike a parallel HEV, is also very simple. If there are hub motors in its propulsion, they can be quickly replaced in case of failure. The above discussion indicates the pros and cons of parallel and SHEVs. But overall reliability, and more specifically survivability needs, can probably be better served by a parallel HEV. Having said that, it should be noted that the decision could depend very much on the application and drive cycle. A logistic or support-type vehicle in the military (or non-combat types of vehicles) which travels longer distances, due to the drive cycle involved, probably will benefit more from a parallel HEV. On the other hand, for a combat vehicle where power demand and quick response to such demand are most important, a SHEV

will be more beneficial. Final decisions on such things are quite complex and systematic trade-off studies by tabulating all the requirements of performance, fuel economy, reliability, and so on, should be done to determine the most optimum decision.

7.2.2 *Vehicles Which Are of Most Benefit*

Military vehicles consist of different types, as shown in Figure 7.1.

In the various types of vehicles shown in the figure, the drive cycles and needs are quite different for these vehicles. Some vehicles run for long distances, some are combat

Figure 7.1 Some military vehicles: (a) HMMWV (High-Mobility Multi-purpose Wheeled Vehicle), (b) Stryker, (c) HEMTT (Heavy Expanded Mobility Tactical Truck), (d) Bradley, (e) Abrams, (f) Fennek (European), (g) MRAP (Mine-Resistant Ambush-Protected), (h) Big dog robot, (i) Gladiator, and (j) Swords. (Courtesy Wikimedia – US military public domain pictures.)

vehicles with extremely high power demand and performance needs, while others are unmanned robotic vehicles, where long-term mission and survivability can be more important than fuel economy. Some have weapons mounted, some do not. Based on these needs, the vehicular architectures could be significantly different.

In order to estimate the benefits from hybridization of military vehicles, some kind of metric should be established. A possible way to systematically do this analysis is suggested below based on the itemized information noted.

Required information and questions to be answered:

- Number of vehicles currently deployed, N
- Cost of the vehicle initially, C
- Average fuel economy of the vehicle, that is, miles per gallon, F
- Power rating of the vehicle, P
- Miles the vehicle travels in its life cycle, M
- Is it a combat vehicle or support vehicle, on a scale of 1 (minimal combat and primarily support) to 10 (highly combat)? K
- How is this vehicle transported to the field, on a scale of 1(by itself), through ship transported (5), to air transported (10)? T
- Ease of maintenance, on a scale of 1 (minimal) to 10 (extremely important), M
- How important is its survivability in terms of failure, on a scale of 1 (minimal) to 10 (extremely important)? S
- Long-term sustainability in terms of mission without any refueling or other intervention from outside, on a scale of 1 (a vehicle which can be easily refueled, that is, fuel is easily available to refuel it) to a vehicle which is deployed and not able to refuel externally, for example, an unmanned robot (10), Q
- Additional cost of hybridization, H
- Loss or gain of reliability if hybridized, compared to the base vehicle on a scale of 0 to 1 (high gain $= 1$; low gain or loss $= 0$), R.

Since the quantities above are in different units, some are dimensionless, and their range can also be numerically very different, it is beneficial to normalize them in some way to bring them within a comparable and manageable range. All these quantities should possibly be normalized except the number of vehicles, since this indicates the total benefit. In addition to normalization, it is instructive to include a weighting factor for each of the criteria above.

All these ideas are incorporated within Table 7.1 for ease of comprehension and with some placeholder numerical values for the purpose of illustration.

The above criteria provide a metric for a particular vehicle. This may not be a perfect metric but at least it allows a comparison of the vehicles against one another. For example, let us say that the benefit of hybridization of a single Abrams tank is much greater than hybridization of a single HMMWV. But there may be many HMMWVs (in terms of numbers deployed) in the field compared to Abrams tanks. Hence it may be more important to introduce hybridization in a HMMWV than in an Abrams, if there is an issue of choice. Similarly, other criteria proposed above are also important. The third column in the table, involving the weighting factor (i.e., how important this particular

Table 7.1 Trade-off mechanism in hybridization decision making

Criteria	Normalization factor	Weighting factor on a scale of 1 (less important) to 10 (most important)
N (number of vehicles)	1	1
C (initial cost per vehicle)	500 000	6
f (miles per gallon): use $1/f$	8	7
P (power rating)	300 kW	5
M (miles in life cycle)	m (to be defined based on the type of vehicle)	5
K (type of vehicle: combat, support, etc.)	5	5
T (transportability)	5	5
M (ease of maintenance)	5	7
S (importance of survivability)	5	8
Q (long-term survivability without refueling)	5	6
H (additional cost for hybridization): use $1/H$	20 000	2
R (gain in reliability due to hybridization)	0.5	8

Total $T = [\{E_{11}\}/\{E_{12}\} \times \{E_{13}\}] \times [\sum\{E_{i1}\}/\{E_{i2}\} \times \{E_{i3}\}_{i=2,3\ldots12}]$, where E_{ij} = element in ith row, jth column in the table above, with $i = 1, 2 \ldots 12$ and j = 1,2,3.

criterion is on a scale of 1–10), is rather critical. Normally all these items have to be initially settled after due discussions with various people who are experienced with the vehicles in terms of their applications and on matters related to the items in different rows of the table.

The concept of normalization and weighting factors introduced in this chapter has not appeared in the literature to the best of the authors' knowledge. Hence it may be an original process for hybridization in military vehicles. With more experience in the field it may be necessary to revise this metric evaluation process and the entries in Table 7.1. Though the concept is introduced for military vehicles, the metric may be equally important for applications in regular commercial civilian vehicles. It could be useful in making decisions about moving to a hybrid platform instead of a regular non-hybrid one.

7.3 Non-ground Vehicle Military Applications

Military vehicles include non-automotive applications as well. This can include air and water-borne vehicles, that is, ships, boats, and aircraft. In addition, some applications are not directly vehicular in nature. For example, a vehicle might use guns or other similar devices, some of which might be better operated electrically. An example could be an electromagnetic gun. Some of this equipment might need an IC engine, or fuel cell, and so on, which could charge a battery or ultracapacitor. The equipment (gun or otherwise)

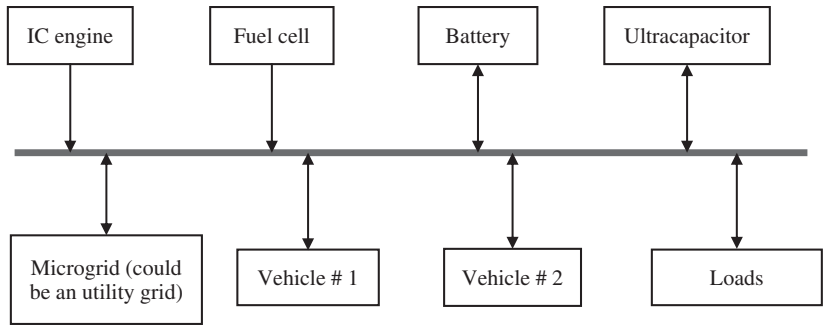

Figure 7.2 A generic hybrid power system architecture

itself could be directly activated by electric power which could later on be replenished by using an IC engine or fuel cell.

Hybridization, though not in the sense of a vehicle, can include matters like interfacing with a utility grid or a microgrid, where a number of vehicles could exchange power through some common bus. Here it is in principle possible to have an IC engine-based generator, some fuel cells, and vehicles all properly synchronized and then exchanging power. A system-level diagram of such a situation is shown in Figure 7.2.

Note that a HEV is merely a special case of the above hybrid power system at an internal vehicular level. Here the hybridization is extended to a higher system level. Vehicles 1 and 2 in the figure could be HEVs or EVs and could be exchanging power with the rest of the system. Similarly, if the vehicle was IC engine based, it could be running the engine and generating power while it is stationary, and it could provide power to another vehicle which has a deficiency in power.

Example applications of non-propulsion types of ground vehicles are as follows.

7.3.1 Electromagnetic Launchers

These can use the electromagnetic force to propel items at very high speed by accelerating them very quickly. In a regular gun the combustion of chemicals causes an explosion and creates the force of acceleration. Whereas the speed of combustion-based systems can be around 2 km/s for high-performance guns, electromagnetic guns could be accelerated to around 6–7 km/s. This is quite spectacular, being three times more than combustion-based systems, and is about the speed needed to put satellites etc. into low Earth orbits.

The principle of an electromagnetic launcher is shown in Figure 7.3 [2]. One of the enabling technologies related to such applications is the availability of very high current and instantaneous power for a very short time. A simple power system cannot provide this since very high pulse power is needed. After each shot of high pulse power, it is necessary to recharge the system through some hybrid power system as noted earlier. If smaller-scale launchers were to be deployed in a mobile vehicle-based system, it would be almost mandatory to use a hybrid power system within the vehicle. This is an example which may not be a hybrid propulsion system in a direct vehicular sense, but is definitely a hybrid power system.

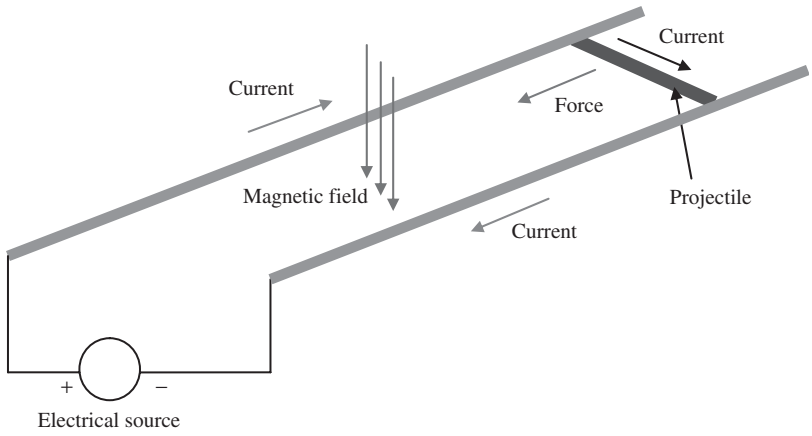

Figure 7.3 Basic principle of the electromagnetic launcher [2]

7.3.2 Hybrid-Powered Ships

In Chapter 6 we discussed electrically propelled ships extensively and will not repeat the information here. The advantages of such systems were clearly shown in that chapter. In one particular effort by the US Navy, diesel will be directly reformed into hydrogen through some chemical process. This hydrogen can then be used in a fuel cell to generate electric power, which can be used to drive an electric motor. It has been indicated [3] that since ships travel at relatively low speed, peak power may not be needed, implying that an additional peak power source like a battery may not be necessary. The advantage of such a system is that an IC engine is not needed and there will not be any pollution. Even if peak power is needed, it may be possible to use an ultracapacitor or some high-power battery to supplement the fuel cell, rather than have any IC engine at all within the ship. Since in a ship there is much more space than in a car, this possibility of having some peak power source should not be ruled out. Further, whereas the gas turbine-based ship engine has about 16–18% efficiency, the fuel cell has 37–52% efficiency, which is significantly higher, thus leading to much better fuel economy. Of course other benefits of a fuel cell-based system could be quiet operation and the ability to place a number of such fuel cell systems in various locations since the connection to the propulsion motor will be through cables. This is unlike an IC engine-based system, which is mechanically rigid in terms of location. This application, noted above, is a typical case of a hybrid power system in the sense that the diesel reformer system is an electrochemical system. This electrochemical system may need initial startup through some pilot electrical system of relatively small size. But once started, the fuel cell itself could maintain the diesel reformer system without the intervention of the startup system. The initial startup system could be a battery of relatively small size.

In a diesel reformer system, diesel, air, and water are used as the input. These components react and a gas mixture with around 30% hydrogen and other inert gases like carbon dioxide, steam, and nitrogen are obtained as the output. This mixture of gases is then fed to a catalytic burner to trigger the fuel cell system. The catalytic burner causes

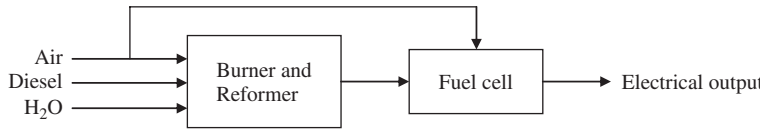

Figure 7.4 A diesel reformer for fuel cell

about 80% of the hydrogen to react with additional air, and produces heat and water as by-products. This is like a fuel cell with a conversion rate of about 80%. Next, another catalytic burner is used to make the remaining hydrogen react with additional air, and converts all the hydrogen to steam. In this particular system hydrogen is not stored as an intermediate process, and the hydrogen that is produced by the reforming process exists only for a very short time (about 15 seconds). This lack of hydrogen storage adds to the safety of the system, since hydrogen is a combustible gas. The system-level diagram for the reformation system is shown in Figure 7.4.

7.3.3 Aircraft Applications

It was indicated in Chapter 6 that, due to the high power and thrust needed, the application of electric power for aircraft propulsion is very much limited at this time, other than in very light aircraft like certain unmanned drones and very small airplanes. For commercial aircraft it is reasonable to assume that the technology (including energy storage) is not yet available for a viable application in this field. Since details on this topic are already given in Chapter 6, they are not included here.

7.3.4 Dismounted Soldier Applications

A dismounted soldier implies a soldier who is not physically within a vehicle and does not have any direct connection for getting power or energy from a vehicle or otherwise. This implies that for whatever equipment carried by the soldier, it is necessary to carry the power or energy sources on the person for those devices. Questions might arise as to why it is even necessary to discuss the power issues for a dismounted soldier in a book on HEVs. The reason is that the architecture of the HEV has some similarity to the architecture of the dismounted soldier, since both are hybrid power systems in the first place. The concept of managing the power here also is similar to that of a HEV. In fact, even though the power level of the soldier's equipment is much smaller than in a HEV, the issue of managing it is no different conceptually. In fact the issue of power management can be more important for a dismounted soldier who can be completely on his or her own under various situations, since the difference between good and poor power management could very well imply the difference between life and death. Hence, even though the dismounted soldier power system may not be a propulsion system, the power system could be hybrid and use similar power management concepts which can be discussed well within the scope of this book.

A general architecture of the power system for the dismounted soldier is shown in Figure 7.5.

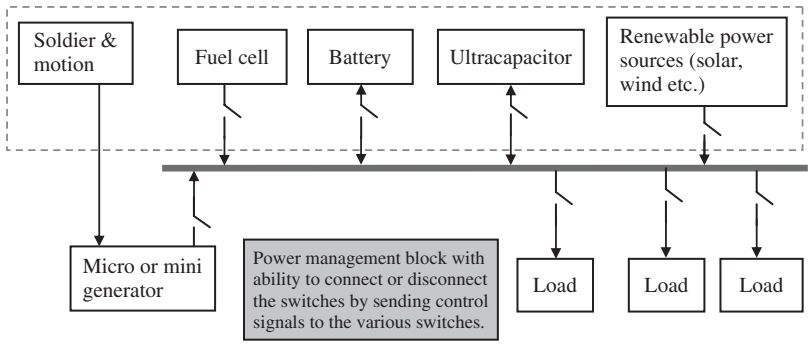

Figure 7.5 A generic hybrid power system for the dismounted soldier

According to the UK Ministry of Defence [4], the equipment and supplies carried by a soldier in the field could be on the order of 45 kg. The environment in which the soldier operates is not very helpful in terms of temperature, which could be around 45 °C, and it could be very cold, say −20 °C. The weight of power sources carried by a soldier could be on the order of 4 kg or more, which can last for 48 hours. In addition, soldiers could in the future carry cooling or heating jackets if needed. The load demand of the dismounted soldier [4] could be as small as 1 W for some small devices or somewhere around 100–200 W for certain electronic equipment.

A dismounted soldier normally uses batteries of various sizes, from AA size to much larger ones which could weigh a few kilograms. These batteries could be both rechargeable and disposable. The energy requirement could be on the order of 65–200 Wh/kg [5, 6].

It is obvious from the above that the dismounted soldier has needs which can be quite demanding, even though the power levels might not compare to the power levels of a vehicle. The expectation is that, in the future, power sources which can be six to eight times lighter than existing batteries could be possible. The specific energy needed in that case could be even 600–800 Wh/kg.

It seems, therefore, that regardless of the available technology, it may be imperative for the dismounted soldier to have power sources which should match the load demand in the best possible way. For example, some power sources may supply high-power but low-energy types of needs, whereas others could be the opposite. If only one type of source is used, then it will definitely lead to an oversizing of the power sources, leading to excessive weight. This is not acceptable for a dismounted soldier. Hence the architecture shown in Figure 7.5 could become important in considering the design of a power system for the dismounted soldier.

The architecture shown in Figure 7.5 implies that for the soldier it would be ideal if the whole system were placed in a single packaging, perhaps with various connecting jacks for different equipment, without requiring the soldier to connect individual sources. Such a single packaging could also include some controlled switches within the power system, as shown in Figure 7.5. Coordinating all these devices by proper switching is done by the power management block, which will monitor the voltage, SOC, and other information, and will accordingly manage the charging process. It will also give an indication to the soldier when the generator is to be cranked.

It may also be possible to use the walking, running, and other motion of the soldier to charge the batteries, without voluntary engagement of the soldier. This should be automatically done by using some mini or micro generators that can work on their own based on the vibrational motion, and so on. Such machines could be under the category of energy harvesting devices. The devices normally should work using inertial motion and periodic motion as in walking, even though the power amount may not be too high. A particular prototype was found to generate 7.3 W, which may still be reasonable [7] for certain loads. Normally, if such energy harvesting devices are carried by the soldier, there will not be any perceivable difference from the point of view of effort, even though the energy is ultimately coming from the soldier.

7.4 Ruggedness Issues

In military applications, in general, devices are ruggedized. In a mechanical sense, this means that physical coverings or boxes containing any components are extremely robust compared to their commercial counterparts. Thus the devices are not easily damaged in physical encounters of any kind. In addition, it is very important that the electrical and other design aspects of the devices are attended to. This can be due to the fact that military applications can mean very large temperature extremes, both hot and cold. In general, high temperature is bad for items like power electronics and batteries. The devices have to be derated accordingly for military use. This means that they can become physically larger and bulky, if performance is to be achieved under these extreme conditions. These considerations can in fact contribute to delays in HEV deployment in the field. It is expected that, in the future, with high-temperature and mechanically robust power electronics, the deployment of HEVs will be expedited by the military.

Basic ruggedness issues, therefore, pertain to mechanical vibration and temperature. Not only the power electronics, but also the regular electronic circuitry, are subject to these issues. In the power electronics area, it is expected that the use of silicon carbide semiconductor materials will significantly alleviate the temperature issues in terms of additional cooling needs. Even if a cooling system is enhanced for extreme temperature, that enhancement itself is also subject to adequate ruggedness questions.

For HEV applications using high-voltage and high-power battery packs, the cooling and heating issue is very important, otherwise HEV performance could be significantly compromised. Examples of ruggedized military batteries are shown in Figure 7.6 (www.mccdc.usmc.mil/OpsDiv/Integration/logistics_integration_files/Power%20Systems.ppt).

Another important issue in connection with HEVs is the connector design. A reliable connector used in cable design is shown on the Hypertronics web site (www.hypertronics.com/en/Products.aspx). This example of such a connector, called the Hypertronics' Hypertac® connector, involves a wire basket, socket contact system. When the pin is inserted into the sleeve or ring shown in Figure 7.6, the wires stretch around it, thus activating several contact paths. Thus, under harsh vibration and similar situations loss of contact can be eliminated or minimized. Pictures of a ruggedized military standard inverter and ruggedized interface connector are shown in Figure 7.7.

Several military standards are applicable in connection with ruggedization, which are applicable in design considerations of the power systems noted above. These include MIL-STD-461 (EMC), MIL-STD-901D, Grade A (shock), MIL-STD-167 (vibration),

(a)

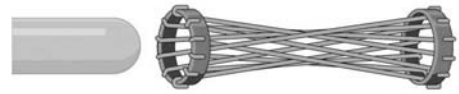

Wire sleeve before insertion of pin

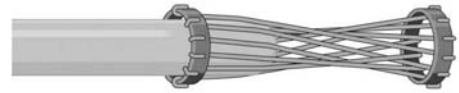

Pin partially inserted into sleeve

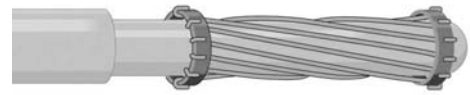

Pin completely inserted into sleeve

(b)

Figure 7.6 Examples of ruggedized battery (courtesy EaglePicher Technologies) and connectors (courtesy Hypertronics Technologies – Hypertac is a registered trademark)

Galaxy MIL-Inverter

Rugged System
Military Connector

Figure 7.7 Examples of a ruggedized inverter (courtesy RIPEnergy AG) and connectors (courtesy Adlink Technology)

MIL-STD-810E (vibration), MIL-STD-1275 (ground–mobile), MIL-STD1399 (interface standard for shipboard systems), and others.

References

1. Ucarol, H., Kaypmaz, A., Tuncay, R., and Tur, O. (n.d.) A performance comparison study among conventional, series hybrid and parallel hybrid vehicles, www.emo.org.tr/ekler/c792a8279211dec_ek.pdf (accessed February 3, 2011).
2. Fair, H. (2003) The Electromagnetic Launch Technology Revolution, Magnetics Magazine, http://www.magneticsmagazine.com/e-prints/UT.pdf (accessed February 3, 2011).
3. Walsh, E. (2004) Hybrids on the High Seas: Fuel Cells for Future Ships, http://www.news.navy.mil/search/display.asp?story_id=12221 (accessed February 3, 2011).

4. UK Ministry of Defence (2004) Reducing the Burden on the Dismounted Soldier Capability Vision Task 3 – The 'Energy-Efficient Soldier', http://www.innovateuk.org/_assets/pdf/competition-documents/briefs/energy_efficient_soldier.pdf (accessed February 3, 2011).
5. Raadschelders, J. and Jansen, T. (2001) Energy sources for the future dismounted soldier: the total integration of the energy consumption within the soldier system. *Journal of Power Sources*, **96** (7), 160–166.
6. Atwater, T., Cygan, P.J., and Leung, F. (2000) Man portable power needs of the 21st century – I. Applications for the dismounted soldier. II. Enhanced capabilities through the use of hybrid power sources. *Journal of Power Sources*, **91**, 27–36.
7. Priya, S. and Inman, D. (eds) (2008) *Energy Harvesting Technologies*, 1st edn, Springer.

Further Reading

Angel, J. (2009) Drone Takes Wing with Linux PCs Onboard, web article, http://www.linuxfordevices.com/c/a/News/Aurora-Excalibur-and-Parvus-DuraCOR-820 (accessed February 3, 2011).
COTS Journal (2009) Rugged Stand-Alone Box System Roundup, http://www.cotsjournalonline.com/articles/view/101098htm (accessed February 3, 2011).
Hypertronics, http://www.hypertronics.com/en/Products.aspx (accessed February 3, 2011).
Marine Corps Electrical Power (2004) https://www.mccdc.usmc.mil/OpsDiv/Integration/logistics_integration_files/Power%20Systems.ppt (accessed July 2004).
Nova Electric, http://www.novaelectric.com/dc_ac_inverters/index.php (accessed February 3, 2011).
The Green Optimistic, http://www.greenoptimistic.com/2008/04/30/HYBRID-ELECTRIC-AIRCRAFT-TO-TAKE-OFF-BY-2009 (accessed February 3, 2011).
http://commons.wikimedia.org/wiki/File:Humvee_of_Doom.jpg (accessed February 3, 2011).
http://commons.wikimedia.org/wiki/File:14_stryker.jpg (accessed February 3, 2011).
http://commons.wikimedia.org/wiki/File:HEMTT.jpg (accessed February 3, 2011).
http://commons.wikimedia.org/wiki/File:Two_M-3_Bradleys.jpg (accessed February 3, 2011).
http://commons.wikimedia.org/wiki/File:M1A1_Abrams_Tank_in_Camp_Fallujah.JPEG (accessed February 3, 2011).
http://commons.wikimedia.org/wiki/File:BundeswehrFennek.jpg (accessed February 3, 2011).
http://commons.wikimedia.org/wiki/File:FBI_Mine_Resistant_Ambush_vehicle.jpg (accessed February 3, 2011).
http://commons.wikimedia.org/wiki/File:Big_dog_military_robots.jpg (accessed February 3, 2011).
http://commons.wikimedia.org/wiki/File:Gladiator _RSTA.jpg (accessed February 3, 2011).
http://commons.wikimedia.org/wiki/File:SWORDS_robot.jpg (accessed February 3, 2011).

8

Diagnostics, Prognostics, Reliability, EMC, and Other Topics Related to HEVs

8.1 Diagnostics and Prognostics in HEVs and EVs

Any vehicle, whether conventional, hybrid, or pure electric, ought to have some sort of diagnostics (find the cause of a problem that has "already happened" to the vehicle) and prognostics (find problems which "will or can possibly happen" in the future), given the present condition of the vehicle based on monitoring of various information within the vehicle. With this in mind, all modern automobiles have onboard diagnostic functions which can give some amount of diagnostics, but not prognostics. Diagnostics can be at several levels. One is at the vehicle level within the vehicle itself, which can inform the driver or basic level service personnel about what might have happened. The second level can be at somewhat deeper maintenance level when the vehicle can be dismantled at different subsystem levels in a repair shop, the problem pinpointed, and the item concerned replaced. The third level can be at the automotive dealer or eventually the vehicle manufacturer level to find out why a subsystem failed. Finally, the diagnostics can be at the subcomponent level or component manufacturer level when more microscopic analysis of the component can be initiated to find design or other flaws, if any. Up to the second level, that is, maintenance level, the correctional step normally is replacement/repair of a part or subsystem, without necessarily trying to find the root cause of the failure. The third and final level can be analyzing the fundamental cause of a failure due to design or manufacturing flaws. Sometimes the fault may be not due to the design of a component or its material defect, rather it could be due to the wrong application or improper use of a device – which may not be due to the vehicle owner or driver, from the engineering design perspective. In that case, redesign of the system or subsystem will be needed on the part of the vehicle manufacturer.

Hybrid Electric Vehicles: Principles and Applications with Practical Perspectives, First Edition.
Chris Mi, M. Abul Masrur and David Wenzhong Gao.

8.1.1 Onboard Diagnostics

Since 1996 all vehicles have been required to have the second version of onboard diagnostics, that is, OBD II. Hybrid vehicles have OBD II as in a regular vehicle, and the role of OBD II in a HEV is the same as in a regular vehicle. As is well known, OBD II is a North American standard which deals with the engine control system, some parts of the chassis, body, and other devices, and the communication and control network diagnostics (control area network or CAN). There are a few variants of the OBD II protocols corresponding to certain standards. In general, for example, GM vehicles use SAE 1850 VPW (Variable Pulse Width Modulation), Ford vehicles use SAE 1850 PWM (Pulse Width Modulation), and Chrysler, all European, and Asian vehicles use ISO 9141 standards. The variations are reflected in the socket connector and the pin uses.

OBD II vehicles nowadays in general have a socket somewhere in the lower region in front of the driver. This may not be immediately visible while sitting, but one can normally see it by lowering the head to look above the pedal region around the plastic trim. This is where the technician or the owner can plug in the diagnostic tool or the scanner. The pins in the socket carry various signals from different sensors spread throughout the vehicle. There are various scanners available on the market. The ones made by the original equipment manufacturers (OEMs) can be quite costly, and after-market products are available at much lesser cost. These scanners normally have display units on them. There are also some rather inexpensive devices (data logger), which may not have a display unit like a full fledged scanner, but can collect the same information as a regular scanner, and the information can then be displayed on a personal computer or laptop using the software provided by the data logger manufacturer. A typical scanner with accessories is shown in Figure 8.1. The price of such a scanner can be close to $100.00, but scanners are available whose price can be from a few hundred dollars to even around $2000.00, depending on features and capabilities.

It is not the intent here to discuss the details of various OBD II signals displayed on a scanner. That information is available in any of the scanner manuals. Basically there

Figure 8.1 Picture of an OBD II scanner. [*Source*: picture taken in authors' lab]

can be 300 or so readings coming from different sensors. They could indicate things like ignition voltage, transmission shift points, or other matters. As an example, the code P0032 could show up on the scanner. One will then find that it corresponds to: Oxygen (A/F) Sensor Heater Control Circuit High. With a little more research, this code can then be related to perhaps a failed oxygen sensor, or a short in the sensor heating circuit, and so on. There may be some other specific reasons connected to this code, which one can find from various manuals. In general, to save time, one might not bother to go further but just replace the whole thing that could be involved with that code. This kind of code will be common to both a HEV and a regular vehicle. Similarly there are codes for other items related to the chassis or common to any vehicle, not just HEVs. Some codes are generic OBD II items which can be read by any scanning tool and related to a corresponding cause.

Certain codes may be proprietary (in terms of how they are arrived at) but manufacturers' manuals will reveal the cause and what needs to be repaired or replaced, even though they may not release the methodology of how they come up with the cause, which may be proprietary.

For HEVs, the specifics could be as follows when it comes to diagnostics. The manufacturer's service manuals should normally reveal the details. Here one has to gain knowledge of HEV technology to be able to correlate the diagnostic code against the symptoms. For example, in a Toyota HEV, the code P3005 will indicate that the "high-voltage fuse is blown," which can mean that the power cable or the fuse itself may need replacement. If after carrying out the replacement one still keeps getting the same code, then a deeper analysis might be called for. Similarly, P3006 will indicate that battery state of charge (SOC) levels are uneven in the battery modules. This may be cured by simply charging the battery for a while. But if the symptom persists, one has to take a serious look at the cause. Unless a repair store technician is knowledgeable enough, the code itself may not reveal the true cause. That is why a very good training program for technicians to cater to the needs of HEVs is needed, since repair-related experience in this field is still evolving [1].

In general, Toyota and other OEMs will present detailed diagnostics charts with step-by-step procedures on how to proceed on a specific diagnostic code. As noted earlier, this will be available even though the details of how these methodologies are developed may be proprietary. The methodology may relate to one or more inner circuit-level diagnostics – and the mechanism of code generation itself might be a research issue. As an example, if the motor is not getting a proper voltage supply due to a failure in the inverter system, it may be necessary to find that out from external sensor readings of the voltages and currents. Although the exact method of how it is done may be vehicle manufacturer specific, some idea can be obtained by following certain engineering principles. Some analyses may be simple electric circuit issues, while others may be quite complex.

In particular, the authors have done research [1, 2] on detecting if a specific inverter switch has become faulty or not, by monitoring the voltages and currents in the motor/inverter circuit. This kind of deeper diagnostics may be of importance because under certain circumstances it may be possible to reconfigure a partially failed system in real time by using software, and then run the vehicle in a gracefully degradable mode at a lower performance. This can significantly contribute toward reliability and safety. Of

course, it will be necessary sooner or later to replace or repair the faulty component or system, to get full functionality of the vehicle.

Similar comments like the above hold, for example, if a vibration is noticed in the vehicle. This could be due to many mechanical things, but it could also be related to a motor failure. Here OBD II codes and hybrid electric (HE) specific codes have to be analyzed together, not in isolation, to come up with a reasonable diagnostic analysis. It is at this stage that an artificial intelligence-based method can come in handy, which can significantly reduce the burden of human guesswork or the personal experience of a technician.

In a purely electric vehicle, which does not have an IC engine, OBD II codes related to emissions and the engine will be unnecessary. But a subset of the existing OBD II codes could still be used for matters related to the brakes, suspension, ABS, chassis, and so on. Everything related to the electric propulsion will be the same as discussed above in connection with HEVs.

8.1.2 Prognostics Issues

Prognosis is an issue involving the prediction of a problem before it happens, or it can also involve getting the health status of a system. In a HEV or EV, the prognostics can focus on basically the battery and power electronics, since these are weaker links in the system. The electric motor itself is important, but it is a more robust element than the battery and power electronics. In addition, prognostics can be important for the steering and braking system of the vehicle. These elements are safety-critical items or subsystems. On the contrary, there are less important items, for example, the air-conditioner, radio, and the like. Some of these are not HEV-specific items. Finally, a vital element in both HEVs and legacy IC-engined vehicles is the computational and networking elements. In fact, since a significant number of items in a HEV are controlled by computers/controllers and the CAN, a failure here can cause a lot of other elements to fail, leading to a system shutdown, if not a dangerous accident. It is no less important to know as well, if possible, the state of health of such computational elements and the communication network involved.

The health status of a system (also called “state of health” or SOH), be it battery, power electronics, or motor, needs to be compared against some benchmark or base system to get an idea of its health, even though it is functioning well. For that, one needs to have various informational data available when the system is healthy, or rather when either it was new or certain components were repaired or replaced. Such data can be logged from (i.e., stored in the database) a healthy system. The alternative to this is a model-based system, where a simulation output is obtained based on ideal or new system parameters, and compared against the current system, supposedly not so new. Hence a prognostics system can have the generic structure shown in the block diagram of Figure 8.2.

In Figure 8.2, three methods of state of health estimation are indicated. Assuming that we want to limit our focus only on the battery, power electronics, and motor system, which are HEV-specific items, the possible approach is as follows.

For the battery we need to monitor (experimentally in hardware) either voltage or current as input, and obtain current or voltage as output in response. In addition, temperature should be monitored as an input. In this immediate discussion, the terms input and output should be construed as input and output for the diagnostic process. They need not

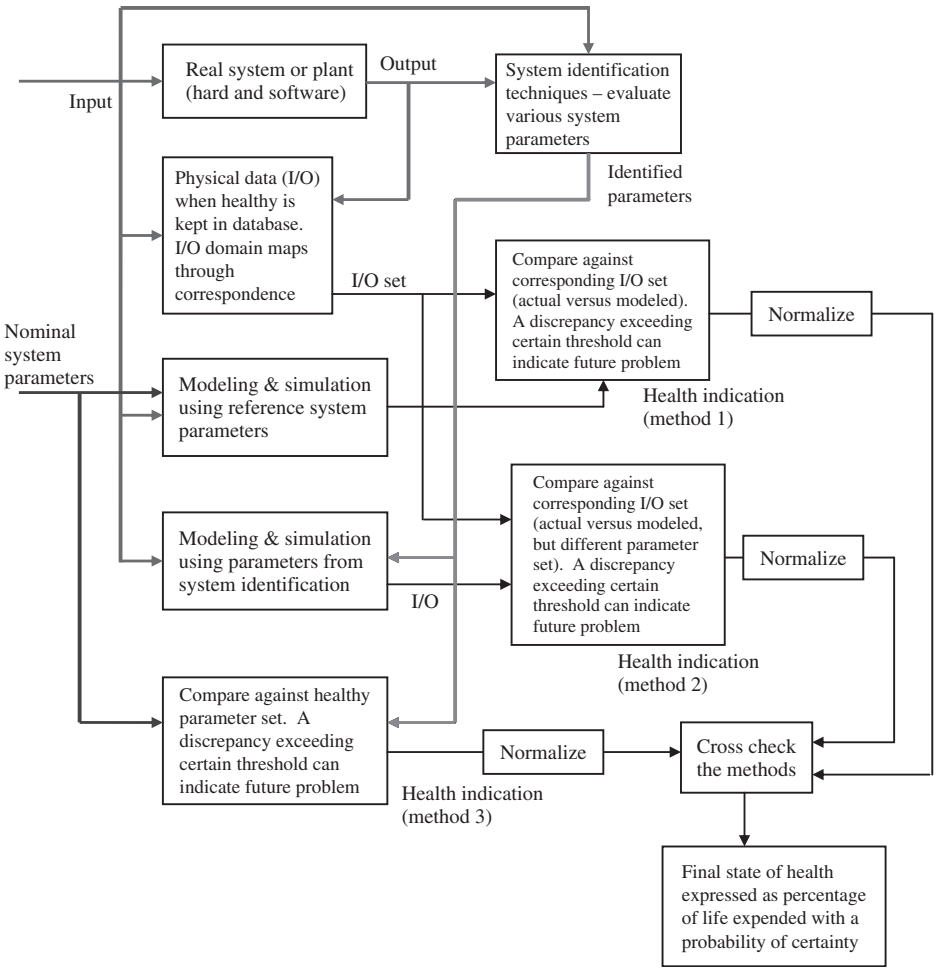

Figure 8.2 A generic methodology illustrating the state of health quantification

necessarily be actual system input or output in a normal electrical engineering sense, which drives the physical system.

For power electronics, we need to monitor the gate signals at each switch, voltage across each switch, and current through each switch. Also, we need to monitor the three-phase terminal voltages and currents coming out of the power electronics system. If placing a current sensor in each switch is too expensive, then it can be omitted, at the cost of losing some fidelity in the accuracy of the conclusion. In this system, diagnostic input can be considered to be the gate signal to each switch and also the voltage across each switch. The current through each switch or the current at the output terminals of the inverter can be considered to be the output of the system. Temperature too should be monitored as an input. In this power electronics example, the voltages across the switches are to be monitored both when the switches are open and when they are closed.

For the motor system, terminal voltage and current can be considered as the input. The output then can be the speed and shaft torque. If torque monitoring hardware is considered expensive or complicated, it is possible to monitor voltage, current, and speed, and infer torque from these measurements.

Once all the above information is in place, we can use the generic process in Figure 8.2 to evaluate the state of health of the system.

8.2 Reliability of HEVs

Recent events reported in the news media regarding faulty vehicles, including HEVs, related to brake failure or sudden acceleration, have led to significant concerns about the safety and reliability of HEVs. While some of these concerns are genuinely important, one should not get too carried away with what is written in the media or make judgments based merely on that. Instead, the authors believe that a more scientific approach of studying reliability should be attempted to see the pros and cons of various aspects accordingly, which will best serve the technical community and the users. In view of this, a reasonably detailed discussion of the subject will be presented here from a system-level perspective.

We all know that a HEV system is considered an important technology in the automotive industry these days. This is due to concerns about fuel economy, worldwide uncertainty of energy supplies, and pollution control. While discussing the subject, it seems that the focus in the technical community and the literature has been primarily on these issues, and also on control of the electric motor drives related to HEVs. In addition, people think in terms of cost premiums, that is, how long it takes to recover the extra cost of the vehicle (compared to a regular non-hybrid vehicle). Various figures have been indicated in the media and elsewhere in the technical community, suggesting that it can take anywhere from five to seven years to recover the extra cost of a HEV through any potential fuel savings. However, very little has been discussed on the issue of overall vehicular system reliability in HEVs. This issue is not trivial and the overall acceptability of these vehicles in the long run will significantly depend on that issue, in addition to fuel economy and extra cost recovery. In this section the intent will be to make the point that, in HEVs, one of the penalties for fuel economy that has to be paid comes in terms of reliability. It is emphasized here that a HEV is not merely a collection of multiple propulsion sources and control systems to extract better fuel economy, rather it has a plethora of items in it. Overall system-level reliable functionality is no less important in making a HEV operate successfully, and be acceptable to the consumer in the long run, than the concern for fuel economy and cost. Unfortunately, the literature on this topic is not available in the public domain to the best of the authors' knowledge. The three references [3–5] that are known deal with similar topics on the reliability of vehicular systems from a quantitative viewpoint, and are also by one of the authors of this book and other co-authors. The primary reason for this lack of published literature on this area of reliability, is, in the opinion of the authors of this book, that people have been predominantly involved until now with only the drive and control technology of hybrid vehicles, and matters related to fuel economy and emissions. A second reason is that hybrid vehicle technology is relatively new, and not much information about its reliability exists in the industry so far. Another important reason is that reliability data on components and subsystems takes a

long time to monitor and collect, and even if it is collected in the industry, the data is normally retained as proprietary information.

The following discussion, prior to the section on software reliability, is extracted and/or modified as needed from Masrur *et al.* [5] which was written by one of the authors of this book.

We will consider here the architecture of a regular IC engine-based vehicle, followed by series and parallel HEV architectures. The overall subsystem and component-level reliabilities are introduced by using some assumed numbers for reliability, and then analyzing them. In addition, the concept of graceful degradation is introduced and its implication from a quantitative point of view is discussed. The numerical values of reliability used in this section are merely to illustrate concepts; the exact reliability situation will depend on the system architecture and precise values of the reliability numbers involved in the system under study. Of course, it should be recognized that finding accurate reliability numbers for various components in a system requires prolonged efforts, sometimes modeling and simulation studies, and also experimental tests; these issues are not within the scope of this discussion.

8.2.1 Analyzing the Reliability of HEV Architectures

For a system-level perspective in studying the reliability of HEVs it is necessary to trace the individual reliability values of the subsystems and components noted in the architectures in Chapter 2 where a slightly different perspective was used. The architecture for parallel HEVs was also discussed briefly in Chapter 6. Some of these architectures are redrawn here.

For this discussion, the term reliability is defined by the probability that a component, subsystem, or a system is functional, that is, performing its intended function at the end of a particular time period, without any change or maintenance activities done within that time period. Thus, reliability is connected with both probability and a time span. In addition we define the term availability where we take a hypothetical system with reliability equal to 1. Such a system will be said to be "fully" available.

One can study the overall system reliability of each of these subsystems in Figure 8.3 by following the simple methodology below. Consider the various items (subsystems) in Figure 8.3, and let the reliability of each of those be as given in Table 8.1 (on page 185).

Note that each of the above items is constructed by using many constituent subsystems and components. However, one can use a single cumulative reliability number for each of the items above; for example, for the motor an overall reliability of 0.999 95 can be used, rather than delving into the individual constituent components within the motor [5].

The numbers in Table 8.1 are used only for the purpose of illustrating the concepts in this section. As noted earlier, component-level reliability numbers are generally kept as proprietary items by the manufacturers. Hence obtaining exact numbers can be extremely difficult, if not impossible. The other issue is that these numbers can vary from one manufacturer to another. Hence during architectural studies in the design phase, one need not be too concerned in trying to find exact numbers for various reliabilities.

Using the definition of reliability given earlier, it is now possible to study the system. The numerical values indicated against each item above mean that at the end of a given (or chosen) period of usage time or mileage of the vehicle (e.g., 100 000 miles (160 000 km)),

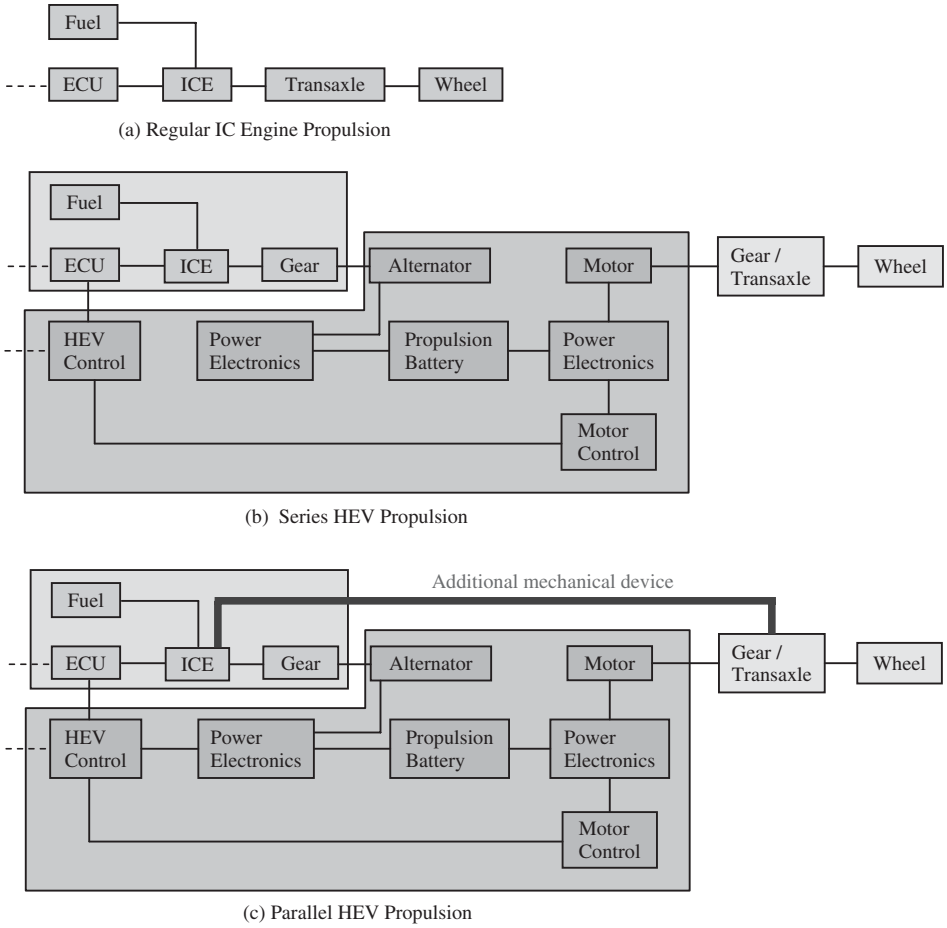

(a) Regular IC Engine Propulsion

(b) Series HEV Propulsion

(c) Parallel HEV Propulsion

Figure 8.3 System-level block diagrams for: (a) regular IC engine, (b) series HEV, and (c) parallel HEV architectures. (From [5], © [2008] IEEE.)

when the reliability is assigned a value of, say, 0.9999 for the IC engine (ICE), it means that the chance of its failure is 1 in 10 000 (within that mileage or usage time starting from when the item was newly installed). It is true that reliability is a function of time as the system ages. However, it will be assumed to be constant for the purpose of the discussion here.

It has been shown [5] that, based on the above concepts, the reliability numbers in this illustrative example in [5] are as follows:

1. For regular ICE propulsion,

$$R_{ICE} = 0.999\,64 \tag{8.1}$$

where R_{ICE} is the reliability (or the probability of being available) of the complete ICE vehicle system.

Table 8.1 Assumed reliability numbers for subsystems shown in Figure 8.3. (From [4], © [2003] IEEE.)

Subsystem/component	Reliability
Fuel system	0.999 9
ECU	0.999 99
ICE	0.999 9
Transaxle	0.999 95
Wheel system	0.999 9
Gear	0.999 95
Alternator	0.999 95
Motor	0.999 95
Power electronics	0.999 92
Propulsion battery	0.999 9
Motor control	0.999 99
HEV control	0.999 99

2. For series HEV propulsion,

$$R_{SH} = 0.999\,210\,280\,440\,917 \tag{8.2}$$

where R_{SH} (reliability of series hybrid architecture) is defined similarly as before.

3. For parallel propulsion,

$$R_{PH} = 0.999\,160\,319\,926\,895 \tag{8.3}$$

where R_{PH} (reliability of parallel hybrid architecture) is defined in an analogous manner to R_{SH}.

8.2.2 Reliability and Graceful Degradation

Consider the parallel HEV propulsion in Figure 8.3c, where demarcation between the ICE-based and the electric propulsion-based subsystems is shown using shaded areas. Using the terminologies EVP (for Electric Vehicle Portion) and ICE (to indicate the ICE portion of the propulsion system) we can write that the following probabilities for various combinations of the EVP and ICE will be [5]:

(a) Both ICE and EVP are good: $0.999\,74 \times 0.999\,62 = 0.999\,36$
(b) ICE good and EVP bad: $0.999\,74 \times (1 - 0.999\,62) = 0.000\,379\,84$
(c) ICE bad and EVP good: $(1 - 0.999\,74) \times 0.999\,62 = 0.000\,259\,87$
(d) Both ICE and EVP bad: $(1 - 0.999\,74) \times (1 - 0.999\,62) = 0.000\,000\,098\,776\,320\,7$
(e) Reliability of the wheel and final transaxle together $= 0.999\,85$.

Hence, the probability of having "some" amount of system functionality during partial failure conditions (i.e., under graceful degradation) is given by the sum of the items (a) through (c)

$$P_{GR} = (\text{a} + \text{b} + \text{c}) \times (\text{e}) = 0.999\,849\,906\,238\,495 \tag{8.4}$$

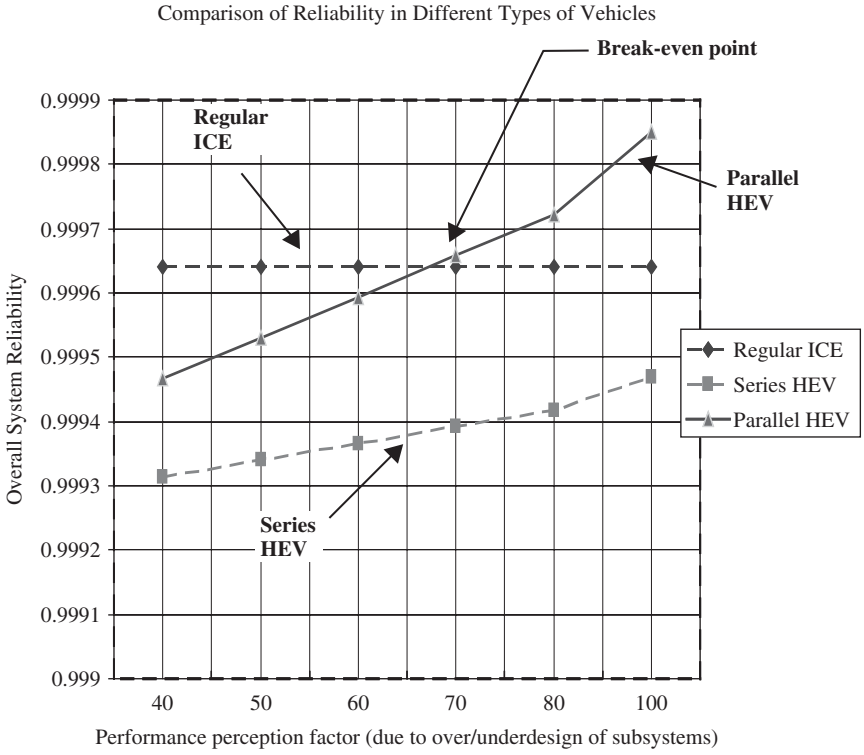

Figure 8.4 Comparison of system reliability vs. performance perception factor as a percentage for three different types of vehicles. (From [5], © [2008] IEEE.)

where P_{GR} is the reliability or probability of the system under graceful degradation, and (a), (b), (c), and (e) in Equation 8.4 are the reliability numbers corresponding to items (a), (b), (c), and (e) in the above list. Thus it can be seen that in a graceful degradation mode the system availability is higher than the situation when the partial availability or graceful degradation mode is not taken into account. However, it should be noted that under conditions (b) and (c), only partial functionality is obtained, not full functionality. Thus for items (b) and (c), one has to amend these items with some weighting factor to indicate that the functionality is degraded. This is explained in greater detail in [5].

Some additional issues pertaining to HEVs should also be considered. For example, if the EVP in a parallel HEV fails, one can still operate the vehicle with the ICE and refill the gas tank as needed, and keep running at a lower performance. If the ICE fails, one can run with the EVP, but only as long as the battery lasts. Thereafter a plug-in operation is required, if there is provision for that; otherwise, there is no option. Here one must not run the battery below the level of allowable SOC, to save battery life. A similar analysis has been done [5] for the series vehicle as well and the outcome can be summarized through the graph in Figure 8.4.

From this graph and from the earlier discussions it is apparent that the overall reliability numbers for a series HEV is quite a bit lower than the parallel HEV. Overall system

reliability of both the series and parallel HEV, without taking any graceful degradation into consideration, is of course lower than the regular ICE-based vehicle. This is due to the fact that the ICE has fewer components and hence initially it has an edge in terms of reliability. The basic idea here is that in a parallel HEV, in general, both the ICE and EVP will be designed at a somewhat lower rating. Hence during partial failure conditions of either the ICE or EVP, the performance of the vehicle is reduced. Thus one cannot get full performance functionality during partial failure. If one intends to have better performance during partial failure, it will be necessary to overdesign the ICE and EVP to some extent. The definition of "performance perception factor" [5] is essentially the ratio of the ICE or EVP rated power in a HEV to the rated power of an ICE of a non-hybrid vehicle. In other words, say, the non-hybrid vehicle has 200 hp (150 kW) nominal. In an equivalent parallel HEV let us assume that the ICE and EVP are each sized to a lower value of, say, 80 hp for the EVP and 120 hp for the ICE. In that case, if the ICE of the HEV fails, one will get only 80/200 of the nominal performance, that is, 40%. This will be called the perceived performance factor. If one needs to get a higher performance, the size of the EVP has to be scaled up. If it is sized higher, obviously the system performance will be even better under graceful degradation. Hence its overall "quality" increases even under degradation. The X axis (in Figure 8.4) basically says that if one overdesigns the EVP or ICE, then its reliability factor, due to better performance, will increase [5]. Thus, without overdesign, the non-hybrid ICE system is more reliable than a HEV, but with overdesign beyond a certain point the parallel HEV is more reliable, which includes the effect of performance along with reliability. But for a series HEV, due to the fact that it has only a single propulsion system, even with overdesign, its overall reliability cannot exceed that of a non-hybrid vehicle, since non-hybrid vehicle has fewer components compared to a series HEV. The interested reader is referred to [5] for further elaboration and details.

8.2.3 Software Reliability Issues

With the proliferation of software in our daily lives and its usage in small electronically controlled devices, to automobiles, aircraft, spacecraft, ships, and so on, the importance of its reliable functioning cannot be overemphasized. In many cases software malfunctioning can merely cause some inconvenience. In a large number of other applications like automotive braking, steering, engine control, aircraft stability control, and so on, or in certain medical and defense applications, malfunctioning software may result in serious accident, injury, and even loss of life. Some examples of catastrophic failures are presented in the article available at www.ece.cmu.edu/~koopman/des_s99/sw_reliability/. These include the tragedies with the Therac 25, a computer-controlled radiation therapy machine, caused by the software's inability to detect a race condition, and the case of the British destroyer HMS *Sheffield* which was sunk because the radar system identified an incoming missile as "friendly." This web site also indicates that sometimes small unnoticeable errors or drifts can cause failure, such as the chopping error that missed 95 ns in precision in every 10th of a second and, accumulated over 100 hours, made a Patriot missile fail to intercept a Scud missile, leading to the loss of 28 lives. Here is a case where errors, considered insignificant, but when accumulated, and apparently not corrected, caused failure. Recent events related to problems in the HEV and also

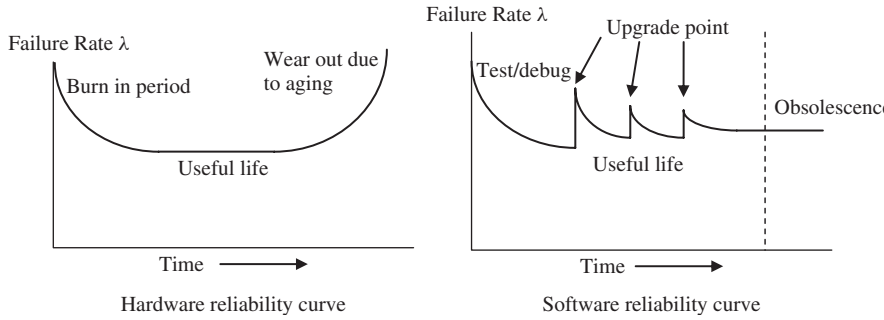

Figure 8.5 Hardware and software reliability curves

regular vehicles, though not yet completely researched, may have both hardware and software-related issues and are yet to be seen.

Software and hardware reliability curves have been compared in www.ece.cmu.edu/~koopman/des_s99/sw_reliability/ through the diagrams in Figure 8.5. It can be seen that hardware passes through an initial burn-in phase, followed by a fairly stable rate, and finally physical wearout occurs and the failure rate rises. At that time hardware replacement may be needed. Unlike hardware, software initially goes through significant failure correction in its testing/debug phase. Thereafter, each upgrade leads to a sort of mini-replication of the initial phase. Eventually the software matures and the reliability factor settles down, but the software also tends to become obsolete as well at that point.

Most people who use a computer operating system (OS) know that an older OS with upgrades works well. An example is Windows XP. But while it operates quite satisfactorily, one may think of new features, and hence obsolescence sets in. For Windows XP, this has led to Vista and Windows 7, and so on.

The bottom line is that there is still no definitive quantitative measure of software reliability and testing method which can assure software reliability under all conditions. Even though people have documented various models for reliability evaluation, in reality none are applicable to all situations.

Hence the question arises: how does all the above relate to the HEV? From the previous chapters it can be noted that the HEV is a complicated system, where various controllers are involved with algorithms making a significant number of decisions. The controllers involved for successful HEV functionality also involve other controllers in the system, which may be legacy items upgraded for a HEV interface. Such examples include the body controller, engine controller, transmission controller, power electronics/motor drive controller, battery management controller, power management controller, to name but a few, and their associated algorithms. All these involve significant amounts of software. Although testing can be done for some selected situations, there is really no guarantee that there does not exist a situation that can render the software ineffective. This means the situation creates a condition such that the output from the command leads to the following: (i) an output which is not supposed to be the desired response to an input as per design; (ii) an algorithm creates an unending loop with either the output remaining unchanged (which is not desirable), or the output flip-flops between a number of different output states. While neither (i) nor (ii) is desirable, as long as they do not lead to any

catastrophically dangerous command to the HEV, they can at least be accepted as a system flaw requiring redesign or repair. If, however, a command is automatically generated, for example, the acceleration is continuously increasing, or if the brake command is not activating the brakes when needed to stop the vehicle, then that can be catastrophic or even fatal.

Some of the reasons for software failure in HEVs are as follows:

1. Design flaw due to inability of the developer to account for all possible scenarios.
2. Improper specifications which can lead to indecision by the software due to lack of sufficient information to carry out the task, even though the software designer or developer is not at fault.
3. Lack of recognition of the need for a higher degree of precision in certain quantities, which can accumulate errors over time and operate with a wrong decision.
4. Lack of thorough testing of the software for all conceivable situations.

Several scenarios for catastrophic failure in the automotive area, and in particular in HEVs (e.g., sporadic noise), can cause a wrong input to the software in the engine or motor control. If the software does not have provision to correct the error, it can give the wrong signal to the engine or motor, leading to very undesirable behavior, perhaps in acceleration.

Another situation can be considered. Let us look at Figure 8.6 and assume that the driver pressed the brake and regenerative action was in place, but the mechanical brake is not activated based on the brake algorithm. Let us also assume that a wheel of the car, which was previously on a smooth surface, momentarily runs over a pothole. At that moment the tire loses contact with the wider road surface, the frictional torque ceases, and the edge of the pothole provides reaction forces F1 and F2, which will be more or less perpendicular to the tire surface. Even if there are any rotational forces (thus creating a torque) tangential to the tire, they will cancel for all practical purposes, due to the directions of forces F1 and F2 shown in the figure (assuming the forces are the same, which is reasonable for the purposes of this discussion). At that very moment the regenerative power from the brake will not be available, and if the mechanical brake does not activate, since it sees the other wheels still doing some regeneration, then the particular wheel of the car shown will accelerate forward even though the driver pressed the brake. If the algorithm did not fully evaluate the situation based on the various wheel conditions and coordinate them properly, it could destabilize the vehicle or fail to slow it

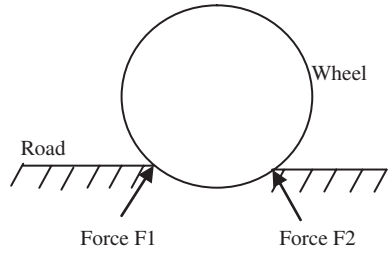

Figure 8.6 A wheel in a pothole

down properly. This is merely a hypothetical situation, since details of the manufacturer's algorithm are in general proprietary and it is difficult to know exactly what will happen in the above scenario. But recent issues like the above are coming to light, and although the problem could be due to sensor issues, or not having sufficient sensors, the software problem could still be one of the reasons.

Notwithstanding the fact that software problems can give rise to significant danger if the software malfunctions, the benefit of having software in general outweighs the drawbacks. Hence the only way one knows about the goodness of software is only after it has been deployed over many years of service. Mere testing in a lab environment can never guarantee this attribute.

8.3 EMC Issues

EMC, or Electromagnetic Compatibility, is an important issue these days in view of the fact that HEVs and EVs use significant amounts of power electronics which result in high-power, high-frequency switching. The EMC issue can be mitigated to a large extent by proper layout of the circuitry on various circuit boards and power distribution systems, in terms of both generation and propagation.

Electromagnetic interference (EMI) is generated by high-power circuits in the power converters and associated controllers. Several standards, for example, EMC Directive 89/336/EEC, the Automotive Directive 95/54/EC, and IEC 61800-3, *EMC Requirements and Test Methods for Adjustable Speed Electrical Power Drive Systems*, are considered to be important. In addition, the CEI EN 55055 standard on radio disturbance characteristics for the protection of receivers onboard has also been considered [6]. The standard SAE J551 on surface vehicle EMC is considered more stringent compared to other applications, unlike automotive ones.

In an electric vehicle the inverter is located near the propulsion motor and housed in a metallic box which shields noise emission [7]. However, the battery module is normally located at a distance and unshielded power cables may be used to connect it to the power electronics. Hence the unshielded cables can lead to a significant amount of noise propagation. The studies by Chen and Xu [7] in an EV indicated that most noise energy is at frequencies below a few megahertz and causes transients which can affect digital systems more than creating radiated noise to the environment. But the radiated noise energy level itself is also high, and not necessarily below limits.

In a very interesting presentation [8], the impact of EMI on HEVs and how it affects various items was studied. Although important for military applications, the information is equally valid for regular vehicles. However, the importance of EMI on communication systems is more vital for military, as opposed to commercial, vehicles. The standards relevant to the military in this context are MIL-STD-461E – *EMI Requirements, Design, and Test*, and MIL-STD-464 – *Vehicle EMC and Lightning Requirements*. The latter is more applicable to commercial aircraft. Other standards, beside those mentioned in the previous paragraph, are RTCA-DO-160 – *EMI and LIT Requirements Including Test Methods*, and AC-20-136 – *FAA LIT Advisory Circular*. In addition, the FCC Rules and Regulations, Title 47, Part 15, Subpart B, are of importance. Several European standards were also indicated earlier.

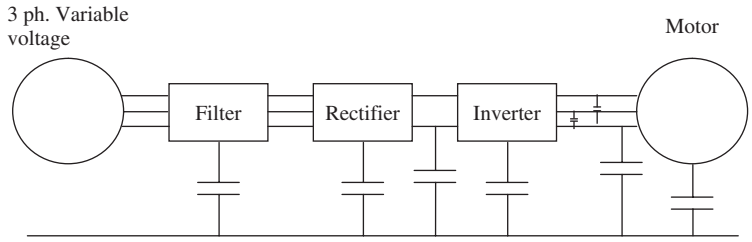

Figure 8.7 Power electronics architecture in EV motor drive

Figure 8.7 shows the block diagram of an electric motor drive. A number of small capacitances, which can be ignored at low frequency, become important, especially when the switching frequency is high [9]. Here, the capacitors are shown between the individual housing elements to the ground or chassis/body of the vehicle. Various currents, in common and differential modes, could flow through these stray capacitances. They can also create problems in the shaft and bearings as follows.

Consider Figure 8.8, showing the bearing and shaft of a motor drive. The stray capacitance shown can give rise to a voltage across the grease layer shown shaded. This can potentially exceed the breakdown voltage of the grease, causing sparks in the bearing's steel material, thus leading to bearing damage and eventual failure. Of course, the other capacitances can also lead to additional stray currents and consequent radiation of noise.

Some of the mechanisms needed to reduce EMI effects include: (i) using very good conducting materials for the housing of power electronics and other equipment; (ii) various joints in the housing should be tight and there should be no abrupt discontinuity in the housing structure, for example, an undesirable tiny gap or hole in the structure which can lead to high emission; (iii) various cables should be shielded properly as far as practicable, and correct terminations should be used; (iv) both magnetic and electric shielding should be used; (v) both common and differential mode filters should be used as applicable; (vi) screw spacing should be made correctly and a conducting gasket should be used as needed. Among other techniques, use of laminated busbars, high-frequency DC link capacitors, good snubbers, and separation of digital and high-power electronic circuits have been suggested for the power electronics circuit. For the electrical wiring, benefits can be obtained by over-braiding high-power bundles. In addition, data buses should be

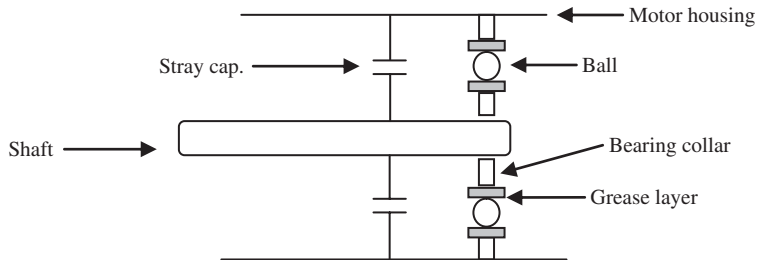

Figure 8.8 Completion of circuit through shaft, stray capacitance, and bearings

shielded properly. In EV high-power wiring, even if it is not shielded, at least the data buses should be shielded to protect malfunctioning of these digital circuits due to EMI.

8.4 Noise Vibration Harshness (NVH), Electromechanical, and Other Issues

As noted earlier in this chapter, in connection with HEVs, normally people are more concerned with matters related to fuel economy and control mechanisms and algorithms, the battery, power electronics, and so on. But the fact that the HEV is subjected to frequent stopping and starting of the engine to conserve fuel, or even too much stopping or starting of the electric motor, deserves some consideration in terms of vibrations or stressing of the engine, motor, or mechanical members associated with the system.

Consider Figure 8.9 showing the configuration of a typical power split-based HEV. In this particular system, a power split device, that is, the planetary gear system, is used to connect the various items shown. This is typical for the Toyota HEV. In this system, since there are no clutches, the traction torque from the ICE and the electric motor is directly transmitted to the wheels. Hence, if there is any engine start/stop action, any accompanying vibration is transmitted to the wheels through the various members in between, including the shafts and the connecting gears. Vibration from the engine can occur both before and after ignition [10]. When there is no ignition, there is compression and pumping pressure in the cylinders. After ignition, there will be a sudden torque change in the engine due to combustion. Note that these are initial changes due to a discontinuous process, that is, starting or stopping of the engine, which is separate from the regular pulsating torque in the engine under normal conditions. Ito *et al*. [10] have studied the vibration problem in an HEV engine in reasonable detail. The vibration was reduced by using two controllers, the first one controlling the ripple due to compression and pumping pressures in the engine cylinders, and the second controlling torsional vibration caused by rapid changes in the torque. The result was promising in terms of reducing the floor acceleration.

Ito *et al*. [10] present their experimental results according to the vibration control method used. A simplified qualitative comparison diagram is given in Figure 8.10 to indicate the difference. It is interesting to note that by using a new control methodology, the

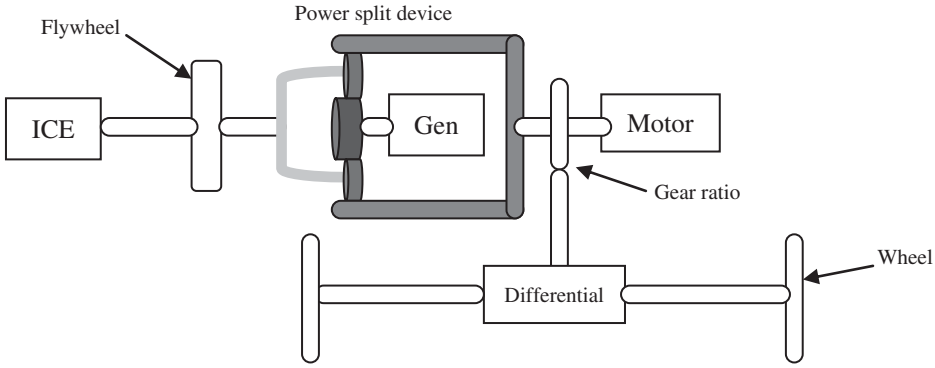

Figure 8.9 Configuration of a typical power split-based HEV

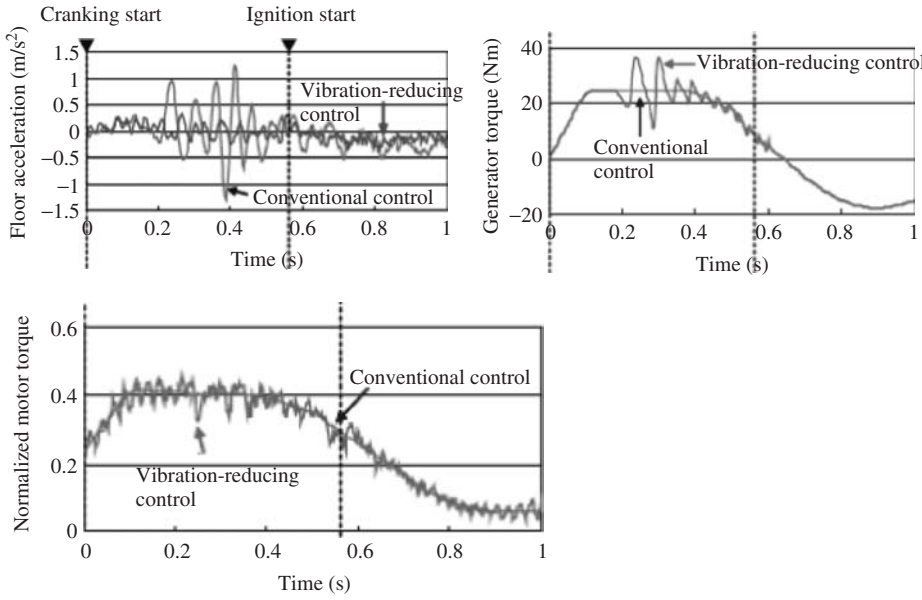

Figure 8.10 Qualitative comparison of reduction of vibration due to control action. Lines representing conventional control and lines showing the vibration reduction control proposed in [10] are indicated by arrows. (Reprinted from *R&D Review of Toyota CRDL*, Vol. 40. No. 2, p.42.)

vibration in floor acceleration has been substantially reduced. However, it should also be noted that concurrently the torque generated at the motor and the generator has increased. This increase is essentially what nullifies the floor vibration. The above phenomenon, though, leads to a reduction of mechanical torque, and indeed needs high-frequency control action through the motor and generator system. This may have some ramifications in terms of faster switching of the power electronics switches and higher frequency currents and magnetic field in the motor, and may actually lead to higher losses in those components. In other words, there is some penalty to pay in one place whenever some benefit is achieved in another. In this particular case the reduction in mechanical vibration is essentially transferred into electrical form. These issues, related to high-frequency control and its ramifications, have not, to the best of the authors' knowledge, been studied.

In the patent [11] the issue of numerous starts and stops was addressed. It was indicated that vehicle designs are normally optimized for minimizing noise vibration harshness (NVH) for both idle speed and above, and particular for high-frequency conditions. But low-speed and low-frequency vibrations are normally difficult to manage. This patent [11] specifically indicates that at 0–800 rpm, the NVH issue and resonance are very problematic. Apparently this situation is caused by compression pulses in the engine and fluctuations in flywheel speed. In addition, the problem is important for gasoline engines, but more so for diesel engines. The former have a compression pressure around 120 psi (827 kPa), and the latter about 400 psi (2758 kPa). It appears that with frequent start/stops every couple of minutes and shutdown of the engine for only a couple of seconds or a little more can be quite important in terms of NVH. The method suggested to improve the

NVH issue includes opening the exhaust port (valve) during the shutdown sequence of the engine. The idea is to reduce the compression pressure in the cylinder, thus reducing the vibration. It was also indicated that the above process influences the change of rotational inertia in the engine which is prevented from transmission to the chassis.

The above issue of NVH is specific to the HEV which has multiple sources of power and involves some shutdown sequence. In a purely electric vehicle the issue is less likely to be of consequence due to the absence of the ICE and also that electric motor torque is much smoother compared to ICE torque.

8.5 End-of-Life Issues

In HEVs and EVs, the end-of-life issue is associated with the life of the various components and overall life cycle management. As far as the mechanical system is concerned, that is, the engine and transmission (power split based or other type of mechanical coupling), this is the same as in a regular ICE vehicle. So, the end of life can be considered to be around 100 000 miles (160 000 km) nominal in terms of company warranty, and, depending on the quality, the life can easily be around 150–200 000 miles. However, important items to consider for HEVs pertain to the battery, power electronics, and motor. The weakest link here is the battery, next is the power electronics, and then the motor. In a HEV, the battery is warranted for around 10 years, which is compatible with the warranted life of the vehicle. The cost of a battery can be around $3000. An Oak Ridge National Laboratory (ORNL) report [12] says that the present cost of power electronics is about $200/kW. Attempts are underway to bring it down in the future to $7/kW. So, for a vehicle with a 60 kW power electronics device, the cost was around $12 000 at the time of the report [12], and hybrid-specific item warranty is around 150 000 miles or 10 years. According to the ORNL study, the cost of a 75 kW motor is a little over $800 to around $1500 depending on the size. The motor is considered the most robust entity within the hybrid-specific components. Although precise information is not available, the authors believe that the life expectancy of the motor itself is probably more than 10 or 12 years, that is, somewhere between 150 000 and 200 000 miles. The life of all the items which are hybrid specific, that is, the battery, motor, and power electronics, is significantly affected by ambient temperature and operational mode. This means that the variation between the continuous drive cycle demands and its peak affects the overall life cycle. This applies to the battery, power electronics, and motor. If there are very high peaks and valleys, with associated harmonics in the voltage and current, it will affect the life expectancy in the long run.

In connection with life cycle issues, it should be noted that some of the materials within a battery and motor could be recycled. For example, the battery casing could be directly reused, and some of the materials inside might be reprocessed. The same applies to the motor. The motor could most likely be reconditioned in terms of winding, and if it is a permanent magnet motor, the magnets could be replaced if they have lost some of their properties. With the power electronics, the silicon components themselves could be replaced, that is, the power electronics switch modules. Control electronics most likely could be retained. The replacement and reconditioning of the components will need some infrastructure, so that the operations of replacement and reconditioning could be done

with least inconvenience to the users. All these processes are rather new and can only evolve with time.

References

1. Murphey, Y.L., Masrur, A., Chen, Z.H., and Zhang, B.F. (2006) Model-based fault diagnosis in electric drives using machine learning. *IEEE/ASME Transactions on Mechatronics*, **11** (3), 290–303.
2. Masrur, M.A., Chen, Z., and Murphey, Y. (2010) Intelligent diagnosis of open and short circuit faults in electric drive inverters for real-time applications. *IET Journal of Power Electronics*, **3** (2), 279–291.
3. Masrur, M.A., Shen, Z.J., and Richardson, P. (2004) Issues on load availability and reliability in vehicular multiplexed and non-multiplexed wiring harness systems. *Society of Automotive Engineers (SAE) Transactions, Journal of Commercial Vehicles*, 2003-01-1096, 31–39.
4. Masrur, A.M., Garg, V.K., Shen, J., and Richardson, P. (2003) Comparison of system availability in an electric vehicle with multiplexed and non-multiplexed wiring harness. IEEE Vehicular Technical Society Conference Proceedings, October, Orlando, FL, pp. 3277–3283.
5. Masrur, A.M. (2008) Penalty for fuel economy – system level perspectives on the reliability of hybrid electric vehicles during normal and graceful degradation operation. *IEEE Systems Journal*, **2** (4), 476–483.
6. Serrao, V., Lidozzi, A., Solero, L., and Di Napoli, A. (2007) EMI characterization and communication aspects for power electronics in hybrid vehicles. European Conference on Power Electronics and Applications, September, Aalborg, Denmark, pp. 1–10.
7. Chen, C. and Xu, X. (1998) Modeling the conducted EMI emission of an electric vehicle (EV) traction drive. IEEE International Symposium on Electromagnetic Compatibility, August, Vol. 2, pp. 796–801.
8. Cortese, S. (2004) EMI in a Hybrid Electric World, www.dtic.mil/ndia/2004tactical/Cortese.ppt (accessed February 3, 2011).
9. Zare, F. (2009) EMI in Modern AC Motor Drive Systems, https://ewh.ieee.org/soc/emcs/acstrial/newsletters/summer09/EMIinModernAC.pdf (accessed February 3, 2011).
10. Ito, Y., Tomura, S., and Moriya, K. Vibration-reducing motor control for hybrid vehicles. Research Report. *R&D Review of Toyota, CRDL*, **40** (2).
11. Stone, K. (2009) Hybrid vehicle vibration reduction system and method. International Patent WO/2009/134695, May 11 2009, pp. 516–521.
12. ORNL Review (2000) Power Electronics: Energy Manager for Hybrid Electric Vehicles, http://www.ornl.gov/info/ornlreview/v33_3_00/power.htm (accessed February 3, 2011).

Further Reading

Toyota Prius Diagnostics, http://www.aa1car.com/library/toyota_prius_diagnostics.htm (accessed February 3, 2011).

9

Power Electronics in HEVs

9.1 Introduction

Power electronics is one of the enabling technologies propelling the shift from conventional gasoline/diesel engine-powered vehicles to electric, hybrid, and fuel cell vehicles. This chapter discusses power electronics used in HEVs and PHEVs. However, the focus of the chapter is on the unique aspects of power electronics in HEVs and PHEVs.

To explain the types of power electronics circuits used in a HEV, we use the configuration of a typical series HEV powertrain as shown in Figure 9.1. In this configuration, the internal combustion engine (ICE) drives a three-phase permanent magnet synchronous generator, whose output is a three-phase voltage with variable frequency and variable voltage. This output needs to be rectified to a direct current (DC) voltage.

The front wheels are driven by an induction motor which needs to be controlled by a voltage source inverter (VSI) or a current source inverter (CSI). An energy storage system is connected to the DC bus, between the generator/rectifier output and the inverter. However, there is a bidirectional DC–DC converter that manages the charge/discharge of the battery, as well as controlling the DC bus voltage.

In conventional vehicles, the air-conditioning (A/C) compressor is driven by the engine through a belt. In advanced HEVs, the engine is turned off very often during stop-and-go driving patterns. In order to have A/C while the engine is off, the A/C compressor needs to be driven by an electric motor which runs from the hybrid battery. There may be an electrically driven hydraulic pressure pump for the vehicle's hydraulic systems, such as frictional brakes, power steering, and so on. The A/C motor and the compressor motor are typically brushless DC motors with an inverter.

In addition, auxiliary components, such as headlights, wipers, entertainment systems, heat seats, and so on, run from the 14 V auxiliary battery. Most advanced hybrid vehicles no longer have an alternator, which means the 14 V battery needs to be charged from the high-voltage (HV) battery. On the other hand, even if an alternator is present, when the engine is off, the 14 V battery can still be drained quickly without proper charge maintenance. Therefore, it is necessary to have a DC–DC converter to charge the 14 V battery from the hybrid battery. For PHEV, there is also a battery charger installed on the vehicle or in the charging station.

Hybrid Electric Vehicles: Principles and Applications with Practical Perspectives, First Edition.
Chris Mi, M. Abul Masrur and David Wenzhong Gao.

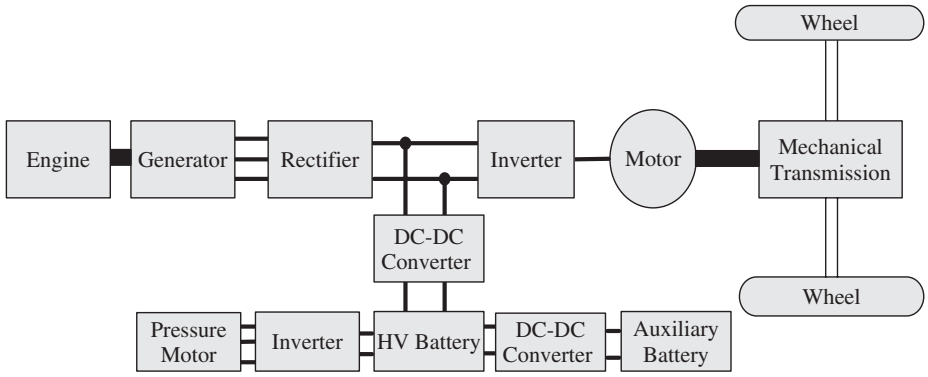

Figure 9.1 Power electronics converters used in a series HEV

Even though there are commonalities between the power converters used in HEVs and the ones used in other industrial, commercial, or residential applications, there are some unique features specific to automotive applications. Examples include wider ambient operating temperature (−20 to 50 °C), vibration and shock, electromagnetic compatibility, and thermal management.

Figure 9.2 shows the integrated main power electronics unit used to control the Toyota Highlander HEV (http://www.toyota.com). The power electronics unit consists of a bidirectional DC–DC converter that links the hybrid battery and the DC bus, and three motor drive circuits that control the front and rear motor/generators.

The issues to be addressed in the design of HEV power electronics circuits cover [1–23]:

- **Electrical design:** Includes main switching circuit design; controller circuitry design; switching frequency optimization; and loss calculations.
- **Control algorithm design:** Includes developing the control algorithm to achieve the desired voltage, current, and frequency at the output, and to realize bidirectional power flow as needed.
- **Magnetic design:** Includes the design of inductors, transformers, and other components such as capacitors needed for filtering, switching, and the gate driver units.
- **EMC design:** Includes understanding the electromagnetic interference (EMI) issues, analyzing switching transients, and circuit layout that minimizes parasitic inductance and capacitances.
- **Mechanical and thermal design:** Includes modeling of the loss of power devices and magnetic components; cooling system, heat sink, and enclosure design; and integration of the power electronics unit.

9.2 Principle of Power Electronics

In broad terms, power electronics is a discipline that studies power converters which process and control power flow using electronic means. It mainly involves the use and control

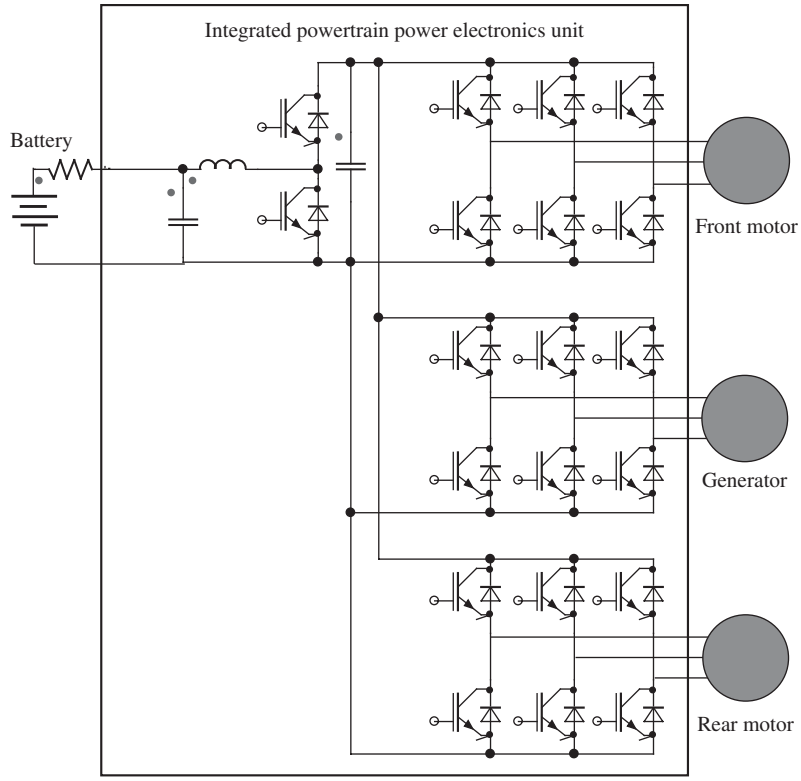

Figure 9.2 The integrated powertrain power electronics unit used to control the Toyota Highlander hybrid vehicle. (Courtesy, CC Chan, The State of the Art of Electric, Hybrid, and Fuel Cell Vehicles, the IEEE Special Issue on Electric, Hybrid and Fuel Cell Vehicles, Vol. 95, No. 4, pp. 704–718, 2007 © [2007] IEEE. Reprinted, with permission, from the Proceedings of the IEEE.)

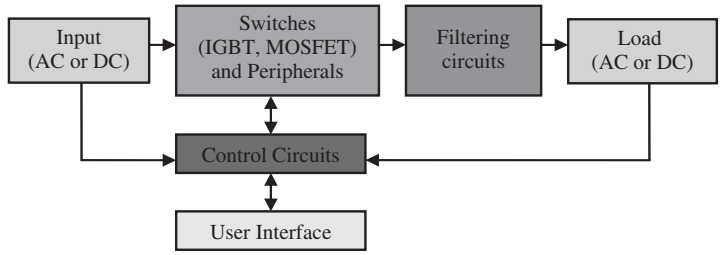

Figure 9.3 Schematics of a power converter

of power semiconductor switches, such as power diodes, insulated gate bipolar transistors (IGBTs), and metal oxide field effect transistors (MOSFETs). Figure 9.3 illustrates the schematics of a power converter.

As can be seen from Figure 9.3, a typical power converter will consist of four segments: switching and peripheral circuits, filtering circuits, control circuits and feedback, and an optional user interface:

- **Types of power converters:** Power converters are usually classified by their input and output. Since the input and output of a power converter can be either alternate current (AC) or direct current (DC), there can be four types of power converters:
  - DC–DC converter
  - DC–AC inverter
  - AC–DC rectifier
  - AC–AC cycloconverter.

  The first three types of power converters are all used in HEVs. The fourth type, AC–AC cycloconverters, is only used in high-power AC–AC systems to control the voltage magnitude and frequency of large motors. However, AC–AC conversion involving an AC–DC circuit and a DC–AC circuit is not unusual. Depending on the powertrain configuration and level of hybridization, a HEV can involve one or more power converters of different types.
- **Main circuit (switches, peripherals):** The main circuit consists of power semiconductor devices (switches and diodes) and peripheral circuits. The semiconductor switches are controlled to turn on and turn off at a frequency ranging from a few kilohertz to a few tens of kilohertz for HEV applications. Depending on the voltage level of the systems, both MOSFETs and IGBTs are used in HEV power converters.
- **Filtering circuit:** Power electronics converters usually involve LC low-pass filters that will filter out the high-frequency components of the output voltage and let the low-frequency components or DC component pass to the load side.
- **Control and feedback circuit:** Control and feedback typically involve the use of microcontrollers and sensors. HEV powertrain applications usually involve feedback torque control. Current feedback is usually necessary.

As a well-developed discipline, power electronics has been very well covered in many textbooks. This chapter will only focus on the unique aspects of power electronics pertaining to HEV applications.

9.3 Rectifiers Used in HEVs

Rectifiers are used to convert an AC input to a DC output. Even though controlled rectifiers exist, they are rarely used in automotive applications. Therefore, we will only discuss uncontrolled passive rectifiers and their unique aspects in HEV applications.

9.3.1 Ideal Rectifier

Figure 9.4 shows a single-phase rectifier and a three-phase ideal rectifier operating from ideal voltage sources. With ideal diode characteristics, the output of a single-phase rectifier can be expressed as

$$V_o = \frac{1}{T/2}\int_0^{T/2} \sqrt{2}V_i \sin(\omega t)dt = 0.9V_i \tag{9.1}$$

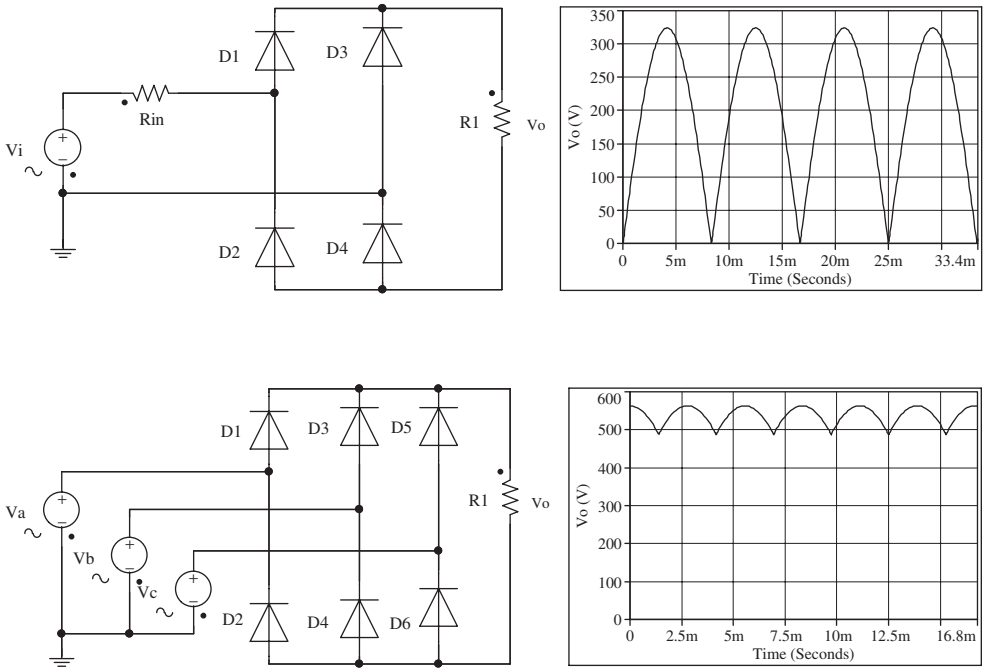

Figure 9.4 Ideal rectifiers: top, single-phase rectifier circuit and output voltage waveforms; bottom, three-phase rectifier circuit and output voltage waveforms

where V_o is the output voltage, V_i is the rms value of the input voltage, T is the period of the input voltage, and ω is the angular frequency of the input.

The output of an ideal three-phase rectifier is

$$V_o = \frac{1}{\pi/3}\int_{-\pi/6}^{\pi/6}(V_a - V_b)dt = \frac{1}{\pi/3}\int_{-\pi/6}^{\pi/6}\sqrt{2}V_{LL}\cos(\omega t)dt = 1.35V_{LL} \tag{9.2}$$

where V_{LL} is the rms value of line-to-line voltage.

9.3.2 *Practical Rectifier*

In HEV applications, the input to a rectifier is usually the output of a synchronous generator (such as in a series HEV or complex HEV), or an alternator (in a belt–alternator–starter HEV). The circuit and output voltage waveforms of a practical HEV rectifier are shown in Figure 9.5. The generator impedance is in series with the voltage source, and the voltage drop of the diodes is also included. It can be seen that there is a significant amount of voltage drop in a practical rectifier when compared to an ideal rectifier. The voltage drop is caused by the impedance of the generator, which is generally not negligible, different from that of rectifiers connected to an infinite AC grid. Besides, there will be commutation loss due to the inductance of the generator. Therefore, the output voltage can be

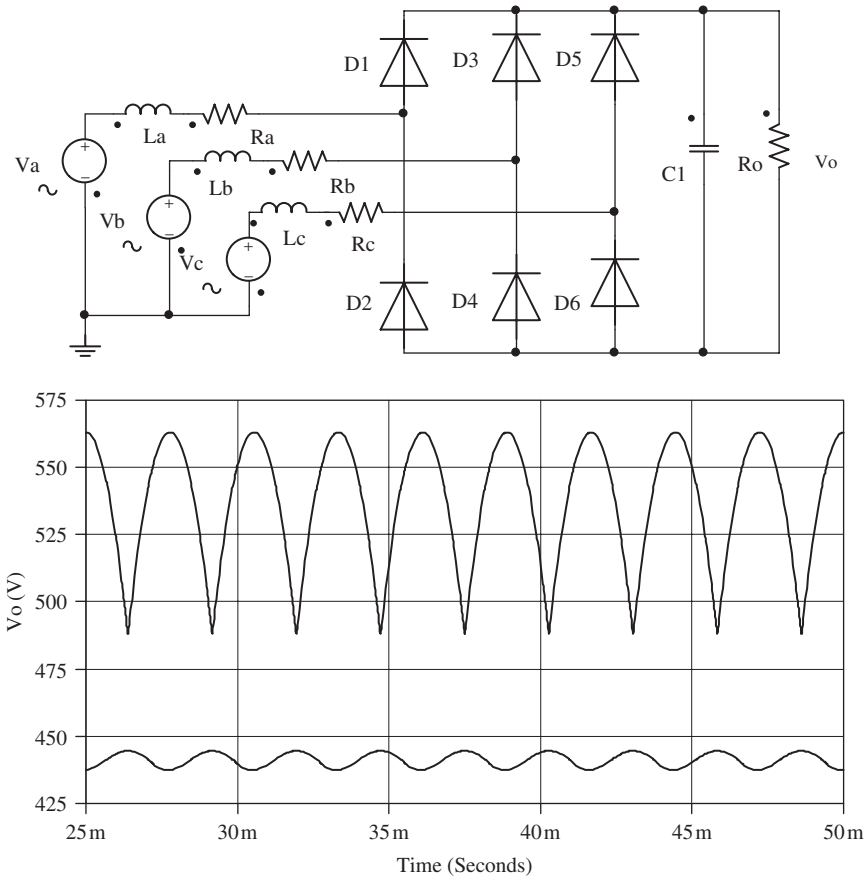

Figure 9.5 Practical rectifiers used in a HEV: top, rectifier circuit; bottom, output voltage in comparison to ideal rectifier (upper curve: ideal rectifier; lower curve: practical rectifier)

significantly different between no-load and loaded conditions. The difference is defined as voltage regulation.

9.3.3 Single-Phase Rectifier

We will use a single-phase circuit to analyze the voltage regulation, voltage ripple, and commutation.

At no-load conditions, due to the existence of the output capacitor, the output voltage will equal the peak of the input voltage, that is,

$$V_o = \sqrt{2}V_a = 1.414V_a \tag{9.3}$$

When load current increases, the impedance of the generator, and the diodes, will have a voltage drop on them. If the DC link capacitor is sufficiently large, then we can assume

that the output voltage V_1 (DC link voltage) is constant. We further assume that diode voltage drop V_D is also a constant.

By solving $\sqrt{2}V_a \sin \omega t = 2V_D + V_1$, we get

$$\theta_1 = \omega t_0 = \arcsin\left(\frac{2V_D + V_1}{\sqrt{2}V_a}\right) \tag{9.4}$$

The analysis can be divided into two scenarios: discontinuous and continuous mode. In discontinuous mode, the AC side current is not continuous. The current starts from zero and builds up when $\omega t \geq \theta_1$; it reaches a maximum when

$$\sqrt{2}V_i \sin \omega t = 2V_D + V_o \quad (\omega t = \pi - \theta_1) \tag{9.5}$$

The current then drops to zero at θ_2, $\theta_2 < \pi + \theta_1$.

Continuous Mode: In continuous mode, the AC side current does not reach 0 at $\pi + \theta_1$. In other words, $\theta_2 > \pi + \theta_1$.

In continuous mode, the voltage equation is

$$V_i - L_a\frac{di}{dt} - R_a i - 2V_D = V_1, \quad i(t_0) = 0 \tag{9.6}$$

$$\frac{di}{dt} + \frac{R_a}{L_a}i = \frac{1}{L_a}\left(\sqrt{2}V_a \sin \omega t - 2V_D - V_1\right) \quad \text{when } \omega t \geq \theta_1 \tag{9.7}$$

Note that the AC input will not have current until the voltage exceeds the output voltage plus the diode drop. However, the current will continue to flow until it reaches zero at angle θ_2.

We further neglect the resistance. The above differential equation can be simplified and the following solution obtained:

$$i(t) = -\frac{\sqrt{2}V_a}{\omega L_a}\cos \omega t - \frac{2V_D + V_1}{\omega L_a}\omega t + C, \quad \theta_1 \leq \omega t \leq \theta_2 \tag{9.8}$$

Since $i(\theta_1) = 0$, from the above equation we get

$$C = \frac{\sqrt{2}V_a}{\omega L_a}\cos \theta_1 + \frac{2V_D + V_1}{\omega L_a}\theta_1 \tag{9.9}$$

Therefore,

$$i(t) = -\frac{\sqrt{2}V_a}{\omega L_a}(\cos \omega t - \cos \theta_1) - \frac{2V_D + V_1}{\omega L_a}(\omega t - \theta_1), \quad \theta_1 \leq \omega t \leq \theta_2 \tag{9.10}$$

To find θ_2,

$$\frac{1}{\omega L_a}\int_{\theta_1}^{\theta_2}\left(\sqrt{2}V_a \sin \omega t - 2V_D - V_1\right) d\omega t = 0 \tag{9.11}$$

$$\cos \theta_2 + \frac{2V_D + V_1}{\sqrt{2}V_a}\theta_2 = \cos \theta_1 + \frac{2V_D + V_1}{\sqrt{2}V_a}\theta_1 \tag{9.12}$$

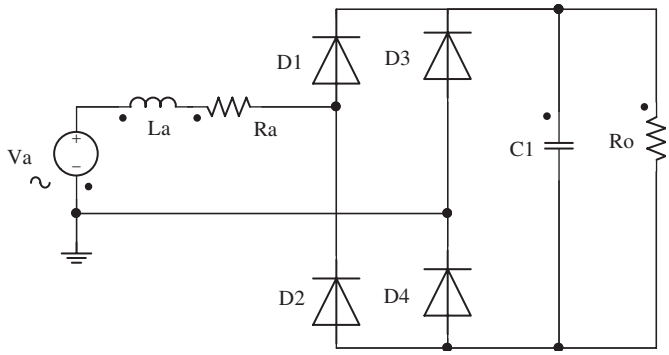

Figure 9.6 Voltage regulation, commutation of practical rectifier used in HEV

The output power of the rectifier must be equal to the power consumed by the load:

$$P = \frac{1}{\pi}\int_{\theta_1}^{\theta_2} \sqrt{2} V_a \sin \omega t^* i(t) d(\omega t) = \frac{V_1^2}{R} \tag{9.13}$$

so the output voltage of the rectifier is

$$V_o = \sqrt{\frac{R}{\pi}\int_{\theta_1}^{\theta_2} \sqrt{2} V_a \sin \omega t^* i(t) d(\omega t)} \tag{9.14}$$

The above expression cannot be directly solved due to the fact that θ_1 and θ_2 are functions of V_o. But it can be seen that the rectifier output is closely related to the impedance of the generator.

The voltage regulation can then be calculated from Figure 9.6. That is,

$$\Delta V_o = \frac{V_1 - V_o}{V_o} \times 100\% \tag{9.15}$$

Apparently, the voltage regulation is a function of the internal impedance of the generator, and the output power.

9.3.4 *Voltage Ripple*

The above derivation assumes that the output voltage is constant. However, it can be seen that the current from the AC input is discontinuous. This means that, during the portion of the cycle when there is no current from the AC side (e.g., from 0 to θ_1, and from θ_2 to π if $\theta_2 < \pi$), the load current is supplied by the capacitor.

However, due to the nonlinearity of the current, when the load current is less than the AC side current, the capacitor still has to supply some current to the load. Therefore, we can assume that if the load current is constant, and also that the capacitor supplies current to the load 50% of the time, then the voltage ripple is

$$\Delta V_o = \frac{1}{2}\frac{1}{C}\frac{V_o}{R}\frac{\pi}{\omega} \tag{9.16}$$

Example: In Figure 9.6, $V_a = 220\,\text{V}$, 400 Hz, $L_a = 1\,\text{mH}$, $R_a = 0.05$ (which can be neglected in the analytical calculations), $C = 10\,\text{mF}$, and $V_D = 0.8\,\text{V}$. The DC output is equivalent to $10\,\Omega$. Find the output voltage and voltage ripple.

Solution: V_o can be solved using the above equations and is illustrated in Figure 9.7a. It is then solved in MATLAB (Figure 9.7b).

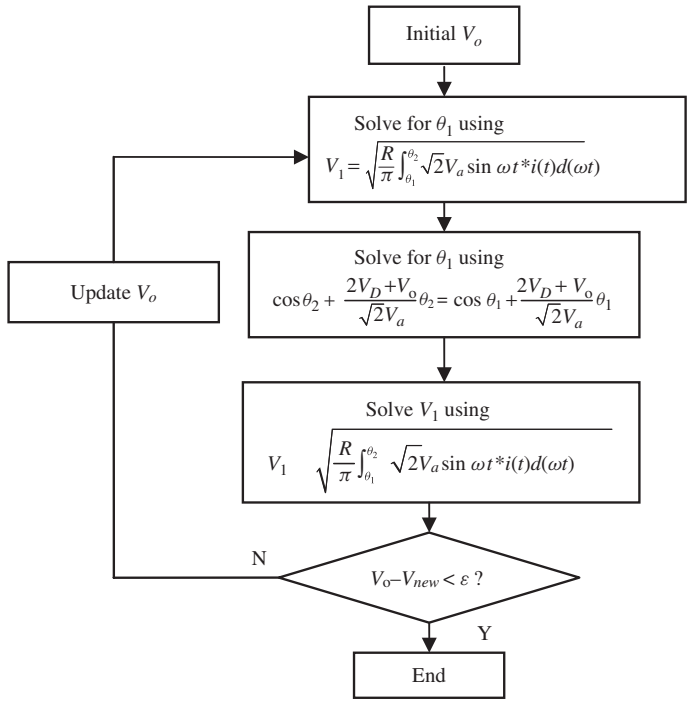

Figure 9.7 (a) Flow chart for solving the circuit shown in Figure 9.6. (b) MATLAB code corresponding to the flow chart in (a)

The solution is $V_o = 206\,\text{V}$. The calculated voltage ripple is 1.3 V.

Simulation: The same circuit is further simulated in Simplorer. The output voltage is 206.3 V, and the voltage ripple is 1 V.

Discontinuous Mode: In discontinuous mode, the AC side current starts at $\omega t = \theta_1 > \theta_2$, and drops to 0 at $\omega t > \pi + \theta_1$:

$$\frac{di}{dt} + \frac{R_a}{L_a} i = \frac{1}{L_a}\left(\sqrt{2}V_a \sin\omega t - 2V_D - V_1\right), \quad \theta_2 \le \omega t \le \theta_2 + \pi \tag{9.17}$$

and

$$i(\pi - \theta_2) = i(\theta_2) = 0 \tag{9.18}$$

```
% Matlab Program to solve for Vo.
clear all
syms wt i v y
delta_error=0.01;
voltage_error=0.1;

VD=0.8;
Va=220*sqrt(2);
w=2*pi*400;
La=1e-3;
RLoad=10;
Ra=0.001;
RD=0.001;
R=RLoad+2*RD+Ra;
x=w*La;

%Initialization
Vo=Va; V1=0;

%Solve for Vo
while abs(V1-Vo)>voltage_error
    Vo=(Vo+V1)/2;
    c0=(2*VD+Vo)/Va;
    theta1=asin(c0);
    c1=cos(theta1)+ c0*theta1;

    %find theta2
    theta2 = pi - theta1;
    c2  = cos(theta2)+ c0*(theta2);
    while abs((c2-c1))>delta_error
        theta2=theta2+0.001;
        c2  = cos(theta2)+ c0*(theta2);
        if theta2 >= pi + theta1 break, end
    end

    i = -Va/x*(cos(wt)-cos(theta1)) -
(2*VD+Vo)/x*(wt-theta1);
    v = Va*sin(wt);
    y = simple(i*v);
    P1 = 1/pi*int(y, wt, theta1, theta2);
    P = abs(real(eval(P1)));
    V1 = real(sqrt(P*R))
    if V1>=Va V1=Va; end
end
Io=P/Vo;
Vo = Vo - (RD*2*Io + 2*VD)
DeltaV=1/C*Vo/RLoad*(theta1+pi-theta2)/w
```

Figure 9.7 (*continued*)

When neglecting R_a,

$$i(t) = -\frac{\sqrt{2}V_a}{\omega L_a}(\cos\omega t - \cos\theta_2) - \frac{2V_D + V_1}{\omega L_a}(\omega t - \theta_2), \quad \theta_2 \le \omega t \le \pi + \theta_2 \tag{9.19}$$

To find θ_2, let

$$\frac{1}{\omega L_a}\int_{\theta_2}^{\pi+\theta_2}\left(\sqrt{2}V_a \sin\omega t - 2V_D - V_1\right)d\omega t = 0 \tag{9.20}$$

$$\theta_2 = \arccos\left[\frac{\pi(2V_D + V_1)}{2\sqrt{2}V_a}\right] \tag{9.21}$$

The boundary condition is $\theta_1 = \theta_2$. Therefore, the boundary condition occurs when

$$2V_D + V_1 = \frac{2\sqrt{2}V_a}{\sqrt{\pi^2 + 4}} \tag{9.22}$$

The above analysis is based on a single-phase generator. Since most generators and motors are three phase, it is worth looking at three-phase circuits.

Again, if the output capacitor is sufficiently large, then we can assume that the output voltage is constant. The diodes only conduct 60° in each cycle. The voltage equation can be written as

$$V_{LL} - 2L_a\frac{di}{dt} - 2R_a i - 2V_D = V_1, \quad -\frac{\pi}{6} \le \omega t \le \frac{\pi}{6} \tag{9.23}$$

where V_{LL} is the line–line voltage, and V_1 is the DC link voltage with load. This equation can be solved using the same method as for the single-phase analysis.

If the generator is a three-phase salient-pole permanent magnet (PM) generator (such as an interior-type PM generator), then the circuit is even more complicated due to the fact that the generator has two equivalent inductances, direct-axis and quadrature-axis inductance.

9.4 Buck Converter Used in HEVs

9.4.1 Operating Principle

A buck converter will step down a higher voltage DC input to a lower voltage DC output. The typical application of a buck converter in a HEV is to step down the hybrid battery voltage (typically 200–400 V) to charge the auxiliary battery (14 V). The uniqueness is the large difference between the input and output voltage of the converter and the small duty ratio (3.5%) needed to control the switching. Figure 9.8 shows the main circuit of a buck converter. It consists of a switch, a freewheeling diode, and an LC filter.

The small duty ratio will make control and regulation very difficult. It also affects the design of the inductor, capacitor, current ripple, and voltage ripple. As a starting point for the analysis, we assume the components are ideal, that is, the voltage drop is zero when turned on. We further assume that the output voltage is constant. When the switch is turned on, the voltage across the inductor is

$$V_L = V_d - V_o \tag{9.24}$$

When the switch is turned off, we assume the circuit is operating in continuous mode; then the voltage drop across the inductor is

$$V_L = -V_o \tag{9.25}$$

In steady state operations, the average voltage of the inductor must be zero. Therefore,

$$(V_d - V_o)DT_s = V_o(1 - D)T_s \tag{9.26}$$

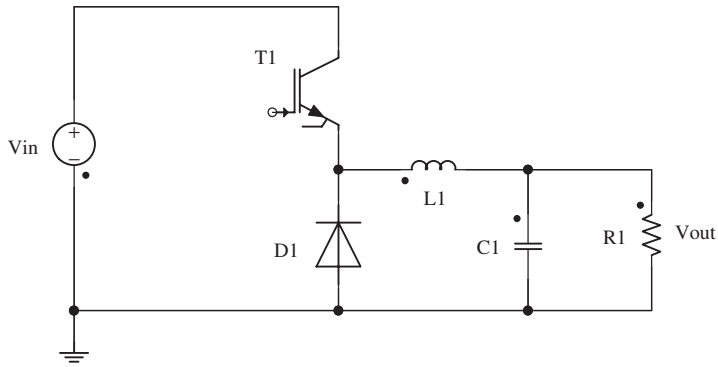

Figure 9.8 A buck converter

and

$$V_o = DV_d \tag{9.27}$$

The current ripple in the inductor is

$$\Delta I_L = \frac{1}{L} V_o (1 - D) T_s \tag{9.28}$$

The voltage ripple of the output can be calculated. We assume the load current is constant; then all the current ripple will enter the capacitor,

$$\Delta V_o = \frac{1}{C} \frac{1}{2} \frac{\Delta I_L}{2} \frac{T_s}{2} = \frac{T_s^2}{8LC} V_o (1 - D) \tag{9.29}$$

9.4.2 *Nonlinear Model*

The above analysis is based on assumptions that the output voltage is relatively constant and the parasitic parameters (resistance, inductance) can be neglected. Due to the fact that the ratio between the input and output voltages is very large, these assumptions may not hold true.

In order to accurately analyze the relationship and the influence of various parameters, we can use a detailed model to describe the system. In continuous mode, when the switch is turned on,

$$V_d = r_d i_L + r_s i_L + L \frac{di_L}{dt} + r_L i_L + V_o \tag{9.30}$$

$$i_L = i_c + i_o = C \frac{dV_o}{dt} + i_o = C \frac{dV_o}{dt} + \frac{V_o}{R} \tag{9.31}$$

where r_d, r_s, and r_L are the equivalent resistance of the diode, switch, and inductor, respectively; and i_o, i_c, and i_L are the current through the load resistance, the capacitor, and the inductor, respectively.

The above equations can be rewritten as

$$\begin{bmatrix} \frac{di_L}{dt} \\ \frac{dV_o}{dt} \end{bmatrix} = \begin{bmatrix} -\frac{r_d + r_s + r_L}{L} & -\frac{1}{L} \\ \frac{1}{C} & -\frac{1}{CR} \end{bmatrix} \begin{bmatrix} i_L \\ V_o \end{bmatrix} + \begin{bmatrix} \frac{1}{L} \\ 0 \end{bmatrix} V_d \tag{9.32}$$

When the switch is closed,

$$\begin{bmatrix} \frac{di_L}{dt} \\ \frac{dV_o}{dt} \end{bmatrix} = \begin{bmatrix} -\frac{r_D + r_L}{L} & -\frac{1}{L} \\ \frac{1}{C} & -\frac{1}{CR} \end{bmatrix} \begin{bmatrix} i_L \\ V_o \end{bmatrix} \tag{9.33}$$

These equations can be solved using numeric tools such as MATLAB.

9.5 Non-isolated Bidirectional DC–DC Converter

The bidirectional DC–DC converter in a HEV is also sometimes called an energy management converter, or boost DC–DC converter. This DC–DC converter is a high-power converter that links the HV battery at a lower voltage with the HV DC bus. The typical voltage of a battery pack is designed at 300–400 V. The best operating voltage for a motor and inverter is around 600 V. Therefore, this converter can be used to match the voltages of the battery system and the motor system. Other functions of this DC–DC converter include optimizing the operation of the powertrain system, reducing ripple current in the battery, and maintaining DC link voltage, hence the high-power operation of the powertrain.

*9.5.1 Operating Principle**

The DC–DC converter provides bidirectional power transfer. The operating principle is show in Figure 9.9.

- **Buck operation:** In buck operation as shown in Figure 9.9b, the power is transferred from V_d to V_B. When T_1 is closed and T_2 is open, since $V_d > V_B$, $V_L = V_d - V_B$ and the inductor current I_L builds up. When T_1 is open, the inductor current I_L continues to flow through D_2. Thus, $V_L = V_B$.
  Assuming ideal components and a constant V_o, the inductor current over one cycle in steady state operation will remain the same, for example,

$$\int_0^{t_{1on}} (V_d - V_o)dt = \int_{t_{1on}}^{t_{1on}+t_{1off}} (-V_o)dt \tag{9.34}$$

$$V_o = \frac{t_{1on}}{T} V_d = D_1 V_d \tag{9.35}$$

* © [2007] Inderscience. Reprinted, with permission, from the International Journal of Electric and Hybrid Vehicles.

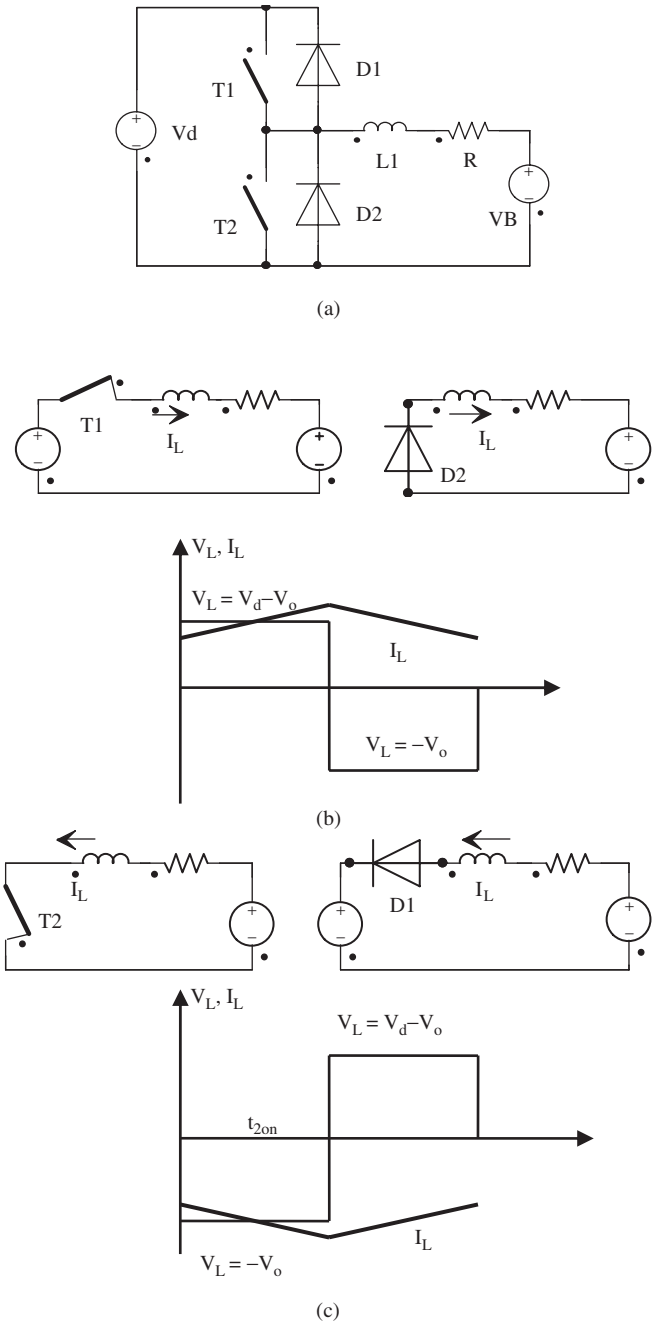

Figure 9.9 Operation of the bidirectional boost converter: (a) circuit topology; (b) inductor voltage and current waveform during buck operation; and (c) inductor voltage and current waveform during boost operation

where D_1 is the duty ratio defined as the percentage of on-time of switch T_1:

$$D_1 = \frac{t_{1on}}{T} \tag{9.36}$$

- **Boost operation:** In boost operation, the power is transferred from V_B to V_d. When T_2 is closed and T_1 is open, V_B and the inductor form a short circuit through switch T_2, as shown in Figure 9.9c, therefore $V_L = V_B$ and the inductor current I_L builds up. When T_1 is open, the inductor current continues to flow through D_1 to V_d, therefore $V_L = V_d - V_B$:

$$\int_0^{t_{2on}} V_o \, dt = \int_{t_{2on}}^{t_{2on}+t_{2off}} (V_d - V_o) dt \tag{9.37}$$

$$V_d = \frac{1}{1 - D_2} V_o \tag{9.38}$$

where D_2 is the duty ratio defined as the percentage of on-time of switch T_2:

$$D_2 = \frac{t_{2on}}{T} \tag{9.39}$$

In the bidirectional boost converter control, since T_1 and T_2 cannot be switched on simultaneously, a practical control strategy is to turn T_2 off while T_1 is on and vice versa. In this case,

$$D_2 = 1 - D_1 \tag{9.40}$$

9.5.2 *Maintaining Constant Torque Range and Power Capability*

The above analysis neglected the internal impedance of the battery. In fact, the impedance is often not negligible. When an electric motor and inverter are directly connected to the battery without a bidirectional DC–DC converter as shown in Figure 9.10, as the current (power or torque) goes up, the battery terminal voltage starts to drop because of the voltage drop on the battery internal impedance. For example, a 16 kWh lithium-ion battery with iron phosphate chemistry will have an internal impedance of 0.5 Ω. If the powertrain inverter/motor is rated at 125 kW, 400 V, 90% efficiency, the rated current is 348 A at 400 V. The battery internal voltage drop is 174 V. This voltage drop will significantly affect the performance of the powertrain motors. In fact, in this example, the maximum power that can be delivered to the motor is only 78 kW. In addition, due to the available voltage at the input, the motor constant torque region is also affected. In the above example, the constant torque region is shortened by 43.5%.

Another factor is that battery voltage is related to battery state of charge (SOC). As the battery SOC drops, the battery voltage will also drop. Therefore, the available voltage at a motor/inverter terminal is also changed, which will make it difficult to maintain the constant torque range.

When a DC–DC converter is inserted between the battery and inverter/motor as shown in Figure 9.11, the DC bus voltage before the inverter can be maintained as a constant.

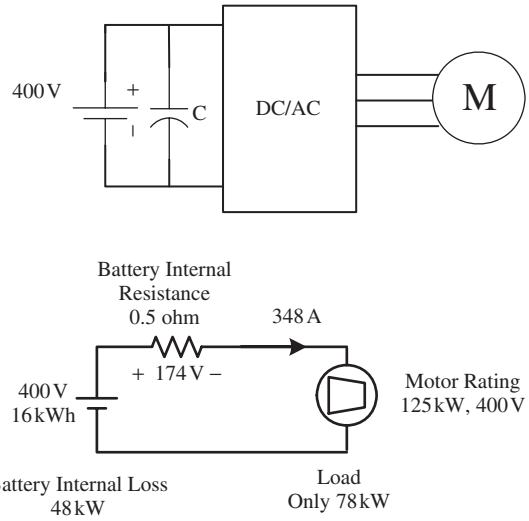

Figure 9.10 Powertrain motor directly connected to battery without the DC–DC converter: top, circuit topology; bottom, equivalent circuit of the circuit

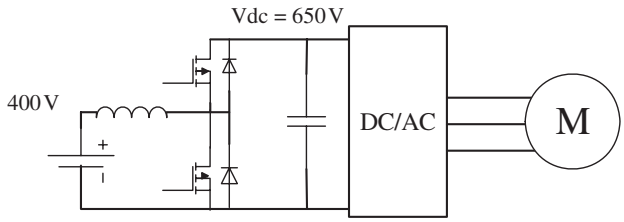

Figure 9.11 Powertrain motor connected to battery through a DC–DC converter

Therefore, the constant torque range will not be affected by the battery SOC or large power drawn by the inverter/motor.

The above analysis assumes that the battery system is designed to handle the large power dissipation during large power draw.

9.5.3 Reducing Current Ripple in the Battery

Due to the switching functions of the inverter used in the powertrain system, there are abundant high-frequency current harmonics on the DC side. The amount of current ripple that goes into/out of the battery depends on the switching methodology, switching frequency, and the capacitance on the DC bus. When there is no DC–DC converter in place, the amount of ripple current of the battery is determined by the DC bus capacitance C and the ratio of capacitor impedance to battery impedance. Without the capacitance, the battery current will be directly determined by the switching status of the DC–AC

inverter, that is, the combination of the three-phase current of the motor, as shown in Figure 9.12. When there is a DC bus capacitor in parallel with the battery, the amount of current ripple flowing into/out of the battery is determined by the capacitance and parasitic impedance of the DC bus capacitor. For example, if $C = 10\,\text{mF}$, the capacitive impedance of the capacitor at switching frequency is only 2.65 mΩ, which is far less than the internal impedance of the battery. Ideally the high-frequency ripple will flow through the capacitor and the battery current is supposed to be constant.

However, the parasitic resistance of the capacitor is also not negligible. A high-quality 10 mF capacitor has 26 mΩ internal resistance and the second-class capacitor has 100 mΩ. The quality of the capacitor affects the current ripple of the battery. The lower the capacitor impedance, the lower the battery ripples, as shown in Figure 9.12. High-frequency ripple current is believed to be harmful to battery life.

When a DC–DC converter is added, the battery current can be maintained with a relatively small ripple, as shown in Figure 9.13.

9.5.4 Regenerative Braking

The regenerative braking of the two topologies, that is, one with and without a DC–DC converter, will also be different. In the topology where there is no DC–DC converter, the DC bus voltage will fluctuate during transition from motoring to braking. For example, if the motor is initially motoring at 50 kW, and the battery internal voltage is 400 V with 0.5 Ω internal resistance, then the battery current is 155 A and the DC bus voltage is 322 V. If the motor is switched to braking at 50 kW, then the battery current is 110 A and the DC bus voltage is 455 V. This dramatic change of DC bus voltage will make motor control, such as vector control, very difficult.

On the other hand, in a system that contains a DC–DC converter between the inverter/motor DC bus and the battery, the DC bus voltage can be maintained relatively constant. Hence, the transition between motoring and braking is easier to handle.

9.6 Voltage Source Inverter*

Voltage source inverters (VSIs) are used in hybrid vehicles to control the electric motors and generators. Figure 9.14 shows the power electronic circuit arrangement of a VSI to control the induction motor, PM synchronous motors, and PM brushless motors. The switches are usually IGBTs for high voltage, high-power hybrid configurations or MOSFETs for low voltage designs.

The output of the VSI is controlled through the means of pulse width-modulated (PWM) signals to produce sinusoidal waveforms. Certain harmonics exists in such a switching scheme. High switching frequency is used to move away the harmonics from the fundamental frequency.

9.7 Current Source Inverter*

Figure 9.15 shows the circuit topology of a current source inverter (CSI). The CSI operates using the same principle as in a VSI, with the input as a current source. Three small commutating/filtering capacitors may be needed on the AC side.

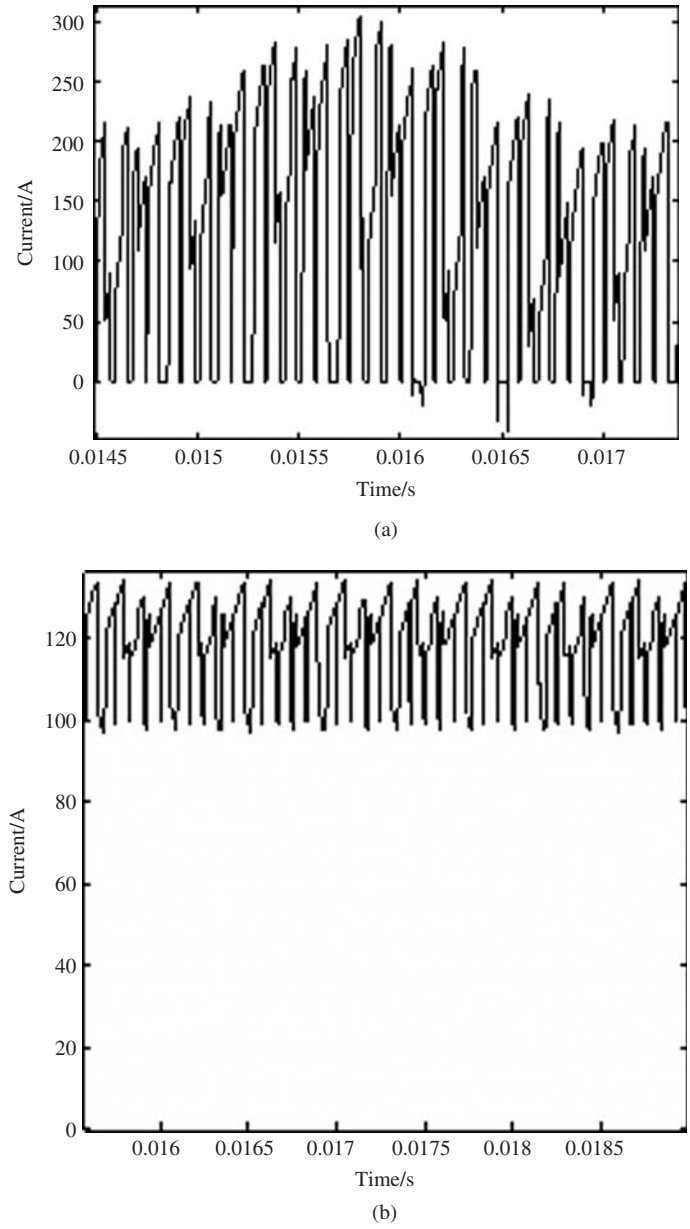

Figure 9.12 Battery current without a DC–DC converter: (a). DC bus current for no DC-bus capacitance; (b). DC bus current for C = 1 mF, Rc = 100 mΩ (c) DC bus current for C = 10 mF, Rc = 100 mΩ

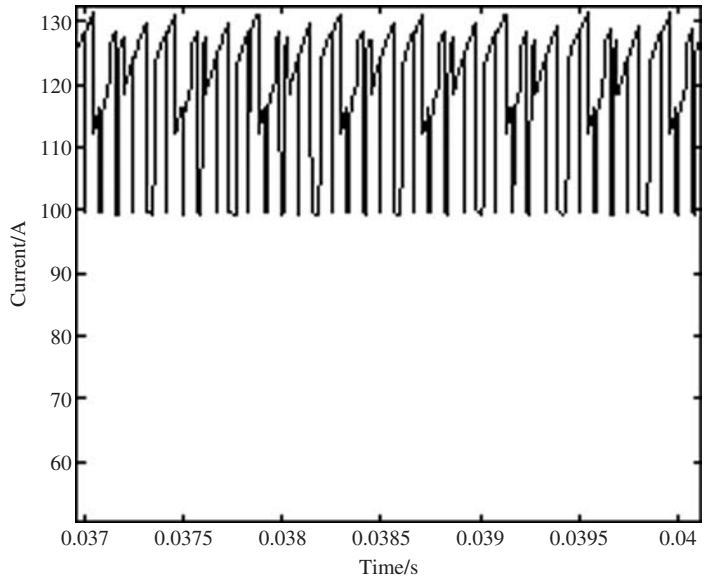

Figure 9.12 (*continued*)

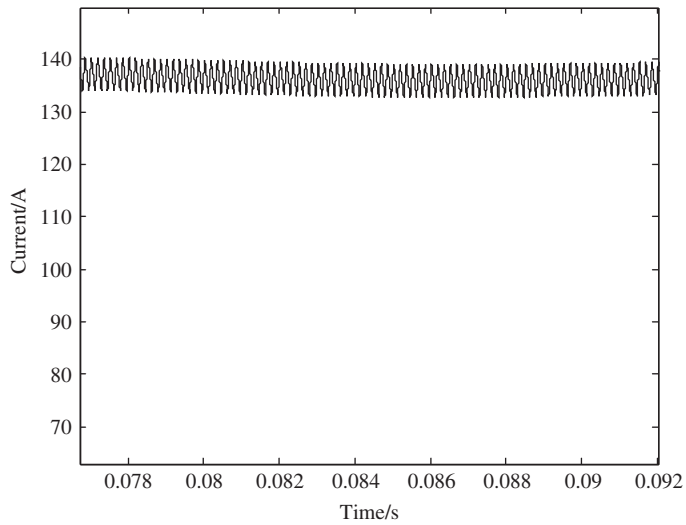

Figure 9.13 Battery current when a DC–DC converter is inserted between the inverter and the battery

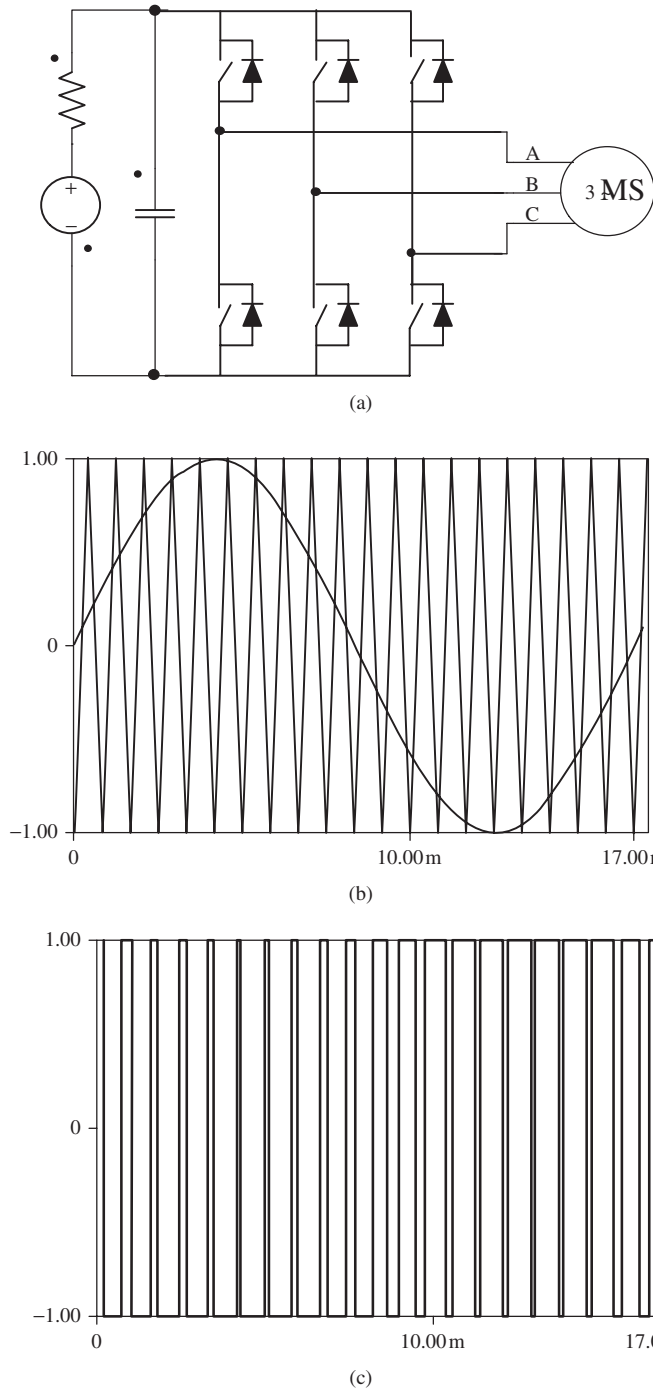

Figure 9.14 Voltage source inverter: (a) circuit diagram; (b) control of the switches; (c) gate control signal via PWM waveform

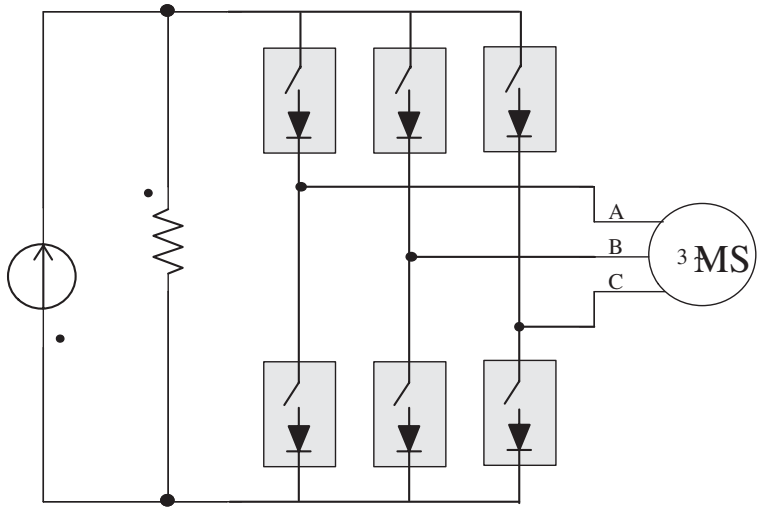

Figure 9.15 Current source inverter

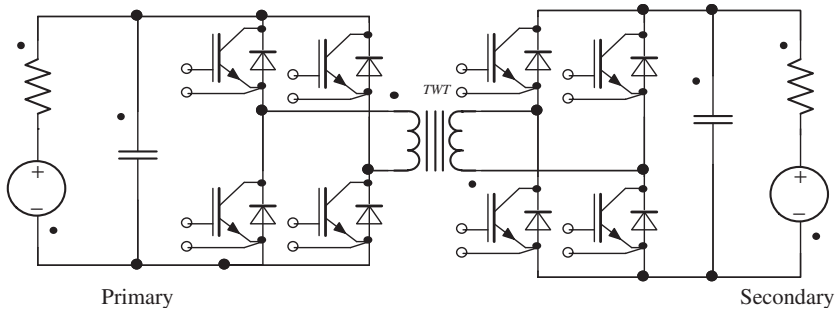

Figure 9.16 Isolated bidirectional DC–DC converter

9.8 Isolated Bidirectional DC–DC Converter*

In some applications, galvanic isolation between the battery and the load units is necessary and desirable [24]. Figure 9.16 shows a full bridge isolated bidirectional DC–DC converter.

In Figure 9.16, the primary bridge inverter switches at 20–50 kHz, with 50% duty ratio. The output of the primary is a square wave voltage which is applied to the primary winding of the isolation transformer. The secondary winding of the transformer therefore will have a square wave voltage. Without any control at the gating of the secondary bridge converter, the voltage of the secondary of the transformer is rectified through the four freewheeling diodes. The output voltage will fluctuate with load conditions and the primary voltage.

* © [2008] IET. Reprinted, with permission, from IET Power Electronics.

9.8.1 Basic Principle and Steady State Operations

Steady state operations of isolated bidirectional DC–DC converters have been studied in detail elsewhere [1, 3, 6]. In this section, we complement these studies by distinguishing the operating modes of isolated bidirectional DC–DC converters according to the phase shift angle, load conditions, and output voltage. In this analysis, the dead-band and switching dynamics will be neglected but will be analyzed later.

In the following analysis, the turns ratio of the transformer is n, the transformer primary voltage is V_1, and the switching frequency is f_s. For the convenience of analysis, we define T_s as one half of the switching period, for example, $T_s = 1/(2f_s)$. The duty cycle or phase shift is based on a half period, $D = t_{on}/T_s$. Therefore, DT_s is the phase shift between the two bridges. Further, I_{L_s} is the current of the leakage inductance of the secondary winding. The output voltage of the secondary bridge is V_2.

9.8.1.1 Heavy Load Conditions

There are a number of different operating modes based on the output current with a boundary condition as illustrated in Figure 9.17. Under heavy load conditions, the inductor current increases from an initial negative value $i(t_0) < 0$ at the beginning of the switching cycle, and reaches a positive value $-i(t_0)$ at the end of the half switching cycle. Six different segments emerge in each switching cycle as shown in Figure 9.17a. In the following analysis, V_2 is assumed to be large than nV_1.

- **Segment 0**, $[t_0, t_1]$: In this segment, Q_1 and Q_4 of the primary bridge are turned on. Therefore V_1 and nV_1 are positive. Q_6 and Q_7 of the secondary bridge are turned on.

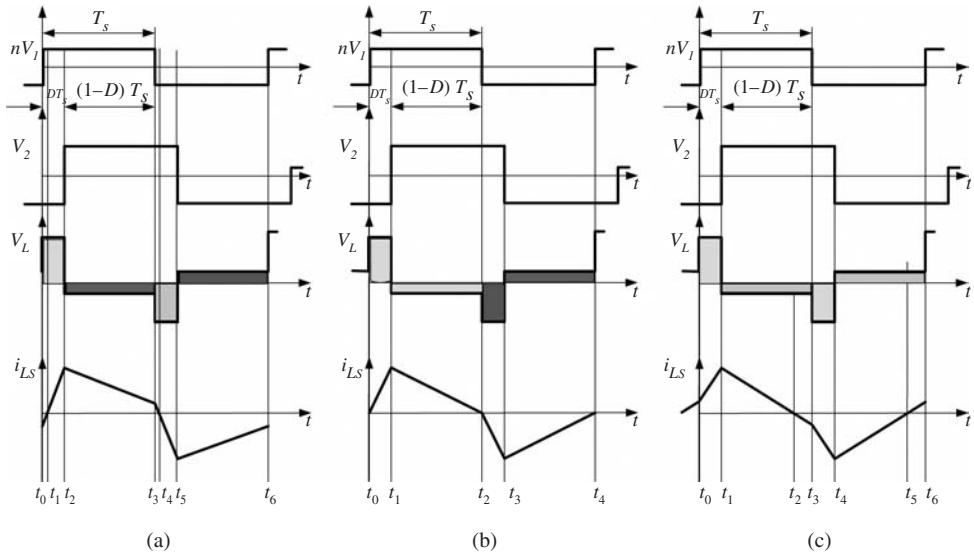

Figure 9.17 Typical voltage and current waveforms for $V_2 > nV_1$: (a) waveforms for i(t_0) < 0; (b) waveforms for Boundary conditions $i(t_0) = 0$; (c) waveforms for $i(t_0) > 0$

Due to the negative current in the inductor, D_6 and D_7 freewheel, and Q_6 and Q_7 do not conduct current. Thus, $V_{L_s} = nV_1 + V_2V$. The inductor current increases linearly from a negative value. At t_1, the inductor current reaches 0.

- **Segment 1**, $[t_1, t_2]$: Switches Q_1 and Q_4 of the primary bridge, and Q_6 and Q_7 of the second bridge, are still turned on; $V_{L_s} = nV_1 + V_2$. The current continues to increase except that it becomes positive, for example, Q_6 and Q_7 conduct the current. The total current increment during interval $[t_0, t_2]$ (**Segments 0 and 1**) is

$$\Delta I_{L_s} = \frac{DT_s}{L_s}(V_2 + nV_1) \tag{9.41}$$

Hence

$$i(t_2) = i(t_0) + \frac{DT_s}{L_s}(nV_1 + V_2) = I_{\max} \tag{9.42}$$

- **Segment 2**, $[t_2, t_3]$: In this segment, switches Q_1 and Q_4 of the primary bridge continue to be turned on, but switches Q_6 and Q_7 are turned off, and switches Q_5 and Q_8 are turned on. Diodes D_5 and D_8 freewheel because the current is positive; $V_{L_s} = nV_1 - V_2 < 0$.
  The leakage inductor current increment during interval $[t_2, t_3]$ is

$$\Delta I_{L_s} = \frac{(1-D)T_s}{L_s}(nV_1 - V_2) \tag{9.43}$$

Hence

$$i(t_3) = i(t_2) + \frac{(1-D)T_s}{L_s}(nV_1 - V_2) \tag{9.44}$$

A similar analysis could be done for the following three segments due to the symmetry of operation.

- **Segment 3**, $[t_3, t_4]$: Switches Q_2 and Q_3 of the primary bridge continue to be turned on, and switches Q_5 and Q_8 are turned on. The primary voltage of the transformer, hence the secondary voltage, is reversed and the current decreases from $i(t_3)$ to zero. D_5 and D_8 freewheel.
- **Segment 4**, $[t_4, t_5]$. Switches Q_2 and Q_3 of the primary bridge are turned on, and switches Q_5 and Q_8 are turned on. The current decreases linearly to the negative maximum. Switches Q_5 and Q_8 conduct current. Hence the current increment in L_s in **Segments 3 and 4** is

$$\Delta I_{L_s} = -\frac{DT_s}{L_s}(nV_1 + V_2) \tag{9.45}$$

- **Segment 5**, $[t_5, t_6]$: Switches Q_5 and Q_8 are turned off, and D_6 and D_7 begin to freewheel. The current increment in L_s is

$$\Delta I_{L_s} = \frac{(1-D)T_s}{L_s}(V_2 - nV_1) \tag{9.46}$$

From the symmetry of the inductance current, $i(t_0) = -i(t_3)$. From Equations 9.41–9.46, the initial inductor current can be obtained

$$i(t_0) = \frac{1}{4f_s L_s}[(1-2D)V_2 - nV_1] \tag{9.47}$$

The maximum current is

$$I_{\max} = i(t_2) = \frac{1}{4f_s L_s}[-(1-2D)nV_1 + V_2] \tag{9.48}$$

The above analysis of operating modes is based on the assumption that $i(t_0) < 0$, that is, $(1-2D)V_2 < nV_1$. If $(1-2D)V_2 = nV_1$, or

$$V_2 = \frac{1}{1-2D}nV_1 \tag{9.49}$$

then $i(t_0) = 0$. This corresponds to the boundary condition as shown in Figure 9.17b which is very similar to the non-isolated boost converter in the steady state operation. Under this circumstance the inductor current increases from zero at the beginning of the switching cycle and drops to zero at T_s.

From Equation 9.49, it seems that V_2 will approach infinity when D reaches 0.5. But it can be seen from Equation 9.47 that when $D = 0.5$, $i(t_0) = -nV_1/4f_s L_s$, that is, $i(t_0)$ will never reach zero for $D = 0.5$. Therefore, the boundary can only be met when D is not equal to 0.5.

9.8.1.2 Light Load Condition

It can be seen from Equation 9.47 that when $(1-2D)V_2 > nV_1$, then $i(t_0) > 0$. This corresponds to light load conditions. The current and voltage waveforms are shown in Figure 9.17c, where the current increases from a positive value at the beginning of the cycle and drops to a negative value at the end of the half switching cycle.

9.8.1.3 Output Voltage

Equations 9.47–9.49 do not give the expression for the output voltage, except for the boundary condition. In order to derive the expression for the output voltage, let us start with the average current in the inductor. The average current of the leakage inductance in the half switching cycle can be derived from Figure 9.17a (note that $i(t_0) < 0$),

$$\bar{I} = \frac{1}{2T_s}[(I_{\max} + i(t_0))DT_s + (I_{\max} - i(t_0))(1-D)T_s] = \frac{1}{2f_s L_s}D(1-D)V_2 \tag{9.50}$$

The supplied power is

$$P_1 = nV_1\bar{I} = \frac{nV_1V_2}{2f_s L_s}D(1-D) \tag{9.51}$$

Assuming that the load has a fixed resistance, then the output power is

$$P_o = \frac{V_2^2}{R_L} \tag{9.52}$$

Neglecting the transformer and the switch losses, $P_1 = P_o$, then

$$V_2 = \frac{nV_1}{2f_s L_s} R_L D(1 - D) \tag{9.53}$$

and

$$I_2 = \frac{nV_1}{2f_s L_s} D(1 - D) \tag{9.54}$$

Equation 9.53 shows that, for a given switching frequency, leakage inductance, and input voltage, the output voltage is proportional to the load resistance and is a function of the duty ratio (phase shift angle). For a given load resistance, the output voltage varies with duty ratio, and reaches a maximum when $D = 0.5$. For a given duty ratio, the output voltage is directly proportional to the load resistance. Therefore, for a given phase shift angle, under heavy load conditions, or

$$R_L < \frac{2f_s L_s}{D(1 - D)} \tag{9.55}$$

V_2 will be less than nV_1.

When V_2 drops to less than nV_1, the initial inductor current is confined to a negative value and the current waveforms are also different from the operations under the condition of $V_2 > nV_1$, as shown in Figure 9.18. The boundary condition occurs when $S_1 = S_2 = S_3 = S_4$ in Figure 9.18b, or $(nV_1 + V_2)DT_s = (nV_1 - V_2)(1 - D)T_s$. Therefore, at the boundary condition,

$$V_2 = nV_1(1 - 2D) \tag{9.56}$$

An extreme mode emerges when $nV_1 = V_2$ as shown in Figure 9.18c, where the inductor current will remain constant during the time interval $[DT_s, T_s]$.

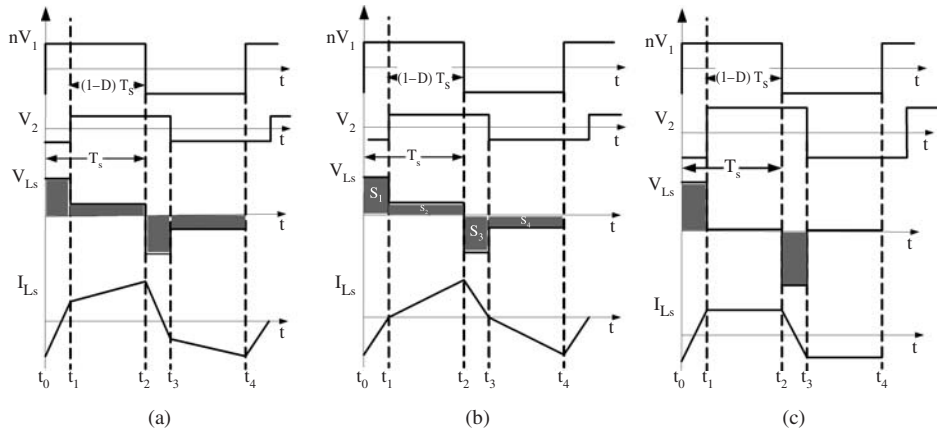

Figure 9.18 Typical voltage and current waveforms for $V_2 < nV_1$ and $V_2 = nV_1$: (a) Common mode; (b) Boundary mode; (c) Extreme mode, $nV_1 = V_2$

It can also been seen from Equation 9.54 that the output current is proportional to the duty ratio (phase shift angle). This may be used to analyze conditions where the output voltage needs to be maintained as constant, and the current can be controlled through the phase shift angle.

9.8.1.4 Output Power

Substituting Equation 9.53 into Equation 9.51, the output power P_o can be obtained as

$$P_o = \left(\frac{nV_1}{2f_sL_s}\right)^2 D^2(1-D)^2R_L \tag{9.57}$$

From Equations 9.51 and 9.57, the output power always has maximum values when and only when $D = 1/2$, whether for a fixed resistance R_L or a constant output voltage V_2.

When the system is in the voltage closed-loop control mode, that is, $V_2 =$ constant, then decreasing R_L will result in the output power increasing since the output power is inversely proportional to R_L as shown in Equation 9.52. To maintain V_2 as a constant, it can be seen from Equation 9.53 that D has to be adjusted accordingly: $D(1-D) \propto 1/R_L$ for a given V_1. For fixed V_1 and V_2, the output power reaches a maximum at $D = 0.5$ as shown in 9.51. At this condition, $R_L = R_C = 8f_sL_sV_2/(nV_1)$.

Further decrease of $R_L < R_C$ will result in the output voltage of the system collapsing and entering the open loop at $D = 0.5$, that is, V_2 cannot be maintained as a constant. Output voltage V_2 and output power P_o will decrease, and are both proportional to R_L as shown in Equations 9.53 and 9.57.

Consider Equations 9.47 and 9.57. When $D \in (0, 1/2]$, if V_1, V_2 are kept constant (closed-loop control), with the increase of D the power will increase accompanying the decrease of the initial current $i(t_0)$. Hence the absolute value and the sign of $i(t_0)$ represent the load condition. The lower the inductor current $i(t_0)$, the higher the output power.

Under open-loop control, that is, for a given D, with the increase of load resistance, V_2 and P_o will increase according to Equations 9.53 and 9.57. At the same time, the initial current increases according to Equation 9.47 due to the increase of V_2. Hence the relations between the initial current and output power are very different in the open-loop and closed-loop operations of the converter.

In order to validate the theoretical analysis, a simulation model was set up with $V_1 = 200\,\text{V}$, $n = 2$, and $L_s = 120\,\mu\text{H}$. In Figure 9.19a,b, with the increase of power, the initial current decreases from a positive value to a negative value. In Figure 9.19c,d, the variation of initial current is the opposite. This analysis is in good agreement with the earlier analysis.

The maximum output power is also a function of L_s and f_s. Increasing the leakage inductance L_s will decrease the current impact to IGBTs but will reduce the capability of the maximum output power of the converter as shown in Equation 9.57. This will be discussed later in this section.

9.8.2 Voltage Ripple

The above switching modes are inherently nonlinear, which will cause voltage ripple on the output capacitor. The capacitor current is a combination of the inductor current I_L and the load current I_o at different operating modes. From Figure 9.17, the capacitor current

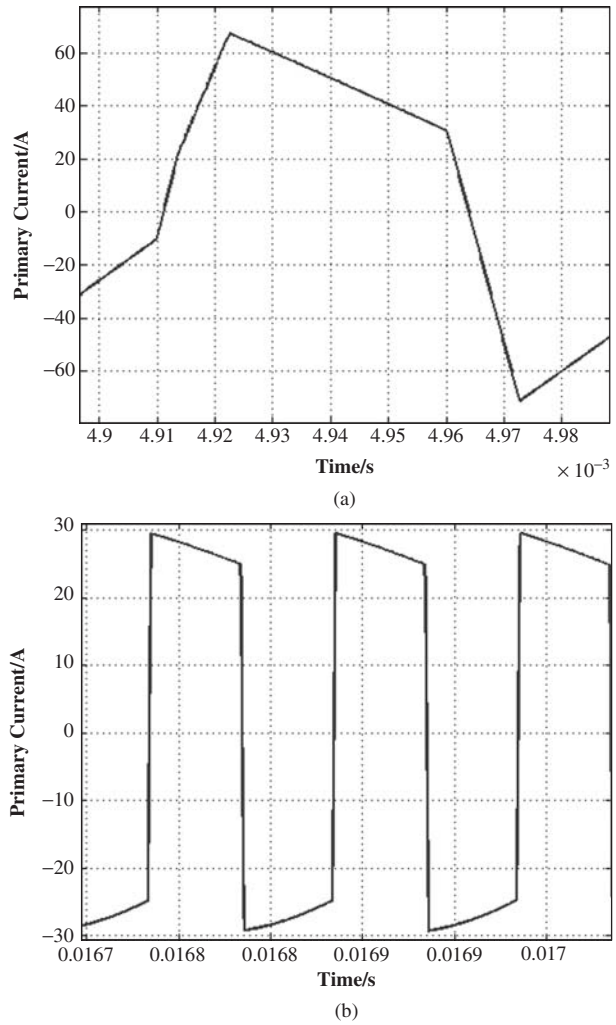

Figure 9.19 Simulated primary current at different voltage and power output: (a) primary current for $V_2 = 500\,\text{V}$, $R = 200\,\Omega$, $P = 1.8\,\text{kW}$; (b) primary current for $V_2 = 600\,\text{V}$, $R = 40\,\Omega$, $P = 9\,\text{kW}$ (c) primary current for $D = 1/8$, $R = 60\,\Omega$, $P = 9.2\,\text{kW}$; (d) primary current for $D = 1/8$, $R = 100\,\Omega$, $P = 13.6\,\text{kW}$

can be written as

$$i_C = -(I_o + i_L), \quad 0 \le t \le DT_s$$
$$i_C = i_L - I_o, \quad DT_s \le t \le T_s \tag{9.58}$$

The capacitor current is shown in Figure 9.20, where at $t = t_1 + \Delta_2$, $I_{L_s} = I_o$, or $I_C(t_1 + \Delta_2) = 0$, that is,

$$I_{\max} + \frac{nV_1 - V_2}{L_s}\Delta_2 = I_o \tag{9.59}$$

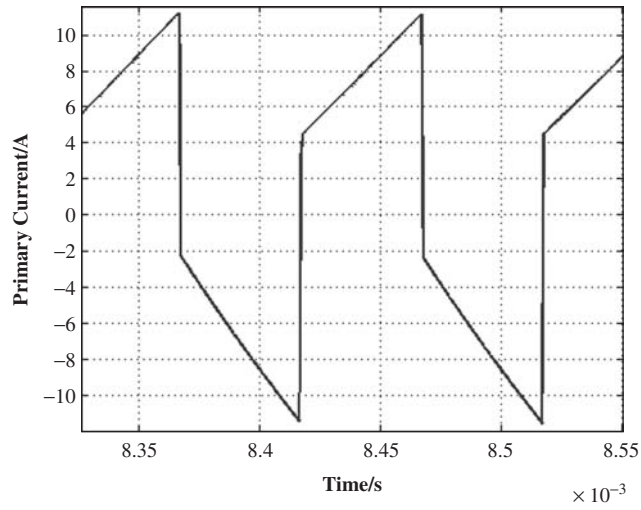

(c)

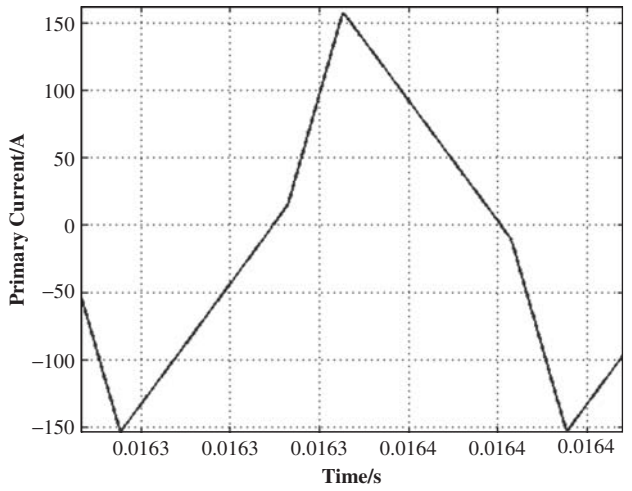

(d)

Figure 9.19 (*continued*)

Therefore

$$\Delta_2 = \frac{I_{\max} - I_o}{V_2 - nV_1} L_s \tag{9.60}$$

Based on energy conservation, $P_1 = P_o$, or $nV_1\bar{I} = V_2 I_o$. Substituting Equation 9.51 for P_o, the output current can be obtained:

$$I_o = \frac{nV_1}{2f_s L_s} D(1 - D) \tag{9.61}$$

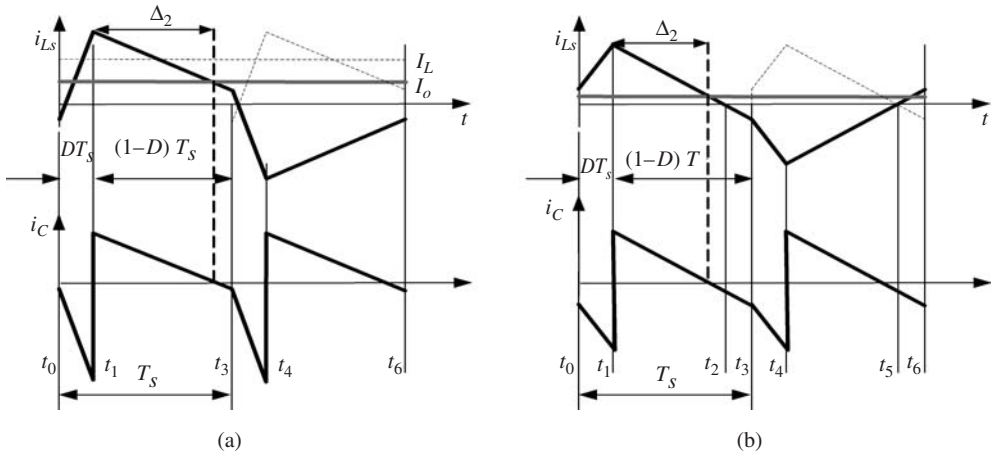

Figure 9.20 The current ripple in the capacitor: (a) current ripple for $i(t_0) < 0$; (b) current ripple for $i(t_0) > 0$

The voltage ripple is

$$\Delta V_2 = \frac{1}{C}\int_{DT_s}^{DT_s+\Delta_2} (i_{L_s}(t) - I_o)dt = \frac{\Delta_2}{C}\frac{I_{\max} - I_o}{2} \tag{9.62}$$

Substitute Equations 9.59–9.61 to Equation 9.62, the voltage ripple can be derived

$$\begin{cases} \Delta V_2 = \dfrac{[V_2 + (2D^2 - 1)nV_1]^2}{32f_s^2 L_s C(V_2 - nV_1)} = \dfrac{[D(1-D)R_L - 2(1-2D^2)f_s L_s]^2}{64f_s^3 L_s^2[D(1-D)R_L - 2f_s L_s]}\dfrac{nV_1}{C} \\ \Delta V_2\% = \dfrac{\Delta V_2}{V_2} = \dfrac{[D(1-D)R_L - 2(1-2D^2)f_s L_s]^2}{32f_s^2 L_s C[D^2(1-D)^2 R_L^2 - 2f_s L_s D(1-D)R_L]} \end{cases} \tag{9.63}$$

Therefore the voltage ripple is a function of D, R, and nV_1. This expression is applicable to both open-loop control and close-loop control. The condition of Equation 9.63 is $V_2 > nV_1$, which implies $D(1-D)R_L > 2f_s L_s$. From Equation 9.63, it is easy to see that ΔV_2 is directly proportional to nV_1/C. In order to further study the influential factors, the voltage ripple under different conditions is shown in Figure 9.21.

From Figure 9.21a, the absolute voltage ripple decreases when R_L decreases under a given D, and the ripple reaches a maximum at $D = 0.5$. However, in Figure 9.21b, the relative ripple is an increasing function of D and only reaches a maximum when $D = 1$. All the curves cross at $D = 0.5$.

When $D < 0.5$, a high resistance will result in a high ripple under a fixed D. When $D > 0.5$ the absolute ripple decreases with D for a given load resistance, but the relative ripple increases with D.

From Figure 9.21c,d, increasing the switching frequency is beneficial to limit both the absolute ripple and the relative ripple of the output voltage.

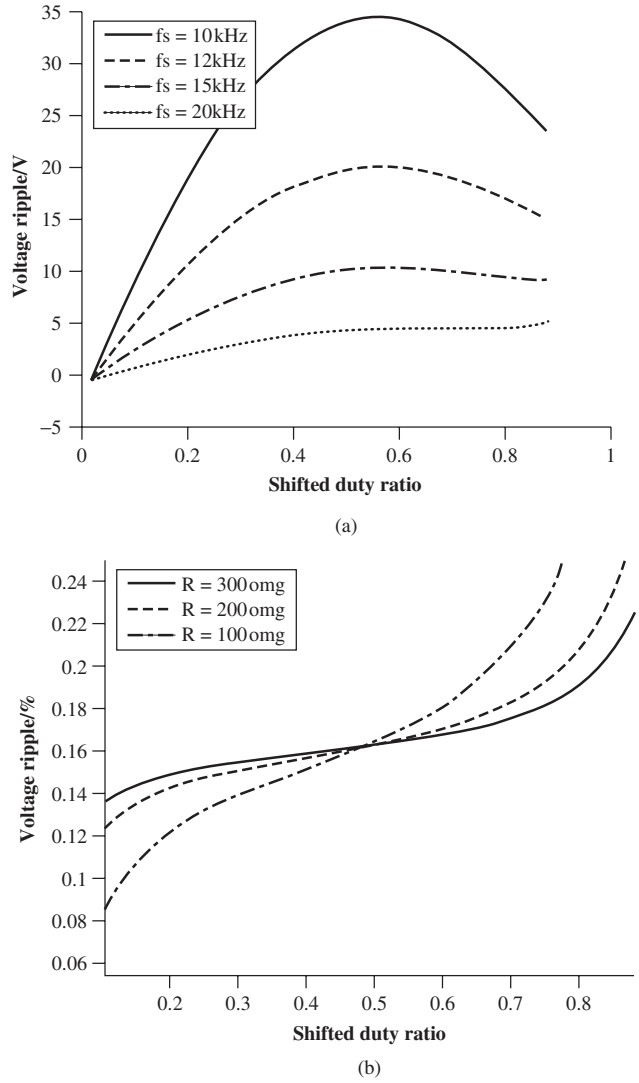

Figure 9.21 Voltage ripple under different operations simulation: (a) Voltage ripple as a function of D and R_L; (b) voltage ripple (%) as a function of D and R_L (c) Voltage ripple as a function of D and f_s; (d) Voltage ripple (%) as a function of D and f_s

9.9 PWM Rectifier in HEVs*

9.9.1 Rectifier Operation of Inverter

In braking mode, the motor is controlled to achieve regenerative braking. The VSI is operated as a PWM rectifier as shown in Figure 9.22. The operating principle of the

* © [2007] Inderscience. Reprinted, with permission, from the International Journal of Electric and Hybrid Vehicles.

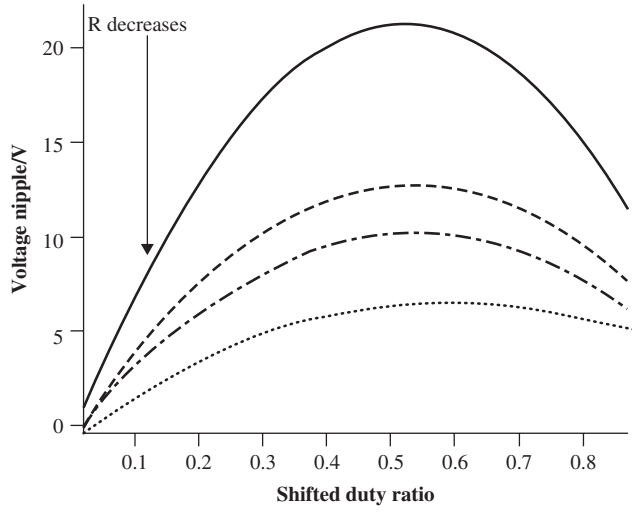

(c)

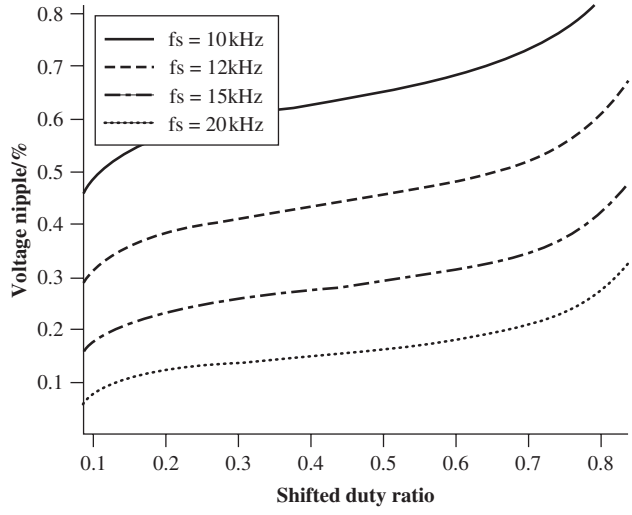

(d)

Figure 9.21 (*continued*)

PWM rectifier, when the motor (operated as a generator) speed is below the base speed of the constant power region, is essentially the same as the boost operation of the isolated DC–DC converter in the previous section.

When the motor speed is above the base speed of the constant power region, the generator develops a back emf much higher than the DC link voltage, especially when a large constant power range is designed. In this case, the motor needs to be controlled in its field weakening region to reduce its winding terminal voltage. Neglecting the stator resistance and salience, the equivalent circuit of the control is illustrated in Figure 9.23,

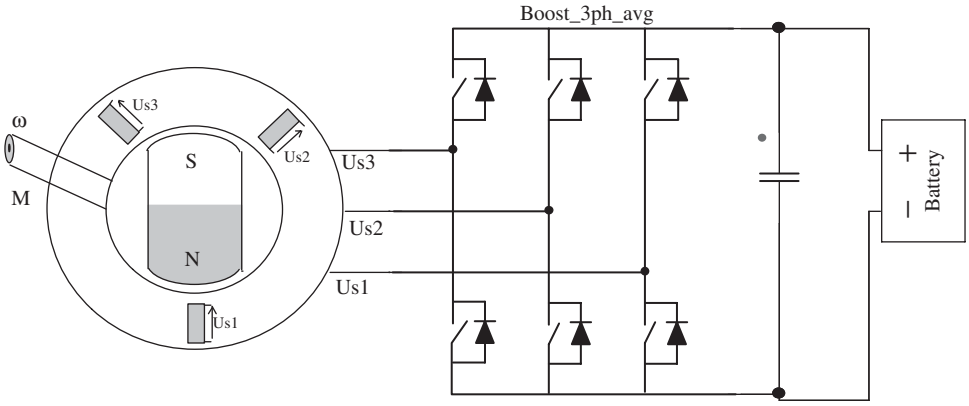

Figure 9.22 PWM rectifier

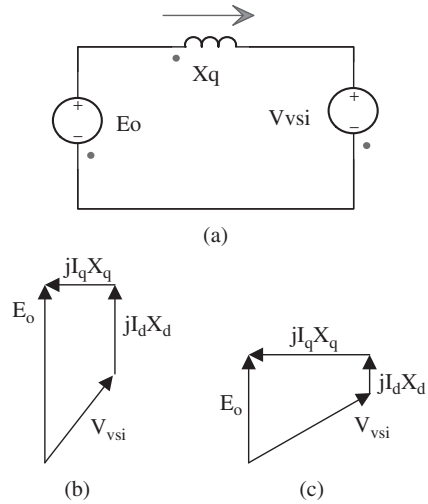

Figure 9.23 Regenerative braking in the constant power region: (a) equivalent circuit; (b) phasor diagram at high speed in the constant power region; and (c) phasor diagram at lower speed in the constant torque region

where E_o is the induced back emf of the PM motor, L_q is the synchronous inductance, and V_{vsi} is the equivalent sine wave output of the VSI:

$$V_{vsi} = E_o - jI_qX_q - jI_dX_d \tag{9.64}$$

The purpose of the field weakening control is to achieve a constant V_{vsi} for higher E_o, by applying a current opposite to the d-axis direction.

9.10 EV and PHEV Battery Chargers

The battery charging system is a critical part of EVs and PHEVs. The efficiency, charging speed, and cost of such chargers are crucial to the commercialization of PHEVs. There are many different topologies available for battery chargers. Due to safety requirements and standards, most battery chargers are required to be isolated from the AC electric grid (such as requirement of SAE J1772). In some cases, bidirectional power flow is necessary in order to realize vehicle-to-grid functions.

A survey conducted by the US Electric Power Research Institute (EPRI) revealed that 78% of the US population drive 40 miles (64 km) or less in their daily commuting. Therefore, PHEVs capable of a 40 mile electric driving range can significantly reduce gasoline usage in passenger cars. For a typical passenger vehicle (car and SUV), the average energy consumption is approximately 150–300 Wh per mile. To achieve a 40 mile electric range, a battery that contains usable energy of 6–12 kWh is appropriate. Lithium-ion batteries are considered as the only viable energy storage solution for PHEVs at the time being. To achieve safe and reliable operation while maintaining the cycle life and health of the batteries in a PHEV, the typical available energy from lithium-ion batteries is approximately 60–70% of the nominal capacity. Therefore, a 10–16 kWh lithium-ion battery pack is very typical in many PHEVs under development.

The battery onboard a PHEV needs to be charged from the grid through either an onboard or offboard charger. For private vehicles, these PHEVs will be charged at home or a public charge station through either 110 or 220 V AC input. In order to make sure that the vehicle is ready for use by the second morning, the battery must be fully charged within a reasonable amount of time, typically 2–8 hours.

In the past few decades, various charging circuits have been developed targeting different applications, such as laptop computers, portable electronics, and uninterruptable power supplies (UPSs). Isolation is one of the basic requirements for all battery chargers for safety. The charging current is usually controlled by continuous feedback of critical battery parameters, such as battery voltage, the SOC, temperature, and so on. As far as the unidirectional charging system is concerned, chargers based on flyback and forward converters are typical examples for low-power applications. Both topologies need only one active switch. However, flyback and forward converters undergo HV spikes when the excessive energy stored in the leakage inductance of the isolation transformer is exhausted at the turn-off moment. Therefore, at higher power operations, an auxiliary snubber circuit is needed. Regardless of the limitations, flyback/forward topologies are being used in PHEV chargers.

Chargers based on half-bridge and full-bridge unidirectional DC–DC converters are favorable alternatives to chargers based on flyback and a forward converter. The magnetization of the isolation transformer in a half-bridge converter is bidirectional, therefore the demagnetizing circuit is eliminated. The leakage inductance of the transformer is a key parameter for energy transfer. The operation of a full-bridge DC–DC converter is similar to a half-bridge converter. The electrical stress of semiconductors in a half-bridge/full-bridge converter is significantly reduced. Soft switching is easy to implement in half-bridge/full-bridge converters. The disadvantages of these converters are the increased number of semiconductor switches.

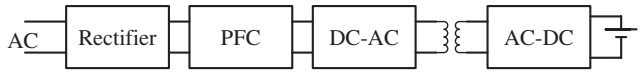

Figure 9.24 Basic PHEV charger architecture

Resonant converters can also be employed as battery chargers at extremely low cost. However, resonant chargers usually provide pulsed charge current, such as the case in inductive heating, other than constant current or constant voltage charging. The impact of pulsed current charging on battery capacity and life cycle is not fully understood at the present time.

Figure 9.24 shows the general architecture of a unidirectional PHEV battery charger. It consists of a front-end rectifier, a power factor correction (PFC) stage, and an isolated DC–DC stage.

9.10.1 Forward/Flyback Converters

Figures 9.25 and 9.26 show the circuit and operation of a forward and flyback converter respectively, where R is the battery internal resistance, E is the battery internal voltage, and V_o is the output voltage across the battery (including the battery internal voltage and voltage drop across the internal resistance). The operation of a forward converter is similar to that of a buck converter. When switch S_1 in Figure 9.25a turns off, the leakage inductance of the transformer will exhaust all the excessive energy through the switches. It therefore induces significant voltage spikes across the switches. The energy stored in the magnetizing inductance could be exhausted through the auxiliary winding shown in Figure 9.25a; however, the excessive energy in the leakage inductance of the transformer could only be mitigated through a snubber circuit, which is also needed in a flyback converter.

In the flyback converter shown in Figure 9.26a, when D_1 conducts, the load voltage will be induced to the primary side. Therefore, in the off-state of S_1, the voltage across S_1 is $V_{in} + V_o/n$, where n is the turns ratio of the isolation transformer. This indicates that although it may not be necessary to have a filtering inductor in the flyback converter, the semiconductor switch will in fact undergo higher voltage stress.

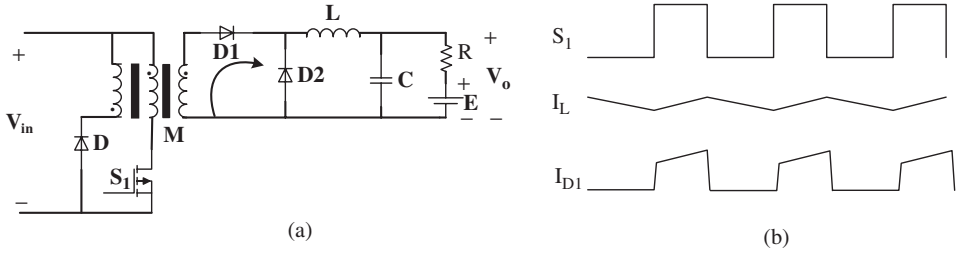

Figure 9.25 Forward converter: (a) Circuit topology; (b) operation waveforms

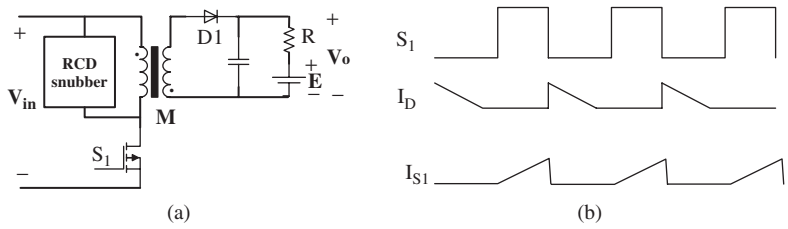

Figure 9.26 Flyback converters: (a) circuit topology; (b) operation waveforms

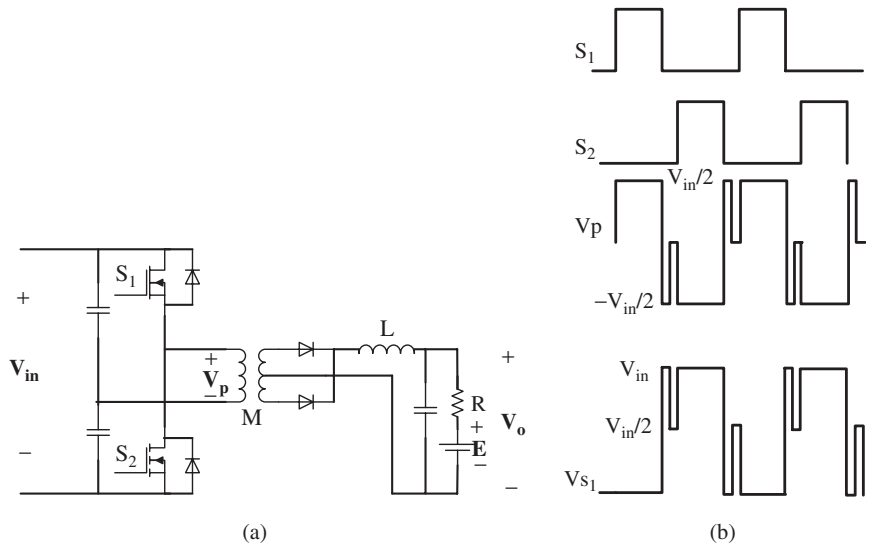

Figure 9.27 Half-bridge converter: (a) circuit topology; (b) operation waveforms

9.10.2 Half-Bridge DC–DC Converter

Figure 9.27 shows a half-bridge DC–DC converter. Switches S_1 and S_2 are switched with their phase shifted by 180°. The leakage inductance of the transformer serves as the component for energy transfer. If the parasitic inductance of the commutating loop is negligible, the voltage spike across the semiconductors will not be of concern.

9.10.3 Full-Bridge DC–DC Converter

Figure 9.28 shows the circuit topology and operation of a full-bridge DC–DC converter. Compared to the half-bridge converter where only half of the DC voltage is imposed on the primary side of the transformer in every switching cycle, the full-bridge converter utilizes the whole DC link voltage. Similar to a half-bridge converter, the leakage inductance of the transformer in a full-bridge converter does not contribute to any voltage spike

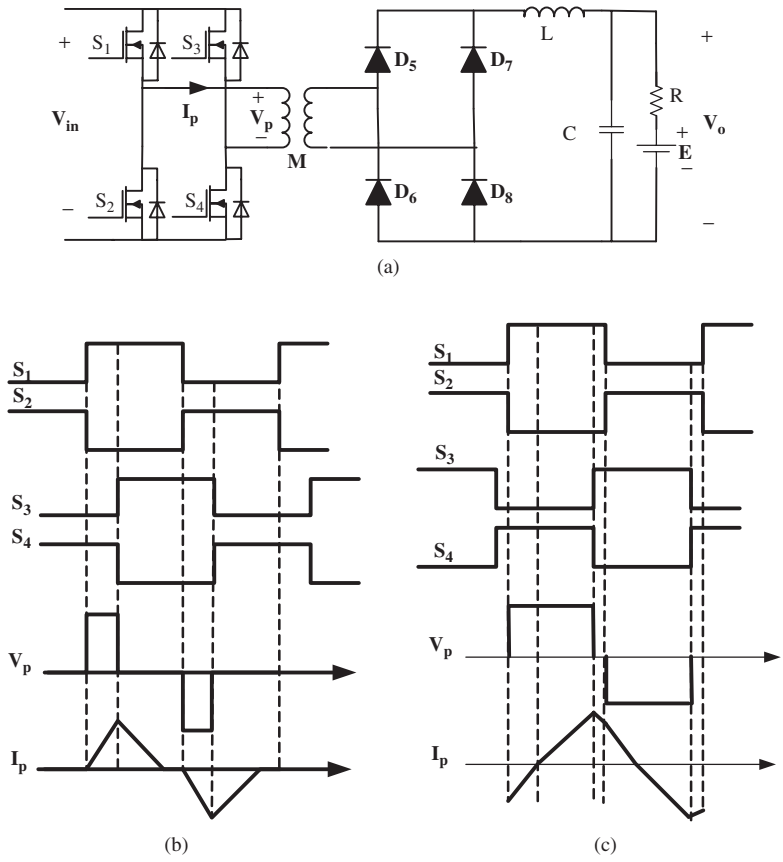

Figure 9.28 Full-bridge converter: (a) circuit topology; (b) discontinuous mode operation; (c) continuous mode operation

across the switches. This leakage inductance should be designed appropriately for best performance [13].

9.10.4 Power Factor Correction Stage

A PFC stage is usually placed between the rectifier and the DC–DC stage to avoid harmonics pollution to the grid as well as to stabilize the DC link voltage. A typical PFC circuit, shown in Figure 9.29, consists of an inductor L, an active switch S, and a freewheeling diode D. Bridgeless PFC circuits have also been used in battery chargers.

9.10.4.1 Decreasing Impact on the Grid

The AC grid side current with and without a PFC stage is shown in Figure 9.30, where the grid voltage is 110 V AC, and the output power of the charger is 5 kW.

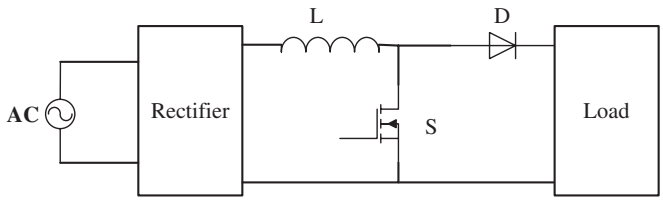

Figure 9.29 Power factor correction stage in a PHEV charger

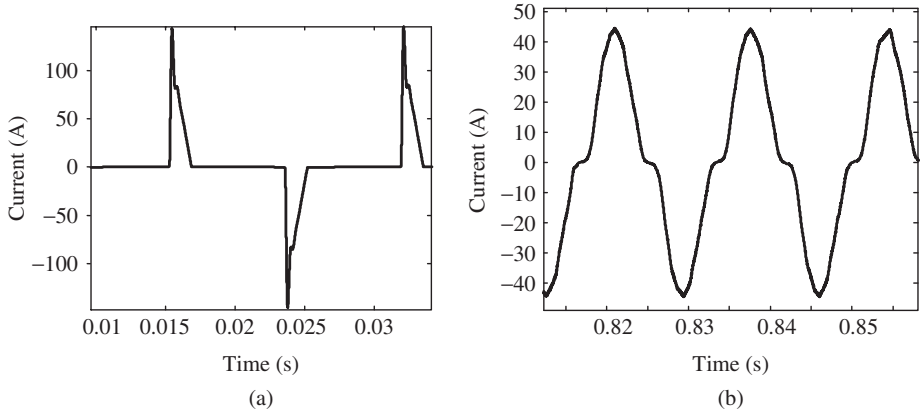

Figure 9.30 AC grid side current with and without PFC: (a) without PFC; (b) with a PFC

It can be seen from Figure 9.30 that with a PFC, the input current is much better. The current is close to sinusoidal and the current peak is significantly decreased. The impact of harmonic currents on the grid is mitigated. Also the primary diode rectifier will undergo smaller current stress. The power factor is close to 1.

9.10.4.2 Decreasing the Impact on the Switches

The PFC circuit also helps boost the DC link voltage to a higher level and stabilize the DC link voltage. Therefore, at the same output power, the current through the switches will be decreased to enhance safety and output capability. Figure 9.31a shows the switch current at different V_{in} with the same output power. When V_{in} is increased to 400 V DC, the switch current is significantly decreased. As long as the voltage across the switches does not exceed the breakdown value, higher DC bus voltage will lead to higher power capability for the same devices used. Figure 9.31b shows the maximum charging current that the system can deliver. Increasing the DC link voltage will benefit the output capability. Here the maximum repetitive switched-off current of the semiconductor switch is set to 70 A.

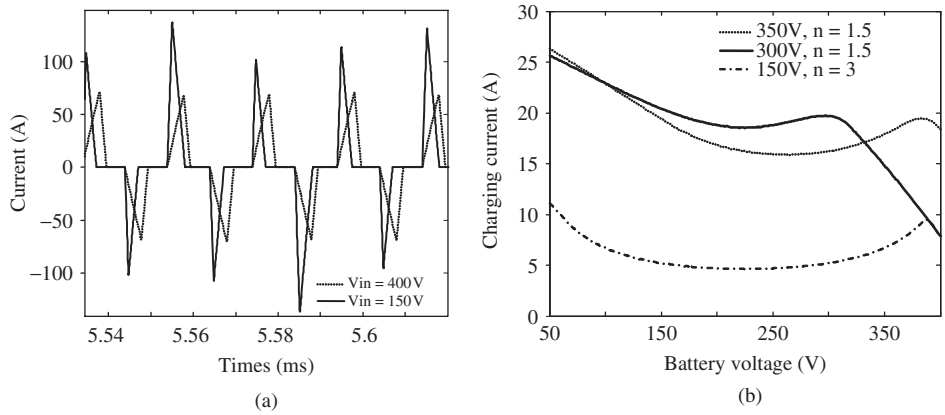

Figure 9.31 Comparison of the switch current without PFC: (a). comparison of switch current; (b) Maximum charging current under different V_{in}

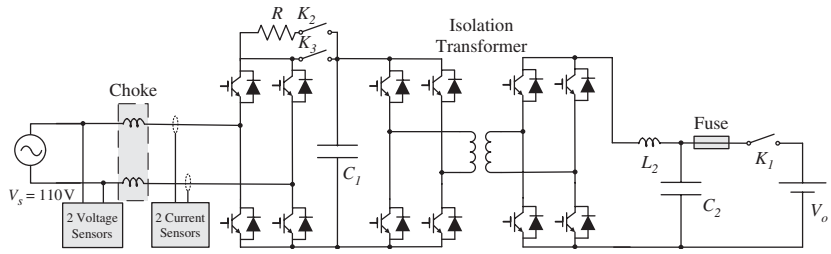

Figure 9.32 Isolation using a high-frequency transformer

9.10.5 *Bidirectional Battery Chargers*

It is possible to equip a PHEV with a bidirectional charger. With bidirectional power transfer capability, the energy stored in a PHEV battery can be sent back to the grid during peak demand hours for peak shaving of the AC electric grid, or to supply power to the home and office during a power outage.

The isolation can be achieved using high-frequency transformers in the DC–DC stage at high-frequency level as shown in Figure 9.32. The isolation can also be achieved using a transformer at the grid frequency level as shown in Figure 9.33. It is difficult to add a PFC stage to the bidirectional chargers but the AC side current can be controlled using the grid side inverter to limit the harmonics and improve power factor.

9.10.6 *Other Charger Topologies*

The above chargers are based on single-phase low-power inputs. In applications such as commercial transportation and recharge stations, it is necessary to quickly charge the

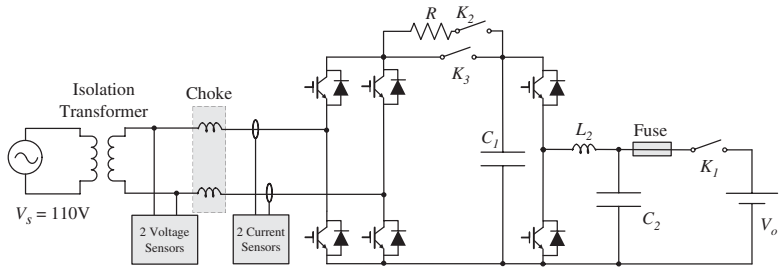

Figure 9.33 Isolation at the grid level with a line frequency transformer

battery in a relatively short time. For example, for a 16 kWh pack, to charge the battery from 30 to 80% SOC in 5 minutes will require 16 kWh × (80% – 30%)/(5/60) = 96 kW. Assuming that the battery is able to accept this type of charging, the charging power will have to be supplied. This is typically done through a three-phase high-power input.

Excessive heat may be generated during high-power fast charging of EV and PHEV batteries. The high charge rate may also impact the long-term capacity or life of the battery.

With more and more renewable energy and distributed generation, DC grids are starting to emerge. Almost all renewable sources, including solar and wind, can be in the form of DC. If a PHEV is connected to a DC grid, then the battery can be charged directly from the DC source. Traditional chargers designed for AC input can be used to take DC input, but a specially designed DC charger will have no need for the rectifier and PFC stage.

9.10.7 Inductive Charging

The above chargers all need an electrical contact with the electric outlet. This hard-wired electrical connection can provide a few caveats. For example, if the cable is pulled out of the electric outlet (whether intentional or unintentional) when the battery is still being charged, then there could be a spark and potential damage or injury. Another example is if somebody (such as children) could get hurt if they happen to play with the cords etc. Charging the vehicle when it is raining could be potentially dangerous. Wear and tear of the plug and cable could also be a source of danger.

Hence inductive charging becomes an alternative. In 1995, the US SAE Electric Vehicle Charging System Group, Japanese manufacturers including Toyota, Nissan, Honda, and DENSO, and IEC/ISO together developed the inductive charging standard SAE J1773. In 1999, SAE J1773 was enacted and recommended as an international standard (http://www.toyota.com). GM has already produced electric vehicles adopting inductive charging in GM's EV1 program in the 1990s. Since inductive charging does not involve direct contact of electricity, it is a safe and convenient way to charge an EV battery. The task can even be completed by a child for 50 kW inductive charging.

Inductive charging involves an isolation transformer where the secondary winding and core can be removed from the primary. Figure 9.34 shows the topology used in inductive chargers.

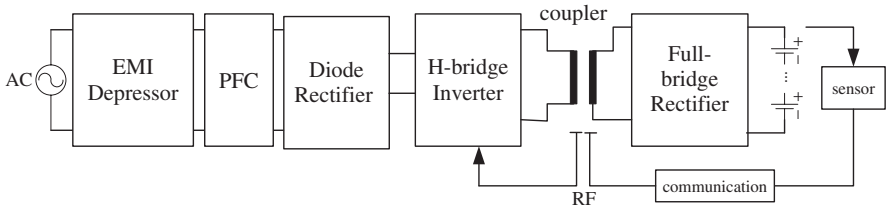

Figure 9.34 Isolated inductive charger

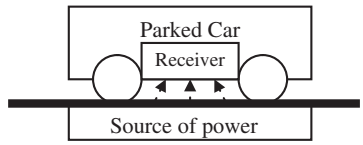

Figure 9.35 Wireless charging of a PHEV/EV on a parking floor

9.10.8 Wireless Charging

Wireless charging involves the use of power and energy transfer at a much longer distance. It is different from inductive charging which involves a transformer with closely placed primary and secondary windings. Although inductive charging can eliminate the direct electric contact, it still needs a plug, cable, and physical connection of the inductive coupler. Wear and tear of the plug and cable could cause danger as well.

Wireless charging could eliminate the cable and plug altogether. In this scenario, a driver can pull the car over to a specially designed parking lot and the car battery is automatically charged without the pulling of any cable or plug as shown in Figure 9.35. It provides the safest approach for EV battery charging.

There have been a few different experiments carried out for wireless energy transfer. The most promising technology is using electromagnetic resonance as shown in Figure 9.36. In this setup, there is a pair of antennas with one placed in the parking structure as the transmitter and one inside the car as the receiver. The two antennas are designed to resonate at the controlled frequency. The limitations are the level of power transfer, and efficiency due to the large air gap between the two antennas.

In the circuit shown in Figure 9.35, R_s is the internal impedance of the source and the resistance of the primary coil, R_o is the load resistance and the resistance of the secondary coil, L_l is the leakage inductance of the each coil, and L_m is the mutual inductance of the two coils. There are two ways to make the circuit resonant. If we design the circuit and select the frequency of the power supply V_1 such that

$$\omega L_l - \frac{1}{\omega C} = -2\omega L_m \tag{9.65}$$

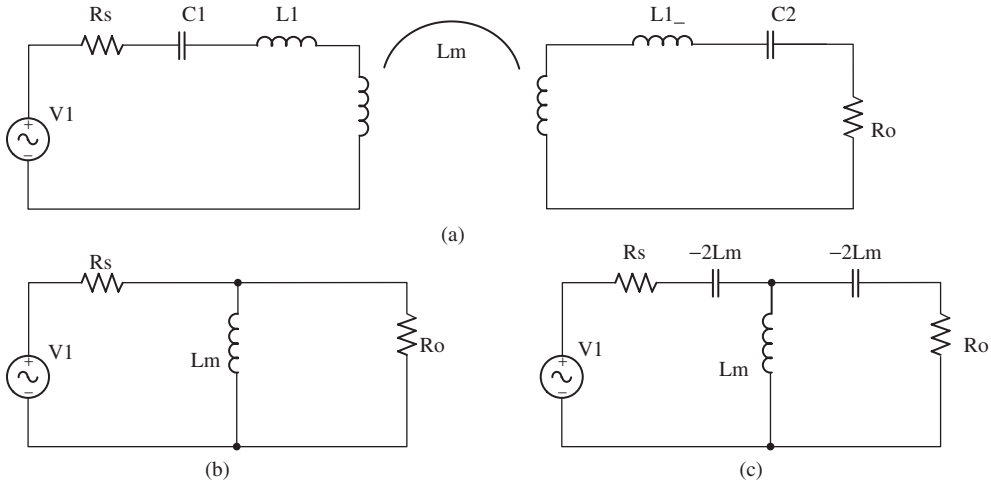

Figure 9.36 Circuits for electromagnetic resonance-based wireless charging: (a) circuit; (b) equivalent circuit at resonance frequency condition 1; (c) equivalent circuit at resonance frequency at condition 2

and the total equivalent impedance is

$$Z = R_s - \frac{j\omega L_m R_o}{R_o - j\omega L_m} \tag{9.66}$$

If we design

$$\omega L_l - \frac{1}{\omega C} = 0 \tag{9.67}$$

and the total equivalent impedance is

$$Z = R_s + \frac{j\omega L_m R_o}{j\omega L_m + R_o} \tag{9.68}$$

then the circuit will be in resonant. However, since both the mutual inductance and leakage inductance change with distance between the two coils, the frequency will have to be tuned based on the distance in real-world applications. Figure 9.36b,c shows the equivalent circuit during resonance of the two conditions. Figure 9.37 shows the simulation results of the circuit. The first plot shows two resonant frequencies. The second plot shows that when the distance between the two coils increases, the two resonant frequencies gets closer.

9.11 Modeling and Simulation of HEV Power Electronics

Modeling and simulation play important roles in the design and development of power electronics circuits. The simulation of power electronics circuits in hybrid vehicle

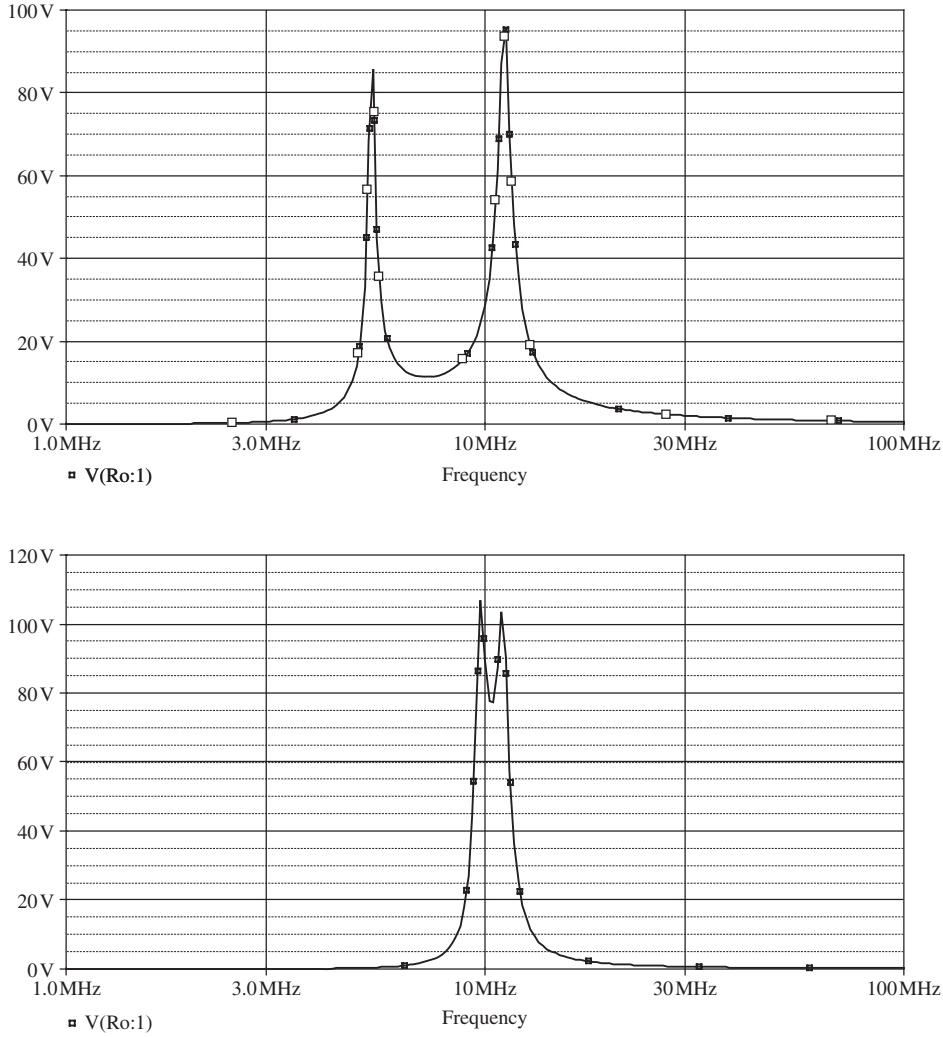

Figure 9.37 Resonance frequency of the wireless charging circuit: top, output voltage for shorter distance; bottom: output voltage for longer distance

applications can be divided into two categories: device-level simulations and system-level simulations [11, 25–29].

9.11.1 Device-Level Simulation

Device-level simulation can reveal the details of the device behavior. To obtain detailed loss data, overvoltages, and other component stresses due to the non-ideal nature of power electronics devices, and the stray inductance and capacitance of the circuitry, it is necessary to simulate a number of cycles of detailed switching pertaining to the worst case scenario.

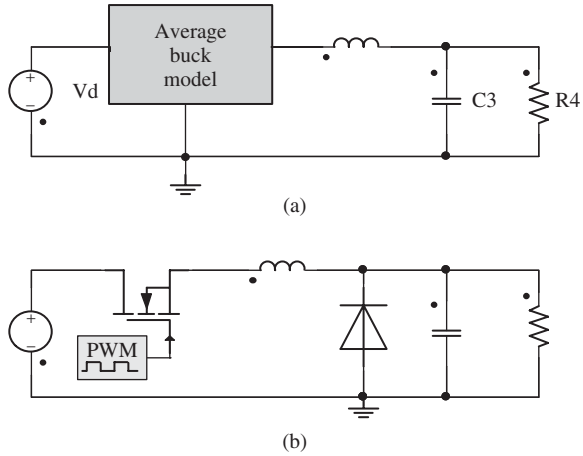

Figure 9.38 Device-level and system-level modeling of a buck converter. (a) System-level model only taking into account the non-linear characteristics of the inductor. (b) Device-level model involving detailed switching of the MOSFET

9.11.2 System-Level Model

Detailed device-level simulation can take a significant amount of time due to the high switching frequency used in the power electronics circuits, whereas the mechanical constants of the vehicle system could be a few seconds or more. Therefore, device-level simulation, although can simulate the dynamic performance of the circuit, is not suitable for simulating the vehicle performance, such as gradability, acceleration, and fuel economy. On the other hand, the electronics circuits have very fast transients, when compared to the vehicle dynamics.

In system-level simulations, the average model is generally used. For example, a buck converter can be represented in the simulation by an average model as shown in Figure 9.38a. A simulation of the system performance of one second only takes two seconds of simulation time, whereas in Figure 9.38b, which uses detailed device-level models, it takes about 20 minutes to obtain the system performance of one second.

9.12 Emerging Power Electronics Devices

The present silicon (Si) technology is reaching the material's theoretical limits and cannot meet all the requirements of hybrid vehicle applications in terms of compactness, light weight, high power density, high efficiency, and high reliability under harsh conditions. New semiconductor materials, such as silicon carbide (SiC), for power devices have the potential to eventually overtake Si power devices in hybrid vehicle powertrain applications [30–37].

SiC power devices potentially have much smaller switching and conduction losses and can operate at much higher temperature than comparable Si power devices. Hence, a SiC-based power converter will have a much higher efficiency than that of converters based on Si power devices if the same switching frequency is used. Alternatively, a

higher switching frequency can be used to reduce the size of the magnetic components in a SiC-based power converter. In addition, because SiC power devices can be operated at much higher temperatures without much change in their electrical properties, ease of thermal management and high reliability can be achieved.

9.13 Circuit Packaging

Electromagnetic interference (EMI) is one of the most challenging problems in power electronics circuits. The high switching frequency and high current generate electromagnetic fields that will permeate the other components in the vehicle system and create large electrical noise. In order to minimize EMI, components must be carefully placed so that EMI is not contained by shielding and will have minimal effect on the rest of the system. All paths must be kept as close as possible so that the generated fields will nullify one another. To minimize parasitics and aid in the EMI issue, the lengths of wires need to be kept as short as possible.

The control circuit needs to provide protection for overcurrent, short circuit, overvoltage, and undervoltage. The capability to detect any fault signal and turn off the gate drive signals to the primary switches is a critical part of power electronic circuit design. Fast fuses need to be used in the circuit to protect the converter from being damaged by any other faults and used for safety.

9.14 Thermal Management of HEV Power Electronics*

At power levels of 100 kW, even with an efficiency of 96–98%, the power losses of each power electronic unit is 2–4 kW. With two or three powertrain motors and associated power electronics circuits, together with the high-power bidirectional DC–DC converter, the heat generated in the hybrid vehicle system could be significant.

Significant advances in the thermal management of both power electronics and motors for HEV propulsion system must be achieved to meet the automotive industry's goals of reduced weight, volume, and cost [37–40]. Through the optimization of existing technologies and the expansion of new pioneering cooling methods, higher power densities, smaller volumes, and increased reliabilities can be realized in the hybrid powertrain components. Investigations and advances in thermal issues can provide a viable path to bridging gaps still plaguing the successful achievement of automotive technical targets while simultaneously enhancing the ability to apply new technologies in automotive applications as they mature.

Thermal performance of a power module is measured by the maximum temperature rise in the die at a given power dissipation level with a fixed heat sink temperature. The lower the die temperature, the better the electrical performance. As the thermal resistance from the junction of the die to the heat sink is reduced, higher power densities can be achieved for the same temperature rise, or for the same power density a lower junction temperature can be attained. It is important to reduce thermal cycling or maintain low ambient temperature to improve the life and reliability of the die.

The main areas of concern in thermal management of power electronics are: operating temperature of IGBTs (it should be less than 125 °C); contact resistance between various

* © [2007] Inderscience. Reprinted, with permission, from the International Journal of Electric and Hybrid Vehicles.

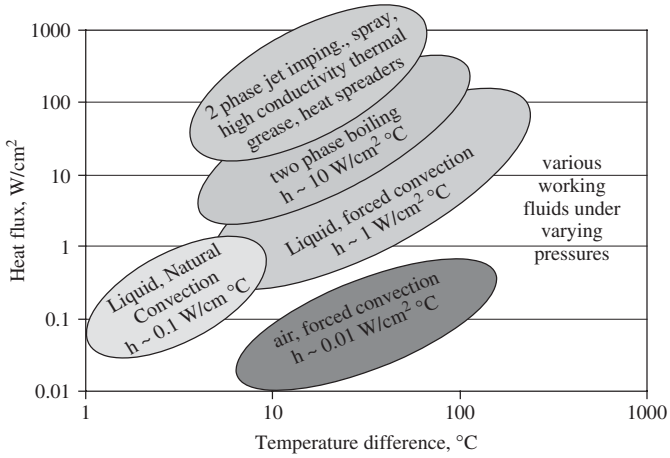

Figure 9.39 Existing cooling technologies

layers of a power module; low-thermal-conductivity thermal paste; heat flux limitations (ideally, faster IGBTs would have to reject heat at a rate of 250 W/cm^2); limitations on the inlet cooling fluid temperature (it is desirable to use the engine coolant at 105 °C); the cost of the cooling system; weight and volume.

The existing cooling technologies are depicted in Figure 9.39. It is shown that conventional cooling techniques such as forced convection and simple two-phase boiling techniques are not capable of removing high heat fluxes (in the range of 250 W/cm^2) at low temperature differences (20 °C). However, this figure shows clearly that employment of enabling technologies such as spray cooling and jet impingement along with some other innovative improvements will be able to meet the goals of the automotive industry.

Ideally, it would be more beneficial if IGBTs could be designed to operate at higher temperatures. The industry is pursuing various long-term research projects to evaluate and achieve that objective. However, to meet the immediate need of the automotive industry, existing IGBTs should be operated at temperatures below 125 °C.

The existing power modules are constructed by bonding together the die, copper layers, substrate, and the base plate. The whole module is then mounted on a heat sink using thermal grease or thermal pad. The existing thermal greases used by the industry that can stand high temperatures have very low conductivities on the order of 0.3–0.5 W/(m K). As a result of this low thermal conductivity, the thermal grease constitutes 30–40% of the total thermal resistance between the junction and the heat sink. Therefore it is crucial to reduce this resistance by increasing the thermal conductivity of the thermal grease. Figure 9.40 shows the impact of the conductivity of the thermal grease on the overall temperature difference between the junction and the heat sink. For a thermal conductivity of 0.5 W/(m K), the temperature difference is about 65 °C. If the thermal conductivity of the thermal grease is doubled to 1.0 W/(m K), the maximum temperature difference can be reduced to 35 °C.

To improve the power density of power modules, higher heat fluxes should be removed from the module because of increased switching frequencies. An important approach for

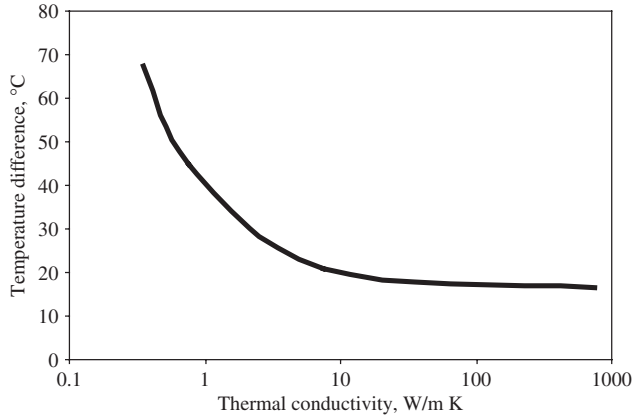

Figure 9.40 Impact of thermal interface material conductivity on temperature difference

removing higher heat fluxes from the IGBTs is to spread out their heat flux over a larger surface. The exiting copper or aluminum base plates spread the heat 20–30%, reducing the maximum heat flux by a corresponding amount. Use of more effective heat spreaders such as highly conductive metal layers, mini-heat pipes, and/or phase change materials inside the cold plate can spread out the high heat flux of the IGBTs over a larger surface area and reduce the maximum heat flux that needs to be removed by as much as 40%. This is a reduction of 50% in the maximum heat flux that needs to be removed and this requirement can be easily met by one of the enabling cooling technologies such as jet impingement and spray cooling currently being considered. Figure 9.41 shows the effect of utilizing a heat spreader that results in an additional 4–6 °C reduced temperature at the junction.

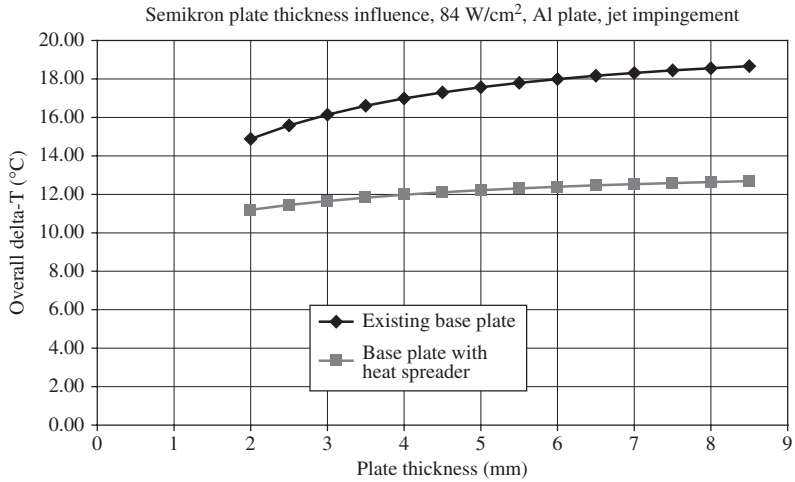

Figure 9.41 The impact of utilizing heat spreaders on junction temperature

One approach to maintaining the power module's temperature at 125 °C or below is to provide a separate cooling loop where the coolant can enter the heat sink at temperatures as low as 85 °C, hence providing an adequate temperature difference to maintain the IGBTs' temperature at the desired value while removing heat fluxes as high as 250 W/cm^2.

9.15 Conclusions*

This chapter presented an overview of the power electronics circuits for HEV applications with a focus on special circuit topologies, analysis, and thermal management. Novel power switching devices and power electronics systems have the potential to improve the overall performance of hybrid vehicles. Continued effort in power electronics circuit research and development will most likely be focused on innovative circuit topologies, optimal control, novel switching devices, and novel thermal management methods.

References

1. Bose, B.K. (2000) Energy, environment, and advances in power electronics. Proceedings of the International Symposium on Industrial Electronics, December, Vol. 1, pp. TU1–T14.
2. Jahns, T.M. and Blasko, V. (2001) Recent advances in power electronics technology for industrial and traction machine drives. *Proceedings of the IEEE*, **89**, 963–975.
3. Miller, J.M. (2003) Power electronics in hybrid electric vehicle applications. Proceedings of the 18th Applied Power Electronics Conference, February, Vol. 1, pp. 23–29.
4. Ehsani, M., Rahman, K.M., and Toliyat, H.A. (1997) Propulsion system design of electric and hybrid vehicles. *IEEE Transactions on Industrial Electronics*, **44**, 19–27.
5. Rahman, M.F. (2004) Power electronics and drive applications for the automotive industry, Proceedings of the Power Electronics Systems and Applications Conference, November, pp. 156–164.
6. Rajashekara, K. (2003) Power electronics applications in electric/hybrid vehicles. Proceedings of IECON'03, November, Vol. 3, pp. 3029–3030.
7. Emadi, A., Williamson, S.S., and Khaligh, A. (2006) Power electronics intensive solutions for advanced electric, hybrid electric, and fuel cell vehicular power systems. *IEEE Transactions on Power Electronics*, **21**, 567–577.
8. Hamilton, D.B. (1996) Electric propulsion power system - overview, *Power Electronics in Transportation*, pp. 21–28.
9. Vezzini, A. and Reichert, K. (1996) Power electronics layout in a hybrid electric or electric vehicle drive system. *Power Electronics in Transportation*, pp. 57–63.
10. Emadi, A., Ehsani, M., and Miller, J.M. (1999) Advanced silicon rich automotive electrical power systems. Proceedings of the Digital Avionic Systems Conference, October, Vol. 2, 8.B.1-1–8.B.1-8.
11. Amrhein, M. and Krein, P.T. (2005) Dynamic simulation for analysis of hybrid electric vehicle system and subsystem interactions, including power electronics. *IEEE Transactions on Vehicular Technology*, **54**, 825–836.
12. Namuduri, C.S. and Murty, B.V. (1998) High power density electric drive for an hybrid electric vehicle. Proceedings of the 13th Applied Power Electronics Conference, February, Vol. 1, pp. 34–40.
13. Xingyi, Xu (1999) Automotive power electronics - opportunities and challenges [for electric vehicles]. International Conference on Electric Machines and Drives, May, pp. 260–262.
14. Ehsani, M., Rahman, K.M., Bellar, M.D., and Severinsky, A. (2001) Evaluation of soft switching for EV and HEV motor drives. *IEEE Transactions on Industrial Electronics*, **48** (1), 82–90.
15. Marei, M.I., Lambert, S., Pick, R. *et al*. (2005) DC/DC converters for fuel cell powered hybrid electric vehicle. Vehicle Power and Propulsion Conference, September, pp. 126–129.
16. Katsis, D.C. and Lee, F.C. (1996) A single switch buck converter for hybrid electric vehicle generators. *Power Electronics in Transportation*, pp. 117–124.

17. Chan, C.C., Chau, K.T., Jiang, J.Z. *et al*. (1996) Novel permanent magnet motor drives for electric vehicles. *IEEE Transactions on Industrial Electronics*, **43**, 331–339.
18. Hayes, J.G. and Egan, M.G. (1999) A comparative study of phase-shift, frequency, and hybrid control of the series resonant converter supplying the electric vehicle inductive charging interface. 14th Applied Power Electronics Conference, March, Vol. 1, 450–457.
19. Krein, P.T., Roethemeyer, T.G., White, R.A., and Masterson, B.R. (1994) Packaging and performance of an IGBT-based hybrid electric vehicle. *Power Electronics in Transportation*, pp. 47–52.
20. Ehsani, M., Rahman, K.M., Bellar, M.D., and Severinsky, A.J. (2001) Evaluation of soft switching for EV and HEV motor drives. *IEEE Transactions on Industrial Electronics*, **48**, 82–90.
21. Tolbert, L.M., Peng, F.Z., and Habetler, T.G. (1998) Multilevel inverters for electric vehicle applications. *Power Electronics in Transportation*, pp. 79–84.
22. Di Napoli, A., Crescimbini, F., Rodo, S. *et al*. (2002) Multiple input DC-DC power converter for fuel-cell powered hybrid vehicles. 33rd Power Electronics Specialists Conference, June, pp. 1685–1690.
23. Solero, L., Lidozzi, A., and Pomilio, J.A. (2005) Design of multiple-input power converter for hybrid vehicles. *IEEE Transactions on Power Electronics*, **20**, 1007–1016.
24. Gargies, S., Wu, H., and Mi, C. (2006) Isolated bidirectional DC/DC converter for hybrid electric vehicle applications. 6th Intelligent Vehicle Symposium, June.
25. Onoda, S. and Emadi, A. (2004) PSIM-based modeling of automotive power systems: conventional, electric, and hybrid electric vehicles. *IEEE Transactions on Vehicular Technology*, **53**, 390–400.
26. Williamson, S., Lukic, M., and Emadi, A. (2006) Comprehensive drive train efficiency analysis of hybrid electric and fuel cell vehicles based on motor-controller efficiency modeling. *IEEE Transactions on Power Electronics*, **21**, 730–740.
27. Filippa, M., Chunting, M., Shen, J. *et al*. (2005) Modeling of a hybrid electric vehicle powertrain test cell using bond graphs. *IEEE Transactions on Vehicular Technology*, **54**, 837–845.
28. Mi, C., Hui, L., and Yi, Z. (2005) Iterative learning control of antilock braking of electric and hybrid vehicles. *IEEE Transactions on Vehicular Technology*, **54**, 486–494.
29. Hak-Geun, J., Bong-Man, J., Soo-Bin, H. *et al*. (2000) Modeling and performance simulation of power systems in fuel cell vehicle. Proceedings of IPEMC 2000, August, **2**, 671–675.
30. Johnson, R.W., Evans, J.L., Jacobsen, P. *et al*. (2004) The changing automotive environment: high-temperature electronics. *IEEE Transactions on Electronics Packaging Manufacturing*, **27**, 164–176. See also *IEEE Transactions on Components, Packaging and Manufacturing Technology, Part C: Manufacturing*.
31. Ozpineci, B., Tolbert, L.M., Islam, S.K. *et al*. (2001) Effects of silicon carbide (SiC) power devices on HEV PWM inverter losses. **2**, 1061–1066.
32. Kelley, R., Mazzola, M.S., and Bondarenko, V. (2006) A Scalable SiC Device for DC/DC Converters in Future Hybrid Electric Vehicles, p. 4.
33. Ozpineci, B., Tolbert, L.M., Islam, S.K. *et al*. (2002) Testing, characterization, and modeling of SiC diodes for transportation applications. 33rd Power Electronics Specialists Conference, June, pp. 1673–1678.
34. Dreike, P.L., Fleetwood, D.M., King, D.B. *et al*. (1994) An overview of high-temperature electronic device technologies and potential applications. *IEEE Transactions on Components, Packaging, and Manufacturing Technology, Part A*, **17**, 594–609. [see also IEEE Transactions on Components, Hybrids, and Manufacturing Technology].
35. Ozpineci, B., Chinthavali, M.S., and Tolbert, L.M. (2005) A 55 kW three-phase automotive traction inverter with SiC Schottky diodes. Vehicle Power and Propulsion Conference, September, p. 6.
36. Ohashi, H. (2003) Power electronics innovation with next generation advanced power devices. International Telecommunications Energy Conference, October, pp. 9–13.
37. Traci, R.M., Acebal, R., and Mohler, T. (1999) Integrated thermal management of a hybrid electric vehicle. *IEEE Transactions on Magnetics*, **35**, 479–483.
38. Alaoui, C. and Salameh, Z.M. (2005) A novel thermal management for electric and hybrid vehicles. *IEEE Transactions on Vehicular Technology*, **54**, 468–476.
39. White, S.B., Gallego, N.C., Johnson, D.D. *et al*. (2004) Graphite foam for cooling of automotive power electronics. *Power Electronics in Transportation*, pp. 61–65.
40. Tatoh, N., Hirose, Y., Nagai, M. *et al*. (2000) Thermal management analysis of high-power electronic modules using Cu bonded AlN substrates. International Conference on Thermal and Thermomechanical Phenomena in Electronic Systems, May, Vol. 2, pp. 297–302.

10

Electric Machines and Drives in HEVs

10.1 Introduction

Advances in electric machines, along with progress in power electronics, are the key enablers for electric, hybrid electric, and plug-in hybrid electric vehicles (HEVs). Induction machines, permanent magnet (PM) synchronous machines, PM brushless DC machines, and switched reluctance machines (SRMs) have all been considered in various types of vehicle powertrain applications [1–20]. Brushed DC motors, once popular for traction applications such as in streetcars, are no longer considered a proper choice due to the bulky construction, low efficiency, the need for maintenance of the brush and commutator, high electromagnetic interference (EMI), low reliability, and limited speed range.

When using electric motors for powertrain applications, there are a few possible configurations. Today's electric motors, combined with inverters and associated controllers, have a wide speed range for constant torque operations, and an extended speed range for constant power operations, which make the design of the powertrain much easier. Depending on the configuration of the hybrid powertrain, the design and selection of electric motor drives can also be different. For example, for series hybrid vehicles, the powertrain motor needs to be able to provide the required torque and speed for all driving conditions. Hence, the size of the motor will be fairly large, usually rated at 100 kW or more for passenger cars. A PM motor or an induction motor is the preferred choice. For mild and micro hybrids, only a small-size motor of a few kilowatts is required. Therefore the motor can be a claw pole DC motor, or a switched reluctance motor.

Traditional automatic transmission or continuous variable transmission (CVT) used in conventional cars are no longer required in electric vehicles (EVs) and many HEVs. However, a fixed gear ratio speed reduction is often necessary. This is due to the fact that a high-speed motor has smaller size and less weight than a low-speed machine. A two-speed automatic transmission may be beneficial in saving vehicle energy consumption.

Hybrid Electric Vehicles: Principles and Applications with Practical Perspectives, First Edition.
Chris Mi, M. Abul Masrur and David Wenzhong Gao.

Electric motors are extensively discussed in various textbooks and many technical publications. In this chapter, we will focus on a few unique aspects of electric motors that are specific to traction applications.

10.2 Induction Motor Drives

Induction motors are popular choices for traction applications due to their robust construction, low cost, wide field weakening range, and high reliability. Especially for EVs, PHEVs, and HEVs that requires a high-power motor, induction motors can provide more reliable operation than other types of electric motors [21–37]. However, when compared to PM motors, induction motors have lower efficiency and less torque density.

Typical induction motors used for traction applications are squirrel cage induction motors. An inverter is used to control the motor so that the desired torque can be delivered for a given driving condition at a certain speed. Advanced control methodologies, such as vector control, direct torque control, and field-oriented control, are popular in induction motor control for traction applications.

10.2.1 Principle of Induction Motors

The basic structure of an induction machine is shown in Figure 10.1. The two main parts of an induction motor are the stator (which houses the winding) and the rotor (which houses the squirrel cage). Both stator and rotor are made out of laminated silicon steel with thickness of 0.35, 0.5, or 0.65 mm. The laminated steel sheets are first stamped with slots and are then stacked together to form the stator and rotor, respectively. Windings are put inside the stator slots while the rotor is cast in aluminum.

There are some additional components to make up the whole machine: the housing that encloses and supports the whole machine, the shaft that transfers torque, the bearing, an optional position sensor, and a cooling mechanism (such as a fan or liquid cooling tubes).

In Figure 10.1c, AX is phase a, BY is phase b, and CZ is phase c. The direction of the phase currents is for a particular moment $\omega t = 60$ electric degrees; "+" indicates positive and "–" indicates negative. It can be seen that conductor AZB forms one group and XCY forms another group. Together they create a magnetic field at 30° NW–SE. The direction of the field will change as the current changes over time.

The stator windings shown in Figure 10.1c are supplied with a three-phase AC sinusoidal current. Assume the amplitude of the currents is I_m amperes, and the angular frequency of the current is ω radians per second; then the three phase currents can be expressed as

$$\begin{aligned} i_a &= I_m \cos(\omega t) \\ i_b &= I_m \cos(\omega t - 120^\circ) \\ i_c &= I_m \cos(\omega t - 240^\circ) \end{aligned} \tag{10.1}$$

Since the currents of each of the three phases are functions of time, the direction of current as shown in Figure 10.1c will change with time. If we mark the direction of the current at any given time, we can see the magnetic field generated by the stator current with its peak changing position over time.

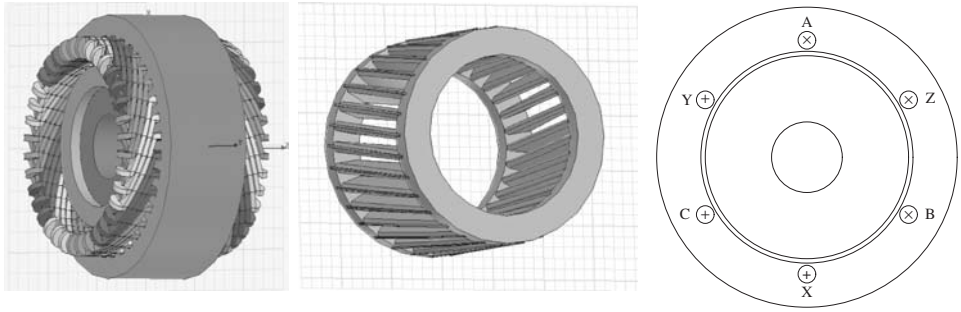

(a) (b) (c)

Figure 10.1 An induction motor: (a) rotor and stator assembly; (b) rotor squirrel cage; and (c) cross-sectional view of an ideal induction motor with six conductors on the stator

Mathematically, we can derive this magnetic field. Each of the three-phase currents will generate a magnetic field. Since the three windings are located 120° from each other in space along the inside surface of the stator, the field generated by each phase can be written as follows, assuming the spatial magnetic field distribution in the air gap due to winding currents is sinusoidal by design:

$$\begin{aligned} B_a &= K i_a(t)\cos(\omega t) \\ B_b &= K i_b(t)\cos(\omega t - 120^\circ) \\ B_c &= K i_c(t)\cos(\omega t - 240^\circ) \end{aligned} \tag{10.2}$$

where K is a constant. Using Equations 10.1 and 10.2, considering that $\cos(\omega t)\cos(\theta) = [\cos(\omega t - \theta) + \cos(\omega t + \theta)]/2$ and $\cos(\omega t + \theta) + \cos(\omega t + \theta - 240^\circ) + \cos(\omega t + \theta - 480^\circ) = 0$, we get

$$\begin{aligned} B_{gap} &= K i_a(\omega t)\cos(\theta) + K i_b(\omega t - 120^\circ)\cos(\theta - 120^\circ) + K i_c(\omega t - 240^\circ)\cos(\theta - 240^\circ) \\ &= \frac{3}{2} K I_m \cos(\omega t - \theta) + \frac{1}{2} K I_m [\cos(\omega t + \theta) + \cos(\omega t + \theta - 240^\circ) \\ &\quad + \cos(\omega t + \theta - 480^\circ)] \\ &= B_m \cos(\omega t - \theta) \end{aligned} \tag{10.3}$$

Equation 10.3 shows that the magnetic field is a traveling wave along the inner surface of the stator. In other words, the total magnetic field is a sinusoidal field with its peak rotating at angular speed ω rad/s.

Since $\omega = 2\pi f$, the rotating speed of the field will be the same as the supply frequency: f revolutions per second or $n_S = 60f$ revolutions per minute (rpm). Noting that the above derivation is based on one pair of poles, a more generic equation for the field speed (or synchronous speed) of an induction machine can be given as

$$n_S = \frac{60f}{p} \quad \text{and} \quad \omega_S = \frac{2\pi n_S}{60} = \frac{2\pi f}{p} = \frac{\omega}{p} \tag{10.4}$$

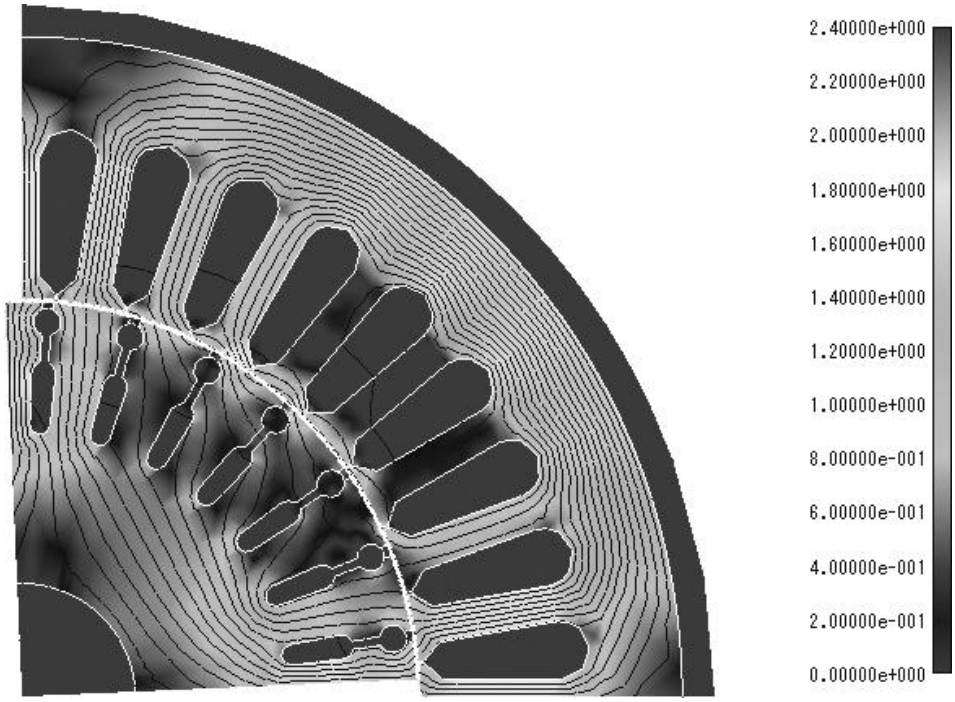

Figure 10.2 The flux distributions of a four-pole induction motor during transient finite element analysis

where p is the number of pairs of poles. Figure 10.2 shows the arrangement of a four-pole squirrel-cage induction motor with flux distribution.

Assuming initially that the rotor is stationary, an electromotive force (emf) will be induced inside the rotor bars of the squirrel cage. A current is therefore formed inside the rotor bars through the end rings. Similarly, since the field is rotating, this current will generate a force on the rotor bars (the rotor bar current is under the stator magnetic field). If the force (or torque) is sufficiently large, the rotor will start to rotate.

The maximum speed of the rotor will be less than the synchronous speed because, if the rotor reaches the synchronous speed, there will be no relative movement between the rotor bars and the stator field, hence no emf or force will be generated. The difference between the rotor speed and the synchronous speed is defined as slip s, that is, $s = (n_S - n_m)/n_S = (\omega_S - \omega_m)/\omega_S$, where n_m and ω_m are the rotor speeds in rpm and radians per second, respectively. Typical slips of induction motors are within 1–3%.

10.2.2 Equivalent Circuit of Induction Motor

We can represent the induction motor by two separate circuits, one for the stator and one for the rotor. Since the three phases are symmetrical, we only need to analyze one phase as shown in Figure 10.3. We use phasors for the analysis of the AC circuit. Here we have defined the direction of current flow using the transformer convention. It is worth noting

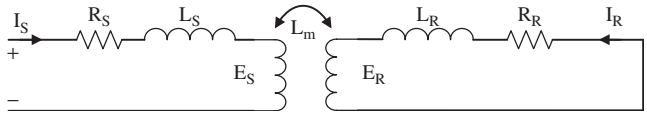

Figure 10.3 Stator and rotor circuits of an induction machine

that the rotor and the stator quantities will have different frequencies except when the rotor is stationary.

The voltage equation of the primary and the secondary circuit can be written as

$$\begin{aligned} V_S &= I_S R_S + j\omega L_S I_S + E_S \\ 0 &= I_R R_R + j\omega_R L_R I_R + E_R \end{aligned} \tag{10.5}$$

where V is the phase voltage, I the phase current, R the phase resistance, and L the leakage inductance of the winding. The subscripts S and R represent the stator and rotor respectively.

Since the field is rotating at synchronous speed ω_S and the rotor is rotating at speed ω_m, the speed of the magnetic field relative to the rotor bar is $\omega_S - \omega_m = s\omega_S = s\omega/p$, and $\omega_R = ps\omega_S = s\omega$ is the frequency of the rotor current.

If we multiply k and divide s for the both sides of the second equation in Equation 10.5, then we get

$$0 = \left(k^2 \frac{R_R}{s}\right)(I_R/k) + j\left(k^2 \frac{\omega_R}{s} L_R\right)(I_R/k) + \frac{kE_R}{s} \tag{10.6}$$

The rotor has AC quantities at slipping frequency $\omega_R = s\omega$. By using the following, $R'_R = k^2 R_R$, $X'_R = k^2 \omega L_R = k^2 X_R$, $I'_R = I_R/k$, $E'_R = kE_R/s$, we have

$$0 = R'_R I'_R + jX'_R I'_R + E'_R \tag{10.7}$$

We will choose k such that $E_S = E'_R$. We can then redraw the equivalent circuit of the induction motor as shown in Figure 10.4a. Here we neglected the magnetic loss in the stator core. If we include the magnetic loss, then the equivalent circuit can be illustrated as in Figure 10.4b.

In the above equivalent circuit, for a given voltage supply the current of the circuit can be written as

$$I_S = \frac{V_S}{R_S + j\omega L_S + (R_m + jX_m)||(R'_R/s + jX'_R)} \tag{10.8}$$

To simplify the analysis, we can neglect $R_m + j\omega X_m$. Under this assumption, the electromagnetic power transferred from the stator to the rotor is

$$P_{em} = mI_S^2 \frac{R'_R}{s} = \frac{mV_S^2}{(R_S + R'_R/s)^2 + (X_S + X'_R)^2} \frac{R'_R}{s} \tag{10.9}$$

Noting that electromagnetic power or rotor power has two parts, namely, the loss of the rotor winding and power transferred to its shaft, the above equation can be rewritten as

$$P_{em} = \frac{mV_S^2}{(R_S + R'_R/s)^2 + (X_S + X'_R)^2} \left[R'_R + \frac{(1-s)}{s} R'\right]_R \tag{10.10}$$

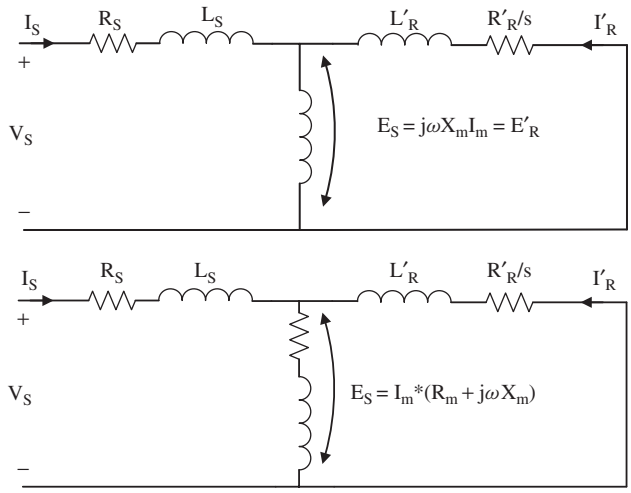

Figure 10.4 Modified equivalent circuit of an induction machine: top, neglecting iron loss; bottom, considering iron loss

The first term represents the rotor copper loss and the second term the mechanical power on the shaft. The electromagnetic torque of the motor can be written as follows:

$$\begin{aligned} T_{em} &= \frac{m}{\omega_S} \frac{V_S^2}{(R_S + R'_R/s)^2 + (X_S + X'_R)^2} \frac{1}{s} R'_R \\ &= \frac{m}{\omega_m} \frac{V_S^2}{(R_S + R'_R/s)^2 + (X_S + X'_R)^2} \frac{(1-s)}{s} R'_R \end{aligned} \tag{10.11}$$

We can plot torque T_{em} as a function of slip s from Equation 10.11 and obtain the torque–speed characteristics of an induction motor as shown in Figure 10.5.

10.2.3 Speed Control of Induction Machine

The speed of an induction motor, in rpm, can be expressed as

$$n = (1-s)n_S = (1-s)\frac{60f}{p} \tag{10.12}$$

Hence, we will have three approaches for changing the speed of an induction motor: change the number of poles, change frequency, and change slip:

1. **Change the number of poles:** The stator winding is designed such that, by changing the winding configuration, the number of poles will change. For example, some induction motors are designed as 4/6, 6/8, or 4/8 pole capable. While changing the number of poles has been used in controlling the induction motor speed in the past, it is used less and less today due to the complexity of the stator winding configuration and low efficiency.

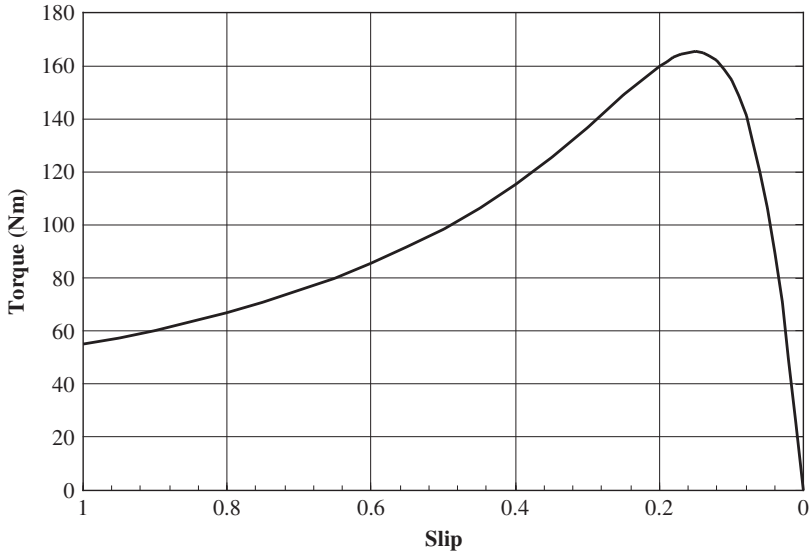

Figure 10.5 The torque–speed characteristics of an induction motor for a constant frequency and constant voltage supply

2. **Change the frequency of the supply voltage:** This is the most popular method for controlling induction motor speed in modern drive systems, including traction drives. This will be discussed in more detail in the next section.
3. **Change slip:** Since the electromagnetic torque of an induction motor is closely related to slip as shown in Equation 10.11, there are a few ways to change the slip to control induction motor speed:
   (a) **Change the magnitude of the supply voltage:** As shown in Figure 10.6, as the voltage is changed, the speed of the motor is also changed. However, this method provides limited variable speed range since the torque is proportional to the square of voltage.
   (b) **Change stator resistance or stator leakage inductance:** This can be done by connecting a resistor or inductor in series with the stator winding.
   (c) **Change rotor resistance or rotor leakage inductance:** This is only applicable to wound-rotor induction motors.
   (d) **Apply an external voltage to the rotor winding:** This voltage has the same frequency as the rotor back emf or rotor current. Modern, doubly fed wind power generators belong to this group. This method is only applicable to wound-rotor induction motors.

When an external resistance is in series with the stator or rotor winding, there is loss associated with this resistor. Hence the system efficiency is compromised. When an external inductor is in series with the stator or rotor, the power factor is compromised. Hence, adding resistance or inductance is no longer a popular method in modern electric drive systems.

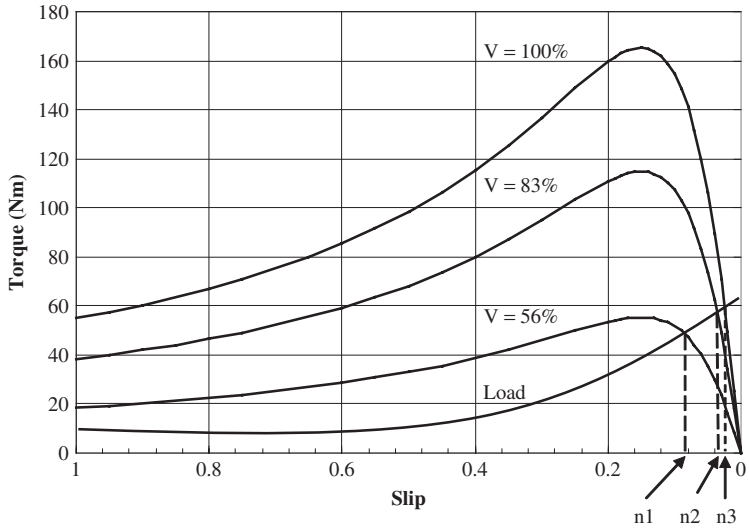

Figure 10.6 Adjusting the speed of an induction motor by varying the terminal voltage

10.2.4 Variable Frequency, Variable Voltage Control of Induction Motors

Varying the frequency of power supply is by far the most effective and most popular method to adjust the speed of an induction motor. If we neglect the stator resistance, leakage inductance, and the magnetic loss, the stator voltage equation can be written as

$$V_S = E_S = k_S \omega \phi = k_S 2\pi f \phi \tag{10.13}$$

where k_S is the machine constant and ϕ is the total flux. Hence, when changing the frequency, the stator voltage should also be changed proportionally in order to maintain a relatively constant flux so that the stator and rotor core do not get saturated, while the output torque can be maintained constant,

$$\frac{V_S}{f} = \text{constant} \tag{10.14}$$

When the frequency and voltage are adjusted, the torque–speed characteristics are as shown in Figure 10.7. Although the above expression is generally true, three observations can be made:

1. For low-frequency operations, the voltage drop across the stator resistance and inductance is no longer negligible. Hence, the stator voltage has to be increased to compensate this.
2. The motor speed corresponding to the rated frequency and rated voltage is called the rated speed or base speed.
3. When the stator voltage reaches its rated supply (maximum), in order to further increase frequency (or speed), the stator flux must be reduced in order to satisfy Equation 10.13

This is called the flux weakening operation. The ratio of the maximum speed to the rated base speed of the motor is defined as the adjustable speed range, or X. Modern induction motors can achieve up to $X = 5$ adjustable speed range.

10.2.5 *Efficiency and Losses of Induction Machine*

The losses in an induction machine are shown in Figure 10.8. The losses include: (i) copper loss in the stator winding; (ii) magnetic loss in the stator iron (or core loss, or iron loss); (iii) copper loss in the rotor winding; (iv) windage loss due to the rotation of the rotor and frictional loss in the bearing; and (v) additional losses that cannot be accounted for by the above components, also called additional loss or stray load loss.

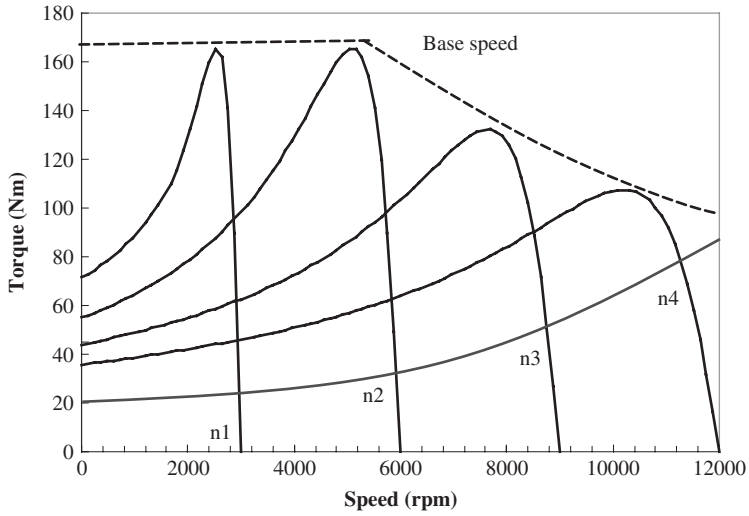

Figure 10.7 Adjusting induction motor speed using variable frequency supply. In this example, the rated speed is 6000 rpm, and the maximum speed is 12 000 rpm. The adjustable speed range $X = 2$

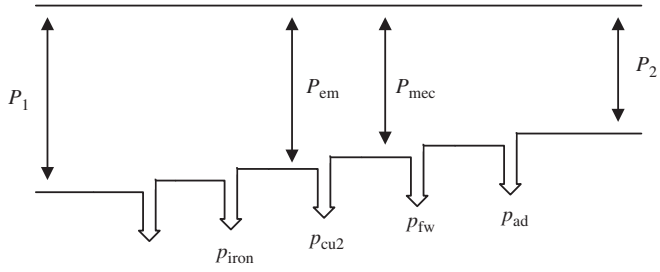

Figure 10.8 Losses in an induction motor

The power balance equations are

$$\begin{aligned} P_{em} &= P_1 - p_{cu1} - p_{iron} \\ P_{mec} &= P_{em} - p_{cu2} \\ P_2 &= P_{mec} - p_{fw} - p_{ad} \end{aligned} \tag{10.15}$$

P_1 is the input power from the voltage supply; P_{em} is the electromagnetic power transferred from the stator to the rotor; P_{mec} is the total mechanical power on the rotor shaft; P_2 is the output power to the load connected to the shaft; p_{cu1} is the copper loss of the stator winding; p_{iron} is the iron loss of the stator core; p_{fw} is the frictional and windage loss; and p_{ad} is the stray load loss.

The efficiency can be expressed as

$$\eta = \frac{P_2}{P_1} = \frac{P_2}{P_2 + p_{cu1} + p_{iron} + p_{cu2} + p_{fw} + p_{ad}} \tag{10.16}$$

One aspect of traction motors for modern HEVs is high-speed operation. Traditionally, laminated silicon steel sheets were designed for use at low frequencies (50 or 60 Hz), and today's traction drives typically operate at about 6000−15 000 rpm. With four-pole designs, the operating frequency is 500 Hz. Some traction motors operate at frequencies as high as 800–1200 Hz. Since eddy current loss and hysteresis loss are proportional to frequency or the square of frequency, the core loss will be significant at high frequencies. In order to keep the core loss within a reasonable range, the magnetic flux in the iron has to be relatively lower than those used in low-speed motors, and the thickness of the silicon steel sheets may have to be reduced as well.

Second, the inverter-operated induction motor will contain harmonics in its voltage and current. These harmonics will introduce additional losses in the winding and stator and rotor core. As is well known, the eddy current loss can be doubled in many induction motors due to the pulse-width-modulated (PWM) supply. These additional losses may cause excessive temperature rise which must be considered during the design and analysis of induction motors.

*10.2.6 Additional Loss in Induction Motors due to PWM Supply**

To analyze the additional losses in an induction motor due to PWM operations, we first take a look at the PWM waveform. The general principle of bipolar PWM supply is shown in Figure 10.9, where the triangular waveform (carrier, V_{tri}) of switching frequency f_c is compared to the control signal ($V_{control}$) of fundamental frequency f_1. The intersections of the two waveforms determine the switching points of power devices. The ratio of switching frequency f_c to fundamental frequency f_1 is defined as the frequency modulation ratio, $m_f = f_c/f_1$. The ratio of the amplitude of the control waveform $V_{control}$ to that of the triangle waveform V_{tri} is defined as the amplitude modulation ratio, $m_a = V_{control}/V_{tri}$ [38, 39].

There are many different methods to determine the switching points, such as the natural sampling rule, regular sampling, and the selected harmonic elimination rule, and so on.

* The permission is from Section 10.2.6 to Figure 10.12. © [2008] IEEE. Reprinted, with permission, from IEEE on Magnetics.

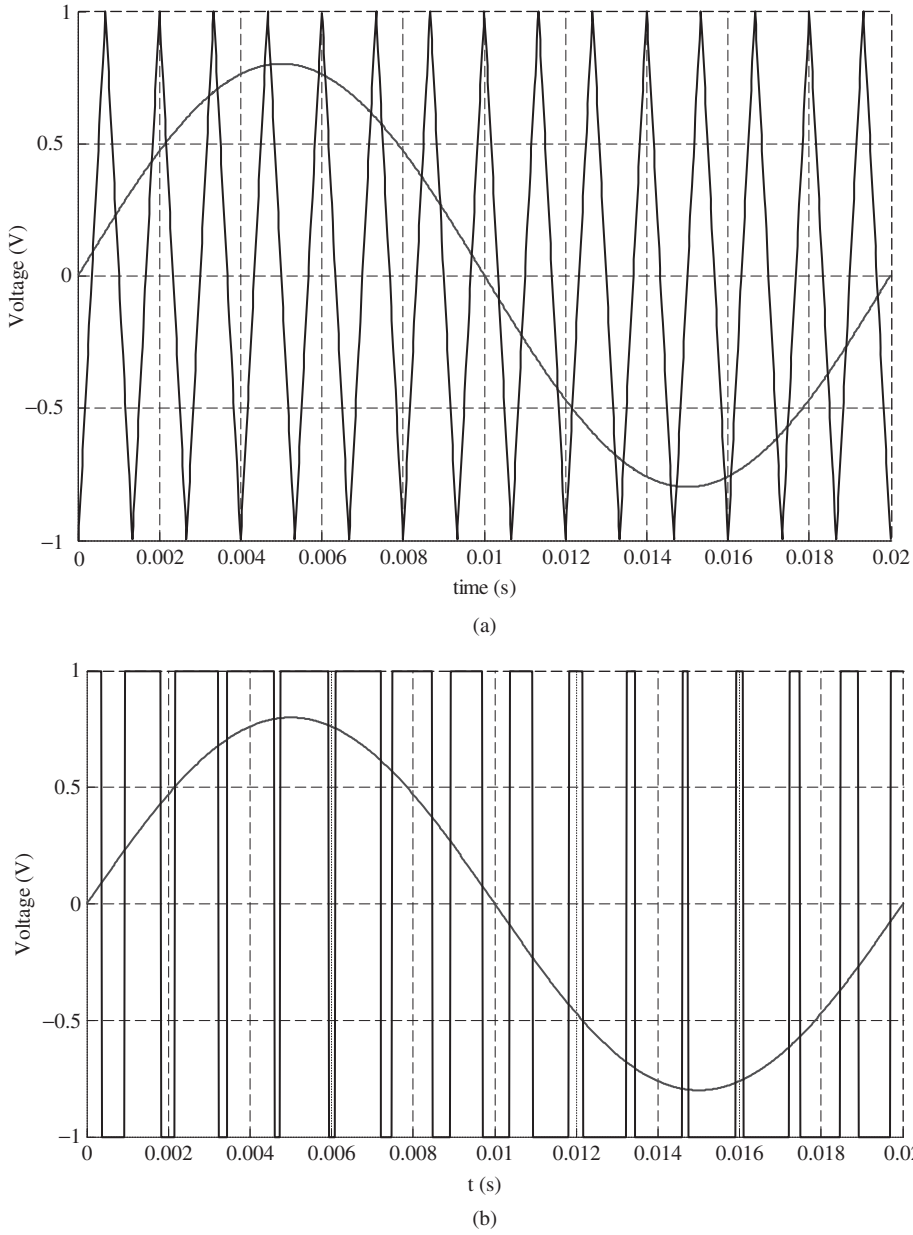

Figure 10.9 Principle of bipolar PWM supply ($m_a = 0.8$, $m_f = 15$, $f_1 = 50$ Hz): (a) carrier waveform V_{tri} and control waveform $V_{control}$; (b) PWM output and its fundamental component

The symmetrical regular sampling rule is a basic method in sampling. The switch points can be determined from Figure 10.9 for this sampling method:

$$\alpha_k = \frac{\pi}{2m_f}\left\{2k - 1 + (-1)^k m_a \sin\left[(k+m)\frac{\pi}{m_f}\right]\right\} \quad k = 1, 2, \ldots, 2m_f$$
$$\text{when } (-1)^k = 1, m = -1; \text{ when } (-1)^k = -1, m = 0 \tag{10.17}$$

where α_k is the switching point.

The output voltage of the inverter contains the fundamental voltage and other high-frequency harmonic voltages. The general Fourier series of the output voltage can be given as follows:

$$v(t) = \sum_{n=1}^{\infty} v_n(t) = \sum_{n=1}^{\infty} (a_n \cos n\omega t + b_n \sin n\omega t) = \sum_{n=1}^{\infty} V_n \sin(n\omega t + \varphi_n) \tag{10.18}$$

where ω is the fundamental angular frequency, n is the order of harmonics, V_n is the amplitude of the nth harmonic, a_n and b_n are the Fourier coefficients; φ_n is the phase angle of the nth harmonic, and

$$a_n = \frac{V_{dc}}{n\pi}\sum_{k=1}^{2m_f} (-1)^k \sin(n\alpha_k) \tag{10.19}$$

$$b_n = \frac{V_{dc}}{n\pi}\sum_{k=1}^{2m_f} (-1)^k \cos(n\alpha_k) \tag{10.20}$$

$$V_n = \sqrt{a_n^2 + b_n^2} = \frac{V_{dc}}{n\pi}\sqrt{\left[\sum_{k=1}^{2R} (-1)^k \cos(n\alpha_k)\right]^2 + \left[\sum_{k=1}^{2R} (-1)^{k+1} \sin(n\alpha_k)\right]^2} \tag{10.21}$$

$$\varphi_n = \arctan\left(\frac{b_n}{a_n}\right) \tag{10.22}$$

where V_{dc} is the DC link voltage.

According to Equation 10.21, the amplitude of the harmonics is dependent on the DC link voltage V_{dc}, the order of the harmonic waveform n, and the switching points α_k. These switching points are determined from the frequency modulation ratio m_f and amplitude modulation ratio m_a. Figure 10.10 shows the harmonic spectrum of the PWM output waveform for $m_f = 15$ and $m_a = 0.8$. The PWM output wave contains carrier frequency-related harmonics with modulation frequency-related sidebands in the form of $mf_c \pm nf_1$, where m and n are integers and $m + n$ is an odd integer.

The total iron loss density p_{iron} is commonly expressed in the following form for sinusoidal varying magnetic flux density B with angular frequency ω [40]:

$$p_{iron} = p_h + p_c = k_h B^{\beta}\omega + k_c B^2\omega^2 \ (\text{W/m}^3) \tag{10.23}$$

where p_h and p_c are the hysteresis loss density and the classical eddy current loss density respectively, k_h and k_c are the hysteresis and eddy current constants respectively, and

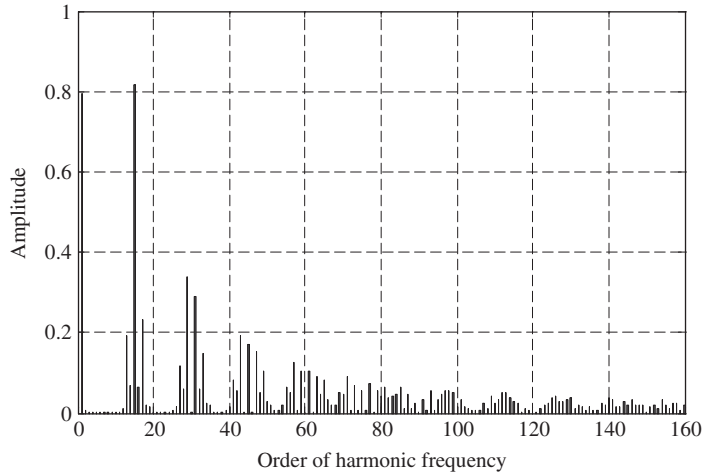

Figure 10.10 Harmonic frequency analysis of output voltage

β is the Steinmetz constant – all of which depend on the lamination material. Because the heavy iron loss increase in the case of PWM supply is mainly induced by the eddy current loss increment, this section will focus on the analysis of the eddy current loss.

Equation 10.23 is only valid for flux densities under sinusoidal time-varying conditions. Under PWM supply, there are many high-frequency harmonic flux density components. With the assumption of a linear material, the flux density harmonic amplitude is proportional to the voltage harmonic amplitude. So the harmonic components of the PWM voltage output can be analyzed, and the eddy current loss of each harmonic component can be calculated. Although such an assumption is not in accordance with the magnetic property of the core material, considering that the objective here is to compare the iron losses influenced by PWM supply, the absolute error caused by the assumption does not affect the final results.

In order to give a clear view of the iron losses associated with the PWM parameters, a single phase was used. Under no-load condition (rotor winding open-circuit condition), the circuit equation is

$$v(t) = e(t) + i(t)R + L_\sigma \frac{di(t)}{dt} \tag{10.24}$$

where $v(t)$ is the applied voltage, $e(t)$ is the back emf, $i(t)$ is the current, L_σ is the leakage inductance of the stator winding, and R is the resistance of the stator winding.

When neglecting the voltage drop on winding resistor R and leakage inductance L_σ,

$$v(t) \approx e(t) = N_1 \frac{d\Phi(t)}{dt} = N_1 A \frac{dB(t)}{dt} \tag{10.25}$$

where N_1 is the number of turns of the winding and A is the cross-sectional area of the core. Under the linear material assumption, the flux density is

$$B(t) = -\sum_{n=1}^{\infty} B_n \cos(n\omega t + \varphi_n) \tag{10.26}$$

where B_n is the flux density of the nth harmonic

$$B_n = \frac{V_n}{N_1 An\omega} \tag{10.27}$$

The eddy current loss can then be obtained by substituting Equation 10.27 into Equation 10.23:

$$p_c = \sum_{n=1}^{\infty} p_n = \sum_{n=1}^{\infty} k_c B_n^2 (n\omega)^2 = \sum_{n=1}^{\infty} k_c \left(-\frac{V_n}{N_1 An\omega}\right)^2 (n\omega)^2$$
$$= \frac{k_c}{(N_1 A)^2} \sum_{n=1}^{\infty} (V_n)^2 \tag{10.28}$$

Combining Equations 10.18 and 10.26, the eddy current losses can be derived as

$$p_c = \frac{k_c}{(N_1 A\pi)^2} \sum_{n=1}^{\infty} \left(\frac{V_{dc}}{n}\right)^2 \left\{ \left[\sum_{k=1}^{2R} (-1)^k \cos(n\alpha_k)\right]^2 + \left[\sum_{k=1}^{2R} (-1)^k \sin(n\alpha_k)\right]^2 \right\} \tag{10.29}$$

$$p_c = K \sum_{n=1}^{\infty} \left(\frac{V_{dc}}{n}\right)^2 \left\{ \left[\sum_{k=1}^{2R} (-1)^k \cos(n\alpha_k)\right]^2 + \left[\sum_{k=1}^{2R} (-1)^k \sin(n\alpha_k)\right]^2 \right\} \tag{10.30}$$

where

$$K = \frac{k_c}{(N_1 A\pi)^2}$$

From the above equations, it can be concluded that the eddy current loss is related to the amplitude of the fundamental and other high-order harmonics. Furthermore, it is related to the switching points α_k and DC link voltage V_{dc}. Switching point α_k is related to the sampling method of switching points. If the regular sampling method is adopted, α_k is determined by the frequency modulation ratio and the amplitude modulation ratio. Each harmonic component will contribute to the total eddy current loss. According to Figure 10.10, the fundamental voltage and the harmonics at the switching frequency contribute more to the eddy current loss.

Figure 10.11 shows the eddy current loss versus switching frequency for an induction motor, where the eddy current loss ratio is defined as the loss from PWM supply to the loss of sinusoidal supply. It can be seen that the eddy current loss is more than doubled with PWM supply. Figure 10.12 shows the iron loss of a 2 kW, 208 V induction motor when operated at 80 V with respect to modulation ratio (the DC bus voltage is adjusted to maintain the fundamental voltage at 80 V). It can be seen that the iron loss increases with the reduction of modulation ratio. The iron loss increases as the amplitude modulation ratio decreases.

An experiment was carried out on a 3 hp induction motor. The motor is a four-pole, 60 Hz, 208 V, Y-connected, three-phase induction motor. Figure 10.13 shows the

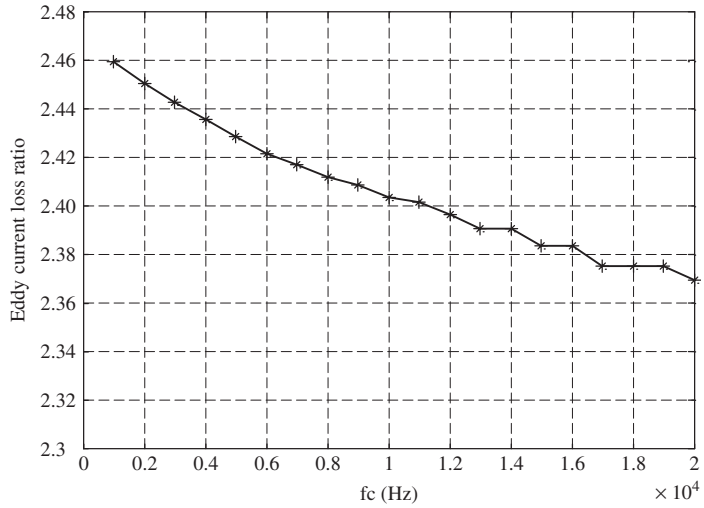

Figure 10.11 Eddy current loss ratio vs. switching frequency at $m_a = 0.9$

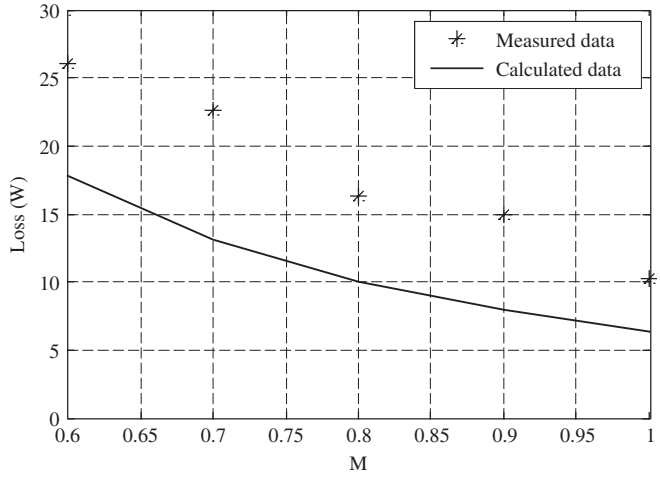

Figure 10.12 The effect of amplitude modulation ratio on PWM iron losses of induction motor for a 2 hp induction motor. (From [38])

cross-section of the machine. The machine has a double-layer, three-phase stator winding, with 36 slots in the stator and 24 slots in the rotor.

The experiment bench is shown in Figure 10.14, which includes the power supply, a unipolar PWM inverter, a power analyzer, an induction motor, a DC generator (as load), and a DC electronic load connected to the output of the DC generator. The solid line shows the induction motor is operated by the sinusoidal supply directly and the dotted line shows it is driven by the PWM inverter. The power analyzer is used to capture the line voltage and phase current.

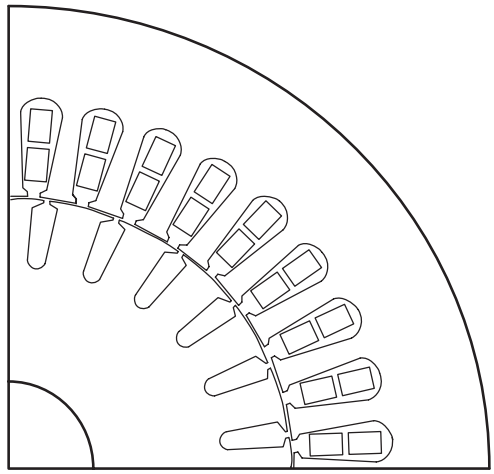

Figure 10.13 Experimental induction motor*

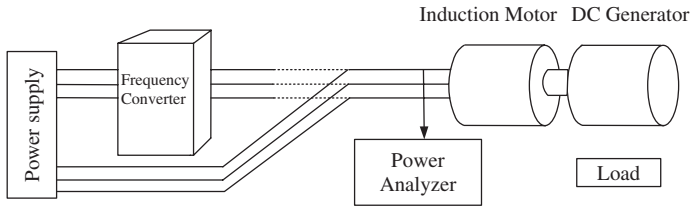

Figure 10.14 Experiment bench

The input power of the induction motor can be obtained directly from the power analyzer. Both no-load and load tests were performed. Moreover, no-load tests with a fundamental frequency of 60 Hz and switching frequency ranging from 3.5 to 9 kHz were carried out to evaluate the influences of switching frequency on the additional losses.

To understand the mechanism of the additional losses and their impact on the temperature, a two-dimensional (2D) finite element model (FEM) was developed to compute the losses. A three-dimensional (3D) FEM model was set up to estimate the thermal profile within the motor.

The simulated iron losses are shown in Figures 10.15 and 10.16 for sinusoidal and PWM supply, respectively. Under no-load operation, the iron loss with PWM supply is 104 W, a 48.2 W increase over the iron loss when operated from the sinusoidal supply (55.8 W). However, when the motor is attached to the load, additional iron losses are induced by the harmonics in the PWM supply, with iron loss at 139.1 W or only 31.1 W more than the sinusoidal iron loss (108 W). All the losses from the simulation and experiments are listed in Tables 10.1 and 10.2 respectively.

* The permission is for Section 10.2.6 from Figure 10.13 to end of Section. © [2007] Inderscience. Reprinted, with permission, from the International Journal of Electric and Hybrid Vehicles.

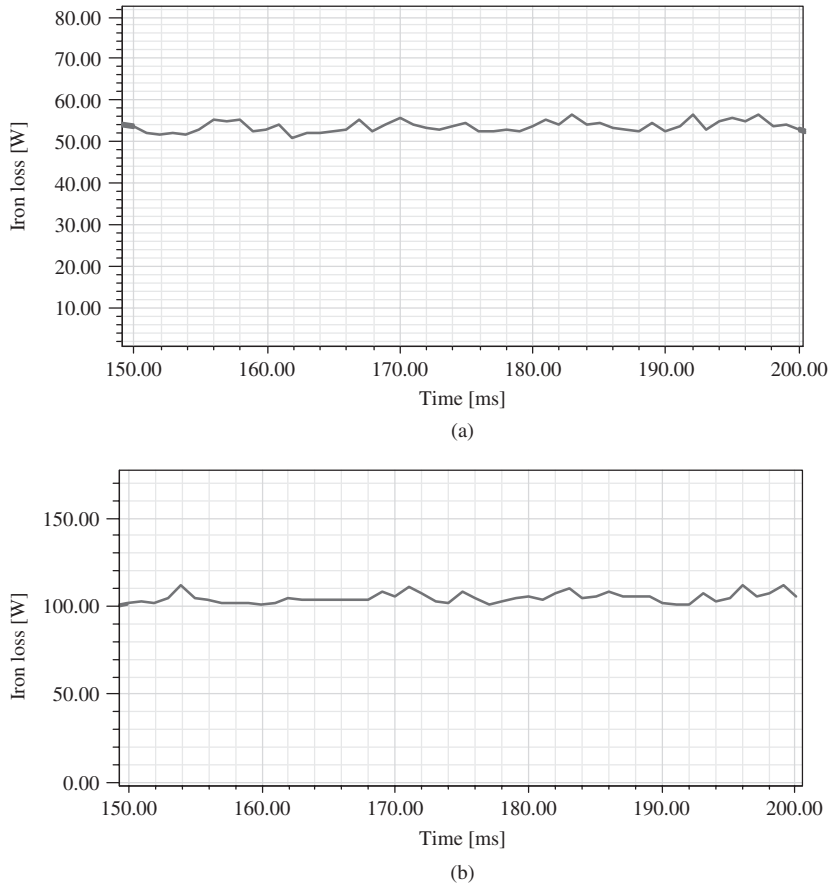

Figure 10.15 Iron losses from simulation for sinusoidal supply: (a) no load and (b) with load

The test results are consistent with the simulation results at fixed switching frequencies. In order to understand the impact of switching frequency on the additional losses, tests have been conducted using several different switching frequencies (3.5–9 kHz) for the PWM inverter. The results are shown in Figure 10.17. The total losses decrease proportionally with the increase of frequency, which is consistent with prior work [41].

By assigning all the losses into the 3D FEM model and incorporating the necessary boundary conditions based on the model of an actual motor, the temperature profile can be obtained. Figure 10.18 shows the temperature distribution in the stator with no load in sinusoidal supply. Tables 10.3 and 10.4 show the entire temperature of the motor, and the location of test points as shown in Figure 10.19 except point 1, which is in the center of the outer surface housing.

It can be seen from Tables 10.3 and 10.4 that the temperature rise of the induction motor is significantly higher when driven by the PWM inverter than by sinusoidal power supply. In conclusion, for induction motor design it is important to consider the additional losses generated due to the harmonics in the PWM supply and possible

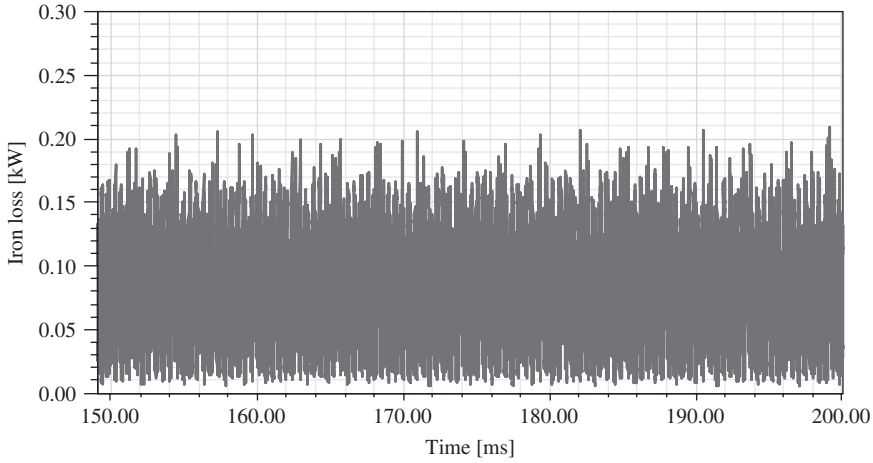

(a)

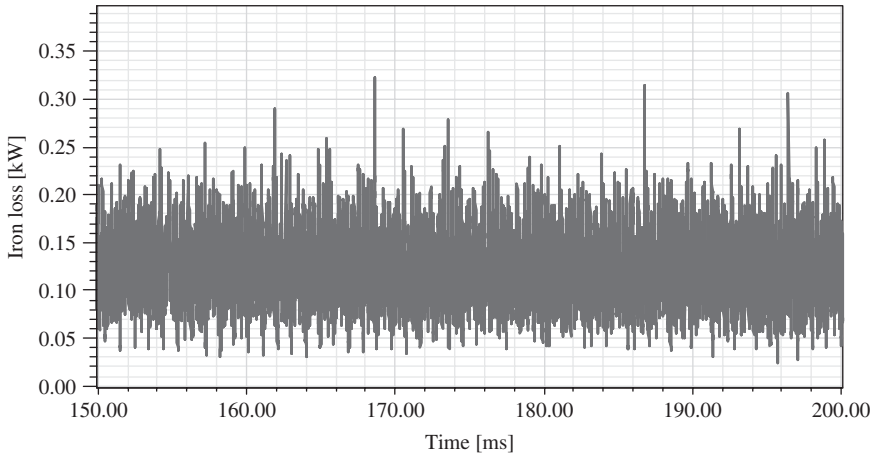

(b)

Figure 10.16 PWM losses from simulation: (a) no load and (b) with load

Table 10.1 Losses from simulation

	No load (W)		Load (W)	
	PWM	Sinusoidal	PWM	Sinusoidal
Iron loss	88.5	53.9	130.0	118.6
Copper loss	139.5	50.1	150.1	113.7

Table 10.2 Losses from experiments

	No load (W)		Load (W)	
	PWM	Sinusoidal	PWM	Sinusoidal
Iron loss	104	55.8	139.1	108
Copper loss	133.7	58.8	148.9	124.5

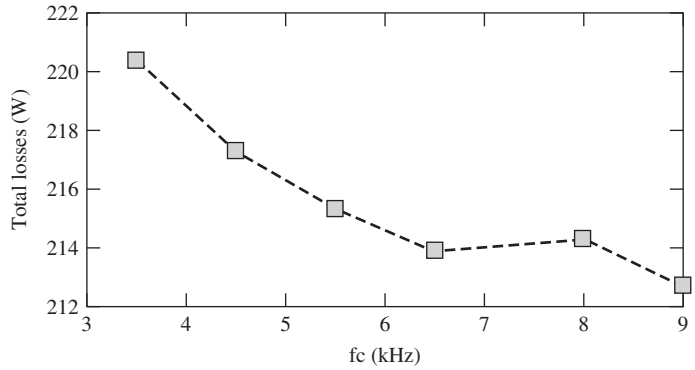

Figure 10.17 Loss with different switching frequencies

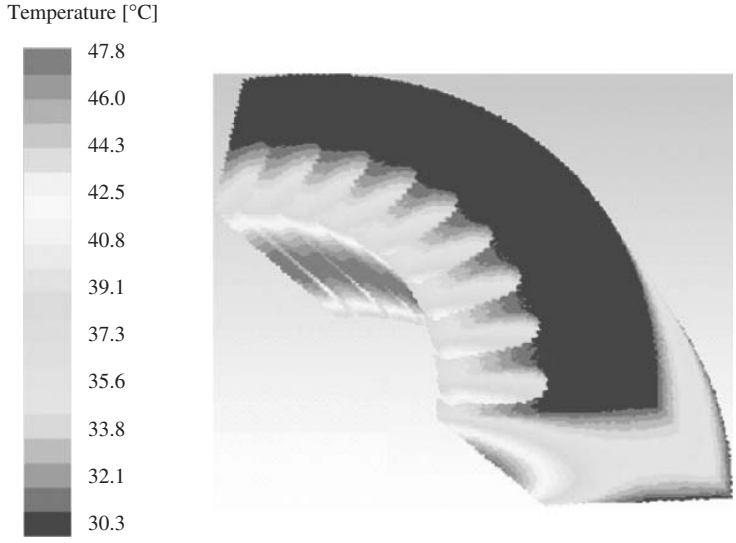

Figure 10.18 Temperature distribution in stator

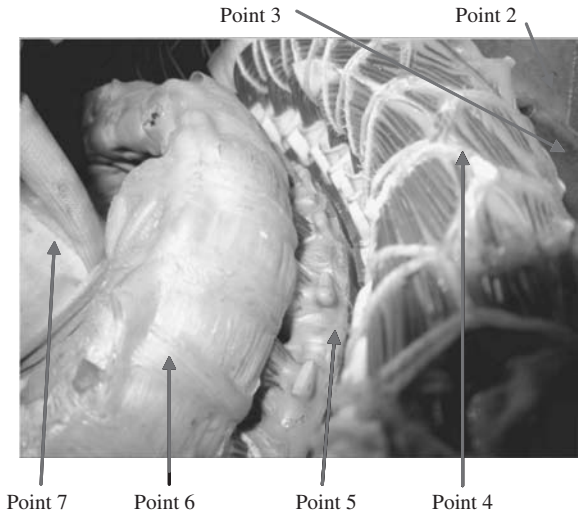

Figure 10.19 Inside view of the experimental motor

Table 10.3 Temperature profile with no load

	Experiment (°C)		Simulation (°C)	
Point 1	31.4	40.9	30.3	37.3
Point 2	36.9	42.4	34.7	38.7
Point 3	38.2	47.1	35.6	45.6
Point 4	39.5	52.7	36.3	49.3
Point 5	40.2	51.1	43.3	47.3
Point 6	39.6	49.7	34.4	45.4
Point 7	50.8	55.7	53.6	53.6

Table 10.4 Temperature profile with load

	Experiment (°C)		Simulation (°C)	
Point 1	34.2	41.8	32.7	37.7
Point 2	41.4	47.8	37.9	42.9
Point 3	47	52.8	44.6	50.6
Point 4	50.8	57.2	49.7	53.7
Point 5	60.5	63.9	55.5	56.3
Point 6	59.9	63.3	52.3	55.3
Point 7	67.6	71.7	63.6	66.7

excessive temperature rise inside the machine. Extra care needs to be taken in applications which experience a wide ambient temperature range, such as the ones used in HEVs.

*10.2.7 Field-Oriented Control of Induction Machine**

With field-oriented control, an induction machine can perform somewhat like a DC machine. This section explains the theory and implementation of the field-oriented control of an induction machine [42].

When expressed in phasors, the voltage equation for a three-phase induction machine with three symmetrical stator windings is given as

$$V_S = R_S i_S + p\lambda_S \tag{10.31}$$

$$V_R = R_R i_R + p\lambda_R \tag{10.32}$$

where p is the differential operand d/dt, and V, I, and λ are phasors of voltage, current, and flux linkage respectively. Subscript S relates to stator quantities and R refers to rotor quantities respectively. Equations 10.31 and 10.32 are expressed in stator and rotor coordinates respectively. Therefore, stator frame S is stationary and rotor frame R is rotational (rotor quantities are at rotor frequency or slip frequency).

Suppose there is a frame B, and the angle between the stator and this frame B is δ, therefore the angle between the rotor and this frame is $(\delta - \theta)$. Multiplying Equation 10.31 by $e^{-j\delta}$ and Equation 10.32 by $e^{-j(\delta-\theta)}$, we get

$$\begin{aligned} V_S \cdot e^{-j\delta} &= R_S i_S \cdot e^{-j\delta} + p\lambda_S \cdot e^{-j\delta} \\ V_R \cdot e^{-j(\delta-\theta)} &= R_R i_R \cdot e^{-j(\delta-\theta)} + p\lambda_R \cdot e^{-j(\delta-\theta)} \end{aligned} \tag{10.33}$$

Let

$$\begin{aligned} V_S^{(B)} &= V_S \times e^{-j\delta}, \quad V_R^{(B)} = V_R \times e^{-j(\delta-\theta)} \\ i_S^{(B)} &= i_S \times e^{-j\delta}, \quad i_R^{(B)} = i_R \times e^{-j(\delta-\theta)} \\ \lambda_S^{(B)} &= \lambda_S \times e^{-j\delta}, \quad \lambda_R^{(B)} = \lambda_R \times e^{-j(\delta-\theta)} \end{aligned} \tag{10.34}$$

By employing the equation

$$p(\lambda_S^{(B)}) = p(\lambda_S \cdot e^{-j\delta}) = -j \cdot \lambda_S(p\delta) \cdot e^{-j\delta} + p\lambda_S \cdot e^{-j\delta} \tag{10.35}$$

or

$$p\lambda_S \cdot e^{-j\delta} = p(\lambda_S^{(B)}) + j \cdot \lambda_S(p\delta) \cdot e^{-j\delta} \tag{10.36}$$

$$p\lambda_R \cdot e^{-j(\delta-\theta)} = p(\lambda_R^{(B)}) + j \cdot \lambda_R e^{-j\delta} p(\delta - \theta) \tag{10.37}$$

Equations 10.31 and 10.32 can then be transferred to a general frame B, where all space phasors are expressed in frame B with the superscript (B) as shown below:

$$V_S^{(B)} = R_S i_S^{(B)} + p\lambda_S^{(B)} + j \cdot \lambda_S^{(B)} p\delta \tag{10.38}$$

$$V_R^{(B)} = R_R i_R^{(B)} + p\lambda_R^{(B)} + j \cdot \lambda_R^{(B)} p(\delta - \theta) \tag{10.39}$$

The superscript (B) will be omitted further in this section for convenience.

* Reproduced with permission from Chunting Mi, "Field Oriented Control of Induction Motor Drives with Direct Rotor Current Estimation for Application in Electric and Hybrid Vehicles," Journal of Asian Electric Vehicle, vol. 5, no. 2, pp. 989–992, December 2007.

When expressed in phasors, the flux linkage can be expressed as

$$\lambda_S = (L_m + L_{1\sigma}) \cdot i_S + L_m \cdot i_R \tag{10.40}$$

$$\lambda_R = L_m \cdot i_S + (L_m + L_{2\sigma}) \cdot i_R \tag{10.41}$$

where L_m is the stator inductance and $L_{1\sigma}$ and $L_{2\sigma}$ are the stator and rotor leakage inductance respectively.

Note that although the phasors are in a different frame, the stator flux and rotor flux are rotating at the same speed.

For squirrel cage induction machines, the rotor current i_R is not accessible. Therefore, a fictitious rotor magnetizing current i_{mr} is defined such that the rotor flux can be expressed in terms of this fictitious rotor magnetizing current and stator inductance in the same way as in Equation 10.40:

$$\lambda_R = i_{mr} \cdot L_m \tag{10.42}$$

The rotor current can then be expressed as a function of magnetizing current and stator current from Equation 10.41:

$$i_R = \frac{i_{mr} - i_S}{1 + \sigma} \tag{10.43}$$

where

$$\sigma = L_{2\sigma}/L_m \tag{10.44}$$

Substituting Equations 10.42 and 10.43 into Equation 10.41 and considering that V_R is normally set to 0 for squirrel cage induction motors, the rotor equation can be rewritten as

$$0 = i_{mr} - i_S + T_r \cdot p i_{mr} + j \cdot T_r i_{mr} \cdot p(\delta - \theta) \tag{10.45}$$

where T_r is the rotor time constant which can be expressed as follows:

$$T_r = L_m(1 + \sigma)/R_R \tag{10.46}$$

As stated above, the rotor magnetizing current is a fictitious current. The magnitude of this current can be observed through the following approach. If the rotor equation is written in the stator frame then $\delta = 0$, $p\theta$ is equal to the speed of the rotor ω, and Equation 10.45 has the following form:

$$0 = i_{mr} - i_S + T_r \cdot p i_{mr} - j \cdot T_r i_{mr} \cdot \omega \tag{10.47}$$

Since this equation is written in the stator frame, we can find the α and β components of phasors i_S and i_{mr}:

$$\begin{aligned} i_S &= i_{S\alpha} + j i_{S\beta} \\ i_{mr} &= i_{mr\alpha} + j i_{mr\beta} \end{aligned} \tag{10.48}$$

Therefore Equation 10.47 becomes

$$\begin{aligned} \frac{di_{mr\alpha}}{dt} &= \frac{1}{T_r}(i_{s\alpha} - i_{mr\alpha}) - i_{mr\beta} \cdot \omega \\ \frac{di_{mr\beta}}{dt} &= \frac{1}{T_r}(i_{s\beta} - i_{mr\beta}) + i_{mr\alpha} \cdot \omega \end{aligned} \tag{10.49}$$

Stator current can be easily transferred from the *abc* system to $\alpha\beta$ system. Equation 10.49 can be implemented discretely in the time domain, therefore, $i_{mr\alpha}$ and $i_{mr\beta}$ can be observed. Once this has been done, i_{mr} and δ_r can finally be calculated:

$$i_{mr} = \sqrt{i_{mr\alpha}^2 + i_{mr\beta}^2}, \quad \cos(\delta_r) = i_{mr\alpha}/i_{mr}, \quad \sin(\delta_r) = i_{mr\beta}/i_{mr} \tag{10.50}$$

where δ_r is the angle between the fictitious current i_{mr} and the stator current $i_{S\alpha}$ as shown in Figure 10.20.

If the frame is chosen such that B is aligned with λ_R as shown in Figure 10.21, i_{mr} will only have real components. Therefore this rotor equation can then be decomposed into its direct and quadrature components as follows:

$$\begin{aligned} i_{sd} &= i_{S\alpha}\cos\delta_r + i_{s\beta}\sin\delta_r \\ i_{sq} &= -i_{S\alpha}\sin\delta_r + i_{s\beta}\cos\delta_r \end{aligned} \tag{10.51}$$

From Equation 10.45, when i_s is decomposed to d–q components, the equation can be written as follows:

$$i_{mr} - i_{sd} + T_r \cdot p i_{mr} = 0 \tag{10.52}$$

$$-i_{sq} + T_r i_{mr} \cdot p(\delta - \theta) = 0 \tag{10.53}$$

From Equation 10.52 it can be seen that i_{mr} is only related to i_{sd}. Therefore, i_{mr} can be controlled by controlling i_{sd}.

The torque in the machine is

$$T_q = \frac{3}{2} \cdot \frac{p}{2} \cdot (\lambda_S \times i_S) \tag{10.54}$$

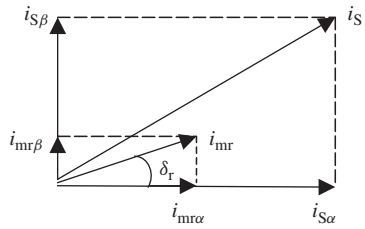

Figure 10.20 Stator and rotor current in α, β coordinates

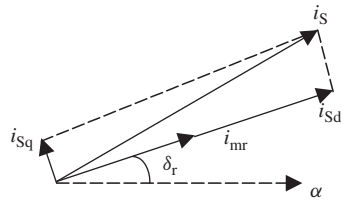

Figure 10.21 Stator current in d, q and α, β coordinates

which has to be balanced with the load and acceleration torque:

$$T_q = T_L + J \cdot p\omega \tag{10.55}$$

where T_q is the developed torque and T_L is the load torque; ω is the angular speed of the motor. If θ is the angle between the stator and the rotor, then $\omega = p\theta$.

It can also be proved that i_{sq} is directly related to motor torque as follows. By substituting i_S and i_R into the torque in Equation 10.54, the torque can be derived:

$$T_q = \frac{3}{2} \cdot \frac{p}{2} \cdot \frac{L_S}{1+\sigma} i_{mr} i_{sq} \tag{10.56}$$

Magnetizing current i_{mr} can be controlled by controlling the real component of stator current, and torque control is achieved by controlling the imaginary component of the stator current.

For ease of implementing control, we will introduce the per-unit system. A per-unit system is essentially a system of dimensionless parameters occurring in a set of wholly or partially dimensionless equations. This kind of system can extensively simplify the phenomena of problems. The parameters of the machines fall in a reasonable narrow numerical range when expressed in a per-unit system related to their ratings and, therefore, this is extremely useful in simulating machine systems and implementing the control of electrical machine by digital computers. Generally, rated power and frequency can be chosen respectively as the base values of power and frequency for normalization, whereas the peak values of rated phase current and phase voltage may be chosen respectively as the base values of current and voltage. Derived base values of impedance, inductance, and flux leakage are as follows (with subscript B indicating the variable as base value):

$$\begin{aligned} Z_B &= V_B / I_B \\ L_B &= Z_B / \omega_B \\ \lambda_B &= L_B I_B \end{aligned} \tag{10.57}$$

Normalized torque can be expressed as

$$T_{qB} = \frac{3}{2}\frac{p}{2}\lambda_B I_B = \frac{3}{2}\frac{p}{2} L_B I_B^2 \tag{10.58}$$

The torque equation can then be normalized. Dividing Equation 10.56 by Equation 10.58, we get

$$T_q^* = \frac{1}{1+\sigma}\frac{L_S}{L_B}\frac{i_{mr}}{I_B}\frac{i_{sq}}{I_B} = \frac{L_S^*}{1+\sigma} i_{mr}^* i_{sq}^* \tag{10.59}$$

Superscript * donates the normalized value. For convenience, superscript * will be omitted in further derivations. To implement the control strategy, a technique has to be developed to identify the magnitude of the magnetizing current i_{mr} and the angle δ_r.

There are two ways to implement the flux observer of Equation 10.49. One way is to take the Laplace transform of Equation 10.49 and apply a bilinear transformation to convert the Laplace transform to the z transform. The inverse z transform can be used to obtain $i_{mr\alpha}$ and $i_{mr\beta}$ in the discrete time domain. An alternative method is to discretize

Equation 10.49 directly in the time domain. Assuming that the sample time is T_s, then the following equation can be obtained from Equation 10.49:

$$\begin{aligned}\frac{(i_{mr\alpha_i} - i_{mr\alpha_{i-1}})}{T_s} &= \frac{1}{T_r}\left(\frac{i_{s\alpha_i} + i_{s\alpha_{i-1}}}{2} - \frac{i_{mr\alpha_i} + i_{mr\alpha_{i-1}}}{2}\right) - \frac{i_{mr\beta_i} + i_{mr\beta_{i-1}}}{2}\cdot\omega \\ \frac{(i_{mr\beta_i} - i_{mr\beta_{i-1}})}{T_s} &= \frac{1}{T_r}\left(\frac{i_{s\beta_i} + i_{s\beta_{i-1}}}{2} - \frac{i_{mr\beta_i} + i_{mr\beta_{i-1}}}{2}\right) - \frac{i_{mr\alpha_i} + i_{mr\alpha_{i-1}}}{2}\cdot\omega\end{aligned} \tag{10.60}$$

Therefore $i_{mr\alpha}$ and $i_{mr\beta}$ can be derived from Equation 10.60:

$$\begin{aligned}i_{mr\alpha_i} &= \frac{1-\kappa}{1+\kappa} i_{mr\alpha_{i-1}} + \frac{\kappa}{1+\kappa}(i_{s\alpha_i} + i_{s\alpha_{i-1}}) - T_r\frac{\kappa}{1+\kappa}(i_{mr\beta_i} + i_{mr\beta_{i-1}})\cdot\omega \\ i_{mr\beta_i} &= \frac{1-\kappa}{1+\kappa} i_{mr\beta_{i-1}} + \frac{\kappa}{1+\kappa}(i_{s\beta_i} + i_{s\beta_{i-1}}) + T_r\frac{\kappa}{1+\kappa}(i_{mr\alpha_i} + i_{mr\alpha_{i-1}})\cdot\omega\end{aligned} \tag{10.61}$$

where κ is the ratio of sampling time to rotor constant,

$$\kappa = T_s/2T_r \tag{10.62}$$

The time variables can also be made dimensionless by multiplying ω_B to the both sides of the equations. Therefore both T_s and T_r are expressed in per-unit values in Equations 10.60 and 10.62. A block diagram of the flux observer is shown in Figure 10.22. The flux observer takes the phase currents and speed as input, and calculates i_{mr}, $\cos\alpha$, and $\sin\alpha$.

It has been shown in the previous sections that it is possible to control the magnetizing component and torque component of the stator current separately. A PI controller is one

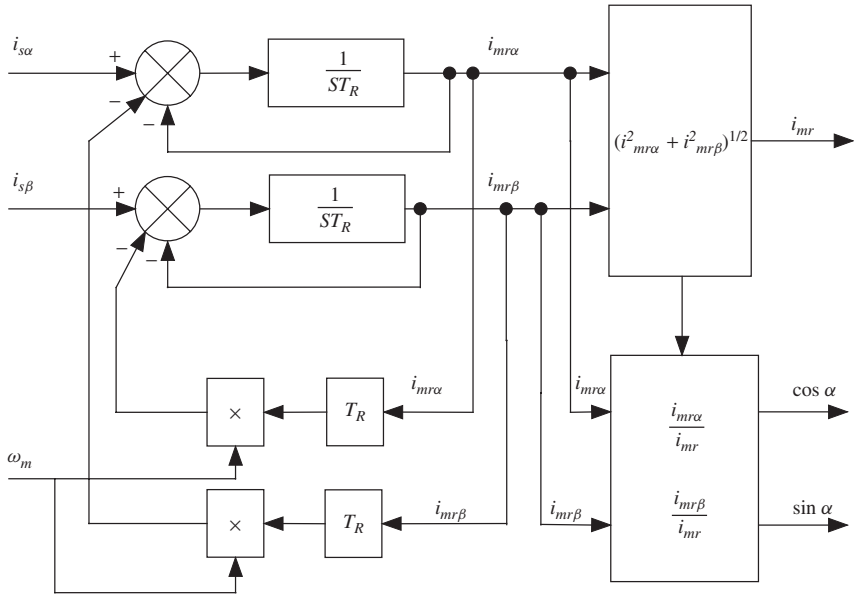

Figure 10.22 Block diagram of the rotor flux observer

way to implement control. The numerical expression for a PI controller is

$$V_o = K_{PI}\left(T_{PI}\varepsilon + \int \varepsilon dt\right) \tag{10.63}$$

where V_o is the output of the PI controller and ε is the error signal of input V_i (here V_i can be the measured current or torque of the motor, and V_o can be the PWM signal). In order to get the time domain discrete expression, we differentiate Equation 10.63:

$$\frac{dV_o}{dt} = K_{PI}\left(T_{PI}\frac{d\varepsilon}{dt} + \varepsilon\right) \tag{10.64}$$

Further implementation is straightforward:

$$\frac{V_{oi} - V_{oi-1}}{T_S} = K_{PI}T_{PI}\frac{\varepsilon_i - \varepsilon_{i-1}}{T_S} + K_{PI}\frac{\varepsilon_i + \varepsilon_{i-1}}{2} \tag{10.65}$$

$$V_{oi} = V_{oi-1} + K_1(\varepsilon_i - K_2\varepsilon_{i-1}) \tag{10.66}$$

where K_1 and K_2 can be expressed as

$$\begin{aligned} K_1 &= (1 + T_S/2T_r)K_{PI}T_{PI} \\ K_2 &= \frac{(1 - T_S/2T_r)}{(1 + T_S/2T_r)} \end{aligned} \tag{10.67}$$

For example, if the gain is chosen as $K_{PI} = 50$, $T_{PI} = 0.02$ seconds, sampling time $T_r = 0.02$ seconds, and $T_s = 0.67$ ms, then the constants K_1 and K_2 are $K_1 = 1.0168$, $K_2 = 0.9671$.

The purpose of field-oriented control is to control an induction machine in such a way that it behaves like a DC motor. A block diagram is shown in Figure 10.23 and the flow chart is shown in Figure 10.24. An incremental encoder is used to measure the speed of the motor. As shown in Equation 10.52, the magnetizing current does not change

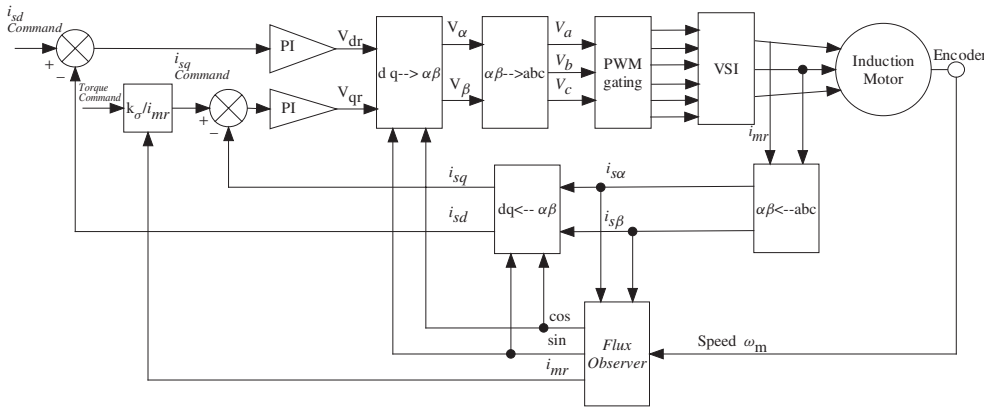

Figure 10.23 Field-oriented control of an induction machine

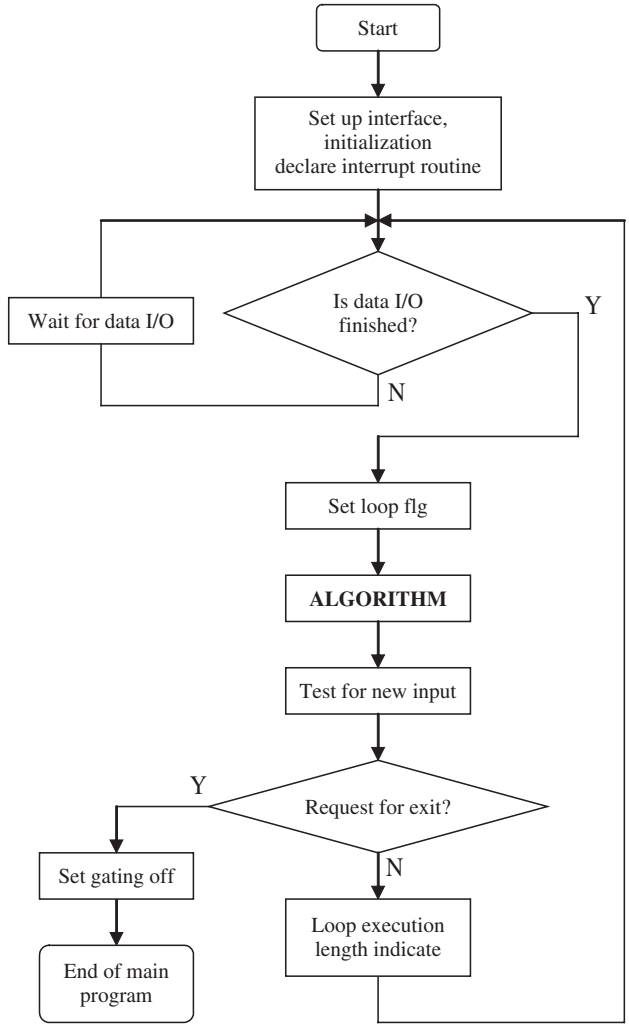

Figure 10.24 Flow chart of the closed-loop control of an induction machine

instantaneously with i_{sd} as it does in a DC motor. Rather, the magnetizing current lags a time constant T_r corresponding to the change of i_{sd}.

In this setup, the flux observer uses the speed signal of an incremental encoder and the current measurement through two external current sensors. Only the currents of two phases are needed to perform the coordinate transformations due to symmetry.

10.3 Permanent Magnet Motor Drives

PM motors are the most popular choices for EV and HEV powertrain applications due to their high efficiency, compact size, high torque at low speeds, and ease of control for regenerative braking [43–90]. The PM motor in a HEV powertrain is operated either as

a motor during normal driving or as a generator during regenerative braking and power splitting, as required by the vehicle operations and control strategies. PM motors with higher power densities are also now increasingly the choice for aircraft, marine, naval, and space applications.

The most commercially used PM material in traction drive motors is neodymium–ferrite–boron (Nd–Fe–B). This material has a very low Curie temperature and high temperature sensitivity. It is often necessary to increase the size of magnets to avoid demagnetization at high temperatures and high currents. On the other hand, it is advantageous to use as little PM material as possible in order to reduce the cost without sacrificing the performance of the machine.

10.3.1 Basic Configuration of PM Motors

When PMs are used to generate the magnetic field in an electric machine, it becomes a PM motor. Both DC and AC motors can be made with PMs. Only PM synchronous motors and PM brushless DC motors are chosen for modern traction drives. We will primarily explain the operation of PM synchronous motors in this book.

A PM synchronous motor contains a rotor and a stator, with the stator similar to that of an induction motor, and the rotor contains the PMs. From the section on induction motors, we know that the three-phase winding, with three-phase symmetrical AC supply, will generate a rotating magnetic field. To generate a constant average torque, the rotor must follow the stator field and rotate at the same synchronous speed. This is also why these machines are called PM synchronous motors.

There are different ways to place the magnets on the rotor, as shown in Figure 10.25. If the magnets are glued on the surface of the rotor, it is called a surfaced-mounted PM motor or SPM motor. If the magnets are inserted inside the rotor in the pre-cut slots, then it is called an interior permanent magnet motor or IPM motor.

For a SPM motor, the rotor can be a solid piece of steel since the rotor iron core itself is not close to the air gap, hence the eddy current loss and hysteresis loss due to slot/tooth harmonics can be neglected. For the IPM motor, the rotor needs to be made out

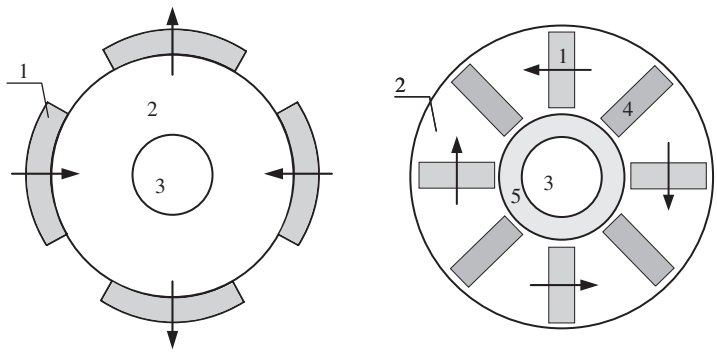

Figure 10.25 Surface-mounted magnets and interior magnets: left, SPM motor; right, IPM motor. 1 – magnet; 2 – iron core; 3 – shaft; 4 – non-magnet material; 5 – non magnet material

of laminated silicon steel since the tooth/slot harmonics will generate eddy current and hysteresis losses.

Due to the large air gap as well as the fact that the magnets have a permeability similar to that of air, SPM motors have similar direct-axis reactance x_d and quadrature-axis reactance x_q. On the other hand, IPM motors have different x_d and x_q. This difference will generate a so-called reluctance torque. It is worth pointing out that although there is a reluctance torque component, it does not necessarily mean an IPM motor will have a higher torque rating than a SPM motor for the same size and same amount of magnetic material used. This is because, in IPM motors, in order to keep the integrity of the rotor laminations, there are so-called "magnetic bridges" that will have leakage magnetic flux. So for the same amount of magnet material used, a SPM motor will always have higher total flux. There are many different configurations for IPM motors as shown in Figure 10.26.

10.3.2 Basic Principle and Operation of PM Motors

The no-load magnetic field of PM machines is shown in Figure 10.27. When the rotor is driven by an external source (such as an engine), the rotating magnetic field will generate

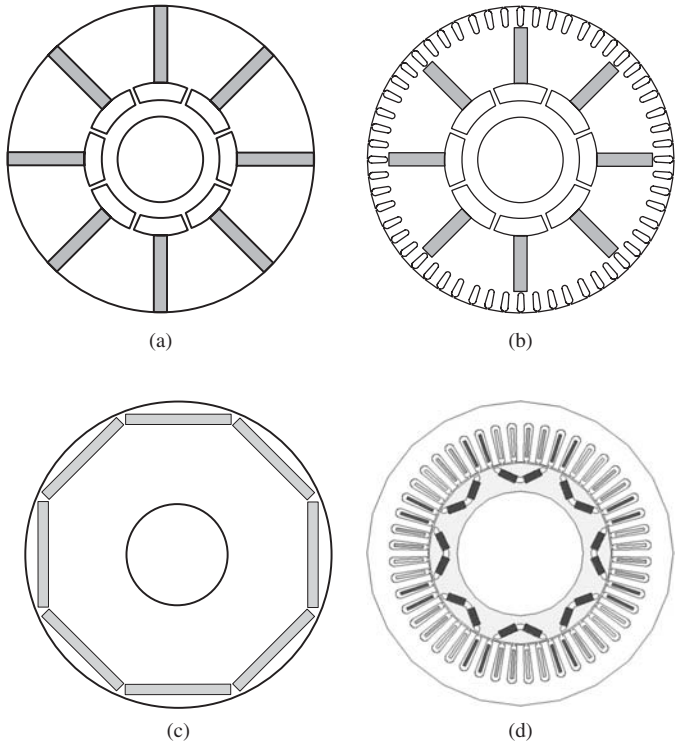

Figure 10.26 Four commonly used IPM rotor configurations: (a) circumferential-type magnets suitable for brushless DC or synchronous motor; (b) circumferential-type magnets for line-start synchronous motor; (c) rectangular slots IPM motor; and (d) V-type slots IPM motor

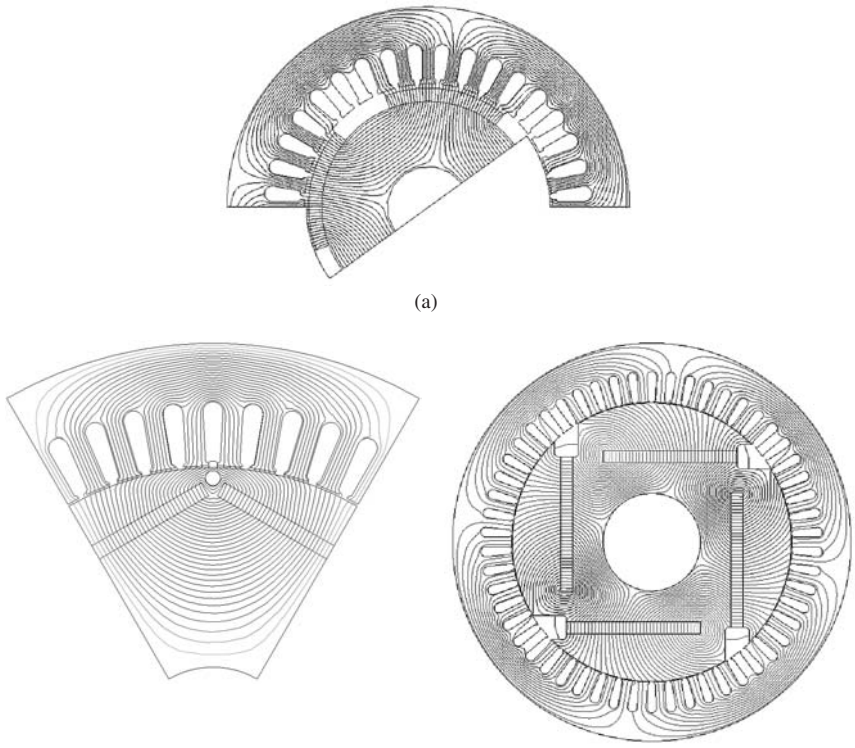

Figure 10.27 The magnetic field distribution of PM machines at no-load conditions (the stator current is zero): (a) a four-pole SPM motor; (b) an eight-pole symmetrical IPM motor; and (c) a four-pole unsymmetrical IPM configuration

three-phase voltage in the three-phase windings. This is the generator mode operation of the PM machine.

When operated as a motor, the three-phase windings, similar to those of an induction motor, are supplied with either a trapezoidal form of current (brushless DC) or sinusoidal current (synchronous AC). These currents generate a magnetic field that is rotating at the same speed as the rotor, or synchronous speed. By adjusting the frequency of the stator current, the speed of the rotor or the synchronous speed can be adjusted accordingly.

The torque is the attraction between the rotor magnetic field and the stator magnetic field in the circumferential direction. Hence, at no-load conditions, the rotor and the stator field are almost lined up. When the angle between the rotor field and the stator field reaches 90 electric degrees, the maximum torque is reached in SPM motors. For IPM motors, the maximum torque occurs at an angle slightly larger than 90° due to the existence of reluctant torque.

Figure 10.28 illustrates how a PM motor operates in different modes. The stator winding generates a rotating field that attracts the rotor magnets. If the two fields are lined up, the attraction between the two magnetic fields is in the radial direction, hence there is no electromagnetic torque. When the stator field is leading the rotor field, the stator will

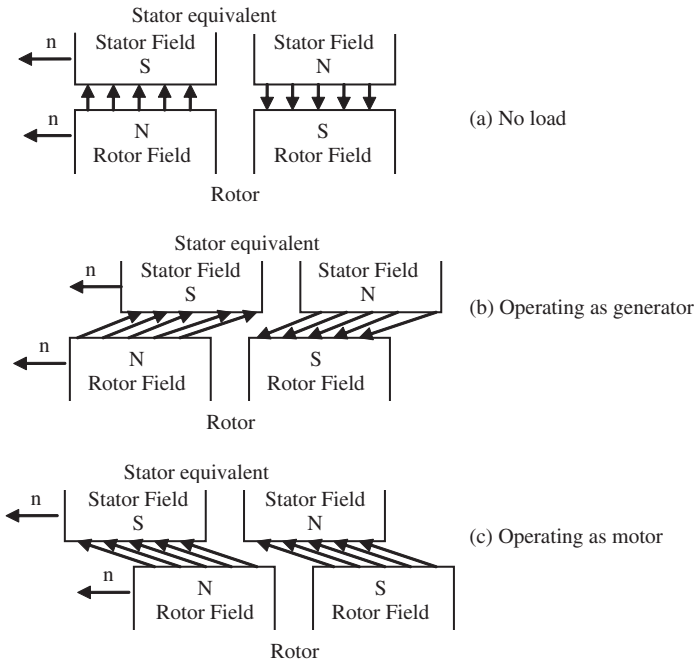

Figure 10.28 The operation of a PM synchronous machine

attract the rotor magnets. The machine then operates as a motor. When the stator field is lagging the rotor field, the machine becomes a generator.

At no load, the rotor magnetic field will generate a back emf E_o in the stator windings. When a voltage with the same frequency is applied to the stator windings, then a current will be generated and the voltage equation can be written as

$$V = E_o + IR + jIX \tag{10.68}$$

where R is the stator resistance and X is the synchronous impedance. The phasor diagram is shown in Figure 10.29 when neglecting the stator resistance. From the diagram, the term jIX can be further decomposed into two components: jI_dX_d and jI_qx_q. In fact, in IPM motors, the d axis and q axis will have different reactances. By using Figure 10.29, Equation 10.68 can be rewritten for IPM motors as

$$V = E_o + IR + jI_dX_d + jI_qX_q \tag{10.69}$$

The real power can be calculated, since from Figure 10.29, $\varphi = \delta + \theta$:

$$\begin{aligned} P_1 &= mIV\cos\varphi = mIE_o\cos\delta = mV(I\cos\delta\cos\theta - I\sin\delta\sin\theta) \\ &= mV(I_q\cos\theta - I_d\sin\theta) \end{aligned} \tag{10.70}$$

where φ is the power factor angle (the angle between the voltage and current), θ is the angle between the voltage and back emf, and δ is the inner power angle (the angle between

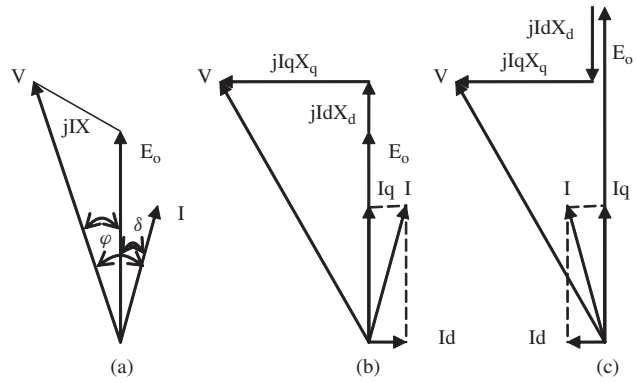

Figure 10.29 Phasor diagram of PM synchronous motors: (a) SPM; (b) IPM; and (c) flux weakening mode of IPM

the back emf and voltage). From Figure 10.29,

$$\begin{aligned} I_q X_q &= V \sin\theta \\ I_d X_d &= V \cos\theta - E_o \end{aligned} \tag{10.71}$$

Therefore, the power of PM motors can be expressed as

$$P = \frac{mE_o V}{X_d} \sin\theta + \frac{mV^2}{2}\left(\frac{1}{X_q} - \frac{1}{X_d}\right)\sin(2\theta) \tag{10.72}$$

The torque can be derived by dividing Equation 10.72 by the rotor speed as shown in Figure 10.30, where the torque–speed characteristics of a typical PM motor are shown. For

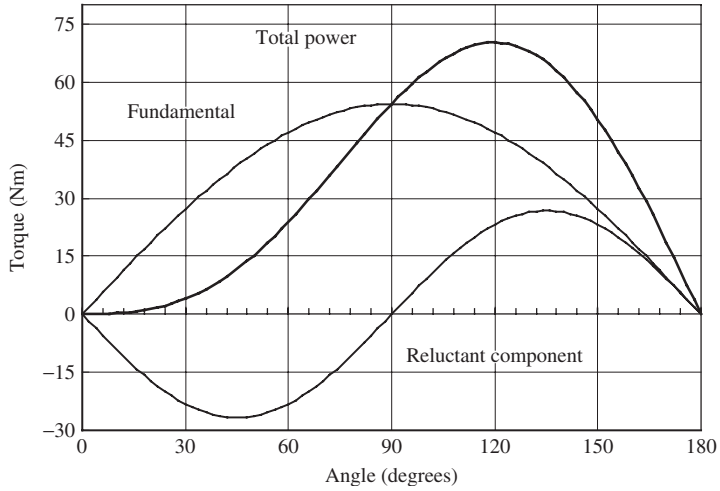

Figure 10.30 Power of IPM motor as a function of inner power angle

SPM motors, since $X_d = X_q$, the second term of Equation 10.72 is zero. For IPM motors, the q axis has less reluctance due to the existence of soft iron in its path, and the d axis has magnets in its path which has larger reluctance. Therefore, X_q is much larger than X_d.

On the other hand, from Equation 10.70, and neglecting losses, we can see that

$$\begin{aligned} T &= \frac{mIE_o \cos\delta}{\omega/p} = \frac{mIk\omega\varphi}{\omega/p}\cos\delta = mpkI\varphi\cos\delta \\ T_{\max} &= mpkI\varphi = \text{constant} \end{aligned} \tag{10.73}$$

Therefore, when inner power angle $\delta = 0$, for a given stator current, the torque of the motor reaches its maximum. In this condition, stator current is in phase with back emf E_o, and

$$\begin{aligned} V^2 &= E_o^2 + (I_q X_q)^2 = (k\omega\varphi)^2 + (I\omega L_q)^2 \\ \frac{V}{\omega} &= \sqrt{(k\varphi)^2 + (IL_q)^2} = \text{constant} \end{aligned} \tag{10.74}$$

Hence, stator voltage must be proportional to frequency to satisfy Equation 10.74 and maintain maximum torque output at the same time. This operation is also called constant torque operation. It can also be seen from Equation 10.72 that for a given θ, the power is inversely proportional to frequency, since V, X_d, and E_o are all proportional to frequency ω. This is similar to the V/f control of induction motors.

When stator voltage reaches its maximum, Equation 10.74 can no longer be maintained. As ω increases, V becomes constant, and a current in the d-axis direction must be supplied, as shown in Figure 10.29c. The relationship of voltage and frequency can be expressed as

$$\begin{aligned} V^2 &= (E_o - I_d X_d)^2 + (I_q X_q)^2 = (k\omega\varphi - I_d\omega L_d)^2 + (I_q\omega L_q)^2 \\ \frac{V}{\omega} &= \sqrt{(k\varphi - I_d L_d)^2 + (I_q L_q)^2} \end{aligned} \tag{10.75}$$

This operation is also called the flux weakening operation region because the d-axis current generate a magnetic flux in the opposite direction to the PM field. Note that due to constraints such as the current limit of the inverter, the q-axis current may have to be decreased from its rated value so that the total current from the inverter is kept the same. Additional losses at higher speeds may make it necessary to further reduce the torque output. It can also be seen from Equation 10.72 that for a given θ, the first term is constant since V is constant, and both X_d and E_o are proportional to frequency ω. In theory, the torque is inversely proportional to frequency in this operation, so the power is constant. Hence this mode is also referred to as the constant power operation range.

*10.3.3 Magnetic Circuit Analysis of IPM Motors**

Although today's motor design is usually aided by finite element analysis (FEA), the initial design stages are still realized through analytical methods. Air-gap flux is one of the most important parameters of PM motor designs and equivalent magnetic circuit analysis is used to calculate the air-gap flux in PM motors. For SPM motors, the equivalent magnetic circuit is straightforward. But for IPM motors, the PMs are buried inside the

* © [2004] IEEE. Reprinted, with permission, from IEEE on Magnetics.

rotor laminations, with magnets inserted into the pre-stamped slots. This arrangement protects the magnets from flying away from the rotor surface due to centrifugal force, fatigue, and aging of material during operation of the motor. Another advantage of IPM motors is that rectangular (cuboid) magnets can be used to simplify the manufacturing process and reduce the cost of manufacturing PM material. Flux concentration structures (such as magnets arranged in a V-shape) are often used to increase air-gap flux density in IPM motors [85].

Calculating air-gap flux in IPM motors is somewhat troublesome due to the existence of so-called "magnetic bridges." When an integrated lamination is used for IPM motors, magnetic short circuits exist around the edges of the magnets. These magnetic bridges are designed to enhance the integrity of the rotor. The magnetic bridges introduce magnetic short circuits and complicate the design and analysis of IPM motors. On the other hand, there are also concerns about how to limit the leakage flux in these magnetic bridges while maintaining the mechanical strength of the rotor. The flux leakage and flux distribution in the magnetic bridges can be precisely obtained through numerical methods such as FEA. However, FEA can only be performed after the preliminary dimensions of the motor have been determined. FEA is also cumbersome and time consuming in the early stages of PM motor design where numerous iterations are usually performed. Analytical calculation and analysis of all types of PM motors are essential in their early design stage.

This section discusses the analytical method to calculate the air-gap flux of IPM machines using an equivalent magnetic circuit model taking into account the assembly gap and saturation in the steel. Factors that affect the flux leakage in an IPM motor will also be discussed.

Figure 10.31 shows the configuration and no-load flux distribution of an eight-pole circumferential-type IPM line-start synchronous motor calculated using FEA. Integrated laminations are used to maintain integrity of the rotor. It contains three magnetic bridges in each pole: *bridge I* between the magnet and rotor slot; *bridges II* and *III* at the

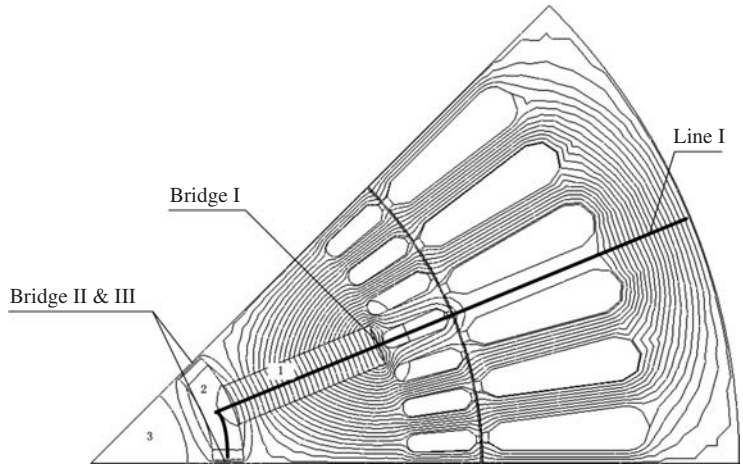

Figure 10.31 The flux distribution of an IPM line-start synchronous motor with circumferential-type magnets: 1, magnet; 2, non-magnetic material; and 3, shaft

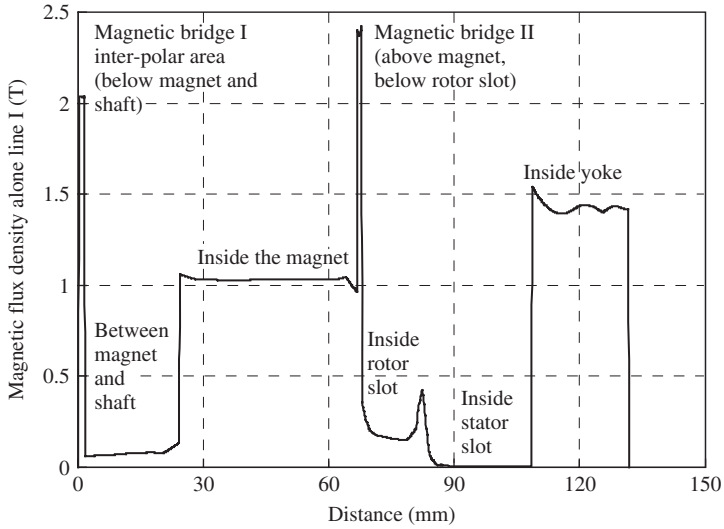

Figure 10.32 Flux density along *line I* of Figure 10.31

inter-polar space between the magnet and the shaft. Figure 10.32 shows the flux density along *line I* of Figure 10.31. It can be seen from Figure 10.32 that the flux densities differ in the two bridges.

It will be shown later that the magnetic flux density in the magnetic bridges is related to the width and length of the magnetic bridge, rather than being constant. For the situation here, there is flux leakage in the rotor slot and the non-magnetic material between the magnet and the shaft. The flux leakage through the stator slot is negligible.

Modern rare earth permanent magnets (REPMs) have a straight demagnetization curve as shown in Figure 10.33. The low cost makes Nd–Fe–B REPMs ideal for motor applications. However, temperature effects, as shown in Figure 10.33, must be taken into consideration when designing a PM motor.

At room temperature (25 °C), the demagnetizing curve of a cuboid REPM can be represented by

$$\Phi_m = \Phi_r - F_m \cdot \Phi_r / F_c = \Phi_r - F_m / R_M \tag{10.76}$$

where Φ_r and F_c are the residual flux and magnetomotive force (mmf) of each pole respectively, and R_M is the reluctance of the magnet, which is the reciprocal of magnet permeance λ_M:

$$R_M = 1/\lambda_M = F_c/\Phi_r \tag{10.77}$$

For parallel or circumferentially magnetized poles as shown in Figure 10.26a,b,

$$\Phi_r = 2B_r A_m, \quad F_c = l_m H_c \tag{10.78}$$

while for series or radially magnetized poles as shown in Figure 10.26c,d,

$$\Phi_r = B_r A_m, \quad F_c = 2l_m H_c \tag{10.79}$$

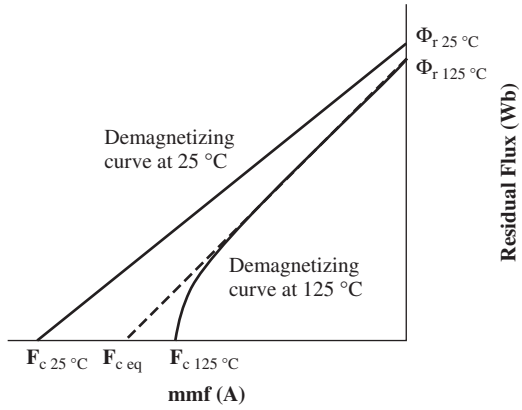

Figure 10.33 Demagnetization curve of Nd–Fe–B magnets considering temperature effects, where subscript 25 °C represents its value at room temperature, whereas subscript 125 °C represents its value at 125 °C; F_{ceq} is the equivalent mmf of the linear portion of the demagnetizing curve

where B_r and H_c are the remanence and coercive force of the magnets respectively, l_m is the length of the magnet, and A_m is the cross-sectional area. Thus

$$A_m = b_m l_{fe} \tag{10.80}$$

where l_{fe} is the length of magnet along the shaft direction and usually equal to the rotor lamination stack length.

At the operating temperature, the above parameters are replaced by their respective values. It is possible that the demagnetizing curve becomes nonlinear at the operating temperature. In this case, F_{ceq} should be used in place of F_c as shown in Figure 10.33. The Norton equivalent of a cuboid magnet is shown in Figure 10.34.

A generic, circumferentially magnetized IPM rotor configuration is shown in Figure 10.35. The equivalent magnetic circuit of this configuration is shown in Figure 10.36, where R_δ, R_{y1}, R_{y2}, R_{t1}, R_{t2}, R_σ, R_1, R_2, R_S are the reluctances of the air gap, stator yoke, rotor yoke, stator teeth, rotor teeth, assembly gap between magnets and

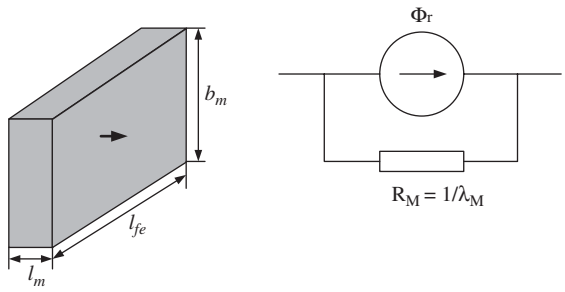

Figure 10.34 Norton equivalent of cuboid magnets

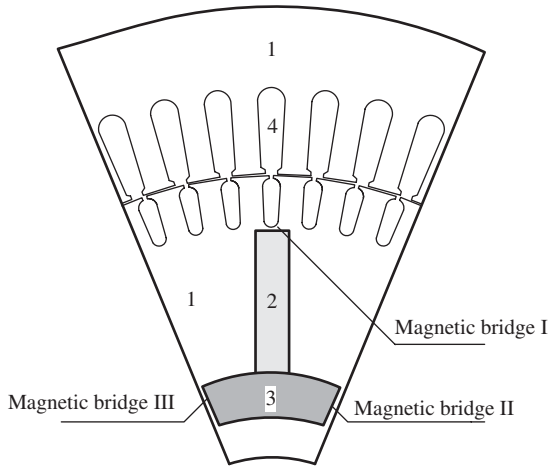

Figure 10.35 Arrangements of magnets of line-start IPM motors: 1, stator and rotor iron laminations; 2, permanent magnets; 3, non-magnetic material; 4, stator slots; and 5, rotor slots. Magnetic bridges are part of the rotor laminations to maintain the integrity of rotor laminations

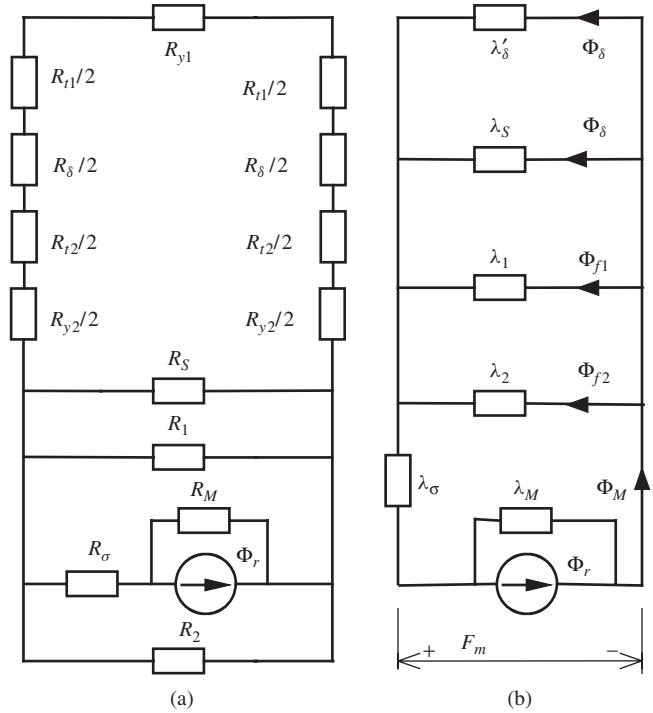

Figure 10.36 The equivalent magnetic circuit of IPM motors with circumferential magnets: (a) exact model and (b) simplified model

laminations, magnetic bridge I, magnetic bridges II and III (combined due to symmetry), and leakage through the rotor slots and the non-magnetic material respectively. End effects are neglected.

Fluxes passing through these bridges are leakage fluxes. These magnetic bridges are highly saturated as can be seen from Figure 10.32.

The magnetic circuit can be simplified as shown in Figure 10.36b, where λ'_δ is the total permeance combining the air gap, stator teeth, stator yoke, rotor teeth (if any), and rotor yoke; λ_1 is the permeance of magnetic bridge I; λ_2 is the permeance of magnetic bridges II and III; and λ_S is the total permeance leakage through the rotor slot and non-magnetic material. Let

$$\begin{aligned} \lambda'_\delta &= 1/(R_\delta + R_{t1} + R_{t2} + R_{y1} + R_{y2}) \\ \lambda_o &= \lambda'_\delta + \lambda_1 + \lambda_2 + \lambda_S \\ \lambda_{ex} &= \lambda_o || \lambda_\sigma \end{aligned} \tag{10.81}$$

where λ_{ex} is the total external permeance.

Solving the magnetic circuit, the magnet operating point and all fluxes can be found:

$$\begin{aligned} F_m &= \Phi_r/(\lambda_M + \lambda_{ex}) \\ \Phi_m &= \Phi_r \lambda_{ex}/(\lambda_M + \lambda_{ex}) \end{aligned} \tag{10.82}$$

$$\begin{aligned} \textstyle\sum F &= F_m - \Phi_m/\lambda_\sigma \\ \Phi_\delta &= \lambda'_\delta \textstyle\sum F \\ \Phi_f &= (\lambda_1 + \lambda_2) \textstyle\sum F \\ \Phi_S &= \lambda_S \textstyle\sum F \end{aligned} \tag{10.83}$$

$$\Phi_m = \Phi_\delta + \Phi_f + \Phi_S \tag{10.84}$$

where Φ_δ is the total air-gap flux, Φ_f is the total leakage flux in the magnetic bridges, and Φ_S is the total leakage flux in the rotor slot and non-magnetic material.

It can be seen from Figures 10.35 and 10.36 that the magnetic bridges should have the same mmf as that of the air-gap branch. Therefore, the magnetic field density of each of the bridges is

$$H_f = \sum F/l_f \tag{10.85}$$

where l_f is the length of the magnetic bridge along the flux path. It can be seen from Equation 10.85 that, if the magnetic bridges have different paths for magnetic fluxes, then the field density will be different.

The flux density in each of the bridges can be found through table lookup or curve-fitting of the lamination material. The total flux leakage in each of the magnetic bridges can be expressed as

$$\Phi_f = B_f A_f \tag{10.86}$$

where B_f is the flux density in the magnetic bridges and A_f is the cross-sectional area of that magnetic bridge.

Although the above equations give an analytical expression for air-gap flux, it can hardly be solved due to saturation in the yoke, teeth, and magnetic bridges. Graphic analysis is an effective method to solve the operating point of the magnets.

10.3.3.1 Unsaturated Motor

If the yoke and teeth of the motor are not saturated but the magnetic bridges are highly saturated, and the assembly air gap is neglected, the air-gap flux can be calculated analytically.

Assume that the flux density in the magnetic bridges is constant due to high saturation. Then

$$\Phi_\delta = \frac{\lambda_\delta}{\lambda_\delta + \lambda_M + \lambda_S}(\Phi_r - \Phi_f) \tag{10.87}$$

where air-gap permeance can be expressed as

$$\lambda_\delta = \frac{\alpha \tau l_{fe} \mu_0}{2\delta k_\delta} \tag{10.88}$$

α is the effective pole width coefficient, τ is the pole pitch, k_δ is Carter's coefficient, δ is air-gap length, and μ_0 is the permeability of air, $\mu_0 = 4\pi \times 10^{-7}$ T m/A.

Carter's coefficient can be calculated for stator slots and rotor slots (if any) separately, that is,

$$k_\delta = k_{\delta 1} k_{\delta 2} \tag{10.89}$$

$$k_{\delta 1} \text{ or } k_{\delta 2} = t/(t - \gamma * \delta) \tag{10.90}$$

$$\gamma = \frac{4}{\pi}\left[\frac{b_0}{2\delta}\arctan\left(\frac{b_0}{2\delta}\right) - \ln\left(\sqrt{1 + \left(\frac{b_0}{2\delta}\right)^2}\right)\right] \tag{10.91}$$

where b_0 is the width of the slot opening and t is the slot pitch.

Leakage permeance λ_S can also be found for rotor slots and the non-magnetic material. The reluctance of the assembly air gap can be expressed as a function of σ, where σ is the average tolerance between the magnet and the lamination steels. The reluctance of the assembly air gap is

$$\lambda_\sigma = \frac{b_m l_{fe} \mu_0}{\sigma} \tag{10.92}$$

10.3.3.2 Saturated Motor

When the IPM motor is saturated, as is the case for most PM motor designs, graphic analysis can be used to solve for the magnetic operating point. Detailed steps of graphic analysis are given in Table 10.5 and Figure 10.37. The calculation procedure is detailed as follows:

1. Assume an air-gap flux density B_δ as in Table 10.5, row 1.
2. Calculate the flux density in the stator tooth (row 2); use table lookup or curve-fitting to find the magnetic field density H_t in the tooth (row 3); calculate the mmf of the tooth (row 4).
3. Repeat step 2 to calculate the mmf of the rotor tooth, stator yoke, and rotor yoke (rows 5–7).

4. Calculate the air-gap mmf (row 8).
5. Calculate the subtotal mmf by summing air-gap mmf and core mmf (row 9).
6. Calculate the magnetic field density of the magnetic bridges (rows 10 and 12); use lookup table or curve-fitting to find the magnetic flux density B_f in the magnetic bridges (rows 11 and 13).
7. Calculate the air-gap flux, leakage flux in the bridges, and leakage flux through the rotor slots (rows 14–17).
8. Calculate the total flux (row 18) and total mmf (row 19).
9. Plot five curves in the second quadrant as shown in Figure 10.37 using Table 10.5. Find on the graph the crossing point A. This is the magnet operating point. Draw a horizontal line to intersect $\Phi_m \sim F_m$ at A′. Draw a vertical line down from point A′. The crossing point of this vertical line with curve $\Phi_\delta \sim F_m$ is the air-ap flux, with $\Phi_S \sim F_m$ the leakage flux through the rotor slot, and with $\Phi_f \sim F_m$ the leakage flux through the bridges.

In Table 10.5, b_{t1} and h_{t1} are the width and height of the stator slots; b_{t2} and h_{t2} are the width and height of the rotor slots; l_{y1} and h_{y1} are the length and height of the stator yoke; l_{y2} and h_{y2} are the length and height of the rotor yoke; A_{f1} and A_{f1} are the cross-sectional areas of each magnetic bridge; and l_{f1} and l_{f2} are the lengths of each magnetic bridge, respectively.

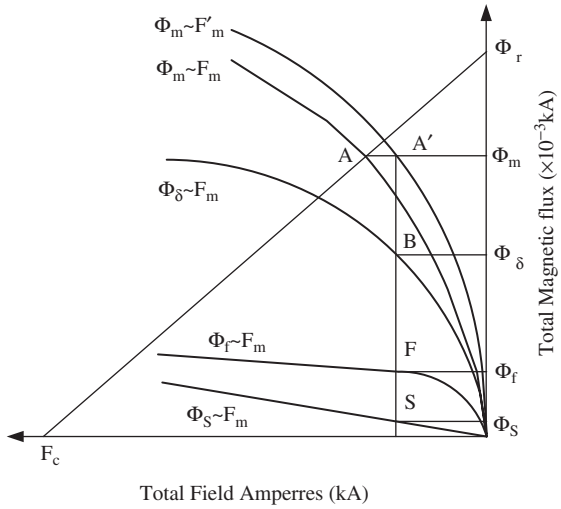

Figure 10.37 Graphic analysis of no-load IPM machine, where crossing point A is the operating point of the magnet, B represents the air-gap flux, F represents the leakage flux in the magnetic bridges, and S represents the leakage flux in rotor slots and the non-magnetic material. Note that the leakage flux in the magnetic bridges contributes a significant portion of the total flux supplied by the magnet as can be seen on the graph

Table 10.5 Magnetic circuit calculation of experimental motor

1	B_δ	(Experimental motor)	0.8	0.9
2	$B_t = t/b_t B_\delta$	$B_t = 2.02 B_\delta$	1.6	1.8
3	H_t(Lookup_Table)	H_t	4 250.0	13 280.0
4	$F_t = h_t H_t$	$F_t = 0.04 H_t$	181.1	565.7
5	$B_y = \Phi_\delta / 2 h_y l_{fe}$	$B_y = 1.38 B_\delta$	1.1	1.2
6	H_y(Lookup_Table)	H_y	498.6	742.8
7	$F_y = l_y H_y$	$F_y = 0.12 H_y$	59.3	88.4
8	$F_\delta = 1.6 \delta k_\delta B / \mu_0$	$F_\delta = 566.8 B_\delta$	907.1	1020.5
9	$\sum F = F_\delta + F_t + F_y$	$\sum F = F_\delta + F_t + F_y$	1147.5	1674.6
10	$H_{f1} = \sum F / l_{f1}$	$H_{f1} = \sum F / l_{f1}$	229 498.0	334 923.3
11	B_{f1}(Lookup_Table)	B_{f1}	2.29	2.43
12	$H_{f2} = \sum F / l_{f2}$	$H_{f2} = \sum F / l_{f2}$	95 624.2	139 551.4
13	B_{f2}(Lookup_Table)	B_{f2}	2.12	2.17
14	$\Phi_\delta = \alpha \tau l_{fe} B_\delta$	$\Phi_\delta = 14.8 \times 10^{-3} B_\delta$	0.011 263	0.012 671
15	$\Phi_{f1} = B_{f1} A_{f1}$	$\Phi_{f1} = 0.38 \times 10^{-3} B_{f1}$	0.001 743	0.001 848
16	$\Phi_{f2} = B_{f2} A_{f2}$	$\Phi_{f2} = 0.608 \times 10^{-3} B_{f2}$	0.001 287	0.001 322
17	$\Phi_s = \sum F \lambda_s$	$\Phi_s = 0.336 \times 10^{-6} F_m$	0.000 771	0.001 125
18	$\Phi_m = \Phi_\delta + \Phi_{f1} + \Phi_{f2} + \Phi_s$	Φ_m	0.015 063	0.016 966
19	$F_m = \sum F + \Phi_m / \lambda_\sigma$	F_m	1462.9	2029.9

10.3.3.3 Operation under Load

The operating point of magnets at rated load can also be solved by shifting the air-gap curve $\Phi_\delta \sim F_m$ by F_{ad} to the left on the graph, where F_{ad} is the armature mmf.

10.3.3.4 Flux Concentration

Flux concentration configurations are often used in IPM machines to increase air-gap flux density as shown in Figure 10.38a. In flux concentration configurations, the assistant magnets are usually designed to have the same mmf as the dominant magnet. However, due to dimensional and other constraints, the assistant magnets may have a different mmf.

There are three possibilities as shown in Figure 10.38b–d. The Norton equivalent of all magnets can still be expressed by (10.76), with Φ_r and F_c the equivalent residual flux and equivalent mmf, and R_M the equivalent reluctance. The equivalent Φ_r and F_c can be expressed as

$$\Phi_r = \Phi_{r1} + \Phi_{r2} \tag{10.93}$$

$$F_c = \frac{\Phi_r}{\Phi_{r1} F_{c2} + \Phi_{r2} F_{c1}} F_{c1} F_{c2} \tag{10.94}$$

where Φ_{r1} and F_{c1} are the residual flux and mmf of the dominant magnet, and Φ_{r2} and F_{c2} are the residual flux and mmf of the assistant magnet.

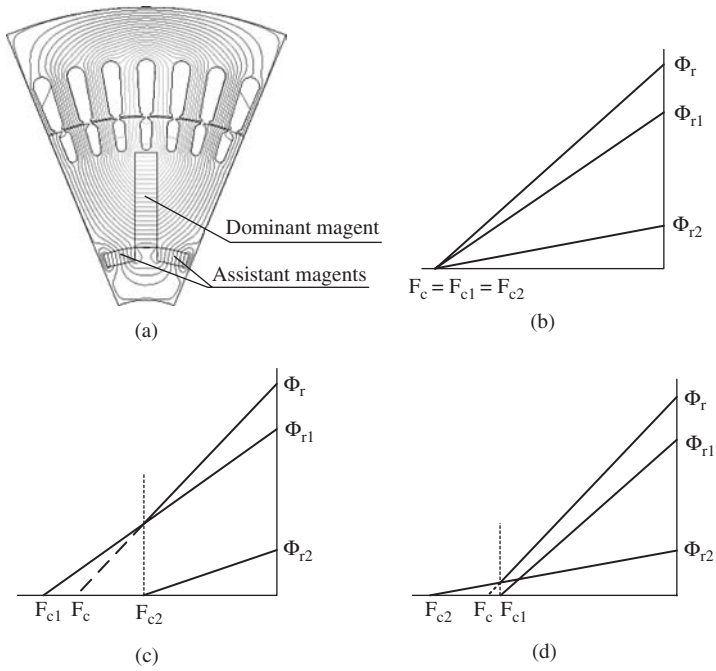

Figure 10.38 Flux concentration configurations: (a) configuration with the assistant magnets in series; (b) equivalent demagnetizing curve when the assistant magnets have the same mmf as that of the dominant magnet; (c) when the mmf of assistant magnets is more than that of the dominant magnet; and (d) when the mmf of assistant magnets is less than that of the dominant magnet

*10.3.4 Sizing of Magnets in PM Motors**

Sizing of magnets is one of the critical tasks of PM machine design. This section discusses the analytical methods to calculate the volume and size of magnets for PM motors. The proposed methods are validated by FEA and experiments [91].

In the following, the formulas will be derived based on a set of assumptions and then modified based on practical design considerations. The assumptions include the following:

- Magnetic pole salience can be neglected
- The stator resistance is negligible.
- Saturation can be neglected.
- The air-gap flux is sinusoidally distributed.

Based on the above assumptions, and using the phasor diagram of a PM synchronous motor as shown in Figure 10.29, the input power of the PM synchronous motor can be written as

$$P_1 = mIV\cos\phi = mIE_0\cos\delta \tag{10.95}$$

* © [2006] IEEE. Reprinted, with permission, from IEEE on Magnetics.

where m is the number of phases, I and V are the phase voltage and phase current, E_o is the induced back emf per phase, φ is the power angle, that is, the angle between phasor I and phasor V, and δ is the inner power angle, that is, the angle between phasor I and phasor E_o.

The back emf of a PM synchronous machine with sinusoidal air-gap flux can be expressed as

$$E_0 = \sqrt{2}\pi K_w f W \Phi \tag{10.96}$$

where W is the number of turns per phase, Φ is the total air-gap flux per pole, and K_w is the winding factor.

The phase current can be expressed in terms of armature maximum direct-axis reactant *mmf* F_{adm}:

$$I = F_{adm} \frac{p}{0.9 m W K_w K_{ad} K_m \sin\delta} \tag{10.97}$$

where K_{ad} is the d-axis armature reaction coefficient, K_m is the maximum possible armature current (per unit), and p is the number of poles.

Substituting Equations 10.97 and 10.98 into Equation 10.96, the input power can be expressed as

$$P_1 = \frac{\sqrt{2}\pi p f}{0.9 K_{ad} K_m \tan\delta} F_{adm} \Phi \tag{10.98}$$

In this chapter, a new term, the magnet usage ratio ξ, is introduced and defined as follows:

$$\xi = \frac{F_{adm} \Phi_m}{F_{mo} \Phi_{mo}} \tag{10.99}$$

where Φ_{mo} is the total residual flux per pole, F_{mo} is the total mmf per pole, Φ_m is the total flux per pole at no-load condition, and F_{adm} is the maximum direct-axis reactant mmf of the motor.

The definition of this magnet usage ratio is illustrated in Figure 10.39, where point A is the magnet operation point at no load, and point B is the magnet operation point at maximum mmf. The air-gap flux per pole Φ can be expressed as a function of flux supplied by the magnet Φ_m and flux leakage coefficient σ_o:

$$\Phi = \Phi_m / \sigma_o \tag{10.100}$$

For series magnets as shown in Figure 10.40a,

$$\left.\begin{aligned} \Phi_{mo} &= B_r S_m \\ F_{mo} &= 2 H_c l_m \end{aligned}\right\} \tag{10.101}$$

For parallel magnets as shown in Figure 10.40b:

$$\left.\begin{aligned} \Phi_{mo} &= 2 B_r S_m \\ F_{mo} &= H_c l_m \end{aligned}\right\} \tag{10.102}$$

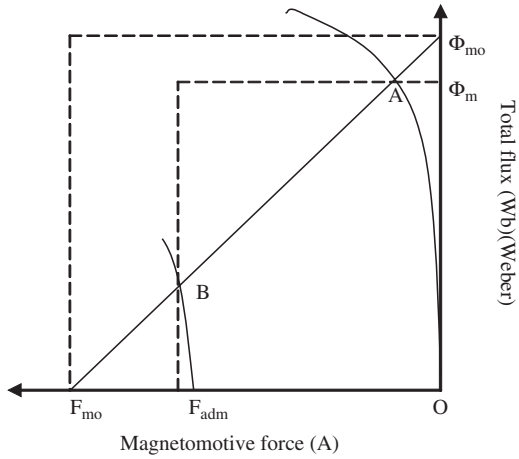

Figure 10.39 Illustration of magnet usage where A is the no-load operation point and B is the maximum reversal current point

where l_m is the thickness of magnet per pole along the magnetizing direction, and S_m is the cross-sectional area of magnet under each pole.

Finally, the input power of the motor can be expressed as follows by substituting Equations 10.100–10.103 into Equation 10.99:

$$P_1 = \frac{\sqrt{2}\pi \xi f}{0.9 K_{ad} K_m \sigma_0 \tan\delta} B_r H_C 2p S_m l_m \tag{10.103}$$

Since the total magnet volume is

$$V_m = 2p S_m l_m \tag{10.104}$$

The magnet volume used in a PM synchronous motor can therefore be expressed as

$$V_m = \frac{0.2\sigma_0 K_m K_{ad}}{\xi} \tan\delta \frac{P_1}{f B_r H_C} = C_V \frac{P_1}{f B_r H_C} \tag{10.105}$$

where C_V is a coefficient

$$C_V = \frac{0.2\sigma_0 K_m K_{ad}}{\xi} \tan\delta \tag{10.106}$$

In order to use the above equations to determine the magnet volume needed for a PM motor, certain parameters of the motor need to be identified.

10.3.4.1 Input Power

At the design stage, the input power of a PM motor is given by

$$P_1 = \frac{P_N}{\eta \cos\phi} \tag{10.107}$$

where η is the target efficiency and $\cos\phi$ is the target power factor of the motor.

10.3.4.2 Direct-Axis Armature Reaction Factor

Salience can be included in the direct-axis armature reaction factor. For a given magnet coverage α, K_{ad} is

$$K_{ad} = \frac{\alpha\pi + \sin\alpha\pi}{4\sin(\alpha\pi/2)} \tag{10.108}$$

10.3.4.3 Magnetic Usage Ratio and Flux Leakage Coefficient

The magnet usage ratio can be designed such that the demagnetization of magnets can be avoided. If one chooses 70–90% residual flux and 70–90% coercive force, then ζ is between 0.5 and 0.81.

Flux leakage for surface-mounted magnets is usually small, that is, σ_0 is approximately 1.0. For IPM motors, $\sigma_0 = 1.2 - 1.5$ and depends on the actual configuration of the motor.

10.3.4.4 Maximum Armature Current

Maximum armature current occurs during transient conditions, or during starting in the case of a line-start PM motor. During transient conditions, when the PM synchronous motor runs out of synchronization, the back emf and terminal voltage may run out of phase. Therefore, the maximum armature current always occurs when the terminal voltage is out of phase with the back emf,

$$I_{\max} = \frac{E_o + V}{X_d} \tag{10.109}$$

where X_d is the direct-axis reactance of the motor.

A typical value of maximum current is 4–8 and must be verified during the design process.

10.3.4.5 Inner Power Angle

The power angle in Equation 10.107 refers to the rated operation point. In PM motor designs, this angle is usually kept around 25°–45°.

By substituting all the above coefficients into Equation 10.107, C_V can be determined. To a reasonable first approximation, C_V can be chosen to be 2. It should be adjusted during the design process.

Usually the length of magnet along the shaft direction is chosen to be the same as the rotor laminations stack length l_{fe}. The thickness of magnet along the magnetization direction is determined by the maximum armature current and operating temperature as shown in Figure 10.33.

For series magnets as shown in Figure 10.40a, the magnet thickness is

$$l_m = K_A \frac{K_m F_{ad}}{H_{c,125\,^\circ\mathrm{C}}} \tag{10.110}$$

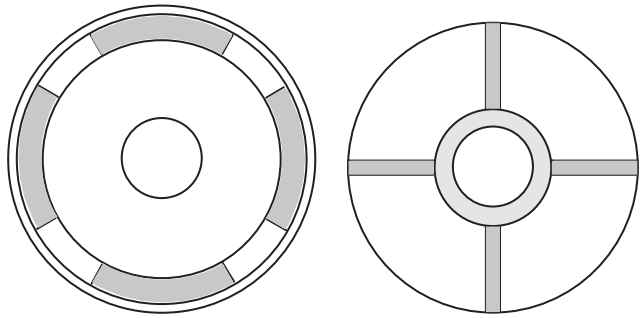

Figure 10.40 Configuration of series and parallel magnets (a) surface mounted with sleeve rings and (b) parallel magnets

For parallel magnets as shown in Figure 10.40b, the magnet thickness is

$$l_m = K_A \frac{K_m F_{ad}}{2H_{c,125\,^\circ\mathrm{C}}} \tag{10.111}$$

where K_A is a safety ratio, which can be chosen to be 1.1, therefore

$$F_{ad} = \frac{0.9mWK_w K_{ad} \sin\delta}{p} I \tag{10.112}$$

The width of rectangular magnets can be determined by

$$b_m = \frac{V_m}{2pl_m l_{fe}} \tag{10.113}$$

The radius of arc-shaped magnets can be determined by

$$R = \frac{V_m}{2\pi\alpha l_m l_{fe}} \tag{10.114}$$

Once the initial magnet volume and size have been determined, FEA can be used for further design analysis and optimization. The numerical calculation will help to identify whether the volume of magnets from the preliminary design is sufficient, insufficient, or excessive. Therefore, magnet volume can be further optimized during the numerical calculations.

In PM motor design and optimization, there are many conflicting design objectives. Multi-objective optimization is usually necessary in order to meet design criteria. In this chapter, the optimization objective is defined as the minimal usage of PM material while satisfying the performance requirements. The optimization problem is defined as

$$\min\{V_m(X)\} \tag{10.115}$$

subject to

$$f_i(X) \le 0, \quad i = 1, 2, \ldots, n \tag{10.116}$$

where X is a vector of the magnet width, thickness, and axial length:

$$X = \{b_m, l_m, l_{fe}\} \tag{10.117}$$

$f_i(X)$ is the motor performance requirements. Here, these requirements are defined as back emf, efficiency, maximum torque, and short-circuit current. These performances are calculated during the optimization process.

The optimization process starts with the preliminary design of the motor. The no-load magnetic field is first calculated using FEA to verify the back emf and short-circuit current. The load magnetic field is then calculated to confirm the maximum power/torque and efficiency. During each FEA, the magnet size is adjusted for given constraints.

The optimization implemented using FEA is shown in Figure 10.41. Saturation, salience, and air-gap flux waveform can also be verified during numerical calculations.

10.3.5 Eddy Current Losses in the Magnets of PM Machines

The eddy current loss in the magnets of PM motors in a HEV and PHEV is usually not taken into consideration in traditional motor design and analysis. However, due to the high conductivity of the rare earth magnet Nd–Fe–B, and slot/tooth harmonics, there is eddy current loss generated inside the magnets. This loss may not greatly affect the efficiency of the motor, but the temperature rise inside the magnets caused by this loss can lead to unpredictable deterioration of the magnets, such as degradation of performance and potential demagnetization. In addition, the output voltage of the PWM inverter contains abundant high-frequency harmonics, which induce excessive loss in the magnets. The excessive heat in PM motors induced by the eddy current loss combined with other losses can degrade the performance of the machine [92].

For sinusoidal supply, the eddy current loss in the magnets of a SPM motor is obtained from time-stepped FEA to be 102 W for a 50 kW PM motor. The eddy current loss in the magnet of an IPM was calculated to be 10 W for the same motor.

For PWM supply, the eddy current loss in the magnets of a SPM is 249 W for a 50 kW PM motor. The eddy current loss in the magnet of an IPMSM was 25 W for the same motor.

10.4 Switched Reluctance Motors

Both switched reluctance motors and synchronous reluctance motors have attracted attention in traction applications due to their simple structure, unnecessary squirrel cage or magnets on the rotor, very little loss on the rotor, and ease of control [93–113].

Although they provide many advantages, PM motors and induction motors both have their own limitations. For example, PM motors face the possibility of demagnetization at extremely high temperature, limited speed range, difficulty in protecting the powertrain during a fault condition, and so on. Induction motors have limited torque capabilities at low speeds, lower torque density and lower efficiency, noise due to stator/rotor slot combinations, and so on.

From the section above we can see that the torque of a synchronous motor has two terms, one related to E_o and X_d, which is induced by the rotor PM field, and one related

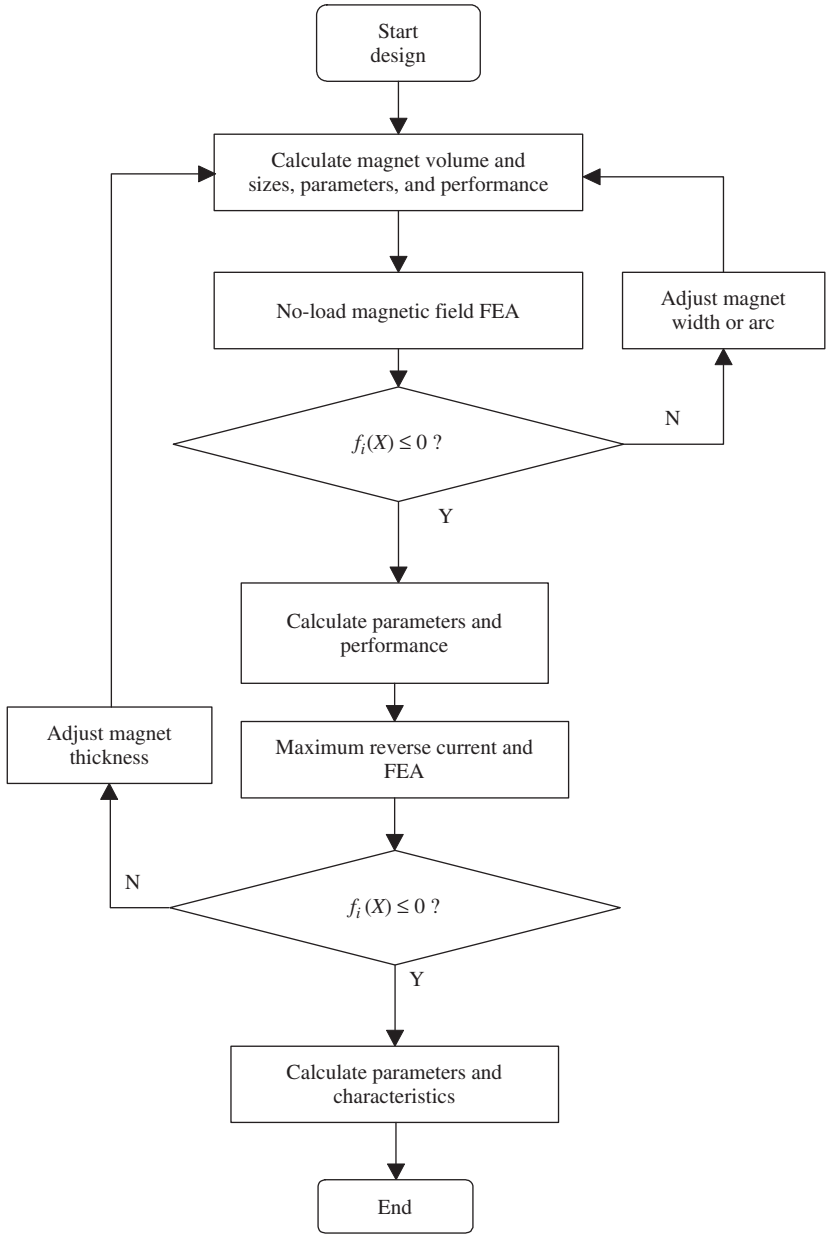

Figure 10.41 Optimization of magnet usage

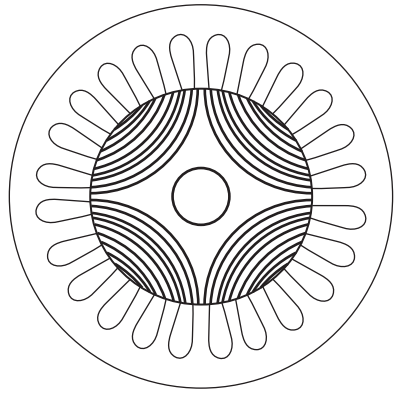

Figure 10.42 The synchronous reluctance motor. (T. Matsuo and T. A. Lipo, "Rotor Design Optimization of Synchronous Reluctance Machine," *IEEE Transactions on Energy Conversion*, Vol. 9, no. 2, pp. 359–365, June 2004. © [2004] IEEE. Reprinted, with permission, from IEEE Transactions on Energy Conversion)

to V, X_d, and X_q, which is induced by the difference in reactance of the d axis and q axis. In other words, even if the magnets are removed, an IPM motor can still generate torque with a sinusoidal supply due to the existence of salience of the rotor. This is called a synchronous reluctance motor. The stator and the rotor of a synchronous reluctance motor have the same number of poles.

Switched reluctance or synchronous reluctance motors do not use magnets or a squirrel cage. They simply use the difference in d-axis and q-axis reactance to produce reluctant torque. Therefore, they are similar to a synchronous motor without excitation and therefore named a switched reluctance motor. Hence only the second term of Equation 10.72 exists. The torque of a switched reluctance motor with sinusoidal supply is

$$T = \frac{mV^2}{2\omega_R}\left(\frac{1}{X_q} - \frac{1}{X_d}\right)\sin(2\theta) \tag{10.118}$$

In order to increase the torque of a switched reluctance motor, the q-axis and d-axis reactance is designed to have a large difference. A cross-section of a synchronous motor is shown in Figure 10.42.

Switched reluctance motors are similar to synchronous motors but will have different numbers of poles on the stator and the rotor. Figure 10.43 shows the cross-section of a switched reluctance motor and its control circuit.

10.5 Doubly Salient Permanent Magnet Machines*

Doubly-salient permanent magnet (DSPM) machines, a new kind of inverter-fed electrical traction motor first proposed in the early 1990s [115, 116], are becoming more and more attractive because of their distinct features, such as high efficiency, high power density, and simple structure. Much progress has been made on the design of DSPM machines. For

* © [2007] IEEE. Reprinted, with permission, from IEEE on Magnetics.

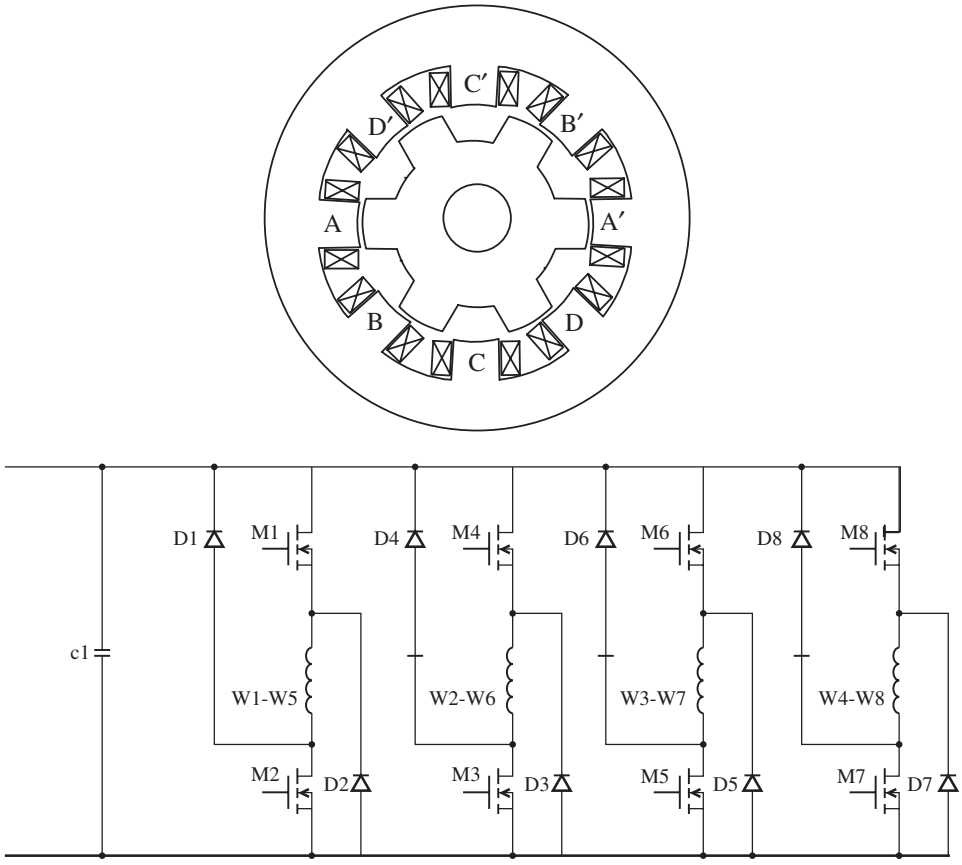

Figure 10.43 The cross-section of a 6/8-pole switched reluctance motor and its control circuit: top cross sectional area of the SRM; bottom, control circuit of the SRM

example, Liao *et al*. discussed the basic principles of DSPM machines in 1992, 1993, and 1995 [116–118]. Cheng and Chau and co-workers studied the steady state characteristics and performance of DSPM machines using nonlinear varying-network magnetic circuit analysis [119–123].

A DSPM machine resembles the structure of a SRM motor except that PMs are inserted in the stator. Therefore some common techniques used in the SRM motor are also adopted in the design and control of DSPM machines. For example, wider rotor pole arc, advanced shutoff angle control, and lagged firing angle control can all be used in the design and control of DSPM machines. However, due to the existence of PMs in the stator, the behavior of a DSPM machine is different from that of a SRM motor. Therefore, new design and control concepts need to be explored to optimize the performance of DSPM machines.

Figure 10.44 shows the typical geometry of a DSPM machine with 6/4 pole pairs, where AX, BY, CZ and A′X′, B′Y′, C′Z′ are the three-phase windings. It resembles the structure of a SRM motor, except that PMs are inserted in the stator. The three-phase flux linkages are shown in Figure 10.45. Because of the existence of PMs in the stator, PM

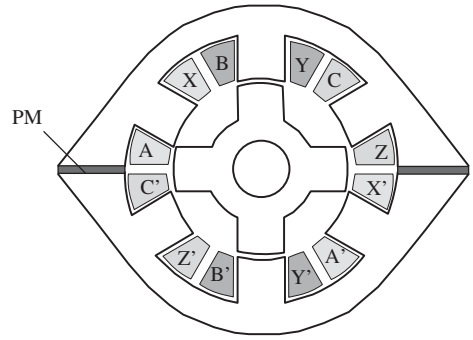

Figure 10.44 Typical DSPM geometry with 6/4 pole pairs

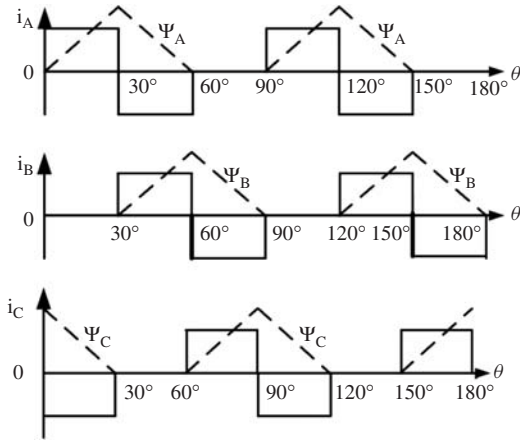

Figure 10.45 Flux linkage (dashed lines) and commutating mode (solid lines)

flux plays a major role in the winding flux linkage. Therefore, dual-polarity control can be employed, as shown in Figure 10.45, to improve the power density.

In the design practices of SRM motors, in order to ensure the winding commutation and self-start capability at any rotor position and either rotating direction, there should be a small overlap between the adjacent stator and rotor salient poles when the axis of the stator pole is aligned with that of the rotor pole. Therefore the width of the rotor pole is usually larger than that of the stator. This technology is also used in DSPM machines [119] because of the structural similarity. But due to the existence of PMs in the stator, cogging torque exists in DSPM machines. According to the flux–mmf diagram of PM machines, cogging torque will reach its minimum if the resultant gap reluctance is uniform at any rotor position [124]. Therefore, for a 6/4 pole-paired DSPM machine, if the width of the rotor pole equals that of the stator and their width is one-half of the pitch, then cogging torque will reach its minimal value; if the rotor pole width is larger than the stator pole width, the cogging torque will increase significantly because the gap reluctance will not be uniform as the rotor position varies. Cogging torque is one of the most important issues

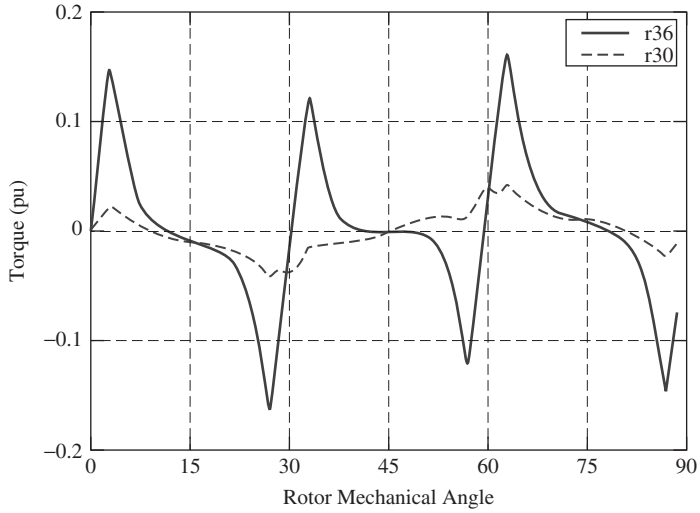

Figure 10.46 Cogging torque with different rotor pole width (unskewed rotor)

of DSPM machines. The cogging torque obtained from FEA is shown in Figure 10.46 for the larger rotor pole width of 36° and uniform width of 30°. The cogging torque was calculated using 2D FEA. It can be seen from Figure 10.46 that the cogging torque is significantly less for the smaller rotor pole width. It can also be seen that the cogging torque has different peaks. This is caused by the different linkage flux from the two PMs. When the rotor poles are aligned with the stator poles that are adjacent to the magnets, there is less flux leakage. Therefore there is more cogging torque. When the rotor poles are aligned with the stator poles that are in the middle of the two magnets, more flux leakage is seen. Therefore there is less cogging torque.

In order to minimize the cogging torque of a DSPM machine, the width of the rotor pole is designed to be the same as that of the stator, both equal to one-half of the pole pitch,

$$\theta_s = \theta_r = \frac{\pi}{N_s} \tag{10.119}$$

For a 6/4 pole-paired DSPM machine, it is 30° mechanical degrees.

Second, a skewed rotor is used to ensure the capability of self-starting at any rotor position and either rotating direction. From the flux linkage curve, a skewed rotor can also lead to overlap between the adjacent stator and rotor salient poles, which provides the same effect as that of the larger rotor pole width used in SRM motors. In order to obtain the largest output capability, the skew angle is chosen to be one-half of the stator salient pole width,

$$\theta_{skew} = \frac{\theta_r}{\mathbf{2}} = \frac{\pi}{\mathbf{2}N_s} \tag{10.120}$$

For a 6/4 pole-paired DSPM machine, the skew angle is 15°.

The flux linkage of the skewed rotor DSPM machine is shown in Figure 10.47. It can be seen that the flux linkages of this machine are different from that of the non-skewed

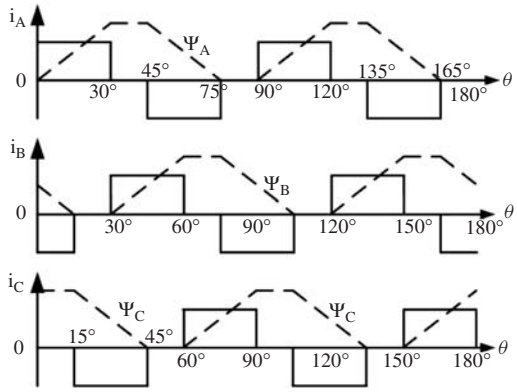

Figure 10.47 Flux linkage (dashed lines) and commutating mode (solid lines) of a skewed rotor DSPM machine

one shown in Figure 10.45, that is, the coverage of flux linkage is increased from 120° to 150°. As a result, the six-state commutating mode can be employed.

In the control of conventional DSPM machines, a three-state commutating mode was used, that is, +A − C, −A + B, and −B + C respectively, as shown in Figure 10.45. This simple commutating mode generally results in poor performance of the DSPM machine. It can be seen that the current commutating from positive to negative is in sequence. But in practice, because of the current continuity, the turn-off angle of the positive current should be advanced, or the freewheeling current will create a reverse torque. This will cause control complications and decrease output ability.

According to the same commutating principle as in conventional DSPM motors, that is, positive current conducts at the rising slope of flux linkage, while negative current conducts at the falling slope, a new commutating mode for the novel skewed rotor DSPM motor can be developed as shown by the solid line in Figure 10.47. It is a six-state commutating mode. The conducting sequences are +A − B, +A − C, +B − C, +B − A, +C − A, and +C − B respectively. Each state will be conducted for 60° electrical degrees continuously, and there is a 60° interval between the positive and negative current commutation. This commutating mode makes it possible to neglect the control of turn-off angle, therefore commutating performance can be improved and reliability enhanced.

10.6 Design and Sizing of Traction Motors

The most important task in the design of a traction drive is to calculate the size of the motor. Take a PM motor as an example. The power of the motor can be expressed as in Equation 10.70 and the back emf can be expressed as in Equation 10.96. Substituting Equation 10.96 into Equation 10.70, we have

$$P = mE_0 I\cos\delta = mI\cos\delta\sqrt{2}\pi K_w f W\Phi \tag{10.121}$$

The linear current density (or specific current density) along the inner stator surface is A (A/m) and the inner diameter of the stator is D. Then

$$2mWI = \pi DA \tag{10.122}$$

The total flux per pole can be expressed in terms of air-gap flux density B:

$$\Phi = \frac{\pi Dl}{2p} B\alpha \tag{10.123}$$

where l is the stack length of the stator, α is the pole enclosure as a percentage of the pole pitch, and B is the air-gap flux density. In PM motor control, we set the inner power angle δ to 0 to achieve maximum torque. Since $f = pn/60$,

$$P = m\frac{\pi DA}{2mW}\sqrt{2}\pi K_w \frac{pn}{60} W \frac{\pi Dl}{2p} B\alpha \tag{10.124}$$

Therefore

$$D^2 l = \frac{60}{\sqrt{2}\pi^3} \frac{4}{\alpha K_w} \frac{P}{AB} \frac{1}{n} \tag{10.125}$$

Since K_w, A, and B are in a relatively narrow range for all types of motors, this expression shows that the effective volume of the motor is proportional to power P and inversely proportional to speed n. Typical values for A are 100 kA/m for small air-cooled motors, and up to 400 kA/m for liquid-cooled motors. The typical range for B is about 0.4 T for small motors, and up to 1.2 T for high-density motors. Considering that $P = T2\pi n/60$, we have

$$D^2 l = k\frac{P}{n} \propto T \tag{10.126}$$

In other words, the size of an electric motor is proportional to its torque rating.

10.6.1 Selection of A and B

In the above equations for sizing traction motors, both A and B are experience-based selections. B shows how much the magnetic material (silicon steel) is utilized and A shows how much the electric material (copper or aluminum) is utilized. B is limited by magnetic losses in the teeth and yoke. A high B means less magnetic material but higher magnetic losses. A high A means less copper material but higher electric losses. Ambient temperature, operating frequency, and cooling method can impact the selection of A and B. Large motors will generally have larger A and B values.

10.6.2 Speed Rating of the Traction Motor

The rotor volume is inversely proportional to rotor speed. Hence, a higher speed rating means a smaller size. But a higher speed means a higher operating frequency, which results in more magnetic losses (eddy current and hysteresis losses). Smaller values of A and B may be necessary to limit the loss in high-speed motors.

For example, a four-pole 1500 rpm motor operates at 50 Hz, but a four-pole 12 000 rpm motor operates at 400 Hz. Since eddy current loss is proportional to f^2, and hysteresis loss is proportional to f^α $(1 < \alpha < 2)$, if the same magnetic flux density is chosen for the two motors, then the losses in the high-speed motor will be many times that of the low-speed motor even if the size of motor is much smaller. This is because loss increases 64 times, but size $(D^2 l)$ reduces by only a factor of 8.

10.6.3 Determination of the Inner Power

In Equation 10.125, the power used in the sizing is inner power (not shaft power). Therefore, for motors, that power is the shaft power divided by the efficiency and power factor, $P' = K_E P_N/(\eta_N \cos\varphi_N)$, and for a generator, $P' = K_E P_N/\cos\varphi_N$, where K_E is the ratio of back emf and rated supply voltage.

Since the efficiency η and power factor are not known until the design is finished, we have to start by making assumptions for these values and validate them at the end of the design.

10.7 Thermal Analysis and Modeling of Traction Motors*

Thermal issues are important aspects in traction motor design and analysis. Traction motors exhibit high frictional and windage losses due to high-speed operation, high magnetic losses due to high-frequency operation, and additional losses caused by PWM harmonics. Thermal analysis is of particular importance for PM motors because the magnets can be demagnetized at high temperatures [125].

Thermal studies on electric motors often approach the subject using FEA. Time-stepping FEA can provide greater accuracy for the thermal distribution in a motor. However, it remains relatively time consuming and does not provide as much insight as an analytical solution. Various analytical and numerical methods have been developed for the thermal analysis of various types of electric motors [126–138]. This section contains a discussion on how to calculate the temperature in a PM motor.

Thermal resistances in the lumped-parameter representation circumscribe the paths for heat transfer and are analogous to resistances in an electric circuit. The model thereby establishes the equivalent parameters between the thermal and electrical domains as given in Table 10.6.

The analogy allows the development of a lumped-parameter thermal model for any electric motor. The thermal capacitances are usually neglected since only steady state operation of the machine is of particular importance. Figure 10.48 shows the thermal equivalent circuit of a SPM. T_{in}, T_{stator}, T_{magnet}, T_{rotor}, T_w, and T_{shaft} respectively describe the temperatures of the inner surface of insulation between stator and casing, the

Table 10.6 Analogy of thermal and electrical domains

Electric circuit	Thermal circuit
Electric voltage u (V)	Temperature T (K)
Current I (A)	Heat loss Q (W)
Electrical resistance R (Ω)	Thermal resistance R (K/W)
Electrical conductivity σ (S/m)	Thermal conductivity k (W/(m K))

* Reproduced with permission from Xiaofeng Ding, Madhur Bhattacharya1, and Chunting Mi., "Simplified Thermal Model of PM Motors in Hybrid Vehicle Applications Taking into Account Eddy Current Loss in Magnets," Journal of Asia Electric Vehicles, vol. 8, no. 1, pp. 1337–1343, June 2010.

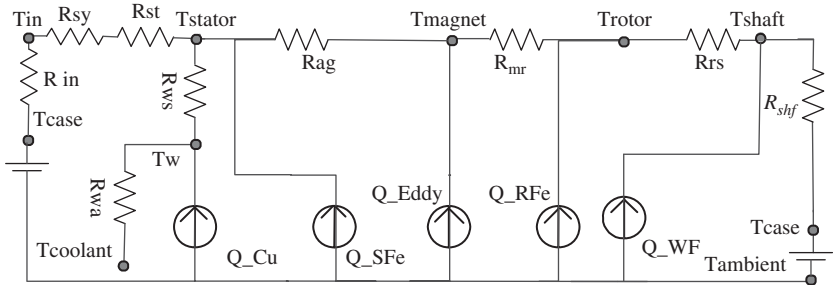

Figure 10.48 Equivalent circuit mode

inner surface of the stator core, the outer surface of the magnet, the outer surface of the rotor, the part of the winding within the stator core, and the part of the shaft under the rotor core. $T_{coolant}$ and T_{case} are assigned as boundary conditions.

The individual thermal resistances are:

R_{ag}, convection thermal resistance of the air gap
R_{mr}, radial conduction thermal resistance of the pole
R_{rs}, radial conduction thermal resistance of the rotor core
R_{shf}, thermal resistance of the shaft
R_{sy}, radial conduction thermal resistance of the stator yoke
R_{st}, radial conduction thermal resistance of stator teeth
R_{ws}, conduction thermal resistance between the windings and stator
R_{in}, contact thermal resistance between the stator and housing.

The Thermal Resistance of the Air Gap, R_{ag}

Within the air gap the heat flow is greater than in the adjoining air as almost 99% heat emitted from the rotor surface is transferred directly across it to the stator.

Taylor [127] developed the dimensionless convection correlation method from testing two concentric cylinders rotating relative to each other, to consider the heat transfer across the air gap; the method was further modified by Gazley [128]. The thermal resistance can be defined in terms of the air-gap length l_g, a dimensionless Nusselt number N_{nu}, the thermal conductivity of motionless air K_{air}, and the average area of the air-gap cylindrical surface A_{ag}:

$$R_{ag} = \frac{l_g}{N_{nu} K_{air} A_{ag}} \tag{10.127}$$

$$\begin{aligned} N_{nu} &= 2, & N_{Ta} &\le 41 \\ N_{nu} &= 0.212 N_{Ta}^{0.63} N_{Pr}^{0.27}, & 41 &< N_{Ta} \le 100 \\ N_{nu} &= 0.386 N_{Ta}^{0.5} N_{Pr}^{0.27}, & N_{Ta} &\le 41 \end{aligned}$$

The values of the Nusselt N_{nu}, Taylor N_{Ta}, and Prandtl N_{Pr} numbers for two rotating smooth cylinders were presented by Taylor. The flow in the air gap is laminar when $N_{Ta} \leq 41$, whereas the flow through the vertex with enhanced heat transfer ranges over $41 < N_{Ta} \leq 100$. If $N_{Ta} > 100$ there is fully turbulent flow in the air gap. Later, Gazley [128] modified the heat transfer with a 10% increase in the experimental results due to the slot effects.

The expression given in (10.127) is applicable to air-cooled electrical motors. In order to analyze liquid-cooled motors, the thermal conductivity of the air gap is assumed to have a constant value, and an equivalent air-gap resistance can be calculated considering the air gap as equal to a cylinder. Hsu *et al*. [139] showed that the thermal conductivity of the Toyota Prius traction motor is 10 W/(m °C) based on an oil and air convective mixture. In this case, the simpler expression for deriving the air-gap thermal resistance is given as follows:

$$R_{ag2} = \frac{\ln(r_{is}/r_{magnet})}{2\pi k_{ag} L_g} \tag{10.128}$$

where r_{magnet} is the outer magnet radius, r_{is} the inner stator radius, and k_{ag} thermal conductivity of the air gap.

The Radial Conduction Thermal Resistance of the Rotor Core, R_{rs}

Figure 10.49 shows the rotor core as a cylinder made of laminations. The radial heat transfer is more pronounced than the axial heat transfer in the laminations, therefore the heat transfer coefficient is calculated for the radial direction:

$$R_{rs} = \frac{\ln(r_{rotor}/r_{shaft})}{2\pi k_{rotor} L_s} \tag{10.129}$$

where r_{shaft} is the shaft radius, k_{rotor} is the thermal conductivity of rotor core, and L_s is axial length of the rotor core.

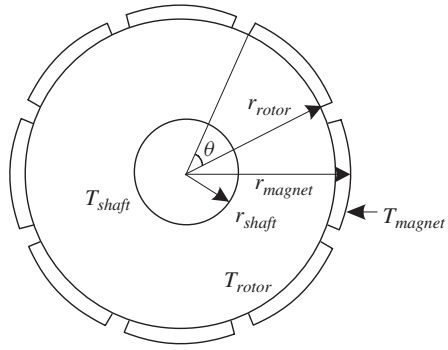

Figure 10.49 Radial dimensions of the rotor

The Radial Conduction Thermal Resistance of the Poles, R_{mr}

The surface-mounted magnets distributed on the rotor core are assumed to be an equivalent cylinder with $n\theta$ radians:

$$R_{mr} = \frac{\ln(r_{magnet}/r_{rotor})}{n\theta k_m L_s} \tag{10.130}$$

where r_{magnet} is the outer rotor radius, r_{rotor} is the rotor core radius, n is the number of poles, θ is the width of each pole in radians, k_m is the thermal conductivity of the magnet, and L_s is the axial length of the poles.

The Thermal Resistance of the Shaft, R_{shf}

The shaft is represented as a cylindrical rod with axial heat conduction and separated into three parts [126]: one that lies under the rotor core; a second that lies under the bearing; and a third that acts as a thermal connection between the mean temperatures of the previous two. As the bearings provide good thermal contact, it is sufficient to consider thermal contact that exists between the shaft and the thermal casing (Figure 10.50). The convection between the shaft and adjoining air is neglected as the heat transfer from the air to the shaft is negligible. Thus

$$R_{shf} = (R_a + R_b)/2 \tag{10.131}$$

where

$$R_a = \frac{1}{2\pi k_{shf} L_s} + \frac{L_{bs}}{2\pi k_{shf}(D_{shf}/2)^2}$$

$$R_b = \frac{1}{4\pi k_{shf} L_b} + \frac{L_{bs}}{2\pi k_{shf}(D_{shf}/2)^2}$$

k_{shf} is the thermal conductivity of the shaft, L_b is the thickness of the bearing, D_{shf} is the radius of the shaft, and L_{bs} is the distance from the bearing center to rotor mean.

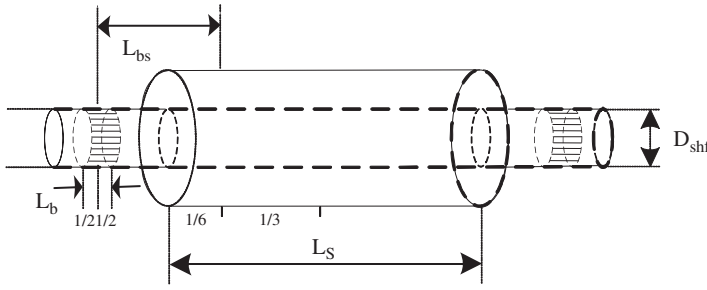

Figure 10.50 Axial dimensions of the shaft

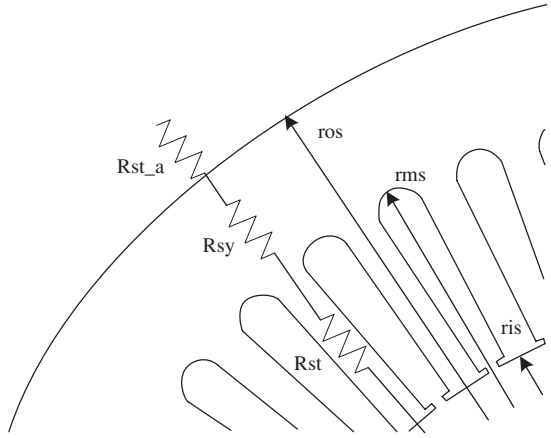

Figure 10.51 Radial dimensions of the stator

The Radial Conduction Thermal Resistance of Stator Teeth, R_{st}

As both the rotor and stator core consist of layers of laminations, only the thermal conductivity in the radial direction is considered (Figure 10.51). In order to calculate the thermal resistance of the stator precisely, the stator is modeled as two parts, one as the stator yoke and the other as the stator teeth. The equivalent cylinder with a reduction factor p is used to model the stator teeth. Thus

$$R_{st} = \frac{\ln(r_{ms}/r_{is})}{2\pi k_{iro} L_s \rho} \tag{10.132}$$

where r_{is} the inner stator radius, r_{ms} is the inner stator yoke radius, k_{iro} is the thermal conductivity of the stator, ρ is the percentage of the teeth section with respect to the total teeth plus all slots section.

The Radial Conduction Thermal Resistance of the Stator Yoke, R_{sy}

This is calculated from

$$R_{sy} = \frac{\ln(r_{os}/r_{ms})}{2\pi k_{iro} L_s} \tag{10.133}$$

where r_{os} is the outer stator yoke radius.

The Conduction Thermal Resistance between the Windings and Stator, R_{ws}

This is obtained from

$$R_{ws} = \frac{S_{slot} - S_{cu}}{l_s k_{cu,ir} A_{slot}} \tag{10.134}$$

where S_{slot} is the stator slot surface, S_{cu} is the copper section in the stator slot, l_s is stator slot perimeter, $k_{cu,ir}$ is the equivalent conductivity coefficient of the air and insulation material in the stator slot, evaluated by simulation, and A_{slot} is the interior slot surface.

Convective Thermal Resistance between Windings External to the Stator and Adjoining Air, R_{wa}

The convection coefficient between the end winding of the stator and adjoining air is found from [126]

$$h_{wa} = 15.5(0.29v + 1) \tag{10.135}$$

where $v = r_{magnet}\omega\eta$ and the speed of inner air v need be no more than 7.5 m/s; ω is the rotor angular velocity and η is fan efficiency.

The value of 50% was assumed for the fan efficiency, usually due to unavailable information on the radial air velocity. Sometimes, there is an oil and air mixture adjoining the winding, so an equivalent increase of fan efficiency is used.

The total surface of the winding external to the stator can be calculated as

$$S_{wa} = (L_c - L_s)2\pi r_{is} \tag{10.136}$$

where L_c is the external casing length.

Therefore, from (10.135) and (10.137), the thermal resistance between the winding external to the stator and adjoining air can be calculated,

$$R_{wa} = \frac{1}{S_{wa}h_{wa}} \tag{10.137}$$

Assigning the losses and casing temperature (90 °C) to the thermal circuit, the temperature of individual components in the motor can be obtained after the calculation.

Consider the equivalent circuit model in Figure 10.48.

At node T_{in}

$$\frac{T_{stator} - T_{in}}{R_{sy} + R_{st}} - \frac{T_{in} - T_{case}}{R_{in}} = 0 \tag{10.138}$$

At node T_{stator}

$$\frac{T_{stator} - T_{in}}{R_{sy} + R_{st}} - \frac{T_w - T_{stator}}{R_l} - \frac{T_{magnet} - T_{stator}}{R_{ag}} = Q_{SFe} \tag{10.139}$$

At node T_w

$$\frac{T_w - T_{stator}}{R_{ws}} - \frac{T_w - T_{coolant}}{R_{wa}} = Q_{cu} \tag{10.140}$$

At node T_{magnet}

$$\frac{T_{magnet} - T_{stator}}{R_{ag}} - \frac{T_{rotor} - T_{magnet}}{R_m r} = Q_{Eddy} \tag{10.141}$$

At node T_{rotor}

$$\frac{T_{rotor} - T_{shaft}}{R_{rs}} + \frac{T_{rotor} - T_{magnet}}{R_{mr}} = Q_{RFe} + Q_{WF} \tag{10.142}$$

At node T_{shaft}

$$\frac{T_{rotor} - T_{shaft}}{R_{rs}} - \frac{T_{shaft} - T_{case}}{R_{shf}} = 0 \tag{10.143}$$

The above equations can be written in matrix form and solved by numerical methods:

$$\begin{bmatrix} -1/(R_{sy}+R_{st}) - 1/R_{in} & R_{sy} + R_{st}a_{12} & 0 & 0 & 0 & 0 \\ -1/(R_{sy}+R_{st}) & 1/R_{ag} + 1/(R_{sy}+R_{st}) + 1/R_{ws} & -1/R_{ws} & -1/R_{ag} & 0 & 0 \\ 0 & -1/R_{ws} & 1/R_{ws} & 0 & 0 & 0 \\ 0 & -1/R_{ag} & 0 & 1/R_{mr} + 1/R_{ag} & -1/R_{mr} & 0 \\ 0 & 0 & 0 & -1/R_{mr} & -1/R_{rs} + 1/R_{mr} & -1/R_{rs} \\ 0 & 0 & 0 & 0 & 1/R_{rs} & -1/R_{rs} - 1/R_{shf} \end{bmatrix} \bullet \begin{bmatrix} T_{in} \\ T_{stator} \\ T_{w} \\ T_{magnet} \\ T_{rotor} \\ T_{shaft} \end{bmatrix} = \begin{bmatrix} -90/R_{in} \\ Q_{SFe} \\ Q_{cu} + 110/R_{wa} \\ Q_{Eddy} \\ Q_{RFe} \\ Q_{WF} + 90/R_{shf} \end{bmatrix} \tag{10.144}$$

The temperature of a PM motor is solved with the temperature shown in Figure 10.52. The temperature of the different components is given in Tables 10.7 and 10.8 for a PM motor operated under pure sinusoidal supply and under PWM supply, respectively.

Figure 10.52 Temperature profiles in magnet

Table 10.7 Temperature distribution under sinusoidal and PWM waveforms

Name	Sinusoidal (°C)	PWM (°C)
Insulation	90–113.23	90–159.14
Stator	113.23–152.35	159.14–198.25
Winding	155.29	202.47
Magnets	154.88–155.47	200.92–201.54
Rotor	155.47–169.76	201.54–213.83
Shaft	90–169.76	90–213.83

Table 10.8 Temperature distribution within the motor fed by a sinusoidal waveform

Name	Analytical method (°C)	Simulation (°C)
Insulation	90–113.23	90–119.45
Stator	113.23–152.35	120.21–156.73
Winding	155.29	162.63–180.39
Magnets	154.88–155.47	158.68–161.13
Rotor	155.47–169.76	156.34–162.90
Shaft	90–169.76	90–163.58

10.8 Conclusions

Electric motors and associated controllers are one of the key enabling technologies for electric, hybrid electric, and plug-in hybrid electric vehicles. Various types of electric motors and drive systems are available for the powertrain of electrified vehicles. Traction motors and drives experience very harsh environmental conditions, such as a wide temperature range (−30 to 60 °C), severe vibration and shock, high electromagnetic noise, size and weight constraints, stringent safety and reliability requirements, and so on. As a result, there are many unique aspects in the design, development, analysis, manufacturing, and research of electric motors and drives for traction applications which are all-important aspects but cannot all be covered in this chapter. Readers might consult the references below for further reading. For example, more in-depth studies about synchronous reluctance motor design and optimization can be found in [114] and studies of the uncontrolled generation in PM drive motors are covered in [140, 141].

References

1. Ehsani, M., Rahman, K.M., and Toliyat, H.A. (1997) Propulsion system design of electric and hybrid vehicles. *IEEE Transactions on Industrial Electronics*, **44**, 19–27.

2. Muta, K., Yamazaki, M., and Tokieda, J. (2004) Development of new-generation hybrid system THS II – drastic improvement of power performance and fuel economy. SAE World Congress, March 8–11, paper no. 2004-01-0064.
3. Chan, C.C., Jiang, K.T., Xia, J.Z. *et al*. (1996) Novel permanent magnet motor drive for electric vehicles. *IEEE Transactions on Industrial Electronics*, **43** (2), 331–339.
4. Ehsani, M., Gao, Y., and Gay, S. (2003) Characterization of electric motor drives for traction applications. Industrial Electronics Society, IECON'03, November 2–6 , Vol. 1, pp. 891–896.
5. Rahman, Z., Butler, K.L., and Ehsani, M. (2000) Effect of extended-speed, constant-power operation of electric drives on the design and performance of EV propulsion system. SAE Future Car Congress, April, paper no. 2001-01-0699.
6. Rahman, K.M. and Ehsani, M. (1996) Performance analysis of electric motor drives for electric and hybrid electric vehicle application. *Power Electronics in Transportation*, pp. 49–56.
7. Rahman, K.M., Fahimi, B., Suresh, G. *et al*. (2000) Advantages of switched reluctance motor applications to EV and HEV: design and control issues. *IEEE Transactions on Industry Applications*, **36** (1), 111–121.
8. Honda, Y., Nakamura, T., Higaki, T., and Takeda, Y. (1997) Motor design considerations and test results of an interior permanent magnet synchronous motor for electric vehicles. Proceedings of the IEEE Industry Applications Society Annual Meeting, October 5–9, pp. 75–82.
9. Kamiya, M. (2005) Development of traction drive motors for the Toyota hybrid system. International Power Electronics Conference, April 4–8.
10. Miller, J.M., Gale, A.R., McCleer, P.J. *et al*. (1998) Starter/alternator for hybrid electric vehicle: comparison of induction and variable reluctance machines and drives. Proceedings of the IEEE 1998 Industry Applications Society Annual Meeting, October 12–15, pp. 513–523.
11. Wang, T., Zheng, P., and Cheng, S. (2005) Design characteristics of the induction motor used for hybrid electric vehicle. *IEEE Transactions on Magnetics*, **41** (1), 505–508.
12. Harson, A., Mellor, P.H., and Howe, D. (1995) Design considerations for induction machines for electric vehicle drives. Proceedings of the IEE International Conference on Electrical Machines and Drives, September 11–13, pp. 16–20.
13. Krishnan, R. (1996) Review of flux-weakening in high performance vector controlled induction motor drives. Proceedings of the IEEE International Symposium on Industrial Electronics, June 17–20, pp. 917–922.
14. Miller, T.J.E. (1993) *Switched Reluctance Motors and their Control*, Magna Physics Publishing and Clarendon Press, Oxford.
15. (a) Miller, T.J.E. (2001) *Electronic Control of Switched Reluctance Machines*, Reed, New York, pp. 227–245; (b) Williamson, S.S., Emadi, A., and Rajashekara, K. (2007) Comprehensive efficiency modeling of electric traction motor drives for hybrid electric vehicle propulsion applications. *IEEE Transactions on Vehicular Technology*, **56** (4), 1561–1572.
16. West, J.G.W. (1994) DC, induction, reluctance and PM motors for electric vehicles. *Power Engineering Journal*, **8** (2), 77–88.
17. Welchko, B.A. and Nagashima, J.M. (2003) The influence of topology selection on the design of EV/HEV propulsion systems. *Power Electronics Letters*, **1** (2), 36–40.
18. Zhu, Z.Q. and Howe, D. (2007) Electrical machines and drives for electric, hybrid, and fuel cell vehicles. *Proceedings of the IEEE*, **95** (4), 746–765.
19. Chan, C.C. (2002) The state of the art of electric and hybrid vehicles. *Proceedings of the IEEE*, **90** (2), 247–275.
20. Jahns, T.M. and Blasko, V. (2001) Recent advances in power electronics technology for industrial and traction machine drives. *Proceedings of the IEEE*, **89** (6), 963–975.
21. Akin, B., Ozturk, S.B., Toliyat, H.A., and Rayner, M. (2009) DSP-based sensorless electric motor fault-diagnosis tools for electric and hybrid electric vehicle powertrain applications. *IEEE Transactions on Vehicular Technology*, **58** (6), 2679–2688.
22. Kou, B., Li, L., Cheng, S., and Meng, F. (2005) Operating control of efficiently generating induction motor for driving hybrid electric vehicles. *IEEE Transactions on Magnetics*, **41** (1), 488–491.

23. Zeraoulia, M., Benbouzid, M.E.H., and Diallo, D. (2006) Electric motor drive selection issues for HEV propulsion systems: a comparative study. *IEEE Transactions on Vehicular Technology*, **55** (6), 1756–1764.
24. Wang, T., Zheng, P., Zhang, Q., and Cheng, S. (2005) Design characteristics of the induction motor used for hybrid electric vehicles. *IEEE Transactions on Magnetics*, **41** (1), 505–508.
25. Li, W., Cao, J., and Zhang, X. (2010) Electrothermal analysis of induction motor with compound cage rotor used for PHEV. *IEEE Transactions on Industrial Electronics*, **57** (2), 660–668.
26. Asano, K., Okada, S., and Iwamam, N. (1992) Vibration suppression of induction-motor-driven hybrid vehicle using wheel torque observer. *IEEE Transactions on Industry Applications*, **28** (2), 441–447.
27. Diallo, D., Benbouzid, M.E.H., and Makouf, A. (2004) A fault-tolerant control architecture for induction motor drives in automotive applications. *IEEE Transactions on Vehicular Technology*, **53** (6), 1847–1855.
28. Benbouzid, M.E.H., Diallo, D., and Zeraoulia, M. (2007) Advanced fault-tolerant control of induction-motor drives for EV/HEV traction applications: from conventional to modern and intelligent control techniques. *IEEE Transactions on Vehicular Technology*, **56** (2), 519–528.
29. Proca, A.B., Keyhani, A., and Miller, J.M. (2003) Sensorless sliding-mode control of induction motors using operating condition dependent models. *IEEE Transactions on Energy Conversion*, **18** (2), 205–212.
30. Salmasi, F.R., Najafabadi, T.A., and Maralani, P.J. (2010) An adaptive flux observer with online estimation of DC-link voltage and rotor resistance for VSI-based induction motors. *IEEE Transactions on Power Electronics*, **25** (5), 1310–1319.
31. Proca, A.B., Keyhani, A., and Miller, J. (2002) Sensorless sliding-mode control of induction motors using operating condition dependent models. *Power Engineering Review*, **22** (7), 50–50.
32. Sudhoff, S.D., Corzine, K.A., Glover, S.F. *et al*. (1998) DC link stabilized field oriented control of electric propulsion systems. *IEEE Transactions on Energy Conversion*, **13** (1), 27–33.
33. Khoucha, F., Lagoun, S.M., Marouani, K. *et al*. (2010) Hybrid cascaded H-bridge multilevel-inverter induction-motor-drive direct torque control for automotive applications. *IEEE Transactions on Industrial Electronics*, **57** (3), 892–899.
34. McCleer, P.J., Miller, J.M., Gale, A.R. *et al*. (2001) Nonlinear model and momentary performance capability of a cage rotor induction machine used as an automotive combined starter-alternator. *IEEE Transactions on Industry Applications*, **37** (3), 840–846.
35. Degner, M.W., Guerrero, J.M., and Briz, F. (2006) Slip-gain estimation in field-orientation-controlled induction machines using the system transient response. *IEEE Transactions on Industry Applications*, **42** (3), 702–711.
36. Kim, J., Jung, J., and Nam, K. (2004) Dual-inverter control strategy for high-speed operation of EV induction motors. *IEEE Transactions on Industrial Electronics*, **51** (2), 312–320.
37. Neacsu, D.O. and Rajashekara, K. (2001) Comparative analysis of torque-controlled IM drives with applications in electric and hybrid vehicles. *IEEE Transactions on Power Electronics*, **16** (2), 240–247.
38. Liu, R., Mi, C., and Gao, W. (2008) Modeling of iron losses of electrical machines and transformers fed by PWM inverters. *IEEE Transactions on Magnetics*, **44** (8), 2021–2028.
39. Ding, X. and Mi, C. (2011) Impact of inverter on losses and thermal characteristics of induction motors. *International Journal on Power Electronics*, in press.
40. Mi, C., Slemon, G.R., and Bonert, R. (2003) Modeling of iron losses of permanent magnet synchronous motors. *IEEE Transactions on Industry Applications*, **39** (3), 734–742.
41. Khluabwannarat, P., Thammarat, C., Tadsuan, S., and Bunjongjit, S. (2007) An analysis of iron loss supplied by sinusoidal, square wave, bipolar PWM inverter and unipolar PWM inverter. International Power Engineering Conference, IPEC 2007, December 3–6, pp. 1185–1190.
42. Mi, C., Shen, J., and Natarajan, N. (2002) Field-oriented control of induction motors. IEEE Workshop on Power Electronics in Transportation (WPET'02), September.
43. Parker, R.J. and Studders, R.J. (1962) *Permanent Magnets and their Application*, John Wiley & Sons, Inc., New York.
44. Merrill, F.W. (1955) Permanent magnet excited synchronous motor. *AIEE Transactions*, **74**, 1754–1760.
45. Binns, K.J., Jabbar, M.A., and Parry, G.E. (1979) Choice of parameters in hybrid permanent magnet synchronous motor. *Proceedings of the IEE*, **126** (8), 741–744.

46. Honsinger, V.P. (1980) Performance of polyphase permanent magnet machines. *IEEE Transactions on Power Apparatus and Systems*, **99** (4), 1510–1518.
47. Rahman, M.A. and Little, T.A. (1984) Dynamic performance analysis of permanent magnet synchronous motors. *IEEE Transactions on Power Apparatus and Systems*, **103** (6), 1277–1282.
48. Rahman, M.A., Little, T.A., and Slemon, G.R. (1985) Analytical models for interior-type permanent magnet synchronous motors. *IEEE Transactions on Magnetics*, **21** (5), 1741–1743.
49. Zhou, P., Rahman, M.A., and Jabbar, M.A. (1994) Field and circuit analysis of permanent magnet machines. *IEEE Transactions on Magnetics*, **30** (4), 1350–1359.
50. Vaez, S., John, V.I., and Rahman, M.A. (1999) An on-line loss minimization controller for interior permanent magnet motor drives. *IEEE Transactions on Energy Conversion*, **14** (4), 1435–1440.
51. Uddin, M.N., Radwan, T.S., and Rahman, M.A. (2002) Performance of interior permanent magnet motor drive over wide speed range. *IEEE Transactions on Energy Conversion*, **17** (1), 79–84.
52. Rahman, M.A., Vilathgamuwa, M., Uddin, M.N., and Tseng, K.J. (2003) Non-linear control of interior permanent magnet synchronous motor. *IEEE Transactions on Industry Applications*, **39** (2), 408–416.
53. Jahns, T.M. (1984) Torque production in permanent magnet synchronous motor drives with rectangular current excitation. *IEEE Transactions on Industry Applications*, **20** (4), 803–813.
54. Morimoto, S., Sanada, M., and Takeda, Y. (1994) Wide-speed operation of interior permanent magnet synchronous motors with high performance current regulator. *IEEE Transactions on Industry Applications*, **30** (4), 920–926.
55. Jahns, T.M. (1987) Flux-weakening regime operation of an interior permanent-magnet synchronous motor drive. *IEEE Transactions on Industry Applications*, **23** (4), 681–689.
56. Morimoto, S., Sanada, M., and Takeda, Y. (1996) Inverter-driven synchronous motors for constant power. *IEEE Industry Applications Magazine*, pp. 18–24.
57. Zhu, Z.Q., Chen, Y.S., and Howe, D. (2000) On-line optimal field weakening control of permanent magnet brushless ac drives. *IEEE Transactions on Industry Applications*, **36** (6), 1661–1668.
58. Zhu, Z.Q., Shen, J.X., and Howe, D. (2006) Flux-weakening characteristics of trapezoidal back-EMF machines in brushless DC and AC modes. Proceedings of the International Power Electronics and Motion Control, August 13–16, pp. 908–912.
59. Shi, Y.F., Zhu, Z.Q., and Howe, D. (2006) Torque-speed characteristics of interior-magnet machines in brushless AC and DC modes, with particular reference to their flux-weakening performance. Proceedings of the International Power Electronics and Motion Control, August 13–16, pp. 1847–1851.
60. Safi, S.K., Acarnley, P.P., and Jack, A.G. (1995) Analysis and simulation of the high-speed torque performance of brushless DC motor drives. *IEE Proceedings – Electric Power Applications*, **142** (3), 191–200.
61. Bose, B.K. (1988) A microcomputer-based control and simulation of an advanced IPM synchronous machine drive system for electric vehicle propulsion. *IEEE Transactions on Industrial Electronics*, **35** (4), 547–559.
62. Bose, B.K. (1988) A high-performance inverter-fed drive system of an interior permanent magnet synchronous machine. *IEEE Transactions on Industry Applications*, **24** (6), 987–997.
63. Lovelace, E.C., Jahns, T.M., Kirtley, J.L. Jr., and Lang, J.H. (1998) An interior PM starter/alternator for automotive applications. Proceedings of the International Conference on Electrical Machines, December, pp. 1802–1808.
64. Lipo, T.A. (1991) Synchronous reluctance machines – a viable alternative for AC drives? *Electric Machines and Power Systems*, **19**, 659–671.
65. Soong, W.L., Staton, D.A., and Miller, T.J.E. (1995) Design of a new axially-laminated interior permanent magnet motor. *IEEE Transactions on Industry Applications*, **31** (2), 358–367.
66. Soong, W.L. and Ertugrul, N. (2002) Field-weakening performance of interior permanent-magnet motors. *IEEE Transactions on Industry Applications*, **38** (5), 1251–1258.
67. Chaaban, F.B., Birch, T.S., Howe, D., and Mellor, P.H. (1991) Topologies for a permanent magnet generator/speed sensor for the ABS on railway freight vehicles. Proceedings of the IEE International Conference on Electrical Machines and Drives, September 11–13, pp. 31–35.

68. Liao, Y., Liang, F., and Lipo, T.A. (1995) A novel permanent magnet machine with doubly salient structure. *IEEE Transactions on Industry Applications*, **3** (5), 1069–1078.
69. Chan, C.C., Jiang, J.Z., Chen, G.H. *et al*. (1994) A novel polyphase multipole square-wave permanent magnet motor drive for electric vehicles. *IEEE Transactions on Industry Applications*, **30** (5), 1258–1266.
70. Wang, J.B., Xia, Z.P., and Howe, D. (2005) Three-phase modular permanent magnet brushless machine for torque boosting on a downsized ICE vehicle. *IEEE Transactions on Vehicular Technology*, **54** (3), 809–816.
71. Russenschuck, S. (1990) Mathematical optimization techniques for the design of permanent magnet machines based on numerical field calculation. *IEEE Transactions on Magnetics*, **26** (2), 638–641.
72. Russenschuck, S. (1992) Application of Lagrange multiplier estimation to the design optimization of permanent magnet synchronous machines. *IEEE Transactions on Magnetics*, **28** (2), 1525–1528.
73. Rasmussen, K.F., Davies, J.H., Miller, T.J.E. *et al*. (2000) Analytical and numerical computation of air-gap magnetic fields in brushless motors with surface permanent magnets. *IEEE Transactions on Industry Applications*, **36** (6), 1547–1554.
74. Boules, N. (1990) Design optimization of permanent magnet DC motors. *IEEE Transactions on Industry Applications*, **26** (4), 786–792.
75. Proca, A.B., Keyhani, A., El-Antably, A. *et al*. (2003) Analytical model for permanent magnet motors with surface mounted magnets. *IEEE Transactions on Energy Conversion*, **18** (3), 386–391.
76. Pavlic, D., Garg, V.K., Repp, J.R., and Weiss, J.A. (1988) Finite element technique for calculating the magnet sizes and inductance of permanent magnet machines. *IEEE Transactions on Energy Conversion*, **3** (1), 116–122.
77. Miller, T.J.E., McGilp, M., and Wearing, A. (1999) Motor design optimization using SPEED CAD software – practical electromagnetic design synthesis. IEE Seminar, Ref. no. 1999/014, pp. 1–5.
78. ANSYS (2005) http://www.ansoft.com (accessed April 11, 2005).
79. Kenjo, T. and Nagamori, S. (1985) *Permanent Magnet and Brushless DC Motors*, Clarendon Press, Oxford.
80. Miller, T.J.E. (1989) *Permanent Magnet and Reluctance Motor Drives*, Oxford Science Publications, Oxford.
81. Slemon, G.R. and Liu, X. (1992) Modeling and design optimization of permanent magnet motors. *Electric Machines and Power Systems*, **20**, 71–92.
82. Bose, B.K. (1997) *Power Electronics and Variable Frequency Drives – Technology and Applications*, IEEE Press, Piscataway, NJ.
83. Balagurov, V.A., Galtieev, F.F., and Larionov, A.N. (1964) *Permanent Magnet Electrical Machines*, Energia, Moscow (in Russian, and translation in Chinese).
84. Gieras, J.F. and Wing, M. (2002) *Permanent Magnet Motor Technology: Design and Applications*, 2nd edn, Marcel Dekker, New York.
85. Mi, C., Filippa, M., Liu, W., and Ma, R. (2004) Analytical method for predicting the air-gap flux of interior-type permanent magnet machines. *IEEE Transactions on Magnetics*, **40** (1), 50–58.
86. Cho, D.H., Jung, H.K., and Sim, D.J. (1999) Multiobjective optimal design of interior permanent magnet synchronous motors considering improved core loss formula. *IEEE Transactions on Energy Conversion*, **14** (4), 1347–1352.
87. Borghi, C.A., Casadei, D., Cristofolini, A. *et al*. (1999) Application of multi objective minimization technique for reducing the torque ripple in permanent magnet motors. *IEEE Transactions on Magnetics*, **35** (5), 4238–4246.
88. Upadhyay, P.R., Rajagopal, K.R., and Singh, B.P. (2004) Effect of armature reaction on the performance of axial field permanent magnet brushless DC motor using FE method. *IEEE Transactions on Magnetics*, **40** (4), 2023–2025.
89. Li, Y., Zou, J., and Lu, Y. (2003) Optimum design of magnet shape in permanent magnet synchronous motors. *IEEE Transactions on Magnetics*, **39** (6), 3523–3526.
90. Fujishima, Y., Wakao, S., Kondo, M., and Terauchi, N. (2004) An optimal design of interior permanent magnet synchronous motor for the next generation commuter train. *IEEE Transactions on Applied Superconductivity*, **14** (2), 1902–1905.

91. Mi, C. (2006) Analytical design of permanent magnet traction drives. *IEEE Transactions on Magnetics*, **42** (7), 1861–1866.
92. Ding, X. and Mi, C. Modeling of eddy current loss and temperature of the magnets in permanent magnet machines. *Journal of Circuits, Systems, and Computers*, submitted.
93. Fahimi, B., Emadi, A., and Sepe, R. (2004) A switched reluctance machine-based starter/alternator for more-electric cars. *IEEE Transactions on Energy Conversion*, **19** (1), 116–124.
94. Rahman, K.M. and Schulz, S.E. (2002) Design of high-efficiency and high-torque-density switched reluctance motor for vehicle propulsion. *IEEE Transactions on Industry Applications*, **38** (6), 1500–1507.
95. Ramamurthy, S.S. and Balda, J.C. (2001) Sizing a switched reluctance, motor for electric vehicles. *IEEE Transactions on Industry Applications*, **37** (5), 1256–1263.
96. Mecrow, B.C. (1996) New winding configurations for doubly salient reluctance machines. *IEEE Transactions on Industry Applications*, **32** (6), 1348–1356.
97. Mecrow, B.C., Finch, J.W., El-Kharashi, E.A., and Jack, A.G. (2002) Switched reluctance motors with segmental rotors. *IEE Proceedings – Electric Power Applications*, **149** (4), 245–254.
98. Krishnamurthy, M., Edrington, C.S., Emadi, A. *et al.* (2006) Making the case for applications of switched reluctance motor technology in automotive products. *IEEE Transactions on Power Electronics*, **21** (3), 659–675.
99. Rahman, K.M., Fahimi, B., Suresh, G. *et al.* (2000) Advantages of switched reluctance motor applications to EV and HEV: design and control issues. *IEEE Transactions on Industry Applications*, **36** (1), 111–121.
100. Long, S.A., Schofield, N., Howe, D. *et al.* (2003) Design of a switched reluctance machine for extended speed operation. Proceedings of IEEE International Electric Machines and Drives Conference, June 1–4, pp. 235–240.
101. Schofield, N. and Long, S.A. (2005) Generator operation of a switched reluctance starter/generator at extended speeds. Proceedings of IEEE Conference on Vehicle Power and Propulsion, September 7–9, pp. 453–460.
102. Edrington, C.S., Krishnamurthy, M., and Fahimi, B. (2005) Bipolar switched reluctance machines: a novel solution for automotive applications. *IEEE Transactions on Vehicular Technology*, **54** (3), 795–808.
103. Dixon, S. and Fahimi, B. (2003) Enhancement of output electric power in switched reluctance generators. Proceedings of IEEE International Electric Machines and Drives Conference, June 1–4, pp. 849–856.
104. Cameron, D.H., Lang, J.H., and Umans, S.D. (1992) The origin and reduction of acoustic noise in doubly salient variable-reluctance motors. *IEEE Transactions on Industry Applications*, **26** (6), 1250–1255.
105. Colby, R.S., Mottier, F., and Miller, T.J.E. (1996) Vibration modes and acoustic noise in a four-phase switched reluctance motor. *IEEE Transactions on Industry Applications*, **32** (6), 1357–1364.
106. Long, S.A., Zhu, Z.Q., and Howe, D. (2001) Vibration behaviour of stators of switched-reluctance machines. *IEE Proceedings – Electric Power Applications*, **148** (3), 257–264.
107. Long, S.A., Zhu, Z.Q., and Howe, D. (2002) Influence of load on noise and vibration of voltage and current controlled switched reluctance machines. Proceedings of IEE International Conference on Power Electronics, Machines, and Drives, April 16–18, pp. 534–539.
108. Blaabjerg, F., Pedersen, J.K., Neilsen, P. *et al.* (1994) Investigation and reduction of acoustic noise from switched reluctance drives in current and voltage control. Proceedings of International Conference on Electrical Machines, December, pp. 589–594.
109. Wu, C.Y. and Pollock, C. (1993) Time domain analysis of vibration and acoustic noise in the switched reluctance drive. Proceedings of International Conference on Electrical Machines and Drives, October, pp. 558–563.
110. Gabsi, M., Camus, F., Loyau, T., and Barbry, J.L. (1999) Noise reduction of switched reluctance machine. Proceedings of IEEE International Electric Machines and Drives Conference, May 12–19, pp. 263–265.
111. Gabsi, M., Camus, F., and Besbes, M. (1999) Computation and measurement of magnetically induced vibrations of switched reluctance machine. *IEE Proceedings – Electric Power Applications*, **146** (5), 463–470.
112. Wu, C.Y. and Pollock, C. (1995) Analysis and reduction of acoustic noise in the switched reluctance drive. *IEEE Transactions on Industry Applications*, **31** (6), 91–98.

113. Long, S.A., Zhu, Z.Q., and Howe, D. (2005) Effectiveness of active noise and vibration cancellation for switched reluctance machines operating under alternative control strategies. *IEEE Transactions on Energy Conversion*, **20** (4), 792–801.
114. Matsuo, T. and Lipo, T.A. (2004) Rotor design optimization of synchronous reluctance machine. *IEEE Transactions on Energy Conversion*, **9** (2), 359–365.
115. Li, Y. and Mi, C. (2007) Doubly salient permanent magnet machines with skewed rotor and six-state communication control. *IEEE Transactions on Magnetics*, **43** (9), 3623–3629.
116. Liao, Y., Liang, F. and Lipo, T.A. (1992) A novel permanent magnet motor with doubly salient structure. Industry Applications Society Annual Meeting, October, pp. 308–314.
117. Liao, Y. and Lipo, T.A. (1993) Sizing and optimal design of doubly salient permanent magnet motors. Sixth International Conference on Electrical Machines and Drives, September, pp. 452–456.
118. Liao, Y., Liang, F., and Lipo, T.A. (1995) A novel permanent magnet motor with doubly salient structure. *IEEE Transactions on Industry Applications*, **31** (5), 1069–1078.
119. Cheng, M., Chau, K.T., and Chan, C.C. (2000) Nonlinear varying-network magnetic circuit analysis for DSPM motors. *IEEE Transactions on Magnetics*, **36** (1), 339–348.
120. Cheng, M., Chau, K.T., and Chan, C.C. (2001) Static characteristics of a new doubly salient permanent magnet motor. *IEEE Transactions on Energy Conversion*, **16** (1), 20–25.
121. Cheng, M., Chau, K.T., Chan, C.C., and Sun, Q. (2003) Control and operation of a new 8/6-pole doubly salient permanent-magnet motor drive. *IEEE Transactions on Industry Applications*, **39** (5), 1363–1371.
122. Cheng, M., Chau, K.T., and Chan, C.C. (2001) Design and analysis of a new doubly salient permanent magnet motor. *IEEE Transactions on Magnetics*, **37** (4), 3012–3020.
123. Chau, K.T., Sun, Q., Fan, Y., and Cheng, M. (2005) Torque ripple minimization of doubly salient permanent-magnet motors. *IEEE Transactions on Energy Conversion*, **20** (2), 352–358.
124. Deodhar, R.P., Staton, D.A., and Miller, T.J.E. (1996) Prediction of cogging torque using the flux-MMF diagram technique. *IEEE Transactions on Industry Applications*, **32** (6), 569–576.
125. Ding, X., Bhattacharyal, M., and Mi, C. (2010) Simplified thermal model of PM motors in hybrid vehicle applications taking into account eddy current loss in magnets. *Journal of Asia Electric Vehicles*, **8** (1), 1–7.
126. Mellor, P.H., Roberts, D., and Turner, D.R. (1991) Lumped parameter thermal model for electrical machines of TEFC design. *IEE Proceedings – Electric Power Applications*, **138** (5), 205–218.
127. Taylor, G.I. (1935) Distribution of velocity and temperature between concentric cylinders. *Proceedings of the Royal Society*, **159** (Pt A), 546–578.
128. Gazley, C. (1958) Heat transfer characteristics of rotational and axial flow between concentric cylinder. *Transactions of the American Society of Mechanical Engineers*, **80**, 79–89.
129. Boglietti, A., Cavagnino, A., Lazzari, M., and Pastorelli, A. (2002) A simplified thermal model for variable speed self cooled industrial induction motor. Industry Applications Conference, 37th IAS Annual Meeting, October 13–17, Vol. 2, pp. 723–730.
130. Tang, S.C., Keim, T.A., and Perreault, D.J. (2005) Thermal modeling of Lundell alternators. *IEEE Transactions on Energy Conversion*, **20** (1), 25–36.
131. Sooriyakumar, G., Perryman, R., and Dodds, S.J. (2007) Analytical thermal modelling for permanent magnet synchronous motors. Universities Power Engineering 42nd International Conference, UPEC 2007, September 4–6, pp. 192–196.
132. Staton, D., Boglietti, A., and Cavagnino, A. (2005) Solving the more difficult aspects of electric motor thermal analysis in small and medium size industrial induction motors. *IEEE Transactions on Energy Conversion*, **20** (3), 620–628.
133. Guo, Y.G., Zhu, J.G., and Wu, W. (2005) Thermal analysis of soft magnetic composite motors using a hybrid model with distributed heat sources. *IEEE Transactions on Magnetics*, **41** (6), 2124–2128.
134. Funieru, B. and Binder, A. (2008) Thermal design of a permanent magnet motor used for gearless railway traction. Industrial Electronics, IECON 2008, 34th Annual Conference, November 10–13, pp. 2061–2066.
135. Staton, D.A. and Cavagnino, A. (2008) Convection heat transfer and flow calculations suitable for electric machines thermal models. *IEEE Transactions on Industrial Electronics*, **55** (10), 3509–3516.
136. Cassat, A., Espanet, C., and Wavre, N. (2003) BLDC motor stator and rotor iron losses and thermal behavior based on lumped schemes and 3-D FEM analysis. *IEEE Transactions on Industry Applications*, **39** (5), 1314–1322.

137. Kim, W.-G., Lee, J.-I., Kim, K.-W. *et al*. (2006) The temperature rise characteristic analysis technique of the traction motor for EV application. Strategic Technology, 1st International Forum, October 18–20, pp. 443–446.
138. Chowdhury, S.K. (2005) A distributed parameter thermal model for induction motors. International Conference on Power Electronics and Drives Systems, PEDS 2005, November 28–December 1 , Vol. 1, pp. 739–744.
139. Hsu, J.S., Nelson, S.C., Jallouk, P.A. *et al*. (2005) Report on Toyota Prius Motor Thermal Management. http://www.ornl.gov/˜webworks/cppr/y2001/rpt/122586.pdf (accessed February 13, 2011).
140. Jahns, T.M. and Caliskan, V. (1999) Uncontrolled generator operation of interior PM synchronous machines following high-speed inverter shutdown. *IEEE Transactions on Industry Applications*, **35** (6), 1347–1357.
141. Liaw, C.Z., Soong, W.L., Welchiko, B.A., and Ertugrul, N. (2005) Uncontrolled generation in interior permanent-magnet machines. *IEEE Transactions on Industry Applications*, **41** (4), 945–954.

11

Batteries, Ultracapacitors, Fuel Cells, and Controls

11.1 Introduction

In this chapter, the requisite energy storage systems for EVs and HEVs are discussed. In a HEV or PHEV, onboard batteries or ultracapacitors are charged from the internal combustion engine/generator set or from the electric power grid. The chemical energy stored in batteries is converted to electrical energy for traction motor and vehicle propulsion. Also, energy storage systems are responsible for recuperating regenerative braking energy to further increase vehicle efficiency. Thus, the performance of EVs and HEVs depends on energy storage systems to a large extent. Therefore, this chapter is devoted to a discussion of battery, ultracapacitor, and fuel cell technology. Here, we will focus on the techniques of modeling, hybridization, equalization, charging control for batteries and ultracapacitors.

Batteries are made of cells where chemical energy is converted to electrical energy and vice versa. The battery energy storage system (BESS) comprises mainly batteries, the power electronics-based conditioning system, and a control system. In HEVs, batteries provide energy for the traction motor and store regenerative energy; a power electronics converter, typically of bidirectional capability, provides an interface between the batteries and power produced by the onboard internal combustion engine or utility power in the case of a PHEV; the control system is responsible for power and energy management including charging/discharging and equalization control. The above description applies as well for the ultracapacitor energy storage system (UESS). The main difference is that the battery is an electrochemical energy conversion device while the ultracapacitor does not involve any chemical reactions. The BESS or UESS topology is illustrated in Figure 11.1.

In order to have the desired voltage rating and current rating for application in HEVs, many cells must be connected in series and/or in parallel in the BESS or UESS. Voltage balancing or equalization is required if more than three cells are connected in series.

Generally speaking, a battery has the characteristics of high energy density and relatively low power density. The internal resistance is the major factor for its limited discharging and charging current capability. The internal equivalent series resistance

Hybrid Electric Vehicles: Principles and Applications with Practical Perspectives, First Edition.
Chris Mi, M. Abul Masrur and David Wenzhong Gao.

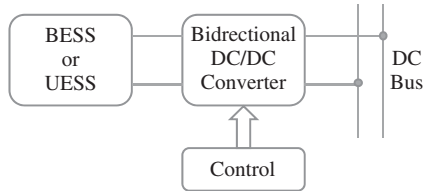

Figure 11.1 HEV BESS/UESS topology

(ESR) has different values under charging and discharging operating conditions. The values are also dependent on the frequency of the discharging current [1]. For lithium-ion batteries, the internal resistance could increase by 50% from 1000 Hz to 100 Hz. The ampere-hour capacity is affected by the discharging current rate and is modeled by Peukert's equation [2], $C_p = I^k t$, where k is the Peukert constant; $k = 1$ for an ideal battery. The charging and discharging efficiencies are nonlinear functions of current and the state of charge (SOC).

The battery can be modeled as an equivalent circuit such as an internal resistance model or a resistance–capacitance (RC) model in ADVISOR [3]. In an internal resistance model, a battery is modeled as a voltage source and an internal resistor. Both the voltage source and the internal resistor are functions of the SOC and temperature, which can be implemented as lookup tables. In a RC model, a battery is represented as a parallel combination of two RC branches. The very large capacitor models the battery's charge capacity while the smaller capacitor models the time constant due to surface effects that limit the current. The model can be implemented as an S function in MATLAB/Simulink.

On the other hand, when compared to common capacitors, the ultracapacitor (electric double-layer capacitor) has a very high energy density, which could be thousands of times greater than a high-capacity electrolytic capacitor. Larger double-layer capacitors can have capacitances up to 5000 F as of 2010. Compared to batteries, an ultracapacitor has the characteristics of high power density and relatively lower energy density. Its equivalent internal resistance is decades lower than that of a battery, thus allowing decades of higher discharging/charging current. Its overall round-trip efficiency is higher than that of a battery. Its capacitance is huge compared to an ordinary electrolyte capacitor, allowing enough energy storage for HEV acceleration power requirements. Note that the internal resistance and capacitance are highly dependent on the frequency because of the porous nature of the electrodes. One big advantage of the ultracapacitor is that its SOC is allowed to vary more widely and thus has longer life cycles. Its capability to provide high power bursts is ideal for hybrid vehicle applications.

An ultracapacitor can also be modeled as an internal resistance model or RC model in the same way as for a battery. The difference is that the ultracapacitor's internal resistance for charging is typically the same as for discharging.

To predict the behavior of battery/ultracapacitor voltage and current during transient operation such as acceleration and deceleration, physics-based dynamic models are needed to account for the time constants due to the electrochemical reactions in batteries or double-layer effects in ultracapacitors.

11.2 Battery Characterization

Capacity (C)

The battery capacity specifies the amount of electric charge a battery can supply before it is fully discharged. The SI unit of battery capacity is the coulomb. A more general unit for battery capacity is *ampere-hour (Ah)*, with 1 Ah = 3600 C. For example, a battery of 20 Ah can supply 1 A current for 20 hours or 2 A for 10 hours, or in theory 20 A for 1 hour. But in general, the battery capacity is dependent on discharge rate.

There are two ways of indicating battery discharge rate: C rate is the rate in amperes, while nC rate will discharge a battery in $1/n$ hours. For example, a rate of $C/2$ will discharge a battery in 2 hours, and a rate of $5C$ will discharge a battery in 0.2 hours. For a 2 Ah battery, the $C/5$ rate is 400 mA, while its $5C$ rate is 10 A.

As mentioned before, C depends on battery discharge current rate according to Peukert's equation. For a lead acid battery, the Peukert constant can range from 2.0 to 1.05 depending on manufacturing technology.

Energy Stored (E)

The energy stored in a battery is dependent on battery voltage and the amount of charge stored within. The watt hour or Wh is the SI unit for energy stored. Assume a constant voltage (CV) for the battery. Then

$$E\ (\text{Wh}) = V \times C \tag{11.1}$$

where V is the voltage and C is the capacity in Ah. The capacity of the battery changes with the discharge rate, and the associated discharging current affects the voltage value. The energy stored is thus not a constant quantity and is a function of two variables, namely, the voltage and capacity of the battery.

State of Charge (SOC)

A key parameter in the electric vehicle is the SOC of the battery. The SOC is a measure of the residual capacity of a battery. To define it mathematically, consider a completely discharged battery. The battery is charged with a charging current of $I_b(t)$; thus from time t_0 to t, a battery will hold an electric charge of

$$\int_{t_0}^{t} I_b(\tau)\, d\tau$$

The total charge that the battery can hold is given by

$$Q_o = \int_{t_0}^{t_2} I_b(\tau)\, d\tau \tag{11.2}$$

where t_2 is the cutoff time when the battery no longer takes any further charge. Then, the SOC can be expressed as

$$\text{SOC}(t) = \frac{\int_{t_0}^{t} I_b(\tau)\, d\tau}{Q_o} \times 100\% \tag{11.3}$$

Typically, the battery SOC is maintained between 20 and 95%.

A common mistake that people may make about a battery's charge is that when a battery "goes dead," the voltage goes from 12 to 0 V (for a 12 V battery). In reality a battery's voltage varies between 12.6 V with a SOC of 100% to approximately 10.5 V with a SOC of near 0%. It is advised that the SOC should not fall below 40%, which corresponds to a voltage of 11.9 V. All batteries have a SOC vs. voltage curve which can be either looked up from the manufacturer's data or determined experimentally. An example of an SOC vs. voltage curve of a lead acid battery is shown in Figure 11.2. Note that for a lithium-ion battery, the curve may be much flatter, especially for the mid-SOC range of 40–80%.

Depth of Discharge (DOD)

The depth of discharge (DOD) is the percentage of battery capacity to which the battery is discharged. The DOD is given by

$$\text{DOD}(t) = \frac{Q_o - \int_{t_0}^{t} I_b(\tau)\, d\tau}{Q_o} \times 100\% \tag{11.4}$$

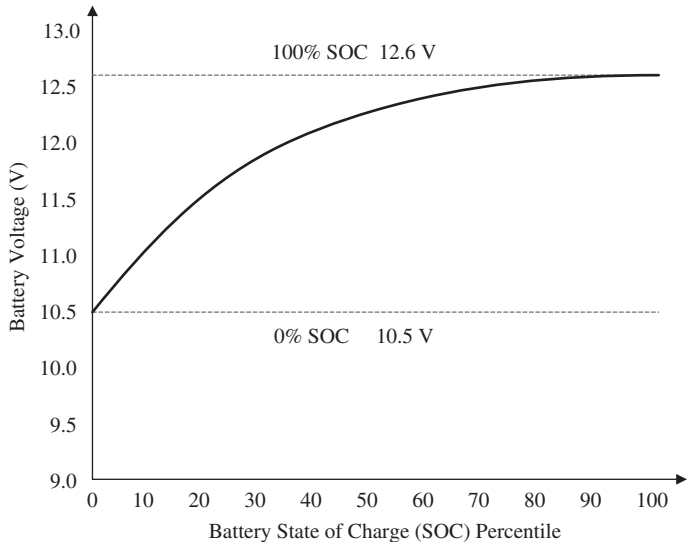

Figure 11.2 Example SOC vs. voltage curve for a 12 V battery

Generally, a battery is prevented from having a low DOD. The withdrawal of at least 80% of battery capacity is regarded as a deep discharge.

One important precaution is that the charge in a battery should never be discharged down to zero voltage, otherwise the battery may be permanently damaged. So, in this case, a cutoff voltage is defined for the battery voltage so that the voltage at the battery terminals will never drop below this cutoff voltage. This point is referenced as 100% DOD.

Specific Energy

Specific energy means how much electrical energy can be stored per unit mass of battery. The SI unit for this quantity is watt hour per kilogram. Knowing the energy stored and specific energy of the battery, the mass of the battery can be easily obtained by dividing the energy by specific energy. Again, the specific energy is not a constant parameter since the energy stored varies with discharge rate. A comparison of the specific energy of various energy sources (typical numbers) is given in Table 11.1.

Energy Density

Energy density means how much electrical energy can be stored per cubic meter of battery volume. It is computed by dividing the energy stored in the battery by the battery volume. The SI unit for energy density is watt hour per cubic meter.

Specific Power and Power Density

Specific power means how much power can be supplied per kilogram of battery. Note that this quantity is dependent on the load served by the battery and is thus highly variable and anomalous. The SI unit of specific power is watt per kilogram. Specific power is the ability of the battery to supply energy. Higher specific power indicates that it can give and take energy quickly. Volume specific power is also called power density or volume power density, indicating the amount of power (time rate of energy transfer) per unit volume of

Table 11.1 Specific energy of different energy sources

Energy source	Specific energy (Wh/kg)
Gasoline	12 500
Natural gas	9350
Methanol	6050
Hydrogen	33 000
Coal	8200
Lead acid battery	35
Nickel metal hydride battery	50
Lithium-polymer battery	200
Lithium-ion battery	120
Flywheel (carbon fiber)	30
Ultracapacitor	3.3

battery. If a battery has high specific energy but low specific power, this means that the battery stores a lot of energy, but gives it out slowly. A Ragone plot is used to depict the relationship between specific power and specific energy of a certain battery.

Ampere-Hour (or Charge) Efficiency

Ampere-hour efficiency is the ratio between the electric charge given out during discharging a battery and the electric charge needed for the battery to return to the previous charge level. In practice, these two values will never be equal, limiting the efficiency to 100%. In fact the typical values of charge efficiency range from 65 to 90%. The efficiency depends on various factors such as the battery type, temperature, and rate of charge.

Energy Efficiency

This important quantity indicates the energy conversion efficiency of the battery, which depends a great deal on the internal resistance of the battery. It can be computed as the ratio of electrical energy supplied by a battery to the amount of charging energy required for the battery to return to its previous SOC before discharging. The efficiency decreases considerably if a battery is discharged and charged very quickly. Typically, the energy efficiency of a battery is in the range of 55–95%.

Number of Deep Cycles and Battery Life

EV/HEV batteries can undergo a few hundred deep cycles to as low as 80% DOD of the battery. Different battery types and design result in different numbers of deep cycles. Also, the usage pattern will affect the number of deep cycles a battery can sustain before malfunction. The United States Advanced Battery Consortium (USABC) has a mid-term target of 600 deep cycles for EV batteries. This specification is very important since it affects battery life time in terms of deep-cycle number. So, generally, we should reduce the chances of DOD in the control strategy for EVs and HEVs in order to limit the operating cost of the vehicles.

Example: The NiMH traction battery of the Toyota Prius 2004 model has the following specifications:

- 168 cells (28 modules)
- 201.6 V nominal voltage
- 6.5 Ah nominal capacity
- 28 hp (21 kW) output power
- 1300 W/kg specific power
- 46 Wh/kg specific energy.

Assume that the voltage is relatively constant.

1. What is the energy rating of the battery in kilowatt hours?
   Solution: $201.6\,\text{V} \times 6.5\,\text{Ah} = 1310\,\text{Wh} = 1.31\,\text{kWh}$
2. If the battery can be discharged at a maximum rate of 100 A, and only 40% can be discharged, for how many seconds can the battery be used when fully charged?
   Solution: $\dfrac{(40\%)6.5\,\text{Ah}}{100\,\text{A}} = 0.026\,\text{h} = 93.6$ seconds
3. If the battery can be charged at a maximum rate of 90 A, and the current SOC is 40%, how long does it take to charge the battery to 80% SOC?
   Solution: $\dfrac{(80\% - 40\%)6.5\,\text{Ah}}{90\,\text{A}} = 0.0289$ hours $= 1.73$ minutes
4. The battery has an internal resistance of 0.15 Ω. What is the efficiency at maximum charge rate?
   Solution: $\eta = 1 - \dfrac{\left(90^2\right)(0.15)}{(90)(201.6)} = 93.6\%$
5. The battery has an internal resistance of 0.1 Ω. What is the efficiency at maximum discharge rate?
   Solution: $\eta = 1 - \dfrac{\left(100^2\right)(0.1)}{(100)(201.6)} = 95\%$
6. How much voltage drop is caused by this internal resistance at maximum charge/discharge?
   Solution: At maximum charge, the voltage drop is $90 \times 0.15 = 13.5\,\text{V}$; at maximum discharge, the voltage drop is $100 \times 0.1 = 10\,\text{V}$.
7. Does the efficiency change with maximum charge/discharge current?
   Solution: Yes, the battery efficiency depends on the maximum charge/discharge current and internal resistance.
8. If the leakage current is 20 mA, how many days does it take for the battery to self-discharge from 80% SOC to 40% SOC?
   Solution: $\dfrac{(80 - 40\%)6.5\,\text{Ah}}{20 \times 10^{-3}\,\text{A}} = 130$ hours $= 5.4$ days.

11.3 Comparison of Different Energy Storage Technologies for HEVs

Different energy storage technologies, including but not limited to those shown in Table 11.2, are available for HEV applications: Li-ion battery, nickel metal hydride battery, lead acid battery, and ultracapacitors. In the table, the typical range of

Table 11.2 Comparison of energy storage technologies suitable for HEVs

Storage technology	Cycle life	Efficiency (%)	Specific power (W/kg)	Specific energy (Wh/kg)
Lead acid battery	500–800	50–92	150–400	30–40
Li-ion battery	400–1200	80–90	300–1500	150–250
Nickel metal hydride battery	500–1000	66	250–1000	30–80
Ultracapacitor	1 000 000	90	1000–9000	0.5–30
USABC long-term goals	1000	80	400	200

specification is given for each type of storage device along with the long-term goal set by the USABC (http://www.uscar.org/, http://en.wikipedia.org/wiki/United_States_Council_for_Automotive_Research). The advanced lead acid and Li-ion batteries are the most promising for application in HEVs. While battery and ultracapacitor technologies have their respective advantages and disadvantages, hybridization could result in better vehicle performance and longer battery life. The vehicle road load transients can be handled by ultracapacitors during acceleration and deceleration.

A battery is an electrochemical cell that can convert chemical energy into electrical energy (redox reaction). There are three main parts in a battery: electrolyte, anode, and cathode. At the anode, the "negative" terminal, an oxidation reaction takes place and the electrode loses electrons. At the cathode, the "positive" terminal, a reduction reaction takes place and the electrode gains electrons. There is also a porous separator between the two electrodes.

Lead Acid Battery

This type of battery is the earliest and the most widely used in automotive applications. For example, it is extensively used as the starting battery to provide "cranking amps" for an automobile's starter motor. One of the plates is made of lead while the other plate is made of lead dioxide. The electrolyte is composed of sulfuric acid. These batteries can last a long time if they are charged and discharged properly.

The energy-to-volume ratio is low for a lead acid battery. This ratio can be used to measure the drive range of an EV. How to treat used lead acid batteries is another serious problem. As a result, this type of battery cannot satisfy the requirements for future environmentally-friendly vehicles. Fortunately, lead acid batteries have very high recyclability with good recycling infrastructure.

The chemical equation for a lead acid battery during discharge is

$$PbO_2 + Pb + 2H_2SO_4 \rightarrow 2PbSO_4 + 2H_2O \tag{11.5}$$

The chemical equation for a lead acid battery during charge is

$$2PbSO_4 + 2H_2O \rightarrow PbO_2 + Pb + 2H_2SO_4 \tag{11.6}$$

According to the chemical equation, electrolyte and the active material on the battery plates are consumed and water and lead sulfate are produced when a lead acid battery is

discharged. On the other hand, during the charging process, electrical energy is absorbed by the battery, water and lead sulfate are consumed, and electrolyte and the active material at the plates are produced.

Nickel Metal Hydride Battery

The NiMH battery is a new type of high-capacity battery. Its technology has grown rapidly in the past five years. It has many advantages such as environmental friendliness, high specific energy and energy density, and a long cycle life. The NiMH battery has already occupied a good market share as energy storage in HEVs.

The overall reversible chemical reaction occurring in a NiMH cell is:

$$\mathrm{MH} + \mathrm{NiOOH} \Leftrightarrow \mathrm{M} + \mathrm{Ni(OH)_2} \tag{11.7}$$

Lithium-Ion Battery

In Li-ion batteries, Li ions alternatively move into and out of host lattices during charging and discharging cycles. This fundamental mechanism has led to the Li-ion battery's nick-name of "rocking-chair" battery. In its physical composition, a Li-ion battery has anode and cathode plates like a lead acid battery, except that these are made of lithium cobalt oxide (or other lithium composites) and carbon. These plates and the separator are immersed in a solvent which is most commonly ether [4]. This type of battery can be made with very high energy density. The overall reversible chemical reaction occurring in a Li-ion cell is

$$\mathrm{Li}_x\mathrm{C} + \mathrm{Li}_{1-x}\mathrm{M}_y\mathrm{O}_z \Leftrightarrow \mathrm{C} + \mathrm{LiM}_y\mathrm{O}_z \tag{11.8}$$

Li-ion batteries do not have the "memory effect" that causes other rechargeable batteries to lose their maximum charge level when repeatedly recharged or not charged to full capacity. Li-ion batteries also impact the environment less due to their composition. Unlike lead acid batteries, they have a much lower self-discharge rate, thus greatly increasing idle period capabilities. These batteries also have a higher power-to-volume ratio which also makes them ideal for automotive applications [5]. Two of the latest EVs, the Nissan Leaf and Chevy Volt, both use lithium batteries. Different materials can be used for anode. The Mn series Li-ion battery has been used in the Nissan Leaf, Mitsubishi i-MiEV, GM Volt, Chrysler S400 Hybrid, BMW 7 series ActiveHybrid, THINK TH!NK City, and Hyundai Sonata Hybrid Blue Drive.

However, lead acid batteries have remained the favored ones due to cost and the fact that Li-ion batteries require a lot more safety attention. These batteries are much more susceptible to overcharging and overdischarging and the associated safety hazards. Overcharging or overdischarging the battery can severely damage the plates inside the case. Overcharging can also cause gassing of the electrolyte and buildup of pressure in the case, which can lead to an explosion, therefore a precise regulatory system is necessary. The reduction in life due to this effect is much greater than in lead acid batteries. The same reaction occurs when they are used improperly, leading to overheating and the risk of an explosion. In the event of charging or discharging a Li-ion battery, the voltage must be monitored carefully because the absolute limits are so close to the required 100% SOC voltage [6].

Ultracapacitors

Ultracapacitors have a very long shelf life, with much lower maintenance requirements, enhanced performance at low temperature, and environmental friendliness. The only downside to ultracapacitors is their initial cost and relatively low energy density when compared to batteries [7]. Unlike batteries, no chemical reactions are needed for storing and retrieving electrical energy with ultracapacitors and thus the energy efficiency is higher. The ultracapacitor's SOC is easier to estimate than that of a battery because the voltage is the only measurement needed (SOC is proportional to V^2). Also, ultracapacitors can be charged to a specific value and, due to their shelf life and charging mechanism, they can hold that charge with virtually no loss. Batteries are incapable of achieving this. Repeated depletion cycles of a lead acid or Li-ion battery can be detrimental to its lifespan; however, this is not the case with an ultracapacitor.

Ultracapacitors provide more freedom in the DC link voltage or wherever else they are used because their charge does not depend on a certain voltage. Whatever voltage they are charged to is what they retain [8]. As a result, a hybrid topology consisting of ultracapacitors is desired when variable voltages are required. This would be beneficial in portable fuel cell/ultracapacitor power supplies that could be used in emergencies or general use. A vast array of loads or devices could be powered by this system.

Ultracapacitors allow rapid charging and discharging. This is especially useful for faster and efficient regenerative energy recovery in HEVs as well as for rapid charging of PHEVs. Simple charging methods can be used without needing a sophisticated SOC detection algorithm, and there is little danger of overcharging so long as the voltage is below the maximum allowable value. Ultracapacitors have a long cycle life (on the order of a million cycles), with little degradation over hundreds of thousands of discharge/charge cycles. In comparison, rechargeable batteries last for only a few hundred deep cycles.

The ultracapacitor's energy density is much lower than that of an electrochemical battery (3–5 Wh/kg for an ultracapacitor compared to 30–40 Wh/kg for a lead acid battery, and 120 Wh/kg or more for a Li-ion battery), and its volumetric energy density is only about 1/1000th of that of gasoline. As in any capacitor, the energy stored is a function of voltage squared. Effective storage and retrieval of energy requires complex electronic control and balancing circuits involving power electronics switches. The self-discharge rate is much higher than that of an electrochemical battery and thus it is only suitable for short-term energy storage. An enormous amount of energy could be released in a fraction of a second from an ultracapacitor and this could be life threatening if precautions were not taken. The internal resistance of ultracapacitors is very low, resulting in high cycle efficiency (95% or more). Environmentally, ultracapacitors are safer since they do not contain corrosive electrolytes or other highly toxic materials. In comparison, the reactive chemical electrolytes of rechargeable batteries present a disposal and safety hazard.

A comparison of the power density and energy density of different energy storage systems (ESSs) is illustrated in Figure 11.3 (Ragone plot or chart).

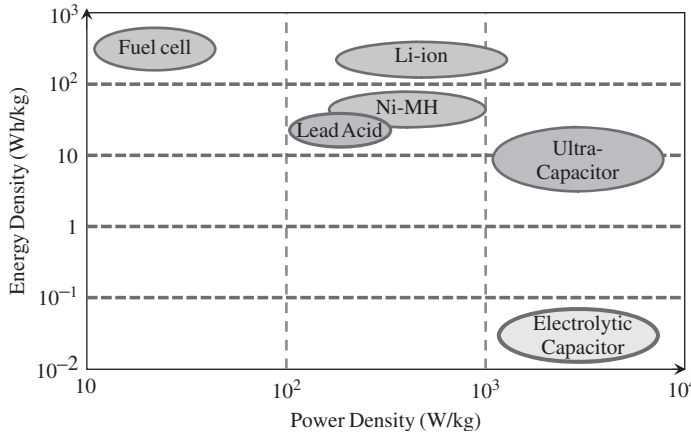

Figure 11.3 Comparison of power density and energy density for ESS in HEVs

11.4 Modeling Based on Equivalent Electric Circuits

11.4.1 Battery Modeling

A commonly used simple battery model is shown in Figure 11.4. It consists of an ideal battery with open-circuit voltage V_{oc} and a constant equivalent internal resistance R_{int}. The battery terminal voltage is V_t. V_{oc} can be obtained from the open-circuit measurement, and R_{int} can be measured by connecting a load and measuring both the terminal voltage and current, at fully charged condition. The terminal voltage V_t can be written as

$$V_t = V_{oc} - I_b R_{int} \tag{11.9}$$

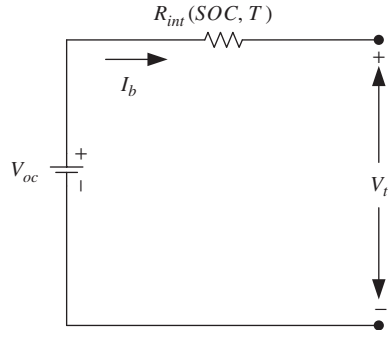

Figure 11.4 Simple battery model

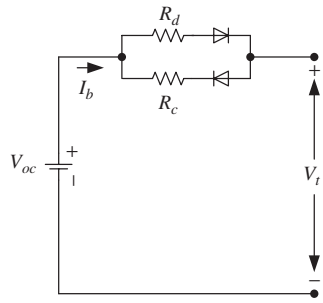

Figure 11.5 Battery model accounting for the different charging and discharging resistances

V_{oc}, the equilibrium potential of the battery, is a nonlinear function of the SOC and temperature T given by Larminie and Lowry [9]:

$$V_{oc} = E_o + (RT/F) \times \ln(\text{SOC}/(1 - \text{SOC})) \tag{11.10}$$

where E_o is the standard potential of the battery, R the ideal gas constant, T the absolute temperature, and F the Faraday constant

This is a fairly good way of predicting the battery voltage. However, the battery open-circuit voltage does not remain constant. As discussed above, the voltage is affected by the SOC/DOD of the battery and temperature. The variation in the open-circuit voltage due to DOD, for a lead acid battery cell, as given by Larminie and Lowry [9] is

$$V_{oc} = (2.15 - \text{DOD} \times (2.15 - 2.0)) \tag{11.11}$$

The main drawback of this model is that it cannot capture the response to dynamic events in a battery. For example, if a load is connected to the battery, the terminal voltage will immediately change to a new, lower value according to this simplified model. In fact this is not true; rather it will take some time for the voltage to settle to a new value.

The internal resistance of the battery has different values on charging and discharging. To account for the different resistance values under charge and discharge conditions, the circuit model in Figure 11.4 can be modified as shown in Figure 11.5. An improved model can be obtained by incorporating a self-discharge resistance R_p in parallel with V_{oc}.

In this model, the internal resistance takes different values during the charging and discharging process: R_c for charging and R_d for discharging. The internal resistance is used to model all energy losses within the battery during charging and discharging, including electrical and non-electrical losses. The ideal diodes are present only for modeling purposes of selecting either R_d or R_c as the internal resistance based on the current direction and have no physical significance in the battery. For a given required power, the battery current I_b is expressed as

$$I_b = \frac{V_{oc} - \sqrt{V_{oc}^2 - 4 \times R \times P_{req}}}{2R} \tag{11.12}$$

where

$$R = \begin{cases} R_{discharge}(\text{SOC}, T) & \text{for } I_b \geq 0, \ P_{req} \geq 0 \\ R_{charge}(\text{SOC}, T) & \text{for } I_b < 0, \ P_{req} \leq 0 \end{cases}$$

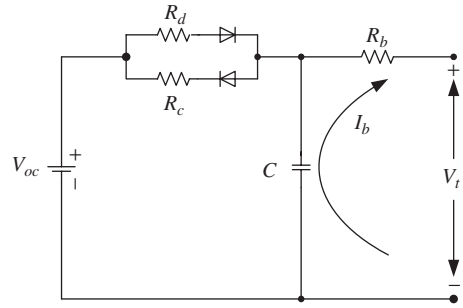

Figure 11.6 Dynamic battery model

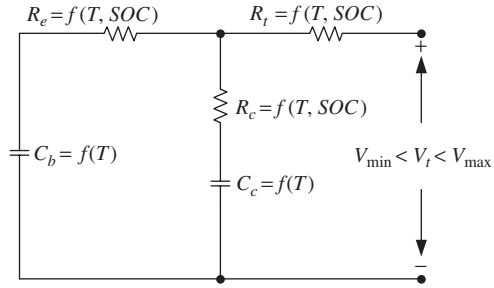

Figure 11.7 RC model of a battery

The sign of the battery current, I_b, appears to be positive in discharging mode and negative in charging mode.

The models in Figures 11.4 and 11.5 have the disadvantage of not being sensitive to dynamic events in the battery. In order to model such dynamic or transient effects in a battery, a capacitor is added to the model as a parallel branch, as shown in Figure 11.6.

The model in ADVISOR [3], given in Figure 11.7, is called the "RC model"; it takes power as an input and maintains the battery output voltage within the high- and low-voltage limits. The "RC model" can predict the average internal battery temperature as a function of time while driving and during soak periods. In this model, the capacitor C_b is large enough to hold the capacity of the battery and the smaller capacitor C_c is used to reflect the dynamic changes in the battery.

11.4.2 Battery Modeling Example

Here, the model in Figure 11.5 is implemented in MATLAB as an example. The SOC is obtained by the following equation:

$$\text{SOC} = 1 - \frac{\text{used Ah capacity}}{\text{max Ah capacity}} \tag{11.13}$$

where the used Ah capacity is calculated from

$$\text{Used Ah capacity} = \begin{cases} \int_0^t i_b(t)dt & \text{for } i_b(t) \geq 0 \text{ discharge} \\ \int_0^t \eta_{coulomb} i_b(t)dt & \text{for } i_b(t) < 0 \text{ charge} \end{cases} \tag{11.14}$$

where $I_b(t)$ is the charge/discharge current for the battery and $\eta_{coulomb}$ is the coulombic efficiency for charging.

In this example, V_{oc} is a function of the SOC; the data is obtained from the experimental tests of a Hawker Genesis 12 V, 26 Ah, 10EP sealed valve-regulated lead acid (VRLA) battery and implemented as a lookup table in MATLAB [3]. The open-circuit voltage of each cell takes values ranging from 11.7 to 12.89 V corresponding to the SOC from 0 to 1. The internal resistors R_d and R_c are also indexed by the SOC and T from two different lookup tables corresponding to discharging and charging respectively. The coulombic efficiency is assumed to be 90%. V_{oc}, R_d, and R_c of this battery model are plotted in Figure 11.8.

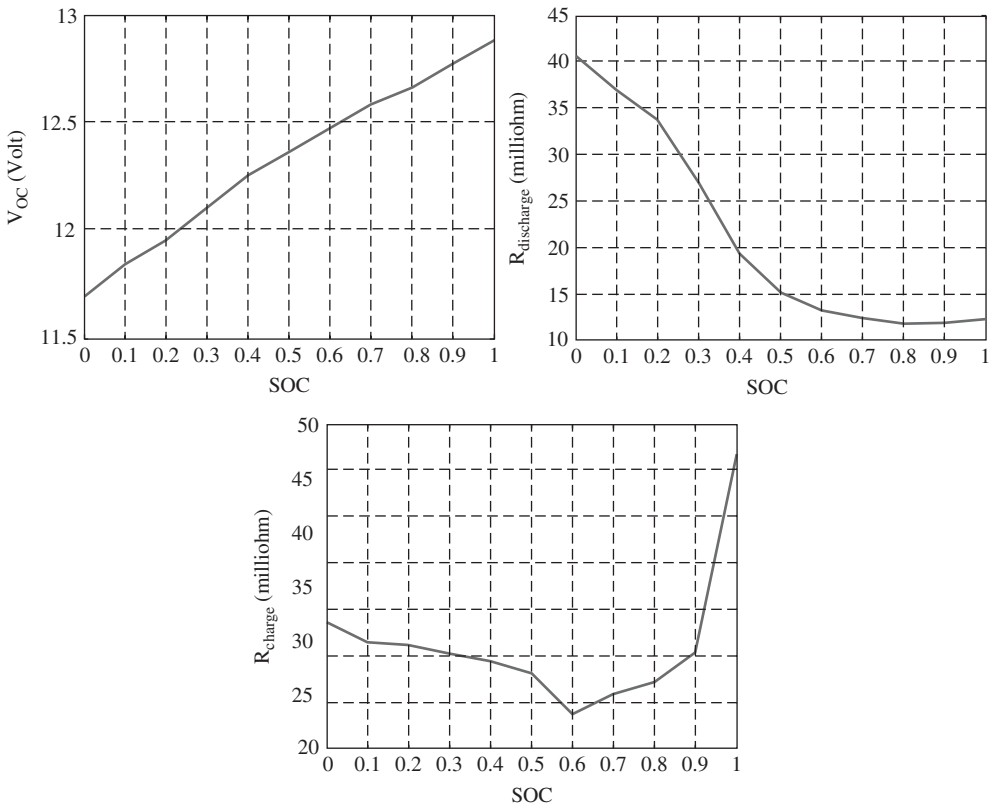

Figure 11.8 V_{oc}, R_d, and R_c of the battery model

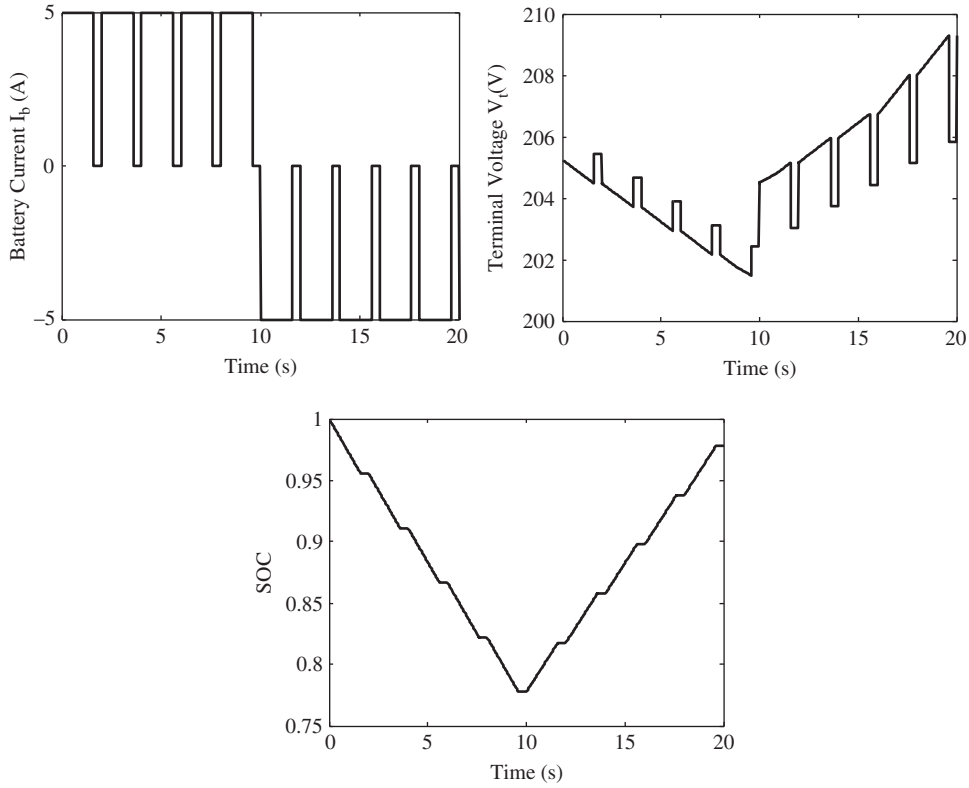

Figure 11.9 Simulation results of the battery model

A battery pack consisting of 16 battery cells in series is simulated to test the developed battery model. The magnitude of battery current pulse is 5 A with a frequency of 0.5 Hz and pulse width of 1.6 seconds. The battery temperature is assumed constant at 34.7 °C. Simulation results are shown in Figure 11.9. From the discharge and charge current pulse profiles, in the first 10 seconds discharge current pulses are applied to the battery model, while in the last 10 seconds charge current pulses of the same magnitude are applied. The battery pack terminal voltage decreases from around 206 V over the first discharging duration in the first 10 seconds. In the last 10 seconds, however, the terminal voltage gains almost linearly over the charging intervals. From the SOC plot, it can be seen that in the first 10 seconds, the SOC is reduced from 1.0 to 0.78 during discharging but increases to 0.975 after the pulsed charge currents are applied.

11.4.3 Modeling of Ultracapacitors

In any capacitor, the electrical energy is stored by using a positively charged electrode surface and a negatively charged electrode surface with a dielectric separator between them. In supercapacitors or ultracapacitors, special carbon-based electrodes are made to

provide an extremely large internal active surface area. The charge and energy stored in a capacitor are given by

$$Q = C \times V \tag{11.15}$$

$$E = \frac{1}{2} C V^2 \tag{11.16}$$

where

Q is the charge in the capacitor,
C is the capacitance in farads,
V is the voltage across the capacitor,
E is the energy of the capacitor.

For ultracapacitors, the SOC can be computed with high accuracy:

$$\text{SOC} = \frac{C\,(V - V_{\min})}{C\,(V_{\max} - V_{\min})} = \frac{(V - V_{\min})}{(V_{\max} - V_{\min})} \tag{11.17}$$

where $V_{\max}$ and $V_{\min}$ denote maximum and minimum allowable voltage for the ultracapacitor.

The capacitance C of a capacitor is given by

$$C = \varepsilon \frac{A}{d} \tag{11.18}$$

where ε is the permittivity of the dielectric medium, A is the plate area, and d is the distance between the plates.

Supercapacitors get their name from their ability to store high energy. This can be done by increasing the area of parallel plates in a capacitor. The capacitance is increased by decreasing the separation distance between the parallel plates. This is the key to modern capacitors, but the voltage across the capacitor must be small otherwise the capacitor may be damaged and act like a short circuit. This puts a limit on the maximum energy a capacitor can store. Connecting capacitors in series decreases the effective capacitance and increases the voltage across them. The energy stored now increases, but not as the voltage squared because of the problem of voltage imbalance among the cells. The fundamental reason for the voltage mismatch between the series-connected cells is due to the variation of capacitance between the cells. The problem can be avoided by charge-equalizing circuits. These circuits balance the charge on the adjacent capacitors keeping the cell voltage the same.

The simplest equivalent electric circuit model for an ultracapacitor consists of a capacitance in series with an internal resistance, which models all the energy losses in the ultracapacitor. This model can capture to a large extent the essential behavior and dynamics of the ultracapacitor for most modeling and analysis needs. However, more detailed and complex models can be developed as outlined in the following.

A slightly more complex model is shown in Figure 11.10. The equivalent circuit of the ultracapacitor unit consists of a capacitor (C), an ESR to model the internal resistance during discharging and charging, and an equivalent parallel resistance (EPR), R_p, which

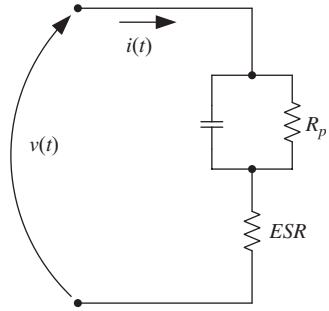

Figure 11.10 Simple electrical equivalent circuit of a supercapacitor

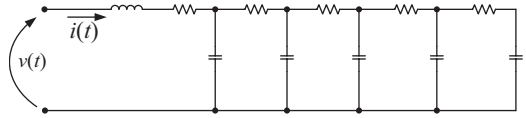

Figure 11.11 The fifth-order ultracapacitor model

is much higher than the ESR, to account for any self-discharging losses. These parameters can be obtained from ultracapacitor data sheets provided by manufacturers.

For an accurate representation of an ultracapacitor, a fifth-order model is needed [10]. The ultracapacitor is represented by a series–parallel connection of resistors and capacitors, and the values of each can be varied to achieve the desired modeling accuracy over a wide range of operating frequency. Figure 11.11 shows the representation of an ultracapacitor by a fifth-order model. For electric vehicle modeling and simulation, the model order can be reduced to third order to account for a frequency range of interest between 0.0034 and 1.44 Hz [10].

11.4.4 Battery Modeling Example for Hybrid Battery and Ultracapacitor

As mentioned previously, hybridization of battery and ultracapacitor could yield a better energy storage system to supply transient loads with the benefit of longer battery life. Based on the battery model described in Section 11.4.2, an electrical model for a hybrid energy storage system (HESS) consisting of a battery and supercapacitor systems is developed and implemented in MATLAB/Simulink to demonstrate the concept of passive HESS. The equivalent circuit of the HESS is shown in Figure 11.12.

In Figure 11.12, the lead acid battery is modeled by the internal emf, E_m, and the internal resistor R_2. The values of the internal series resistance R_2 are dependent on the charge/discharge current. $R_{2,c}$ and $R_{2,d}$ correspond to charging resistance and discharging resistance respectively. In this HESS model, the internal parameters, including E_m and R_2, are SOC and temperature, T dependent.

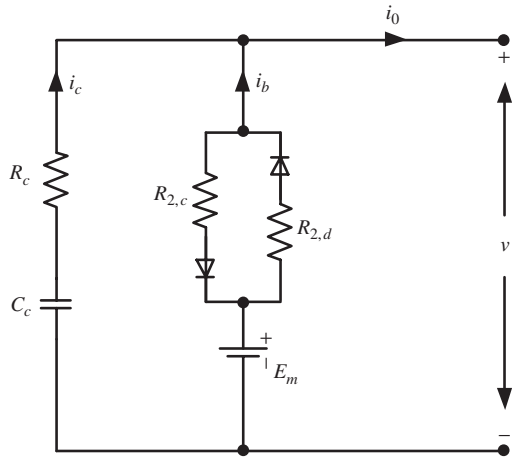

Figure 11.12 Equivalent circuit model for HESS consisting of lead acid battery and ultracapacitor

Though the charge/discharge characteristic of the ultracapacitor can be modeled in more complex forms as shown in previous section, the ultracapacitor model used in this example is represented by a single lumped capacitance, C_c, and a single lumped resistance, R_c. In this model, C_c is the capacitance between the double layers of the ultracapacitor and R_c models the internal loss inside the supercapacitor.

For a given discharge current i_0, one can assume it is distributed between the battery and ultracapacitor branches based on the impedances of the two branches, as denoted by i_b and i_c respectively in Figure 11.12. The calculation of i_b and i_c for a given i_0 will be detailed in the following.

The Thévenin equivalent circuit of the HESS as shown in Figure 11.12 can be depicted as in Figure 11.13, where the Thévenin equivalent voltage and impedance of the HESS

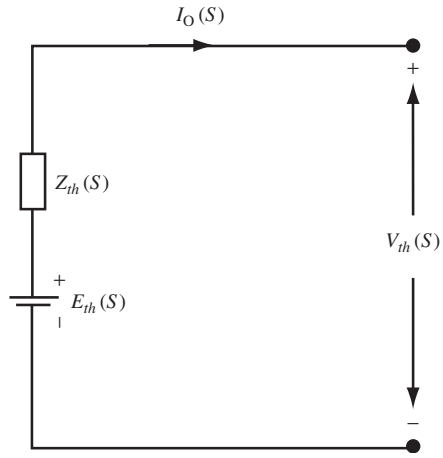

Figure 11.13 Thévenin equivalent circuit of the HESS

circuit are denoted by $E_{th}(s)$ and $Z_{th}(s)$ respectively. Note that Figure 11.13 is derived in the frequency domain and $E_{th}(s)$ and $Z_{th}(s)$ are obtained by

$$E_{th}(s) = \frac{R_c}{R_2 + R_c} E_m \frac{s+\alpha}{s(s+\beta)} + \frac{R_2}{R_2 + R_c} V_{c0} \frac{1}{s+\beta} \tag{11.19}$$

$$Z_{th}(s) = \frac{R_2 R_c}{R_2 + R_c} \frac{s+\alpha}{s+\beta} \tag{11.20}$$

where s is the complex frequency, V_{c0} is the initial voltage across the ultracapacitor, and

$$\alpha = \frac{1}{R_c C_c} \tag{11.21}$$

$$\beta = \frac{1}{(R_2 + R_c) C_c} \tag{11.22}$$

By assuming the charge/discharge current is a pulsed signal with period T_1 and duty ratio D, the current for the first N pulses can be expressed as

$$i_0(t) = I_0 \sum_{k=0}^{N-1} [\Phi(t - kT_1) - \Phi(t - (k+D)T_1)] \tag{11.23}$$

where I_0 is the magnitude of the current and $\Phi(t)$ is a unit step change function at $t = 0$. By applying the Laplace transform operation to this equation, one can readily obtain the current in the frequency domain as

$$I_0(s) = I_0 \sum_{k=0}^{N-1} \left[\frac{e^{-kT_1 s}}{s} - \frac{e^{-(k+D)T_1 s}}{s} \right] \tag{11.24}$$

Based on this, the internal voltage drop due to internal equivalent impedance inside the HESS, $V_i(s)$, is given by

$$V_i(s) = I_0(s) \cdot Z_{th}(s) = \frac{R_2 R_c}{R_2 + R_c} I_0 \left[\left(\frac{\alpha}{\beta} \frac{1}{s} + \frac{\beta - \alpha}{\beta} \frac{1}{s+\beta} \right) \times \left(e^{-kT_1 s} - e^{-(k+D)T_1 s} \right) \right]. \tag{11.25}$$

Thus, the terminal voltage of the HESS, $V_{th}(s)$, can be calculated by

$$V_{th}(s) = E_{th}(s) - V_i(s) \tag{11.26}$$

Performing the inverse Laplace transform, we get

$$\begin{aligned} v(t) = E_{th}(t) - v_i(t) = E_m + \frac{R_2}{R_2 + R_c}(V_{c0} - E_m) e^{-\beta t} \\ - R_2 I_0 \sum_{k=0}^{N-1} \left[\left(1 - \frac{R_2}{R_2 + R_c} e^{-\beta(t - kT_1)} \right) \Phi(t - kT_1) \right. \\ \left. - \left(1 - \frac{R_2}{R_2 + R_c} e^{-\beta[t - (k+D)T_1]} \right) \Phi[t - (k+D)T_1] \right] \end{aligned} \tag{11.27}$$

Note that the second term in this equation is caused by the energy redistribution between the battery and supercapacitor at the beginning of the discharge. This item decays as time lapses. The Thévenin voltage of the HESS finally approaches E_m.

After obtaining the HESS terminal voltage, the charge/discharge currents flowing through the battery and the ultracapacitor can be calculated by the following two equations respectively:

$$i_b(t) = \frac{1}{R_2}[E_m(t) - v(t)] \tag{11.28}$$

$$i_c(t) = i_0(t) - i_b(t) \tag{11.29}$$

The above HESS model equations are implemented in MATLAB/Simulink. To verify the validity of this HESS model, a pulsed signal with a magnitude of 8 A, period $T_1 = 2$ seconds, and duty ratio $D = 0.8$ is applied in the model. Note that positive values of i_0 correspond to discharge currents, while negative values correspond to charge currents. The battery pack consists of 16 Hawker Genesis 12 V, 26 Ah, 10EP sealed VRLA batteries connected in series to obtain 206.24 V at the original state. The ultracapacitor system consists of 77 modules of Nesscap 2.7 V/600 F capacitors connected in series to match the BESS terminal voltage. We assume that the ultracapacitors are fully charged at the initial stage having an initial voltage of 207.9 V. The internal resistance of the ultracapacitor is 1mΩ. The simulation results are shown in Figure 11.14.

The discharge/charge current applied to the HESS is given in Figure 11.14a. The battery (BESS) current is shown in Figure 11.14b, from which one can find that the BESS current increases gradually to approach the pulse magnitude, 8 A, after five periods or 10 seconds. The current balance between the applied current and that taken by the BESS is compensated by the parallel-connected supercapacitor, which can be found from Figure 11.14c. This contribution of the supercapacitor will reduce the negative effect of the high discharge/charge current on the battery and hence effectively extends the lifetime of the BESS. The terminal voltage and SOC of the battery over the simulated interval are depicted in Figure 11.14d,e respectively. The exchange current between the BESS and supercapacitor is shown in Figure 11.14f. The exchange current originates from the second term in the equation for $v(t)$, which is due to the difference between the initial voltage of the ultracapacitor V_{c0} and E_m. The negative exchange current indicates that the ultracapacitor provides a decaying charging current to the battery. It can be observed that the exchange current decays to 0 after about 25 seconds, which verifies the analysis regarding $v(t)$.

11.5 Battery Charging Control

Charging technology plays a key role in maximizing battery performance. A proper battery charging technique ensures battery safety and increases system reliability. The primary requirement of the charging process is to provide a fast and efficient way of charging without degrading the battery. Some of the factors to be taken into account while charging the battery are:

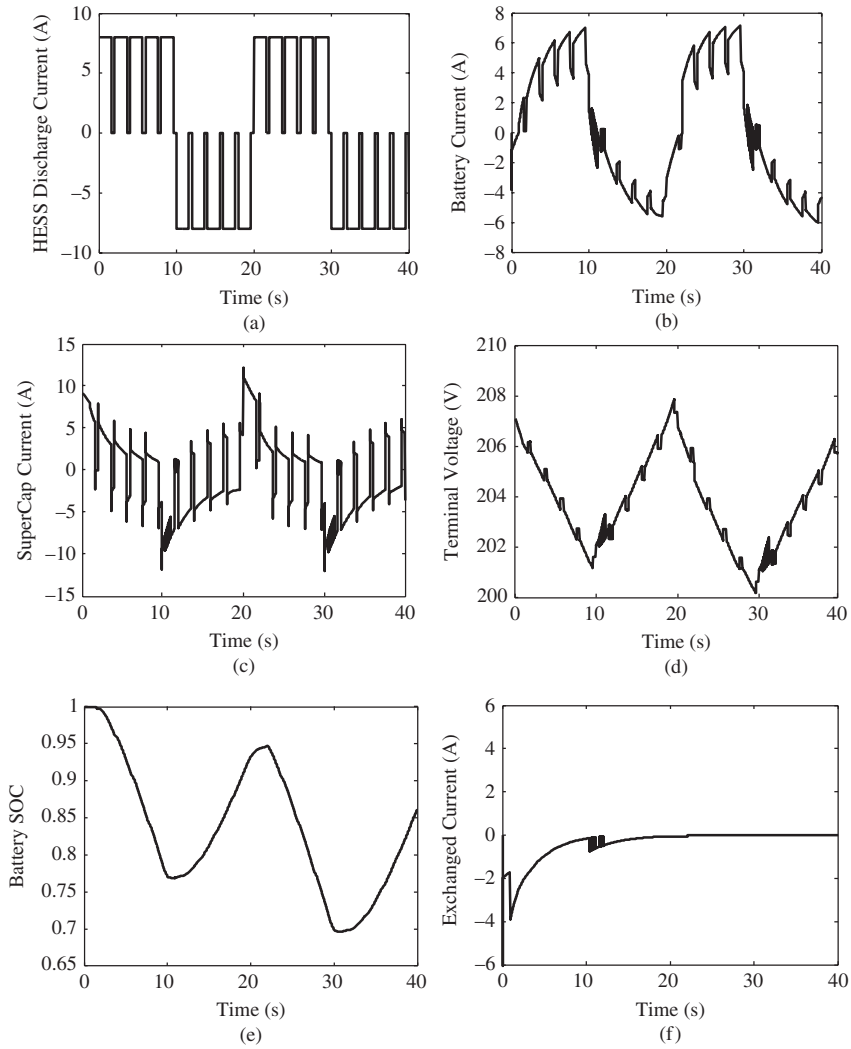

Figure 11.14 Simulation results of the HESS model: (a) applied discharge/charge current; (b) BESS current; (c) ultracapacitor current; (d) BESS terminal voltage; (e) SOC of the BESS; and (f) the exchange current between the BESS and the ultracapacitor

- Avoiding overcharging and undercharging.
- Fast charging without affecting the battery life.
- Maintaining a good quality of charging current.

Conventional charging methods include passive charging, constant current (CC) charging, CV charging, and CC–CV charging. The pulse charging method is gaining popularity

because of its advantages over CC and CV charging. In this section, different charging techniques will be reviewed and discussed.

The simplest method is passive charging. This method is also the worst method for the health of a battery. In passive charging, the battery is connected to a DC link which has a fixed voltage higher (hopefully by only a small percentage) than the rated voltage of the battery. The charging current is unregulated in this method and can spike greatly and possibly stay at a charging current above the safe value. As a result, there is the risk of overcurrent and definitely overvoltage. This method is not recommended for critical systems.

The second method is CV charging. For example, for a 12 V battery, the charging voltage would be maintained at a value of about 12.1 V regardless of the SOC. As a result of CV charging, the current supplied to the battery is unregulated. In turn, with a low initial SOC there is a high current spike of unknown duration that could exceed the safe charging current for the battery. This is a very fast method of charging with an exponential profile; however, the initial current spike can be damaging.

In the CC scheme, the charging voltage is varied and tracks the SOC of the battery to maintain a CC at the battery's DC link. As a result, the charging current profile of the battery stays well below the safe charging rate. A great advantage of this method is that it prevents heat from building up during the charging process and thus increases the life of the battery. The disadvantage of this method is that the constant higher current, even at the end of the charging cycle, could lead to the growth of deposits which could short the plates in the batteries. As a result, the method is harmful at the end of the charging cycle. This method also requires monitoring of both voltage and current measurements. It is slower than CV charging and has a linear charging profile.

In the CC–CV charging method, in the first stage a CC is maintained for charging the battery. This current level is regulated at the safe charge limit by increasing or decreasing the terminal voltage level of the charging source. Once the battery reaches a certain SOC or voltage value, the current is decreased (voltage decreased) to prevent damaging currents at the end stage. This particular charging stage is usually called the floating charge. This method combines the best attributes of both the CV and CC methods and eliminates their disadvantages. It is slower than the previously mentioned methods; however, it is the safest for the battery [11].

The final charging method to mention is the pulsed current method. This method is similar to pulse width modulation in that the pulse duration is proportional to the SOC. When the SOC is low, the pulses have a longer duration; when the SOC approaches 100%, the pulse duration is reduced to near zero. At any pulse duration, there will be a rest period in which the charging current is low. The relaxation period between pulses equalizes the chemical reaction in the battery as the ions diffuse and distribute evenly throughout the battery. This process normalizes the ion concentration in the battery and thus prevents the negative effect experienced in CC charging. Because of the equal charge distribution, battery performance as well as battery life are enhanced. The charging rate can be controlled by varying the width of the pulses. This type of charging is advantageous over CC charging in that the charging rate is higher and battery internal impedance is kept lower [12]. This is the fastest method of the above-mentioned

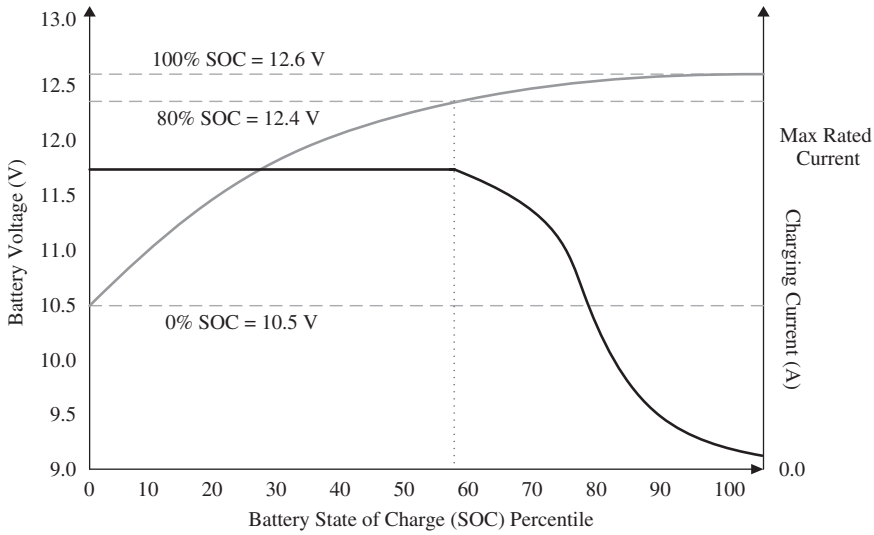

Figure 11.15 Plot of the battery voltage and charging current vs. SOC for a three-stage charger

methods and is becoming more popular with charging protocols. However, it would require a power electronics converter with a dedicated control algorithm.

The three-stage charger is an example of a controlled charging method on the market today and is mainly used for 12 V lead acid batteries. The CC–CV scheme is used. The first stage is called the bulk charge stage. In this stage, the maximum current that the batteries are rated for is delivered until the SOC reaches about 80–90%. The charging voltage at this stage exists between 10.5 and 15 V. The second stage, called the absorption stage, delivers reduced current and maximum voltage in the range of 14.2–15.5 V. The third stage, the float charge stage, occurs when the batteries have reached nearly 100% SOC and all that is needed is to keep them at full charge. In this stage the voltage can vary between 12.8 and 13.2 V [13]. A sketch of a three-stage charger for a 12 V lead acid battery is shown in Figure 11.15. An example of battery charge and discharge versus the SOC of a Li-ion battery is shown in Figure 11.16.

11.6 Charge Management of Storage Devices

The voltage of energy storage devices in electric vehicles is designed to be in the range of 300–400 V in order to provide adequate power for traction motors. As a result, many cells must be connected in series. When dealing with long battery or ultracapacitor strings, charge distribution must be equalized between the individual cells in order to prevent under- or overcharging and extend energy storage life. For HEV batteries, the cells will undergo many charge/discharge cycles, where major amounts of power are consumed from and injected into them [14]. In HEVs, the battery bank is charged with power from the IC engine or via regenerative braking. The charge/discharge lapses can cause

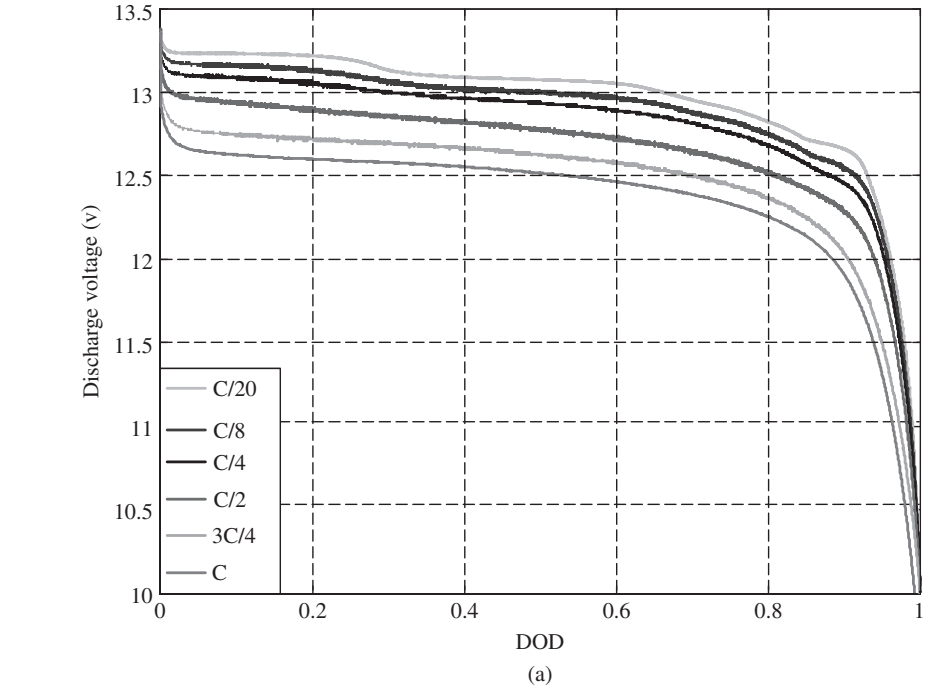

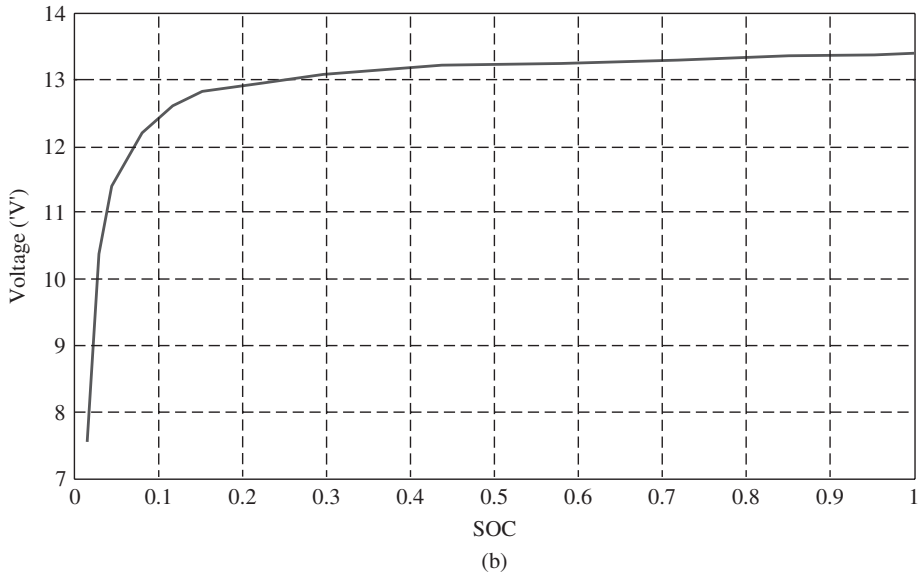

Figure 11.16 Lithium-ion battery discharge and charge characteristics. (a) Voltage versus depth of discharge (DOD) during the discharge of lithium ion battery at different discharge rates, at room temperature. (b) Battery voltage versus state of charge of a lithium ion battery, calibrated through testing data. (c) Charge current during pulsed charge of lithium ion battery. (d) Terminal voltage during pulsed charge using the charging current shown in (c)

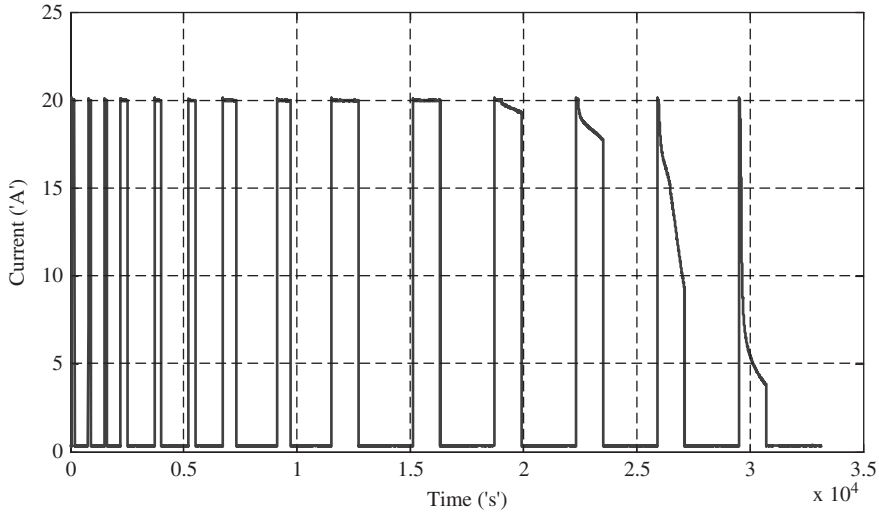

(c)

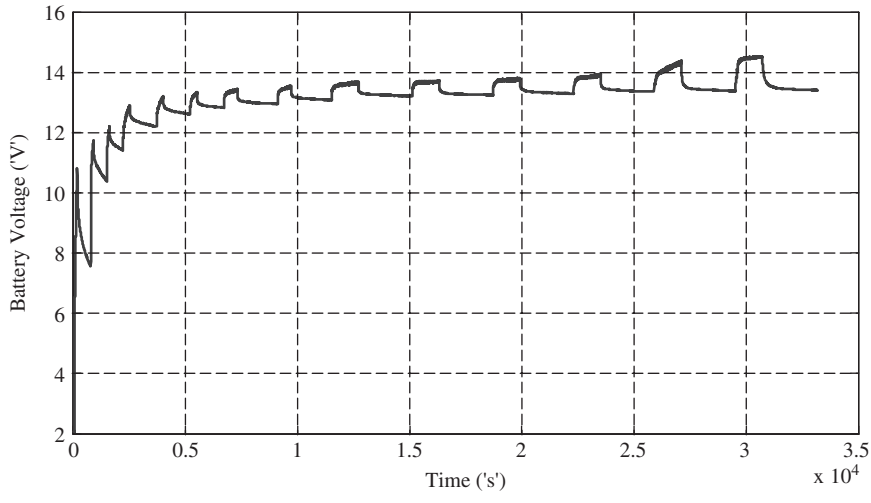

(d)

Figure 11.16 (*continued*)

lasting damage to an unprotected battery string. A battery cell usually can act differently from other cells in a string. Some may charge or discharge faster than others due to differences in internal impedance, temperature, and so on. This can cause an imbalance in charges among individual cells. If left unchecked, some can become over/undercharged or over/underdischarged. As a result, battery longevity is severely shortened and the overcharged batteries in an unprotected string could overheat, build up gas pressures, and explode. The battery string presents a safety hazard and must be carefully maintained [6, 15–17]. Thus, a carefully controlled charge equalization system is needed. Our

discussion is focused on the battery system; a good discussion on cell balancing for an ultracapacitor system can be found in [18].

The general principle behind the charge equalization circuit is to distribute an equal amount of energy or voltage to every cell in the series-connected string. In order to do this, the circuit must remove the energy from the more strongly charged cells and redistribute it to the weaker cells in order to obtain a uniform voltage or uniform energy distribution. This process is not instantaneous, it will happen over time, the length of which is determined by the method used. Of course, this can be done in many different ways. Charge equalization methods fall into several different categories. The two top categories are dissipative and non-dissipative equalizers. In the dissipative charge equalizing method, resistive shunts are used. An active version of the resistive shunt method utilizes a PWM control switch in line with the resistive shunt. This method is the simplest but very inefficient.

Moving on to non-dissipative equalizers, there exist three more tiers in classification. First of all, there is the charge type, discharge type, and the charge–discharge (bidirectional) type. With respect to the charge–discharge type, the classification splits again into current-fed equalizers and voltage-fed equalizers. For the former case, the equalizers contain bidirectional converters; and for the latter case, the circuit contains switched capacitors. An equalization scheme using switched capacitors is shown in Figure 11.17.

The circuit in the figure is the double-tiered method. In this method, as in the single-tiered method, no dedicated control system is necessary. The switches are set to a fixed frequency and are all switched at the same time. As a result, only one switching signal is necessary for this configuration. Even as the batteries reach an equalized state, the switching action remains; however, this consumes negligible energy. The addition of the second tier allows batteries 1 and 3 to also exchange charge between each other. This allows for faster equalization. Another advantage is that sensors are not necessary, resulting in cost savings [19].

As for the current-fed bidirectional converter type, the system presented by Lee and Cheng [5] utilizes two bidirectional converters sharing one capacitor shown in Figure 11.18.

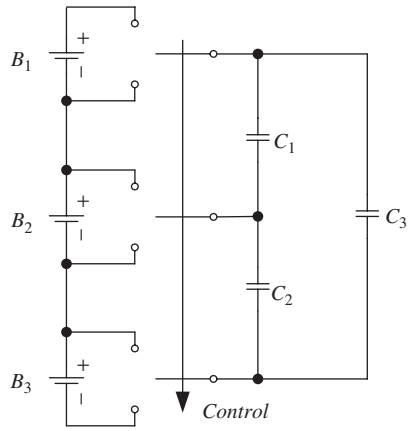

Figure 11.17 Circuit diagram of non-dissipative equalization with switched capacitors

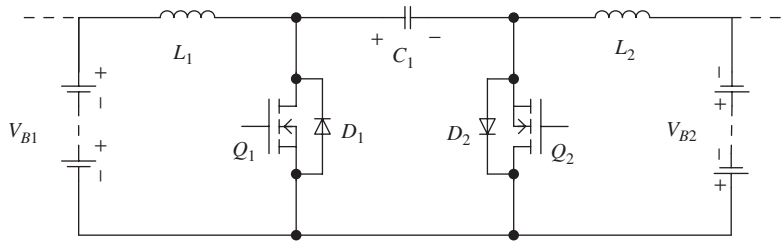

Figure 11.18 Circuit diagram of the current-fed bidirectional converter method

In the process of equalization, if battery 1 has a higher voltage than battery 2, then the first switch turns on at the duty cycle specified by the control system depending on the system's current state and measured values. This action charges the first inductor and then releases that energy through the capacitor and into the second battery, charging it. Hence the method is named a current-fed charge–discharge type. When the second battery has a greater voltage than the first battery, the same process happens, just with reversed currents, with the first battery being charged. PWM signals for controlling the converters' switches regulate the amount of current going into and out of each battery cell. This would be dependent on the SOC of the batteries. Different methods can be designed to control the PWM signals.

With respect to the discharge type, there exist two more tiers, namely, direct transfer and indirect transfer. With direct transfer, a serial recovery method uses step-up converters and a parallel recovery method uses primary multiple windings. With indirect transfer, a two-step method uses buck–boost converters and a multi-step method uses unidirectional converters. As with the charge type, there also exist two more tiers. The first is an automatic method which uses secondary multiple windings. The second is a selective method which uses secondary multiple windings plus switches [14].

11.7 Flywheel Energy Storage System

Flywheels are becoming of increasing interest in hybrid vehicle design, particularly for larger passenger transit vehicles. This is because of the following reasons. First, the requirements on specific power and specific energy of the battery can be decoupled, affording optimization of the battery's specific energy density and hence cycle life. Second, as the high-rate power demand and high-current discharge are greatly reduced by the load leveling effect of the flywheel, the usable energy, endurance, and battery cycle life can be increased. Third, the flywheel can allow rapid interim recharges with high efficiency during periods of low power demand or regenerative braking. Due to the combined effect of load leveling of the main energy source and improved energy recovery during regenerative braking, the range of the vehicle can be remarkably extended. The energy density is primarily related to the flywheel's speed of rotation. Increasing the speed of rotation produces improved specific energy, but increases the potential safety hazard, and also the cost, since special bearings and high-strength materials are required. Instead of using a battery or fuel cell, an EV can potentially be powered solely by an ultrahigh-speed flywheel. The corresponding long-term potential benefits for EV applications are possible,

since it can potentially provide higher specific energy and higher specific power than any batteries. Its specific power may possibly be even higher than the IC engine. The flywheel should also mitigate the problem of limited cycle life suffered by other sources because the life cycle of a flywheel is practically unlimited or at least longer than vehicle life [20]. The mechanical energy stored in a flywheel can be expressed as

$$E = \frac{1}{2} J\omega^2 \tag{11.30}$$

where J is the moment of inertia and ω the rotational speed. The above equation clearly indicates that there is a squared relation between energy stored in the flywheel and its rotational speed. Several companies have developed practical flywheel storage systems, like CCM of the Netherlands and Magnet Motor in southern Germany, and have accumulated considerable experience in the running of production flywheel–electric hybrid vehicles [21]. CCM's flywheels rotate at speeds of 15 000 rpm and operate with regenerative electronic drives of modern design; energy storage efficiencies of up to 93% have been achieved [21].

Some basic concepts related to flywheels are important to consider. As noted above, a flywheel involves the need to transfer one form of energy into another, that is, the kinetic energy of the flywheel. In some cases electrical energy may be converted and stored in a flywheel in mechanical form. But if mechanical energy from one body is needed to be transferred into another, that is, to a flywheel in this case, then it will be necessary to convert motion of the first body into motion of the flywheel. Consider the case of regenerative braking in a hybrid vehicle. Here it is necessary for motion of the vehicle's wheel to be reduced and the energy of motion to be transferred to the flywheel. In principle it is possible to transfer motion from one wheel to another as indicated in Figure 11.19.

In this figure, J_v and ω_v represent the inertia and angular velocity of the vehicle's wheel, and J_{FW} and ω_{FW} represent the same quantities for the flywheel. If the energy from the wheel is to be transferred to the flywheel, and assuming there is no loss in the process, at the end of the energy transfer the following relationship should hold:

$$\tfrac{1}{2} J_v \omega_v^2 = \tfrac{1}{2} J_{FW} \omega_{FW}^2 \tag{11.31}$$

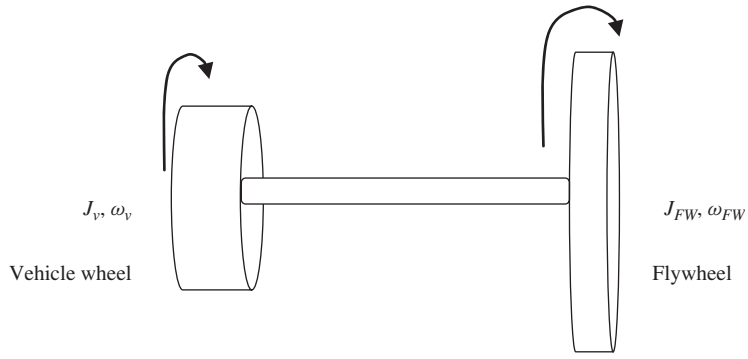

Figure 11.19 A simple connection between the vehicle's wheel and the flywheel

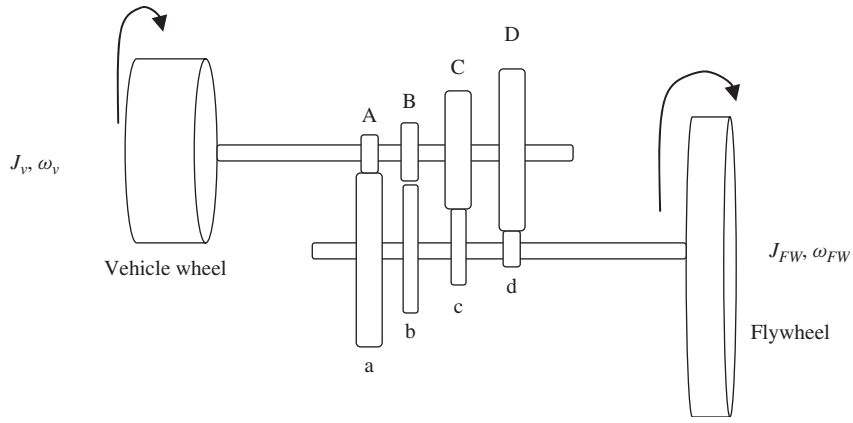

Figure 11.20 Use of gears to mechanically transfer motion between the vehicle's wheel and the flywheel

where ω_v is the original angular velocity of the wheel and ω_{FW} is the final angular velocity of the flywheel after the energy transfer is complete. When the flywheel speed has satisfied the above equation, the full vehicle wheel energy will be transferred to the flywheel, and the wheel's speed should then be zero, theoretically speaking.

The question is: how is the motion transferred? If the transfer is to be done purely mechanically, then one can introduce two sets of gears in the vehicle wheel shaft and the flywheel shaft respectively and slowly transfer the motion in a seamless manner as shown in Figure 11.20.

The idea is that initially the gears *Aa* will mesh together and other gears will be displaced laterally by some gear shifting scheme so that they are not engaged. With gear *A* having a very small diameter and gear *a* having a very large diameter, the flywheel will slowly start moving. The angular velocity will be such that the energy is conserved, that is, if the initial velocity of the wheel was ω_v, then after *Aa* meshing, the relationship at steady state should be

$$\tfrac{1}{2}J_v\omega_v^2 = \tfrac{1}{2}J_{FW}\omega_{FW}^2 + \tfrac{1}{2}J_v\omega_{v(new)}^2 \tag{11.32}$$

The value of $\omega_{v(new)}$, the vehicle wheel velocity after some transfer of motion, will obviously be smaller than the original value ω_v. Next time the gear *Aa* can be disengaged (by sliding the gears sideways) and *Bb* can be engaged. Following the same logic, the speed of the flywheel now increases a little more and the speed of the wheel will be reduced a little more. Similarly, continuing with the process of engaging *Cc*, and then *Dd*, and each time disengaging the previous gear set, the speed of the wheel will reduce more and more and the speed of the flywheel will increase ultimately until the energy of the flywheel will be equal to the energy of the wheel at its original speed prior to motion transfer. In principle this will be best achieved if the gears are continuously variable, rather than a discrete set of gears as in Figure 11.20. Obviously, due to the fact that an infinite number of gears are not possible, the process will be achieved through some discrete jumps if Figure 11.20 is followed. Also, note that the final energy of the flywheel will be somewhat less than the original energy of the wheel due to losses in the system.

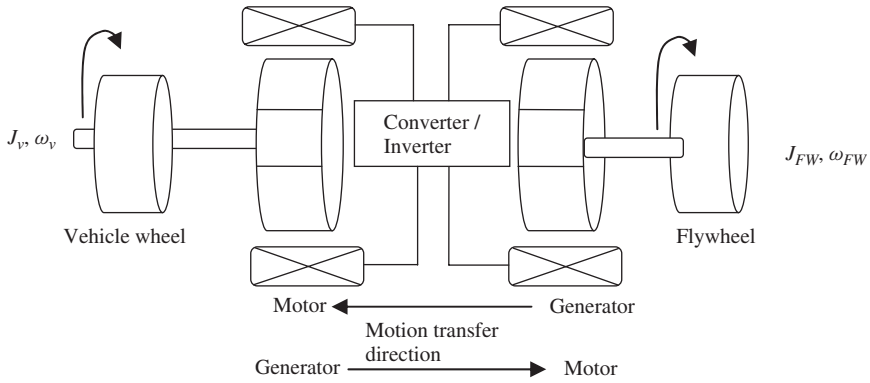

Figure 11.21 Electromechanical means to transfer motion between the vehicle's wheel and the flywheel

The other way of transferring motion is by electromechanical means but using the same principle as above. Here a motor generator scheme is used, which provides the continuously variable speed ratio and motion transfer through electromechanical means. This is illustrated in Figure 11.21.

In this figure, if the motion is to be transferred from the wheel on the left to the flywheel on the right, then the left electric machine will be a generator, and the power converter will convert the generator power properly to energize the other electric machine on the right. This one will then become a motor and will accelerate the flywheel. The motor generator sets and the power converter serve as a continually variable transmission if one wants to see it from that perspective. Eventually the speed of the wheel will be reduced and the speed of the flywheel will increase by an amount such that the reduction of mechanical energy of the wheel will be equal to the mechanical energy increase of the flywheel, less any losses. If it is intended to accelerate the vehicle again, the process will be reversed.

One final note regarding the flywheel is that, when it is rotating, it can cause a gyroscopic effect if the vehicle suddenly tries to turn quickly. This problem can be generally remedied by having two rotational masses with the same inertia but moving in opposite directions. This can be easily implemented by placing the two rotating members in a single housing with a gear in between.

11.8 Hydraulic Energy Storage System

Energy can also be stored by using a hydraulic system, where it is stored in the form of a compressed fluid or gas in a cylinder or similar means, known as an accumulator. To pressurize a compressible fluid, one needs mechanical power and energy, which can come from an IC engine or any other engine used to activate a hydraulic pump. Of course, in this case the original source of energy which drives the engine is chemical energy of the gasoline or diesel. While extracting the energy back from the hydraulic storage, one can use a hydraulic motor. The system-level scheme for realizing a hydraulic energy

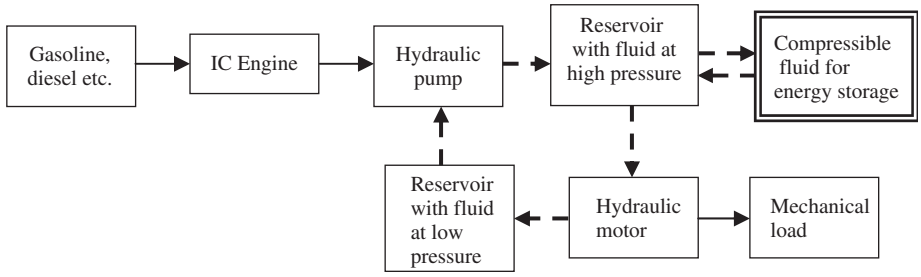

Figure 11.22 Generic scheme for hydraulic energy storage and extraction

storage and extraction mechanism is shown in Figure 11.22. In this figure, the dashed lines indicate the fluid flow path.

In Figure 11.22, chemical energy of the gasoline or diesel will drive an IC engine. The engine will drive a hydraulic pump which will basically draw an incompressible fluid from a low-pressure reservoir and increase its pressure. The high-pressure incompressible fluid can be used to drive a hydraulic motor which can drive some mechanical load. In the hydraulic motor, the mechanical fluid enters at high pressure and exits at low pressure, doing mechanical work in the process. Upon exiting the hydraulic motor, the low-pressure fluid flows to the low-pressure reservoir and the fluid flow circuit is completed. The high-pressure reservoir fluid can also move a piston or similar mechanism which in turn can push against a compressible gas. This compression will cause energy to be stored in the gas. Once some predefined pressure has been achieved, a valve can be used to prevent further pressurization of the gas. While extracting energy from the accumulator, an appropriate valve can be opened and the compressed gas will work against some piston and pressurize the incompressible fluid in the high-pressure reservoir, which in turn will drive a hydraulic motor.

In Figure 11.22, it can be seen that the dashed fluid flow path forms a closed loop system. It can also be seen that the fluid path can be bidirectional between the accumulator and the high-pressure fluid reservoir. Note that energy itself is stored in the compressible gas or fluid. The incompressible fluid (liquid) provides a flexible path or actuator, which replaces any mechanical linkage which otherwise would have been used for actuation.

Note also that an accumulator by itself is not of much use without the peripheral equipment or subsystems shown in Figure 11.22, since ultimately the goal is to be able to use the stored energy in a beneficial manner when needed, or, when extra energy is available, to store it in the accumulator. All the above items shown in Figure 11.22 together form the overall hydraulic energy extraction and storage system mechanism. Further details on hydraulic systems are given in Chapter 6.

11.9 Fuel Cells and Hybrid Fuel Cell Energy Storage System

11.9.1 Introduction to Fuel Cells

Research and development have been carried out on fuel cells as possible alternative power sources for a wide range of applications, from portable power sources, to the distributed

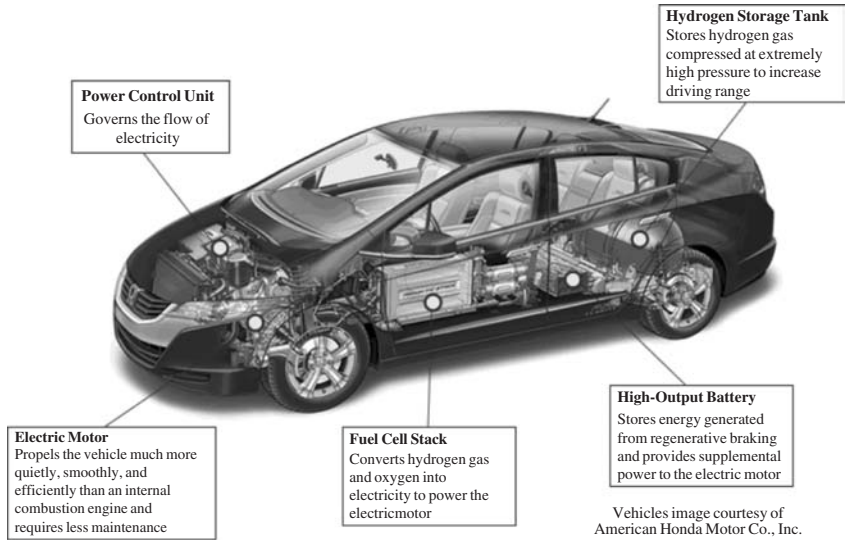

Figure 11.23 Honda 2008 FCX Clarity fuel cell car. (*Source*: http://www.fueleconomy.gov/feg/fuelcell.shtm. Courtesy American Honda.)

generation (DG) of electricity, to use in a new generation of fuel cell-powered electric vehicles, and so on. There are different types of fuel cells, such as the proton exchange membrane fuel cell (PEMFC), alkaline fuel cell, phosphoric acid fuel cell, molten carbonate fuel cell, solid oxide fuel cell, and direct methanol fuel cell. Among them, PEMFCs are primary candidates as power sources to drive next-generation vehicles, mainly due to their relatively low operating temperature (around 80 °C). In the PEMFC, hydrogen fuel is converted to electricity based on an electrochemical process involving the use of precious catalytic materials such as platinum. Some fuel cell prototype vehicles have already been built for the purpose of proof-of-concept and commercial demonstration. Examples include the GM HydroGen3, Honda 2008 FCX Clarity (as shown in Figure 11.23), Toyota FCHV-adv, among many others. Many fuel cell buses have been developed and are in operation around the world for demonstration purposes; an example fuel cell bus is shown in Figure 11.24.

High cost, unsatisfactory durability, poor transient performance, and subzero temperature startup issue are the main obstacles for the commercialization of clean fuel cell vehicles. Further, current fuel cell systems do not allow bidirectional energy flow and thus have difficulty in recovering braking energy. Therefore, some kind of hybridization of fuel cells with other energy storage devices such as batteries and ultracapacitors will be advantageous for a long period of time. For example, the Toyota FCHV fuel cell vehicle uses a NiMH battery pack as the secondary energy source, and the Honda FCX fuel cell vehicle uses ultracapacitors as an energy buffer to achieve powerful, responsive driving [22, 23]. In hybrid powertrains, the fuel cell system provides the base power for constant speed driving, while other energy storage devices provide additional peak power during acceleration and high-load operation and recover braking energy by regeneration.

Figure 11.24 The AC Transit Fuel Cell Bus – San Diego, 2005. (Courtesy ISE Corporation.)

Hence, the fuel cell system power rating and cost will be reduced; the powertrain transient performance will be improved; and energy efficiency will be increased.

There have been some studies and experiments involving hybrid fuel cell vehicles [22, 24, 25]. In [22], the requirements on energy storage devices in a fuel cell vehicle are analyzed. A mid-size SUV and a mid-size car are designed and simulated using ADVISOR in order to help the FreedomCar technical teams properly size the energy storage devices onboard fuel cell vehicles. It is concluded that the powertrain cost and volume can be greatly reduced over the pure fuel cell vehicle due to fuel cell downsizing via hybridization. In [24], a fuel cell system with a nominal power of 48 kW is hybridized with supercapacitors with a storage capacity of 360 Wh. The hybrid system is implemented on a road vehicle and tested. The test results demonstrate that good transient performance and impressive energy efficiency are achieved. In [25], optimization tools are linked to ADVISOR for the optimal design of a battery fuel cell SUV. In particular, ratings of fuel cell and battery and energy management strategy are optimized to maximize fuel economy, while meeting the pre-specified vehicle performance constraints. For a US city/highway composite test procedure, the optimizer chose a 66 kW fuel cell system and a 28-module battery pack with a large ampere-hour capacity of 50 Ah per module.

A fuel cell may be considered as an "open" battery in that the energy capacity is not limited by the reductant and oxidant contained within a cell. Instead, the energy generating capacity is determined by the amount of onboard hydrogen fuel. As a power source, a fuel cell can be three times more efficient (typical efficiency value of 60%) than an IC

engine (typical efficiency value of 20%) [23] because the fuel cell is not subject to the "Carnot cycle" efficiency limit [26, 27]. Except for water as the only by-product, there are no CO_2 and other harmful emissions. Thus, a fuel cell is a clean energy source. However, current fuel cell systems still have a low power density (10–100 times lower) compared to combustion engines. The short-term goal of power density for fuel cell systems is 0.5 kW/l [22], while current IC engines can reach up to 50 kW/l. The fuel cell vehicle drive range is still much shorter than conventional vehicles and is limited by the hydrogen storage energy density and cost. In addition, the fuel cell system has the disadvantages of slow startup and slow power response. Hence, a pure fuel cell vehicle has an unsatisfactory acceleration performance. Further, a fuel cell system cannot make use of any braking energy for improving fuel economy and driving range because of its inability to regenerate energy. Another characteristic of the fuel cell system is that its efficiency peaks near 25% of the rated power, with relatively lower efficiency at low and high output power. Thus, a vehicle control strategy should avoid the fuel cell system's low-efficiency operating regions.

The general construction of a fuel cell consists of two plates between which a membrane layer and catalyst are compressed. One plate serves as the anode and the other plate is the cathode. These plates have channels which are etched in the material and let the reactant fuels uniformly make contact with the catalyst. In the case of the PEMFC, these plates are made of carbon and the polymeric ion exchange membrane is coated with a platinum catalyst. The interconnections of the PEMFC are also made of carbon or some other type of metal. This cell can generate approximately 0.6 V DC. In order to increase the current capabilities, the surface area of the plates is increased. This also results in a power increase.

Similar to batteries and ultracapacitors, many individual fuel cells are connected in series/parallel to form a fuel cell stack to achieve the desired voltage, current, and power ratings for a particular application. A fuel cell system is composed of more than just the stack and the hydrogen and oxygen fuel. A complete fuel cell system is composed of blowers, pumps, fans, ejectors, turbines, compressors, valves, and regulators. All these components work together to deliver and regulate the proper amounts of fuel and ensure system safety. This management system is known as the balance of plant or (BOP). The main objectives of the BOP are hydrogen fuel preparation, air supply, thermal management, and water management. Fuel cell performance depends on the following parameters: temperature, reactant gas stoichiometric flow rates, anode and cathode pressures, anode and cathode humidification.

Once the reactant fuels flow through the channels and come into contact with the catalyst, a chemical process takes place. On the anode side (+), pressurized hydrogen flows through the network of small pathways. Through these pathways the hydrogen comes into contact with the platinum catalyst and splits into positive hydrogen ions and negative electrons. The polymer electrolytic membrane only allows positive ions to flow through. As a result, the hydrogen ions pass through the membrane and the electrons are forced to pass through an external electric circuit. On the cathode side (−), the oxygen gas (or ambient air) is passed through its own set of pathways. When it comes into contact with the catalyst, the bonded oxygen atoms split into two independent atoms. Once the hydrogen ions have passed through the membrane, they join up with the oxygen atoms. Two hydrogen ions bond with one oxygen atom and two electrons pass through the cathode. As a result, the "exhaust" of the PEMFC is water vapor and heat [26, 27].

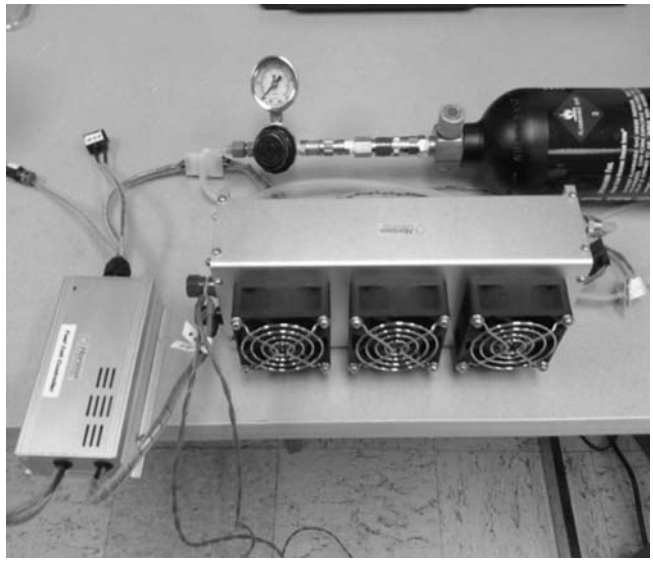

Figure 11.25 A 300 W fuel cell stack with BOP controller and hydrogen connections

Figure 11.25 shows a fuel cell power source with a power rating of 300 W, made by Horizon Fuel Cell Technologies. It has a maximum current output of 7 A at 42 V.

The fuel cell system contains the controller, electrical connections, rubber hydrogen lines for secondary hydrogen connections, primary valve, and purge valve. Details concerning the physical characteristics of the stack are given in Table 11.3. A 12 V source is required to power its BOP controller.

*11.9.2 Fuel Cell Modeling**

The relationship between cell current and voltage is modeled as the polarization curve and is based on the fuel cell's steady state performance. In particular, the fuel cell output voltage is modeled as the thermodynamic potential with three types of overvoltages subtracted: activation overvoltages, ohmic overvoltages, and concentration overvoltages. The activation-related losses, or kinetic regime, are caused by the chemical reactions themselves. The chemical reactions are not instantaneous when the reactants come into contact with the catalyst; that is, the reaction must first be activated. This is mainly due to the surface area of the catalyst. Ohmic losses are due to electrical resistances in the leads, connections, and the plates of the stack. This type of loss is greatly affected by heat, the surface area of the plates in the stack, and the types of materials used in the fuel cell system. As for the concentration overvoltage or transport losses, these are caused by the limit on mass transport rate of hydrogen and oxygen reactants.

In practical application such as powertrains of land-based vehicles, the output power from the fuel cell system undergoes large variations, especially during acceleration and

* © [2008] Inderscience. Reprinted, with permission, from the International Journal of Electric and Hybrid Vehicles.

Table 11.3 List of technical specifications for the Horizon Fuel Cell

Technical specifications	
Type of fuel cell	PEM
Number of cells	72
Rated power	300 W
Performance	43 V at 7 A
H_2 supply valve voltage	12 V
Purging valve voltage	12 V
Blower voltage	12 V
Reactants	Hydrogen and air
External temperature	5–35 °C
Maximum stack temperature	65 °C
Composition	99.999% dry H_2
Hydrogen pressure	5.8–6.5 psi
Humidification	Self-humidified
Cooling	Air (integrated cooling fan)
Weight	2 kg
Dimensions	32.4 cm × 10.9 cm × 9.4 cm
Hydrogen flow rate	3.9 l/m at max power
Stack efficiency	40% at 43 V
Controller weight	250 g
Low-voltage shutdown	36 V
Overcurrent shutdown	12 A
Over-temperature shutdown	65 °C

deceleration. During such transient operating periods, due to the existence of the double-layer capacitance at the interface between the electrodes and the electrolyte, the reactant gas manifold filling dynamics, cell surface dynamics, and other effects, the fuel cell stack system's performance cannot be adequately represented by a pure algebraic steady state model. Hence, a dynamic fuel cell model is needed to provide more accurate predictions of fuel cell system performance for the dynamic simulation and analysis of the fuel cell power system. Such a model is illustrated in Figure 11.26.

In this equivalent circuit model, E_{cell} represents the internal potential of the fuel cell. The output of fuel cell voltage V_d is E_{cell} with three types of voltage drop subtracted: activation voltage drop, ohmic voltage drop, and concentration voltage drop. Activation voltage drop can be separated into two parts: the one affected by internal temperature and the other one caused by the equivalent resistance of activation. Capacitor C is the equivalent capacitor due to the double-layer charging effect. The formula for calculating these parts is as follows [28, 29]:

$$V_d = E_{cell} - V_{act1} - V_{act2} - V_{conc} - R_{ohmic} I \tag{11.33}$$

where

$$E_{cell} = E_{0,cell} + \frac{RT}{2F} \ln\left[P^*_{H_2} \left(P^*_{O_2}\right)^{0.5}\right] - k_E\,(T - 298)$$

and where $E_{0,cell}$ is the standard reference potential at standard state (298 K and 1 atm pressure), R is the gas constant, and F is the Faraday constant. P_{H_2} and P_{O_2} represent

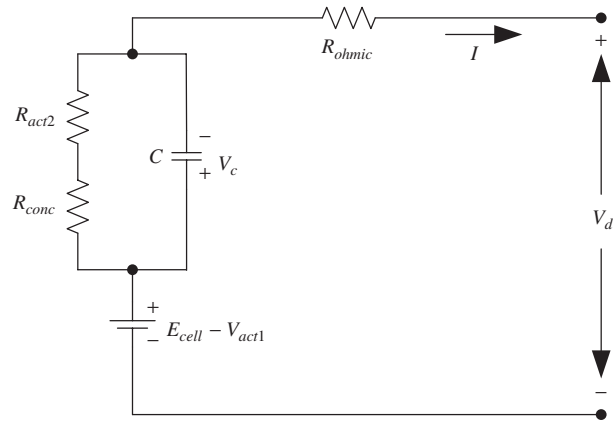

Figure 11.26 A dynamic fuel cell model

the partial pressure of H_2 and O_2 activated inside the fuel cell. The asterisk * represents the effective value of the parameter. k_E is an empirical constant in volts per kelvin and T is the actual temperature when the fuel cell is operating. Thus

$$V_{act1} = \eta_0 + a\,(T - 298) \tag{11.34}$$

where η_0 is the temperature-invariant part of V_{act1} and a is an empirical constant in volts per kelvin. Similarly,

$$V_{act2} = R_{act2} I \tag{11.35}$$

$$V_{conc} = R_{conc} I \tag{11.36}$$

$$V_C = \left(I - C\frac{dV_C}{dt}\right)(R_{act} + R_{conc}) \tag{11.37}$$

At steady state, the static characteristics of the fuel cell are as depicted in the following equation, in which the relationship between the output voltage and current of the fuel cell can be approximately considered as linear by ignoring V_{act2} and V_{conc} due to small values of the two parameters at steady state:

$$V_d = E_{cell} - V_{act1} - R_{ohm} I \tag{11.38}$$

At steady state, E_{cell}, V_{act1}, and R_{ohm} can be considered as constants; therefore, the above equation can be modified approximately with the following expression:

$$V_d = K_1 + K_2 I \tag{11.39}$$

where

$$K_1 = E_{cell} - V_{act1} \quad \text{and} \quad K_2 = -R_{ohm}$$

Typical values of the parameters of the fuel cell model are given in Table 11.4.

Figure 11.27 shows $I-V$ polarization characteristics and the power–current curve for a typical PEMFC model.

Table 11.4 Parameters of a typical fuel cell

$E_{0,cell}$(V)	R(J/(mol K))	F(C/mol)	P_{H_2}(Pa)	P_{O_2}(Pa)
58.9	8.3143	96 487	1.5	1.0
k_E(V/K)	η_0(V)	a(V/K)	$R_{ohm}(\Omega)$	T(K)
0.00085	20.145	−0.1373	0.2793	307.7

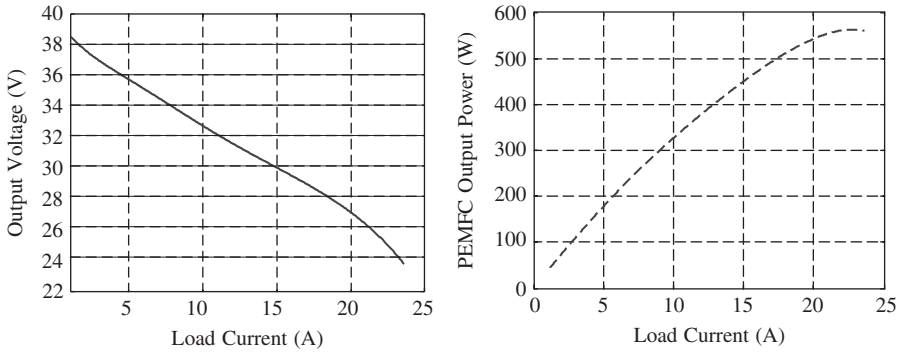

Figure 11.27 Fuel cell characteristic curve

11.9.3 Hybrid Fuel Cell Energy Storage Systems

The continuous power output of PEMFCs is satisfactory, but the voltage regulation is poor and their response to instantaneous transient power load requirements is often too sluggish. To meet such peak power requirements economically, that is, to eliminate fuel cell overdesign, the PEMFCs are hybridized with batteries or ultracapacitors. Fuel cells have a high specific energy while supercapacitors have high specific power, with secondary batteries lying in between. The fuel cell/ultracapacitor hybrid system will ideally provide both high power and energy densities at low cost. Further, since supercapacitors have limited energy storage capability compared to batteries, a fuel cell/battery/supercapacitor hybrid system will have better power supplying capability. In vehicular applications, the battery is also needed to start up the fuel cells. This kind of hybrid system has the flexibility to be optimally sized for different applications so that the advantages of each device can be utilized to maximum extent. At the IEEE Vehicular Power and Propulsion Conference held on 6–8 September 2006 in Windsor, UK, faculty members at the University of Manchester presented their hybrid fuel cell–battery electric London Taxi project with a 6 kW PEMFC and ZEBRA Z5C traction battery [30]. Their results show that the hybridization of a fuel cell and battery can extend the driving range and reduce fuel cell size under dynamic urban driving cycles.

There are several configurations for the design of hybrid systems. In the simplest topology, the output of the fuel cell stack is connected through a DC–DC converter to a DC link, where fuel cells can be hybridized with other energy storage devices such as batteries or ultracapacitors. The load is also connected in parallel at the DC link. Note that the load can be a DC traction motor or an inverter-driven AC traction motor in

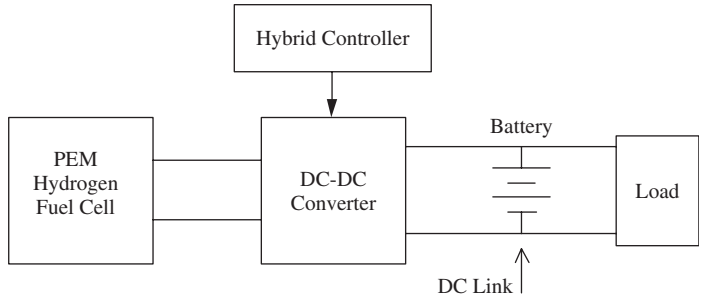

Figure 11.28 A simple hybrid fuel cell system

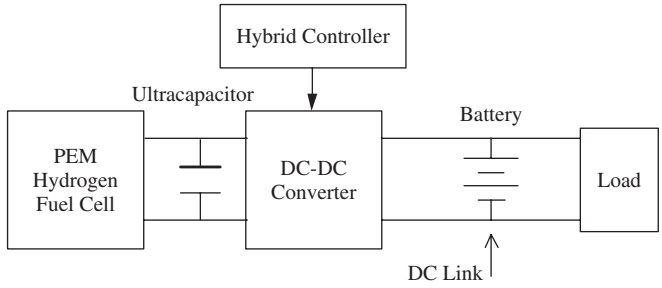

Figure 11.29 A hybrid fuel cell system with both batteries and ultracapacitors

vehicle applications. Such a topology is shown in Figure 11.28. One key component is the hybrid controller that will control the power flow among the different power sources under different load conditions. The hybrid controller will be responsible for the hybrid system's power and energy management.

The use of batteries can restrict the DC link voltage. Depending on the number of cells in series, batteries have a definite voltage value. As a result, the output of the converter must maintain a value corresponding to the battery voltage. However, with the use of ultracapacitors, which are not voltage dependent, the output of the converter can be set to whatever voltage is needed by a particular load. If the use of batteries is desired at the output of the converter, ultracapacitors can still be used at the input of the converter or the output of the fuel cell to further stabilize the system and reduce current spikes in the fuel cell. This hybrid topology is shown in Figure 11.29.

We can also use a double input DC–DC converter (DIC) to accommodate a PEMFC and a battery unit. This hybrid system is illustrated in Figure 11.30. The PEMFC and the battery unit are connected in parallel so that both sources can supply the load. This topology will allow each power source to operate independently with the benefits of each fully utilized in an appropriate hybrid control strategy. For example, the battery unit can be voltage controlled to maintain constant DC link voltage V_{DC}, while the PEMFC is current controlled in order to provide the connected load with the required current. The DIC can be based on the buck–boost converter, which allows the voltage levels of each power source to be above or below the DC link voltage level. The battery in Figure 11.30

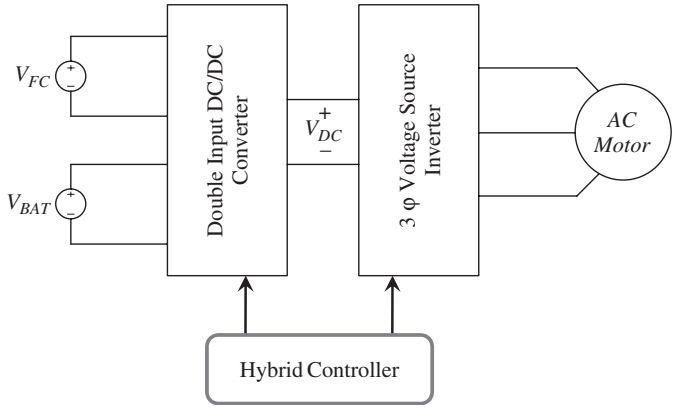

Figure 11.30 A hybrid fuel cell–battery system using a double-input DC–DC converter

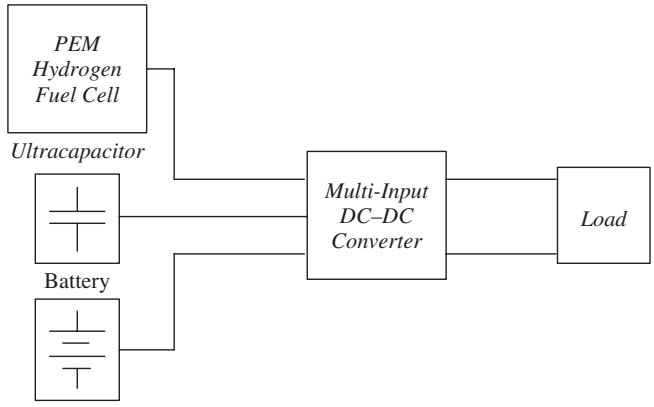

Figure 11.31 Hybrid system with a multi-input DC–DC converter

can be replaced by an ultracapacitor to achieve another hybrid fuel cell–ultracapacitor system, but a different control strategy will be needed due to the different characteristics of the battery and ultracapacitor.

Since the buck–boost converters are connected in parallel, the topology can be extended by connecting additional converters allowing the use of additional sources (i.e., supercapacitor and/or IC engines). Such a topology is illustrated in Figure 11.31, in which a multiple input DC-DC converter is used to allow connections of fuel cell, battery, and ultracapacitor to the load. Again, the load can be a DC load or inverter-driven AC load.

A variation of the topology in Figure 11.31 is shown in Figure 11.32, where multiple converters can be used. The fuel cell would have either a buck or boost converter and the batteries or ultracapacitors would have a bidirectional buck–boost converter. Bidirectional DC–DC converters allow currents to flow into or out of the energy storage devices and thus allow the devices to supply power to the load or to be charged by either the fuel

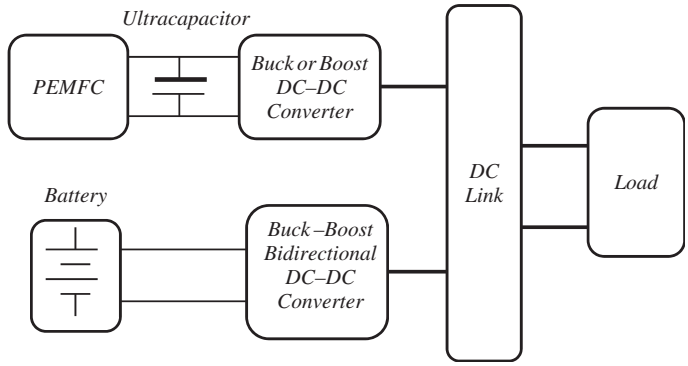

Figure 11.32 Hybrid fuel cell energy storage system with a bidirectional converter [27]

cell or electric generator. This topology would also allow for a variable DC link voltage. Both topologies in Figures 11.31 and 11.32 require sophisticated hybrid control strategies for the power and energy management.

*11.9.4 Control Strategy of Hybrid Fuel Cell Power System**

In this section, a hybrid power source consisting of a PEMFC and a lead acid battery is used as a case study. The PEMFC is used as the main energy source while the battery is used as the auxiliary part to improve power quality. A DC–DC boost converter is connected between the fuel cell and the battery to ensure a proper voltage level at the DC bus and also to control the power flow.

The control strategy takes into account the load profile and the battery SOC. In order to protect the fuel cell, load transients mitigation control is utilized to filter out the peak values of the load. The fuel cell is controlled to provide the steady state load current after mitigation and the battery supplies the peak currents. The SOC is estimated using the battery's voltage and current, which are constantly measured.

In case the SOC is below a specified limit, the fuel cell supplies the charging current to the battery, until the desired SOC is achieved. Additionally, the control strategy also improves fuel cell efficiency, limits its maximum power output, and controls the load bus voltage, thus ensuring longer lifetime for the fuel cell and providing reliable working conditions for the load.

The configuration of the hybrid PEMFC–battery system is shown in Figure 11.33. The PEMFC, battery, and load are connected in parallel so that both power sources can supply the load. The PEMFC voltage varies over a large range, depending on the load current. In order to maintain a constant voltage at the DC bus, the fuel cell is isolated from the battery and the load using a DC–DC boost converter. Using the measured load current, battery current, and DC bus voltage, the main controller calculates the reference current I_{ref}, which together with the converter output current i_{con_out} is used to determine the duty ratio for the DC–DC converter via the current controller. A three-step-starting DC motor with a rated voltage of 220 V and a rated power of 2 kW is used as a load.

* © [2009] IEEE. Reprinted, with permission.

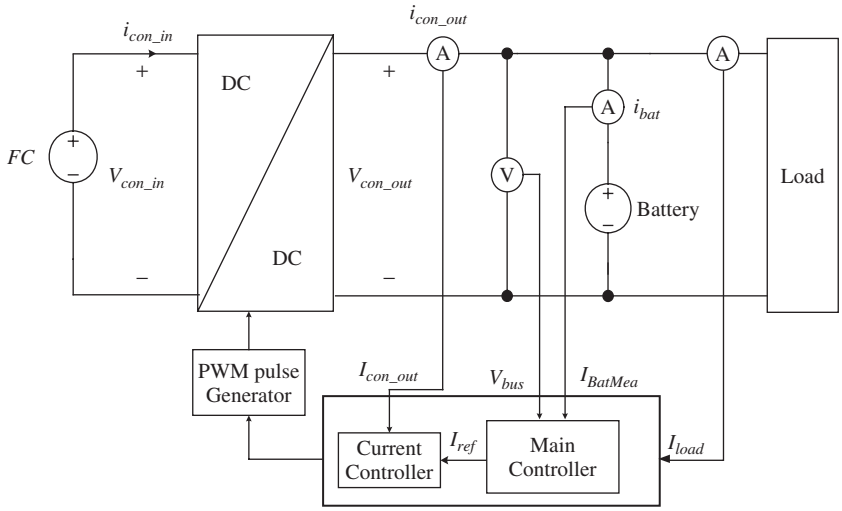

Figure 11.33 Configuration of the hybrid fuel cell–battery system

The main objective of the hybrid control strategy is to use the fuel cell to satisfy the energy demands of the load, while the transient peak power demand is covered by the battery. In order to improve the lifetime of the battery and to maintain the DC bus voltage within a small range (±5%) around 220 V, the battery's SOC is controlled as well. In case of a low SOC, the fuel cell will provide a charging current.

Two controllers are required for the hybrid control strategy: a current controller and a main controller. The current controller, a PI controller, regulates the output current i_{con_out} of the DC–DC converter by controlling the duty ratio of the PWM generator. Reference current I_{ref} is provided by the main controller. The tasks of the main controller consist of regulating the steady energy for the load and any additional charging energy for the battery, both provided by the PEMFC. Thus, the main controller is split into two parts: the load transient mitigation controller [31], which supplies steady load current $i_{LoadREF}$; and the battery SOC controller, which supplies the battery charging reference current i_{BatREF}. Details of the two controllers can be found in [32]. The flow chart of the overall control strategy is shown in Figure 11.34. The objective of the control strategy is to provide an optimum response to the load demand, to maintain the SOC of the battery (i.e., maintaining the energy reserve), and to ease operation of the PEMFC (i.e., extending the life cycle of the fuel cell).

Two different simulation scenarios are presented. The first scenario includes a lead acid battery pack, consisting of 17 cells connected in series, with a relatively high capacity of 1 Ah for each battery cell up to a total of 17 Ah for the battery stack. With such a high capacity the battery stack should be able to provide the load with enough peak power without needing to be charged. The second scenario includes a battery pack, with the same amount of batteries, with a significantly lower capacity of 0.05 Ah each up to a total of 0.85 Ah for the battery stack. The batteries in this scenario should be discharged to a point where charging will become necessary.

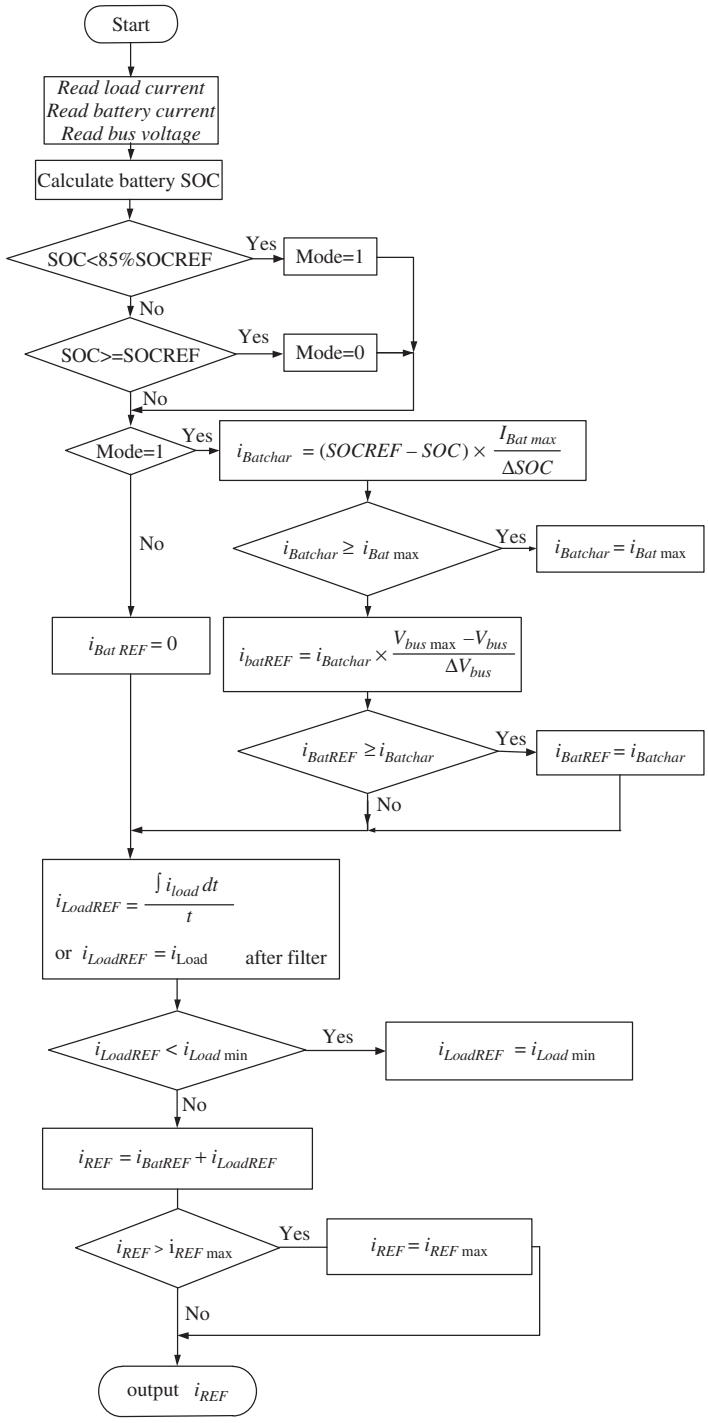

Figure 11.34 Flow chart of the hybrid control strategy

The purpose of using two different battery capacities is to illustrate the battery charging control algorithm implemented in the system, where the fuel cell is used not only to supply the load demand, but also to maintain the SOC of the battery.

It is assumed that at the beginning of the simulations the batteries are fully charged with the SOC equal to 1.

11.9.4.1 Maximum Capacity of 1 Ah per Battery Cell

As expected, the SOC of the battery stack with such a high capacity remains above 85%. Thus no charging current provided by the fuel cell is necessary in this scenario. Therefore, the main controller output i_{ref} equals the converter output current i_{con_out}, which is shown in Figure 11.35. The low-pass filter, implemented in the load mitigation controller, smoothes the transients of the load current providing a steadily growing reference current, resulting in a smooth converter output current. At the same time, the battery covers all peak power transients of the load and is zero at steady state load, as shown in Figure 11.36.

The fuel cell output current as shown in Figure 11.37 has the same profile as the converter output current. As can be seen at the starting point, the fuel cell is controlled to have a rapidly increasing output current to avoid low efficiency due to small output current.

As an auxiliary part of the fuel cell system, the battery may not need a very high capacity. In comparison the fuel cell is supposed to be a large energy storage source. Therefore a simulation for a smaller battery capacity (0.05 Ah per battery cell) was performed.

11.9.4.2 Maximum Capacity of 0.05 Ah per Battery Cell

The output current of the fuel cell shows a smooth profile, as seen from the inset in Figure 11.38, until the third transient of the load at around five seconds of the simulation, when the battery SOC drops below 85% and the charging of the battery is triggered. The fuel cell is controlled to provide charging current until the battery is fully charged again,

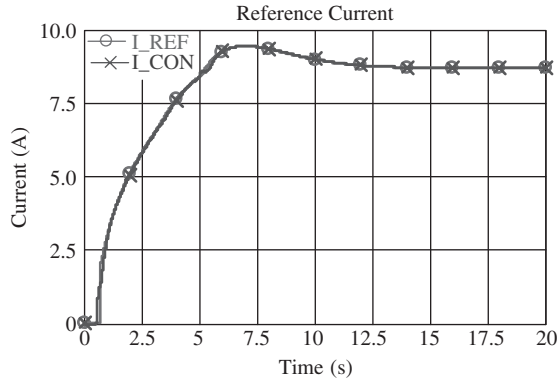

Figure 11.35 Reference current and converter output current (1 Ah/battery cell)

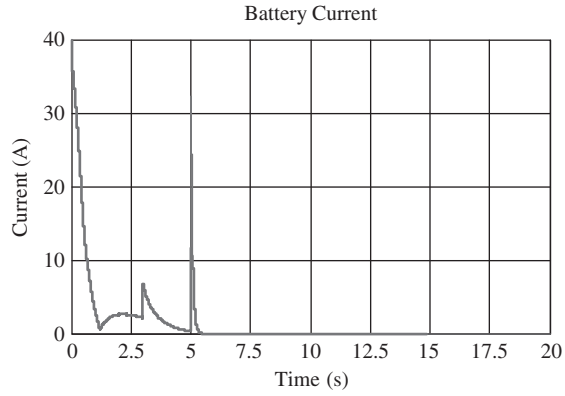

Figure 11.36 Battery output current (1 Ah/battery cell)

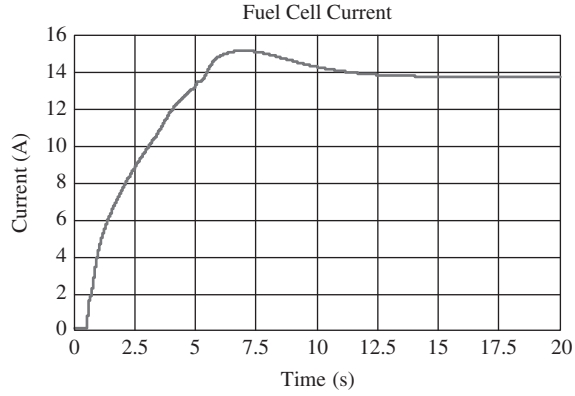

Figure 11.37 Fuel cell output current (1 Ah/battery cell)

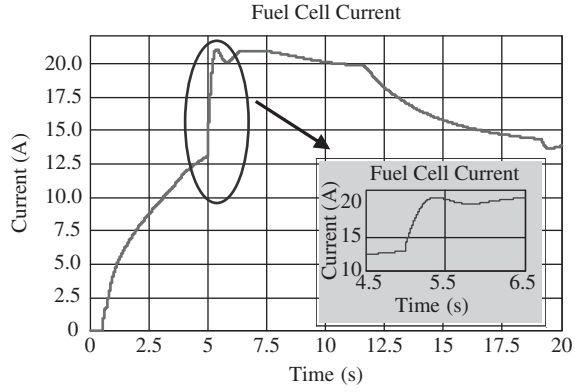

Figure 11.38 Fuel cell output current (0.05 Ah/battery cell)

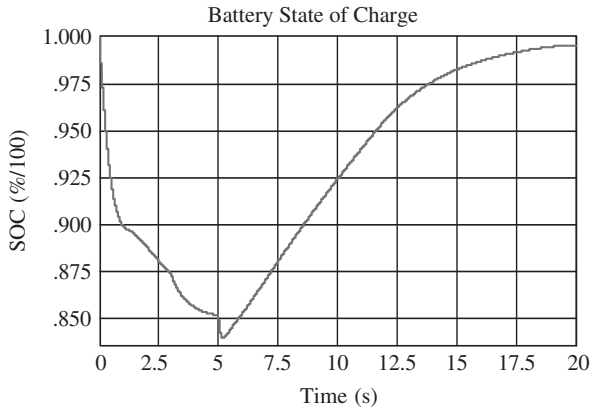

Figure 11.39 Battery state of charge (0.05 Ah/battery cell)

as shown in Figure 11.39. A dead-band is necessary to avoid the chattering effect of the controller from charging/discharging the battery at a faster rate. At the beginning of the charging mode, the current output of the fuel cell significantly steps up, following the increase of the reference current from the current controller, providing charging current to the battery and mitigated load current to the DC motor. However, the increase in the fuel cell current seems to be smooth enough due to the low-pass filter action in the load current measurement, thus assuring a longer life cycle for the fuel cell in applications with dynamic load profiles.

The simulation results show that the whole system works well and both the fuel cell current and battery current can be controlled as desired to meet different load demands.

11.10 Summary and Discussion

In this chapter, the most important energy storage devices – batteries, ultracapacitors, flywheel energy storage systems, hydraulic energy storage systems, and fuel cells – are discussed in detail. Since many cells of batteries and ultracapacitors are connected in series and parallel to achieve desired voltage and current ratings, equalizing circuits are indispensible for the energy management and control of onboard energy storage devices. Different battery charging techniques that are commonly used for charging the battery in HEVs are compared. There are different advantages and disadvantages for each charging method. Conventional methods like CC and CV have many disadvantages; the pulse charging technique is gaining popularity and will be a better option for HEV battery charging. Integration of an ultracapacitor with a battery can potentially mitigate the disadvantages of each component and deliver superior performance for a HEV or PHEV. Fuel cell technologies are promising for future clean vehicles, but current PEMFCs cannot meet the requirements of high peak power, low cost, and robustness. Therefore, hybridization of fuel cells with batteries or ultracapacitors will result in higher energy efficiency with regenerative braking capability under dynamic driving cycles.

References

1. Zheng, J.P., Jow, T.R., and Ding, M.S. (2001) Hybrid power sources for pulsed current applications. *IEEE Transactions on Aerospace and Electronic Systems*, **37** (1), 288–291.
2. Van Mierlo, J., Van den Bossche, P., and Maggetto, G. (2004) Models of energy sources for EV and HEV: fuel cells, batteries, ultracapacitors, flywheels and engine-generators. *Journal of Power Sources*, **128**, 76–89.
3. Brooker, A., Haraldsson, K., Hendricks, T. *et al*. (2002) ADVISOR Documentation (Version 2002), National Renewable Energy Laboratory.
4. Brian, M. (2006) How Lithium-ion Batteries Work. HowStuffWorks.com. http://electronics.howstuffworks.com/lithium-ion-battery.htm (accessed November 14, 2006).
5. Lee, Y. and Cheng, M. (2005) Intelligent control battery equalization for series connected lithium-ion battery strings. *IEEE Transactions on Industrial Electronics*, **52** (5), 1297–1307.
6. Affanni, A., Bellini, A., Franceschini, G. *et al*. (2005) Battery choice and management for new-generation electric vehicles. *IEEE Transactions on Industrial Electronics*, **52** (5), 1343–1349.
7. Maxwell Technologies, (2006) Fuel Cells and Ultracapacitors – A Proven Value Proposition Versus Incumbent Technologies, San Diego.
8. Maxwell Technologies, (2011) Ultracapacitors Help P21 to Provide Fuel Cell-Based Backup Power for Telecoms, San Diego.
9. Larminie, J. and Lowry, J. (2003) *Electric Vehicle Technology Explained*, John Wiley & Sons, Ltd, Chichester.
10. Dougal, R.A., Gao, L., and Liu, S. (2004) Ultracapacitor model with automatic order selection and capacity scaling for dynamic system simulation. *Journal of Power Sources*, **126**, 250–257.
11. Sule, V. and Santoso, S. (n.d.) Constant Current and Voltage Battery Charging Schemes for Stand-Alone Wind Turbines, Department of Electrical and Computer Engineering, University of Texas.
12. Jiang, Z. and Dougal, R.A. (2004) Synergetic control of power converters for pulse current charging of advanced batteries from a fuel cell power source. *IEEE Transactions on Power Electronics*, **19** (4), 1140–1150.
13. Nemeth, M.S. (2002) The 12 volt Side of Life, http://www.ccis.com/home/mnemeth/12volt/12volt.htm (accessed March 3, 2002).
14. Park, H., Kim, C.-E., Kim, C.-H. *et al*. (2009) A modularized charge equalizer for an HEV lithium-ion battery string. *IEEE Transactions on Industrial Electronics*, **56** (5), 1464–1476.
15. Kutkut, N., Wiegman, H.L.N., Divan, D., and Novotny, D. (1998) Charge equalization for an electric vehicle battery system. *IEEE Transactions on Aerospace and Electronic Systems*, **34** (1), 235–245.
16. Moo, C., Hsieh, Y., and Tsai, I. (2003) Charge equalization for series-connected batteries. *IEEE Transactions on Aerospace and Electronic Systems*, **39** (2), 704–710.
17. Kutkut, N.H., Wiegman, H.L.N., Divan, D., and Novotny, D. (1999) Design considerations for charge equalization of an electric vehicle battery system. *IEEE Transactions on Industry Electronics*, **35** (1), 28–35.
18. Miller, J.M. (2004) *Propulsion Systems for Hybrid Vehicles*, IEE, London.
19. Baughman, A. and Ferdowsi, M. (2008) Double-tiered switched-capacitor battery charge equalization technique. *IEEE Transactions on Industrial Electronics*, **55** (6), 2277–2285.
20. Chan, C.C. and Chau, K.T. (2001) *Modern Electric Vehicle Technology*, Oxford University Press, Oxford.
21. Jefferson, C.M. and Barnard, R.H. (2002) *Hybrid Vehicle Propulsion*, WIT Press, Boston, MA.
22. Markel, T., Zolot, M., Wipke, K.B., and Pesaran, A.A. (2003) Energy storage requirements for hybrid fuel cell vehicles. Advanced Automotive Battery Conference, June 10–13, Nice, France.
23. Matsumoto, T., Watanabe, N., Sugiura, H., and Ishikawa, T. (2002) Development of fuel-cell hybrid vehicle. SAE World Congress, March 4–7, Detroit, MI, paper 2002-01-0096.
24. Rodata, P., Garcia, O., Guzzella, L. *et al*. (2003) Performance and Operational Characteristics of a Hybrid Vehicle Powered by Fuel Cells and Supercapacitors, SAE paper 2003-01-0418, Society of Automotive Engineers.
25. Wipke, K.B., Markel, T., and Nelson, D. (2001) Optimizing energy management strategy and degree of hybridization for a hydrogen fuel cell SUV. 18th International Electric Vehicle Symposium (EVS 18), October, Berlin, Germany.

26. Larminie, J. and Dicks, A. (2000) *Fuel Cell Systems Explained*, John Wiley & Sons, Ltd, Chichester.
27. O'Hayre, R., Cha, S-W., Colella, W., and Prinz, F.B. (2005) *Fuel Cell – Fundamentals*, John Wiley & Sons, Inc., New York.
28. Wang, C., Nehrir, M.H., and Gao, H. (2006) Control of PEM fuel cell distributed generation systems. *IEEE Transactions on Energy Conversion*, **21** (2), 586–595.
29. Wang, C. and Nehrir, M.N. (2003) A dynamic model for PEM fuel cells using electrical circuit. Proceedings of 35th North American Power Symposium, October, Rolla, MO, pp. 30–35.
30. Lachichi, A. and Schofield, N. (2006) Comparison of DC-DC converter interfaces for fuel cells in electric vehicle applications. Proceedings of the IEEE Vehicle Power and Propulsion Conference, September 6–8, Windsor, UK.
31. Wang, C. and Nehrir, M.H. (2007) Load transient mitigation for stand-alone fuel cell power generation systems. *IEEE Transactions on Energy Conversion*, **22** (4), 864–872.
32. Zheglov, V., Gao, W., Muljadi, E., and Wang, G. (2009) New control strategy for stand-alone fuel cell-battery hybrid power supply system. IEEE PES General Meeting, July, Calgary, Canada.

12

Modeling and Simulation of Electric and Hybrid Vehicles*

12.1 Introduction

Compared to conventional vehicles, there are more electrical components used in electric, hybrid, and fuel cell vehicles, such as electric machines, power electronics, electronic continuously variable transmissions (CVTs), and embedded powertrain controllers [1, 2]. Advanced energy storage devices and energy converters, such as Li-ion batteries, ultracapacitors (UCs), and fuel cells are introduced in the next-generation powertrains. In addition to these electrification components or subsystems, conventional internal combustion engines (ICEs), mechanical systems, and hydraulic systems may still be present. The dynamic interactions among various components and the multidisciplinary nature make it difficult to analyze a newly designed hybrid electric vehicle (HEV). Each of the design parameters must be carefully chosen for better fuel economy, enhanced safety, exceptional drivability, and a competitive dynamic performance – all at a price acceptable to the consumer market. Prototyping and testing each design combination is cumbersome, expensive, and time consuming. Modeling and simulation are indispensable for concept evaluation, prototyping, and analysis of HEVs. This is particularly true when novel hybrid powertrain configurations and controllers are developed.

Furthermore, the complexity of new powertrain designs and dependence on embedded software are a cause for concern among automotive research and development efforts. This results in increasing difficulty in predicting interactions among various vehicle components and systems. In such situations, a modeling environment that can model not only components but also embedded software, such as the electronic throttle controller (ETC) software, is needed. Effective diagnosis also presents a challenge. Modeling can play an important role in the diagnostics of the operating components. For example, running an embedded fuel cell model and comparing the actual fuel cell operating variables to those obtained from the model can help fault diagnosis of fuel cells.

Hybrid Electric Vehicles: Principles and Applications with Practical Perspectives, First Edition.
Chris Mi, M. Abul Masrur and David Wenzhong Gao.

A face-off with modeling and simulation tools in the electronics industry has demonstrated that similar tools in the automotive domain still lack the power, sophistication, and automation required by and available to the electronics designers [3]. Advances in electronic design tools have validated Moore's law (as applied to the complexity of integrated circuits) and have helped achieve amazing standards in computing power while simultaneously decreasing costs. For designers of automotive systems to duplicate and manage similar levels of complexity, design tools that automate the low-level details of the design process need to be developed [3, 4].

Depending on the level of detail of how each component is modeled, the vehicle model may be steady state, quasi-steady, or dynamic [5–15]. For example, an ADVISOR (ADvanced VehIcle SimulatOR) [5, 6] model can be categorized as a steady state model, a powertrain system analysis toolkit (PSAT) [7] model as quasi-steady, and PSIM [8] and virtual test bed (VTB) [9] models as dynamic. On the other hand, depending on the direction of calculation, vehicle models can be classified as forward-looking or backward-facing models [5]. In forward-looking models, vehicle speed is controlled to follow a driving cycle during the analysis of fuel economy, thus facilitating controller development.

The main advantage of employing a steady state model or quasi-steady model is fast computation, while the disadvantage is inaccuracy for dynamic simulation. On the contrary, physics-based models can facilitate high-fidelity dynamic simulations for the vehicle system at different time scales. This kind of dynamic model should be useful for developing an effective powertrain control strategy [10]. The models are tied closely to the underlying physics through a link such as a lumped-coefficient differential equation or some digital equivalent model.

This chapter addresses different modeling and simulation methods for electric and hybrid vehicles. The chapter is organized as follows: Section 12.2 reviews the fundamentals of vehicle system modeling. Sections 12.3 and 12.4 provide an overview of the existing vehicle modeling tools ADVISOR and PSAT, with application examples, using ADVISOR to study a hybrid battery–ultracapacitor energy storage system, and using PSAT to optimize a parallel powertrain design. Section 12.5 looks at physics-based dynamic modeling, introducing the resistive companion form (RCF) of modeling method with examples of a DC machine, a DC–DC boost power converter, and vehicle dynamics including a wheel slip model. Section 12.6 looks at bond graphs and other modeling tools such as PSIM, Simplorer, V-ELPH, Saber, and Modelica for hybrid powertrain modeling. Section 12.7 addresses the issue and mitigation methods of numerical oscillations for dynamic simulation involving power electronics. Finally, conclusions are given in Section 12.8.

12.2 Fundamentals of Vehicle System Modeling

It is important to define the common terms used in modeling. The following definitions are based on the text by Dr Peter Fritzson of Linköping University in Sweden [16] and are related to HEV modeling:

- **System:** The object or objects we wish to study. In the context of this chapter, the system will be an electric vehicle or HEV.
- **Experiment:** The act of obtaining information from a controllable and observable system by intelligently varying system inputs and observing system outputs.

- **Model:** A surrogate for a real system upon which "experiments" can be conducted to gain insight about the real system. The types of experiments that can be validly applied to a given model are typically limited. Thus, different models are typically required for the same target system to conduct all of the experiments one wishes to conduct. Although there are various types of models (e.g., scale models used in wind tunnels), in this chapter we will mainly discuss physics-based mathematical models.
- **Simulation:** An experiment performed on a model.
- **Modeling:** The act of creating a model that sufficiently represents a target system for the purpose of simulating that model with specific predetermined experiments.
- **Simulator:** A computer program capable of performing a simulation. These programs often include functionality for the construction of models and can often be used in conjunction with advanced statistical engines to run trade (sensitivity) studies, design of experiments, Monte Carlo routines, and other routines for robust design.

Vehicle system modeling is conducted over various areas of interest to answer vastly different questions (i.e., different experiments). Traditional areas include modeling for the analysis of noise vibration harshness (NVH); modeling of vehicle performance (e.g., acceleration, gradability, and maximum cruising speed); modeling for the prediction, evaluation, and optimization of fuel economy; modeling for safety, stability, and crashworthiness; modeling of vehicle controls; modeling for structural integrity; modeling to facilitate component testing and validation; modeling for preliminary conceptual design/design exploration; modeling for cost and packaging; and modeling for the prediction of emissions.

There are various types of mathematical models and simulators available to perform vehicle system simulations. For example, some simulators can be used to construct models that use macro statistics from duty cycles and cycle-averaged efficiencies of components for near-instantaneous prediction of fuel consumption and performance, whereas other simulators perform detailed sub-second transient simulations for more detailed experiments. There is also a typical tradeoff in the vehicle modeling between the amount of engineering assumptions the modeler has to make and the amount of time required to set up and construct a model. A simple high-level model can estimate fuel consumption using the engineer's knowledge of "typical" cycle-averaged component efficiencies. A more detailed model would actually simulate each of the components over time and mathematically determine cycle-averaged efficiencies. In addition to the assumption/specificity tradeoff, there is also a tradeoff between model detail and run time. In general, the more detailed the results, the longer the total time for model setup, simulation, and interpretation of the results.

Detailed vehicle system models typically contain a mix of empirical data, engineering assumptions, and physics-based algorithms. Good simulators provide a large variety of vehicle components along with data sets to populate those components. The components can then be connected together as the user desires to create a working vehicle powertrain, body, and chassis. Connections between components mathematically transmit effort and flow (e.g., torque and speed or voltage and current) during a simulation.

Depending upon the desired degree of detail, there are various models available such as steady state spreadsheet models, transient power–flow models, and transient effort–flow models (effort–flow refers to the combinations of torque–angular speed, voltage–current, force–linear speed, etc.).

The transient vehicle system models can be divided into two categories based on the direction of calculation. Models that start with the tractive effort required at the wheels and

"work backward" toward the engine are called backward-facing models. Models that start from the engine and work in transmitted and reflected torque are called forward-facing models. So-called non-causal models allow for forward or backward operation depending on the experiment being performed. Backward-facing models are typically much faster than forward-facing models in terms of simulation time. Forward-facing models better represent real system setup and are preferred where controls development and hardware-in-the-loop (HIL) will be employed. Forward models must typically use some kind of "driver model" such as a proportional–integral–derivative (PID) controller to match a target duty cycle. Some "hybrid" models include both concepts.

In addition, vehicle system models may interact with any number of more detailed models such as structural analysis models, vibrational models, thermal models, and so on.

Driven by the need for fast simulation times, complex components such as engines and motors are typically simulated using "lookup maps" of energy consumption versus shaft torque and angular speed. Once the average torque and angular shaft speed for a given time step are determined, an interpolation on empirical data is performed to determine the component's energy consumption rate.

There have been extensive studies in the modeling and simulation of hybrid and electric vehicles [4–15]. Modeling tools such as ADVISOR and PSAT are available in the public domain, and are discussed in more detail in the following sections.

12.3 HEV Modeling Using ADVISOR

ADVISOR is a modeling and simulation tool developed by the US National Renewable Energy Laboratory (NREL) [5, 6]. It can be used for the analysis of performance, fuel economy, and emissions of conventional, electric, hybrid electric, and fuel cell vehicles. The backbone of the ADVISOR model is the Simulink block diagram shown in Figure 12.1, for a parallel HEV as an example. Each subsystem (block) of the block diagram has a MATLAB file (m-file) associated with it, which defines the parameters of that particular subsystem. The user can alter both the model inside the block as well as the m-files associated with the block to suit the modeling needs. For example, the user may need a more precise model for the electric motor subsystem. A different model can replace the existing model as long as the inputs and the outputs are the same. On the other hand, the user may leave the model intact and only change the m-file associated with the

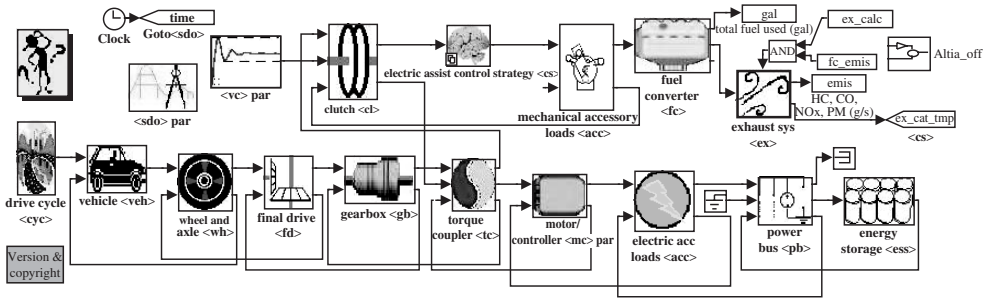

Figure 12.1 Block diagram of the parallel HEV in ADVISOR [6]

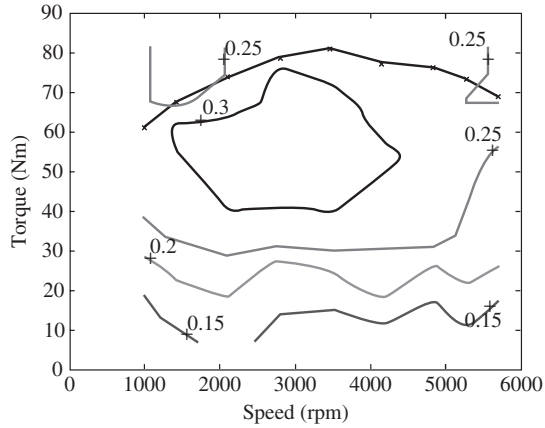

Figure 12.2 Geo 1.01 (43 kW) spark ignition engine efficiency map

block diagram. This is equivalent to choosing a different make of the same component (e.g., choosing a 12 Ah battery manufactured by Hawker Genesis instead of a 6 Ah battery manufactured by Caterpillar). ADVISOR provides modeling flexibility for a user.

ADVISOR models fit empirical data obtained from the component testing to simulate a particular subsystem. In general, the efficiency and limiting performances define the operation of each component. For example, the ICE is modeled using an efficiency map that is obtained via experiments. The efficiency map of a Geo 1.01 (43 kW) engine is shown in Figure 12.2. Various contour lines on this diagram indicate particular efficiency values labeled beside the corresponding contour. The maximum torque curve is also shown in this map. The engine cannot perform beyond this maximum torque constraint. Maximum torque change is another constraint on the engine subsystem. In other words, the model considers the inertia of the component in the simulation.

The program also allows for the linear scaling of components. For an ICE, this means linear scaling of the torque so as to provide the required maximum power. This type of scaling is valid only in the neighborhood near the actual parameter where the efficiency map for a slightly larger or smaller component would not change drastically. Scaling of the Geo ICE is shown in Figure 12.3 so that the ICE gives a maximum power of 50 kW instead of the nominal 43 kW.

In the latest version of ADVISOR, the functionality of the software was improved by allowing links to other software packages such as Ansoft Simplorer [17] and Synopsys Saber [18]. These powerful packages allow for a more detailed look at the electric systems of the vehicle.

As an application example, ADVISOR is used to simulate a hybrid battery–ultracapacitor energy storage system. More extensive applications can be found in [19], where ADVISOR is used to model a hybrid fuel cell/battery powertrain and hybrid fuel cell/ultracapacitor powertrain and simulate their fuel economy and performance. The concept of using a hybrid energy storage system consisting of a battery and a UC is well known and well documented in the literature [20, 21]. The UC provides and absorbs the current peaks, while the battery provides the average power required for the electric

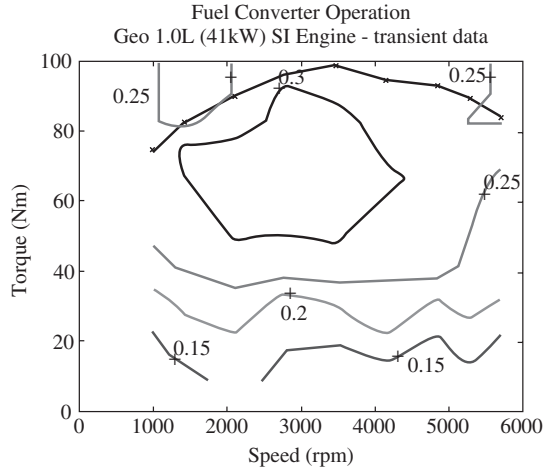

Figure 12.3 Geo 1.01 engine scaled to give a maximum power of 50 kW by linear alteration of the torque characteristics

motor. This arrangement of hybrid energy storage in a HEV extends the life of the battery and allows the motor to operate more aggressively. Simulating such a system in ADVISOR allows the user to visualize the fuel economy benefit. At the same time, the program allows the user to design the best control strategy for the battery–ultracapacitor hybrid to improve the battery life and the overall system performance. Finally, the size of the components can be optimized and, thus, the cost and weight of the system can be reduced.

The default battery model in ADVISOR operates by requesting a specific amount of power from the battery as decided by the vehicle control strategy. Depending on the amount of power that the battery is able to supply, the battery module will send out the power available from the battery to the other subsystems. Due to the hybrid backward/forward simulation method of ADVISOR, the amount of power that the batteries are able and required to supply in a given time step is calculated in a single iteration. From this value, the battery model calculates the battery variables like current, voltage, and temperature.

However, hybrid battery–ultracapacitor energy storage systems cannot be modeled within ADVISOR using the above default battery model. Here, we have to replace the energy storage model with a more complex model. Fortunately, the subsystem model in ADVISOR can be altered as long as the types of inputs and outputs to the rest of the vehicle are not altered. In our simulation, we replaced the battery model by a model of the combination of a battery and a UC connected to a local control strategy unit that splits the power demand between the battery and the UC. Detailed information about the control strategy is available in [21]. The block diagram representation of the system is shown in Figure 12.4.

The use of the model described above gives the user a way to quickly and easily simulate the battery–ultracapacitor subsystem in a vehicle environment. It allows the user to observe the benefit of using the UC on the fuel economy of the vehicle as well as the benefit to the battery by making the battery's state of charge more even and by reducing

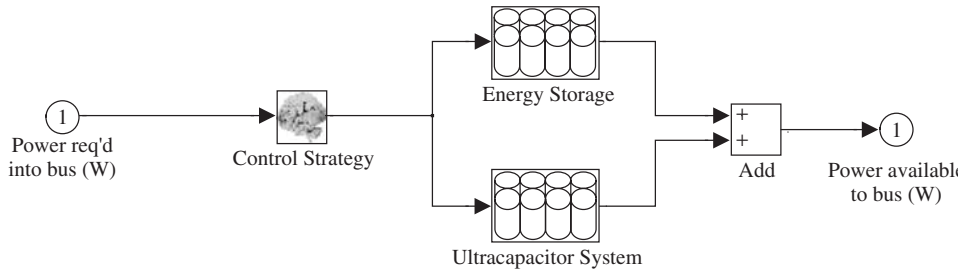

Figure 12.4 Block diagram representation of the new battery subsystem that consists of the battery and ultracapacitor. The input/output relation with the rest of the system is left unchanged

the peaks of the battery current that the battery has to accept. It also allows the user to validate whether the system operates as efficiently as it would if the battery size were reduced. Finally, the user can optimize the battery–ultracapacitor control strategy (in other words, how the power demand will be split) without having to think about the complexities of designing the power electronics to make this control system feasible. In addition, the system can be optimized before any system is built and the system cost and possible savings can be easily calculated at the early design stage. Once the control strategy is optimized, the actual DC–DC converter with the required control strategies can be integrated into the simulation by interfacing with Saber or Ansoft Simplorer software [20].

12.4 HEV Modeling Using PSAT

PSAT (AUTONOMIE) is state-of-the-art flexible simulation software developed by Argonne National Laboratory and sponsored by the US Department of Energy (DOE) [7]. PSAT is modeled in a MATLAB/Simulink environment and is set up with a graphical user interface (GUI) written in C#, which makes it user friendly and easy to use. Being a forward-looking model, PSAT allows users to simulate more than 200 predefined configurations, including conventional, pure electric, fuel cell, and hybrids (parallel, series, power split, and series–parallel). The large library of component data enables users to simulate light-, medium-, and heavy-duty vehicles.

The level of detail in component models can be flexible; for example, a lookup table model or high-fidelity dynamic model can be used for a component, depending on the user's simulation requirements. To maintain modularity, every model must have the same number of input and output parameters. The use of quasi-steady models and control strategies including propelling, braking, and shifting strategies in PSAT sets it apart from other steady state simulation tools like ADVISOR. This feature allows PSAT to predict fuel economy and performance of a vehicle more accurately. Its modeling accuracy has been validated against the Ford P2000 and Toyota Prius. PSAT is designed to co-simulate with other environments and is capable of running optimization routines. HIL testing is made possible in PSAT with the help of PSAT-PRO, a control code to support the component and vehicle control [7].

As an application example, PSAT is used to optimize a parallel HEV for maximum fuel economy on a composite driving cycle. Four global algorithms, namely, divided

rectangle (DIRECT), simulated annealing (SA), genetic algorithm (GA), and particle swarm optimization (PSO), are used in the model-based design optimization [22]. Details can be found in Chapter 13.

12.5 Physics-Based Modeling

PSAT and ADVISOR are based on experiential models in the form of lookup tables and efficiency maps. The accuracy of these tools may not be good enough for vehicles operating under extreme conditions. For detailed dynamic modeling and simulation of a HEV system, physics-based modeling is needed. VTB, PSIM, Simplorer, and V-Elph are good examples of physics-based modeling tools, where the state variables of a component or subsystem are modeled according to the physical laws representing the underlying principles. The resulting model is a function of device parameters, physical constants, and variables. Such physics-based models can facilitate high-fidelity simulations for dynamics at different time scales and also controller development.

In this section, the physics-based modeling technique, RCF [23] modeling in particular, is explored. The RCF method originates from electrical engineering, but is suitable for multidisciplinary modeling applications such as the hybrid powertrain.

RCF Modeling Technique

The RCF method has been used successfully in a number of industry-standard electronic design tools such as SPICE [24] and Saber. Recently, it has also been applied in VTB [9, 23], which is recognized as the leading software for prototyping of large-scale, multi-technical dynamic systems. Using the RCF modeling technique, we can obtain high-fidelity physics-based models of each component in modular format. These models can be seamlessly integrated to build a system simulation model suitable for design. Just as a physical device is connected to other devices to form a system, the device can be modeled as a block with a number of terminals through which it can be interconnected to other component models, as shown in Figure 12.5. Each terminal has an associated across variable and a through variable. If the terminal is electrical, these variables are the terminal voltage with respect to a common reference and the electric current flowing into the terminal, respectively. Note that the concept of across and through variables in RCF is similar to the effort–flow concepts used in ADVISOR and PSAT.

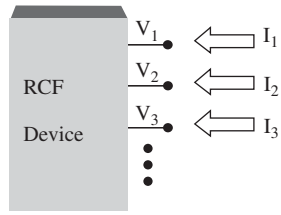

Figure 12.5 Physics-based resistive companion form (RCF) modeling technique

The general form of the RCF model can be expressed as follows, which is obtained by numerically integrating the differential–algebraic equations describing the dynamics of the component:

$$\begin{bmatrix} \mathbf{i}(t) \\ \mathbf{0} \end{bmatrix} = \mathbf{G}[\mathbf{v}(t), \mathbf{v}(t-h), \mathbf{i}(t), \mathbf{i}(t-h), \mathbf{y}(t), \mathbf{y}(t-h), t] \times \begin{bmatrix} \mathbf{v}(t) \\ \mathbf{y}(t) \end{bmatrix} - \begin{bmatrix} \mathbf{b}_1[\mathbf{v}(t), \mathbf{v}(t-h), \mathbf{i}(t), \mathbf{i}(t-h), \mathbf{y}(t), \mathbf{y}(t-h), t] \\ \mathbf{b}_2[\mathbf{v}(t), \mathbf{v}(t-h), \mathbf{i}(t), \mathbf{i}(t-h), \mathbf{y}(t), \mathbf{y}(t-h), t] \end{bmatrix} \tag{12.1}$$

where $\mathbf{i}$ is a vector of through variables; $\mathbf{v}$ is a vector of across variables; $\mathbf{y}$ is a vector of internal state variables; h is the numerical integration time step; $\mathbf{G}$ is a Jacobian matrix; $\mathbf{b}_1$, $\mathbf{b}_2$ are vectors depending in general on past history values of through and across variables and internal states, and on values of these quantities at time instant t. Note that $\mathbf{G}$, $\mathbf{b}_1$, and $\mathbf{b}_2$ depend on the chosen integration method. The most common integration methods that can be used are the trapezoidal rule and second-order Gear's method.

After all the powertrain components are modeled in RCF, they can be integrated into one set of algebraic equations by applying the connectivity constraints between neighboring modular components, which can then be solved to get system state variables.

Hybrid Powertrain Modeling

Modeling examples for powertrain components are given for a DC machine, a DC–DC boost power electronics converter, and vehicle dynamics. Through these modeling examples, the principles of physics-based modeling techniques are demonstrated. Extensive coverage of models for all the powertrain components is not intended for this chapter.

Modeling of a DC Machine

An equivalent circuit model of the DC machine is illustrated in Figure 12.6, where R and L are the armature resistance and inductance, respectively. The DC machine has two electrical terminals (0,1) and one mechanical terminal (2).

The through variables are: $\mathbf{i} = [i_0, i_1, T_{sh}]^t$, where T_{sh} $(= i_2)$ is the mechanical torque at the machine shaft; the superscript t indicates matrix transpose. The across variables are: $\mathbf{v} = [v_0, v_1, \omega]^t$, where ω $(= v_2)$ is the rotational speed of the machine shaft.

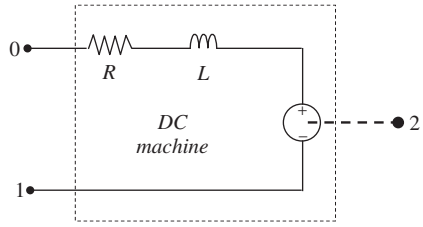

Figure 12.6 DC machine modeling

The differential algebraic equations describing the machine dynamics are

$$\begin{cases} i_0 = -\dfrac{L}{R}\dfrac{di_0}{dt} + \dfrac{1}{R}(v_0 - v_1) - \dfrac{k_e\phi}{R}v_2 \\ i_1 = -i_0 \\ i_2 = -(k_T\phi)\, i_0 + J\dfrac{dv_2}{dt} + d \bullet v_2 \end{cases} \tag{12.2}$$

where J is shaft inertia, d is the drag coefficient, and ϕ is the flux per pole. Applying the trapezoidal integration rule, we get the following RCF model:

$$i(t) = G(h) \bullet v(t) - b(t-h) \tag{12.3}$$

where

$$G(h) = \begin{bmatrix} \dfrac{h}{hR+2L} & \dfrac{-h}{hR+2L} & \dfrac{-hk_e\phi}{hR+2L} \\ \dfrac{-h}{hR+2L} & \dfrac{h}{hR+2L} & \dfrac{hk_e\phi}{hR+2L} \\ \dfrac{-hk_T\phi}{hR+2L} & \dfrac{hk_T\phi}{hR+2L} & \left(\dfrac{hk_e\phi k_T\phi}{hR+2L} + \dfrac{2J}{h}\right) \end{bmatrix} \tag{12.4}$$

$$b(t-h) = \begin{bmatrix} b_0(t-h) \\ -b_0(t-h) \\ b_2(t-h) \end{bmatrix} \tag{12.5}$$

$$\begin{aligned} b_0(t-h) = {} & \frac{hR-2L}{hR+2L}i_0(t-h) - \frac{h}{hR+2L}v_0(t-h) \\ & + \frac{h}{hR+2L}v_1(t-h) + \frac{hk_e\phi}{hR+2L}v_2(t-h) \end{aligned} \tag{12.6}$$

$$b_2(t-h) = -k_T\phi b_0(t-h) + k_T\phi i_0(t-h) + i_2(t-h) + \frac{2J}{h}v_2(t-h) \tag{12.7}$$

Modeling of DC–DC Boost Converter

An equivalent circuit model of the DC–DC boost converter is illustrated in Figure 12.7. The DC–DC boost converter has three electrical terminals (0, 1, and 2). Here, we derive the average state space model, based on the two states of the circuit when the switch is on or off.

When the switch Q is ON, we have the following state space dynamic equations:

$$\begin{aligned} \frac{di_0}{dt} &= \frac{1}{L}(v_0 - v_1) \\ \frac{d(v_2 - v_1)}{dt} &= \frac{1}{C}i_2 \end{aligned} \tag{12.8}$$

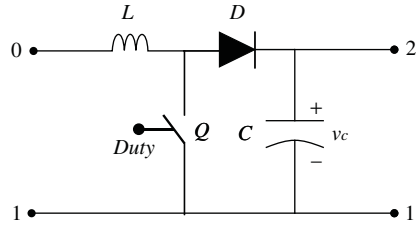

Figure 12.7 DC–DC boost converter modeling

When the switch Q is OFF, we have the following state space dynamic equations:

$$\begin{aligned} \frac{di_0}{dt} &= \frac{1}{L}(v_0 - v_2) \\ \frac{d(v_2 - v_1)}{dt} &= \frac{1}{C}(i_0 + i_2) \end{aligned} \tag{12.9}$$

Hence, the Middlebrook state space averaging model is as follows (d = duty):

$$\begin{aligned} \frac{di_0}{dt} &= \frac{d}{L}(v_0 - v_1) + \frac{(1-d)}{L}(v_0 - v_2) \\ \frac{d(v_2 - v_1)}{dt} &= \frac{d}{C}i_2 + \frac{(1-d)}{C}(i_0 + i_2) \end{aligned} \tag{12.10}$$

Applying the trapezoidal integration rule, we get the following RCF model for the boost power converter:

$$i(t) = G(h) \bullet v(t) - b(t-h) \tag{12.11}$$

where

$$G(h) = \begin{bmatrix} \frac{h}{2L} & \frac{-hd}{2L} & \frac{-h(1-d)}{2L} \\ \frac{-hd}{2L} & \frac{hd^2}{2L} + \frac{2C}{h} & \frac{hd(1-d)}{2L} - \frac{2C}{h} \\ \frac{-h(1-d)}{2L} & \frac{hd(1-d)}{2L} - \frac{2C}{h} & \frac{hd(1-d)^2}{2L} + \frac{2C}{h} \end{bmatrix} \tag{12.12}$$

$$b(t-h) = \begin{bmatrix} b_0(t-h) \\ -b_0(t-h) - b_2(t-h) \\ b_2(t-h) \end{bmatrix} \tag{12.13}$$

$$b_0(t-h) = -i_0(t-h) - \frac{h}{2L}v_0(t-h) + \frac{hd}{2L}v_1(t-h) + \frac{h(1-d)}{2L}v_2(t-h) \tag{12.14}$$

$$\begin{aligned} b_2(t-h) = &-(1-d)b_0(t-h) + (1-d)i_0(t-h) + i_2(t-h) \\ &- \frac{2C}{h}v_1(t-h) + \frac{2C}{h}v_2(t-h) \end{aligned} \tag{12.15}$$

Modeling of Vehicle Dynamics

The vehicle dynamic model can be derived from Newton's second law considering all the forces applied to the vehicle. The driving force comes from the powertrain shaft torque, which can be written as the wheel torque:

$$T_{wh} = R_g \eta_{trans} T_{sh} \tag{12.16}$$

where R_g and η_{trans} are the transmission gear ratio and transmission efficiency, respectively. This wheel torque provides the driving force to the vehicle:

$$F_d = \frac{T_{wh}}{r} \tag{12.17}$$

where r is the wheel radius.

The total resistance force consists of rolling resistance, aerodynamic resistance, and gravitational force. Hence, the vehicle dynamic equation can be obtained:

$$\begin{aligned} F_d &= F_{gxt} + F_{roll} + F_{ad} + ma \\ &= mg\sin(\alpha) + mg\,(C_0 + C_1 v)\,\mathrm{sgn}(v) \\ &\quad + \frac{1}{2}\rho C_d A_F\,(v + v_0)^2\,\mathrm{sgn}(v) + \left(m + \frac{J_{wh}}{r^2}\right)\frac{dv}{dt} \end{aligned} \tag{12.18}$$

where F_{gxt} is the gravitational force on a grade, F_{roll} is the rolling resistance, F_{ad} is the aerodynamic resistance, m is the vehicle mass, g is the natural acceleration, α is the angle of grade, C_0 and C_1 are the rolling coefficients, ρ is the air density, C_d is the aerodynamic drag coefficient, A_F is the vehicle frontal area, v_0 is the wind speed, v is the vehicle linear speed, and J_{wh} is the wheel inertia.

Similarly, applying the trapezoidal integration rule, we get the following RCF model for the vehicle dynamics:

$$i(t) = G(h) \bullet v(t) - b(t-h) \tag{12.19}$$

where the through variable is $i(t) = F_d$ and the across variable $v(t) = v$ (vehicle velocity).

Note that Equation 12.18 is a nonlinear model, requiring an iterative Newton–Raphson solution procedure at each simulation time step; the Jacobian $G(h)$ is as follows:

$$G(h, v(t)) = mgC_1\,\mathrm{sgn}(v) + \rho C_d A_F\,(v(t) + v_0)\,\mathrm{sgn}(v) + \frac{2}{h}\left(m_{veh} + \frac{J_{wh}}{r^2}\right) \tag{12.20}$$

Other RCF models for induction machine, batteries, UCs, and so on, can be found in [23, 25, 26] respectively. Based on the same principles, an ICE model and fuel cell model can be developed.

Finally, as an example of employing RCF techniques for HEVs, a hybrid fuel cell–ultracapacitor–battery vehicle model is modeled in VTB, as shown in Figure 12.8. Upon simulation, variables that are of interest can be plotted, as shown in Figure 12.9, where the reference vehicle speed, battery, UC, and DC motor currents are plotted. Details of how to use VTB can be found in [9].

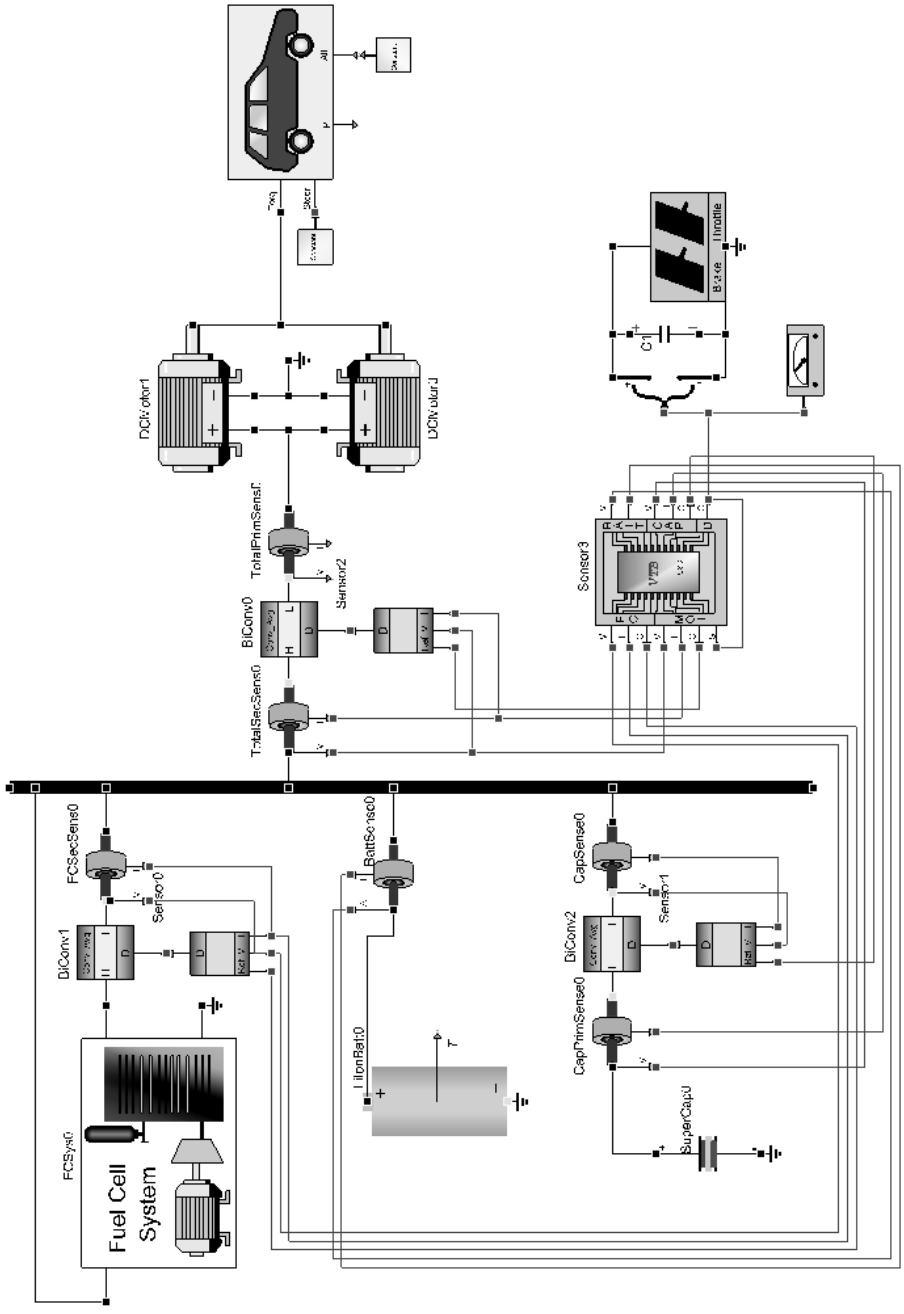

Figure 12.8 Modeling a hybrid fuel cell/ultracapacitor/battery vehicle in VTB [9]

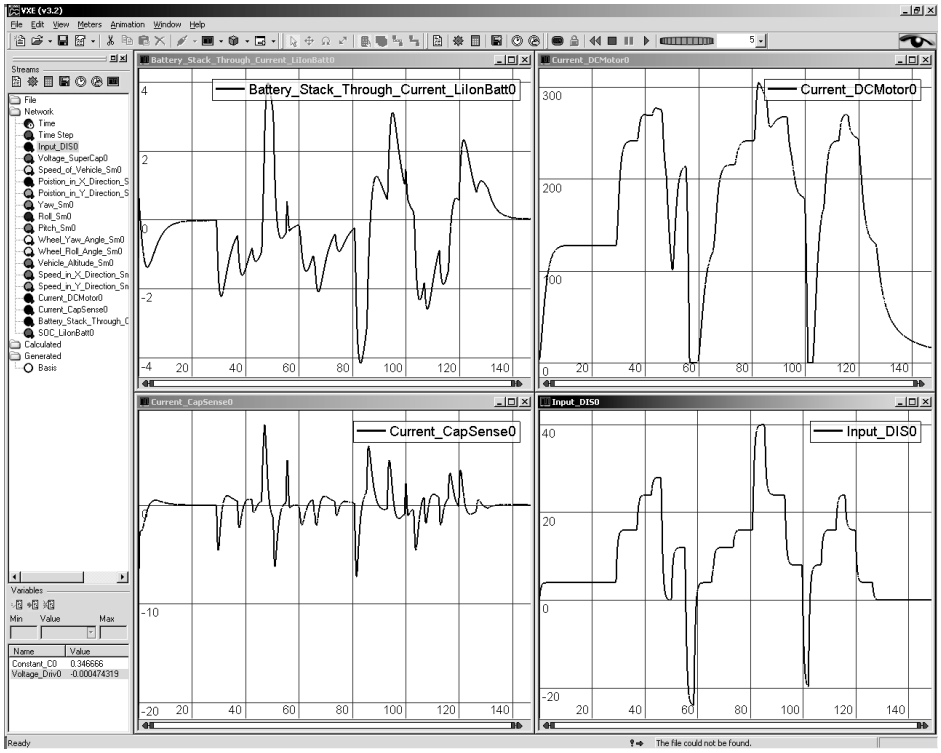

Figure 12.9 Simulation results of hybrid vehicle in VTB

Wheel Slip Model

In simulations involving vehicle dynamics, the wheel slip model must be implemented. Figure 12.10 shows the one-wheel model of a HEV. Applying a driving torque or a braking force F_m to a pneumatic tire produces tractive (braking) force F_d at the tire–ground contact patch due to the wheel slip. The slip ratio λ is defined as

$$\lambda = \frac{V_\omega - V}{\max\{V, V_\omega\}} \tag{12.21}$$

where V is the speed of the vehicle and V_ω is the linear speed of the wheel.

The wheel speed can be expressed as

$$V_\omega = \omega r \tag{12.22}$$

where ω is the angular speed of the wheel and r is the radius of the wheel.

During normal driving, $\lambda > 0$, there exists a friction force on the wheel in the direction of the forward motion. This friction force, also known as traction force, is caused by the slip between the road surface and the tire. This force contributes to the forward motion of the vehicle during normal driving. During braking, external forces are applied to the

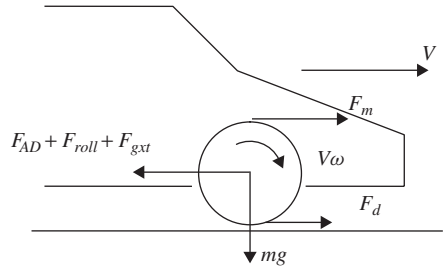

Figure 12.10 One-wheel model of vehicles, where F_m is the force applied to the wheel by the powertrain, F_d is the tractive force caused by tire slip, m is the vehicle mass, and g is the natural acceleration rate

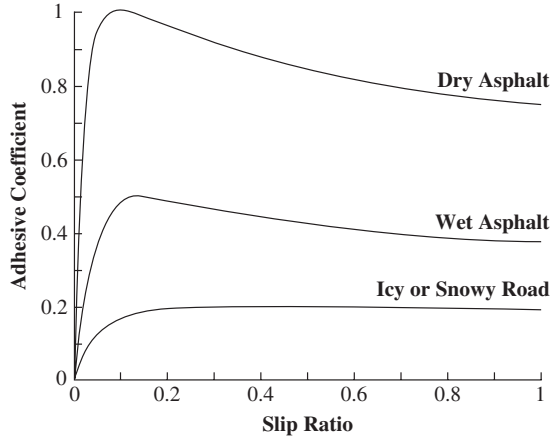

Figure 12.11 Typical adhesive coefficient between the road surface and the tires, as a function of slip ratio and road surface conditions

wheel so that the wheel linear speed is less than the vehicle speed; for example, $\lambda < 0$. Therefore, there exists a braking force opposite to the forward motion.

The traction force, or braking force in the case of braking as shown in Figure 12.10, can be expressed as follows:

$$F_d(\lambda) = \mu(\lambda)mg \tag{12.23}$$

where $\mu(\lambda)$ is the adhesive coefficient between the road surface and the tire. $\mu(\lambda)$ is a function of slip ratio λ and is a function of tire condition and road condition as shown in Figure 12.11.

The equation of the vehicle motion can be expressed as

$$m\frac{dV}{dt} = F_d(\lambda) - (F_{gxt} + F_{AD} + F_{roll}) \tag{12.24}$$

This equation is similar to Equation 12.18 but the tractive force is linked with the slip ratio.

During normal driving, the external torque applied to the wheels is positive. In order to enter braking mode, an external torque must be applied to the wheel to slow it down. In a HEV, this torque is the sum of the motor regenerative braking torque and additional braking torque provided by the mechanical braking systems, in case the motor torque is not enough to provide effective braking.

During normal driving, the powertrain torque tries to accelerate the wheel while the tractive force will try to slow it down. During braking, the powertrain torque applied to the wheel is in the opposite direction of the wheel's rotation and slows down the wheel. The tractive force, on the other hand, is in the same direction as the wheel rotation and therefore will accelerate the wheel, as shown in Figure 12.10.

Therefore, the equation of motion of the wheel can be expressed as follows:

$$J_\omega \frac{d\omega}{dt} = T_m - r F_d(\lambda) \tag{12.25}$$

where J_ω is the inertia of the wheel and T_m is the total braking torque, $T_m = F_m r$.

12.6 Bond Graph and Other Modeling Techniques

Bond Graph Modeling for HEVs

Created by H. M. Paynter in 1959, bond graphs are a graphical tool used to describe and model subsystem interactions involving power exchange. This formulation can be used in hydraulics, mechatronics, thermodynamics, and electrical systems. Bond graphs have been proven effective for the modeling and simulation of multi-domain systems including automotive systems [27–38].

In a bond graph model, a physical system is represented by basic passive elements that are able to interchange power: *resistances* (R), *capacitances* (C), and *inertias* (I). Although these names suggest a direct application in electrical systems, they are used in any other domains as well; for example, friction as a mechanical resistance, a compressible fluid as a capacitance, and a flywheel as an inertial element.

Each element has one or more ports where power exchange can occur. This *power* (P) is expressed as a product of two variables: *effort* (e) and *flow* (f). These names are used extensively in all domains, but have a unique name in each domain: force and speed in mechanical systems, voltage and current in electrical systems, pressure and flow in hydraulics, and so on. Additional variables are defined: *momentum* (p) as the time integral of effort and *displacement* (q) as the time integral of flow.

Additional elements are needed to fully describe a system: *sources of effort* (S_e) and *sources of flow* (S_f) are active elements that provide the system with effort and flow, respectively; *transformers* (TFs) and *gyrators* (GYs) are two-port elements that transmit power, but scale their effort and flow variables by its modulus; and *one junction* (1) elements are multi-port elements that distribute power sharing equal flow, while *zero junction* (0) elements distribute power, having equal effort among all ports.

Bond graph elements are linked with half arrows (bonds) that represent power exchange between them. The direction of the arrow indicates the direction of power flow when both effort and flow are positive. Full arrows are used when a parameter is to be passed between elements, but no power flow occurs.

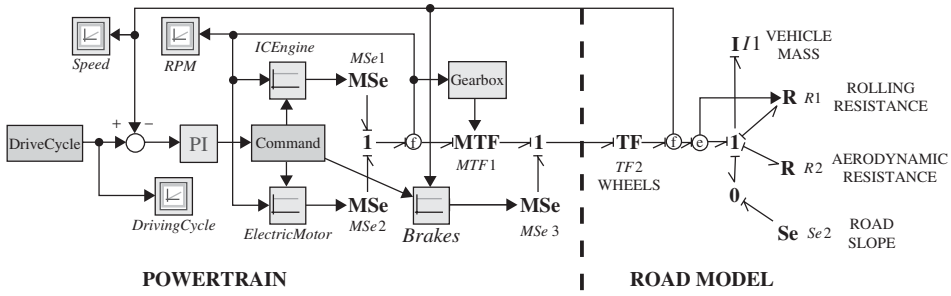

Figure 12.12 A bond graph modeling example: a HEV powertrain model connected to a road model

A bond graph can be generated from the physical structure of the system. For example, the HEV powertrain connected to the road load model can be drawn as shown in Figure 12.12, where the road load is described by Equation 12.18

Causality in bond graph models is indicated with a vertical stroke at the start or end of the bond arrow. This causal stroke establishes the cause and effect relationships between elements. Causality in bond graphs enables the extraction of system dynamics equations. It also provides an insight into the dynamic behavior of the model and is useful to predict modeling problems such as algebraic loops, differential causality, and causal loops.

Modeling presented in [37, 38] demonstrated that bond graph modeling is an appropriate tool for the modeling and simulation of hybrid and electric vehicles.

HEV Modeling Using PSIM

PSIM is a user-friendly simulation package that was originally developed for simulating power electronics converters and electric machine drives. Its new version allows interactive simulation capability and provides magnetic and thermal models for more flexible and accurate analysis of automotive mechatronics design. However, with a few additional customer-built models, it can also be used to model and simulate electric and hybrid vehicles.

Module boxes for necessary electrical systems and also mechanical, energy storage, and thermal systems are created. These modules include ICEs, fuel converters, transmissions, torque couplers, and batteries. Once these modules are made and stored in the PSIM model library, the user can build an electric or a hybrid vehicle model. As an example, a series hybrid configuration, shown in Figure 12.13, is modeled in PSIM [39].

Since load torque is imposed only on the propulsion motor, the ICE can be operated at its optimal efficiency all the time regardless of the load torque. Therefore, the energy management strategy is simple. The main design task is focused on how and where to operate the ICE in an optimum region [39, 40].

Simulation results of the engine speed for the UDDS drive cycle are presented in Figure 12.14.

This simulation model assumed that the power produced by the engine is equal to the power generated by the generator and stored directly in the battery. It can be observed that power is produced when the engine is on (Figure 12.15).

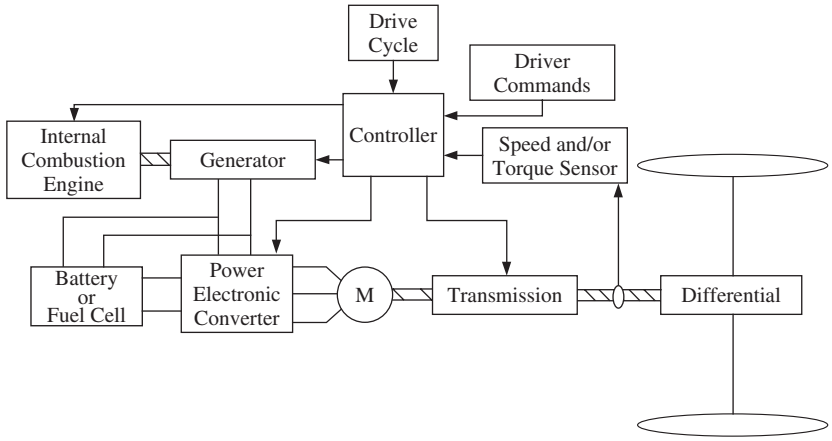

Figure 12.13 Series HEV configuration

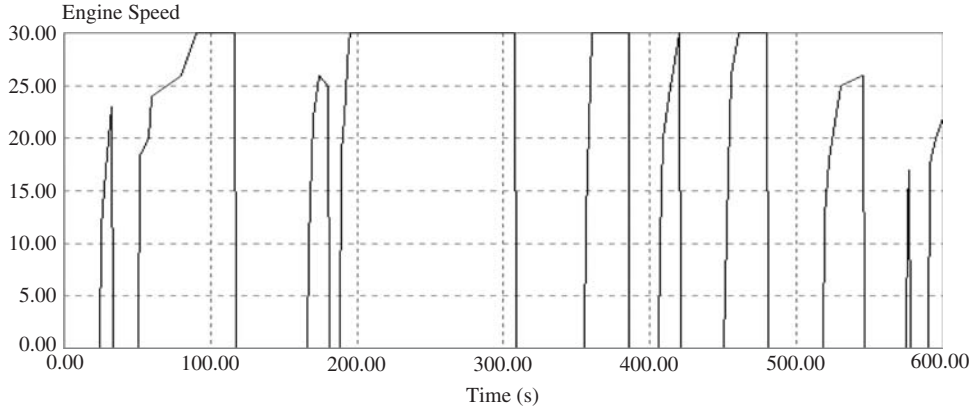

Figure 12.14 Engine speed (×100 rpm) vs. time in seconds

HEV Modeling Using Simplorer and V-Elph

Simplorer is a multi-domain simulation package that can be used for system-level HEV modeling. It has a comprehensive automotive component library, including batteries, fuel cells, wires (conductors), fuses, lamps, electric motors, alternators, engine models, relays, in addition to the electronics, power electronics, and controller models. Further, Simplorer can be linked for co-simulation with a finite element-based electromagnetic field simulation package, Maxwell [17]. This capability provides even greater modeling and simulation accuracy for automotive electronics and machine design. In [41], a series hybrid electric HMMWV is modeled in Simplorer. The vehicle model consists of an ICE/generator, a PM DC motor, a DC–DC converter, a battery and battery management system, PI controller, and vehicle model. The simulation facilitates the development and

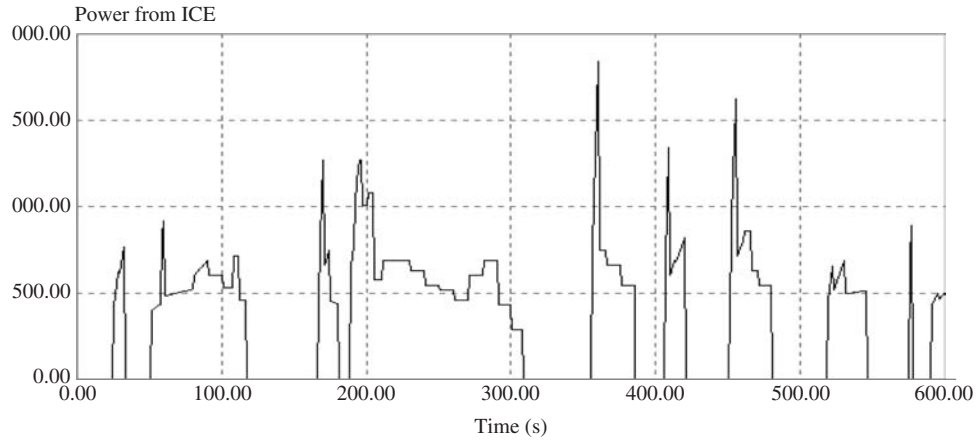

Figure 12.15 Power ($\times 100$ W) from the ICE vs. time in seconds

functional verification of controller and battery management. Dynamic/transient responses of battery voltage, motor torque, and motor voltage under different drive cycles can be simulated. Also, the vehicle's response to the incline of road grades can be obtained to predict overall system performance.

V-Elph [12] is a system-level MATLAB/Simulink-based modeling, simulation, and analysis tool developed at Texas A & M University. This package uses detailed dynamic models of electric motors, ICEs, batteries, and the vehicle. The dynamic performance and fuel economy, energy efficiency, emissions, and so on, can be predicted for hybrid and electric vehicles.

In addition, software packages such as Modelica [42, 43] are also used in the physics-based modeling and simulation of hybrid and electric vehicles.

12.7 Consideration of Numerical Integration Methods

Numerical integration of differential equations or state equations is essential for performing dynamic system simulation. Therefore, discussion of numerical integration methods is an integral part of a study focusing on modeling and simulation. There are several varieties of numerical integration methods: backward Euler's, trapezoidal, Simpson's, Runge–Kutta, Gear's method, and so on. Among these methods, trapezoidal integration is the most popular one in dynamic modeling and simulation due to its merits of low distortion and absolute stability (A-stable). For example, the trapezoidal integration rule is used in EMTP, Spice, and VTB. However, numerical oscillations are often encountered, especially in the simulation of power electronics circuits, which are very often used in hybrid powertrains. Specifically, the numerical values of certain variables oscillate around the true values. In other words, only the average values of the simulated results are correct. The magnitude and frequency of these numerical oscillations are directly related to the parameters of the energy storage elements and the simulation time step. Sometimes, this problem is so severe that the simulation results are erroneous.

Two techniques can be used to mitigate the problem for this kind of numerical oscillation: the trapezoidal with numerical stabilizer method and Gear's second-order method. Elimination of numerical oscillations is of great significance in performing a meaningful simulation for power electronics circuits in which switching of semiconductor devices cause current interruptions.

12.8 Conclusion

This chapter has presented an overview of the modeling and simulation of HEV, with specific emphasis on physics-based modeling. Methods for the mitigation of numerical oscillations in dynamic digital simulations are briefly discussed. Additional simulation techniques, such as bond graph modeling, provide added flexibility in HEV modeling and simulation [44].

With the advent of powerful computing, development of computational methods, and advances in software-in-the-loop (SIL) and HIL modeling and simulations, it is now possible to study numerous iterations of different designs with combinations of different components and different topology configurations. HIL is becoming increasingly important for rapid prototyping and development of control systems for new vehicles such as X-by-Wire [45].

With the evermore stringent constraints on energy resources and environmental concerns, HEVs will attract more interest from the automotive industry and the consumer. Although the market share is still insignificant today, it can be predicted that HEVs will gradually gain popularity in the market due to their superior fuel economy and vehicle performance. Modeling and simulation will play important roles in the success of HEV design and development.

References

1. Muta, K., Yamazaki, M., and Tokieda, J. (2004) Development of new-generation hybrid system THS II – drastic improvement of power performance and fuel economy. SAE World Congress, March 8–11, Detroit, MI, SAE paper no. 2004-01-0064.
2. Horie, T. (2006) Development aims of the new CIVIC hybrid and achieved performance. SAE Hybrid Vehicle Technologies Symposium, February 1–2, San Diego, CA.
3. Struss, P. and Price, C. (2004) Model-based systems in the automotive industry. *AI Magazine*, **24** (4), 17–34.
4. Gao, W., Neema, S., Gray, J. *et al*. (2005) Hybrid powertrain design using a domain-specific modeling environment. Proceedings of the IEEE Vehicle Power and Propulsion Conference, September, Chicago, pp. 6–12.
5. Wipke, K.B., Cuddy, M.R., and Burch, S.D. (1999) ADVISOR 2.1: a user-friendly advanced powertrain simulation using a combined backward/forward approach. *IEEE Transactions on Vehicular Technology*, **48** (6), 1751–1761.
6. Markel, T., Brooker, A., Hendricks, T. *et al*. (2002) ADVISOR: a systems analysis tool for advanced vehicle modeling. *Journal of Power Sources*, **110** (2), 255–266.
7. PSAT Documentation, http://www.transportation.anl.gov/software/PSAT/ (accessed 2006).
8. PSIM web site, http://www.powersimtech.com/ (accessed February 9, 2011).
9. VTB web site, http://vtb.ee.sc.edu/ (accessed February 9, 2011).
10. Powell, B., Bailey, K., and Cikanek, S. (1998) Dynamic modeling and control of hybrid electric vehicle powertrain systems. *IEEE Control Systems Magazine*, **18** (5), 17–22.

11. Lin, C.C., Filipi, Z., Wang, Y. *et al*. (2001) Integrated, feed-forward hybrid electric vehicle simulation in Simulink and its use for power management studies. Proceedings of SAE 2001 World Congress, March, Detroit, MI.
12. Butler, K.L., Ehsani, M., and Kamath, P. (1999) A Matlab-based modeling and simulation package for electric and hybrid electric vehicle design. *IEEE Transactions on Vehicular Technology*, **48** (6), 1770–1778.
13. Rizzoni, G., Guzzella, L., and Baumann, B.M. (1999) United modeling of hybrid electric vehicle drivetrains. *IEEE Transactions on Mechatronics*, **4** (3), 246–257.
14. He, X. and Hodgeson, J.W. (2002) Modeling and simulation for hybrid electric vehicles, I. Modeling. *IEEE Transactions on Intelligent Transportation Systems*, **3** (4), 235–243.
15. He, X. and Hodgson, J. (2002) Modeling and simulation for hybrid electric vehicles – Part II. *IEEE Transactions on Transportation Systems*, **3** (4), 244–251.
16. Fritzson, P. (2004) *Principles of Object Oriented Modeling and Simulation with Modelica 2.1*, IEEE Press, Piscataway, NJ.
17. Ansoft Simplorer web site, http://www.ansoft.com/ (accessed February 9, 2011).
18. Saber web site, http://www.synopsys.com/saber/ (accessed 2006).
19. Gao, W. (2005) Performance comparison of a hybrid fuel cell–battery powertrain and a hybrid fuel cell–ultracapacitor powertrain. *IEEE Transactions on Vehicular Technology*, **54** (3), 846–855.
20. Baisden, A.C. and Emadi, A. (2004) An ADVISOR based model of a battery and an ultra-capacitor energy source for hybrid electric vehicles. *IEEE Transactions on Vehicular Technology*, **53** (1), 199–205.
21. Bose, B.K., Kim, M.H., and Kankam, M.D. (1996) Power and energy storage devices for next generation hybrid electric vehicle. Proceedings of the 31st Intersociety Energy Conversion Engineering Conference, August, Washington, DC, Vol. 3, pp. 1893–1898.
22. Gao, W. and Porandla, S. (2005) Design optimization of a parallel hybrid electric powertrain. Proceedings of the IEEE Vehicle Power and Propulsion Conference, September, Chicago, pp. 530–535.
23. Gao, W., Solodovnik, E., and Dougal, R. (2004) Symbolically-aided model development for an induction machine in Virtual Test Bed. *IEEE Transactions on Energy Conversion*, **19** (1), 125–135.
24. SPICE web site, http://bwrc.eecs.berkeley.edu/Classes/IcBook/SPICE/ (accessed February 9, 2011).
25. Gao, L., Liu, S., and Dougal, R.A. (2002) Dynamic lithium-ion battery model for system simulation. *IEEE Transactions on Components and Packaging Technologies*, **25** (3), 495–505.
26. Gao, L., Liu, S., and Dougal, R.A. (2003) Active power sharing in hybrid battery/capacitor power sources. Applied Power Electronics Conference and Exposition, APEC'03, February, Miami Beach, FL, Vol. 1, pp. 497–503.
27. Xia, S., Linkens, D.A., and Bennett, S. (1993) Automatic modeling and analysis of dynamic physical systems using qualitative reasoning and bond graphs. *Intelligent Systems Engineering*, **2**, 201–212.
28. Gissinger, G.L., Chamaillard, Y., and Stemmelen, T. (1995) Modeling a motor vehicle and its braking system. *Journal of Mathematics and Computers in Simulation*, **39**, 541–548.
29. Suzuki, K. and Awazu, S. (2000) Four-track vehicles by bond graph-dynamic characteristics of four-track vehicles in snow. 26th Annual Conference of the IEEE Industrial Electronics Society, IECON 2000, October, Nagoya, Japan, Vol. 3, pp. 1574–1579.
30. Kim, J.-H. and Cho, D.D. (1997) An automatic transmission model for vehicle control. IEEE Conference on Intelligent Transportation System, ITSC'97, November, Boston, MA, pp. 759–764.
31. Nishijiri, N., Kawabata, N., Ishikawa, T. *et al*. (2000) Modeling of ventilation system for vehicle tunnels by means of bond graph. 26th Annual Conference of the IEEE Industrial Electronics Society, IECON 2000, October, Nagoya, Japan, Vol. 3, pp. 1544–1549.
32. Kuang, M.L., Fodor, M., Hrovat, D. *et al*. (1999) Hydraulic brake system modeling and control for active control of vehicle dynamics. Proceedings of the 1999 American Control Conference, June, San Diego, CA, Vol. 6, pp. 4538–4542.
33. Khemliche, M., Dif, I., Latreche, S. *et al*. (2004) Modeling and analysis of an active suspension 1/4 of vehicle with bond graph. Processing of the First International Symposium on Control, Communications and Signal Processing, March, Hammamet, Tunisia, pp. 811–814.
34. Truscott, A.J. and Wellstead, P.E. (1990) Bond graphs modeling for chassis control. IEE Colloquium on Bond Graphs in Control, April, London, UK, pp. 5/1–5/2.
35. Coudert, N., Dauphin-Tanguy, G., and Rault, A. (1993) Mechatronic design of an automatic gear box using bond graphs. International Conference on Systems, Man, and Cybernetics, October 17–20, Le Touquet, France, pp. 216–221.

36. Jaume, D. and Chantot, J. (1993) A bond graph approach to the modeling of thermics problems under the hood. International Conference on Systems, Man and Cybernetics, October 17–20, Le Touquet, France, pp. 228–233.
37. Hubbard, G.A. and Youcef-Toumi, K. (1997) Modeling and simulation of a hybrid-electric vehicle drivetrain. Proceedings of the 1997 American Control Conference, June 4–6, Albuquerque, NM, Vol. 1, pp. 636–640.
38. Filippa, M., Mi, C., Shen, J., and Stevenson, R. (2005) Modeling of a hybrid electric vehicle test cell using bond graphs. *IEEE Transactions on Vehicular Technology*, **54** (3), 837–845.
39. Onoda, S. and Emadi, A. (2004) PSIM-based modeling of automotive power systems: conventional, electric, and hybrid electric vehicles. *IEEE Transactions on Vehicular Technology*, **53** (2), 390–400.
40. Juchem, R. and Knorr, B. (2003) Complete automotive electrical system design. Proceedings of the 2003 Vehicular Technology Conference, October 6–9, Orlando, FL, Vol. 5, pp. 3262–3266.
41. Ducusin, M., Gargies, S., Berhanu, B. *et al*. (2005) Modeling of a series hybrid electric high mobility multipurpose wheeled vehicle. Proceedings of the IEEE Vehicle Power and Propulsion Conference, September, Chicago, pp. 561–566.
42. Otter, M. and Elmqvist, H. (2001) Modelica Language, Libraries, Tools, Workshop, and EU-Project RealSim, The Modelica Organization, http://www.modelica.org/documents/ModelicaOverview14.pdf (accessed June 2001).
43. Glielmo, L., Natale, O.R., and Santini, S. (2003) Integrated simulations of vehicle dynamics and control tasks execution by Modelica. IEEE/ASME International Conference on Advanced Intelligent Mechatronics, July 20–24, Kobe, Japan, Vol. 1, pp. 395–400.
44. Gao, W., Mi, C., and Emadi, A. (2007) Modeling and simulation of electric and hybrid vehicles. *Proceedings of the IEEE*, Special Issue on Electric and Hybrid Fuel Cell Vehicles, **95** (4), 729–745.
45. Chu, L., Wang, Q., Liu, M. *et al*. (2005) Control algorithm development for parallel hybrid transit bus. Proceedings of the IEEE Vehicle Power and Propulsion Conference, September, Chicago, pp. 196–200.

13

HEV Component Sizing and Design Optimization

13.1 Introduction

One key research and development topic for hybrid electric vehicles (HEVs) is an innovative hybrid powertrain, whose parameters must be tuned for desired performance of the hybrid vehicle [1]. A hybrid powertrain comprises electric motors, power electronics converters, energy storage devices such as batteries and ultracapacitors, and sophisticated controllers in addition to such classical components as internal combustion engines (ICEs), transmissions, clutch, drive shafts, differentials, and so on. Therefore, a hybrid powertrain is much more complicated than a conventional powertrain. The component sizing and system prototyping of a hybrid powertrain is difficult because of the many design options and the rapidly developing technologies in the automotive industries [2]. The cost and performance of the designed hybrid powertrain are determined by the chosen configuration and hundreds of design variables and parameters. A parametric design method can be used to determine hybrid vehicle component sizes. Example design variables include the power ratings of the fuel converter (ICE), motor controller, number of battery cells, the final drive ratio, and control strategy parameters. The parametric design can yield a hybrid vehicle with better performance than the baseline vehicle. The overall design is unlikely to be optimal, but can be used as a rough design for further optimization so as to maximize fuel economy and minimize emissions, weight, and cost. At the same time, vehicle performance requirements must be satisfied [3, 4].

There are a variety of optimization algorithms available for HEV design. They can be categorized in different ways: for example, the local optimization algorithm versus the global optimization algorithm; the deterministic optimization algorithm versus the stochastic optimization algorithm; or the gradient-based algorithm versus the derivative-free algorithm. A good selection of optimization algorithms for the application of hybrid powertrain design is not very obvious. In this chapter, four optimization algorithms are thoroughly discussed. Design optimization examples are given for a parallel HEV and a series HEV. Since an analytical expression for the objective function does not exist, a

Hybrid Electric Vehicles: Principles and Applications with Practical Perspectives, First Edition.
Chris Mi, M. Abul Masrur and David Wenzhong Gao.

vehicle simulation model is used for function evaluations. PSAT (Powertrain System Analysis Toolkit) and ADVISOR are chosen as HEV modeling tools for the optimization study.

This chapter explores the feasibility of different global optimization algorithms by comparing their performance and accuracy. The chapter is organized as follows. Section 13.2 reviews the principles and procedures of four global optimization algorithms. Section 13.3 presents the methodology of the model-in-the-loop design process used for this study. In Section 13.4, the constrained HEV design optimization problem is set up; the results are presented with the associated comparison. Section 13.5 presents another design example of a series HEV using the non-dominated sorting genetic algorithm (NSGA). Finally, conclusions are given in Section 13.6.

13.2 Global Optimization Algorithms for HEV Design*

For HEV design, the performance and design objectives, such as fuel economy, can be evaluated from a vehicle model and computer simulation. The value is also called the response function, which is typically multimodal (involving many local minima), and sometimes noisy and discontinuous [3]. Gradient-based algorithms such as sequential quadratic programming (SQP) [5] use the derivative information to find the local minima. The major disadvantage of local optimization algorithms is that they do not search the entire design space and cannot find the global minimum. Derivative-free algorithms such as divided rectangles (DIRECT) [6, 7], simulated annealing (SA) [8], genetic algorithm (GA) [9], and particle swarm optimization (PSO) [10, 11] do not rely on the derivatives and can therefore work exceptionally well when the objective function is noisy and discontinuous. Derivative-free methods are often the best global algorithms because they must often sample a large portion of the design space to be successful. A comparison of the gradient-based and derivative-free algorithms for the optimization of a HEV is given in [3, 12]. Note here that even though DIRECT, SA, GA, and PSO algorithms search the design space globally, the main difference is that DIRECT is a deterministic algorithm, whereas SA, GA, and PSO are stochastic algorithms.

13.2.1 DIRECT

DIRECT is a sampling algorithm, developed by Donald R. Jones [6]. This global optimization algorithm is a modification of the standard Lipschitz approach that eliminates the need to specify the Lipschitz constant [7]. This constant is a weighing parameter, which determines the different emphasis on the global or local search [7]. The use of the Lipschitz constant is eliminated in [6] by searching all possible values for it, thus putting a balanced emphasis on both the global and local search.

A brief introduction to the DIRECT algorithm is presented here. A detailed explanation of it can be found in [6]. DIRECT is a modification of a one-dimensional Lipschitz algorithm by Shubert [13] and extension to multidimensional problems. The approach proposed by Shubert is given as follows.

A function $f(x)$ defined in the closed interval $[l, u]$ is said to have a lower bound such that there exists a positive Lipschitz constant K that satisfies the following condition:

$$\left|f(x) - f\left(x'\right)\right| \leq K\left|x - x'\right| \text{ for all } x, x' \in [a, b] \tag{13.1}$$

* © [2005] IEEE. Reprinted, with permission.

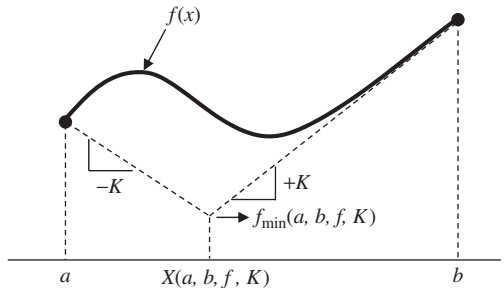

Figure 13.1 Lower bound of a function $f(x)$ using the Lipschitz constant

From Equation 13.1, the change in the value of function $f(x)$ should be less than the change between x and x' multiplied by a constant K. Further, let us substitute a or b for x' in Equation 13.1; then the following inequality constraints are obtained for $f(x)$:

$$f(x) \leq f(a) + K(x - a) \tag{13.2}$$

$$f(x) \leq f(b) - K(x - b) \tag{13.3}$$

These two equations correspond to two lines with slopes $-K$ and $+K$ as shown in Figure 13.1. These two lines form a V shape and the smallest value that $f(x)$ can possibly be is at the bottom of the V shape; that is, $X(a, b, f, K)$. So, $f_{\min}(a, b, f, K)$ corresponds to the lower bound of $f(x)$:

$$X(a, b, f, K) = (a + b)/2 + \left[f(a) - f(b)\right]/2K \tag{13.4}$$

$$f_{\min}(a, b, f, K) = \left[f(a) + f(b)\right]/2 - K(b - a) \tag{13.5}$$

where $f(a)$ and $f(b)$ are the function values of f at a and b.

This minimum point is taken as x_1, which is used to divide the search space into two intervals. Then one of the two intervals with the least function value $f_{\min}$ is selected for further division. This division is continued until some pre-specified tolerance of the final solution is met. Equation 13.5 explains the local and global search of the algorithm. The first term leads to the local search and the second term leads to the global search. The relative weight between the local and global search is determined by the Lipschitz constant. The larger the value of K, the higher the emphasis on the global search.

However, the Lipschitz approach followed by Shubert has the following two main disadvantages:

1. The need to specify the correct value of the Lipschitz constant K.
2. The need for 2^n function evaluations for n-dimensional design space.

These problems are fixed in the DIRECT algorithm, in which the sampling is done at the center point of the interval rather than at the endpoints to reduce the number of function evaluations [6]. The balance between the local and global search in the DIRECT algorithm is achieved by selecting the optimal intervals (optimal rectangles) assuming all possible values for the Lipschitz constant. For example, assume that Figure 13.1 is

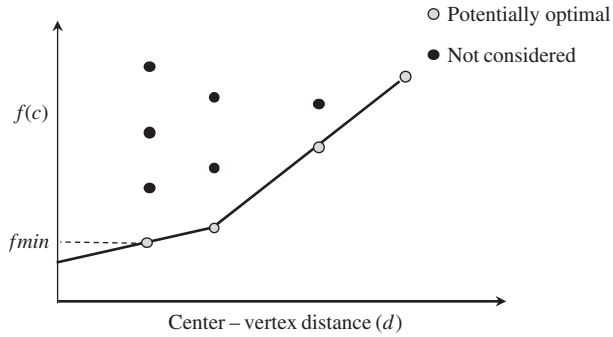

Figure 13.2 Rectangle selection using all possible K

divided into 10 intervals so that 10 center points are obtained. The function values at the center points of the intervals are evaluated. A plot showing these 10 points with the width of the interval on the x axis and the corresponding function value is given in Figure 13.2. If a line with a slope given by the Lipschitz constant K is drawn from a point, then the y intercept is the local bound for the function. Instead of fixing one value of K, various possible values of K are taken. This gives the lowest lower bound intervals represented by the lower convex hull of points shown in Figure 13.2. The same procedure will be followed to select the optimal rectangles in the DIRECT algorithm for the n-dimensional problem.

The DIRECT algorithm is based on the above theoretical background, and is basically a sampling algorithm. At the beginning of the algorithm, the n-dimensional design space box is scaled to an n-dimensional unit hypercube. To initiate the search, the design objective function is evaluated at the center point of the hypercube. DIRECT then trisects this hyperrectangle and samples the center points of the two resulting hyperrectangles. From here, DIRECT selects the optimal hyperrectangles using various values of the Lipschitz constant and trisects them. An example selection of the optimal hyperrectangles is shown by the lower convex hull of dots in Figure 13.2. The selection of optimal hyperrectangles selects the larger rectangles (global search) as well as smaller rectangles (local search). This division process continues until pre-specified function evaluations are reached or convergence is achieved. The division of rectangles in the first three iterations of a two-dimensional problem is illustrated in Figure 13.3. In this figure, d denotes the distance between center and vertex and each center point is labeled with a numeral for the sake of explanation.

In the first iteration, the unit hypercube is trisected into three rectangles. The objective function value is evaluated at the center points of the three resulting rectangles. The objective function values are plotted versus the center–vertex distance as shown in Figure 13.4a. Then the rectangle with the least objective value in each column of dots is selected as the optimal rectangle. In the first iteration, there is only one column of dots; therefore rectangle 1 is selected as the optimal rectangle and trisected in the second iteration. Similarly, in the second iteration, rectangle 4 and rectangle 2 have the least

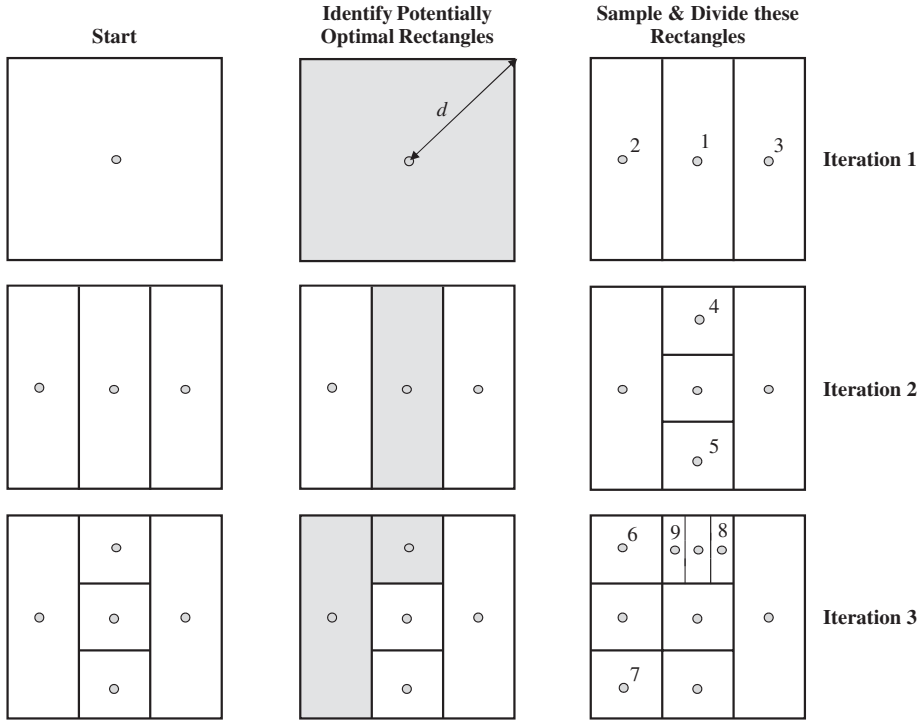

Figure 13.3 First three iterations of a two-dimensional problem

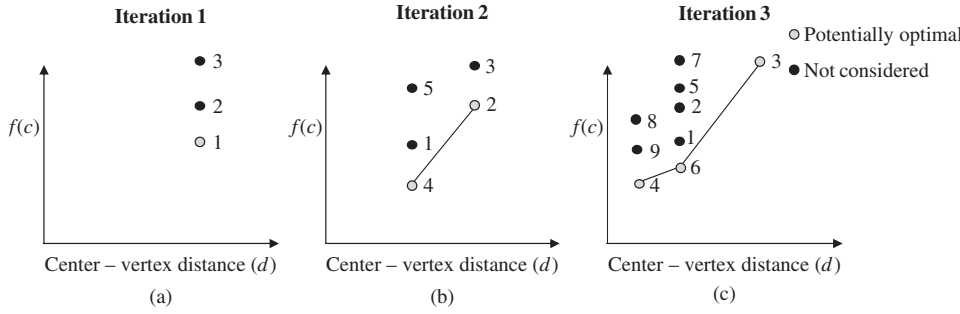

Figure 13.4 Selection of optimal rectangles in each iteration

objective function values as shown in Figure 13.4b. These two rectangles are selected as optimal rectangles and further trisected in the third iteration. This process is continued until the maximum number of function evaluations is exhausted.

The inequality constraints are handled by an auxiliary function given in [6] that combines the information of the objective and constraint functions. The auxiliary equation is

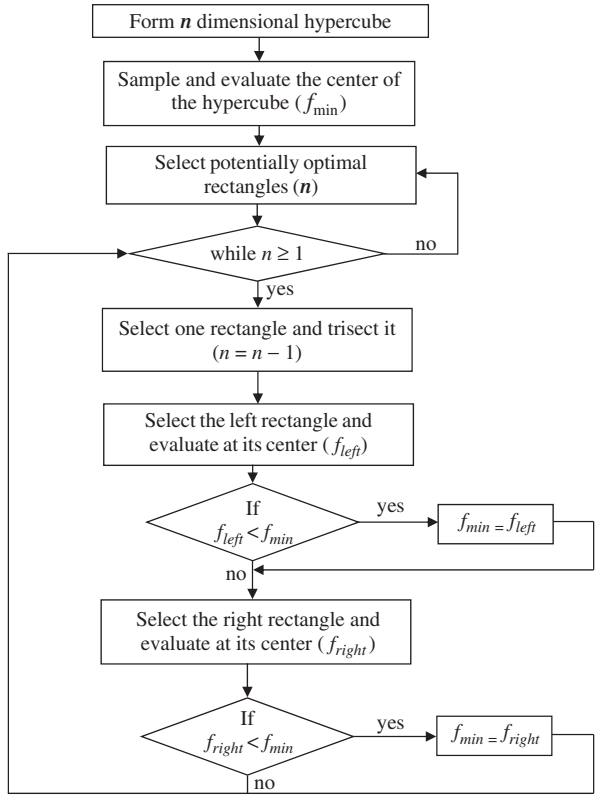

Figure 13.5 Flow chart showing the DIRECT algorithm

given in Equation 13.6 and is a weighed sum of the violated constraints and the deviation of the objective function value from a projected global minimum:

$$\max\left(f_r - f^*, 0\right) + \sum_{j=1}^{m} c_j \max\left(g_{rj}, 0\right) \tag{13.6}$$

In this equation, f_r is the objective function value at the center point of the rectangle r, f^* is the assumed global minimum, m is the number of inequality constraints, c_j are the positive weighing coefficients, and g_{rj} is the constraint violation of the jth constraint at the mid-point of rectangle r.

A flow chart explaining the DIRECT algorithm is shown in Figure 13.5.

Initially, DIRECT converts the n-dimensional design space into an n-dimensional unit hypercube. It samples and evaluates at the center point of this rectangle. This function value is assigned to a variable $f_{\min}$ which holds the minimum function objective value. Then a set of optimal rectangles is selected assuming various possible values for the Lipschitz constant. These rectangles form the lower convex hull of dots as shown in Figure 13.4. However, in the first iteration, the only present rectangle is selected as the optimal rectangle. Each rectangle in the optimal rectangle set is trisected to give two more

rectangles (left and right rectangles). The objective function is evaluated at the center points of the left and right rectangles and $f_{\min}$ is updated if there is an improvement in the objective function. The whole process is continued until a pre-specified number of function evaluations is reached.

13.2.2 Simulated Annealing

SA belongs to the class of stochastic hill-climbing algorithms, which means that they follow a random path in every searching process for the global optimum. SA has been presented by a large number of authors but Kirkpatrick *et al.* in 1983 [8] started using it in various combinatorial problems. SA is based on the Metropolis *et al*. Monte Carlo simulation proposed in [14].

13.2.2.1 Algorithm Description

The SA algorithm is analogous to the physical annealing process occurring in metals and function minimization. This analogy is explained briefly here. When metals are at high temperatures, the atoms in the lattice structure can move relatively freely in the higher energy states due to heating, but as the temperature is decreased slowly, the atoms can move freely enough and begin adopting the most stable orientation by taking the lowest possible energy state. If the temperature is decreased rapidly, the atoms become frozen at a high energy state. Attaining the lowest possible state can be thought of as reaching a global minimum in the optimization process. The temperature is decreased slowly (cooling) so that the design will find the global minimum (lowest energy state). At the beginning of the algorithm, the objective function value is evaluated at a random feasible design point. From this design point, a new, random, design point is selected and the objective function value and feasibility of the new design point are evaluated. If the new neighbor is better than the previous one, then the new point is accepted as the optimal point; otherwise, acceptance or rejection of the new design point depends on the Metropolis *et al*. probability criterion

$$P(f, T) = e^{-[(f_{new} - f_{current})/T]} \tag{13.7}$$

From this equation, it can be seen that the new point is more likely to be accepted if the new design point function value is close to the current design point function value. Also, the probability of accepting a design point is higher when the temperature is high. Note here that a new design point might be accepted even when it is not as good as (i.e., the function value at the new point is higher) the current design point. However, this feature will help the method avoid becoming trapped in a local minimum. So, initially, when the temperature is high, the algorithm does a global search where even the worse design points are more likely to be accepted, and then switches to a local search when the temperature is decreased, where worse design points are less likely to be selected. Thus, switching from the global search to local search depends on the value of the temperature; this is called gradual cooling – to gradually reduce the probability of accepting a neighbor design point with worse performance. Another parameter that is responsible for switching from the global to local search is the maximum step size. This variable is reduced as

the algorithm progresses, forcing it to search more locally. If either the specified number of temperature reduction cycles or the predetermined number of function evaluations is exceeded, then the algorithm will stop.

13.2.2.2 Tunable Parameters

SA has many parameters that need to be tuned to improve the efficiency of the algorithm. So, particular attention should be given to these parameters. The parameters used in this algorithm are described below:

- *num_steps*: The number of steps before reducing the temperature and maximum step size.
- T_0*_init*: The initial temperature.
- V_0*_init*: The initial step size (maximum).
- *temp_red*: The temperature reduction factor. The temperature for the next cycle is reduced by this factor.
- V_0*_red*: This factor is multiplied by the initial step size to get the step size for the next design point.

13.2.2.3 Flow Chart

A flow chart showing the core of SA is given in Figure 13.6.

SA starts by initializing a temperature t. Next, a random design point x_n is selected such that it satisfies all the constraints and all the design variables are within the bounds (i.e., a feasible point). This point is passed as the current point to the algorithm core. SA is carried out in two loops. The outer loop defines the number of function evaluations that the algorithm must run before terminating. This parameter is defined by the *max_funevals* parameter. The inner loop defines the number of steps after which the temperature and the step size for x_n to jump to x_{n+1} are reduced. This parameter is defined by the *num_steps* parameter. As discussed above, this parameter is responsible for switching from the global to local search. As shown in the flow chart, the feasible point found initially is made the current point x_n. Then, it makes a random step to x_{n+1} and the objective function value and the constraints are calculated in the next step. The current step size is used in finding the new design point. In the next step, the function value and the constraints at this design point are evaluated. Then the new design point is compared to the old design point to see whether it is better or not. This comparison is done by a penalty method. The following quadratic penalty function is used:

$$Penalty(x_i) = f(x_i) + \sum_{j=1}^{n} \left\{ f(x_i) \left[\frac{\max\left(0, g_j(x_i)\right)}{boundingvalue_j} \right] \right\}^2 \tag{13.8}$$

where g_j indicates the design constraint and n is the total number of design constraints. This function gives a higher penalty value to the design points which violate the design constraints more. So, if the penalty value of the current point x_{n+1} is less than the penalty for the design point x_n then it is accepted and tested if it is better than the current optimum. If it is better, then it is assigned as the current optimum and this point is fed

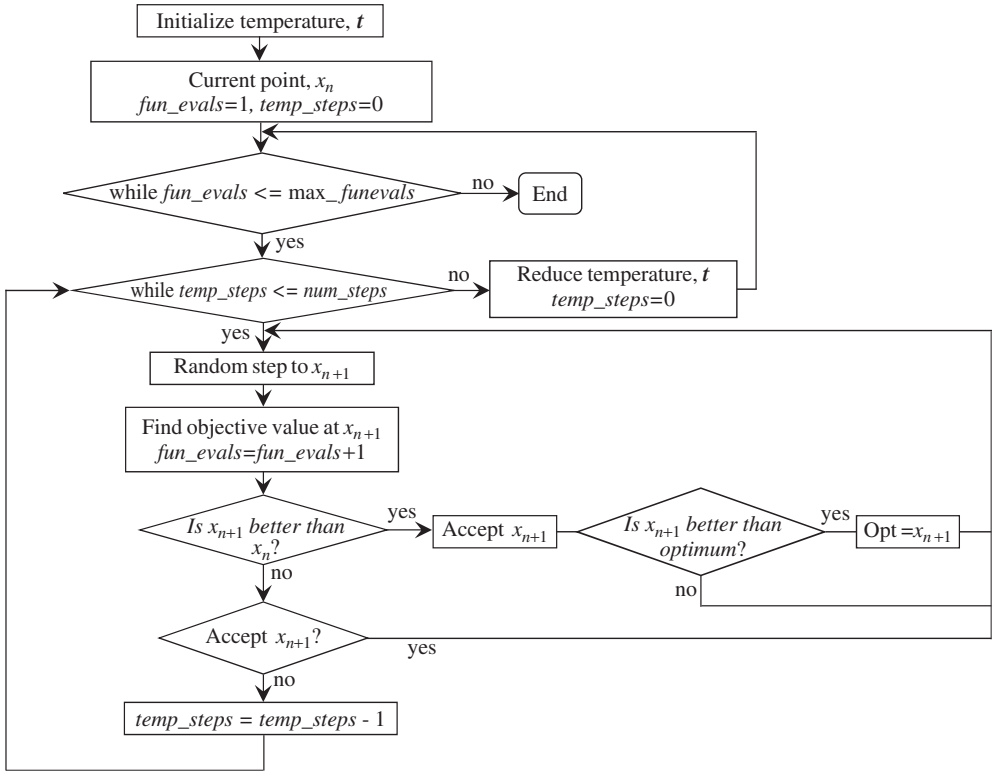

Figure 13.6 Flow chart showing the simulated annealing algorithm

back to generate a new design point. If the penalty of the current point x_{n+1} is more than the penalty for the design point x_n then the decision of its acceptance is taken using the Metropolis criterion given in Equation 13.7. If the current point is accepted then a new design point is generated based on the design point x_{n+1}. If it is not accepted then *temp_step* is increase by 1 and then a new design point is generated from the previous design point x_n.

13.2.3 Genetic Algorithms

GAs [9] are based on evolutionary processes and Darwin's concept of natural selection. In this selection, only the fittest populations survive and are allowed to produce offspring while the bad populations are weeded out. During the process, several natural processes like crossover, mutation, and natural selection are used to select the best fit population. The same concept is extended to mathematical optimization problems where only good design points are selected while bad design points are neglected. In this context, the objective function is usually referred to as a fitness function, and the process of "survival of the fittest" implies a maximization procedure. The design constraints can be incorporated as penalties in the fitness function.

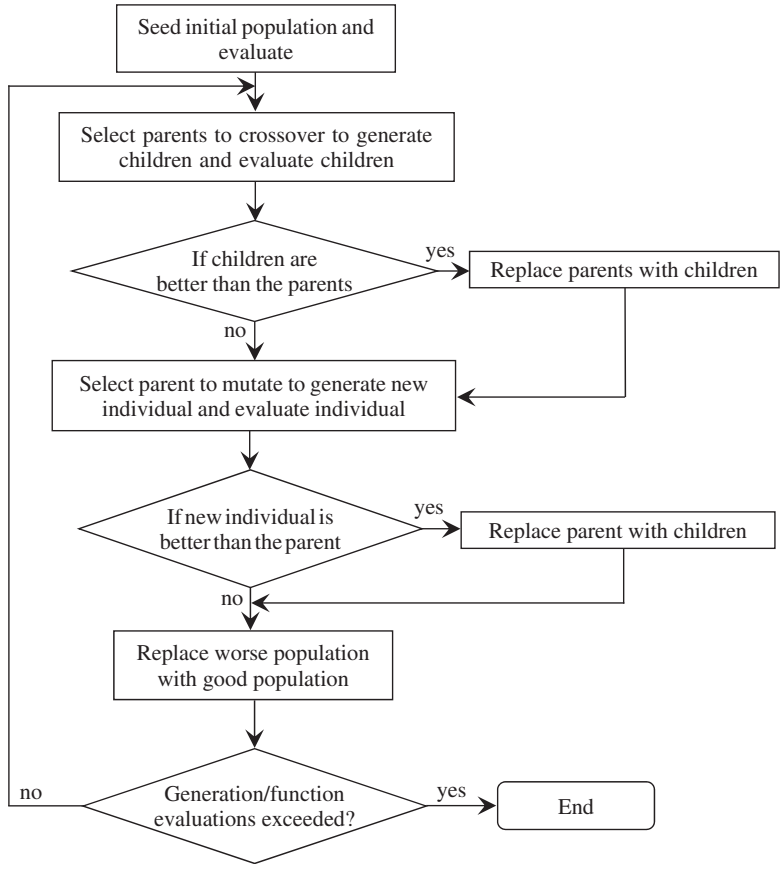

Figure 13.7 Flow chart showing the genetic algorithm

13.2.3.1 Flow Chart

The flow chart for the GA is given in Figure 13.7. The GA begins by randomly generating or seeding an initial population of candidate solutions (design points). Starting with the initial random population, the GA then applies a sequence of operations like the design crossover where two individuals (parents) from the initial population are selected randomly and reproduced to get two new individuals (children), and mutation where one individual from the initial population is slightly changed to get a new individual. If the newly generated individuals created by the crossover and the mutation operators are better than the parents used, then the parents are replaced by the newly created individuals. Again, at the end, the worst design points are weeded out from the population in order to improve the fitness function. The entire process can be termed as one generation and continued for multiple generations or until the maximum number of function evaluations is exhausted in order to further improve the fitness function.

13.2.3.2 Operators and Selection Method

There are numerous operators for the GA. The *arithmetic crossover* operator is described as follows. Two parents reproduce to generate two new individuals (children). The parent individuals are selected randomly. The newly generated individuals can be represented as a linear combination of the parents as follows:

$$\begin{aligned} X_{ind1} &= r.X_{par1} + (1-r).X_{par2} \\ X_{ind2} &= (1-r).X_{par1} + r.X_{par2} \end{aligned} \tag{13.9}$$

In Equation 13.9, X_{ind1}, X_{ind2} represent the two newly created individuals, X_{par1}, X_{par2} represent the parents, and r represents a random variable between 0 and 1.

In mutation, a parent is selected and is altered to get a new individual.

A selection method is needed to choose the best fit individuals. A *normalized geometric* selection method, which is a ranking-type method, is used as the selection method. The ranking method was chosen because of the presence of negative fitness. With this selection method, a probability is assigned to each individual of the population given by Equation 13.10, where q denotes the probability of choosing the best design, r denotes rank of the individual, and P denotes the population size:

$$\text{Each individual probability} = \frac{q}{1-(1-q)^P}(1-q)^{r-1} \tag{13.10}$$

13.2.3.3 Tunable Parameters

Like SA, the GA has many parameters that need to be tuned for a better performance, although the GA has fewer tunable parameters compared to SA. The tunable parameters and their description are given below:

- *Pop_size*: The number of individuals in a generation.
- *xoverFNs*: The number of times the crossover operation is to be done.
- *mutFNs*: The number of times the mutation operation is to be done.

13.2.4 Particle Swarm Optimization

PSO was developed by Kennedy and Eberhart and belongs to evolution-based stochastic global optimization techniques [10, 11]. The idea of PSO came from the swarm intelligence found in many natural systems with group behavior. Such systems are typically made up of a population (swarm) of simple agents or particles interacting locally with their neighbors and with their group organization. Ant colonies, bird flocks, and animal herds are a few of the examples of such natural systems. In these systems, the agents interact locally and this can result in a global behavior. For example, individuals can change position or velocity locally and a global behavior pattern can be observed. The underlying principle is used to develop a technique to find global maxima in optimization problems.

13.2.4.1 Algorithm Description

Just like the GA, PSO is a population-based search procedure. At the beginning, random solutions called *particles* are initialized in the multidimensional design space. In a PSO system, each particle flies in the multidimensional design space seeking the global maximum. Each particle in the PSO is defined by a point in the design space called *position* and its flight speed is called *velocity*. Also, each particle is aware of its best position reached so far (*pbest*) and the best position of the group so far (*gbest*). During flight, each particle adjusts its position according to its own experience (*pbest* value), and also according to the experience of its neighboring particles (*gbest* value). The position is modified using the concept of velocity. The velocity of each particle is updated as follows:

$$v_i^{n+1} = kv_i^n + \alpha_1 rand_1 \left(pbest_i - p_i^n\right) + \alpha_2 rand_2 \left(gbest - p_i^n\right) \tag{13.11}$$

where v_i^{n+1} is the velocity of particle i at iteration $n+1$, k is the weighing function, α_1 and α_2 are the weighing factors, $rand_1$ and $rand_2$ are two random numbers between 0 and 1, p_i^n is the position of particle i at iteration n, $pbest_i$ is the best position of particle i, and *gbest* is the best position of the group (best of all *pbests*). For the study example in section 13.4, $k = 0.6$ and $\alpha_1 = \alpha_2 = 1.7$ are taken for better convergence [11]. Similarly, the position is updated as follows:

$$p_i^{n+1} = p_i^n + v_i^{n+1} \tag{13.12}$$

The velocity and position updating for particle i is illustrated in Figure 13.8. Note that this figure represents a two-dimensional problem.

From Figure 13.8, it can be seen that the position of the particle is adjusting itself toward the *gbest* position. This is because the velocity has changed its direction toward the *pbest* and *gbest* values.

The constraints in PSO are treated the same way as in SA and the GA. A penalty is assigned to each design point using Equation 13.8. The penalty is used to update *pbest* and *gbest* for each particle. For a particle i, the *pbest* value is updated if the penalty

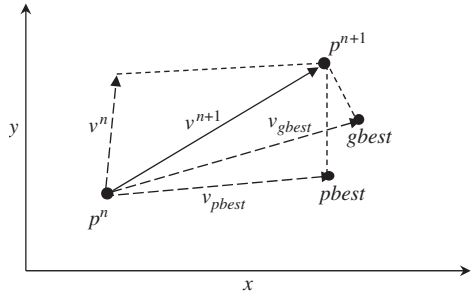

Figure 13.8 Velocity and position updating in particle swarm optimization

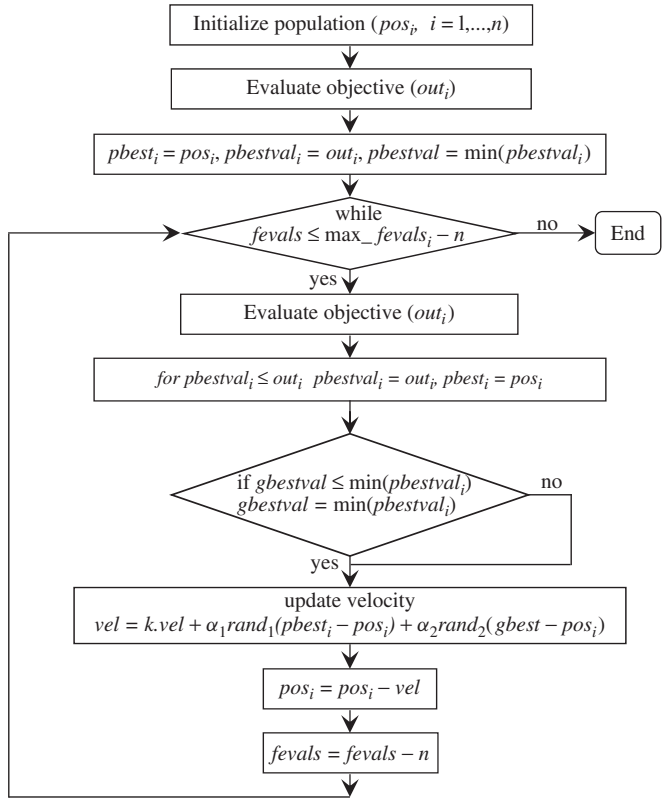

Figure 13.9 Flow chart of particle swarm optimization

of the particle is less than the previous best penalty. The same is done when *gbest* is updated. This makes sure that the objective function is maximized.

13.2.4.2 Flow Chart

The flow chart representing the PSO algorithm is shown in Figure 13.9. The algorithm starts by initializing a population (particles) of random design points. In the case of PSO, the random solutions are normalized for a better performance. The population size (n) is defined by the user. The random design points are evaluated to give the next step. Initially, the best position values (*pbest*) and the best objective values (*pbestval*) of each particle are assigned to starting position values (*pos*) and the best starting values (*out*).

The best value of all the particles (*gbestval*) is the least value of all the *pbest*. The variable *gbestval* holds the current best global maximum of the objective function. Next, a while loop is run for a specified number of function evaluations. The while loop updates

the *pbest* and *pbestval* values if there is any improvement in the current *pbestval* value. It also updates *gbestval* if there is an improvement. The updated *pbest* and *gbest* are used in determining the new velocity (*vel*) and position (*pos*). The function evaluations (*fevals*) are incremented by the population size every iteration.

13.2.5 Advantages/Disadvantages of Different Optimization Algorithms

In the following, the advantages and disadvantages of the above four different optimization algorithms are discussed.

13.2.5.1 DIRECT

DIRECT has no tuning parameters in order to get good algorithmic performance. Also, the user is not required to specify the starting point since DIRECT starts at the center point of the design space as its initial point. Therefore, it eliminates the problem of choosing a good starting point. Note here that the local optimizers require a good initial point to reach the optimum value. Another advantage is that DIRECT covers the entire design space, avoiding any chance of missing the global optimum.

DIRECT can converge to a global optimal region after fewer function evaluations, but in order to actually reach the global optimum point more function evaluations are often required. The algorithm can be implemented for paralleling computing.

13.2.5.2 SA

The main advantage of SA is that it is a very efficient algorithm for finding global minima. It accepts some worse points during the process in the expectation of finding global minima.

The disadvantage of SA is the tuning parameters discussed above. The right set of parameters is needed to improve the efficiency of the algorithm. This tuning in turn becomes an optimization problem. Similar to DIRECT, SA is efficient in finding the region of global minima, but in order to reach the true global minima more function evaluations are often required.

13.2.5.3 GA

The initial population generated primarily determines a good starting point for the GA. So, it can be seeded by some good design points to improve its efficiency. According to the nature of the design problem, different types of selection method and operators for crossover and mutation can be chosen in using GA.

The major disadvantage is the tuning of the parameters. Also, the initial population is randomly chosen. This random initial population may not cover the entire design space uniformly. It was observed that most of the design points generated by the crossover and mutation operators were not able to meet the constraints (infeasible points) because the operators have no knowledge of the constraints. This resulted in many infeasible points.

This was the reason why the algorithm had difficulty in improving the best objective function value found in the initial random population.

13.2.5.4 PSO

The major advantage of the PSO algorithm is that fewer parameters need to be adjusted compared to SA and the GA. The constants for updating velocity are very critical in obtaining better performance. Many sets of constants are available and suitable for specific problems. Moreover, no natural operators such as crossover, mutation, and selection are needed in PSO. Also, PSO is easier to understand with simpler equations. The disadvantage lies in the selection of the constants in updating the velocity. If inappropriate constants are chosen then the problem may not converge to the optimum.

13.3 Model-in-the-Loop Design Optimization Process

The approach for HEV design optimization is typically a model-in-the-loop design optimization process, as illustrated in Figure 13.10. In the middle of the diagram, the vehicle is modeled in a simulation tool such as PSAT [15], ADVISOR [16], or VTB [17], and this model is embedded in a computational loop. Initially, the vehicle model is simulated using the initial values of the design variables, and we get the numerical values of the objective function, in this case the composite fuel economy measured in mpgge (miles per gallon gasoline equivalent). At the same time, the constraint functions, in this case the vehicle performance, are evaluated. Then these simulated results are fed back to the optimization algorithm, which generates a new set of values for the design variables. Subsequently, the vehicle model is simulated again to get the values for the objective function and the constraint functions. The simulation results are fed back to the optimization algorithm again to generate yet another new set of design variables. This iteration process goes on and on until some stopping criteria are reached for the optimization process. Note that the design variables are restricted within their bounds during this process.

For illustration purposes, in this chapter PSAT is used as the modeling and simulation tool. PSAT was developed by Argonne National Laboratory, sponsored by the US Department of Energy (DOE) [15]. It can help a vehicle designer to size components and develop a realistic hybrid powertrain and its control system. PSAT can accurately simulate vehicle performance, fuel economy, and emissions. In using PSAT, we mainly

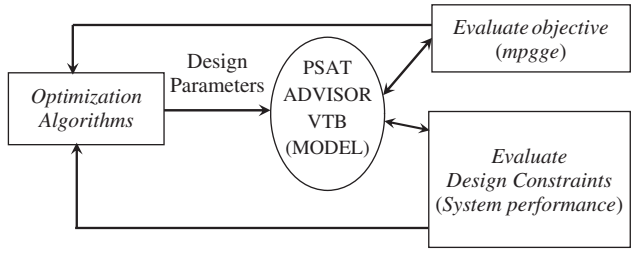

Figure 13.10 Model-in-the-loop design optimization process

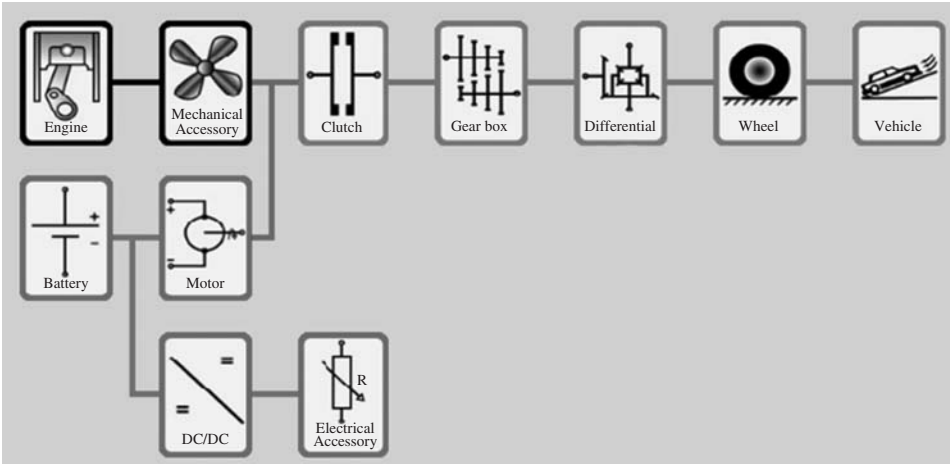

Figure 13.11 Configuration of the selected parallel HEV in PSAT [15]

need to select powertrain topology, define components sizes, and construct the control strategy. Note that the component sizing is automated by the model-in-the-loop process.

13.4 Parallel HEV Design Optimization Example*

As an application example, PSAT is used to optimize a parallel HEV for maximum fuel economy on a composite driving cycle. Four global algorithms, DIRECT, SA, GA, and PSO, are used in the model-based design optimization. The main focus of the example is to show the comparison of different optimization algorithms for optimal vehicle design rather than the result. The vehicle model "gui_par_midsize_cavalier_ISG_in" (available in the PSAT model library) has been chosen for this optimization study. This vehicle is a two-wheel-drive starter–alternator parallel configuration with manual transmission. The basic configuration of the parallel HEV used for the simulation study is illustrated in Figure 13.11 and the main components of the HEV are listed in Table 13.1.

The objective is to maximize the composite fuel economy, which is computed based on city fuel economy and highway fuel economy. For example, composite fuel economy can

Table 13.1 Parallel HEV components

Component	Description
Fuel converter	84 kW and 2.2 l Cavalier gasoline engine
Motor	ECOSTAR motor model with continuous power of 33 kW and peak power of 66 kW
Battery	Panasonic NiMH battery with a capacity of 6.5 Ah and 240 cells
Transmission	Four-speed manual gearbox with final drive ratio 3.63
Control strategy	Default propelling, shifting, and braking strategies

* © [2007] Inderscience. Reprinted, with permission, from the International Journal of Electric and Hybrid Vehicles.

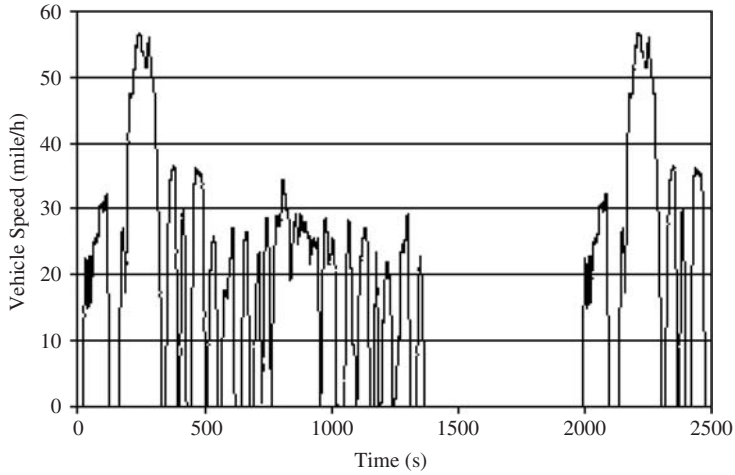

Figure 13.12 The FTP-75 drive cycles

be computed as the weighted average of the state of charge (SOC) balanced fuel economy values during the city drive cycle and highway drive cycle, as given below [18]:

$$\text{Composite fuel economy} = \frac{1}{\frac{0.55}{\text{City\_FE}} + \frac{0.45}{\text{Hwy\_FE}}}$$

where City_FE and Hwy_FE denote the city and highway fuel economy values, respectively.

The driving cycles selected are Federal Test Procedure city driving cycle FTP-75 and Highway Fuel Economy Test drive cycle HWFET. The two drive cycles are shown in Figures 13.12 and 13.13, respectively.

The design problem's constraints come from the following required vehicle performance:

- Acceleration time 0–60 mph (0–96 km/h) $\leq$ 18.1 seconds
- Acceleration time 40–60 mph (64–96 km/h) $\leq$ 7 seconds
- Acceleration time 0–85 mph (0–136 km/h) $\leq$ 35.1 seconds
- Maximum acceleration $\geq$ 3.583 m/s^2.

Table 13.2 shows the six design variables used in this study. The first two define the power ratings of the fuel converter (the engine) and motor controller. The third, fourth, and fifth variables define the number of battery modules, minimum battery SOC allowed, and maximum battery SOC allowed. Note that the SOC values are part of the control strategy parameters. Although they are not related to component sizing, they have a direct impact on fuel economy of a HEV design. The sixth design variable defines final drive ratio. Each design variable is also restricted within a lower and an upper bound.

The problem now becomes quite challenging since this is a constrained multi-variable optimization problem.

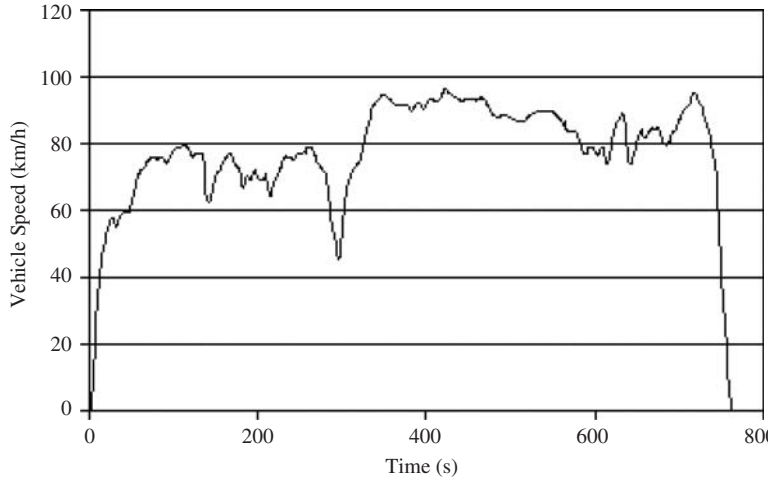

Figure 13.13 The HWFET drive cycles

Table 13.2 Upper and lower bounds of design variables

Design variable	Description	Lower bound	Upper bound
eng.scale.pwr_max_des	Fuel converter power rating	40 kW	100 kW
mc.scale.pwr_max_des	Motor controller power rating	10 kW	80 kW
ess.init.num_module	Battery number of cells	150	350
ess.init.soc_min	Minimum SOC allowed	0.2	0.4
ess.init.soc_max	Maximum SOC allowed	0.6	0.9
fd.init.ratio	Final drive ratio	2	4

Table 13.3 Initial design variable values

Design variable	Initial value
eng.pwr_max_des	86 kW
mc.pwr_max_des	65.9 kW
ess.init.num_module	240
ess.init.soc_min	0
ess.init.soc_max	1
fd.init.ratio	3.63

First, the default vehicle is simulated in PSAT. The design variables and their initial values are listed in Table 13.3. The fuel economy was observed to be 35.1 MPG (6.7 *l*/100 km) as given in Table 13.4 under the first column.

Second, the optimization algorithms, DIRECT, SA, GA, and PSO, are looped with the PSAT Vehicle Simulator and the optimization is carried out. For this step, the same default

Table 13.4 Comparison of fuel economy

Fuel economy				
Before optimization	After optimization			
	DIRECT	SA	GA	PSO
35.1 MPG	39.64 MPG	40.37 MPG	37.6 MPG	37.1 MPG

Table 13.5 Final design variable values

Design variable	Initial value	Final value			
		DIRECT	SA	GA	PSO
eng.pwr_max_des (kW)	86	83.1	82.4	95.5	87.1
mc.pwr_max_des (kW)	65.9	20.2	21.9	24.2	14.8
ess.init.num_module	240	245	311	300	238
ess.init.soc_min	0	0.25	0.22	0.34	0.26
ess.init.soc_max	1	0.84	0.78	0.89	0.78
fd.init.ratio	3.63	3.9	4.0	3.49	3.42

vehicle configuration given in Figure 13.12 and Table 13.1 is taken and the bounds for the design variables are taken as given in Table 13.2. The four algorithms are allowed to run for 400 function evaluations. Using the same number of function evaluations will allow us to compare the performance of the different optimization algorithms. A comparison of the fuel economy before and after the optimization is given in Table 13.4. A significant improvement in the fuel economy is seen due to optimization (to a less extent in the case of PSO and the GA, though). Of all the four algorithms, SA performs well with an approximate improvement of 5 MPG.

Table 13.5 shows the final values of the six design variables after optimization. Note that the rating of the electric motor is greatly reduced, implying that downsizing of the electric motor has been achieved. On the other hand, the engine is downsized to a lesser extent in the DIRECT and SA cases, while upsized in the GA and PSO cases. Given the vehicle performance constraints, the tradeoff of engine downsizing and motor downsizing can be realized by adjusting the lower and upper bounds of the design variables.

Table 13.6 shows the performance results of the hybrid powertrain after optimization. Essentially, all the optimization algorithms resulted in improved vehicle performance.

The vehicle mass changes as the design variables change because the mass of the vehicle depends directly on some design variables. In particular, of the chosen six design variables, three design variables (power ratings of engine and motor, and energy modules) affect the vehicle mass. The vehicle mass before and after the optimization is given in Table 13.7. The vehicle mass decreased for the DIRECT and SA cases and increased slightly in the case of the GA and PSO.

Figure 13.14 shows how the objective function (fuel economy) value improves versus the design iteration number. The cross curve is for the SA case; the circle curve is for the DIRECT case; the star curve is for the GA case; and the square curve is for the PSO case.

Table 13.6 Comparison of the HEV performance

Constraint	Constraint value	Before optimization	After optimization			
			DIRECT	SA	GA	PSO
0–60 mph	≤18.1 s	18.1 s	15.5 s	10.8 s	11.9 s	11.1 s
40–60 mph	≤7 s	7 s	6.8 s	5 s	4.4 s	4.9 s
0–85 mph	≤35.1 s	35.1 s	30.6 s	20.7 s	21.2 s	20 s
Maximum acceleration	≥3.583 m/s^2	3.583 m/s^2	3.97 m/s^2	4.07 m/s^2	3.94 m/s^2	3.99 m/s^2

Table 13.7 Mass of HEV before and after optimization

Mass of the vehicle (kg)				
Before optimization	After optimization			
	DIRECT	SA	GA	PSO
1683	1635	1656	1694	1690

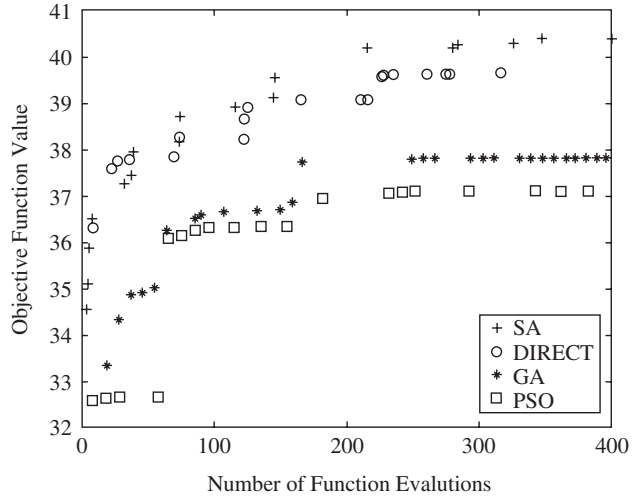

Figure 13.14 Performance comparison of DIRECT, SA, GA, and PSO

We can see that fuel economy improvement with the SA and DIRECT algorithms is very close until about 125 function evaluations, after which SA leaped ahead of DIRECT. The GA is slow to catch SA and DIRECT initially because it takes some function evaluations to generate the initial populations. After about 50 function evaluations, the GA did not find any good design point to get further improvement in the fuel economy. The performance of PSO is similar to that of the GA. Overall, SA performed the best for this particular design optimization problem.

13.5 Series HEV Design Optimization Example*

In this section, NSGA-II is applied for design optimization of a series HEV [19, 20]. NSGA-II is one of the most efficient evolutionary algorithms. Three different operators (crowded tournament selection, simulated binary crossover, and polynomial mutation) are applied to the population to yield a better population at each iteration. The main task of a selection operator is to emphasize good solutions of the population by making multiple copies of them to replace bad solutions of the population. The task of a crossover operator is to exchange partial information between two or more reproduced solutions and to create new offspring solutions. The task of a mutation operator is to locally perturb the offspring solutions. Successive applications of such iterations have been demonstrated to converge close to the true optimal solution of the problem both theoretically and computationally [21, 22].

Figure 13.15 illustrates the major computational steps in NSGA-II. The parent population P_t is first initialized based on the range and constraints of the design variables. Through crowded tournament selection, simulated binary crossover, and polynomial mutation, the offspring population Q_t is generated. Then the parent population P_t and the offspring population Q_t are combined together to form R_t of size $2N$. After that, a non-dominated sorting procedure is applied to classify the entire population R_t into a number of hierarchical non-dominated fronts. Once the non-dominated sorting is completed, the crowding distance of each solution is also calculated. The new parent population P_{t+1} of size N is derived from R_t of size $2N$ through the following calculation [19, 20]. The calculation starts with the best non-dominated front and continues with the solutions of the second non-dominated front, and so on. When the last allowed front is being considered and there are more solutions in the last front than the remaining slots in the new population, the crowding distance has to be considered to choose the members of the last front, which reside in the least crowed region in the front. The iteration of generating new populations repeats until some terminating conditions are met. As the generation progresses, the solutions in the new populations are optimized.

13.5.1 Control Framework of a series HEV Powertrain

A typical powertrain configuration of a series HEV is shown in Figure 13.16. The vehicle is propelled by a traction motor. The traction motor is powered by a battery pack and/or an engine/generator unit. The engine/generator unit either helps the batteries to power the traction motor when load power demand is high, or charges the batteries when load demand is low. The electric motor can also be used as a generator to charge batteries by regenerative braking. The motor controller is to control the traction motor to produce the power required by the vehicle.

The series thermostat control strategy uses the generator and engine to generate electrical energy for use by the vehicle. The powertrain control strategy is described as follows [23]:

- To maintain charge in the battery, the engine turns on when the SOC reaches the low limit.
- The engine turns off when the SOC reaches the high limit.
- The engine operates at the most efficient speed and torque level.

* © [2009] IEEE. Reprinted, with permission, from IEEE VPPC Conference.

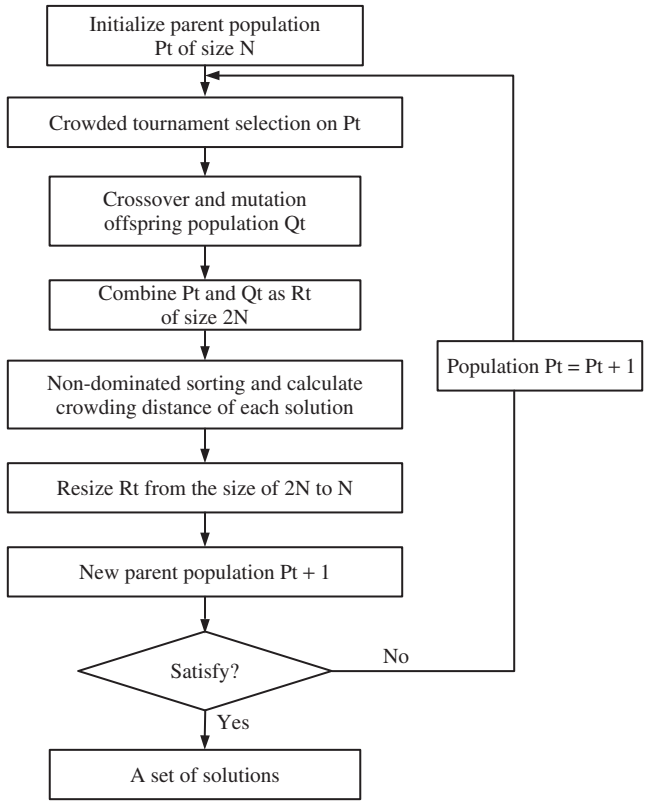

Figure 13.15 Computational steps in NSGA-II

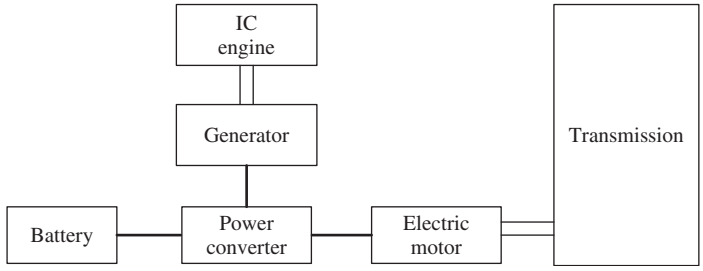

Figure 13.16 Powertrain configurations of series HEV

Table 13.8 Vehicle parameters

Gross mass (kg)	Full load mass (kg)	Wheelbase (m)
1373	1659	2.6
Windward area (m^2)	Rolling coefficient	Aerodynamic coefficient
2.0	0.015	0.335

Table 13.9 Series HEV main components

Component	Description
Fuel converter	Geo 1.01 SI 41 kW
Motor	75 kW Westinghouse AC induction motor
Battery	Hawker Genesis 12 V, 26 Ah, 10EP sealed valve-regulated lead acid (VRLA) battery

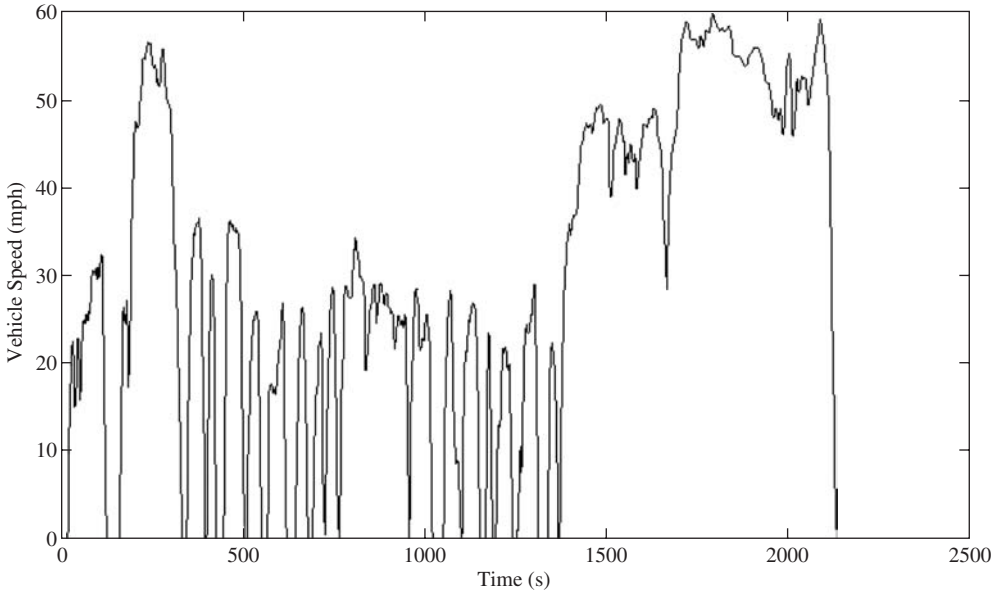

Figure 13.17 Combined UDDS and HWFET drive cycle

The major vehicle parameters and main components of the series HEV are given in Tables 13.8 and 13.9.

13.5.2 Series HEV Parameter Optimization

ADVISOR is used to evaluate the vehicle performance. ADVISOR is a vehicle simulation package developed on the MATLAB/Simulink software platform, which adopts forward and backward modeling methods. Figure 13.17 shows the test drive cycle used in our simulation. The test drive cycle is composed of city driving represented by UDDS and highway driving represented by HWFET. Table 13.10 shows that the optimization is initially limited to eight design variables, three component parameters, and five control strategy parameters. The initial default values and the boundaries of design parameters are also given in the table.

Before optimization, the vehicle model has the following dynamic performances:

- 0–60 mph: 10.5 seconds
- 40–60 mph: 5.6 seconds
- 0–85 mph: 24.6 seconds
- Gradability: 6.8% grade at 55 mph (88 km/h).

Since the dynamic performance must be kept during optimization, the above performances are imposed constraints in the optimization process. At the same time, in order to eliminate the influence of initial battery energy on the fuel consumption and emissions, the SOC correction has to be selected, so the initial and final SOC can be set at almost the same level and the delta SOC tolerance is within [−0.5%, +0.5%]. We can consider that the entire output energy for the cycle is from the engine alone.

For each solution in a population, which contains eight design variables, the algorithm calls ADVISOR to run a simulation using these parameters specified for the test drive cycle to obtain the fuel consumption and emission data. The optimization algorithm calculates the fitness value for each solution, and then generates a new set of solutions by the crossover and mutation operations. The non-dominated sorting algorithm is applied to the newly generated solutions to select the next population. This iteration process repeats until the terminating condition (such as the maximum number of generations) is satisfied.

13.5.3 Optimization Results

The NSGA-II algorithm shown in Figure 13.15 is implemented in ADVISOR. The initial population is 40 randomly selected individuals of the design parameters given in Table 13.10 from the solution space. The terminating condition is set to 80 generations. For each individual, the drive cycle simulation for the evaluation including the objective function and constraints takes an average of about 1 minute on a 3.4 GHz Pentium computer, and takes about four days for the whole program to run. Figure 13.18 shows the fuel consumption and emission data generated by the 40 solutions after 80 generations of

Table 13.10 Design variables

Design variable	Description	Default value	Lower bound	Upper bound
eng_pwr	Engine power	41 kW	25 kW	53 kW
mc_pwr	Motor power	75 kW	38 kW	112 kW
ess_cap	Capacity of batteries	26 Ah	13 Ah	39 Ah
cs_high_soc	Highest SOC allowed	0.8	0.7	0.85
cs_low_soc	Lowest SOC allowed	0.6	0.3	0.5
cs_max_pwr	Maximum power commanded of fuel converter	30 kW	25 kW	40 kW
cs_low_pwr	Minimum power commanded of fuel converter	20 kW	5 kW	20 kW
cs_off_time	The shortest allowed period of fuel converter off	Inf.	10 s	1000 s

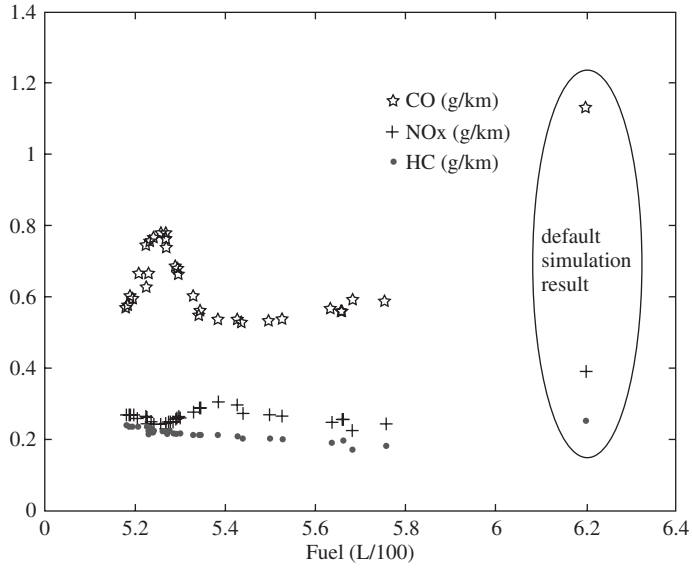

Figure 13.18 The fuel consumption and emission data generated by the tradeoff solutions generated by the optimization algorithm

optimization, along with the result generated by the default controller in ADVISOR. All 40 solutions consumed less fuel than the default controller, and all 40 solutions generated less emission in CO, NO_x, and HC than the default controller.

In order to illustrate progress through the generations during the optimization, we use the following equation as an evaluation function to select the best one from the 40 solutions at each generation:

$$F = 0.7 \cdot \text{fuel} + 0.1 \cdot \text{HC} + 0.1 \cdot \text{CO} + 0.1 \cdot \text{NO}_x$$

The results are illustrated in Figure 13.19. The data in the figure shows that the algorithm converges to the evaluation value of 3.72 after 50 generations.

Table 13.11 lists the optimization results generated by the top-ranked five solutions in the final population based on the non-dominated sorting method. Take solution 1, for example: the fuel consumption and the three emissions are reduced by 15, 14, 31, and 40%, respectively, in comparison to the performances generated by the default controller. This suggests that if the design parameters suggested by this solution are used in the series HEV design, an online controller can be optimized to reach the same or better performances than those generated by this optimal solution.

Corresponding to the five solutions in Table 13.11, Table 13.12 shows the value of the design variables and performance after optimization. Although the engine power is scaled down, by increasing the motor power and battery capacity, the acceleration ability and gradability of vehicle performance are still improved.

Table 13.13 shows the optimization results generated by the top five solutions selected by the evaluation function from the final population. We can see that the solutions in Table 13.13 are different from those shown in Table 13.10. We use this example to show

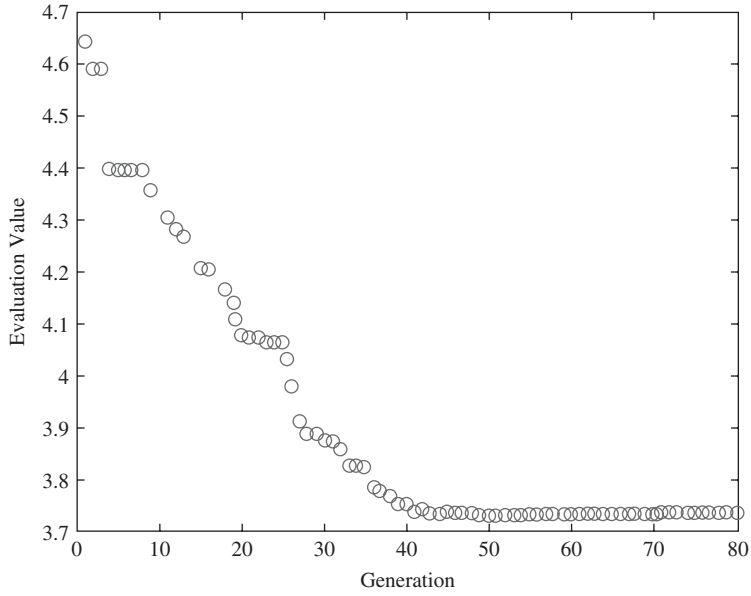

Figure 13.19 Evaluation of generation progress during optimization

Table 13.11 The optimization results generated by the top five solutions selected by the non-dominated sorting

No.	Fuel (l/100 km)	HC (g/km)	CO (g/km)	NO_x (g/km)
1	5.268	0.213	0.779	0.231
2	5.681	0.170	0.593	0.223
3	5.439	0.201	0.526	0.272
4	5.183	0.238	0.568	0.270
5	5.758	0.184	0.589	0.242

the importance of the proposed optimization algorithm: it generates a population of multiple tradeoff optimal solutions. Vehicle designers and control engineers can use their own evaluation criteria to select optimal solutions from this population of tradeoff solutions.

13.6 Conclusion

Based on the optimization results of the example parallel HEV, the following observations can be made. The fuel economy of the parallel HEV is increased from 35.1 to 39.64 MPG with the DIRECT algorithm, and from 35.1 to 40.37 MPG with the SA algorithm. The performance of the optimized HEV shows a great improvement. The power rating of the traction motor is reduced significantly [24]. The second example uses the evolutionary

Table 13.12 The value of design variables and performance after optimization

No.	1	2	3	4	5
eng_pwr	25 kW	25.1 kW	25 kW	25.1 kW	25 kW
mc_pwr	82.8 kW	81.4 kW	86.7 kW	80.9 kW	82.9 kW
ess_cap	39 Ah	38.2 Ah	38.9 Ah	38.3 Ah	38 Ah
cs_high_soc	0.73	0.75	0.75	0.74	0.74
cs_low_soc	0.49	0.48	0.50	0.48	0.49
cs_max_pwr	33.1 kW	33.5 kW	32.2 kW	33 kW	31.9 kW
cs_low_pwr	13.2 kW	6.7 kW	9.8 kW	5.6 kW	12.4 kW
cs_off_time	750 s	538 s	598 s	519 s	711 s
0–60 mph	10.2 s	10 s	10 s	10.3 s	9.9 s
40–60 mph	5.4 s	5.3 s	5.3 s	5.5 s	5.2 s
0–85 mph	23.8 s	23.4 s	23.4 s	24 s	22.8 s
Gradability at 55 mph	8.1%	7.9%	7.9%	8.0%	7.2%
Delta SOC	0.21%	0.26%	0.31%	−0.17%	−0.24%

Table 13.13 The optimization results generated by the top five solutions selected by the evaluation function

No.	Fuel (l/100 km)	HC (g/km)	CO (g/km)	NO_x (g/km)	Evaluation value
1	5.183	0.238	0.568	0.270	3.7357
2	5.188	0.234	0.578	0.268	3.7396
3	5.193	0.238	0.582	0.268	3.7439
4	5.194	0.237	0.601	0.266	3.7462
5	5.199	0.238	0.592	0.267	3.7490

algorithm, NSGA-II, for the multi-objective optimization problem in a series HEV. The algorithm has the capability of simultaneously optimizing fuel economy as well as three emissions. At the end of the optimization process, the algorithm generates 40 optimal tradeoff solutions and performances. All of these solutions are better, in all four categories, than the performances generated by the default controller in ADVISOR. We also demonstrated that vehicle designers and control engineers can derive their own tradeoff criteria to select the solutions that best suit their specific needs.

In these studies, only global optimization algorithms are tested for a hybrid vehicle design, which generally have slower convergence. On the other hand, derivative-based algorithms are known for their faster convergence. In fact, a hybrid optimization algorithm can be used that combines the benefits of both global and local algorithms. The global algorithm can reach a design point near the global optimum region after a certain number of optimization steps. Then a local algorithm kicks in and the process is continued until a global optimum is found.

For the parallel HEV example, the design optimization takes about 100 hours running PSAT on a single PC. This long design time necessitates the development of a more efficient optimization methodology such as using parallel and distributed computing.

References

1. Moore, T.C. (1996) Tools and Strategies for Hybrid-electric Drive System Optimization. SAE Technical Paper Series, No. SP-1189.
2. Miller, J. (2003) *Propulsion Systems for Hybrid Vehicles*, Peter Peregrinus, Stevenage.
3. Fellini, R., Michelena, N., Papalambros, P. *et al*. (1999) Optimal design of automotive hybrid powertrain systems, in *Proceedings of EcoDesign 99 – First International Symposium on Environmentally Conscious Design and Inverse Manufacturing* (ed. H. Yoshikawa *et al*.), Tokyo, pp. 400–405.
4. Gao, W. and Porandla, S. (2005) Design optimization of a parallel hybrid electric powertrain. Proceedings of the IEEE Vehicle Power and Propulsion Conference, Chicago, September, pp. 530–535.
5. Schittkowski, K. (1985) NLQPL: a FORTRAN-subroutine solving constrained nonlinear programming problems. *Annals of Operations Research*, **5**, 485–500.
6. Jones, D.R. (2001) DIRECT global optimization algorithm, in *Encyclopedia of Optimization*, Kluwer Academic, Dordrecht.
7. Jones, D.R., Perttunen, C.D., and Stuckman, B.E. (1993) Lipschitz optimization without Lipschitz constant. *Journal of Optimization Theory and Applications*, **79** (1), 157–181.
8. Kirkpatrick, S., Gelett, C., and Vechhi, M. (1983) Optimization by simulated annealing. *Science*, **220** (4598), 671–680.
9. Holland, H.J. (1975) *Adaptation in Natural and Artificial Systems*, The University of Michigan.
10. Kennedy, J. and Eberhart, R. (1995) Particle swarm optimization. Proceedings of the IEEE International Conference on Neural Networks, Perth, Australia, November–December, Vol. IV, pp. 1942–1948.
11. Trelea, I.C. (2003) The particle swarm optimization algorithm: convergence analysis and parameter selection. *Information Processing Letters*, **85** (6), 317–325.
12. Wipke, K. and Markel, T. (2001) Optimization techniques for hybrid electric vehicle analysis using ADVISOR. Proceedings of the ASME, International Mechanical Engineering Congress and Exposition, New York, November.
13. Shubert, B. (1972) A sequential method seeking the global maximum of a function. *SIAM Journal of Numerical Analysis*, **9**, 379–388.
14. Metropolis, N., Rosenbluth, A.W., Rosenbluth, M.N. *et al*. (1958) Equations of state calculations by fast computing machines. *Journal of Chemical Physics*, **21**, 1087–1092.
15. PSAT Documentation, http://www.transporation.anl.gov/software/PSAT (accessed 2006).
16. Wipke, K.B., Cuddy, M.R., and Burch, S.D. (1999) ADVISOR 2.1: A User-Friendly Advanced Powertrain Simulation using a Combined Backward/Forward Approach. NREL/JA-540-26839, September.
17. Gao, W., Solodovnik, E., and Dougal, R. (2004) Symbolically-aided model development for an induction machine in Virtual Test Bed. *IEEE Transactions on Energy Conversion*, **19** (1), 125–135.
18. Wipke, K., Markel, T., and Nelson, D. (2001) Optimizing energy management strategy and a degree of hybridization for a hydrogen fuel cell SUV. 18th Electric Vehicle Symposium (EVS-18), Berlin, Germany, October 20–24.
19. Deb, K. (2001) *Multi-Objective Optimization Using Evolutionary Algorithms*, John Wiley & Sons, Ltd, Chichester.
20. Deb, K., Pratap, A., Agarwal, S. *et al*. (2002) A fast and elitist multiobjective genetic algorithm: NSGA-II. *IEEE Transactions on Evolutionary Computation*, **6** (2), 182–197.
21. Deb, K., Jain, P., Gupta, N.K. *et al*. (2004) Multiobjective placement of electronic components using evolutionary algorithms. *IEEE Transactions on Components and Packaging Technologies*, **27** (3), 480–492.
22. Vose, M. (2001) *Simple Genetic Algorithm: Foundation and Theory*, MIT Press, Cambridge, MA.
23. ADVISOR 2004 Documentation, http://www.avl.com (accessed January 27, 2011).
24. Gao, W. and Mi, C. (2007) Hybrid vehicle design using global optimisation algorithms. *International Journal of Electric and Hybrid Vehicles*, **1** (1), 57–70.

14

Vehicular Power Control Strategy and Energy Management

14.1 A Generic Framework, Definition, and Needs

The terms power and energy management are "almost" synonymous when used in the context of vehicular systems. To be more precise, power is an instantaneous quantity, whereas energy involves a period of time over which the power is applied. Although the meaning will become clearer as we progress through this chapter, normally when power is "managed," in general energy will be managed as well.

The question of management of power or energy arises due to the following reasons. Consider Figure 14.1 which represents a very generic system involving several power/energy sources and loads, including distribution of power to the loads.

In this diagram we have several sources [1]. Each of these sources could be of any particular type. For example, it could be an IC engine, which is a power source, that is, an energy converter which translates chemical energy into mechanical power. It could also be a battery, which is an electrical energy storage device, or it could be a fuel cell, which converts chemical energy into electrical power, or it could be a flywheel, which stores kinetic energy in mechanical form. In the case of the flywheel, energy could be injected into the flywheel by running through an electric motor and speeded up. The sources could be hydraulic or pneumatic power sources as well.

It is apparent from the above that the sources could be of a different nature, but they could be similar as well, or even identical. For example, sources 1 and 2 in Figure 14.1 could both be IC engines. Or one could be a diesel and the other a gasoline engine. Similarly, one source could be a battery, the other a fuel cell.

Loads could also be of different types as well. Again, for a hybrid or electric vehicle the load could be a propulsion motor type of electrical (or rather electromechanical) load, or it could be an electric light or heater, that is, some kind of resistive load. It could also include auxiliary motors like pumps, air-conditioners, and so on. Thus it is obvious that in a vehicle there are various kinds of loads due to needs. But the question is: why should one have multiple sources in a vehicular system?

Hybrid Electric Vehicles: Principles and Applications with Practical Perspectives, First Edition.
Chris Mi, M. Abul Masrur and David Wenzhong Gao.

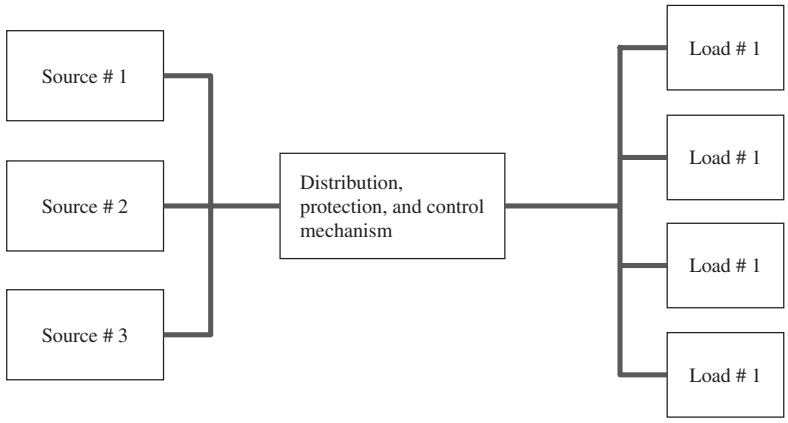

Figure 14.1 A block diagram schematic showing the source and load distribution system

Even in a regular non-hybrid vehicle we have the IC engine and also a battery. Here we have at least two sources to cater for two different types of loads, that is, mechanical propulsion and electrical loads. In a HEV we also have two sources at least. The only difference is that in a HEV the battery can be much larger (actually consisting of a number of separate battery modules combined together) than in a regular non-hybrid vehicle. The simple answer as to why we have different types of sources is that we have a heavy mechanical propulsion load which can be catered for by means of IC engines. Then of course we can use the battery to deliver smaller loads like electric lights, pumps, and so on. But a more complex answer regarding the need for multiple sources is due to the fact that the load demand (amount of power) varies with time, and the characteristics of the load (i.e., torque–speed characteristics of a mechanical load like propulsion) also change with time. Sources also have characteristics in terms of their power delivery profile, and efficiency. In other words, to deliver a particular load at a particular moment, if it is found that a particular source is capable of doing so at the best efficiency compared to several choices of sources, then obviously one should select the best source accordingly. Here one has to first see if one or more sources (individually or collectively) can meet the particular load demand in terms of load performance. If there are more than one source which can do the job, then one has to choose the most efficient source (or a combination of the most efficient ones) to do the job.

The reason why the above situation arises is due to the fact that the IC engine has better efficiencies in a certain torque–speed region of its engine efficiency map. The same thing applies to the electric motor, but electric machines have much higher efficiencies over a wide range in the torque–speed region, compared to an IC engine. Similarly, for the sake of discussion, if we assume that a system has both a diesel and a gasoline engine (multi-engine, multi-fuel system), then their efficiency characteristics will be different, and at a certain torque–speed point a diesel engine will be better than a gasoline engine, and vice versa.

This idea forms the main rationale behind power management from performance and efficiency points of view. This can also be termed energy management since this rationale also increases overall system efficiency and reduces energy consumption.

In addition, other things which fall within the scope of power management involve the overall means through which the power is distributed to various loads. For example, the mechanism used to connect the loads to the source and the protection mechanism used for problems like short circuits in an electrical system are also within the scope of power management.

14.2 Methodology to Implement

We will treat power management and control from two different perspectives, one related to optimization and the other to distribution and control. Optimization deals with things like energy efficiency, or maintaining the battery's state of charge (SOC) within some threshold values, and has more to do with generation control and management, based on load demand. Although the second perspective relates to distribution and control, there is some, or rather a good, interrelationship between the two as will be evident in the following.

First let us consider the characteristics of power/energy sources and look at the characteristics of the following: gasoline IC engine, diesel engine, alternator, battery, and fuel cell.

For these engines, the curves shown in Figure 14.2 actually should contain a family of curves corresponding to different throttle positions or fuel input (additional discussion can be found in the web article cited in further reading at the end of this chapter). One could have another set of curves showing the relationship between speed and efficiency at different throttle positions (or equivalently the fuel input) for each of the sources. Both of these sets, that is, speed–torque and speed–efficiency curves, together constitute the engine map.

Similarly, for the electrical components, like motors and generators, one could have another set of curves showing the relationship between speed and efficiency for a given

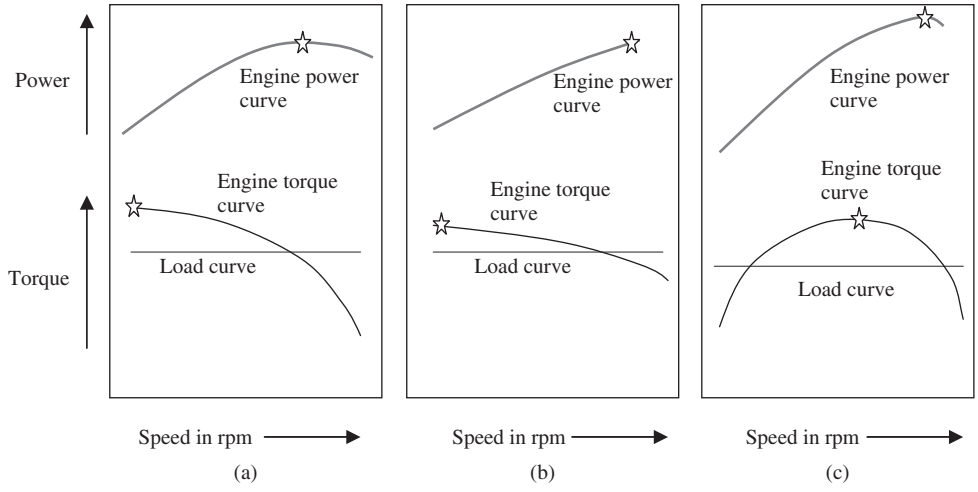

Figure 14.2 (a) Diesel engine with relatively high torque rise, (b) diesel engine with relatively low torque rise, and (c) gasoline engine (maximum torque and power points are shown by ☆)

power output (or equivalently the speed versus power input at a given efficiency). For static components like a battery and fuel cells, one could plot voltage versus current at a given SOC (or equivalently the power input versus current). These characteristics for components such as a generator and battery can constitute the required information in terms of the operating point of these devices.

For the characteristic curves in Figure 14.2, the engine curves and the load curves are indicated. As noted previously, the curves involving an IC engine are for a specific throttle position corresponding to the engine fuel intake. The intersection points between the load curves and the source (e.g., engine, battery, etc.) curves dictate the exact operating point of the load and source. When we want to drive a load, this means we want to generate a specific speed at a specific torque. The load and its characteristics are dependent on things outside of the engine (or source). To meet the load speed and torque, it is in general necessary to include some gear train in the system, since engines in general cannot handle the wide range of load demand, even after controlling the throttle. Once the throttle position and gear ratio are chosen, they define the precise engine operating point. At that point the engine operates at a given efficiency or fuel economy.

The electrical system characteristics and their nature are shown in Figure 14.3. For convenience of comparison we have made the curves identical in form to show what variables change in each case. The variables are voltage and current on the Y and X axis respectively. The parameter that is fixed is the SOC in the case of a battery, and fuel (could be hydrogen) flow rate in the case of a fuel cell. For the generator the speed is held constant while the load changes. Some electrical load can be connected or applied to each of these electrical source devices, as depicted by the respective load curves. For example, an electrical resistance (could be a light) characteristic could be the straight line in the figure. In each of these graphs, the operating point is defined by the intersection point between the curves. Corresponding to each of these diagrams, a companion diagram showing the actual energy input needed at the operating point might be drawn, which would indicate the energy used and would depend on the efficiency at each operating point. That might be one of the ingredients in defining the cost of power production at each point.

At this point we can define the above situation mathematically as follows:

$$\text{Engine: } T_{e1} = f_{e1}(\omega_{e1}, \Gamma_{e1}) \tag{14.1}$$

which is the torque corresponding to a specific engine e1, where ω_{e1}, Γ_{e1} are speed and throttle positions.

As noted earlier, the engine will also have another equation involving its power consumption or energy, or equivalently the efficiency, which can be written as follows:

$$\eta_{e1} = \zeta_{e1}(\omega_{e1}, \Gamma_{e1}) \tag{14.2}$$

Similarly one can write an equation for another engine

$$T_{e2} = f_{e2}(\omega_{e2}, \Gamma_{e2}) \tag{14.3}$$

which can have different characteristics than e1. Together, the engines can deliver the total load.

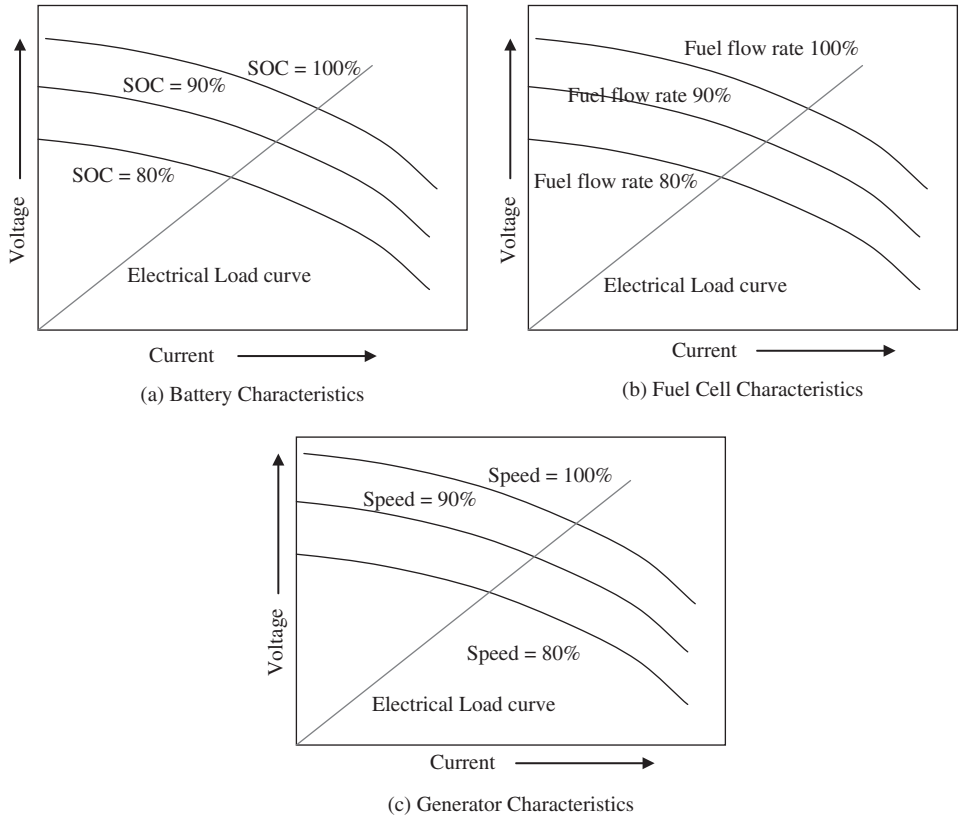

Figure 14.3 Characteristic curves for (a) battery, (b) fuel cell, and (c) generator

The second engine can have an efficiency defined by

$$\eta_{e2} = \zeta_{e2}(\omega_{e2}, \Gamma_{e2}) \tag{14.4}$$

and the load is assumed to have the characteristics

$$T_L = f_L(\omega_L, \Gamma_L) \tag{14.5}$$

where T_L is the torque, ω_L is the load speed, and Γ_L depends on the road profile and external environmental issues and driver demand. Γ_L also depends on any auxiliary load demand within the vehicle due to direct action of the driver (e.g., increased electrical load, which can lead to a higher torque on the generator) or due to indirect control actions taken within the vehicle automatically, for example, some mechanical or electrical pump being activated. Even if the quantity Γ_L is dependent on only the driver input in terms of desire to accelerate, the functional nature of the torque, that is, f_L, will depend on the road characteristics and other factors outside the vehicle. Hence this function f_L will change from one road to another or from one drive cycle to another.

There may be a gear ratio between the load and the individual engine. In other words,

$$\omega_L/\omega_{e1} = g_1 \tag{14.6}$$

and

$$\omega_L/\omega_{e2} = g_2 \tag{14.7}$$

Assume that the gears are ideal and lossless for the sake of discussion. Under the above scenario, if the loads are driven by the two engines together, and assuming the conservation of power, the power equation will be

$$T_L\omega_L = T_{e1}\omega_{e1} + T_{e2}\omega_{e2} \tag{14.8}$$

So, the total fuel consumption in this case will correspond to a total input power to the two engines taken together:

$$\begin{aligned} P_{in} &= \{\text{power of engine 1/efficiency of engine 1}\} \\ &\quad + \{\text{power of engine 2/efficiency of engine 2}\} \\ &= T_{e1}\omega_{e1}/\eta_{e1} + T_{e2}\omega_{e2}/\eta_{e2} \\ &= \{f_{e1}(\omega_L/g_1, \Gamma_{e1}) \times (\omega_L/g_1)\}/\{\zeta_{e1}(\omega_L/g_1, \Gamma_{e1})\} \\ &\quad + \{f_{e2}(\omega_L/g_2, \Gamma_{e2}) \times (\omega_L/g_2)\}/\{\zeta_{e2}(\omega_L/g_2, \Gamma_{e2})\} \end{aligned} \tag{14.9}$$

and of course

$$T_L = \{f_{e1}(\omega_L/g_1, \Gamma_{e1})/g_1)\} + \{f_{e2}(\omega_L/g_2, \Gamma_{e2})/g_2)\} \tag{14.10}$$

It can be immediately seen from this equation that fuel input is dependent only on the gear ratios and the throttle position. The strategy in this case will be: given the load torque T_L and load speed ω_L, choose gear ratios g_1, g_2, and throttle positions Γ_{e1}, Γ_{e2}, such that the fuel consumption rate corresponding to P_{in} is a minimum, while satisfying the torque and speed demand. It is of course understood that the various function expressions for torque and efficiency are available from the engine specifications or manufacturer's data. If this objective can be met, it will deliver the correct torque and speed to the load at a minimum fuel intake, which is very much desirable. In a real system these actions are coordinated through the fuel/throttle controller and transmission controller. If the transmission is not a continually variable type, then the choice for g_1 and g_2 will be limited. In addition, the engine controller and other sensor information in the vehicle will become involved in the above decision process. But the point here is that, in principle, the best strategy can be realized to meet the load demand with minimum fuel consumption.

On top of the equations indicated above, it may be necessary to impose certain constraints. For example, we can impose the requirement that the engine speed, for either engine 1 or 2, should not exceed a certain limit, due to the engine's structural design, physical size, and other factors. This can be written in the form

$$\omega_{e1} \leq \omega_{threshold1} \tag{14.11}$$

$$\omega_{e2} \leq \omega_{threshold2} \tag{14.12}$$

and similarly for the torques:

$$T_{e1} \leq T_{threshold1} \tag{14.13}$$

$$T_{e2} \leq T_{threshold2} \tag{14.14}$$

In other words, we have not only to observe certain engine characteristics defined previously through an engine map or equivalent information, but also to make sure that we are within the maximum threshold limits of the devices based on the manufacturer's specifications. Hence our optimization problem has to take into account these constraints, and then try to minimize the fuel economy, and so on.

We will present the methodology of optimization after further discussion on other multi-source systems.

Continuing with the previous plots (torque vs. speed etc.) showing the characteristics of various sources, the idea can be extended as follows. Just as we have done for the engines, we can write similar equations for the other sources. For example, for the electrical source or storage elements such as the generator, battery, fuel cell, and so on, we can write the following for their electrical characteristics based on the previous diagrams showing their characteristics:

$$I_{G1} = f_{G1}(V_{G1}, \omega_{G1}) \tag{14.15}$$

(the voltage–current relationship at fixed speed, for the generator)

$$\eta_{G1} = \zeta_{G1}(V_{G1}, \omega_{G1}) \tag{14.16}$$

(the efficiency relationship at fixed speed, for the generator)

$$I_{B1} = f_{B1}(V_{B1}, \mathrm{SOC}_{B1}) \tag{14.17}$$

(the voltage–current relationship at fixed SOC, for the battery)

$$\eta_{B1} = \zeta_{G1}(V_{B1}, \mathrm{SOC}_{B1}) \tag{14.18}$$

(the efficiency relationship at fixed SOC, for the battery)

$$I_{FC1} = f_{FC1}(V_{FC1}, \mathrm{FR}_{FC1}) \tag{14.19}$$

(the voltage–current relationship at fixed fuel rate, for the fuel cell)

$$V_{FC1} = \zeta_{FC1}(V_{FC1}, \mathrm{FR}_{FC1}) \tag{14.20}$$

(the efficiency relationship at fixed fuel rate, for the fuel cell)

In the equations above the subscripts G, B, and FC stand for generator, battery, and fuel cell, respectively. SOC indicates the state of charge, and FR indicates the fuel rate. The equations imply that the current of the generator is dependent on its speed and output voltage. Similarly the battery current is dependent on the battery voltage for a given SOC, and the fuel cell current is dependent on the fuel cell voltage for a given fuel rate. The efficiency of each of these devices depends on the voltage (or equivalently the current)

and the other parameters like speed, SOC, or FR, which are also included above. Again, we might have some constraints imposed on these devices as follows:

$$I_{G1} \leq I_{G1threshold} \tag{14.21}$$

$$I_{B1} \leq I_{B1threshold} \tag{14.22}$$

$$I_{FC1} \leq I_{FC1threshold} \tag{14.23}$$

$$\mathrm{SOC}_{B1} \leq \mathrm{SOC}_{B1\_high\_threshold} \tag{14.24}$$

$$\mathrm{SOC}_{B1} \geq \mathrm{SOC}_{B1\_low\_threshold} \tag{14.25}$$

Here the upper bounds of current limits in the devices, and upper and lower bounds for the SOC of the battery, are shown as constraints.

For the sake of simplicity we can write

$$\mathrm{SOC}_{B1} = f_{SOC\_B1}(V_{B1}) \tag{14.26}$$

which indicates that the SOC is related to voltage. This is a simple equation for the sake of illustration only, since SOC equations can be quite complex and a method to evaluate them can include various nonlinearities as well.

We can also assume that there is a total electrical load current and load voltage in the system, which can be written as follows:

$$I_L = f_L(V_L) \tag{14.27}$$

$$I_L = I_{G1} + I_{B1} + I_{FC1} \tag{14.28}$$

These are just examples. In a similar manner, additional constraints, depending on the needs and specifications, could be included. Once all these constraints and equations are in place, which can involve a large number of equations, some formal method has to be introduced to deal with them. We will now briefly touch on some of these methods, since there are quite a number available nowadays, as well as computer-based modeling, design, and development, which are often necessary and effective.

14.2.1 Methodologies for Optimization

One stage in the process of dealing with the above is the development of a "cost function," where a single function is developed such that the equations and the constraints are all included in a manner such that if the energy consumption in a particular device increases, the cost function increases. Similarly, if a constraint is violated, the cost function increases. The word "cost" in this context implies that some "undesirable" thing happens somewhere in the system when the "cost" increases. It can mean more fuel intake indicating fuel cost, or it can be an overcurrent or overvoltage in a component, or exceeding the SOC in a battery, and so on, all ultimately somehow related to something "undesirable" and in some sense having the connotation of actual cost in terms of expense or money.

As an example, one can develop a cost function with the following philosophy.

One can directly include the number $1 - \eta$ (i.e., inefficiency of the device) as a "cost." Similarly, one can say that if the current I in a device exceeds the threshold, then

$|(|I| - |I_{threshold}|)|$, that is, absolute value of the amount exceeded, multiplied by some constant, can form part of a cost function. The constant multiplier can serve as a weighting function, that is, how important this threshold item is, and taken into account through this multiplier. Say, for example, that the "cost" of exceeding the SOC in a battery by 5% may be much higher than the "cost" of going below the lower threshold. The physical meaning of this is that the "cost" or damage to the battery will be much higher if the upper SOC limit is exceeded compared to the lower one. Similar judgment has to be exercised in developing the individual ingredients of the cost function corresponding to other devices. As we indicated earlier, it is obvious that the word "cost" in cost function can be construed as system inefficiency (which is tantamount to actual cost of fuel), or damage done in terms of cost, or it could be in terms of poor performance of a device which can lead to undesirable ramifications and hence is "costly" in some sense. Thus, a proper development of the cost function is very important in terms of system optimization.

In a real system it may be necessary to implement the above in real time. Hence, depending on the complexity of the system, a significant amount of computational power might be necessary. It is therefore beneficial to develop a cost function which serves the needs of optimization and at the same time it is not too complex.

Considering the above system, with two engines (for the sake of generality), which need not necessarily be IC engines (one could be an IC engine and the other an electric propulsion system), and with one battery, one fuel cell, and one generator, we could set up an overall cost function as follows:

$$\begin{aligned} C = {} & P_{in} + K_{prop} \times |P_{prop\_actual} - P_{prop\_demand}| \\ & + \eta_{G1} \times (V_{G1} \times I_{G1}) + \eta_{B1} \times (V_{B1} \times I_{B1}) + \eta_{FC1} \times (V_{FC1} \times I_{FC1}) \\ & + K_{B\_high} \times |\mathrm{SOC}_{B1} - \mathrm{SOC}_{B1\_high\_threshold}| + K_{B\_low} \times |\mathrm{SOC}_{B1} - \mathrm{SOC}_{B1\_low\_threshold}| \\ & + K_{FC\_high} \times |I_{FC1} - I_{FC1\_threshold}| + K_{G1} \times |(|I_{G1}| - |I_{G1threshold}|)| \\ & + K_{B1} \times |(|I_{B1}| - |I_{B1threshold}|)| \end{aligned} \tag{14.29}$$

In this equation the power input to the engine, P_{in}, is dependent on the propulsion power demand and also any auxiliary power, for example, the power needed to drive a generator, pumps, and so on. Other terms in C involve the efficiency of individual items like the generator, battery, any fuel cell, and so on. The remaining terms involve the exceeding of current and SOC thresholds, which is penalized. Since P_{in} is the input fuel to the engine, the higher its value, the higher the value of C. The term $K_{prop} \times |P_{prop\_actual} - P_{prop\_demand}|$ tells us that if the actual power output from the engine does not meet the demand for some reason, then we incorporate a penalty in C. Here this discrepancy in the actual power output from the demand can be an indicator of lack of performance by the engine, and not necessarily as inefficiency. The values of various constant multipliers can be chosen depending on their importance. For example, if engine performance is very important, we should use a relatively high value for the multiplier K_{prop}. Similarly, if an item is less important it should be given a lower value.

Once again, the items above are all included for the sake of a general discussion and merely to give an idea of what a cost function can imply. A real system might include more of these items or less, depending on the situation.

Although the function C above is already quite involved, it should be noted that the full expression for each of the individual functions, based on all the previous equations, should be inserted to make it complete. Once that is done, the issue will be to minimize this cost function C, which will, in our illustrative example, already have taken into account the various constraints.

As noted above, the input from the driver is provided to the vehicular system through the accelerator pedal and brake pedal positions. The input basically serves as the desire of the driver to either increase or decrease speed, which is implemented through the accelerator and brake pedals. This is compared against the actual speed and a control action is invoked. The situation on the road and the environment outside the vehicle are also taken into account through various sensors. The power management algorithm includes all of these and integrates them together to come up with a control action. This mechanism is shown in Figure 14.4.

The diagram is self-explanatory. The only input to the system comes through the accelerator and brake pedals. In addition, depending on certain actions by the driver or through the various controllers, different electrical or mechanical loads might be engaged. Examples could be the window lift motor, which is due to an action by the driver; or the activation of the air-conditioner, depending on the cabin temperature; or perhaps the water pump motor, depending on the engine temperature. All these inputs, together with the environmental and road conditions, dictate what the real fuel intake will be or the battery current will be. The outcome of the above situations (due to driver action etc.) will be transmitted through various sensor data, or certain indirectly computed information like the battery SOC will be generated, which will then be fed into the power management algorithm. The algorithm looks at the cost function (as in the equation for C above),

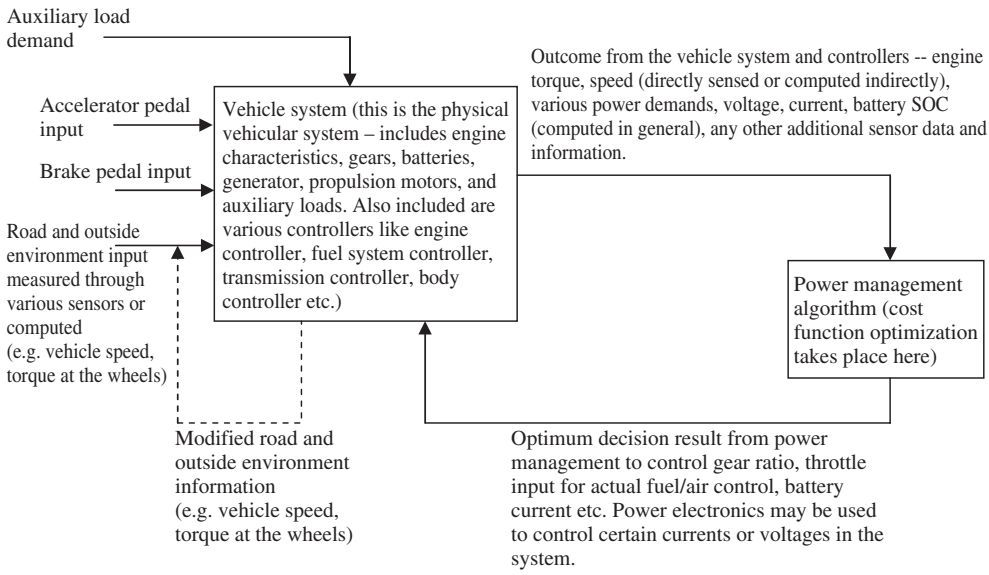

Figure 14.4 Schematic diagram of the overall power management control implementation interface for a vehicular system

created through the use of all this information. The algorithm then tries to optimize C, and its end result could be the updated choice of a particular gear ratio, throttle position, or battery current value. These updated values will be used to tell the various controllers to command a new status for the respective quantities. In consequence, information on speed, torque, and so on, is also updated – which also depends on the road and environmental conditions. This update is shown by the dashed line in Figure 14.4. This line can be considered to be the outcome of the various controller updates which interact with the environment and road outside, and generate new information. In reality the dashed line should not exist – it is shown for the sake of convenience. Note that the road and outside environment are outside the vehicle, so information on them has to be acquired through various sensors or otherwise computed.

It is apparent, therefore, that the ultimate outcome in Figure 14.4 on power management control is due to cost function optimization within the power management algorithm block. This optimization can be done as follows.

14.2.2 Cost Function Optimization

In our example above, the only things that can be controlled are the throttle, gear ratios in the two engines, and current control in the alternator or battery through some power electronics. It is assumed that the propulsion and non-propulsion load powers have already been decided based on the driver demand and external conditions. Hence the optimization is involved with trying to minimize the function C while observing various constraints. The idea here will be to achieve a global optimization (or rather minimization in our case) so that cost C is minimized. In essence, it involves identifying various local minima in the system, and then trying to find the one which gives the global minimum. There are certain numerical techniques available to do this.

Assume the situation shown in Figure 14.5 with two engines in a vehicle. Let us say that the vehicle is at point A and intends to go to point B, where A and B are defined in time. Between these two points the path or drive cycle is defined by the load power

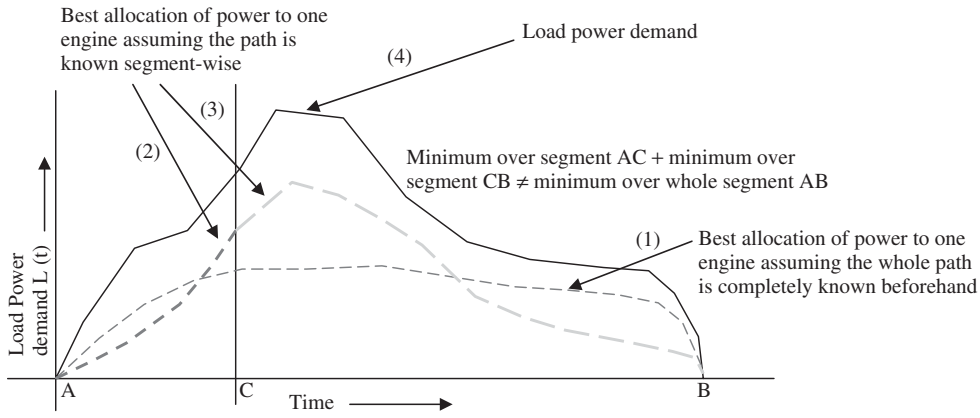

Figure 14.5 Load demand cycle segments as a function of time

demand of the vehicle $L(t)$, which depends on the speed between A and B, the actual road surface, and other external environmental inputs. Sometimes an alternative way to define a drive cycle is by means of speed as a function of time, along with information on the type of road. But ultimately, the end result of the drive cycle will be mapped to some power demand $L(t)$ which will be used by the power management process to generate the optimization decision. The statement of the problem is as follows: given $L(t)$, we have to find the individual power allocations in the two engines, as discussed in more detail below.

In our example where we have two engines, the objective is to select the torque and speed of the engines, and also the gear ratios as a function of time, in a manner such that the "cost" C (which can be equivalent to fuel cost, but not necessarily so) is minimized. As long as the total power demand is met, we have the freedom to choose any combination of individual engine torques and speeds along with the corresponding gear ratios. In meeting the power demand we may be meeting the various constraints in terms of a certain quantity being less than or equal to some threshold. Thus it is very possible that in going from A to B, we have some unique (torque–speed) profile for the individual engines which gives the minimum C. Let us put this minimum C equal to C_{AB} for the sake of specificity, with the subscripts AB indicating the path. Then let us split the span AB into AC and CB. If we just focus on AC and come up with a sequence of engine (torque–speed) profiles to keep the cost C_{AC} to a minimum, and then do the same for the segment CB, then the question is whether or not

$$C_{AC}|_{\min} + C_{CB}|_{\min} = C_{AB}|_{\min} \tag{14.30}$$

The answer is: not necessarily in general.

In Figure 14.5, the dashed line labeled (1) shows the path $C_{AB}|_{\min}$, assuming the whole path is known beforehand; the dashed line labeled (2) shows the path $C_{AC}|_{\min}$ without knowing anything after AC; and similarly the dashed line labeled (3) shows $C_{CB}|_{\min}$ within the segment CB and without knowing anything prior to CB.

Before we introduce additional mathematical terminology, the reason why pre-emptive knowledge of the whole path can lead to a different result when minimizing, compared to segmented minimization, can be understood through a simple numerical example, which is very hypothetical but provides a suitable illustration.

Consider that in Figure 14.5 we have at our disposal two different engines running on two different fuels. Let us consider the following numbers.

Assume that path AC needs 40 gallons (151 l) of fuel regardless of which engine, 1 or 2, is used. Also assume that path CB needs 80 gallons (303 l) of fuel regardless of which engine is used. In addition, assume that we have 42 gallons (159 l) of fuel in engine 1 and 80 gallons in engine 2 to begin with. Let us also assume some numerical values for the cost of fuel as indicated below. These numerical values will give a simple picture of the illustration for ease of understanding the idea.

Let us say that C_{AC1} is the cost of fuel over segment AC for engine 1 = \$2.00/gal for engine 1 and, as indicated above, we have 42 gallons of fuel for engine 1. Similarly, let us say that C_{AC2} is the cost of fuel over segment AC for engine 2 = \$5.00/gal for engine 2 and we have 80 gallons of fuel for engine 2.

These dollar values can be due to the type of engines and other reasons, and in principle the values can be different.

Assume that for the second segment CB, for whatever reason, the hypothetical engines need some special additives or whatever to make them go, perhaps due to some slope conditions etc., and that the cost of fuel increases as follows: $C_{CB1} = \$5.00$/gal for engine 1 and $C_{CB2} = \$20.00$/gal for engine 2. These numbers are chosen for ease of clearly showing the distinction.

Say we know nothing about segment CB and we are asked to find the minimum cost over AC. Obviously we will (or, rather, will be tempted to) use only engine 1, since the fuel cost of engine 1 is cheaper over AC, and use 40 gallons at a cost of

$$\$2.00 \times 40 = \$80.00$$

Now, after we have completed our journey through AC, assume that we are told that we have to go to another segment, CB. Our engine 1 has already used 40 gallons and has only 2 gallons left, so we have no choice and our cost for segment CB will be

$$\$5.00 \times 2 = \$10.00$$

since we have only 2 gallons of fuel for engine 1, and from engine 2 we have

$$\$20.00 \times 78 = \$1560.00$$

Hence the total cost of traversing the distance AC + CB or AB is

$$\$80 + 10 + 1560 = \$1650$$

Now, consider that we are told beforehand that we will have to traverse the whole path AB and that the price of fuel will vary between AC and CB for special reasons as indicated earlier. Then we may decide as follows.

For AC, we use engine 2 fully and the cost is $\$5.00 \times 40 = \$200$. Notice here that even though using engine 1 is cheaper, we decided to withhold its use. So, engine 2 will be left with 40 gallons at the end of AC. During segment CB we can use engine 1 fully for a cost of $\$5.00 \times 42 = \$210$. For the remaining 38 gallons we use engine 2 for a cost of $\$20.00 \times 38 = \$760.00$. Hence the total cost of the path AC + CB or AB will now be $\$200 + 210 + 760 = \$1170$.

This artificial numerical example illustrates the point that forward knowledge of the path, that is, knowledge of the load and various cost items ahead during the whole path, allows one to make a decision in a more prudent way so that the absolute minimum is not necessarily equal to the individual minima over different segments added together.

If we know load $L(t)$ over the whole path for a period of time t, along with the different cost values of different entities like engines, then with a system involving only two entities (engines in our case), this can be written mathematically as follows:

Min J = minimum of the integrated cost function over the individual segments t_1 and t_2 will be

$$\int_0^{t_1} \underbrace{\{C_1(p_1(t)) + C_2(L(t) - p_1(t))\}}_{\min} dt + \int_{t_1}^{t_2} \underbrace{\{C_1(p_1(t)) + C_2(L(t)) - p_1(t)\}}_{\min} dt$$

which is not necessarily equal to

$$\int_0^t \underbrace{\{C_1(p_1(t)) + C_2(L(t) - p_1(t))\}}_{\min} dt \tag{14.31}$$

where $t_1 + t_2 = t$, $p_1(t)$ is the power allocation for engine 1 as a function of time t, and the minimization is done subject to certain constraints. The constraints, in the case of entities like engines, can be in the form of expressions indicating that the torque and/or speed of the engine cannot exceed a given threshold. If the particular items related to constraints involve sources such as a battery or generator, then those thresholds could take the form of overcurrent, overvoltage, SOC, and so on. For the equation above, $C_1(p_1(t))$ is a cost function corresponding to entity 1 (which can be an engine or anything else) and similarly for entity 2. In this case it is assumed that the cost function C_1 for entity 1 depends on how many units $p_1(t)$ of some item (which can be energy or power, or other attributes as well) is delivered by this entity 1.

Once again it is important to emphasize that, although we gave a numerical example using figures to illustrate the point, the term cost can imply anything in the sense of penalty due to violation of some constraint like overcurrent and so on, and hence cost should not necessarily be construed as something only in the sense of fuel economy and so on. The minimization process of the cost function normally will penalize the cost function if the constraints are violated in some way. For example, in the case of an engine, exceeding the torque above its rating of 100% to a value of 110% might be assigned some numerical increase in cost through some penalty value, and if it is between 110 and 120%, the penalty value may be much higher. Similarly for the SOC of a battery, if it is overcharged the penalty might be quite a bit higher compared to when it is undercharged – which is due to the damage done to a battery during overcharging.

The point above can also be explained by introducing a term incremental cost which is the additional cost of the cost function C for producing one additional unit of power (in our case), where C is dependent on the operating power of the various entities (IC engine, motor, etc.) involved in producing it. In addition, C is dependent on various other items or parameters which can be gear ratio, throttle position, or anything else. Hence the final incremental cost will depend on both the operating power and the parameters. This can be expressed mathematically as follows, where i is an index which indicates the various controllable variables corresponding to different resources:

$$\text{Total incremental cost} = \Delta C$$

$$= \sum_{i=1,n} [\partial C / \partial(\text{parameter}_i)] \times [\text{change in the parameter}_i \text{ value}]$$

To minimize ΔC at a particular moment, it is necessary to choose the best parameter set in the above equation to achieve this. The operating power itself can be considered a parameter, and hence the incremental cost ΔC will depend, in our example, on the allocation of power to the various engines or devices delivering it.

In general the incremental cost will change with time, depending on various factors, including, but not limited to, the possibility of running out of fuel, battery SOC too low, and so on. If the incremental cost remained constant for each of the resources involved,

independent of operating conditions, and regardless of which zone of operation they are in, and if resource quantity were unlimited, then the answer to the question posed earlier (i.e., whether minimization of cost function C over individual segments leads to the same result as minimization over the total amount of all the segments) would be affirmative. In other words, if we know the complete path AB beforehand, we can decide exactly what the individual power generation (or something else) should be throughout the journey, to make the total C a minimum at the end of the journey. This can be considered to be a pre-emptive minimization effort. The discussion tells us that knowing the whole path ahead beforehand allows us to choose the best combination of resources to make C a minimum at the end of the journey.

In a complex system, with multiple resources and constraints, the above issue of minimization of a complex function can be quite laborious. Numerical and mathematical methods like dynamic programming (DP) [2] can help in such situations (details are abundant in the literature on this topic [2]). DP depends on knowing the whole path beforehand.

In a real system, however, often it is difficult to know the path ahead. Hence people have to resort to minimizing the cost based on what is known now, that is, instantaneous minimization in real time. In a real-time scenario this can mean moving forward incrementally in little segments. In particular, for the equation related to ΔC above, as time progresses, one would see which particular parameter$_i$, when adjusted, helps minimize ΔC of the cost function. Intuitively speaking, the algorithm might just take one parameter at a time and minimize it as much as it can, then take the next one, and so on, and then come back and iterate the process until there is no further benefit. But there is no guarantee that this process will yield the best or absolute minimum for the cost function, nor will it ensure that this method will help achieve the absolute minimum for the complete path, if we had known the path ahead beforehand. Some methods also tend to predict the path forward to come up with hopefully something better than knowing nothing at all about the path ahead. In addition, there are methods like artificial neural networks and fuzzy algorithms that have been used [3] to come up with more optimal solutions to a cost function minimization problem.

Some practical details related to the previous paragraph can be stated. In a real-time scenario, one can create tables that can be stored in a microprocessor memory based on the information of different resources as a function of operating point, which can be engine torque–speed and efficiency–speed maps at different throttle positions, or information about generator voltage as a function of speed and current drawn, or of a battery voltage vs. current at different SOC. At different operating points, the data can be extracted from the memory at nearby points to calculate $\partial C/\partial(\text{parameter}_i) \times [\text{change in parameter}_i]$, and thus find ΔC, the incremental cost of C at an operating point. By doing so one can find which resource has the minimum cost increment and choose the one to deliver the next unit of power or energy. If a single particular resource cannot provide it all, then an additional next best resource has to be brought in. Since the incremental cost changes with time, the priority list indicating which resource should be delivering how much power at a particular moment will also change. As discussed earlier, if the future needs of system loads can be predicted beforehand, then one can make decisions differently. Thus, even if the cost of one resource in terms of its immediate cost is higher than another at a particular moment, the costlier resource can still be engaged to deliver the load, notwithstanding the fact that it is not the best option at that particular moment. In this case, this apparently

costlier decision is taken in anticipation that cost reduction due to "non-engagement" of this "presently higher" cost device at a future operating point will more than offset the loss encountered now.

It can be seen from the above that to obtain the optimal numerical solution to the cost function minimization problem, mathematical manipulations and computations are necessary. Normally this calls for the incorporation of processors with significant amounts of computational power, especially if calculations are to be done in real time. With the artificial neural network method it is possible to train a system through various drive scenarios and then use the trained network to come up with a real-time solution based on various inputs from different sensor signals. These may not be the best solutions in a rigorous mathematical sense, but could practically be very good with significant benefits. By properly training a neural network, one can derive a simple matrix of constant numbers, which are normally used to multiply different variables, so the computational demand is not too high once the network is trained. Similar reasoning holds for fuzzy algorithms too.

The above discussion ultimately relates to the power management block shown in Figure 14.4, where the goal is to deliver the desired load under different constraints while minimizing some cost, which can be a real cost in the sense of fuel economy, or a penalty factor corresponding to violation of some SOC or current thresholds, which are minimized.

14.3 Benefits of Energy Management

Based on the previous discussions, it is easily appreciated that energy management has multiple goals. It of course involves the distribution of energy (implying instantaneous power as well) depending on load demand. It also implies protection of the system in case some threshold is exceeded, for example, voltage, current, SOC, and so on. Further, since the resource is not unlimited, it involves the best allocation of resources, with the objective of minimizing fuel consumption while observing various constraints. Thus good energy management leads to better fuel economy and/or lower emissions, and it also leads to enhanced life of devices. For example, by controlling the SOC properly, it may be possible to better maintain the battery's health, thus requiring less replacement. To be more precise, power management has the goal to take a holistic view of the system, not just from the point of view of fuel economy; or rather, it is to achieve a minimum life cycle cost of the system, from the point of view of operation, maintenance, and longevity, all taken together.

Note also that power and energy management is a post-design situation. It is an operational-level strategy after the system has already been built and deployed. Knowing beforehand what kind of power management strategy and algorithm will be used can help one make a better choice of devices in terms of size of engine, battery, and so on, during the design phase, so that the same performance can be achieved by using smaller equipment and making best or optimum use of it. Thus it is important to coordinate the power management process during the design phase, which can help design a more compact system. Once a system has been designed, however, little further changes can be done, though it is still possible to improve the power management algorithm from time

to time in an adaptive manner. This may be required because various parameters within the system might change (i.e., due to aging and other reasons) with time, and hence the algorithm should adaptively be able to change accordingly to take care of this.

References

1. Murphey, Y., Chen, Z., Kiliaris, L., and Masrur, M. (2010) Intelligent power management in a vehicular system with multiple power sources. *Journal of Power Sources*, **196** (2), 835–846.
2. Bertsekas, D. (2007) *Dynamic Programming and Optimal Control*, 3rd edn, Athena Scientific, Nashua, NH.
3. Murphey, Y. (2008) *Intelligent Vehicle Power Management: An Overview*, Studies in Computational Intelligence (SCI), Vol. 132, Springer, Berlin, pp. 169–190.

Further Reading

Understanding Horsepower and Torque, http://www.imagelegacies.com/HPandTorque.html (accessed February 10, 2011).

15

Commercialization and Standardization of HEV Technology and Future Transportation

15.1 What Is Commercialization and Why Is It Important for HEVs?

By commercialization we normally mean that a product is produced in volume quantities and whose technology has been developed to a reasonable degree of maturity such that systematic large-scale production is viable and sustainable. One important reason behind commercialization is that it allows mass production, hence the price can come down and more people can afford the product. Without commercialization, a technology may be good yet remain unused. In connection with HEVs, the situation is no different. It involves various technologies and with the commercialization of HEVs all these technologies will benefit.

15.2 Advantages, Disadvantages, and Enablers of Commercialization

There are several benefits of commercialization. As noted above, it allows mass production of the product where the whole manufacturing process can be streamlined. This leads to a fall in price and more people can then afford the product. As more people use it, its price can fall further. In HEVs, various technologies are involved, for example, motor technology, power electronics, cables, electromagnetic interference (EMI), to name but a few, which have to be addressed. Hence to commercialize HEVs, for mass production it is necessary for all the constituent ingredients and the corresponding technologies to be mature

Hybrid Electric Vehicles: Principles and Applications with Practical Perspectives, First Edition.
Chris Mi, M. Abul Masrur and David Wenzhong Gao.

as well. Once a product is commercialized, additional incentives arise for the manufacturer and designer to improve the various technologies further and invest accordingly.

While discussing benefits, it is also instructive to see if there are any disadvantages to commercialization. In fact, there are. When something is commercialized, there is the potential that individual developers of the technology will try to keep it as a proprietary item and not share it. Thus outsiders may not have the chance to provide any worthwhile input to the technology which could have been of benefit. This situation is comparable to commercial software versus open-source software. In the latter everyone can provide input and thus enrich the software, even though it is not financially profitable for any particular company or entity. The same holds for HEV-related technology. Thus commercialization can deprive the technical community and society from further enrichment of a technology, some of which might not even be conceivable until someone proposes it. Another disadvantage of commercialization is the fact that a particular manufacturer can make things in such a way that maintenance is very difficult without proprietary parts and no generic replacement can be used. While commercialization can lead to a fall in the price of a commodity, it can also lead to monopolization as well by a manufacturer, especially if the technology is proprietary and not shared, leading to a high price. Another issue related to commercialization, especially in the case of HEVs, is that many smaller industries and businesses cannot participate in the whole process except as suppliers. Even though sometimes small businesses can participate as suppliers, big businesses cannot normally afford to use too many relatively smaller suppliers to get the same product.

Thus we see that there are both advantages and disadvantages of commercialization, and one needs to reckon with these.

Some of the enablers for commercialization can be investments put toward technology development. In addition, partnerships between various industries can lead to better technology development at a lesser cost. One example of such a collaboration is between GM, BMW, and Daimler-Chrysler, which formed a consortium to develop HEV technology and improve it. Once the job is done, the partnership will not need to exist and the partners can get on with their own products. In the case of HEVs, it can undoubtedly be said that the US Department of Energy plays a major role in terms of funding various projects jointly with industry. This has paved the way to the very commendable objective of developing a viable HEV product.

15.3 Standardization and Commercialization

Commercialization of HEVs obviously calls for cooperation between various manufacturers, since there are multiple technologies involved. These technologies, such as batteries, power electronics, motors, charging mechanism of batteries in the case of plug-in hybrid vehicles, all need to conform to certain standards. These standards can concern the perspective of safety, but also the perspective of conforming to some commonality between what one technology can give and what another can receive. Regardless of the manufacturer, it is very likely that power electronics are purchased from only a handful of suppliers, hence battery and motor- related design must match the basis of what is available from the power electronics. Then there is the EMI issue, for which there are various standards. It is very important to observe these standards to make sure there is no problem with any microcontroller system due to EMI, nor should it disrupt anything

in another nearby vehicle. In connection with plug-in vehicle infrastructure, it is very likely in the future that there will be battery charging stations, just like gas stations, or perhaps more likely within existing gas stations. It is very important that the charging interfaces between vehicles of different brands and the charging stations follow the recommendations of standards. Other issues of standardization pertain to maintenance of the vehicles. Just like their ICE counterparts, HEVs will need appropriate testing equipment, which need not necessarily be procured from the vehicle manufacturer. In general it is likely that diagnostic instruments from the HEV manufacturer will be more costly than generic ones. Hence some standardization, such as OBD II, will be called for. From the customer's point of view perhaps the perfect standardization is one in which a component for the vehicle, including motors, batteries, and power electronics, could be replaced by generic counterparts readily available on the market. To make this a reality, the generic components must adhere to some minimum safety and other standards. This situation could cause another difficulty, in terms of warranty. A manufacturer might say that if a particular part is replaced within the vehicle using generic components, then the warranty will be void. All of the above are legitimate concerns, and need the participation of the manufacturer, consumer, various professional societies, organizations like the ISO, IEEE, SAE, and so on, and the government, in order to achieve successful standardization.

15.4 Commercialization Issues and Effects on Various Types of Vehicles

Commercialization may not have the same effect on all types of vehicles. That is, the effect might be different for a regular small passenger vehicle compared to things like heavy trucks, military vehicles, delivery trucks, refuse or garbage trucks, utility vehicles, construction vehicles and equipment, locomotives, ships, and so on. Commercialization ultimately has to do with profit and money. Thus it depends on the cost per unit and the volume produced. The impact of commercialization and its implementation need to take all of the above into account.

It appears that the effect of commercialization is more important for smaller vehicles, since a larger number of the population are affected in that case, in terms of vehicle cost per unit. Heavier vehicles, especially those with less volume, may sometimes be developed based on need and use very special designs developed by a few niche industries. Some of these industries might need flexible manufacturing processes in order to meet low-volume production which can be changed to produce other items. Military vehicles in particular may be less affected by commercialization in the sense that the military can afford to select multiple suppliers for the same thing. However, they can benefit from commercialization as well, since it is always more cost effective to use commercial off-the-shelf (COTS) items to help ease maintenance and provide overall life cycle benefits. Locomotives, ships, and similar vehicles, which are very expensive items and produced in relatively low volumes, and sometimes custom ordered and built according to requirements, can benefit from the commercialization of various constituent components used to build the vehicle, rather than commercialization of the finished product, which does not happen in a true sense for such high-cost, low-volume items.

15.5 Commercialization and Future of HEVs and Transportation

It is apparent from the previous discussion that commercialization in general can lead to the delivery of better value to customers who want HEVs. With commercialization and standardization, prices will most likely be cheaper, since commercialization can lead to better competition and provide more options to users. The same applies to suppliers of various components. If commercialization of some vital item like a battery becomes broader, that will lead to a fall in the cost of the battery. As is well known, the cost, size, and weight of a battery are now real challenges which stand in the way of the overall popularity of HEVs. The cost issue is one item, but the size and weight will depend on the technology. With more competition in the industry, various manufacturers might invest in developing new and better technologies, which in essence can be the deciding factor in the success or failure of an item ultimately leading to people wanting to own a HEV rather than a regular ICE vehicle. Currently the fundamental issues on batteries, related to their chemistry, remain big challenges and cannot claim to have been fully addressed. In future, if battery technology can be really made to improve through some quantum jump, then that can lead to the next stage of development of pure electric vehicles (EVs). In addition, serious research is presently being done on fuel cells. Fuel cell technology exists in a relatively mature form for very high-power fuel cells, but for portable vehicular applications it still has quite a way to go. If the fuel used in the fuel cell can directly convert the high-specific-energy content fuel to hydrogen (rather than carrying hydrogen in cylinders) then this will help significantly toward increasing the range of a pure EV. In a HEV, having both ICE and electric propulsion leads to a complexity of manufacturing, control, and maintenance. In a pure EV these can be significantly simplified. Hence a future goal of commercialization should have the objective of achieving a pure EV. This applies equally to even high-power construction equipment as well. In some of these vehicles, it is possible to have ultracapacitor-type high-specific-power devices to supplement the fuel cell. Combining a fuel cell and ultracapacitor can lead to both longer range and overall longevity of dispensable items, that is, an ultracapacitor instead of a battery. Thus it appears that the HEV is an intermediate step between the ICE and pure EV, and will depend very much on the technology of the fuel cell, ultracapacitor, and battery. Other technologies like power electronics and motors will benefit from commercialization in terms of cost reduction since they are already very efficient devices. But thermal management still remains a challenge for power electronics, and high-temperature devices based on silicon carbide and perhaps something else in the future can be important enablers toward future EV transportation.

Further Reading

Britton, D. (2010) Barriers to Commercialization Still Exist For Hybrid Truck Industry, http://www.truckinginfo.com/clean-green/news-detail.asp?news_id=69076&news_category_id=63 (accessed January 19, 2010).

Browning, L. and Unnasch, S. (2001) Hybrid electric vehicle commercialization issues. The 16th Annual Battery Conference on Applications and Advances, August, Long Beach, CA, p. 45.

Kramer, F. (2009) Commercializing Plug-In Hybrids, The California Cars Initiative, http://www.calcars.org/calcars-photos.pdf (accessed July 14, 2009).

Van Amburg, B. (2007) Heavy Hybrid Vehicle Commercialization Progress and Directions: Clean Transportation Solutions, http://files.harc.edu/Sites/TERC/About/Events/ETAC200705/HybridCommercialization.pdf (accessed May 3, 2007).

Index

Hybrid Electric Vehicles: Principles and Applications with Practical Perspectives, First Edition.
Chris Mi, M. Abul Masrur and David Wenzhong Gao.